

Evaluation of Used Fuel Disposition in Clay-Bearing Rock (Vol. I)

(FCRD-UFD-2015-000124)

Fuel Cycle Research & Development

***Prepared for
U.S. Department of Energy
Used Fuel Disposition Campaign***

***Carlos F. Jové Colón, Philippe F. Weck,
Glenn E. Hammond, Kristopher L. Kuhlman (SNL)***

***Liange Zheng, Jonny Rutqvist,
Kunhwi Kim, James Houseworth (LBNL)***

***Florie A. Caporuscio, Michael Cheshire,
Sarah Palaich, Katherine Norskog (LANL)***

Mavrik Zavarin, Thomas J. Wolery (LLNL)

***James Jerden, Jacqueline M. Copple,
Terry Cruse, William Ebert (ANL)***

September 4th, 2015

SAND2015-7827 R



DISCLAIMER

This information was prepared as an account of work sponsored by an agency of the U.S. Government. Neither the U.S. Government nor any agency thereof, nor any of their employees, makes any warranty, expressed or implied, or assumes any legal liability or responsibility for the accuracy, completeness, or usefulness, of any information, apparatus, product, or process disclosed, or represents that its use would not infringe privately owned rights. References herein to any specific commercial product, process, or service by trade name, trade mark, manufacturer, or otherwise, does not necessarily constitute or imply its endorsement, recommendation, or favoring by the U.S. Government or any agency thereof. The views and opinions of authors expressed herein do not necessarily state or reflect those of the U.S. Government or any agency thereof.

Prepared by:

Sandia National Laboratories

Albuquerque, New Mexico 87185

Sandia National Laboratories is a multi-program laboratory managed and operated by Sandia Corporation, a wholly owned subsidiary of Lockheed Martin Corporation, for the U.S. Department of Energy's National Nuclear Security Administration under contract DE-AC04-94AL85000.



**U.S. DEPARTMENT OF
ENERGY**



Sandia National Laboratories

APPENDIX E FCT DOCUMENT COVER SHEET ¹

Name/Title of Deliverable/Milestone/Revision No. Evaluation of Used Nuclear Fuel Disposition in Clay-bearing Rocks (M2FT-15SN0806071)

Work Package Title and Number Argillite Disposal R&D – SNL

Work Package WBS Number 1.02.08.06

Responsible Work Package Manager Carlos F. Jove Colon
(Name/Signature)

Date Submitted: 09/04/2015

Quality Rigor Level for Deliverable/Milestone ²	<input checked="" type="checkbox"/> QRL-3	<input type="checkbox"/> QRL-2	<input type="checkbox"/> QRL-1 Nuclear Data	<input type="checkbox"/> Lab/Participant QA Program (no additional FCT QA requirements)
--	---	--------------------------------	--	---

This deliverable was prepared in accordance with Sandia National Laboratories
(Participant/National Laboratory Name)

QA program which meets the requirements of
 DOE Order 414.1 NQA-1-2000 Other

This Deliverable was subjected to:


Technical Review

Technical Review (TR)

Review Documentation Provided

- Signed TR Report or,
 Signed TR Concurrence Sheet or,
 Signature of TR Reviewer(s) below

Name and Signature of Reviewers

Yifeng Wang 

Peer Review

Peer Review (PR)

Review Documentation Provided

- Signed PR Report or,
 Signed PR Concurrence Sheet or,
 Signature of PR Reviewer(s) below

9/3/2015

NOTE 1: Appendix E should be filled out and submitted with the deliverable. Or, if the PICS:NE system permits, completely enter all applicable information in the PICS:NE Deliverable Form. The requirement is to ensure that all applicable information is entered either in the PICS:NE system or by using the FCT Document Cover Sheet.

NOTE 2: In some cases there may be a milestone where an item is being fabricated, maintenance is being performed on a facility, or a document is being issued through a formal document control process where it specifically calls out a formal review of the document. In these cases, documentation (e.g., inspection report, maintenance request, work planning package documentation or the documented review of the issued document through the document control process) of the completion of the activity, along with the Document Cover Sheet, is sufficient to demonstrate achieving the milestone. If QRL 1, 2, or 3 is not assigned, then the Lab / Participant QA Program (no additional FCT QA requirements) box must be checked, and the work is understood to be performed and any deliverable developed in conformance with the respective National Laboratory / Participant, DOE or NNSA-approved QA Program.

ACKNOWLEDGEMENTS

The authors acknowledge our gratitude to Yifeng Wang (SNL), Ernest Hardin (SNL), Kevin McMahon (SNL), Geoff Freeze (SNL), David Sevougian (SNL), William Spezialetti (DOE NE-53), Prasad Nair (DOE NE-53), Mark Tynan (DOE NE-53), and Tim Gunther (DOE NE-53) for their helpful discussions and contributions on various topics covered in this report.

SUMMARY

Deep geological disposal of nuclear waste in clay/shale/argillaceous rock formations has received much consideration given its desirable attributes such as isolation properties (low permeability), geochemically reduced conditions, slow diffusion, sorptive mineralogy, and geologically widespread (Jové Colón et al., 2014). There is a wealth of gained scientific expertise on the behavior of clay/shale/ argillaceous rock given its focus in international nuclear waste repository programs that includes underground research laboratories (URLs) in Switzerland, France, Belgium, and Japan. Jové Colón et al. (2014) have described some of these investigative efforts in clay rock ranging from site characterization to research on the engineered barrier system (EBS). Evaluations of disposal options that include nuclear waste disposition in clay/shale/argillaceous rock have determined that this host media can accommodate a wide range of waste types. R&D work within the Used Fuel Disposition Campaign (UFDC) assessing thermal effects and fluid-mineral interactions for the disposition of heat-generating waste have so far demonstrated the feasibility for the EBS and clay host rock to withstand high thermal loads. This report represents the continuation of disposal R&D efforts on the advancement and refinement of coupled Thermal-Hydrological-Mechanical-Chemical (THMC), hydrothermal experiments on clay interactions, used fuel degradation (source term), and thermodynamic modeling and database development. The development and implementation of a clay/shale/argillite reference case described in Jové Colón et al. (2014) for FY15 will be documented in another report (Mariner et al. 2015) – only a brief description will be given here. This clay reference case implementation is the result of integration efforts between the GDSA PA and disposal in argillite work packages.

The assessment of *sacrificial zones* in the EBS is being addressed through experimental work along with 1D reactive-transport and reaction path modeling. The focus of these investigations into the nature of *sacrificial zones* is to evaluate the chemical effects of heterogeneous chemical reactions at EBS interfaces. The difference in barrier material types and the extent of chemical reactions within these interfacial domains generates changes in mineral abundances. These mineralogical alterations also result in volume changes that, although small, could affect the interface bulk porosity.

As in previous deliverables, this report is structured according to various national laboratory contributions describing R&D activities applicable to clay/shale/argillite media. These activities are summarized as follows:

- **Evaluation of Used Fuel Disposition in Clay-Bearing Rock: Reactive Transport and Barrier Interactions in the Near Field Environment (Part I)**
 - Brief overview of the reference case implementation for disposal in argillite.
 - Results are described in Mariner et al. (2015) for the GDSA PA implementation.
 - Repository layout refinements included addition of stratigraphic units (interbeds, aquifer sediments) and related hydrogeological properties consistent with clay rock formations.
 - Numerical simulations were conducted using PFLOTRAN with a 3D structured grid having variable spacings.

- Sampling, sensitivity analysis, and uncertainty quantification is conducted using the code DAKOTA. The PFLOTRAN and DAKOTA coupling are the core of the GDSA PA computational framework.
 - Evaluation of repository performance is based on ^{129}I concentration given its conservative nature.
 - 1D reactive-transport modeling of the EBS.
 - Construction of a layered multi-barrier case of a 1D reactive diffusion simulation using the PFLOTRAN code.
 - Results show significant changes in pH and $\text{H}_4\text{SiO}_4(\text{aq})$ concentration in pore water at the EBS interfaces between cement and outer clay buffer, and between cement and clay rock.
 - Relative changes in porosity are concentrated at the cement-clay interfaces, as expected.
 - A noticeable decrease in pH in the inner and outer clay regions due to pyrite decomposition.
 - While small, porosity reduction or clogging as a result of mineral precipitation was discernable in the outer-clay – cement interface region.
 - Thermodynamic evaluation of barrier clay interactions using reaction path modeling.
 - Overall agreement between experimental observations and thermodynamic modeling predictions suggest clay phases in bentonite will be relatively stable over a wide range of temperatures.
 - Evaluation of clay and zeolite stability relations with comparisons to experimental data suggest the predominance of localized alteration of pre-existing unstable phases (glass, zeolite) in the stabilization of secondary analcime and silica phases.
 - The feedback from secondary mineralization of analcime and silica phases is to control aqueous silica at elevated temperatures.
 - DOE-Managed HLW and SNF research and applicability to disposal in clay rock environments.
 - The projected lower thermal loading of DOE-Managed HLW waste (relative to commercial SNF) demonstrates the applicability of disposal in clay/shale/argillaceous rock of this waste type.
- **Investigation of Coupled Processes and Impact of High Temperature Limits in Argillite Rock (Part II)**
 - Investigation of the Impacts of High Temperature Limits with THMC modeling:
 - Progress on computer simulations to analyze the impact of elevated temperature on the bentonite backfill and near-field clay host rock in a geologic repository for radioactive waste.

- Implementation of a time-step management scheme in the TOUGHREACT-FLAC3D simulator to reduce the simulation time.
 - The effect of chemical changes on swelling stress was analyzed for a time period of 100,000 years.
 - In general, chemical change does not have significant impact on the stress in the clay formation.
 - Developing THMC models for FEBEX-DP:
 - Consideration of bentonite barrier mechanical change in the prediction of relative humidity across the whole domain.
 - Non-Darcian flow into the TH model needs further study due to significant underestimation of the relative humidity data in the entire bentonite barrier.
 - The preliminary prediction of chemical change upon dismantling Heater 2 shows concentration levels of aqueous species will continue to decrease in bentonite near the heater. Carbonate minerals like calcite dissolve and dolomite precipitates along with illite clay near the bentonite/granite interface.
 - THM modeling: FE heater test and DECOVALEX:
 - Successfully conducted model predictions of the THM responses at all three of these experiments (Mont Terri HE-E, Horonobe EBS, and Mont Terri FE experiments) using state-of-the-art constitutive models for bentonite and host rocks.
 - Heating has just started in 2015 for the Horonobe EBS experiment and the Mont Terri FE experiment, and comparison between measured and predicted responses can be started once the data is provided to the modeling teams.
 - Discrete Fracture Network (DFN) Approach for THM Damage Modeling in Argillaceous Rock:
 - An effective coupling between the TOUGH2 and the RBSN approach has been implemented and applied to hydraulic fracturing simulations.
 - Equations of motion of Voronoi cells are solved to get the nodal accelerations, which are integrated through a time-stepping procedure to derive the nodal velocities and displacements.
- **Summary of Baseline Experiments for Generic Repository Engineered Barriers (Part III)**
 - Summary of four years of hydrothermal experiments containing (1) SEM images, (2) electron microprobe data for major mineral phases, and (3) aqueous geochemistry data is given for 17 major experiments. This includes a large data set of zeolite compositional analyses describing the analcime-wairakite solid solution.

- Discussion of copper corrosion based on more recent characterization results and interpretation of corrosion rates.
- **Evaluation of Thermodynamic and Sorption Data; Applications of First-Principles Modeling in the Assessment of Thermal-Mechanical Properties of Kaolinite Clay (Part IV)**
 - Progress on the assessment of thermodynamic and sorption data:
 - Evaluation of a thermodynamic data using the concept of “links” to the chemical elements in their reference forms. Manuscript has been prepared describing this approach: “Chemical Thermodynamic Data. I. The Concept of Links to the Chemical Elements and the Historical Development of Key Thermodynamic Data”. This work has been carried in collaboration between LLNL and SNL.
 - Proposal of an alternative approach to evaluate and test various surface complexation models based on a PHREEQC module (PreeqcRM) coupled with parameter estimation / optimization software to facilitate equilibrium calculations on individual batch sorption data.
 - Summary NEA TDB project activities and upcoming releases of new data compilations.
 - **Structural and Thermal-Mechanical Properties of Argillite Disposal Systems: First-Principles Study of Kaolinite Clay:**
 - Application of first-principles computational approaches in the retrieval of thermal and mechanical properties for kaolinite clay ($\text{Al}_2\text{Si}_2\text{O}_5(\text{OH})_4$):
 - Application of the density functional theory corrected for dispersion (DFT-D) with the generalized gradient approximation (GGA) to describe van der Waals interactions in layered silicate structures like kaolinite.
 - Kaolinite bulk modulus, shear modulus, transverse wave velocity, longitudinal wave velocity, Poisson’s ratio, and Young’s modulus components were calculated using the Reuss, Voigt, and Hill approximations.
 - Bulk moduli of kaolinite predicted with DFT-D2 at 298.15 K using the Vinet and Birch-Murnaghan EoS are in good agreement with the recent experimental data.
 - Proposal to apply this methodology in a systematic way to other clays (e.g., montmorillonite clay).

- **Fuel Matrix Degradation Model: Integration with Performance Assessment and Canister Corrosion Model Development (Part V)**
 - Added a working noble metal particle (epsilon phase) domain on fuel surface to account for the protective hydrogen effect.
 - Completed a model validation study in which results from the state of the art FMDM were compared to experimental data from international geologic repository programs. This study was published in the Journal of Nuclear Materials.
 - Completed conversion of the state of the art FMDM (version 2.3) to Fortran to facilitate integration with the Generic Disposal System Analysis (GDSA) repository Performance Assessment (PA) code PFLOTRAN.
 - ANL worked with SNL scientists to complete and test a prototype integrated PFLOTRAN-FMDM repository model.
 - Completed preliminary model runs focused on expanding the FMDM to account for corrosion of the used fuel steel canister.
 - Completed scoping experiments investigating the possible poisoning of the Noble Metal Particles (NMP), which are known to catalyze the oxidation of H₂, thus shutting down the oxidative dissolution of used fuel.

Overall Future Perspectives:

- Expand integration work with GDSA PA on the reference case built for disposal in argillite. Further analyses on the performance metric based on radionuclide transport and consideration of near- and far-field processes through PA analyses.
- Development of coupled-process model representations of near-field chemical interactions and transport through integrated thermodynamic modeling and experimental work. This should also comprise waste package degradation plus other materials exerting important effects on EBS interfaces. Programmatic engagements and collaborations with international R&D activities in repository sciences are an integral part of these efforts.
- Further integrate various modeling activities towards the assessment of thermal limits in the EBS. Experimental and modeling efforts have contributed to the elucidation of key processes affecting the fate and performance of barrier materials at elevated temperatures.
- Coupling of source term models (radiolysis and MPM) with the effects of waste package degradation. This effort is guided by further integration of these model representations with PA.

TABLE OF CONTENTS

AKNOWLEDGEMENTS.....	iv
SUMMARY	v
ACRONYMS.....	xxv

Part I: Evaluation of Used Fuel Disposition in Clay-Bearing Rock: Reactive Transport and Barrier Interactions in the Near Field Environment

1. Evaluation of Used Fuel Disposition in Clay-Bearing Rock.....	2
1.1 Introduction.....	2
1.2 Reference Case for Disposal in Clay/Shale/Argillite: Brief Description	2
2. Reactive Transport in the Near-Field Environment.....	5
2.1 1D Reactive-Transport Model Description of the EBS	6
2.2 Results and Discussion.....	12
3. Thermodynamic Evaluation of Barrier Clay Interactions: Equilibrium Phase Relations and Reaction Path Modeling	15
3.1 Reaction Path Modeling.....	17
3.2 Discussion and Conclusions.....	17
4. DOE-Managed HLW and SNF Research	20
5. Concluding Remarks	22
5.1 Proposed Research Outlook for FY16	23
6. References	25

Part II: Investigation of Coupled Processes and Impact of High Temperature Limits in Argillite Rock

1. Introduction	32
2. Investigation of the Impacts of High Temperature Limits with THMC Modeling	34
2.1 Introduction.....	34
3. Developing THMC Models for FEBEX-DP	83
4. THM Modeling: FE Heater Test and DECOVALEX	127
5. Discrete Fracture Network (DFN) Approach for THM Damage Modeling in Argillaceous Rock.....	161

5.7	References.....	186
6.	Summary.....	188
Part III: Summary of Baseline Experiments for Generic Repository Engineered Barriers		
1	Introduction	194
2	Background.....	195
3	Methods	199
4	Results/Discussion.....	201
5	New Information and Interpretation from Characterization of Experiments in FY15	209
5.5	Copper corrosion rate determination.....	220
6	Conclusions	223
7.	References	225
Part IV: Evaluation of Thermodynamic and Sorption Data; Applications of First-Principles Modeling in the Assessment of Thermal-Mechanical Properties of Kaolinite Clay		
1	Introduction	230
2	Thermodynamic and Sorption Data Evaluation	230
3	Thermodynamic Database Development.....	231
4	Surface Complexation and Ion Exchange Model and Database Development	233
5	NEA Thermodynamic database development	235
6	Planned FY16 Efforts	236
7	References	238
8.	Interplay Between Structural and Thermal-Mechanical Properties of Argillite Disposal Systems: First-Principles Study of Kaolinite Clay	240
8.1	Background	240
8.2	Computational Methods.....	241
9.	Results and Discussion	244
9.1	Crystal structure:	244
9.2	Mechanical properties:.....	247

9.3	Thermodynamic properties:	254
10.	Conclusions	260
10.1	Proposed Work Scope for FY16	261
11.	References	262
Part V: Fuel Matrix Degradation Model: Integration with Performance Assessment and Canister Corrosion Model Development		
1	Introduction and Objective	268
2	Fuel Matrix Degradation Model Development and Integration with PFLOTRAN.....	270
2.1	Conversion of FMDM from MATLAB to Fortran	270
2.2	Summary of Technical Changes Made to the FMDM Incorporated into Version 2.3	273
2.3	Demonstration of Prototype Integrated PFLOTRAN – FMDM Model for PA	278
3	Scoping Work for the Development of a Canister Corrosion Model	282
4	Results from Scoping Experiments on Poisoning of Noble Metal Particle.....	285
5	Conclusions and Future Work	289
6	References	290

TABLE OF FIGURES

(Part I) Evaluation of Used Fuel Disposition in Clay-Bearing Rock: Reactive Transport and Barrier Interactions in the Near Field Environment

Figure 1. Schematic representation of the stratigraphy and repository footprint dimensions considered for the reference case for disposal in clay/shale/argillite rock (Mariner et al. 2015).....	3
Figure 2. X-Z slice of the clay reference case model at the Y midpoint of the first drift pair in the repository (see Fig. 1).....	3
Figure 3. (a) 3D unstructured mesh representation of a longitudinal section of a backfilled drifts with multiple waste canisters and a multi-layered EBS. Inset shows a 2D cross-sectional view of the drift. (b) Example of a 3D thermal simulation using PFLOTRAN with the unstructured mesh for a repository in argillite.....	5
Figure 4. Schematic representation and dimensional characteristics of the 1D reactive-transport.....	10
Figure 5. Profile of pH vs. time (up to 10,000 years) of the reactive transport calculations for the multi-layered EBS.....	13
Figure 6. Enlarged view of the pH vs. time (up to 200 years) profile from the previous figure.....	13
Figure 7. Profile of porosity vs. time (up to 10,000 years) of the reactive transport calculations for the multi-layered EBS.....	14
Figure 8. Enlarged view of the porosity vs. time (up to 10,000 years) profile outlining the small porosity decrease at the outer-clay – cement interface observation point.....	14
Figure 9. Log activity $\text{SiO}_2(\text{aq})$ vs. temperature phase diagram for the system Ca-Na-Al-Si-Fe- H_2O generated using CHNOSZ containing : (a) illite (IMt-2) and (b) illite-smectite (ISCz1).....	16
Figure 10. Log activity $\text{SiO}_2(\text{aq})$ vs. temperature phase diagram for the system Ca-Na-Al-Si-Fe- H_2O generated using CHNOSZ.....	19
Figure 11. Existing and projected relative volumes of SNF and HLW in the USA (SNL, 2014).	20
Figure 12. Projected waste decay heat per canister for Hanford HLW glass, SRS HLW glass, and UOX SNF (20 GWd/MT burnup; 21-PWR assemblies).	21
Figure 13. Chronological evolution of Thermal-Chemical processes in a shale/argillite repository (modified after Jové Colón et al., 2014).	24

(Part II) Investigation of Coupled Processes and Impact of High Temperature Limits in Argillite Rock

Figure 2-1. The coupling scheme for TOUGHREACT-FLAC3D.....	36
Figure 2-2. Domain for the test example of a bentonite back-filled horizontal emplacement drift at 500 m (Rutqvist et al., 2014)	37
Figure 2-3. Swelling pressure versus mass fraction of smectite for various bentonites.....	39
Figure 2-4. Temperature evolution at points A, B, C, and D.....	45
Figure 2-5. The temporal evolution of water saturation at points A, B, C, and D.....	46
Figure 2-6. The temporal evolution of pore pressure at points A, B, C, and D.....	47
Figure 2-7. The temporal evolution of smectite volume fraction at points A, B, C, and D.....	49

Figure 2-8. The temporal evolution of illite volume fraction at points A, B, C, and D.....	50
Figure 2-9. The temporal evolution of smectite volume fraction at points A and B, with X-axis plotted in linear scale.....	50
Figure 2-10. The temporal evolution of K-feldspar volume fraction at points A and B, with X-axis plotted in linear scale.....	51
Figure 2-11. The temporal evolution of quartz volume fraction at points A, B, C, and D.	51
Figure 2-12. The temporal evolution of K-feldspar volume fraction at points A, B, C, and D for the “high T” base run and a sensitivity run with K-feldspar dissolution rate two orders of magnitude higher.....	54
Figure 2-13. The temporal evolution of smectite volume fraction at points A, B, C, and D for the “high T” base run and a sensitivity run with K-feldspar dissolution rate two orders of magnitude higher.	55
Figure 2-14. The temporal evolution of smectite volume fraction at points A, B, C, and D for the “high T” base run and a sensitivity run with K-feldspar dissolution rate two orders of magnitude higher.	56
Figure 2-15. The temporal evolution of calcite volume fraction at points A, B for the case with Ca-smectite and Na-smectite in Kunigel-VI bentonite.....	57
Figure 2-16. The temporal evolution of smectite volume fraction at points A, B for the case with Ca-smectite and Na-smectite in Kunigel-VI bentonite.....	57
Figure 2-17. The temporal evolution of illite volume fraction at points A, B for the case with Ca- smectite and Na-smectite in Kunigel-VI bentonite.....	58
Figure 2-18. Simulation results of mean total stress, pore pressure, and thermal stress at point A for the “low T” and “high T” scenario, respectively.	59
Figure 2-19. Simulation results of mean total stress, pore pressure, and thermal stress at point B for the “low T” and “high T” scenario, respectively.	60
Figure 2-20. Simulation results of swelling stress at point A for the “low T” and “high T” scenarios, respectively.	60
Figure 2-21. Simulation results of swelling stress at point B for the “low T” and “high T” scenarios, respectively.	61
Figure 2-22. Simulation results of mean total stress, pore pressure, and thermal stress at point C for the “low T” and “high T” scenario, respectively.	62
Figure 2-23. Simulation results of mean total stress, pore pressure, and thermal stress at point D for the “low T” and “high T” scenario, respectively.	62
Figure 2-24. Simulation results of mean total stress at point C for the “high T” scenarios in three cases: the ‘high T, base case” in which the effect ion concentration and smectite change on stress are considered; the “high T, no Sc” case in which the contribution of smectite change to stress is neglected and the “high T, no C, no Sc” case in which both the contribution of smectite change and ion concentration to stress are neglected.	63
Figure 2-25. Simulation results of mean total stress at point D for the “high T” scenarios in three cases: ‘high T, base case”, “high T, no Sc”, and “high T, no C, no Sc” case.....	63
Figure 2-26. The temporal evolution of smectite volume fraction at points A, B, C, and D for Kunigel and FEBEX bentonite.	66

Figure 2-27. The temporal evolution of illite volume fraction at points A, B, C, and D for Kunigel and FEBEX bentonite.....	67
Figure 2-28. The temporal evolution of K-feldspar volume fraction at points A, B, C, and D in the base case with Kunigel bentonite and a sensitivity case with FEBEX bentonite.	68
Figure 2-29. The temporal evolution of quartz volume fraction at points A, B, C, and D in the base case with Kunigel bentonite and a sensitivity case with FEBEX bentonite.	69
Figure 2-30. The temporal evolution of calcite volume fraction at points A and B for the case with Ca-smectite and Na-smectite in FEBEX bentonite.....	70
Figure 2-31. The temporal evolution of Ca-smectite/Na-smectite volume fraction for 200 years at points A and B for the case with Ca-smectite and Na-smectite in FEBEX bentonite.	70
Figure 2-32. The temporal evolution of illite volume fraction at points A and B for the case with Ca-smectite and Na-smectite in FEBEX bentonite.....	70
Figure 2-33. The temporal evolution of illite volume fraction at points A, B for the case with Ca-smectite and Na-smectite in FEBEX bentonite.	71
Figure 3-34. Simulation results of mean total stress, pore pressure, swelling stress, and thermal stress at point A in the sensitivity case with FEBEX bentonite for the “low T” and “high T” scenarios, respectively.	72
Figure 2-35. Simulation results of mean total stress, pore pressure, swelling stress, and thermal stress at point B in the sensitivity case with FEBEX bentonite for the “low T” and “high T” scenarios, respectively.	72
Figure 2-36. Simulation results of mean total stress at point A for Kunigel-VI and FEBEX bentonite for the “low T” and “high T” scenarios, respectively.	73
Figure 2-37. Simulation results of mean total stress at point B for Kunigel-VI and FEBEX bentonite for the “low T” and “high T” scenarios, respectively.	73
Figure 2-38. Simulation results of swelling stress at point A for the FEBEX bentonite for the “low T” and “high T” scenarios, respectively, focusing on the stress range from 4.5 to 5 MPa.....	75
Figure 2-39. Simulation results of swelling stress at point A for the FEBEX bentonite for the “low T” and “high T” scenarios, respectively, focusing on the stress range from 4.5 to 5 MPa.....	76
Figure 2-40. Simulation results of swelling stress at point B for the FEBEX bentonite for the “low T” and “high T” scenarios, respectively, focusing on the stress range from 4.5 to 5 MPa.....	76
Figure 2-41. Simulation results of swelling stress at point B for the FEBEX bentonite for the “low T” and “high T” scenarios, respectively, focusing on the stress range from 4.5 to 5 MPa.....	77
Figure 3-1. The operational stages of FEBEX <i>in situ</i> test (Vomvoris, personal communication).....	84
Figure 3-2. Schematic design of the heating and hydration laboratory experiment in the cell CT23 (ENRESA, 2006a).	85
Figure 3-3. Schematic design of mock-up test (Martín et al., 2006).	86
Figure 3-4. The initial configuration of FEBEX <i>in situ</i> test at the Grimsel underground laboratory (Switzerland) (ENRESA, 2000).	87

Figure 3-5. The moisture content (gravimetric water content) at section 15(Vomvoris, personal communication).....	88
Figure 3-6. Layout of the sampling sections during the dismantling of heater 1 in 2002. In blue color are the common sections for THG and THM analyses (Fernandez and Rivas, 2003).....	88
Figure 3-7. <i>In situ</i> test configuration following dismantling of heater 1 (Huertas et al., 2005).....	89
Figure 3-8. Mesh used for the model, not to the scale.	91
Figure 3-9. Measured temperature by sensors located at radial distance of 0.48 m in sections E2 and F2 and model results from the base TH model.	97
Figure 3-10. Measured temperature by sensors located at radial distance of 0.8 m in sections E2 and F2 and model results from the base TH model.	97
Figure 3-11. Measured temperature by sensors located at radial distance of 1.05 m in sections E2 and F2 and model results from the base TH model.	98
Figure 3-12. Measured temperature by sensors located at radial distance of 1.09 m in sections E2 and F2 and model results from the base TH model.	98
Figure 3-13. Measured relative humidity by sensors located at radial distance of 0.52 m in sections E2 and E1 and model results from the base TH model.....	99
Figure 3-14. Measured relative humidity by sensors located at radial distance of ~0.8 m in sections E1, E2, F1 and F2 and model results from the base TH model.	99
Figure 3-15. Measured relative humidity by sensors located at radial distance of ~1.05 m in section F2 and model results from the base TH model.....	100
Figure 3-16. Measured relative humidity by sensors located at radial distance of ~1.1 m in sections E1, E2 and F1 and model results from the base TH model.	100
Figure 3-17. Measured relative humidity by sensors located at radial distance of 0.52 m and model results from the base model and two sensitivity runs with different permeability for granite.	101
Figure 3-18. Measured relative humidity by sensors located at radial distance of 0.8 m and model results from the base model and two sensitivity runs with different permeability for granite.	102
Figure 3-19. Measured temperature by sensors located at radial distance of ~1.05 m and model results from the base model and two sensitivity runs with different permeability for granite.	102
Figure 3-20. Measured relative humidity by sensors located at radial distance of 1.1 m and model results from the base model and two sensitivity runs with different permeability for granite.	103
Figure 3-21. Saturated hydraulic conductivity as a function of dry density (ENRESA, 2000)	104
Figure 3-22. Measured relative humidities by sensors located at radial distance of 0.52 m and model results from the base model and two sensitivity runs with different permeability for bentonite.....	104
Figure 3-23. Measured relative humidities by sensors located at radial distance of 0.8 m and model results from the base model and two sensitivity runs with different permeability for bentonite.....	105

Figure 3-24. Measured relative humidities by sensors located at radial distance of 1.1 m and model results from the base model and two sensitivity runs with different permeability for bentonite.....	105
Figure 3-25. Schematic design of the permeation test (Samper et al., 2008b).....	107
Figure 3-26. Measured cumulative water flux data and Darcy flow model, marked “Darcy” in the figure and Non-Darcian flow model, marked as “ND” in the figure with different A values while keeping B equal to -0.78.....	108
Figure 3-27. Measured cumulative water flux data and Darcy flow model, marked “Darcy” in the figure and Non-Darcian flow model, marked as “ND” in the figure with different B values while keeping A equal to 2×10^{-13}	108
Figure 3-28. Measured relative humidities by sensors located at radial distance of 0.52 m and model results from the base model and the Non-Darcian flow model.	109
Figure 3-29. Measured relative humidities by sensors located at radial distance of 0.8 m and model results from the base model and the Non-Darcian flow model.	110
Figure 3-30. Measured relative humidities by sensors located at radial distance of 1.1 m and model results from the base model and the Non-Darcian flow model.	110
Figure 3-31. Measured temperature by sensors located at radial distance of 0.48 m and model results from the base model and the Non-Darcian flow model.	111
Figure 3-32. Measured temperature by sensors located at radial distance of 1.1 m and model results from the base model and the Non-Darcian flow model.	111
Figure 3-33. The positions where samples were taken for geochemical analyses at section 29 after the dismantling of heater 1 in 2002 (Zheng et al., 2011).....	113
Figure 3-34. The concentration profile of chloride at 1930 days (Zheng et al., 2011) and model results from the base model.	114
Figure 3-35. The concentration profile of sodium at 1930 days (Zheng et al., 2011) and model results from the base model and sensitivity run that does not consider any chemical reaction.	115
Figure 3-36. The concentration profile of calcium at 1930 days (Zheng et al., 2011) and model results from the base model and sensitivity run that does not consider any chemical reaction.	115
Figure 3-37. The concentration profile of magnesium at 1930 days (Zheng et al., 2011) and model results from the base model and sensitivity run that does not consider any chemical reaction.	116
Figure 3-38. The concentration profile of potassium at 1930 days (Zheng et al., 2011) and model results from the base model and sensitivity run that does not consider any chemical reaction.	116
Figure 3-39. Computed profile of volume fraction change of smectite at the 1930 days (after the dismantling of heater 1) and at 6698 days (July 1, 2015).....	117
Figure 3-40. Computed profile of volume fraction change of dolomite at the 1930 days (after the dismantling of heater 1) and at 6698 days (July 1, 2015).....	117
Figure 3-41. Computed profile of volume fraction change of calcite at the 1930 days (after the dismantling of heater 1) and at 6698 days (July 1, 2015).....	118

Figure 3-42. Computed profile of volume fraction change of illite at the 1930 days (after the dismantling of heater 1) and at 6698 days (July 1, 2015).....	118
Figure 6-84. The profile of pH at 1930 days (Zheng et al., 2011) and model results from the base model.	119
Figure 3-44. The concentration profile of bicarbonate at 1930 days (Zheng et al., 2011) and model results from the base model.	119
Figure 3-45. The concentration profile of sulfate at 1930 days (Zheng et al., 2011) and model results from the base model.	120
Figure 3-46. The concentration profile of chloride at 1930 days (Zheng et al., 2011) and model results from the base model and two sensitivity runs with different permeability for granite.	121
Figure 3-47. The concentration profile of chloride at 1930 days (Zheng et al., 2011) and model results from the base model and two sensitivity runs with different chloride initial concentrations.	121
Figure 4-1. Schematic of linking of TOUGH2 and FLAC3D in a coupled TOUGH-FLAC simulation.	129
Figure 4-2. Numerical procedure of a linked TOUGH2 and FLAC3D simulation.	129
Figure 4-3. BBM constitutive model showing the yield surface in q-p-s space.	130
Figure 4-4. (a) Pore size distribution and (b) schematic representation of the two structural levels considered in the dual structure model. Clay particles are represented by the gray lines.	132
Figure 4-5. Schematic setup of HE-E experiment at Mont Terri and photo of micro-tunnel (Garritte, 2012).	133
Figure 4-6. TOUGH-FLAC 3-D model of the Mont Terri HE-E experiment.	134
Figure 4-7. Vertical cross-section through the model grid.	135
Figure 4-8. Steps for modeling the Mont Terri HE-E experiment.	136
Figure 4-9. Calculated evolution of (a) liquid saturation and (b) temperature.	137
Figure 4-10. Calculated evolution of (a) liquid saturation relative humidity and (b) temperature at monitoring points in the granular bentonite (above heater) and bentonite blocks (below heater).	138
Figure 4-11. Comparison of predicted (dashed lines) and measured (solid lines) evolutions of (a) liquid saturation relative humidity and (b) temperature.	138
Figure 4-12. Comparison of predicted (dashed lines) and measured (solid lines) evolutions of pore pressure in Opalinus Clay at a point located 3.54 m from the tunnel wall.	139
Figure 4-13. Layout of the Horonobe URL in Hokkaido, Japan.	140
Figure 4-14. General description of the EBS experiment at the Horonobe URL Project in Japan.	141
Figure 4-15. Early time monitored fluid pressure in the test pit and temperature evolution at the heater surface that will help to define boundary conditions in the interpretive modeling of the Horonobe EBS experiment.	142
Figure 4-16. TOUGH-FLAC 3-D numerical grid of the Horonobe EBS experiment.	144
Figure 4-17. TOUGH-FLAC simulation results of temperature in the buffer and rock.	146

Figure 4-18. TOUGH-FLAC simulation results of liquid saturation in the buffer, sand layer and rock.	146
Figure 4-19. TOUGH-FLAC simulation results of extensometer displacements in the rock.	147
Figure 4-20. Comparison of simulated temperature profiles at 10 and 365 days among the DECOVALEX modeling teams.	147
Figure 4-21. Comparison of simulated saturation profiles at 10 and 365 days among the DECOVALEX modeling teams.	148
Figure 4-22. Images from the construction and installation of heaters, bentonite buffer and plugs from NAGRA daily reports by Herwig Müller, NAGRA.	149
Figure 4-23. Plan view of experiment setup and borehole layout.	150
Figure 4-24. View of FE tunnel face from the FE niche showing beddings dipping 45°.	152
Figure 4-25. TOUGH-FLAC 3-D numerical grid of the FE experiment.	153
Figure 4-26. Capillary curves for Bentonite and Opalinus clays.	155
Figure 4-27. Model prediction of temperature and liquid saturation for staged power in first emplaced heater.	156
Figure 5-1. Discretization process: a) nodal point generation; b) Delaunay tessellation; and c) Voronoi tessellation.	163
Figure 6-117. Typical RBSN element ij : a) within a Voronoi grid; b) isolated from the network; and c) a zero-size spring set located at centroid C of Voronoi cell boundary area A_{ij}	164
Figure 5-3. Stress tensor at a Voronoi cell node: a) components of spring force local coordinates; b) a set of nodal forces satisfying the equilibrium; and c) complete stress tensor at Voronoi cell node.	166
Figure 5-4. Mohr-Coulomb fracture surface with tension cut-off.	167
Figure 5-5. Flow diagram of the coupling procedure between TOUGH2 and RBSN (adapted from Asahina et al., 2014).	169
Figure 5-6. Fracture mapping and discretization within an unstructured Voronoi grid.	170
Figure 5-7. Adjustment of nodal connections for flow modeling with discrete fractures: a) original matrix nodes and connections; and b) insertion of fracture nodes and connections.	171
Figure 5-8. Hydraulic fracturing simulation of a single fracture: a) 2-D model set up; and b) comparison between the numerical model and the analytical approximation in terms of fracture aperture profiles.	172
Figure 5-9. Modeling of discrete fracture networks: a) geometric topology of fracture networks; and mapping of the fracture pattern onto unstructured Voronoi grids with different mesh density: approximately b) 5000 and c) 10000 Voronoi cells, respectively.	172
Figure 5-10. Simulation results at a final stage of hydraulic fracturing: a) deformed shape; and b) fracture propagation paths overlaid on the pre-existing fracture network.	173
Figure 5-11. Pressure distributions captured at: a) at the point of fracture initiation; b) at the early stage; c) at the latter stage; and d) at the final stage of fracture propagation.	174
Figure 5-12. Evolutions of injected fluid pressure for different compressibility coefficients of the borehole region.	175

Figure 5-13. Abnormal break-up of the domain due to numerical instability: a) final time step as a meaningful result; and b) abrupt fracture generation at the next time step.	176
Figure 5-14. Free-body diagram of a Voronoi cell: a) with external nodal forces; and b) with internal spring forces.	177
Figure 5-15. Conceptual drawing of mass-spring system.	179
Figure 5-16. Propagation of a disturbance in the mass-spring system: a) no damping except for mass 1; and b) damping for masses 11 through 20 and mass 1.	182
Figure 5-17. Comparison of damping with no damping of masses 11 through 20. Black lines for damped case, red lines for undamped case (except mass 1 which is damped in both cases).	183

(Part III) Summary of Baseline Experiments for Generic Repository Engineered Barriers

Figure 1. Bounding backfill temperature histories at the waste package surface, for in-drift emplacement in crystalline rock (2.5 W/m-K) with a compacted bentonite backfill (0.6 W/m-K) (From Caporuscio et al., 2014)	195
Figure 2. Cartoon of corrosion processes related to EBS experiments containing 316SS.....	207
Figure 3. A) Colony Wyoming Bentonite starting material- Image of clinoptilolite pseudomorphing glass shard. B) EBS 5 post reaction material. Euhedral analcime crystal in bed of smectite clay. C) EBS 14 post reaction material. Image of wairakite crystals in platy smectite bed. D) EBS 15 post reaction material. E) EBS 14 Back Scattered Electron (BSE) image of euhedral wairakite crystals.	211
Figure 4. Plot of the analcime—wairakite solid solution compositions for the Na-Ca join.....	212
Figure 5. Pentlandite (white) sitting on a bed of Fe-saponite, all of which form as a mantling material on 316 stainless steel.	214
Figure 6. BSE image of steel and Fe-saponite interface from experiment EBS-13.....	215
Figure 7. SEM image of pyrrhotite nested in bed of Fe-saponite rosettes. Sample EBS-6: the growth substrate is low carbon steel.....	215
Figure 8. BSE image of iron metal with concentric alteration zones.....	216
Figure 9. Corroded copper surface and the covering chalcocite secondary growth.....	217
Figure 10. Plan view of pit corrosion in Sample EBS-4	218
Figure 11. Sample EBS-8. Initial growth of chalcocite on copper	219
Figure 12. Total coverage of copper by chalcocite. Sample EBS-8.	219
Figure 13. Atacamite (orthorhombic laths) resting on top of chalcocite crystals.	220
Figure 14 Experiment EBS-17. Note that pit corrosion of this copper foil has progressed to nearly 50% of the total thickness of the sample.	222

(Part IV) Evaluation of Thermodynamic and Sorption Data; Applications of First-Principles Modeling in the Assessment of Thermal-Mechanical Properties of Kaolinite Clay

Figure 1. Layered crystal structure of kaolinite, $\text{Al}_2\text{Si}_2\text{O}_5(\text{OH})_4$, relaxed with DFT-D2 at the GGA/PBE level of theory. The unit cell is indicated by solid black lines..... 244

Figure 2. Energetics of the hydrostatic and uniaxial (z-axis) deformations of the kaolinite unit cell calculated with DFT-D2 at the GGA/PBE level of theory. 253

Figure 3. Thermal evolution of the entropy of kaolinite computed with DFT-D2 at the GGA/PBE level along with the experimental values of Robie and Hemingway (1995) and Schieltz and Soliman (1966). 255

Figure 4. Thermal evolution of the bulk modulus of kaolinite computed with the Vinet and third-order Birch-Murnaghan EoS with DFPT-D2 at the GGA/PBE level of theory. Experimental data and Reuss-Voigt-Hill values computed with DFPT and DFPT-D2 from Table 8 are also displayed for comparison..... 257

Figure 5. Thermal evolution of the isobaric heat capacity of kaolinite calculated at constant atmospheric pressure with DFPT-D2 at the PBE/GGA level of theory for uniaxial and hydrostatic deformations. The experimental values of Robie and Hemingway (1995) and Schieltz and Soliman (1966) are also depicted for the sake of comparison..... 257

Figure 6. Thermal evolution of the enthalpy function of kaolinite calculated at the DFPT-D2/GGA/PBE level of theory. Experimental estimates derived from calorimetric data by Robie and Hemingway (1995) are also displayed for comparison purpose. 259

Figure 7. Thermal evolution of the Gibbs energy function of kaolinite calculated at the DFPT-D2/GGA/PBE level of theory. Experimental estimates derived from calorimetric data by Robie and Hemingway (1995) are also displayed for comparison purpose. 260

(Part V): Fuel Matrix Degradation Model: Integration with Performance Assessment and Canister Corrosion Model Development

Figure 1. Conceptual diagram identifying the key dissolution rate-determining processes in the FMDM and highlighting the FY 2016 priorities. 269

Figure 2. Conceptual flow diagram showing the individual calculations within a single time step of the FMDM..... 272

Figure 3. The burnup – dose rate function derived from the MCNPX results of Radulescu 2011 as a polynomial fit..... 274

Figure 4. shows three types of results: (1) points from Radulescu 2011, (2) dose rate with time from an example simulation with the Fortran FMDM for 60 GWd/MTU (red), (3) dose rate with time from an example simulation with the MATLAB FMDM for 40, 60 and 80 GWd/MTU..... 275

Figure 5. The alpha particle dose rate as a function of distance from the fuel surface..... 276

Figure 6. Results from three simulation cases performed with both the MATLAB and Fortran versions of the FMDM.. 277

Figure 7. Schematic diagrams summarizing the workflow in the prototype PFLOTRAN – FMDM model (from Hammond, 2015). 279

Figure 8. Results from a scaled-down PFLOTRAN repository model in which the FMDM process model has been integrated to determine the dissolution rate of the used fuel and thus the source term of a non-sorbing tracer.....	280
Figure 9. Conceptual summary of the flow of information between the GDSA PA model and the FMDM.....	281
Figure 10. Conceptual layout for the extended FMDM version 3.0 that includes a module quantifying steel corrosion.	283
Figure 11. Results from an older version of the FMDM that included a corroding steel surface.....	284
Figure 12. Photograph and schematic diagram of the type of cell used for the electrochemical experiments.....	285
Figure 13. Results from scoping electrochemical tests showing the open circuit potential of the $\text{Ru}_{56}\text{Mo}_{20}\text{Rh}_{11}\text{Pd}_{11}\text{Tc}_2$ (NMP) electrode for three different tests.....	287
Figure 14. Results from the FMDM v2.3 showing the dramatic decrease in fuel dissolution rate caused by the oxidation of H_2 on the NMP and the possible effect of poisoning of the NMP surface.....	288

LIST OF TABLES

(Part I) Evaluation of Used Fuel Disposition in Clay-Bearing Rock: Reactive Transport and Barrier Interactions in the Near Field Environment

Table 1 Dimensional characteristics of the reference case for disposal in clay (Mariner et al., 2015).....	4
Table 2 Properties and dimensions of EBS components for the 1D PFLOTTRAN simulation.....	8
Table 3 Initial volume fractions inputs for the 1D PFLOTTRAN simulations.....	8
Table 4 Initial molal concentration of aqueous components for each barrier zone in the PFLOTTRAN input card.	9
Table 5 Kinetic rates and reactive surface areas of mineral phases.	9
Table 6 Present and projected disposal volumes of SNF and HLW in the USA (SNL, 2014).	21

(Part II) Investigation of Coupled Processes and Impact of High Temperature Limits in Argillite Rock

Table 2-1. Mineral volume fraction (dimensionless, ratio of the volume for a mineral to the total volume of medium) of the Kunigel-VI bentonite (Ochs et al., 2004), FEBEX bentonite (ENRESA, 2000; Fernández et al., 2004; Ramírez et al., 2002) and Opalinus Clay (Bossart 2011; Lauber et al., 2000).	41
Table 2-2. Pore-water composition (mol/kg water, except pH) of Kunigel-VI bentonite (Sonnenthal et al., 2008), FEBEX bentonite (Fernández et al., 2001) and Opalinus Clay (Fernández et al., 2007).	41
Table 2-3. Thermal and hydrodynamic parameters.	42
Table 2-4. Kinetic properties for minerals considered in the model (Xu et al., 2006).	43
Table 2-5. The geochemically induced swelling stress for Kunigel and FEBEX bentonite at points A and B for “high T” scenario. Stress reduction by ion concentration is the difference between the swelling stress obtained with “ $\sigma=f(SI)$ ” and “ $\sigma=f(SI,C)$ ”, and the stress reduction by smectite dissolution is the difference between the swelling stress obtained with “ $\sigma=f(SI,C)$ ” and “ $\sigma=f(SI,C,Ms)$ ” (see Figure 2-26), where the relative amount (%) use the results from “ $\sigma=f(SI)$ ” as the basis.	75
Table 3-1. Thermal and hydrodynamic parameters.	92
Table 3-2. Mass fraction of minerals for FEBEX bentonite from different publications (%)	93
Table 3-3. Mineral volume fraction (dimensionless, ratio of the volume for a mineral to the total volume of medium) FEBEX bentonite (ENRESA, 2000; Fernández et al., 2004; Ramírez et al., 2002) and granite (Zheng et al., 2011).	93
Table 3-4. Pore-water composition (mol/kg water except for pH) of FEBEX bentonite (Fernández et al., 2001) and granite (Zheng et al., 2011).	94
Table 3-5. Aqueous complexes and their dissociation constants.....	95
Table 3-6. Surface protonation reactions on montmorillonite (Bradbury and Baeyens, 2005)	95
Table 3-7. Cation exchange reactions on montmorillonite and illite (Bradbury and Baeyens, 2005).....	95
Table 3-8. Equilibrium constants for mineral precipitation/dissolution	95
Table 3-9. Kinetic properties for minerals considered in the model (Xu et al., 2006).	96

Table 4-1. Parameters used in the modeling of the Mont Terri HE-E experiment.	135
Table 4-2. Details on the sequence of construction and installation of the Horonobe EBS experiment	141
Table 4-3. DECOVALEX research teams and numerical simulators in modeling Horonobe EBS experiment	143
Table 4-4. Material parameters for modeling Horonobe EBS experiment.	145
Table 4-5. Parameters for the Opalinus and Bentonite clay used in the modeling of the FE experiment.	154
(Part III) Summary of Baseline Experiments for Generic Repository Engineered Barriers	
Table 1 Initial components and reaction conditions for EBS experiments.	196
Table 2 Synthetic groundwater chemistries used in the hydrothermal experiments.	197
Table 3 Synthetic groundwater chemistry used in the Opalinus Clay experiments.	198
Table 4 Quantitative X-Ray Diffraction (QXRD) analyses of the buffer clay (Wyoming Bentonite) the wall rock (Opalinus Clay) and end product results of all seventeen experiments.	204
Table 5 Average (post reaction) zeolite compositions from mineral sample analyses.	213
Table 6 Copper corrosion rate data. Note that the EBS-16 (6 month experiment) corrosion rate is an order of magnitude lower than the other 3 experiments (5-6 week run time).	221
(Part IV) Evaluation of Thermodynamic and Sorption Data; Applications of First- Principles Modeling in the Assessment of Thermal-Mechanical Properties of Kaolinite Clay	
Table 1 G-H-S data for Al(OH) ₃ (Gibbsite) at 298.15K, 1 bar.	233
Table 2 G-H-S data for Al ³⁺ at 298.15K, 1 bar.	233
Table 3. Summary of NEA TDB Activities.	236
Table 4 Parameters used in the empirical force-field of Grimme for the elements in kaolinite.	243
Table 5 Structural unit-cell parameters of kaolinite.	245
Table 6 Selected interatomic distances (Å) in the structure of kaolinite.	246
Table 7 Calculated and measured elastic constants of kaolinite (in GPa).	249
Table 8 Calculated bulk modulus (<i>K</i>), shear modulus (<i>G</i>), transverse wave velocity (<i>V_s</i>), longitudinal wave velocity (<i>V_p</i>), Poisson's ratio (<i>ν</i>), and Young's modulus components along the <i>a</i> , <i>b</i> , <i>c</i> directions (<i>Y_x</i> , <i>Y_y</i> , <i>Y_z</i>) of kaolinite.	251
Table 9 Coefficients of the Haas-Fisher heat capacity polynomial <i>C_p(T)</i> for kaolinite calculated from DFPT-D2.	258

ACRONYMS

1D, 1-D	One Dimensional
2D, 2-D	Two Dimensional
3D, 3-D	Three Dimensional
ANDRA	Agence Nationale pour la Gestion Des Déchets Radioactifs (France)
BBM	Barcelona Basic Model
BExM	Barcelona Expansive Model
CEC	Cation Exchange Capacity
CIEMAT	Centro de Investigaciones Energéticas, Medioambientales y Tecnológicas (Spain)
DECOVALEX	DEvelopment of COupled Models and their VALidation against EXperiments
DFN	Discrete Fracture Network
DFT	Density Functional Theory
DFT-D	Density Functional Theory Corrected for Dispersion
DI	Deionized
DOE	Department of Energy
DOE-NE	Department of Energy, Office of Nuclear Energy
DRZ	Disturbed Rock Zone
DSEF	Disposal Systems Evaluation Framework
EBS	Engineered Barrier System
EBS-NS	Engineered Barrier System-Natural System
EC	European Community
EDL	Electric Double Layer
EDX	Energy dispersive X-ray spectroscopy
EDZ	Excavated Disturbed Zone
EMP	Electron Microprobe
ENRESA	Empresa Nacional de Residuos Radioactivos SA
EoS or EOS	Equation of State
EPCA	Elasto-Plastic Cellular Automata
FCRD	Fuel Cycle Research and Development
FMDM	Fuel Matrix Degradation Model
FE	Full-Scale Emplacement Experiment

FEBEX	Full-scale Engineered Barriers Experiment
FEBEX-DP	Full-scale Engineered Barriers Experiment-Dismantling Project
FEP	Features, Events, and Processes
FY	Fiscal Year
GDSA	Generic Disposal System Analysis
GW	Gigawatt
GWd	Gigawatt days
GWd/MT	Gigawatt (thermal) - days per Metric Ton
HC	Hydrological and Chemical
HKF	Helgeson-Kirkham-Flowers
HLW	High-Level nuclear Waste
HM	Heavy Metal
HPLC	High Pressure Liquid Chromatograph
IAEA	International Atomic Energy Association
IC	Ion Chromatography
I-S	Illite-Smectite
JAEA	Japan Atomic Energy Agency
JNC	Japan Nuclear Cycle Development Institute
LANL	Los Alamos National Laboratory
LBNL	Lawrence Berkeley National Laboratory
LC	Load Collapse
LLNL	Lawrence Livermore National Laboratory
MC	Mechanical-Chemical
MCC	Modified Cam Clay
MT	Metric Ton
MTHM	Metric Tons Heavy Metal
NAGRA	National Cooperative for the Disposal of Radioactive Waste
NE	DOE-Nuclear Energy
NEA	Nuclear Energy Agency
NIST	National Institute of Standard and Technology
NS	Natural (Barrier) System
NW	Nuclear Waste

OECD	Organization for Economic Co-operation and Development
PA	Performance Assessment
PWR	Pressurized Water Reactor
QA	Quality Assessment
QXRD	Quantitative X-ray Diffraction
R&D	Research and Development
RBSN	Rigid-Body-Spring Network
RH	Relative Humidity
SEM	Scanning Electron Microscopy
SIT	Specific Interaction Theory
SNF	Spent Nuclear Fuel
SNL	Sandia National Laboratories
T	Temperature
TC	Thermal and Chemical
TDB	Thermodynamic Database
TEM	Transmission Electron Microscopy
TH	Thermal and Hydrological
THM	Thermal-Hydrological-Mechanical
THMC	Thermal-Hydrological-Mechanical-Chemical
TM	Thermal-Mechanical
TPHM	Two-Part Hooke's Model
UFD	Used Fuel Disposition
UFDC	Used Fuel Disposition Campaign
UOX	Uranium Oxide Fuel
UPC	University of Catalonia
URL	Underground Research Laboratory
WP	Waste Package
XRD	X-ray Diffraction
XRF	X-ray Fluorescence

**Evaluation of Used Fuel Disposition in Clay-Bearing Rock: Reactive Transport
and Barrier Interactions in the Near Field Environment
(Part I)**

1. Evaluation of Used Fuel Disposition in Clay-Bearing Rock

1.1 Introduction

Deep geological disposal of nuclear waste (NW) in clay/shale/argillaceous rock formations has received much consideration given its desirable attributes such as isolation properties (low permeability), geochemically reduced conditions, slow diffusion, sorptive mineralogy, and are geologically widespread (Bianchi et al., 2013, 2014; Gonzales and Johnson, 1984; Hansen et al., 2010; Mazurek et al., 2003; Neuzil, 2013; Schurr, 1977). A brief discussion on the sedimentological characteristics of clay/shale/argillite rock is given in Jové Colón et al. (2014) but it will be repeated here for completeness: “Clay/shale rock formations are characterized by high content of clay minerals such as smectites and illites. From here on, the term ‘shale’ and/or ‘argillite’ will be used interchangeably and generically to delineate mudrock composed primarily of clay minerals plus other minor phases such as quartz, Fe oxides, pyrite, and feldspar. Common definitions of clay/shale rock are based on mineralogical content and textural features such as grain size, fissility, and the presence of laminations. For simplicity, no rigorous distinction between shale and argillite on the basis of metamorphic grade or level of clay induration will be made in this report. It should be noted that the term ‘argillite’ is commonly referred in sedimentology to a mud- or clay-shale having a low degree of metamorphism (Boggs, 2006). This is different from ‘argillaceous’ rock where this term refers to sedimentary rocks having argillite components. Hansen et al. (2010) summarizes the classification of clay-bearing rocks on the basis of texture and level of induration.”

There is a wealth of gained knowledge on the behavior on clay/shale/ argillaceous rock given its focus in international nuclear waste repository programs that includes underground research laboratories (URLs) in Switzerland, France, Belgium, and Japan (ANDRA, 2005; NAGRA, 2002; Hansen et al., 2010). The DOE Used Fuel Disposition Campaign (UFDC) supports a diversified disposal R&D program that include: experimental/modeling studies on diffusion and hydrothermal interactions in clay, coupled Thermal-Hydrological-Mechanical-Chemical (THMC) modeling for clay, SNF degradation, and thermodynamic analysis of fluid-mineral interactions on barrier materials (Jové Colón et al., 2014; Rutqvist et al. 2014, Zheng et al. 2014). Some of these modeling activities have benefited from cross-cutting international collaborations and partnerships such as DECOVALEX and the Mont. Terri project. Jové Colón et al. (2014) documented the characteristics of a reference case for disposal in clay/shale/argillite within the development of a generic disposal concept for argillite. One key study is that of Hardin et al. (2012) analyzing reference disposal concepts based on thermal load management for various host media. Another important contribution is a large scale 2-D hydrogeologic model by Bianchi et al. (2013, 2014) describing radionuclide transport at the repository scale capturing the complexity of hydrogeological units and disposal structures. All these studies have provided important insight on the build up a of reference case for disposal in argillite and related modeling activities for the safety assessment.

1.2 Reference Case for Disposal in Clay/Shale/Argillite: Brief Description

The development and implementation of a reference case for NW disposal in argillite is an important phase within the Used Fuel Disposition Campaign (UFDC) to evaluate repository performance in this host media. Although the initial descriptions of the reference case for argillite was initiated in Jové Colón et al. (2014), the current development will be documented separately in Mariner et al. (2015) as part of the generic disposal system analysis (GDSA) and

performance assessment (PA). This development is based on the framework adopted for the generic salt repository reference case described in Freeze et al. (2013). The characteristics of the clay/shale/argillite reference case described in Mariner et al. (2015) differ (to a certain extent) from those described in Jové Colón et al. (2014). For example, some differences include the addition of stratigraphic units (interbeds, aquifer sediments) and related hydrogeological properties considered for this reference case scenario (see Figures 1 and 2).

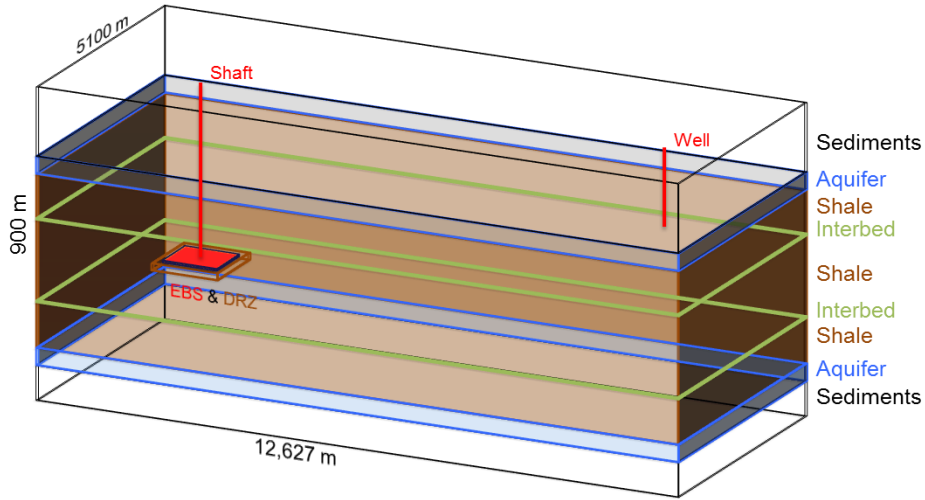


Figure 1. Schematic representation of the stratigraphy and repository footprint dimensions considered for the reference case for disposal in clay/shale/argillite rock (Mariner et al. 2015).

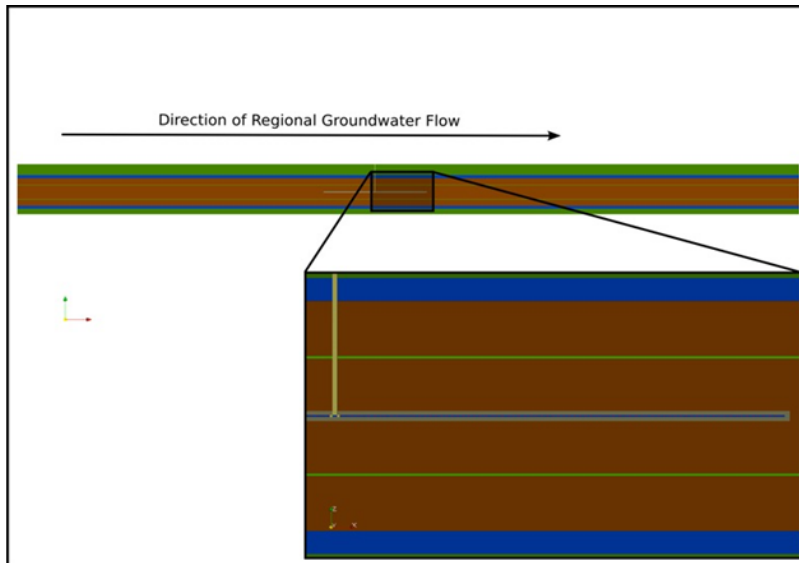


Figure 2. X-Z slice of the clay reference case model at the Y midpoint of the first drift pair in the repository (see Fig. 1). Clay rock is shown in dark brown, dark green is sediment, aquifers are shown in royal blue, grey is the disturbed rock zone (DRZ), interbeds are shown in bright green, bentonite/quartz buffer is shown in dark blue and the shaft and seals are shown in yellow (Mariner et al. 2015).

However, overall repository attributes such as depth, diposal drift layout, shale formation thickness, lithology, etc., were based on the on Jové Colón et al. (2014). Other repository characteristic such as waste inventory and disposal capacity which are based on the salt disposal concept were retained for the clay disposal reference case. The subsurface repository layout consists of horizontal disposal galleries emplaced end-to-end with waste packages in drifts lined with cement and/or metal support structures. Table 1 summarizes the dimensions adopted for the reference case for disposal in clay given by Mariner et al. (2015). Numerical simulations were conducted using PFLOTRAN with a 3D structured grid having variable spacings. The DAKOTA software toolkit is used for sampling, sensitivity analysis, and uncertainty quantification. The interfacing between PFLOTRAN and DAKOTA embodies the GDSA PA computational framework. Evaluation of repository performance is based on ^{129}I concentration due its nature as a conservative tracer. The results of this reference case implementation and development of the GDSA PA capability are documented in Mariner et al. (2015).

Table 1 Dimensional characteristics of the reference case for disposal in clay (Mariner et al., 2015)

Parameters	Value
Waste Package (WP)	
WP length (m)	5.00
WP outer diameter (m)	1.29
WP center-to-center spacing in-drift (m)	10.0
Inventory per 12-PWR WP (MTHM)	5.225
Approx. number of WPs for 70,000 MTHM	13,397.4
Emplacement Drift	
Drift diameter (m)	4.5
Drift center-to-center spacing (m)	20.0
Pillar width (m)	15.5
Number of WPs per drift	80
Drift seal length (m)	10.0
Drift length, including seals (m)	805.0
Central access hallway height (m)	4.5
Central access hallway width (m)	8.0
Approx. number of drifts needed for 70,000 MTHM	167.5
Repository	
Number of drift pairs (rounded up)	84
Repository length (m)	1,618.0
Repository width (m)	1,664.5
Repository Depth (m)	500.0
Total length of all drifts (m)	135,240

Jové Colón et al. (2013, 2014) presented a 3D unstructured mesh for a single-drift multi-canister thermal problem. Figure 3 shows the expansion of this geometry consisting of three parallel (horizontal) disposal galleries emplaced end-to-end with multiple waste packages including a layered EBS. The 3D mesh was built using the Cubit software for use with the multiphysics FEM code Albany (see Jové Colón et al., 2013, 2014) for the analysis of thermal limits in a multi-drift multi-canister repository layout. This unstructured 3D mesh has been adapted for use with the computer code PFLOTRAN through a format conversion using Python scripting for potential applications to THC modeling and compatibility with GDSA PA. The capability for 3D thermal evaluation using the Albany FEM code will continue for the evaluation of thermal limits of EBS design concepts with material heterogeneities. It should be noted that PFLOTRAN is the chosen code to conduct the GDSA PA work described in Mariner et al. (2015) for the implementation of the reference case for disposal in clay/shale/argillaceous rock. As noted in the previous paragraph, the 3D mesh used with PFLOTRAN for the clay reference case is structured and different from the one shown Figure 3 which captures more detail of the EBS.

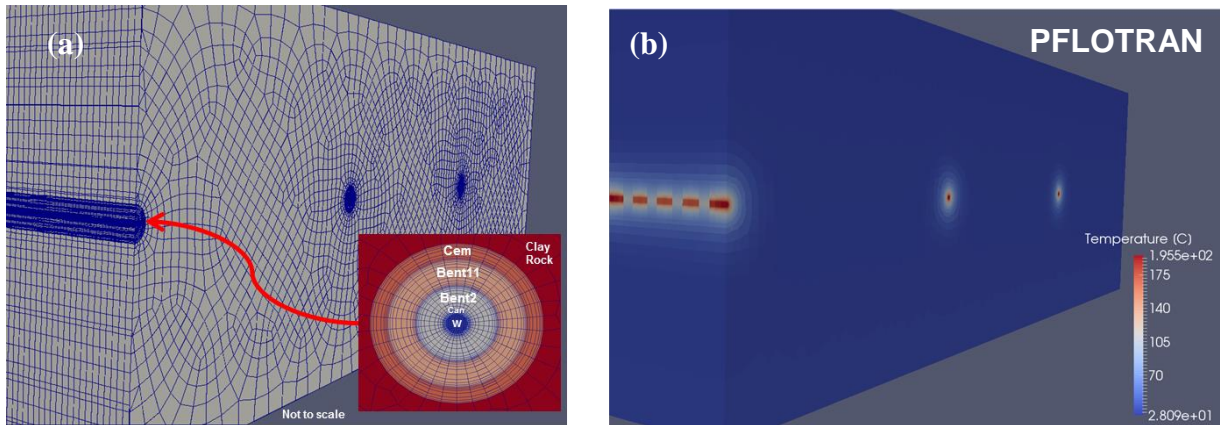


Figure 3. (a) 3D unstructured mesh representation of a longitudinal section of a backfilled drifts with multiple waste canisters and a multi-layered EBS. Inset shows a 2D cross-sectional view of the drift where CEM represents cement liner, and Bent1 and Bent2 refers to the outer and inner clay buffers, respectively. Can and W stands for the canister and heat-generating waste, respectively. (b) Example of a 3D thermal simulation using PFLOTRAN with the unstructured mesh for a repository in argillite.

2. Reactive Transport in the Near-Field Environment

The evaluation of multi-layered engineered barrier system (EBS) interactions between barrier material components (e.g., clay, cement, metal) and pore fluids is key to the assessments of near-field processes and long-term isolation performance of repository design concepts. Field- and laboratory-scale investigations performed at dedicated experimental facilities have provided important information to evaluate these physico-chemical interactions at various scales. As summarized in Jové Colón et al. (2014), multiple studies on the performance of EBS materials and their interactions with fluids have been carried out to evaluate cement-clay interactions (Dauzères et al., 2010; Gaboreau et al., 2012; Sanchez et al., 2006; Savage, 2011; Trotignon et al., 2006), reactive-transport simulations of multi-barrier EBS concepts (Kosakowski and Berner, 2013; Marty et al., 2010; Marty et al., 2009; Montes-H et al., 2005), and characterization studies of reactive-diffusion and sorption in clay-bearing barrier materials (González Sánchez et al.,

2008; Joseph et al., 2011; Joseph et al., 2013; Kozai et al., 2001; Kozaki et al., 2001; Van Loon et al., 2003).

The assessment of *sacrificial zones* in the EBS goes beyond the thermal perturbation caused by heat-generating waste. Understanding the effects (long- and short-term) of heterogeneous chemical reactions (dissolution/precipitation), phase transformation phenomena, and the coupling of these with thermal effects are key to the overall barrier isolation performance in the near-field environment. In particular, chemical effects are expected to be intensified at EBS interfaces between different barrier materials inducing changes in porosity and permeability. This spatially localized phenomena then becomes a focus of investigation given the significance to transport in the assessment of a multi-barrier EBS.

Cement-clay interactions at the clay rock / cement interface play a central role defining the boundary between the near- and far-field regions in deep geological nuclear waste repositories. Given the reactivity of clay and other silicates to highly alkaline solution, such interfacial domain is key to the sealing performance of disposal galleries (Berner et al., 2013; Gaboreau et al., 2012; Kosakowski and Berner, 2013; Soler, 2012; Soler and Mader, 2010). However, other EBS interfaces such as those defined by multi-layered clay barriers and interactions with metal (steel) overpack/canister are also crucial to long-term waste isolation performance (Jové Colón et al., 2013; Jové Colón et al., 2014; Marty et al., 2010; Wilson et al., 2015).

The effects of porosity enhancement and reduction (i.e., clogging) due to mineral dissolution and precipitation have been the focus in various reactive-transport modeling efforts including benchmark test cases for computer code inter-comparisons (Marty et al., 2015; Xie et al., 2015). The main motivation behind these model / code assessments lies in the complexity and non-linearity of geochemical interactions (kinetic vs. transport controlled) and transport phenomena represented by reactive-transport models (Marty et al., 2015). Moreover, the extent to which these models capture relevant physico-chemical processes with sufficient realism and adequacy still needs to be examined and reconciled with the limited amount of synthetic data available. Nevertheless, the coupling of thermal-hydrological-chemical (THC) processes is in itself a challenge but the last two decades or so has brought important advances in the theoretical representation and thus computational simulation capabilities of these coupled phenomena.

The main purpose of this reactive-transport work is to formulate a 1D representation of geochemical interactions with diffusive transport in a multilayered EBS using the computer code PFLOTRAN. This code has been selected as part of the core simulation platform for GDSA PA in the evaluation of disposal concepts (Mariner et al. 2015). A 1D reactive-transport model offers the advantages of performing expeditious simulations thus allowing for rapid analysis of key input and output variables. The next section describes details of the model built and implementation in PFLOTRAN.

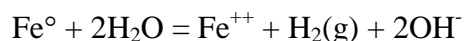
2.1 1D Reactive-Transport Model Description of the EBS

The PFLOTRAN simulation tool is an open source, state-of-the-art massively parallel subsurface flow and reactive transport code with extensive modeling capabilities of THC processes (Lichtner et al., 2013). A major feature of PFLOTRAN is its performance on massively parallel or high performance computing (HPC) platforms where efficient scalability becomes important for large coupled process problems that otherwise could present a computational limitation in

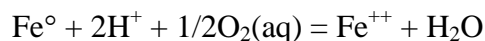
other simulation codes. Parallelization is achieved through domain decomposition using the PETSc (Portable Extensible Toolkit for Scientific Computation) libraries. Lichtner et al. (2013) provides details on PFLOTRAN simulation capabilities, reactive-transport formulations, and geochemical treatment of mineral-fluid interactions.

As noted previously, there are various studies of 1D reactive-transport modeling of EBS material interactions exemplified by cases of multi-barrier domains (Kosakowski and Berner, 2013; Marty et al., 2010; Marty et al., 2009; Montes-H et al., 2005). The scenario considered in this study is depicted in Figure 4. The 1D structured grid has a cylindrical symmetry with 1000 grid cells in the horizontal direction covering a total domain of 13 meters. The dimensional characteristics of each zone (also given in Figure 4) represent barrier thicknesses for the EBS concept proposed for the argillite reference case in Jové Colón et al. (2014). All zones are assumed to be fully saturated and isothermal at 25°C. Tables 2 list some of the thermal and transport properties of each zone. Tables 3 and 4 provide the mineral volume fractions and initial pore solution chemical composition, respectively, for each barrier material zone. Two types of initial pore water chemistries for the clay barrier zones were considered: (a) dilute (Table 2) and (b) “FEBEX-like” pore water given in Jové Colón et al. (2014). The reason for considering diluted pore solution composition is for reduced complexity, improved run stability, and the ability for better scoping the response of barrier-fluid interactions. The $\text{H}_4\text{SiO}_4(\text{aq})$ concentration in the inner clay zone is assumed to be in equilibrium with quartz given that 14% volume fraction of this mineral is present in this zone. The FEBEX pore water composition is considered nominal for bentonite pore waters reported in the literature. The clay rock pore water chemistry is based on the work of Turrero et al. (2006) for Opalinus Clay. Pore water compositions in the cement zone are mainly controlled by equilibria with respect to the calcite aggregate and the presence of CSH(1.6) and portlandite plus other cementitious phases. Future work will explore other cement compositions (e.g., shotcrete) with variable amounts of cementitious phases.

Canister material is currently represented in the model by Fe metal, similar to other reactive transport studies (Marty et al. 2010; Wilson et al. 2015). However, there are differences in the treatment of steel corrosion usually represented by an anaerobic corrosion reaction given by (Marty et al. 2010; Wilson et al., 2015):



A similar reaction is adopted for the “Fe(element)” phase in the THERMOPDEM thermodynamic database representing the steel material in this work:



As expected, the above reaction results in an increase in pH due to H^+ consumption where $\text{H}_2(\text{g})$ is controlled by the equilibria with other relevant species such as $\text{O}_2(\text{aq})$, $\text{O}_2(\text{g})$, and $\text{H}_2(\text{aq})$. As noted by Wilson et al. (2015), the fate of $\text{H}_2(\text{g})$ is not well constrained and as such it imposes an important uncertainty in the chemical interactions at this EBS interface. The current simulations show large reactivity, as expected, with a sharp increase in pH. At this moment, the reaction product for steel corrosion considered in the simulations is magnetite. Given the importance of these interactions to waste package degradation, future work will look at this issue in more detail to advance an adequate set of reaction products that include Fe oxy-hydroxides and Fe-bearing Al-silicates.

Table 2 Properties and dimensions of EBS components for the 1D PFLOTRAN simulation.

	Thickness (m)	Porosity (-)	Permeability (m ²)	Tortuosity (-)	Particle Density (kg/m ³)	Thermal Conductivity (Dry) (W/m K)	Remarks
Waste Form	0.475	0.3	1.0E-22	0.3	8720	11	Assumed to be inert
Metal Canister	0.1	0.001	1.0E-22	0.001	7850	46	Stainless steel overpack
Inner Clay Barrier	1.24	0.3	1.0E-17	0.3	2700	1.7	Bentonite + Quartz
Outer Clay Barrier	1.24	0.2	1.0E-20	0.2	2700	1.3	Bentonite
Cement Liner	0.75	0.15	1.0E-17	0.15	2700	1.7	Cement + aggregate
Argillite Rock	9.2	0.12	5.0E-20	0.12	2700	1.7	Based on argillite properties

Table 3 Initial volume fractions inputs for the 1D PFLOTRAN simulations.

	Smectite (MX80)	Illite (IMt2)	Quartz (alpha)	Uraninite	Fe (element)	Pyrite	Calcite	Siderite	CSH(1.6)	Portlandite	Ettringite	Monosulfo aluminate	Gypsum	Remarks
Waste Form	-	-	-	0.7	-	-	-	-	-	-	-	-	-	Assumed to be inert
Metal Canister	-	-	-	-	0.999	-	-	-	-	-	-	-	-	Fe metal in the model
Inner Clay Barrier	0.55	-	0.14	-	-	0.004	0.003	-	-	-	-	-	0.003	Bentonite + Quartz
Outer Clay Barrier	0.79	-	-	-	-	0.004	0.003	-	-	-	-	-	0.003	Bentonite
Cement Liner	-	-	-	-	-	-	0.663	-	0.09	0.062	0.033	0.002	-	Cement + calcite aggregate
Clay Rock	0.06	0.43	0.24	-	-	0.01	0.139	0.001	-	-	-	-	-	Opalinus clay rock

Table 4 Initial molal concentration of aqueous components for each barrier zone in the PFLOTTRAN input card.

	Na ⁺	K ⁺	Ca ⁺⁺	Mg ⁺⁺	H ₄ SiO ₄ (aq)	Al ⁺⁺⁺	Fe ⁺⁺	U ⁺⁺⁺⁺	Cl ⁻	SO ₄ ⁻	HCO ₃ ⁻	pH	Remarks
Waste Form	1.0E-07	1.0E-08	1.0E-07	1.0E-07	5.0E-06	6.0E-08	5.0E-15	trace	1.0E-07	1.0E-07	1.0E-05	7.51	Assumed to be inert
Metal Canister	1.0E-07	1.0E-08	1.0E-07	1.0E-07	5.0E-06	6.0E-07	5.0E-05	trace	1.0E-07	1.0E-07	1.0E-05	7.51	Stainless steel overpack
Inner Clay ^(a) Barrier	1.0E-06	1.0E-08	1.0E-04	1.0E-07	5.0E-06	6.0E-07	5.0E-06	trace	1.0E-07	1.0E-05	1.0E-05	7.51	Dilute water. H ₄ SiO ₄ (aq) in equilibrium with Quartz
Outer Clay ^(a) Barrier	1.0E-06	1.0E-08	1.0E-05	1.0E-07	5.0E-06	6.0E-07	5.0E-07	trace	1.0E-06	1.0E-05	1.0E-03	7.51	Dilute water. Ca ⁺⁺ in equilibrium with calcite
Cement Liner	1.0E-05	1.0E-08	2.0E-03	1.0E-07	6.0E-03	6.0E-07	5.0E-07	trace	1.0E-05	1.0E-09	1.0E-07	11.3	Cement + calcite aggregate
Clay Rock	0.261	0.0027	0.0201	0.0165	2.95E-04	6E-07	2.3E-05	trace	0.332	1.0E-07	1.0E-06	7.6	Based on Turrero et al. (2006) for Opalinus Clay pore water

^(a) Dilute pore water composition (see text).

Table 5 Kinetic rates and reactive surface areas of mineral phases.

Mineral Phase	Dissolution Rate (mol/ m ² s)	Reactive Surface Area (m ² /m ³)	Source	Remarks
Smectite(MX80)	8.0E-14	1	Marty et al. (2009)	-
Illite(IMt2)	1.585E-15	1	Köhler et al., 2003	pH~7
Quartz(alpha)	1.99E-14	1	Rimstidt and Barnes (1980)	-
Uraninite	-	1	-	Assumed unreactive
Fe(element)	2.232E-12	1	Marty et al. (2010)	Rate constant for steel
Pyrite	2.884E-11	1	Williamson and Rimstidt (1994)	pH~7.5; 7.24E-7 molal dissolved oxygen
Calcite	1.778E-05	1	Pokrovsky et al. (2009)	-
Siderite	1.007E-09	1	Golubev et al. (2009)	pH~7
CSH(1.6)	2.75E-12	1	Baur et al. (2004)	pH range 11-12
Portlandite	5E-04	1	Giles et al. (1993)	Transport-independent rate
Ettringite	1.12E-12	1	Baur et al. (2004)	-
Monosulfoaluminate	1.12E-12	1	-	Sames as ettringite
Gypsum	1.3d-3	1	Jeschke et al. (2001)	-

The diffusive flux in PFLOTRAN is defined according to porosity, saturation, reference diffusivity, and tortuosity (Lichtner et al., 2013):

$$F_i = -\phi S D \tau \nabla C \quad (1)$$

where F_i is the diffusive flux of the solute constituent i , ϕ stands for porosity, S refers to saturation, τ represents tortuosity, D denotes the diffusion/dispersion coefficient, and C symbolizes solute concentration. Tortuosity in each zone is assumed to be equal to porosity following Archie's Law with the exponent $n = 2$. Boudreau (1996) compared tortuosity-porosity data for sedimentary environments along with formulations to represent tortuosity-porosity relations including Archie's Law. Considering the scatter in the data, Boudreau (1996) found that Archie's Law with $n = 2.14$ provides a reasonable description of this tortuosity-porosity relation. All media domains are fully saturated. The diffusion coefficient is set to $1.5 \text{ E-}12 \text{ m}^2/\text{s}$ to be consistent with the range of effective diffusion coefficient values adopted in the study of Kosakowski and Berner (2013). Although this value may seem to be on the lower end, diffusivities for compacted clay-rich barrier material and clay rock can be as low as $10^{-13} \text{ m}^2/\text{s}$. Porosities are updated in the simulations according to the volume fraction of minerals and their dissolution/precipitation rates.

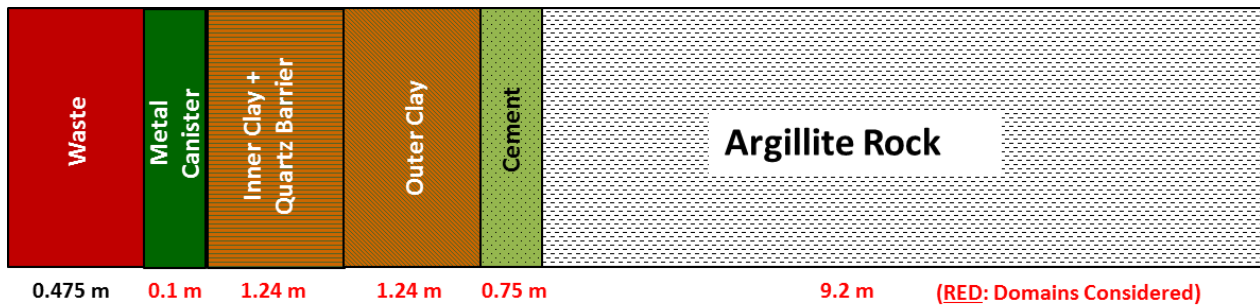


Figure 4. Schematic representation and dimensional characteristics of the 1D reactive-transport simulation domain including the EBS and argillite rock. Interactions with waste are not considered in this study.

The reactive surface areas of all constituent minerals are all set to unity. This modeling assumption deviates from other reactive-transport modeling studies but it allows for simpler evaluation of simulation outputs. PFLOTRAN updates reactive surface area of minerals as a result of mineral dissolution and precipitation. This is captured in the code runs by changes in mineral volume fractions and hence porosity. Other modeling studies such as that of Marty et al. (2009) evaluated modeling sensitivities to reactive surface areas. Given the range of reactive surface areas adopted in reactive-transport modeling studies, it appears that these are mostly based on modeler choice built on literature values or estimates of specific and/or geometric mineral surface areas. In the future, PFLOTRAN simulations will sensitivities for comparisons with other studies such as that of Marty et al. (2009).

Sensitivity analyses were conducted with regards to reactive surface areas of pyrite given its strong effect on pH. In the diluted pore water cases, reactive surface areas were set in the order of $\sim 10^{-3}$ to reduce the effects of pH drop which can be significant even when using relatively small pyrite volume fractions. According to Cheshire et al. (2014), the drop in pH as a result of

pyrite decomposition is ~2 pH units according to their clay hydrothermal experiments. In the cases for the FEBEX pore water chemistry, the drop in pH was observed but of lesser magnitude than in the diluted pore water case.

Thermodynamic data for all mineral phases were obtained from the THERMODDEM database (Blanc et al., 2012; Blanc et al., 2006). This database contains a comprehensive set of relevant mineral solids and aqueous species such as smectite (MX-80) and illite (IMt2) clays. Its development is borne out from the traceability requirements demanded by rigorous quality assessment of data to be used in (geo)chemical modeling of radioactive waste and engineered barrier materials. THERMODDEM also contains a comprehensive set of solid phases relevant to cementitious materials such as CSH(1.6), portlandite, and monosulfoaluminate among others. The cement liner composition considered in these simulations approximates that of ordinary Portland cement (OPC) with ~70% volume of calcite aggregate (see Table 3).

Dissolution rates of mineral solids are listed in Table 5. A linear dissolution rate law is assumed at this point for simplicity. More sophisticated rate law formulations available in PFLOTRAN will be considered in the future to evaluate sensitivities to kinetic rates, pH dependencies, and the effects on transport. Although uraninite as a waste form source term is part of the EBS solid phase assemblage, the current simulations do not consider the contributions of this phase to the solution chemistry.

The dissolution rate for pyrite is obtained from Williamson and Rimstidt (1994) for a near-neutral pH 7.5. The smectite (MX-80) dissolution rate is taken from Marty et al. (2009) and it's based on the work of Amram and Ganor (2005), Huertas et al. (2001), and Golubev et al. (2006). The illite dissolution rate for pH~7 is from the experimental work of Kohler et al. (2003). The aqueous dissolution rate for magnetite is obtained from the electrochemical work of White et al. (1994) at pH 7. Dissolution rates for calcite and siderite were obtained from the studies of Pokrovsky et al. (2009) and Golubev et al. (2009), respectively.

The dissolution rate of the CSH phases was obtained from Baur et al. (2004) for pH 11-12. Dissolution rates for ettringite is based on the rates given for ettringite-Ca(2) in Baur et al. (2004). The dissolution rate tobermorite(11) is assumed to be equal to that of ettringite. The dissolution rate of portlandite was obtained from Giles et al. (1993). This rate was retrieved from spinning disk dissolution experiments for the "reaction-controlled" or transport-independent rate. The portlandite dissolution rate obtained from this study is orders of magnitude faster than that adopted by Marty et al. (2009). It's also more realistic for a pure portlandite phase since the spinning disk methodology provides insight into transport effects on dissolution rates which in this case are attributed to Ca diffusion through the interface (Giles et al., 1993). The dissolution rate of gypsum was taken from the study by Jeschke et al. (2001). It is assumed that precipitation rates are the reverse of dissolution rates given the very limited kinetic data available. This is consistent with the PFLOTRAN implementation of transition-state theory (TST) where the equilibrium constant can be defined as the ratio of backward and forward rates. Simulations were conducted up to time lengths of 1,000, 5,000, 10,000, 100,000, and 500,000 years. For simplicity, only results at 10,000 years are presented. Observation points were located at the center of each zone and at interfaces between EBS material domains.

2.2 Results and Discussion

The code simulations results show distinctive trends that are summarized as follows:

- Rapid increase in pH and $\text{H}_4\text{SiO}_4(\text{aq})$ concentration in pore water is observed at the interfaces between cement and outer clay buffer, and between cement and clay rock (Figure 5). This is expected for the alkaline reaction front migration even when clay dissolution is a slow process (Marty et al., 2009). However, the inner clay zone did not experience an increase in pH, as expected, given the distance between this zone and the cement liner interfaces. At extended times (in the order of thousands of years) the pore solution pH in the inner clay zone also increases.
- A noticeable decrease in pH in the inner and outer clay regions due to pyrite decomposition (Figure 6). This observation is consistent with experiments on bentonite clay interactions (Cheshire et al., 2014). However, the magnitude of this decrease was not as large as that observed in this experimental study. The extent of such pH drop could be attributed to the nature of initial pore solution composition and the amount of pyrite in the clay mass. The temporal extent for this pH drop will depend on the amount of mineral present in the zone, kinetic rates, and solution chemistry. It is assumed that pyrite decomposition will be more predominant during the thermal pulse period of elevated temperatures. Extension of this modeling approach to higher temperatures is planned for future work.
- The largest changes in porosity are concentrated at the cement-clay interfaces, as expected (Figure 7). Overall, there is porosity enhancement at these interfacial locations but the extent of mineral volume fraction changes as a result of mineral dissolution is relatively small. Consequently, the overall changes in porosity are also small.
- Porosity reduction or clogging as a result of mineral precipitation was discernable in the outer-clay – cement interface region but the magnitude of such change is small (Figure 8). The volume fractions of precipitated minerals were too small as to generate any significant reduction in porosity. Future work will assess this aspect of porosity reduction in more detail.

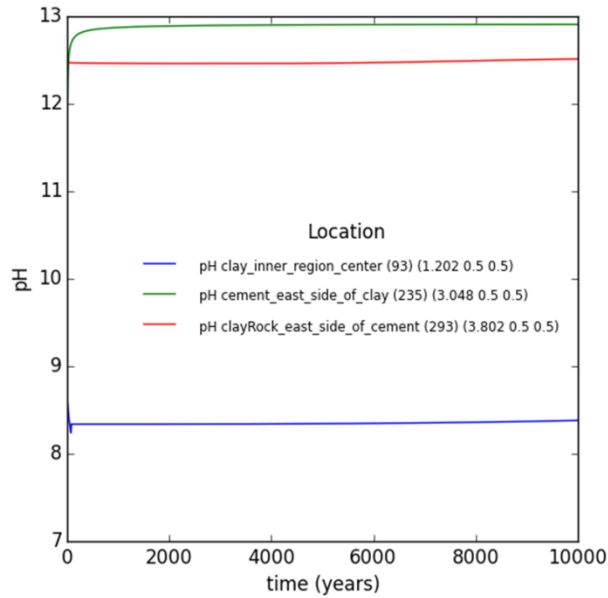


Figure 5. Profile of pH vs. time (up to 10,000 years) of the reactive transport calculations for the multi-layered EBS. The selected locations for observation points are the center of the inner clay zone (clay_inner_region_center), interface between cement and outer clay zone (cement_east_side_of_clay), and interface between cement and clay rock. The number triplet in the second set parentheses in the legend refers to the observation location (x, y, z) distances starting from the waste leftmost coordinate.

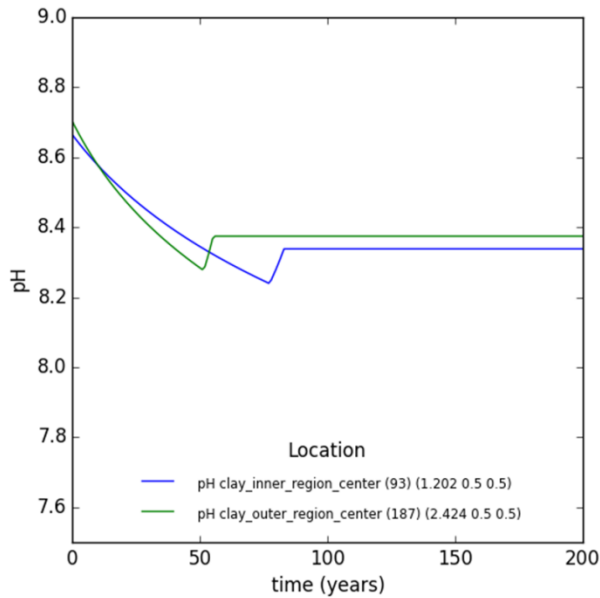


Figure 6. Enlarged view of the pH vs. time (up to 200 years) profile from the previous figure. Notice the drop in pH in the ~50-75 years due to pyrite decomposition. Observations points located at the inner and outer clay center regions. See previous figure caption for location legend explanation.

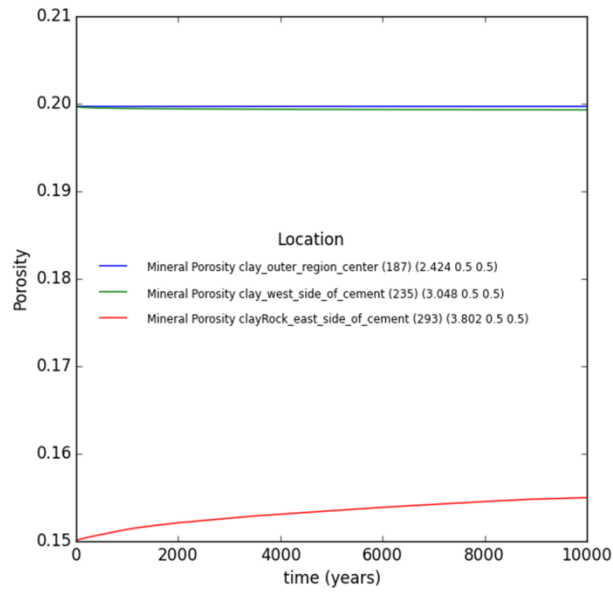


Figure 7. Profile of porosity vs. time (up to 10,000 years) of the reactive transport calculations for the multi-layered EBS. The selected locations for observation points are the center of the outer clay zone (clay_outer_region_center), interface between cement and outer clay zone (clay_west_side_of_cement), and interface between cement and clay rock. Porosity increase/decrease is more marked at the interfaces but their overall magnitude is relatively minimal in these simulations (see text).

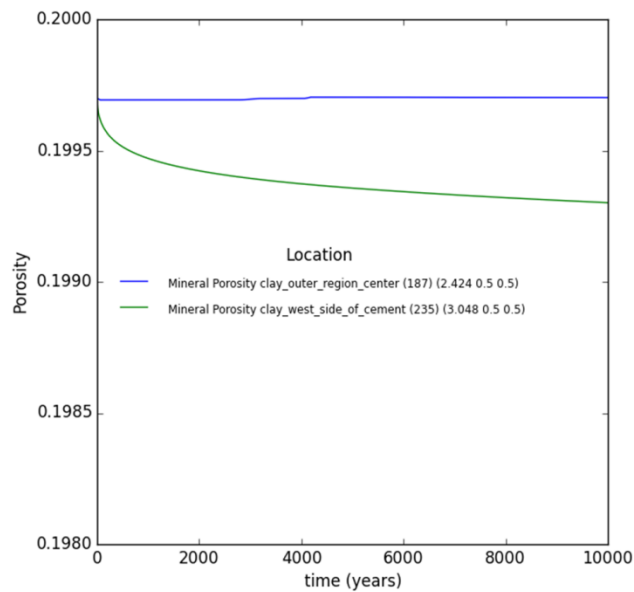


Figure 8. Enlarged view of the porosity vs. time (up to 10,000 years) profile outlining the small porosity decrease at the outer-clay – cement interface observation point.

3. Thermodynamic Evaluation of Barrier Clay Interactions: Equilibrium Phase Relations and Reaction Path Modeling

The description of equilibrium phase relations for the system Na-Ca-Mg-K-Si-Al-H₂O requires accurate information of the thermodynamic properties of Al-silicate solids and related aqueous species. The widespread use and applications of thermodynamic data in the description of mineral phase stability relations and retrieval of thermodynamic parameters has placed a longstanding emphasis in the analysis of these data for complex systems. Previous work discussed in Jové Colón et al. (2013) and Jové Colón et al. (2014) described recent updates to thermodynamic data focus on Al-silicate solids and relevant aqueous species. These updates were considered necessary based not only on recent assessments of thermodynamic data and their internal consistency but also for comparison with experimental observations of clay interaction at elevated temperatures (Cheshire et al., 2014). Updates to existing data include the minerals kaolinite, smectites, diaspore, quartz, Si-rich analcime, and corundum (Blanc et al., 2012; Blanc et al., 2006; Gailhanou et al., 2013; Gailhanou et al., 2012; Gailhanou et al., 2007; Holland and Powell, 2011; Neuhoff et al., 2004; Rimstidt, 1997; Tutolo et al., 2014). Other updates to aqueous species were considered for SiO₂(aq), Al⁺⁺⁺, and AlO₂⁻ (Rimstidt, 1997; Tagirov and Schott, 2001). This information will be used as key inputs in the construction of phase diagrams using CHNOSZ (Dick, 2008), reactive transport calculations described previously, and reaction path calculations described in this section. An example on the application of this tool is the equilibrium representation of clay phases as a function of SiO₂(aq) activity and temperature. Figures 9a and 9b illustrate the relative stability of clays (smectite (MX-80), saponite (SapCa-1)) with illite (IMt-2) and illite-smectite (ISCz1) clays. The resulting topology for illite (IMt-2) is consistent with the occurrence of this phase under conditions of silica undersaturation. It should be noted that the construction of these diagrams assumes fixed aqueous activities of system components. In this case Figure 9a is consistent with $\log(a\text{Na}^+/a^2\text{H}^+)$ and $\log(\text{K}^+/a^2\text{H}^+)$ ratios of 4.89 and 5 in figures 9a and 9b, respectively. Aqueous species activities were adjusted to resolve the clay stability fields in these figures.

Future work will evaluate sensitivities of stability relations of co-existing mineral assemblages to a given set aqueous species activities. This type of sensitivity analysis is key to make comparisons between experimental observations of mineral parageneses and predictive thermodynamic relations under given conditions of temperature, pressure, and solution composition.

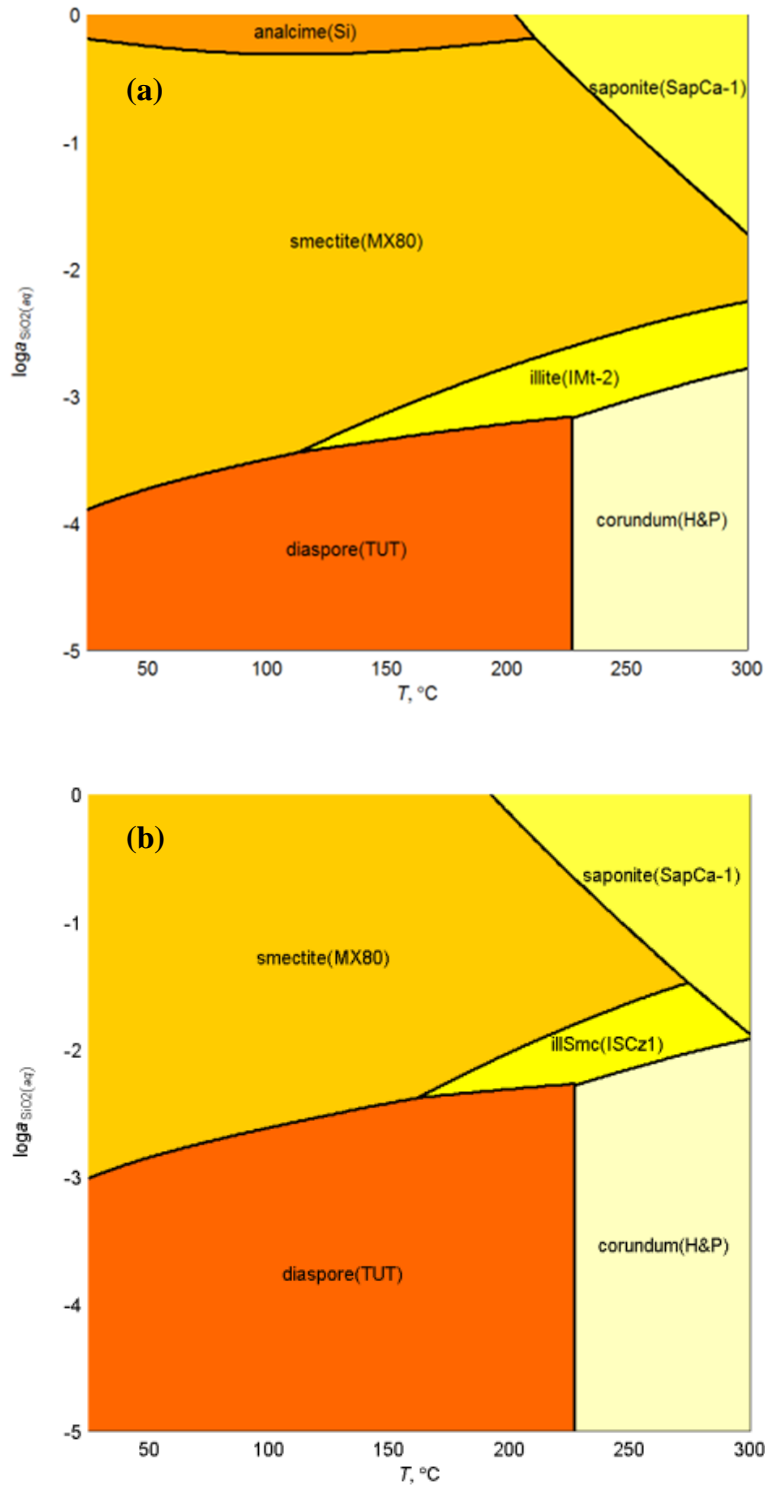


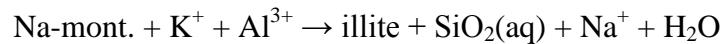
Figure 9. Log activity $\text{SiO}_2(\text{aq})$ vs. temperature phase diagram for the system Ca-Na-Al-Si-Fe- H_2O generated using CHNOSZ containing : (a) illite (IMt-2) and (b) illite-smectite (ISCz1). Thermodynamic input data for smectite(MX-80), illite (IMt-2), and saponite (SapCa-1) is from Gailhanou et al. (2007, 2012, 2013). Data for diaspore (TUT) and corundum (H&P) are from Tutolo et al. (2014) and Holland and Powell (2011), respectively. Analcime(Si) data is from Neuhoff et al. (2004). Note that the construction of these diagrams assumes fixed aqueous activities of system components.

3.1 Reaction Path Modeling

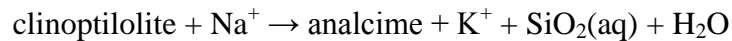
Reaction path modeling is a useful tool to map the evolution of solution composition during fluid-mineral interactions as a function of reaction extent and temperature (Wolery and Jarek, 2003). The purpose of this analysis is to develop a relatively simple problem describing the expected reaction path for clay degradation. Reaction path runs were conducted using the EQ3/6 software package (Wolery and Jarek, 2003) with a modified thermodynamic database to accommodate data updates for Al-silicates (see previous section). The reaction path runs were performed with the option of ramping up temperature with linear increments of the reaction progress variable (ξ). Such approach allows for the evaluation of mineral saturation effects with respect to silica (e.g., quartz, cristobalite) or zeolite phases (e.g., analcime) as a function of temperature. The reactant phases considered in the simulations are pyrite, $\text{SiO}_2(\text{am})$, Na-clinoptilolite, smectite (MX-80), and iron metal. Product phases are constrained to represent the cases for analcime- and silica-saturated reaction path curves. The relative mineral molar proportions adopted for these simulations are 0.05, 0.1, 0.05, 0.6, and 0.2, respectively. The starting temperature is 125°C in 0.1°C increments yielding a final temperature of 294.9°C , close to 300°C . The pressure calculations follow the liquid vapor saturation curve of water. The reacting solution composition is based on a synthetic Stripa groundwater chemistry after Cheshire et al. (2014). Multiple simulations were conducted to evaluate mineral inclusions and suppressions when investigating the effects of silica (quartz, cristobalite) and zeolite (siliceous analcime saturation) on aqueous silica concentrations and overall silica phase equilibria of reaction products.

3.2 Discussion and Conclusions

The importance of silica concentration on clay barrier degradation at elevated temperatures has been emphasized by many authors with regards to Na-montmorillonite (Na-mont.) dissolution, illite formation, and silica cementation (Pusch et al., 1998; Wersin et al., 2007):



and Al-silicate mineral dissolution and zeolite / $\text{SiO}_2(\text{am})$ formation (Cheshire et al., 2014):



The last two reactions were advanced by Cheshire et al. (2014) to exemplify alternate controls of silica concentrations by minerals other than those associated to illitization. The transformation of clinoptilolite to siliceous analcime in bentonite is significant given that the former, along with volcanic glass, is a common component in Na-bearing bentonites. These authors also noted that even at high temperatures, smectite experienced negligible levels of dissolution and therefore limited degradation. The alteration of silica glass remnants can produce $\text{SiO}_2(\text{aq})$ in large enough concentrations to stabilize siliceous analcime and/or cristobalite. Post-experiment observations

did not indicate silica cementation as a result of smectite degradation which has been suggested in other studies. This is an important observation since silica cementation affects the bulk thermal and hydrological properties of bentonite in addition to smectite swelling.

Figure 10 shows a simplified activity-temperature phase diagram displaying the range of $\text{SiO}_2(\text{aq})$ concentrations from the experimental data all falling within the stability field of smectite (MX-80). This is consistent with observations by Cheshire et al. (2014) on the overall stability of the bulk smectite phase in the temperature range of their experiments. These experimental $\text{SiO}_2(\text{aq})$ concentrations are also consistent with quartz saturation at $T < 200^\circ\text{C}$. However, as noted in Cheshire et al. (2014) and earlier in the text, this close correspondence may be indicative of equilibrium with a silica phase such as quartz or cristobalite but also with siliceous analcime equilibrium. Figure 10 also shows the EQ3/6 reaction path simulation allowing for quartz saturation (or quartz-bounded simulations) depicting the expected trend overlap with temperature. Even with the rather broad range of $\text{SiO}_2(\text{aq})$ concentrations, comparison of this experimental $\text{SiO}_2(\text{aq})$ trend indicate good agreement with quartz saturation at $T < 200^\circ\text{C}$. However, there is a slight deviation towards higher $\text{SiO}_2(\text{aq})$ activities with increasing temperature ($T \geq 200^\circ\text{C}$). This is consistent with cristobalite saturation above that of quartz. The same figure shows the cristobalite-bounded reaction path simulations consistent with the experimental $\text{SiO}_2(\text{aq})$ activities. Although reaction path modeling confirms the experimental observations of Cheshire et al. (2014) and the agreement with thermodynamic relations with silica phase equilibria as a function of temperature, none of these simulations predict saturation with respect to siliceous analcime which is problematic. Figure 10 illustrates the siliceous analcime-bounded simulation predicting a much larger $\text{SiO}_2(\text{aq})$ activities to attain siliceous analcime saturation at $T \leq 200^\circ\text{C}$. Such large $\text{SiO}_2(\text{aq})$ activities are inconsistent with the observed concentrations in the experiments and puts into question the stability of siliceous analcime predicted in this system representation. Therefore, reaction path simulations suggest that if siliceous analcime stability is to be associated with silica phase saturation, then it must be assumed that there is no significant role of smectite (MX-80) in this equilibrium scenario. That is, the formation of siliceous analcime is local to clinoptilolite degradation and silica-rich phases but not necessarily in equilibrium with respect to smectite (MX-80). If smectite (MX-80) is excluded from the equilibrium mineral assemblage, the stability field of siliceous analcime enlarges with the phase boundaries coinciding with that of silica phase saturation. This scenario of smectite exclusion then explains the experimental observations of Cheshire et al. (2014) and provides a key elucidation of local equilibrium in a subsystem dominated by an unstable silicates under given experimental conditions. Such a “local” equilibria is consistent with textural observations of post-experiments analyses confirmed by negligible levels of smectite degradation and localized formation of siliceous analcime from the clinoptilolite precursor. This leads to the conclusion that the cristobalite-bounded reaction path is more representative of high temperature alteration of bentonite. As previously noted, this activity phase diagram assumes fixed aqueous activities of system components which is a limitation in representing reaction path simulation results. For example, the $\log(a\text{Na}^+/a^2\text{H}^+)$ and $\log(\text{K}^+/a^2\text{H}^+)$ ratios may change along the reaction path and consequently the mineral stability fields in the diagram will also change. The purpose of presenting all output results in figure 10 is to delineate the overall $\text{SiO}_2(\text{aq})$ evolution with temperature mapped within a reasonable bounds of clay stability. Additional sensitivity analyses to mineral inclusion and suppressions plus data consistency are planned for future work.

Cheshire et al. (2014) discussed the significance of $\text{SiO}_2(\text{aq})$ saturation with respect to cristobalite at $T > 200^\circ\text{C}$ and its crystallization observed in the 300°C isothermal experiments. The agreement of siliceous analcime stability along quartz saturation at $T \leq 200^\circ\text{C}$ is consistent with the analysis of Neuhoﬀ and Ruhl (2006). The trend of increasing $\text{SiO}_2(\text{aq})$ activities with temperature towards equilibrium with respect to cristobalite exemplifies the stabilization of a higher temperature silica phase along with the analcime phase. The work of Neuhoﬀ and Ruhl (2006) evaluates the relationship between silica and siliceous analcime phase stability but is limited to temperatures up to 150°C . Nevertheless, their analysis of Si/Al ratios in analcime solid solution shows the tendency of siliceous analcime being stable at higher $\text{SiO}_2(\text{aq})$ activities – almost overlapping with cristobalite saturation. This is consistent with Cheshire et al. (2014) experimental observations where siliceous analcime compositions are predominant in their reaction products. Future work on how mineral solid solutions affect the overall stability relations of the alteration mineralogy is anticipated.

In conclusion, reaction path modeling is a very useful tool to simulate multiphase multicomponent solution-mineral equilibria mapped as a function of temperature and solution chemistry. It allows the evaluation of phase equilibria and textural relations from experiments in testing scenarios where local and/or global phenomena may be key in explaining the degradation of the bentonite clay barrier material. This analysis also illustrates the key importance of accurate thermodynamic data and its use in predictive models to represent complex interactions in the EBS. This is important for mineral precursors such as existing zeolites and silica-rich phases in bentonite clay in controlling clay-solution interactions. The role of localized mineral parageneses is also described in part III of this report for the description of hydrothermal experiment results showing wairakite precipitation in cracks of Opalinus Clay rock.

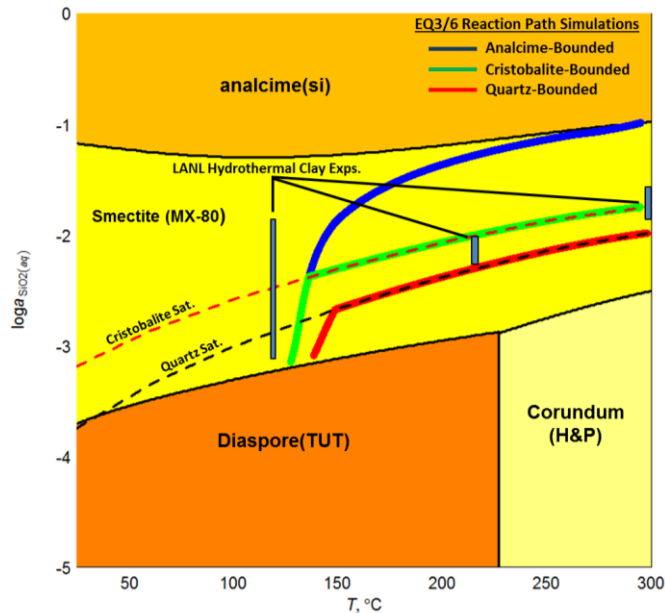
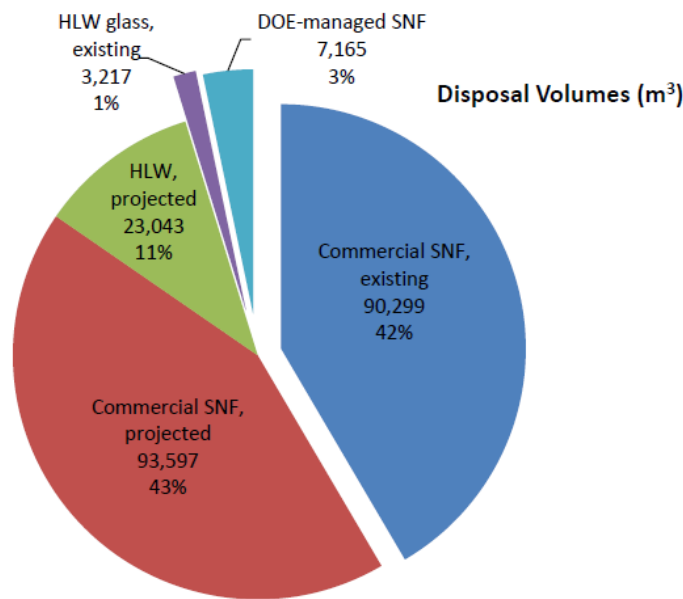


Figure 10. Log activity $\text{SiO}_2(\text{aq})$ vs. temperature phase diagram for the system Ca-Na-Al-Si-Fe- H_2O generated using CHNOSZ. The trend lines for “Analcime-Bounded”, “Cristobalite-Bounded”, and “Quartz-Bounded” are the EQ3/6 reaction path results described in the text. Thermodynamic input data for smectite (MX-80) is from Gailhanou et al. (2012, 2013). Data for diaspore(TUT) and corundum (H&P) are from Tutolo et al. (2014) and Holland and Powell (2011), respectively. Analcime(Si) data is from Neuhoﬀ et al. (2004). The “LANL hydrothermal Exps.” refers to the ranges of $\text{SiO}_2(\text{aq})$ concentrations from the work of Cheshire et al. (2014).

4. DOE-Managed HLW and SNF Research

The disposition of DOE-managed high-level radioactive waste (HLW) and spent nuclear fuel (SNF) was recently considered in terms of starting the process of evaluating the development of a repository. This section provides a brief description of the alignment and applicability of the concept of disposal in argillite or clay-rock media to DOE-managed HLW and SNF. As described in SNL (2014), DOE-managed HLW and SNF represent a relatively small portion of the total existing and projected estimates of nuclear waste types (e.g., relative to commercial SNF). Figure 11 and Table 6 indicate that although present disposal volumes of HLW glass are relatively small, however, projected volumes of HLW (most of it in vitrified form) will exceed those DOE-managed SNF. Therefore, consideration of waste type for disposal on argillaceous media is mainly given to HLW glass.

DOE HLW comprises various forms ranging from tank waste processed into borosilicate glass, calcine and sodium-bearing HLW, and cesium/strontium capsules stored at the Hanford site. Existing and projected amounts of vitrified waste will generate thermal loads per canister that would be lower than those of commercial SNF. This is exemplified in Figure 12 by comparing projected HLW glass (Hanford and SRS) and UOX SNF (21-PWR assemblies) heat decay curves as a function of time.



NOTE: Volume estimates assume (1) constant nuclear power generation in commercial reactors and disposal of all commercial SNF in dual-purpose canisters, and (2) relative volumes of various HLW based on calcine processed by hot isostatic pressing with additives, (3) sodium-bearing waste treated by fluidized bed steam reforming, (4) sodium-bonded fuels undergo electrometallurgical treatment, and (5) all other waste forms are vitrified. For simplicity, all DOE-managed SNF is shown as "existing"; approximately 3,500 m³ of naval SNF remains to be generated.

Figure 11. Existing and projected relative volumes of SNF and HLW in the USA (SNL, 2014).

Table 6 Present and projected disposal volumes of SNF and HLW in the USA (SNL, 2014).

Waste	Present Volume (m ³)	Additional Projected Volume in 2048 (m ³)	Total Volume (m ³)
Commercial SNF disposed of in dual-purpose canisters	90,299	93,597	183, 896
DOE-managed SNF	7,165	0	7,165
Savannah River Site vitrified HLW	2,969 (through macrobatch 8)	3,988	6,957
Hanford site vitrified HLW	0	14, 089	14, 089
Calcine waste after treatment by hot isostatic pressing	0	3,661	3,661
Sodium-bearing waste after treatment by fluidized bed steam reforming	0	721	721
Vitrified Cs/Sr capsules	0	453	453
West Valley Demonstration Project vitrified HLW	245	0	245
Treated sodium-bonded fuel (electrometallurgical treatment)	0	132	132
Federal Republic of Germany HLW glass	3	0	3
Total	100,681	116,641	217,332

Note: Table assumes constant nuclear power generation in commercial reactors. For simplicity, all DOE SNF is shown as "existing," although approximately 3,500 m³ of naval SNF remains to be generated. In addition, all the waste from electrometallurgical treatment of Na-bonded fuel is shown as "projected" even though a small quantity was generated during demonstration of the treatment process.

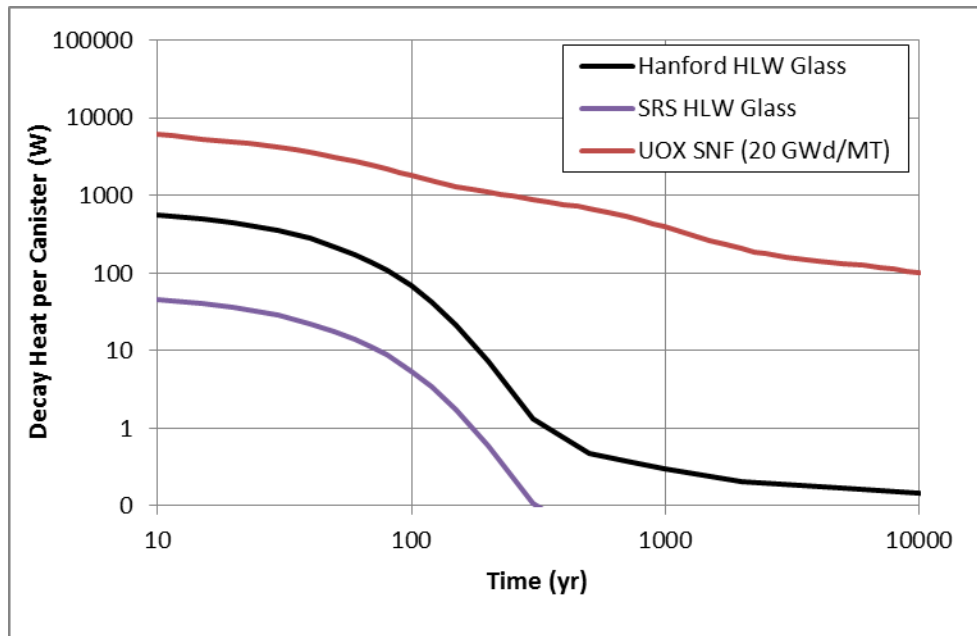


Figure 12. Projected waste decay heat per canister for Hanford HLW glass, SRS HLW glass, and UOX SNF (20 GWd/MT burnup; 21-PWR assemblies). These projections were computed based on inventory decay energy information given in Miller (2004).

The lower thermal loads for HLW glass relative to commercial spent fuel through at least 10,000 years of the post-closure period indicate a low impact to the long-term radionuclide isolation performance of a repository in clay/shale/argillaceous rock. Therefore, the work developed in this work package and documented in this section of the report also applies to the disposition of DOE-Managed HLW and SNF in clay rock environments that are not particularly affected by thermal issues concerning heat-generating nuclear waste.

5. Concluding Remarks

Reactive (diffusive) transport phenomena and reaction path modeling are valuable tools to evaluate the effects of chemical reactions key to EBS and NS interfaces. This modeling effort is informed by experimental studies on hydrothermal interactions of clay with other barrier materials. This model-experiment synthesis and cross-fertilization provides key observations on the geochemical behavior of barrier materials:

- Heterogeneous chemical reactions at interfaces can be localized to unstable phases in bentonite and are accompanied with porosity changes (enhancement/reduction). The resulting of these processes can limit mass fluxes in the near-field environment.
- Experimental observations and thermodynamic modeling predictions suggest clay phases in bentonite will be relatively stable over a wide range of temperatures. Zeolite parageneses should be related to localized pre-existing zeolite (e.g., clinoptilolite) and glass remnants in bentonite to produce analcime and silica phases. The latter two phases exert control on aqueous silica at elevated temperatures.
- Porosity reduction through mineral precipitation may lead to localized compartmentalization of fluids at barrier interfaces. This could also lead to a decrease in diffusive transport and consequently towards a chemically closed system in the long-term.

Figure 13 shows an expanded version of the chronological evolution of thermal-chemical processes relevant to barrier performance in a clay/shale/argillite repository. Hydrological and mechanical processes are omitted for simplicity. The temporal extents of the chemical processes outlined in this figure are roughly based on their expected predominance during the thermal pulse. The timing is also highly uncertain since it can be specific to mineral types and relative abundances, and solution chemistries. However, it still provides a reasonable picture of key chemical processes affecting the EBS. The current 1D reactive-transport model is relatively simple with a limited set of mineral phases but it demonstrates the capability to examine these processes. This model will be expanded to larger mineral assemblages, thermal regimes, and solution chemistries. Once the stability of coupled chemical and transport aspect are attained, the model can be expanded to higher dimensions if necessary.

5.1 Proposed Research Outlook for FY16

Some extension of the current work on the reference case for disposal in clay/shale/argillite by the GDSA PA work package is anticipated. Factors influencing repository design and variations in layout due to radionuclide releases and thermal considerations will be assessed in the future. This effort is part of the integration between the GDSA PA and disposal in argillite work packages. 3D Evaluation of thermal limits with a detailed EBS representation using the Albany FEM code will continue.

1D reactive-transport modeling at the scale of the EBS using PFLOTRAN is a powerful tool to evaluate the effects of diffusive reaction fronts at EBS interfaces. This work should be expanded to examine the following:

- Evaluation of the chemical effects of waste package degradation on the adopted reactive transport modeling scheme. This includes an analysis of reaction product phases to be considered along with details on the adequate kinetic and transport representation.
- Temperature effects: Conduct isothermal runs above-ambient and in excess of 100°C. Also conduct simulations capturing heat decay from the waste form to evaluate thermal effects at spatio-temporal scales relevant to repository performance.
- Re-saturation: A reactive-transport model evaluating different boundary conditions for EBS re-saturation coupled with chemical effects.
- Effects of cement chemistry: Look into the effect of varying cementitious components in the liner (e.g., CSH types) along with their relative amounts in the cement mix.
- Porosity reduction or clogging: Explore further the effects of mineral precipitation on porosity reduction and transport at EBS interfaces.

Thermodynamic evaluation of barrier clay interactions and reaction path modeling will encompass the following:

- Sensitivity analyses on aqueous species activities to evaluate stability relations of co-existing mineral assemblages. This also includes the effects of mineral inclusion and suppressions to assess localized mineral parageneses.
- Comparisons between modeling and experimental data generated from activities in this work will be conducted as validation but also as guidance in developing a robust mechanistic picture of processes affecting barrier performance. For example, the compositional characterization of zeolite (wairakite, analcime) in the experimental work described in Part III of this report demonstrates the importance of solid solutions in the alteration mineral mineral assemblage at elevated temperatures. Work on how mineral solid solutions affect their overall stability relations is anticipated.
- The above-mentioned efforts will cross-fertilize with thermodynamic database development work jointly with staff from LLNL.

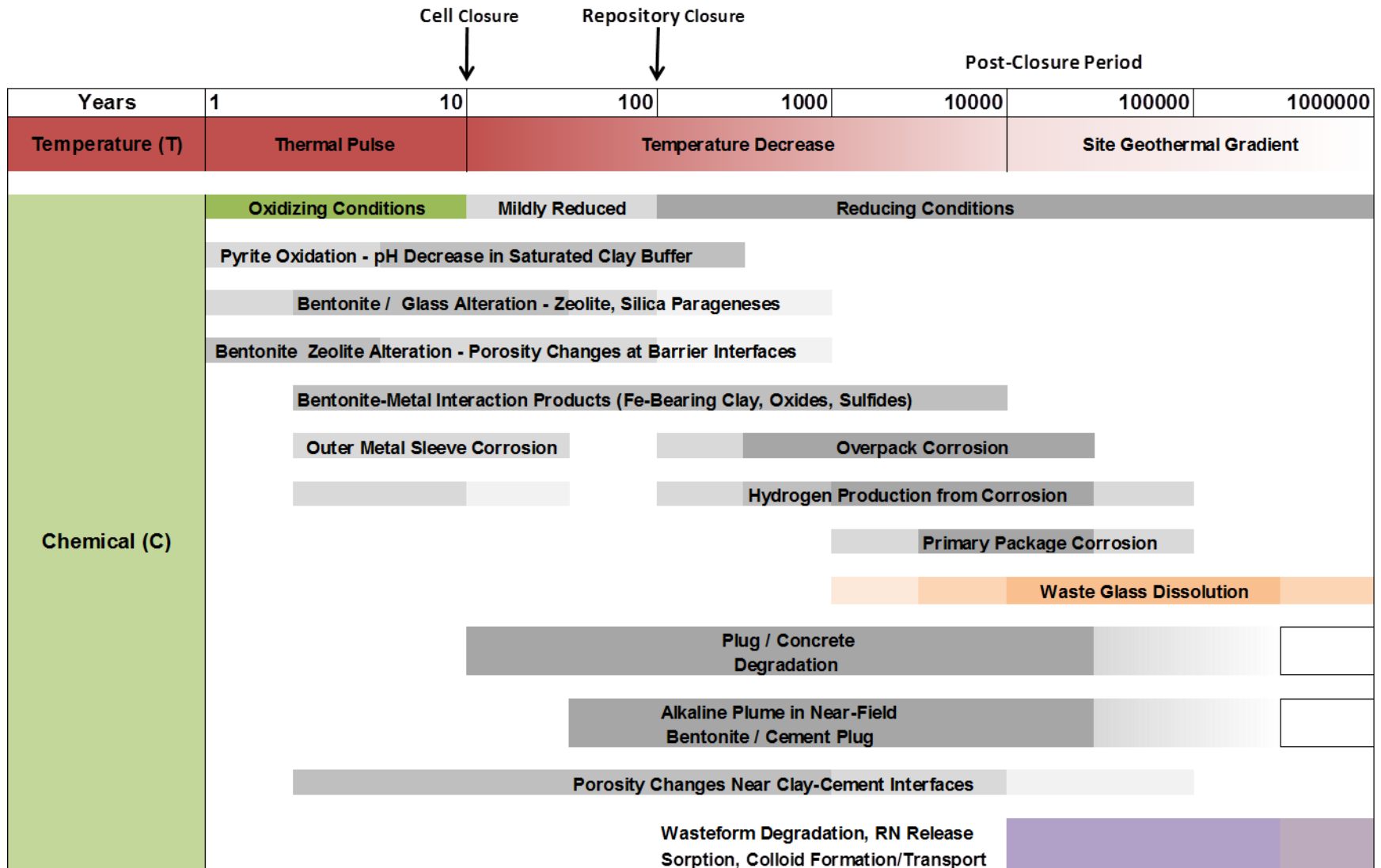


Figure 13. Chronological evolution of Thermal-Chemical processes in a shale/argillite repository (modified after Jové Colón et al., 2014). Hydrological and mechanical processes are not shown for simplicity.

6. References

- Amram, K., and Ganor, J., 2005, The combined effect of pH and temperature on smectite dissolution rate under acidic conditions: *Geochimica et Cosmochimica Acta*, v. 69, no. 10, p. 2535-2546.
- ANDRA, 2005, "Dossier 2005 Argile", Tome: Evaluation of the feasibility of a geological repository in an argillaceous formation. Andra Report Series.
- Baur, I., Keller, P., Mavrocordatos, D., Wehrli, B., and Johnson, C. A., 2004, Dissolution-precipitation behaviour of ettringite, monosulfate, and calcium silicate hydrate: *Cement and Concrete Research*, v. 34, no. 2, p. 341-348.
- Berner, U., Kulik, D. A., and Kosakowski, G., 2013, Geochemical impact of a low-pH cement liner on the near field of a repository for spent fuel and high-level radioactive waste: *Physics and Chemistry of the Earth, Parts A/B/C*, v. 64, no. 0, p. 46-56.
- Bianchi, M., H.-H., Liu, and J. T. Birkholzer. (2013). Diffusion Modeling in a Clay Repository: FY13 Report. . FCRD-UFD-2013-000228 Report, Lawrence Berkeley National Laboratory, Berkeley, USA.
- Bianchi, M., H.-H., Liu, and J. T. Birkholzer. (2014). Radionuclide Transport Behavior in a Generic Geological Radioactive Waste Repository. *Groundwater*. doi: 10.1111/gwat.12171.
- Blanc, P., Lassin, A., Piantone, P., Azaroual, M., Jacquemet, N., Fabbri, A., and Gaucher, A., 2012, Thermodem: A geochemical database focused on low temperature water/rock interactions and waste materials: *Applied Geochemistry*, v. 27, p. 2107-2116.
- Blanc, P., Piantone, P., Lassin, A., and Burnol, A., 2006, Thermochimie : Sélection de constantes thermodynamiques pour les éléments majeurs, le plomb et le cadmium, Rapport final BRGM/RP-54902-FR: France, BRGM, p. 157.
- Boggs, S., 2006, Principles of Sedimentology and Stratigraphy, Pearson Prentice Hall.
- Boudreau, B. P., 1996, The diffusive tortuosity of fine-grained unlithified sediments: *Geochimica Et Cosmochimica Acta*, v. 60, no. 16, p. 3139-3142.
- Cheshire, M., Caporuscio, F. A., Rearick, M. S., Jové Colón, C. F., and McCarney, M. K., 2014, Bentonite evolution at elevated pressures and temperatures: An experimental study for generic nuclear repository designs: *American Mineralogist*, v. 99, p. 1662-1675.
- Dauzeres, A., Le Bescop, P., Sardini, P., and Coumes, C. C. D., 2010, Physico-chemical investigation of clayey/cement-based materials interaction in the context of geological waste disposal: Experimental approach and results: *Cement and Concrete Research*, v. 40, no. 8, p. 1327-1340.
- Dick, J. M., 2008, Calculation of the relative metastabilities of proteins using the CHNOSZ software package: *Geochemical Transactions*, v. 9, no. 10.
- Gaboreau, S., Lerouge, C., Dewonck, S., Linard, Y., Bourbon, X., Fialips, C. I., Mazurier, A., Pret, D., Borschneck, D., Montouillout, V., Gaucher, E. C., and Claret, F., 2012, In-Situ Interaction of Cement Paste and Shotcrete with Claystones in a Deep Disposal Context: *American Journal of Science*, v. 312, no. 3, p. 314-356.

- Gailhanou, H., Blanc, P., Rogez, J., Mikaelian, G., Horiuchi, K., Yamamura, Y., Saito, K., Kawaji, H., Warmont, F., and Grenèche, J.-M., 2013, Thermodynamic properties of saponite, nontronite, and vermiculite derived from calorimetric measurements: *American Mineralogist*, v. 98, no. 10, p. 1834-1847.
- Gailhanou, H., Blanc, P., Rogez, J., Mikaelian, G., Kawaji, H., Olives, J., Amouric, M., Denoyel, R., Bourrelly, S., Montouillout, V., Vieillard, P., Fialips, C. I., Michau, N., and Gaucher, E. C., 2012, Thermodynamic properties of illite, smectite and beidellite by calorimetric methods: Enthalpies of formation, heat capacities, entropies and Gibbs free energies of formation: *Geochimica Et Cosmochimica Acta*, v. 89, p. 279-301.
- Gailhanou, H., van Miltenburg, J. C., Rogez, J., Olives, J., Amouric, M., Gaucher, E. C., and Blanc, P., 2007, Thermodynamic properties of anhydrous smectite MX-80, illite IMt-2 and mixed-layer illite-smectite ISCz-1 as determined by calorimetric methods. Part I: Heat capacities, heat contents and entropies: *Geochimica Et Cosmochimica Acta*, v. 71, no. 22, p. 5463-5473.
- Giles, D. E., Ritchie, I. M., and Xu, B. A., 1993, The Kinetics of Dissolution of Slaked Lime: *Hydrometallurgy*, v. 32, no. 1, p. 119-128.
- Golubev, S. V., Bauer, A., and Pokrovsky, O. S., 2006, Effect of pH and organic ligands on the kinetics of smectite dissolution at 25 degrees C: *Geochimica Et Cosmochimica Acta*, v. 70, no. 17, p. 4436-4451.
- Golubev, S. V., Benezeth, P., Schott, J., Dandurand, J. L., and Castillo, A., 2009, Siderite dissolution kinetics in acidic aqueous solutions from 25 to 100 degrees C and 0 to 50 atm pCO(2): *Chemical Geology*, v. 265, no. 1-2, p. 13-19.
- Gonzales, S. and K.S. Johnson, (1984). Shale and other argillaceous strata in the United States. Oak Ridge National Laboratory. ORNL/Sub/84-64794/1.
- González Sánchez, F., Van Loon, L. R., Gimmi, T., Jakob, A., Glaus, M. A., and Diamond, L. W., 2008, Self-diffusion of water and its dependence on temperature and ionic strength in highly compacted montmorillonite, illite and kaolinite: *Applied Geochemistry*, v. 23, no. 12, p. 3840-3851.
- Hansen, F.D., E.L. Hardin, R. P. Rechar, G. A. Freeze, D.C. Sassani, P.V. Brady, C. M. Stone, M. J. Martinez, J. F. Holland, T. Dewers, K.N. Gaither, S. R. Sobolik, and R. T. Cygan, 2010, Shale Disposal of U.S. High-Level Radioactive Waste. SAND2010-2843. Albuquerque, NM: Sandia National Laboratories.
- Hardin, E., T. Hadgu, D. Clayton, R. Howard, H. Greenberg, J. Blink, M. Sharma, M. Sutton, J. Carter, M. Dupont, and P. Rodwell, 2012, Repository Reference Disposal Concepts and Thermal Load Management Analysis. FCRD-UFD-2012-000219 Rev. 2. U.S. Department of Energy, Office of Used Nuclear Fuel Disposition, Washington, DC.
- Holland, T. J. B., and Powell, R., 2011, An improved and extended internally consistent thermodynamic dataset for phases of petrological interest, involving a new equation of state for solids: *Journal of Metamorphic Geology*, v. 29, p. 333-383.
- Huertas, F. J., Caballero, E., de Cisneros, C. J., Huertas, F., and Linares, J., 2001, Kinetics of montmorillonite dissolution in granitic solutions: *Applied Geochemistry*, v. 16, no. 4, p. 397-407.

- Jeschke, A. A., Vosbeck, K., and Dreybrodt, W., 2001, Surface controlled dissolution rates of gypsum in aqueous solutions exhibit nonlinear dissolution kinetics: *Geochimica Et Cosmochimica Acta*, v. 65, no. 1, p. 27-34.
- Joseph, C., Schmeide, K., Sachs, S., Brendler, V., Geipel, G., and Bernhard, G., 2011, Sorption of uranium(VI) onto Opalinus Clay in the absence and presence of humic acid in Opalinus Clay pore water: *Chemical Geology*, v. 284, no. 3-4, p. 240-250.
- Joseph, C., Van Loon, L. R., Jakob, A., Steudtner, R., Schmeide, K., Sachs, S., and Bernhard, G., 2013, Diffusion of U(VI) in Opalinus Clay: Influence of temperature and humic acid: *Geochim. Cosmochim. Acta*, v. 109, p. 74-89.
- Jové Colón, C. F., Greathouse, J. A., Teich-McGoldrick, S., Cygan, R. T., Weck, P. F., Hansen, G. A., Criscenti, L. J., Caporuscio, F. A., Cheshire, M., Rearick, M. S., McCarney, M. K., Greenberg, H. R., Wolery, T. J., Sutton, M., Zavarin, M., Kersting, A. B., Begg, J. B., Blink, J. A., Buscheck, T., Benedicto-Cordoba, A., Zhao, P., Rutqvist, J., Steefel, C. I., Birkholzer, J., Liu, H.-H., Davis, J. A., Tinnacher, R., Bourg, I., Zheng, L., and Vilarrasa, V., 2013, EBS Model Development and Evaluation Report (FCRD-UFD-2013-000312): Albuquerque, NM, Sandia National Laboratories, SAND2013-8512 P, p. 508.
- Jové Colón, C. F., Weck, P. F., Sassani, D. C., Zheng, L., Rutqvist, J., Steefel, C. I., Kim, K., Nakagawa, S., Houseworth, J., Birkholzer, J., Caporuscio, F. A., Cheshire, M., Rearick, M. S., McCarney, M. K., Zavarin, M., Benedicto-Cordoba, A., Kersting, A. B., Sutton, M., Jerden, J. L., Frey, K. E., Copple, J. M., and Ebert, W. L., 2014, Evaluation of Used Fuel Disposition in Clay-Bearing Rock (FCRD-UFD-2014-000056): Albuquerque, NM, Sandia National Laboratories, SAND2014-18303 R, p. 434.
- Kohler, S. J., Dufaud, F., and Oelkers, E. H., 2003, An experimental study of illite dissolution kinetics as a function of pH from 1.4 to 12.4 and temperature from 5 to 50 degrees C: *Geochimica Et Cosmochimica Acta*, v. 67, no. 19, p. 3583-3594.
- Kosakowski, G., and Berner, U., 2013, The evolution of clay rock/cement interfaces in a cementitious repository for low- and intermediate level radioactive waste: *Physics and Chemistry of the Earth*, v. 64, p. 65-86.
- Kozai, N., Inada, K., Kozaki, T., Sato, S., Ohashi, H., and Banba, T., 2001, Apparent diffusion coefficients and chemical species of neptunium (V) in compacted Na-montmorillonite: *Journal of Contaminant Hydrology*, v. 47, no. 2-4, p. 149-158.
- Kozaki, T., Inada, K., Sato, S., and Ohashi, H., 2001, Diffusion mechanism of chloride ions in sodium montmorillonite: *Journal of Contaminant Hydrology*, v. 47, no. 2-4, p. 159-170.
- Lichtner, P. C., Hammond, G. E., Lu, C., Karra, S., Bisht, G., Andre, B., Mills, R. T., and Kumar, J., 2013, PFLOTRAN User Manual: <http://www.pflotran.org>.
- Mariner, P.E., W.P. Gardner, G.E. Hammond, D. Sevougian, and E. Stein, Application of Generic Disposal System Models (FCRD-UFD-2015-000126), 2015, Sandia National Laboratories: Albuquerque, NM.
- Marty, N. C., Bildstein, O., Blanc, P., Claret, F., Cochapin, B., Gaucher, E. C., Jacques, D., Lartigue, J.-E., Liu, S., and Mayer, K. U., 2015, Benchmarks for multicomponent reactive transport across a cement/clay interface: *Computational Geosciences*, p. 1-19.

- Marty, N. C. M., Fritz, B., Clement, A., and Michau, N., 2010, Modelling the long term alteration of the engineered bentonite barrier in an underground radioactive waste repository: *Applied Clay Science*, v. 47, no. 1-2, p. 82-90.
- Marty, N. C. M., Tournassat, C., Burnol, A., Giffaut, E., and Gaucher, E. C., 2009, Influence of reaction kinetics and mesh refinement on the numerical modelling of concrete/clay interactions: *Journal of Hydrology*, v. 364, no. 1-2, p. 58-72.
- Mazurek, M., F.J. Pearson, G. Volckaert, and H. Bock, Features, Events and Processes Evaluation Catalogue for Argillaceous Media, (2003). Organisation for Economic Co-operation and Development (OECD) - Nuclear Energy Agency (NEA): Paris, France. 379 pp.
- Miller, H., 2004, Initial Radionuclide Inventories (ANL-WIS-MD-000020 REV 01): Las Vegas, Nevada, Bechtel SAIC Company, LLC, U.S. Department of Energy, Office of Civilian Radioactive Waste Management, Office of Repository Development, p. 178.
- Montes-H, G., Marty, N., Fritz, B., Clement, A., and Michau, N., 2005, Modelling of long-term diffusion-reaction in a bentonite barrier for radioactive waste confinement: *Applied Clay Science*, v. 30, no. 3-4, p. 181-198.
- NAGRA (2002) Project Opalinus Clay: safety report. Demonstration of disposal feasibility for spent fuel, vitrified high-level waste and long-lived intermediate level waste (Entsorgungsnachweis). Nagra Technical Report NTB 02-05, Wettingen, Switzerland.
- Neuhoff, P. S., Hovis, G. L., Balassone, G., and Stebbins, J. F., 2004, Thermodynamic properties of analcime solid solutions: *American Journal of Science*, v. 304, no. 1, p. 21-66.
- Neuhoff, P. S., and Ruhl, L. S., 2006, Mechanisms and geochemical significance of Si-Al substitution in zeolite solid solutions: *Chemical Geology*, v. 225, no. 3-4, p. 373-387.
- Neuzil, C. (2013). Can Shale Safely Host US Nuclear Waste? *Eos, Transactions American Geophysical Union* 94(30): 261-262.
- Pokrovsky, O. S., Golubev, S. V., Schott, J., and Castillo, A., 2009, Calcite, dolomite and magnesite dissolution kinetics in aqueous solutions at acid to circumneutral pH, 25 to 150 degrees C and 1 to 55 atm pCO₂: New constraints on CO₂ sequestration in sedimentary basins: *Chemical Geology*, v. 265, no. 1-2, p. 20-32.
- Pusch, R., Takase, H., and Benbow, S., 1998, Chemical processes causing cementation in heat-affected smectite-the Kinnekulle bentonite, *Svensk Kärnbränslehantering*.
- Rimstidt, J. D., 1997, Quartz solubility at low temperatures: *Geochimica Et Cosmochimica Acta*, v. 61, no. 13, p. 2553-2558.
- Rutqvist, J., L. Zheng, F. Chen, H.-H. Liu and J. Birkholzer, 2014a, Modeling of Coupled Thermo-Hydro-Mechanical Processes with Links to Geochemistry Associated with Bentonite-Backfilled Repository Tunnels in Clay Formations. *Rock Mechanics and Rock Engineering* 47(1): 167-186.
- Sanchez, L., Cuevas, J., Ramirez, S., De Leon, D. R., Fernandez, R., Dela Villa, R. V., and Leguey, S., 2006, Reaction kinetics of FEBEX bentonite in hyperalkaline conditions resembling the cement-bentonite interface: *Applied Clay Science*, v. 33, no. 2, p. 125-141.

- Savage, D., 2011, A review of analogues of alkaline alteration with regard to long-term barrier performance: *Mineralogical Magazine*, v. 75, no. 4, p. 2401-2418.
- Shurr, G.W., 1977, The Pierre Shale, Northern Great Plains; A Potential Isolation Medium for Radioactive Waste. United States Geological Survey Open File Report 77-776.
- SNL, 2014, Evaluation of Options for Permanent Geologic Disposal of Spent Nuclear Fuel and High-Level Radioactive Waste in Support of a Comprehensive National Nuclear Fuel Cycle Strategy (FCRD-UFD-2015-000125), Volume I: Albuquerque, NM, Sandia National Laboratories, p. 302.
- Soler, J. M., 2012, High-pH plume from low-alkali-cement fracture grouting: Reactive transport modeling and comparison with pH monitoring at ONKALO (Finland): *Applied Geochemistry*, v. 27, no. 10, p. 2096-2106.
- Soler, J. M., and Mader, U. K., 2010, Cement-rock interaction: Infiltration of a high-pH solution into a fractured granite core: *Geologica Acta*, v. 8, no. 3, p. 221-233.
- Tagirov, B., and Schott, J., 2001, Aluminum speciation in crustal fluids revisited: *Geochimica Et Cosmochimica Acta*, v. 65, no. 21, p. 3965-3992.
- Trotignon, L., Peycelon, H., and Bourbon, X., 2006, Comparison of performance of concrete barriers in a clayey geological medium: *Physics and Chemistry of the Earth*, v. 31, no. 10-14, p. 610-617.
- Turrero, M., Fernández, A., Peña, J., Sánchez, M., Wersin, P., Bossart, P., Sánchez, M., Melón, A., Garralón, A., and Yllera, A., 2006, Pore water chemistry of a Paleogene continental mudrock in Spain and a Jurassic marine mudrock in Switzerland: Sampling methods and geochemical interpretation: *Journal of Iberian Geology*, v. 32, no. 2, p. 233-258.
- Tutolo, B. M., Kong, X.-Z., Seyfried, W. E., Jr., and Saar, M. O., 2014, Internal consistency in aqueous geochemical data revisited: Applications to the aluminum system: *Geochimica et Cosmochimica Acta*, v. 133, p. 216-234.
- Van Loon, L. R., Soler, J. M., and Bradbury, M. H., 2003, Diffusion of HTO, $^{36}\text{Cl}^-$ and $^{125}\text{I}^-$ in Opalinus Clay samples from Mont Terri: Effect of confining pressure: *Journal of Contaminant Hydrology*, v. 61, no. 1-4, p. 73-83.
- Wersin, P., Johnson, L. H., and McKinley, I. G., 2007, Performance of the bentonite barrier at temperatures beyond 100°C: A critical review: *Physics and Chemistry of the Earth*, v. 32, no. 8-14, p. 780-788.
- White, A. F., Peterson, M. L., and Hochella, M. F., 1994, Electrochemistry and Dissolution Kinetics of Magnetite and Ilmenite: *Geochimica Et Cosmochimica Acta*, v. 58, no. 8, p. 1859-1875.
- Williamson, M. A., and Rimstidt, J. D., 1994, The Kinetics and Electrochemical Rate-Determining Step of Aqueous Pyrite Oxidation: *Geochimica Et Cosmochimica Acta*, v. 58, no. 24, p. 5443-5454.
- Wilson, J. C., Benbow, S., Sasamoto, H., Savage, D., and Watson, C., 2015, Thermodynamic and fully-coupled reactive transport models of a steel-bentonite interface: *Applied Geochemistry*.

- Wolery, T. J., and Jarek, R. L., 2003, EQ3/6, Version 8.0: Software User's Manual: Sandia National Laboratories.
- Xie, M. L., Mayer, K. U., Claret, F., Alt-Epping, P., Jacques, D., Steefel, C., Chiaberge, C., and Simunek, J., 2015, Implementation and evaluation of permeability-porosity and tortuosity-porosity relationships linked to mineral dissolution-precipitation: Computational Geosciences, v. 19, no. 3, p. 655-671.
- Zheng, L., James Houseworth, Carl Steefel, Jonny Rutqvist, Jens Birkholzer (2014), Investigation of Coupled Processes and Impact of High Temperature Limits in Argillite Rock. FCRD-UFD-2014-000493, U.S. Department of Energy, Washington DC.

**Investigation of Coupled Processes and Impact of High Temperature Limits in
Argillite Rock
(Part II)**

1. Introduction

Shale and clay-rich geological formations have been considered as potential host rock for geological disposal of high-level radioactive waste throughout the world, because of their low permeability, low diffusion coefficient, high retention capacity for radionuclides, and capability to self-seal fractures. The low permeability of clay and shale rock are well-known in the hydrogeology community where these rock types represent aquitards that severely limit groundwater movement, and in petroleum geology, where they act as caprocks limiting the rise of buoyant petroleum fluids. While fractures can occur, clay and shale often demonstrate the tendency to self-seal fractures, which reduces the effects of fractures on bulk permeability. Other favorable characteristics of clay/shale rock are the strong sorptive behavior for many radionuclides, reducing conditions because of the lack of oxygen transport from the surface, and chemical buffering of introduced materials.

A large body of information concerning the behavior of clay/shale geologic environments using bentonite backfill/buffers for nuclear waste disposal has been developed through the repository programs with underground research laboratories in Switzerland, France, Belgium, and Japan. Here we document modeling of tests conducted at Switzerland's Mont Terri underground rock laboratory and the Horonobe underground research laboratory in Japan.

The focus of research within the UFD Campaign is on repository-induced interactions that may affect the key safety characteristics of an argillaceous rock. These include thermal-hydrological-mechanical-chemical (THMC) process interactions that occur as a result of repository construction and waste emplacement. Some of the key questions addressed in this part of the report include the development of fracturing in the excavation damaged zone (EDZ) and THMC effects on the near-field argillaceous rock and buffer minerals and petrophysical characteristics, particularly the impacts of induced temperature rise caused by waste heat.

Within the Natural Barrier System (NBS) group of the Used Fuel Disposition (UFD) Campaign at the Department of Energy's (DOE) Office of Nuclear Energy, LBNL's research activities have focused on understanding and modeling EDZ evolution and the associated coupled processes, and impacts of high temperature on parameters and processes relevant to performance of a clay repository to establish the technical base for the maximum allowable temperature. This work documents results from some of these activities. These activities address key Features, Events and Processes (FEPs), which have been ranked in importance from medium to high, as listed in Table 7 of the *Used Fuel Disposition Campaign Disposal Research and Development Roadmap* (FCR&D-USED-2011-000065 REV0) (Nutt, 2011). Specifically, they address FEP 2.2.01, Excavation Disturbed Zone, for clay/shale, by investigating how coupled processes affect EDZ evolution; FEP 2.2.05, Flow and Transport Pathways; and FEP 2.2.08, Hydrologic Processes, and FEP 2.2.07, Mechanical Processes and FEP 2.2.09, Chemical Process—Transport, by studying near-field coupled THMC processes in clay/shale repositories. The activities documented in this part of the report also address a number of research topics identified in *Research & Development (R&D) Plan for Used Fuel Disposition Campaign (UFDC) Natural System Evaluation and Tool Development* (Wang, 2011), including Topics S3, Disposal system modeling – Natural system; P1, Development of discrete fracture network (DFN) model; P14, Technical basis for thermal loading limits; and P15 Modeling of disturbed rock zone (DRZ) evolution (clay repository).

This part of the report documents the following research activities:

- Section 2 presents the development and application of thermal-hydrological-mechanical-chemical (THMC) modeling capabilities to assess engineering-barrier-system (EBS) responses to different temperatures and pressures, and to evaluate impacts of the interaction between EBS and host rocks. Model results are presented that help to understand the impact of high temperatures on the properties and behavior of clay.
- Section 3 presents a pre-test modeling exercise for the FEBEX-DP dismantling experiment. This has been done using THMC predictive modeling of the FEBEX EBS response after almost two decades of heating, prior to the actual dismantling.
- Section 4 presents THM modeling for the FE heater tests at Mont Terri, Switzerland. THM modeling of the FE Heater test was performed using TOUGH-FLAC simulator. The Full-Scale Emplacement Experiment (FE) at the Mont Terri site, Switzerland is one of the largest and longest-duration heater tests worldwide. The analyses have been used to calibrate clay properties by modeling lab tests and through model-result comparisons with other teams. THM modeling is also presented for the HE-E heater test at Mont Terri and the Horonobe EBS experiment as part of the DECOVALEX tasks for this year. Modeling of the Mont Terri HE-E Experiment and the EBS Horonobe experiment are compared with results from international modeling teams.
- Section 5 presents the development of a THM fracture damage model for investigating coupled processes in the EDZ. Simulations of fracturing for a laboratory experiment on hydraulic fracturing are presented. Issues concerning the effects of boundary conditions and computational efficiency are identified along with the potential resolution of these issues through the development of a dynamic discrete fracture damage model.
- Section 6 summarizes the main research accomplishments for FY 2015 and proposes future work activities.

2. Investigation of the Impacts of High Temperature Limits with THMC Modeling

2.1 Introduction

Radioactive waste from spent fuel emanates a significant amount of thermal energy due to decay processes, which causes temperature increases in the surrounding environment particularly in the early stages of waste emplacement. The temperature to which the EBS (engineered barrier system) and natural rock can be exposed is one of the most important design variables for a geological repository, because it determines waste package spacing, distance between disposal galleries, and therefore the overall size (and cost) of repository for a given amount of heat-emitting waste (Horseman and McEwen, 1996). This is especially important for a clay repository, because argillaceous rocks have relatively small heat conductivity. All disposal concepts throughout the world, despite their differences in design concepts, unanimously impose a temperature limit of about 100 °C (Hicks et al., 2009). Chemical alteration and the subsequent changes in mechanical properties are among the determining factors. A high temperature could result in chemical alteration of buffer and backfill materials (bentonite) within the EBS through illitization and cementation, which compromise the function of these EBS components by reducing their plasticity and capability to swell when wetting (Pusch and Karnland, 1996; Pusch et al., 2010; Wersin et al., 2007). The swelling capability of clay minerals within the bentonite is important for sealing gaps between bentonite blocks, between bentonite and other EBS components, and between the EBS and the surrounding host rock. Chemical alteration may also occur in the near-field host rock, which could reduce the clay capability for self-sealing within the excavation damaged zone (EDZ). Because the permeability of clay rock is low, a high temperature may induce significant pore pressure build-up (through pore water expansion and vaporization) in the near field, which could generate adverse mechanical deformation (such as fracturing), damaging the integrity of the host rock (Horseman and McEwen, 1996).

Regarding the concern of chemical alteration and the associated mechanical changes, Wersin et al. (2007), after reviewing a number of data sets, concluded that the criterion of 100°C for the maximum temperature within the bentonite buffer is overly conservative. Their conclusion was based on their findings that no significant changes in bentonite hydraulic properties occur at temperatures of up to 120°C under wet conditions and that bentonite is chemically stable to much higher temperature under dry conditions. The impact of a high temperature on bentonite and clay host rock behavior, and the consequences on repository performance, are largely open questions for a clay repository system. While various studies shed light on certain aspects of this question, there is no study that integrates the relevant THMC processes and considers the interaction between EBS and host rock.

Since FY13, in UFDC, LBNL has used coupled THMC modeling to evaluate the chemical alteration and mechanical changes in EBS bentonite and the NS (natural system) clay formation under various scenarios, attempting to provide necessary information for decisions on temperature limits. In the FY13 report (Liu et al., 2013), after an extensive review of the THMC alteration of EBS and argillite under various temperature conditions, fully coupled THMC simulations were developed for a nuclear waste repository in a clay formation with a bentonite-backfilled EBS. Two scenarios were simulated for comparison: a case in which the temperature in the bentonite near the waste canister can reach about 200°C and a case in which the

temperature in the bentonite near the waste canister peaks at about 100°C. In these simulations, it was assumed that the EBS bentonite was Kunigel-VI bentonite (Ochs et al., 2004) and that the host rock properties were representative of Opalinus Clay (Bossart 2011; Lauber et al., 2000). Simulations showed that the decrease in smectite volume fraction in bentonite ranges from 0.004 to a maximum of 0.085, or up to about 27% of the initial volume fraction of smectite for the 200 °C scenario in 1,000 years. This decrease in smectite volume fraction led to a reduction in swelling stress ranging from 16-27%, subject to a great deal of variation depending on smectite volume fraction and swelling pressure under different chemical conditions. In FY14, we continued to analyze more scenarios based on Kunigel-VI bentonite, including sensitivity analyses to key mechanical-chemical coupling parameters. In addition, THMC models were developed for FEBEX (ENRESA, 2000) bentonite, which differs from Kunigel-VI bentonite in terms of the content of smectite and swelling pressure. By comparing the model results for Kunigel-VI and FEBEX bentonite, we found out the illitization is enhanced at high temperature for both bentonites. However, the magnitude of illitization varies a great deal and has to be evaluated case by case. During FY15, we continued to improve our modeling capability and refine the model so that we can better understand coupled processes in bentonite and a clay formation. One of the major achievements is the implementation of a time-step management scheme in the TOUGHREACT-FLAC3D simulator, which reduces simulation time and enables us to extend the simulations from 1,000 years to 100,000 years. The simulator was also modified to include chemical-mechanical coupling for a clay formation. We also performed an evaluation of Ca-smectite illitization (in FY13 and FY14, we evaluated Na-smectite illitization), which sheds light on the potential for calcite to interfere with smectite illitization.

2.2 Model Development

Because the model used in this part of the report is similar to that in previous years (Liu et al., 2013; Zheng et al., 2014), we briefly describe each element of the THMC model here, focusing on the updates in FY15. Additional details on the THMC model are presented in Liu et al.(2013).

2.2.1 Simulator

The numerical simulations are conducted with TOUGHREACT-FLAC3D, which sequentially couples the multiphase fluid flow and reactive transport simulator, TOUGHREACT (Xu et al., 2011), with the finite-difference geomechanical code FLAC3D (Itasca, 2009). The coupling of TOUGHREACT and FLAC3D was initially developed in Zheng et al. (2011) to provide the necessary numerical framework for modeling fully coupled THMC processes. It included a linear elastic swelling model (Zheng et al., 2012; Rutqvist et al., 2013) to account for swelling as a result of changes in saturation and pore-water composition and the abundance of swelling clay (Liu et al., 2013; Zheng et al., 2014). The major improvement in TOUGHREACT-FLAC3D is the implementation of a time-step management scheme to reduce the simulation time. Figure 2-1 shows the coupling scheme of TOUGHREACT-FLAC3D. In each time step, TOUGHREACT calculates the primary variables for THC processes including temperature (T), liquid pressure (P_l) or gas pressure (P_g), water saturation (S_l), ion concentrations of pore water (C_i) and concentration of exchangeable cations and/or abundance of swelling clay minerals (X_i). These primary variables are then passed to FLAC3D via a coupling module to conduct stress and strain analysis (see Figure 2-1). The coupling between THC processes (provided by TOUGHREACT)

and the mechanical part (FLAC3D) is carried out at every time step. The FLAC3D stress and strain analysis consumes a large portion of the total computation time. For example, in the base case for FEBEX bentonite described below, a THC run took about 4.5 hours but the THMC runs (which calls FLAC3D at every time step) took about 4 days. The length of time step is constrained by the chemical calculation to accommodate small changes in the concentrations. However, such small changes in chemical conditions lead to very minimal changes in stress and it is unnecessary to update the stress every time step. Therefore, a time step management scheme was implemented in TOUGHREACT-FLAC3D. A subroutine was inserted in TOUGHREACT to check the change of primary variables from the previous time step and decide if the change is large enough to warrant an update in stress/strain based on the predetermined criteria. The choice of criteria is arbitrary. We tested several values and a criterion of 2% reduces computation time significantly and the calculated stress is very close (within 0.1% difference) to that obtained by updating stress/strain every time step.

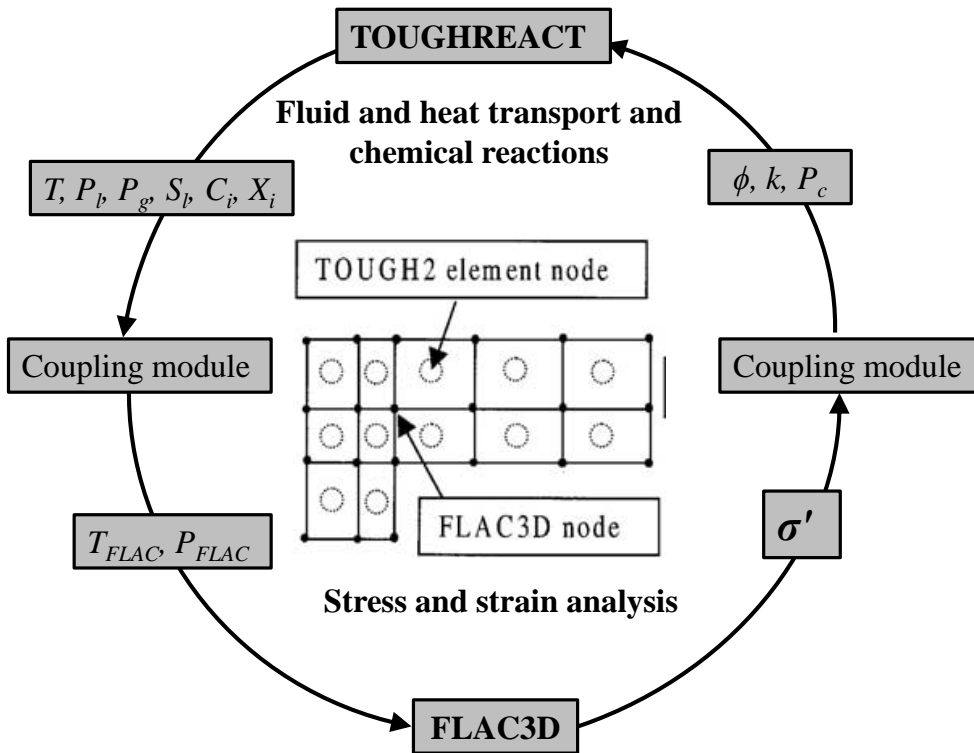


Figure 2-1. The coupling scheme for TOUGHREACT-FLAC3D.

2.2.2 Modeling scenario

The model scenario is still the same as in Liu et al. (2013) and Zheng et al., (2014). The model is applied to a hypothetical bentonite-backfilled nuclear waste repository in clay rock, a repository example that involves a horizontal nuclear waste emplacement tunnel at 500 m depth (Figure 2-2) (Rutqvist et al., 2013). The Z-axis is set as vertical, while the horizontal Y- and X-axes are aligned parallel and perpendicular to the emplacement tunnel, respectively (Figure 2-2) in this 2-D model. Note that while the canister is modeled as a heat source with mechanical properties of

steel, the THC changes in the canister and their interactions with EBS bentonite are not considered here for the sake of simplicity.

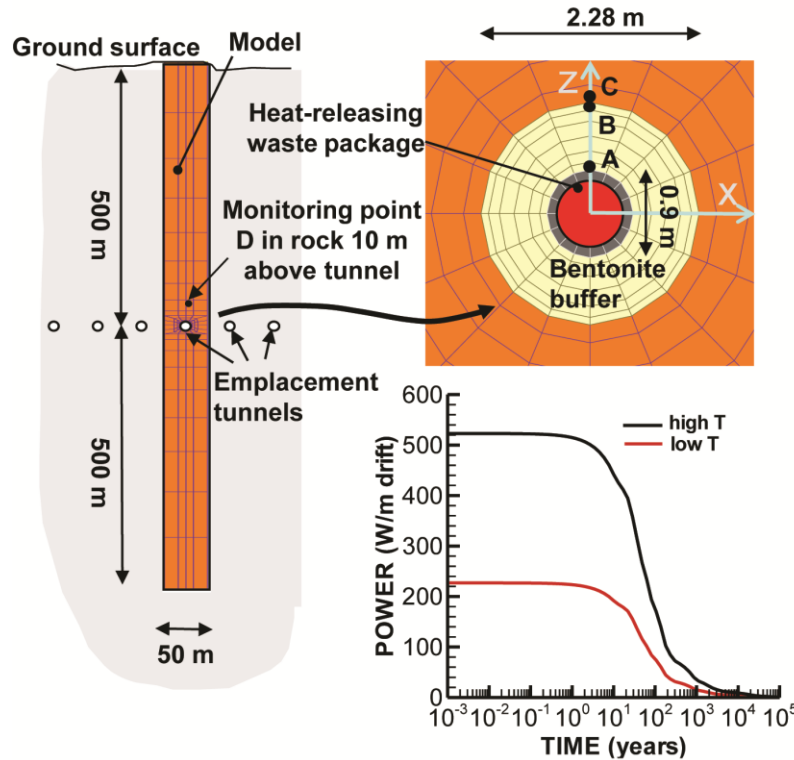


Figure 2-2. Domain for the test example of a bentonite back-filled horizontal emplacement drift at 500 m (Rutqvist et al., 2014). Modeling monitoring points: A: inside the bentonite near the canister, B: inside the bentonite and near the EBS-NS interface, C: inside the clay rock formation and near the EBS-NS interface, D: inside the clay rock formation at a distance of 10 m from the canister. “High T”: 200 °C; “Low T”: 100°C.

An initial stress field is imposed by the self-weight of the rock mass. Zero normal displacements are prescribed on the lateral boundaries of the model. Zero stress is applied to the top and vertical displacements are prevented at the bottom. An open boundary is applied to the liquid pressure at top and bottom and initially the model domain is in a hydrostatic state. The initial temperature at the top is about 11 °C, with a thermal gradient of 27 °C/km, the initial temperature at the bottom is 38 °C. The model simulation was conducted in a nonisothermal mode with a time-dependent heat power input (Rutqvist et al., 2014). The power curve in Figure 2-2 was adopted from representative heating data from the U.S. DOE's Used Fuel Disposition campaign for pressurized water reactor (PWR) used fuel. This heat load is then scaled in the 2-D model to represent an equivalent line load, which depends on the assumed spacing between individual waste packages along an emplacement tunnel. The heat load for the “low-T” case corresponds to an initial thermal power of 3144 W for a 4-PWR-element waste package after aging for 60 years, a 50-m spacing between emplacement tunnels, and 3-m spacing between the 5-m long packages. The heat load for the “high T” case represents similar waste package and spacing, except with only 20 years of aging. Initially the EBS bentonite has a water saturation of 65% and the clay

formation is fully saturated. From time zero, the EBS bentonite undergoes simultaneously re-saturation, heating, chemical alteration, and stress changes.

2.2.3 Mechanical Model

Details of mechanical model implemented in the TOUGHREACT-FLAC3D are given in Rutqvist et al., (2014). Here we briefly describe the mechanical models for the EBS bentonite and clay formation. For nonisothermal behavior of unsaturated soils, we may partition the total incremental strain into elastic (ε^e), plastic(ε^p), suction(ε^s), thermal strains (ε^T)and chemical strains(ε^c):

$$d\varepsilon = d\varepsilon^e + d\varepsilon^p + d\varepsilon^s + d\varepsilon^T + d\varepsilon^c \quad (2-1)$$

where the suction strain represents the strain associated with changes in suction and chemical strain represents the strains associated with change in chemical conditions, including changes in ion concentration and abundance of swelling clays. Each of these types of strain, except chemical strain, is described in Rutqvist et al., (2014).

Similar to thermally induced strains, chemical strains are purely volumetric:

$$d\varepsilon^c = -A_n^* dC + A_{sc}^* dM_s \quad (2-2)$$

where A_n^* is a constant that linearly relates ion concentration (C) variation and the corresponding strain change. A_{sc}^* is a constant that relates the change in mass fraction of swelling clay, m_s , to change in strain.

A linear elastic swelling model essentially defines the suction stress as a function of water saturation:

$$d\varepsilon^s = \beta_{sw} dSl \quad (2-3)$$

where Sl is the water saturation and β_{sw} is a moisture swelling coefficient.

Under mechanically constrained conditions and considering the linear relationship between swelling stress and suction strain, $d\sigma_s = 3Kd\varepsilon^s$, we have a swelling stress that is linearly proportional to the saturation:

$$d\sigma_s = 3K\beta_{sw} dSl \quad (2-4)$$

where K is the bulk modulus. Equation (2-4) is what was used for EBS bentonite in Rutqvist et al. (2011). In this case, the value of β_{sw} is 0.048, calibrated based using the swelling pressure of 1 MPa for Kunigel-VI bentonite (Börgesson et al. 2001) under the condition that bentonite is saturated with dilute solution (e.g. deionized water), and K is 20 MPa (Rutqvist et al., 2011).

To consider the swelling due to both moisture and chemical changes, we include the stress due to a change of ion concentration in the pore water and abundance of swelling clay:

$$d\sigma_s = 3K(d\varepsilon^s + d\varepsilon^c) = 3K(\beta_{sw}dSl + A_n^*dC + A_{sc}^*dMs) = 3K\beta_{sw}dSl + A_ndC + A_{sc}dMs \quad (2-5)$$

where $A_n = 3KA_n^*$ is a constant that linearly relates ion concentration (C) variation and the corresponding swelling stress change. $A_{sc} = 3KA_{sc}^*$ is a constant that relates the change in mass fraction of swelling clay, Ms , to change in swelling stress.

A_n is typically calculated from swelling pressures measured using a different solution (e.g. deionized water versus 1 M NaCl solution) to saturate the bentonite. Laredj et al. (2010) proposed the following expression for A_n :

$$A_n = \frac{(5.312 \ln C - 23.596)}{\sqrt{C}} - \frac{7.252 \times 10^{-4}}{C^2} \quad (2-6)$$

An empirical value for A_{sc} is derived through a linear regression of swelling pressure versus smectite mass fractions as shown in Figure 2-3, and A_{sc} is the slope of the linear correlation. However, probably because these bentonite materials differ not only in the mass fraction of smectite but also in other properties, these data points are fairly scattered. This makes it impossible to establish a unique linear regression between swelling pressure change and mass fraction change of smectite. Therefore, we chose a linear correlation line that crosses the measured swelling pressure for Kunigel VI bentonite and used the slope of this line as the value of A_{sc} which is 2.5×10^6 Pa. For FEBEX bentonite we used the slope of line that crosses the measured swelling pressure of FEBEX bentonite as the value of A_{sc} which is 6.5×10^6 Pa.

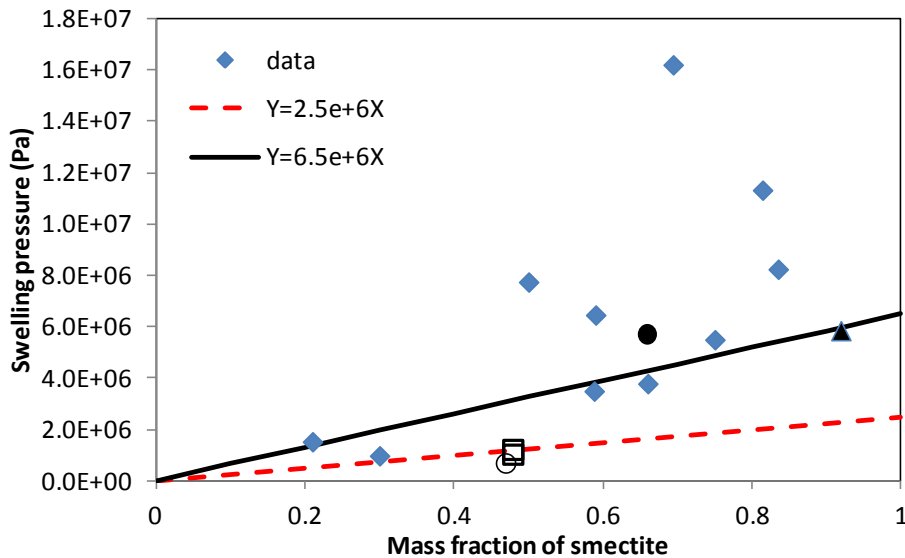


Figure 2-3. Swelling pressure versus mass fraction of smectite for various bentonites. ▲, FEBEX bentonite (ENRESA, 2000); ●, Montigel bentonite (Bucher and Muller-Vonmoos,

1989); □, Kunigel VI bentonite (JNC, 1999); ○, Kunigel bentonite (Komine and Ogata, 1996), ◆ are data for reference material from Czech, Danish, Friedland, Milos Deponit CA-N, Kutch (Indian) and Wyoming MX-80 (Karlund et al., 2006).

More sophisticated and realistic mechanical models are available in the literature and have been successfully used for bentonite and clay formations, such as the state surface approach (e.g. Nguyen et al., 2005) and the dual structure Barcelona Expansive Clay model (Alonso et al., 1999; Sánchez et al., 2005). Here we use a rather simple elastic model because it allows us to incorporate the contribution from the chemical components and parameters and the model can be relatively easily calibrated as discussed above.

For clay formations, we extend the elastic model used in Rutqvist et al., (2014) to consider the chemical strain as in Equation (2-2). The parameters, A_n and A_{sc} , are same as those used for bentonite, with an assumption that compact bentonite and clay rock behave similarly in terms of the effect of chemical change on strain. However, the validity of this assumption needs to be confirmed with more data.

2.2.4 Chemical Model

In these generic cases, it is assumed that the host rock properties are representative of Opalinus Clay (Bossart 2011; Lauber et al., 2000). Two cases are used for the EBS backfill: one is Kunigel-VI bentonite (Ochs et al., 2004) and the other is FEBEX bentonite (ENRESA, 2000). The mineral compositions of the bentonite and clay formation are listed in Table 2-1. The pore-water compositions of the Kunigel-VI bentonite (Sonnenthal et al., 2008), FEBEX bentonite (Fernández et al., 2001) and the clay formation (Fernández et al., 2007) are listed in Table 2-2. Table 2-3 lists the thermal and hydrodynamic parameters used in the model. The majority of these parameters are taken from Sonnenthal et al. (2008) for Kunigel-VI bentonite and from Thury (2002) for the EBS bentonite and the NS clay formation. Permeability for the clay formation is from Soler (2001) and bentonite permeability is from JNC (1999).

FEBEX and Kunigel-VI bentonite also have distinct hydrological and thermal parameters, with the most relevant ones being thermal conductivity and permeability. However, here we use the same thermal conductivity and permeability for both bentonites. These parameters are actually fairly similar for the two types of bentonite — thermal conductivity for saturated Kunigel-VI bentonite is 1.5W/m-°C (see Table 2-2) and that for FEBEX bentonite is 1.3 W/m °C (ENRESA, 2000); permeability for Kunigel-VI bentonite is 2E-21 m² and that for FEBEX ranges from 1E-21 to 3.75E-21 m² (ENRESA, 2000; Zheng et al., 2011; Chen et al. 2009). Moreover, by using the same values of thermal conductivity and permeability for both bentonites, we can isolate the effect of variations in chemical and CM coupling parameters on the stress changes.

Table 2-1. Mineral volume fraction (dimensionless, ratio of the volume for a mineral to the total volume of medium) of the Kunigel-VI bentonite (Ochs et al., 2004), FEBEX bentonite (ENRESA, 2000; Fernández et al., 2004; Ramírez et al., 2002) and Opalinus Clay (Bossart 2011; Lauber et al., 2000).

Mineral	EBS Bentonite: Kunigel-VI	EBS Bentonite: FEBEX	Clay formation: Opalinus Clay
Calcite	0.016	0.0065	0.093
Dolomite	0.018	0.0	0.050
Illite	0.000	0.0	0.273
Kaolinite	0.000	0.0	0.186
Smectite	0.314	0.6	0.035
Chlorite	0.000	0.0	0.076
Quartz	0.228	0.026	0.111
K-Feldspar	0.029	0.0065	0.015
Siderite	0.000	0.0	0.020
Ankerite	0.000	0.0	0.045

Table 2-2. Pore-water composition (mol/kg water, except pH) of Kunigel-VI bentonite (Sonnenthal et al., 2008), FEBEX bentonite (Fernández et al., 2001) and Opalinus Clay (Fernández et al., 2007).

	EBS Bentonite: Kunigel-VI	EBS Bentonite: FEBEX	Clay formation: Opalinus Clay
pH	8.40	7.72	7.40
Cl	1.50E-05	1.60E-01	3.32E-01
SO ₄ ⁻²	1.10E-04	3.20E-02	1.86E-02
HCO ₃ ⁻	3.49E-03	4.1E-04	5.18E-03
Ca ⁺²	1.37E-04	2.2E-02	2.26E-02
Mg ⁺²	1.77E-05	2.3E-02	2.09E-02
Na ⁺	3.60E-03	1.3E-01	2.76E-01
K ⁺	6.14E-05	1.7E-03	2.16E-03
Fe ⁺²	2.06E-08	2.06E-08	3.46E-06
SiO ₂ (aq)	3.38E-04	1.1E-04	1.10E-04
AlO ₂ ⁻	1.91E-09	1.91E-09	3.89E-08

Table 2-3. Thermal and hydrodynamic parameters.

Parameter	Clay formation : Opalinus Clay	EBS Bentonite
Grain density [kg/m ³]	2700	2700
Porosity ϕ	0.162	0.33
Saturated permeability [m ²]	2.0×10^{-20}	2.0×10^{-21}
Relative permeability, k_{rl}	$m = 0.6, S_{rl} = 0.01$	$K_{rl} = S^3$
Van Genuchten α [1/Pa]	6.8×10^{-7}	3.3×10^{-8}
Van Genuchten m	0.6	0.3
Compressibility, β [1/Pa]	3.2×10^{-9}	5.0×10^{-8}
Thermal expansion coeff., [1/°C]	1.0×10^{-5}	1.5×10^{-4}
Dry specific heat, [J/kg-°C]	860	800
Thermal conductivity [W/m-°C] dry/wet	1.48/1.7 ^s	1.1/1.5
Tortuosity for vapor phase	$\phi^{1/3} S_g^{10/3}$	$\phi^{1/3} S_g^{10/3}$
Bulk modulus, (GPa)	4.17	0.02
Shear modulus, (GPa)	1.92	0.0067

From http://www.mont-terri.ch/internet/mont-terri/en/home/geology/key_characteristics.html

Mineral dissolution/precipitation is kinetically controlled. The kinetic law for mineral dissolution/precipitation is given in Xu et al. (2011):

$$r = kA \left| \left(1 - \left(\frac{K}{Q} \right)^\theta \right) \right|^\eta \quad (2-7)$$

where r is the kinetic rate, k is the temperature-dependent rate constant (mol/m²-s), A is the reactive surface area per kg water, K is the equilibrium constant for the mineral–water reaction (written for the destruction of one mole of mineral), and Q is the reaction quotient. Here, for simplicity, the exponents θ and η are assumed equal to 1.

The kinetic rate constants can usually be summed for three mechanisms (Lasaga et al., 1994):

$$k = k_{25}^{nu} \exp \left[\frac{-E_a^{nu}}{R} \left(\frac{1}{T} - \frac{1}{298.15} \right) \right] + k_{25}^H \exp \left[\frac{-E_a^H}{R} \left(\frac{1}{T} - \frac{1}{298.15} \right) \right] a_H^{n_H} + k_{25}^{OH} \exp \left[\frac{-E_a^{OH}}{R} \left(\frac{1}{T} - \frac{1}{298.15} \right) \right] a_{OH}^{n_{OH}} \quad (2-8)$$

where superscripts nu , H and OH indicate neutral, acid, and alkaline mechanisms, respectively, E is the activation energy, k_{25} is the rate constant at 25 °C, R is the gas constant, T is the absolute temperature, α is the activity of the species, and n is a power term (constant). It should be noted that reaction rates depend on the reactive surface area A in Equation (2-7), which is a function of

the product of the specific surface area and the volume fraction of each mineral. Therefore, the calibrated values of specific surface area and volume fraction should be viewed as arbitrary and non-unique (co-linearly varying) values, the product of which is relevant but not each value separately.

The kinetic rates and surface areas for the minerals considered in the model were taken mostly from Xu et al. (2006) (Table 2-4). However, the illitization rate (the rate of illite precipitation and smectite dissolution) was calibrated (Liu et al., 2013) based on the measured illite percentage in an illite/smectite (I/S) mixed layer from Kinnekulle bentonite, Sweden (Pusch and Madsen, 1995). The thermodynamic data were taken from the Data0.dat.YMPv4.0, an EQ3/6 (Wolery, 1993) database qualified by the U.S. Department of Energy for the Yucca Mountain project.

Table 2-4. Kinetic properties for minerals considered in the model (Xu et al., 2006).

Mineral	A (cm ² /g)	Parameters for Kinetic Rate Law							
		Neutral Mechanism		Acid Mechanism			Base Mechanism		
		k ₂₅ (mol/m ² /s)	E _a (kJ/mol)	k ₂₅ (mol/m ² /s)	E _a (kJ/mol)	n(H ⁺)	k ₂₅ (mol/m ² /s)	E _a (kJ/mol)	n(H ⁺)
Quartz	9.8	1.023×10 ⁻¹⁴	87.7						
K-feldspar	9.8	3.89×10 ⁻¹³	38	8.71×10 ⁻¹¹	51.7	0.5	6.31×10 ⁻¹²	94.1	-0.823
Kaolinite	151.6	6.91×10 ⁻¹⁴	22.2	4.89×10 ⁻¹²	65.9	0.777	8.91×10 ⁻¹⁸	17.9	-0.472
Illite	1.18×10 ⁴ (¹)	1.66×10 ⁻¹³	105 (²)						
Chlorite	9.8	3.02×10 ⁻¹³	88	7.76×10 ⁻¹²	88	0.5			
Calcite	3.5	1.63×10 ⁻⁷	23.5						
Dolomite	12.9	2.52×10 ⁻¹²	62.76	2.34×10 ⁻⁷	43.54	1			
Ankerite	9.8	1.26×10 ⁻⁹	62.76	6.46×10 ⁻⁴	36.1	0.5			
Smectite	1.18×10 ⁴ (¹)	1.66×10 ⁻¹³	105 (²)						

(¹) calibrated based on the field illitization data (Liu et al., 2013)

(²) from Pusch and Madsen (1995)

2.3 Model Results

In Liu et al. (2013) and Zheng et al. (2014), the model results for first 1000 years, expressed as the evolution of temperature, pore pressure, water saturation, concentration and stress, were discussed in detail and a sensitivity analyses to key chemical and mechanical parameters were conducted to understand the coupling processes. The simulations were only conducted for a period of 1,000 years because the older version of TOUGHRACT-FLAC3D was not fast enough for longer simulation time periods and because it is assumed that coupled process effects are most pronounced in the first 1,000 years. One of the general observations based on these simulations is that illitization is enhanced at higher temperature, although the amount of illitization depends on chemical and hydrological conditions and varies a great deal. These results lead to questions about illitization at longer times (i.e., 100,000 years). For example, does illitization continue at the same rate or does it stabilize at long times and how does illitization effect stress at long times? In this part of the report, we have been able to address these questions with the improved version of TOUGHRACT-FLAC3D, which can carry out simulations to 100,000 years.

2.3.1 Cases for Kunigel-VI Bentonite

In the generic cases we used to study the effect of high temperature on the THMC evolution in bentonite and clay formation, two bentonites have been simulated: Kunigel-VI and FEBEX bentonite. In this section, model results for Kunigel-VI bentonite are presented. We first briefly discuss the changes in temperature, water saturation and the volume fraction of smectite because their changes essentially determine the evolution of stress; then the changes in stress are discussed.

2.3.1.1 *THC Evolution*

The evolution of heat release from decaying waste is shown in Figure 2-2. The heat release rates have been adjusted to make two cases for comparison: a “high T” case, in which the temperature near the canister can reach 200 °C; and a “low T” case, in which the temperature near the canister peaks at about 100 °C. In this part of the report, the temporal evolution at the four monitoring points (shown in Figure 2-2) is used to present thermal, hydrological, chemical and mechanical results: point A is inside the bentonite near the canister, point B is inside the bentonite near the EBS-NS interface, point C is inside the clay formation near the EBS-NS interface, and point D is inside the clay formation at a distance of 10 m from the canister. The temperature evolution at the four monitoring points A, B, C, and D is shown in Figure 2-4. After 100,000 years, as expected from the heat release function shown in Figure 2-2, the temperature drops to about 27 °C. The clay formation near the EBS-NS interface goes through desaturation (Figure 2-5), which interestingly lasts much longer for the “low T” case than the “high T” case. Desaturation in the clay formation occurs because the host rock is not able to replenish water as fast as it is being imbibed by the EBS bentonite. For the “high T” case, the hydration of bentonite is slower because the high temperature leads to stronger outward vapor flow and higher pore pressure in the EBS bentonite, which gives the host rock more time to replenish the water lost to EBS bentonite and the outward vapor flow hydrates the outer portion of the bentonite. As a result, the clay formation saturation near the EBS-NS interface does not decrease as much for the “high T” case as for the “low T” case. Pore pressure increases as a result of re-saturation and heating. The “high T” case exhibits much higher pore pressure than the “low T”, with a difference of about 5 MPa after 1,000 years (Figure 2-6), but by the end of 100,000 years, the difference is fairly small.

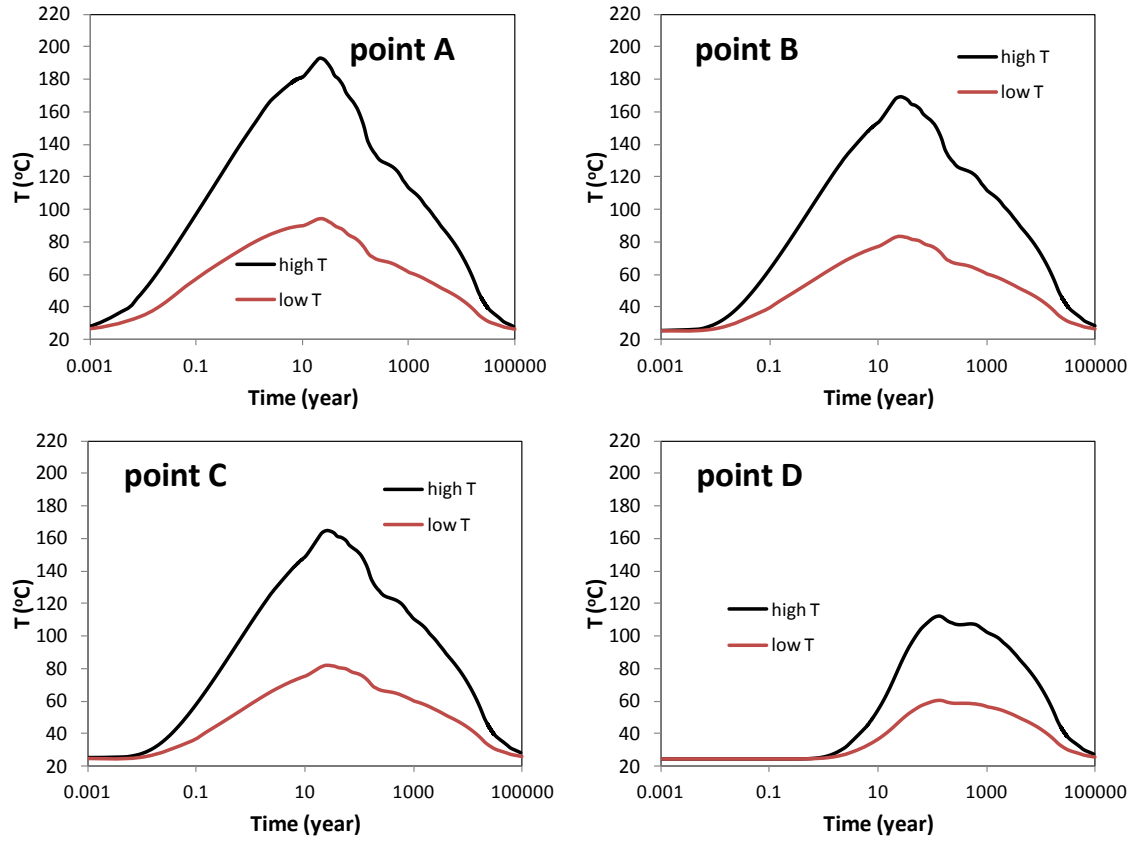


Figure 2-4. Temperature evolution at points A, B, C, and D.

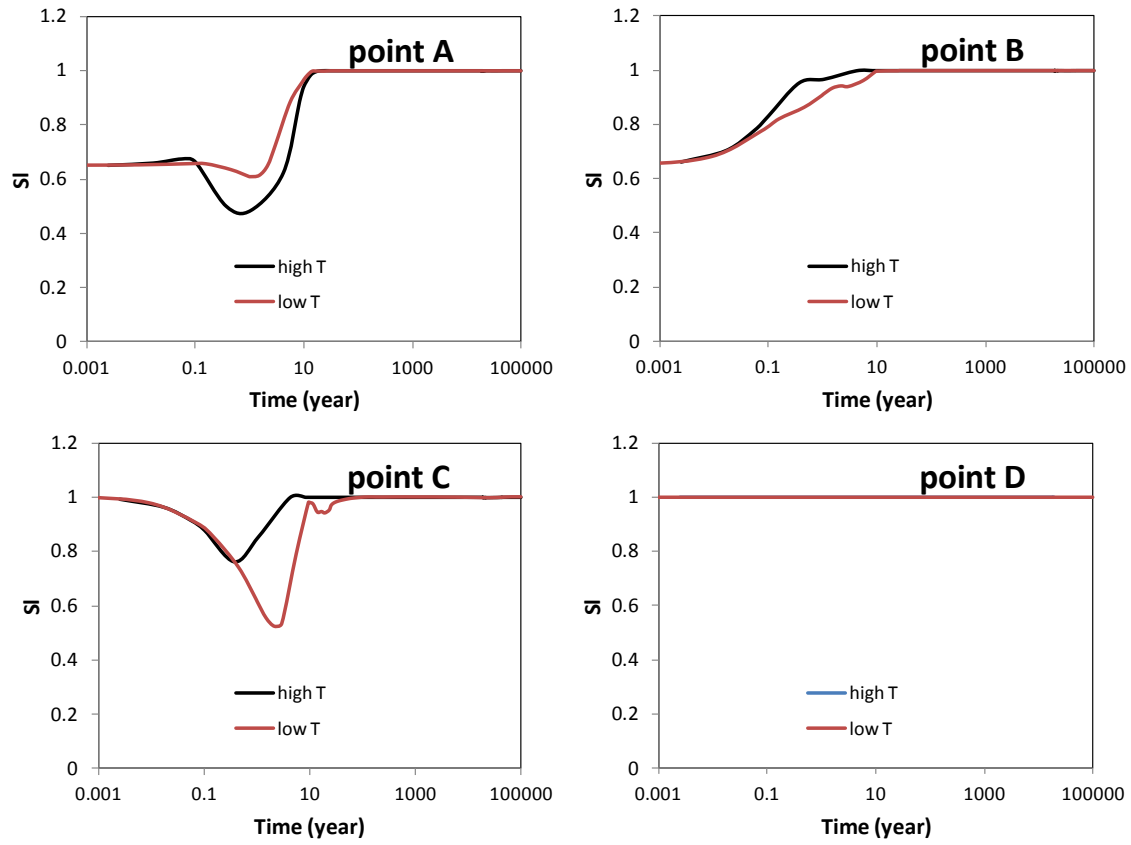


Figure 2-5. The temporal evolution of water saturation at points A, B, C, and D.

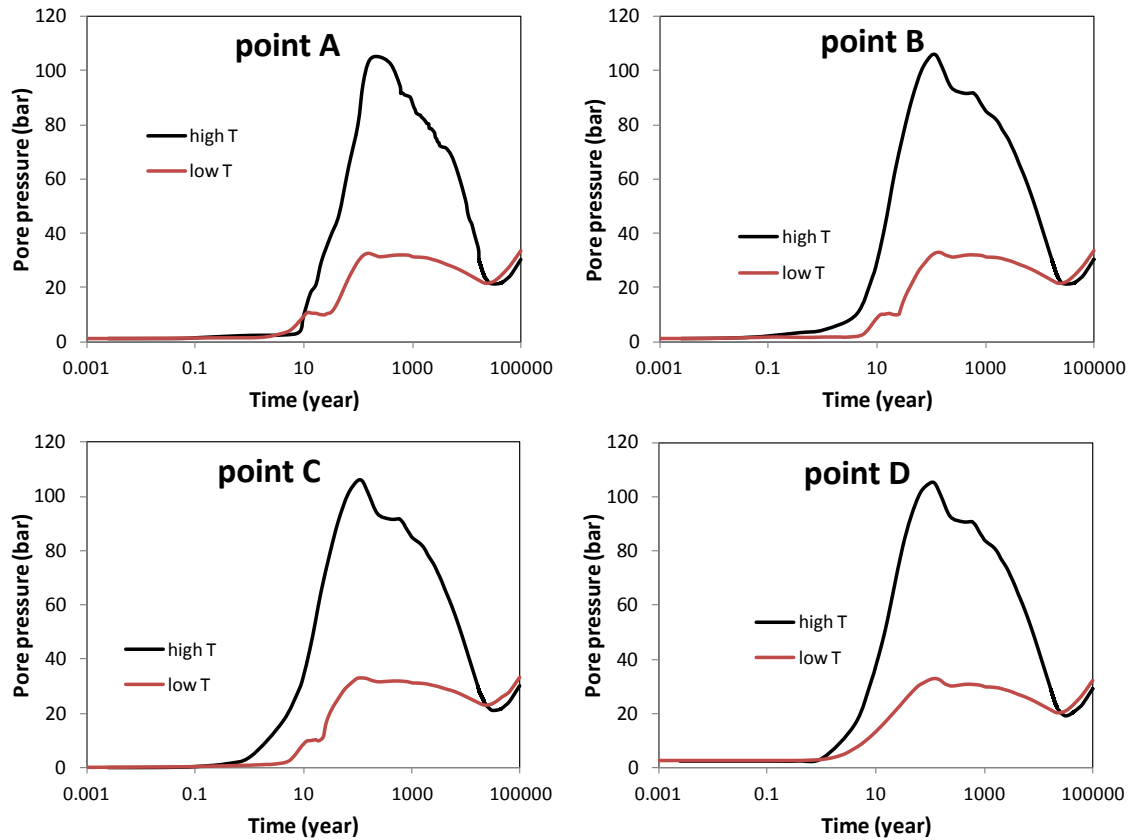
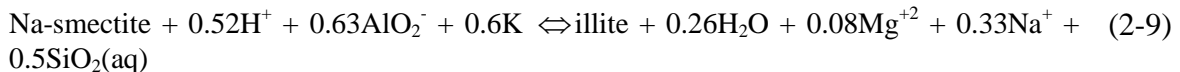


Figure 2-6. The temporal evolution of pore pressure at points A, B, C, and D.

In the base case, illitization is modeled as the dissolution of Na-smectite and precipitation of illite. The overall reaction can be written as:



Other chemical parameters in the base case, such as reaction rate for Na-smectite and illite, K-feldspar, water compositions in bentonite and the clay formation, are presented in Section 2.2.4. As revealed from Liu et al., (2013) and Zheng et al., (2014), many factors can affect the chemical reactions such as the initial water-mineral disequilibrium in bentonite (since the water used for making bentonite blocks is not necessarily in equilibrium with the mineral phase in bentonite, and it takes time to reach that equilibrium), as well as the thermal and hydrological disturbances in response to emplacement.

Smectite volume fraction changes at points A through D are shown in Figures 2-7 (log time scale) and 2-9 (linear time scale); illite volume fraction changes are shown in Figures 2-8 (log time scale). Figures 2-7 and 2-8 show that illitization does occur in the EBS bentonite. In addition to temperature effects, illitization is affected by the initial disequilibrium between the pore-water solution and mineral phases. Initially, the pore water in the bentonite buffer is

oversaturated with respect to illite and undersaturated with respect to smectite. In addition, the pore water in the clay formation contains a much higher concentration of K and Al, and thus provides a source of Al and K for the EBS bentonite alteration through diffusion and advection. Note that the increase in Al and K concentrations in bentonite is caused not only by diffusion and advection, but also by the dissolution of other minerals, such as K-feldspar. In fact, as shown in Liu et al., (2013), the dissolution of K-feldspar is the major source of K for illitization, especially in the area that is away from the EBS-NS interface, such as point A. The pore water in the clay formation also has a higher concentration of Mg and Na, which inhibits illitization. But it seems that the factors in favor of illitization outpace those against illitization. After 1,000 years (the simulation time of previous models in Liu et al. (2013)) the smectite volume fraction in the bentonite decreases by 0.035 (or 11%) for the ‘high T’ case and 0.006 (or 2%) for the ‘low T’ case, which corresponds to an illite volume fraction increase of similar magnitude. Smectite volume fraction changes are similar at point A and B. However, after 2,000 years, illitization exhibits distinct behavior at points A and B for the ‘high T’ case. At point A, illitization is stagnant, which is more clearly illustrated in Figure 2-9 where time is plotted on a linear scale. This is mainly caused by the drop of temperature, which significantly slowed down the dissolution of K-feldspar (Figure 2-10) and subsequently the supply of K. The reduced temperature also significantly decreases the reaction rate of smectite and illite. Conversely, at point B, the illitization continues at fairly fast rate due to the interaction with clay formation. Although the dissolution rate of K-feldspar at point B is significantly reduced (which limits the supply of K), bentonite near the EBS-NS interface receives K from the clay formation. This source of K is depleted before 2,000 years by illitization in the clay formation. However, illitization ceases in the clay formation after 2,000 years such that K is free to move into the bentonite. After 100,000 years, for the ‘high T’ case, at point A, smectite volume fraction decreases by about 0.05, equivalent to 17% of the initial amount of smectite, while at point B, smectite volume fraction decreases by about 0.19, close to 60% of the initial amount of smectite. The difference between the illitization at points A and B shows that without interaction with host rock, the thermal-induced chemical alteration in the EBS bentonite stabilizes after 2,000 years (e.g. results at point A), but the interaction with host rock may lead to dramatic changes in EBS bentonite as illustrated by the model results at point B. For the ‘low T’, smectite volume fraction decreases about 0.03 (10% of initial amount) at points A and B after 100,000 years, which is substantially lower than that for ‘high T’ case, especially at point B.

In Figures 2-7 and 2-8, model results are also shown for a simulation (‘no heat’) that assumes there is no heat release from waste package. This simulation illustrates the chemical alteration in EBS bentonite is caused mostly by the interaction between EBS bentonite and the clay formation. Even though there is no temperature increase, Kunigel-VI bentonite tends to undergo slight illitization which results in a decrease of smectite volume fraction of 0.02 (5% of the initial amount) in 100,000 years. In the ‘no heat’ simulation, the model result at point D represents the chemical evolution for undisturbed temperature conditions — which shows a slow illitization in the clay formation, with a decrease of smectite volume fraction about 0.005 in 100,000 years.

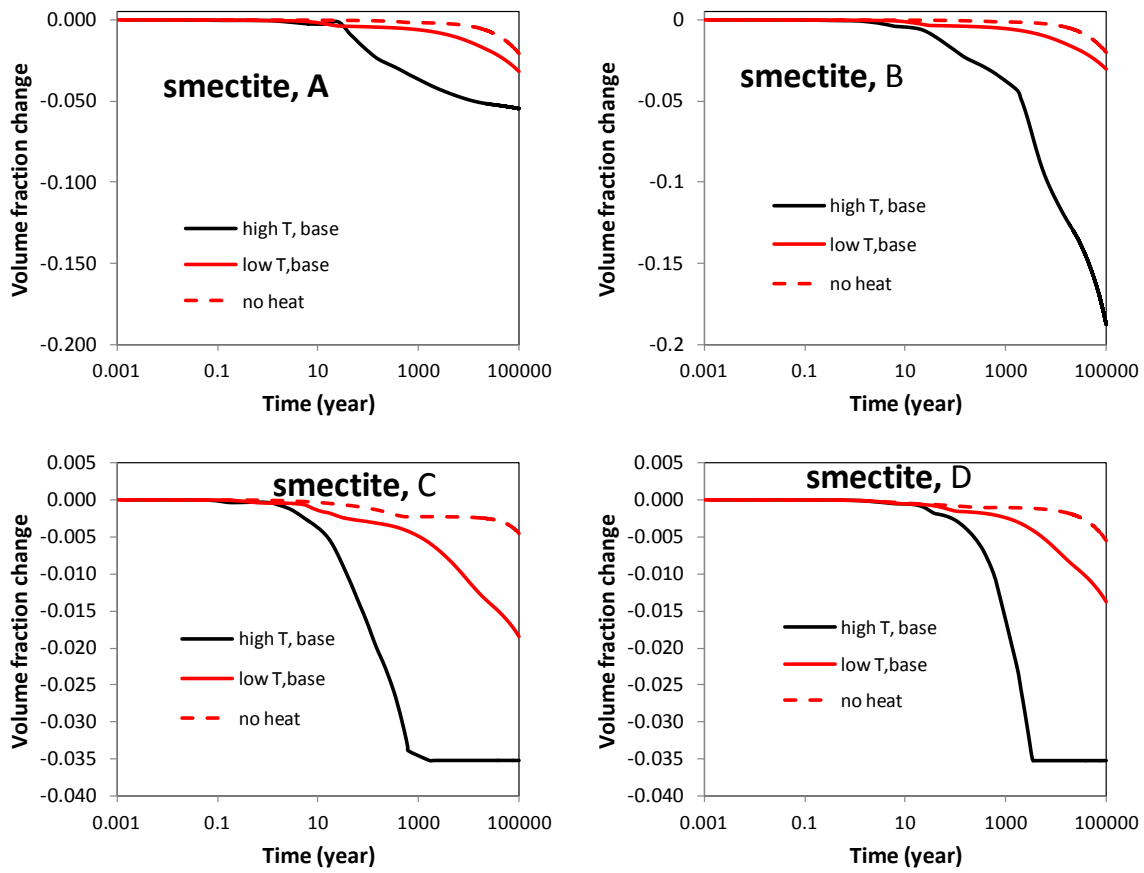


Figure 2-7. The temporal evolution of smectite volume fraction at points A, B, C, and D.

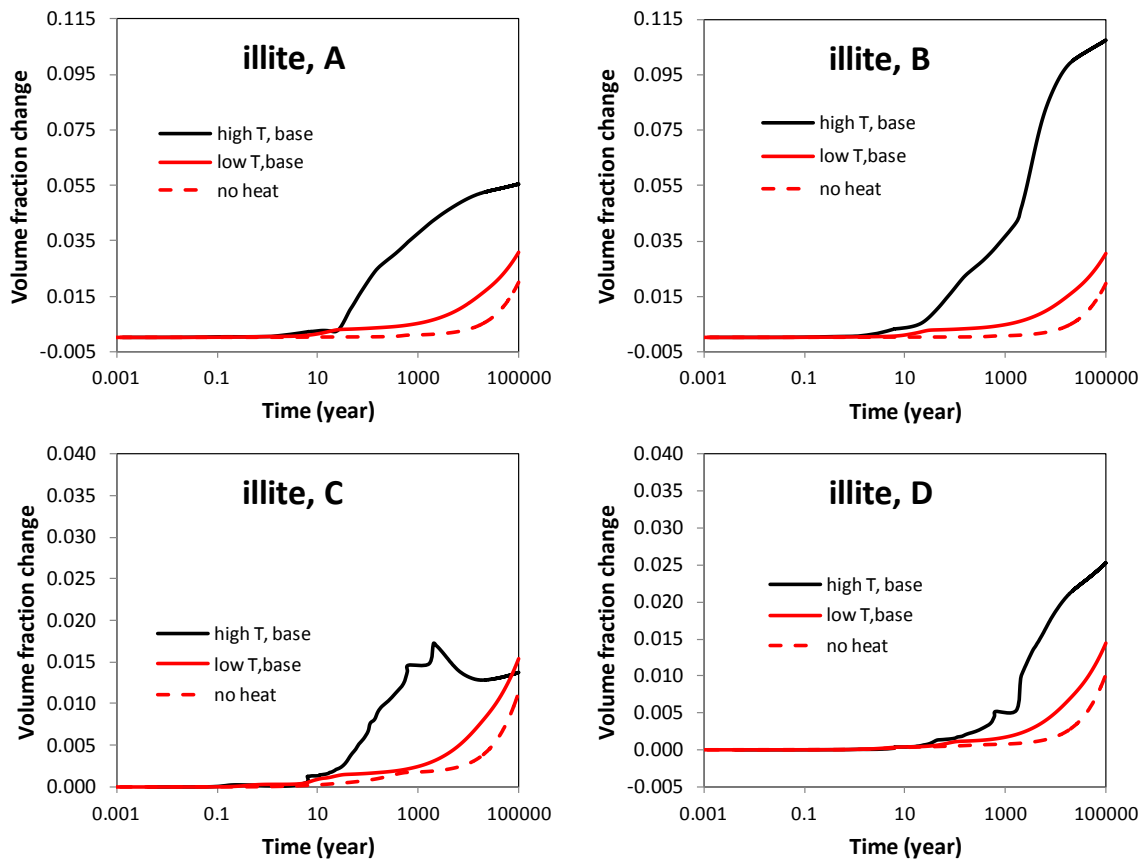


Figure 2-8. The temporal evolution of illite volume fraction at points A, B, C, and D.

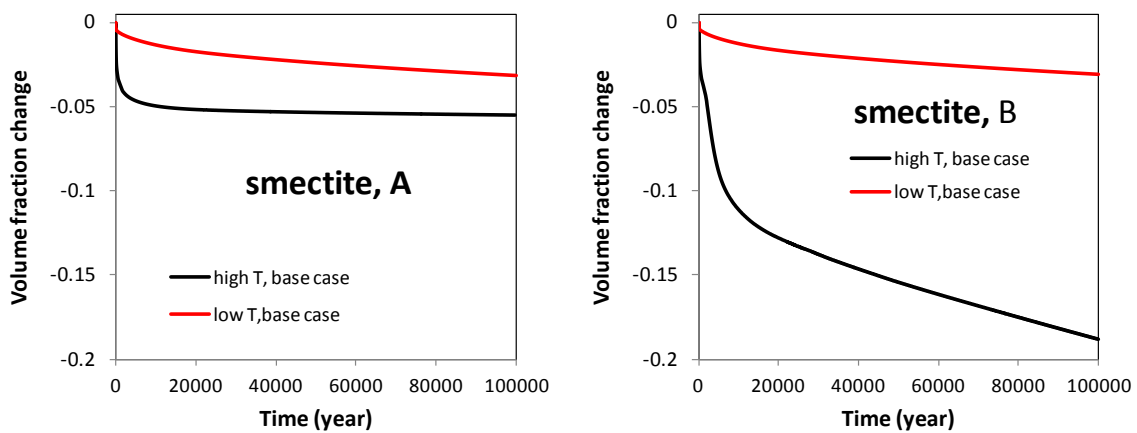


Figure 2-9. The temporal evolution of smectite volume fraction at points A and B, with X-axis plotted in linear scale.

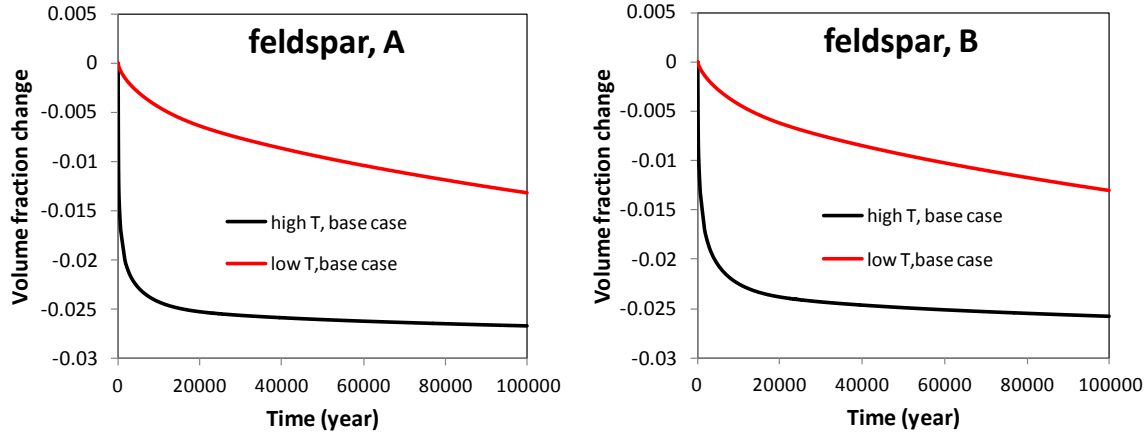


Figure 2-10. The temporal evolution of K-feldspar volume fraction at points A and B, with X-axis plotted in linear scale.

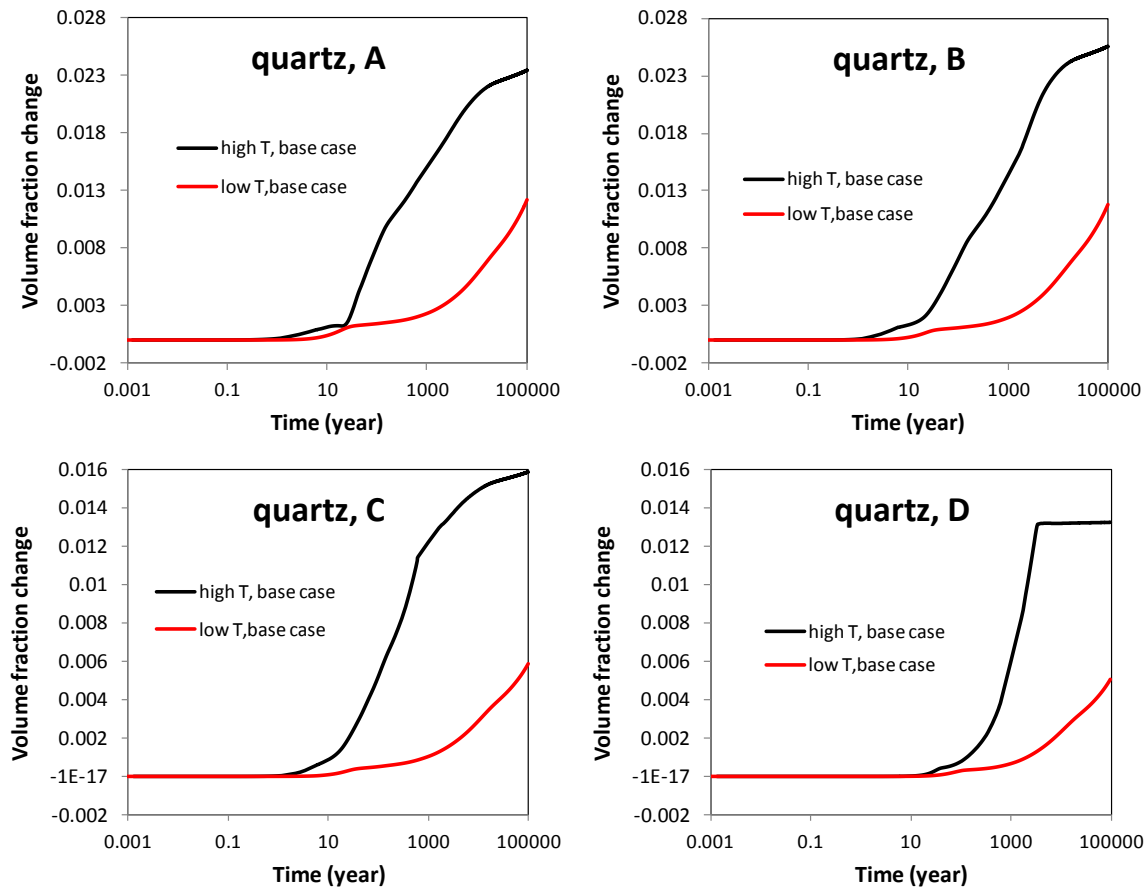


Figure 2-11. The temporal evolution of quartz volume fraction at points A, B, C, and D.

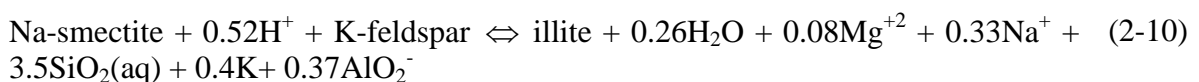
As a by-product of illitization, a moderate amount of quartz is formed after 100,000 years, as shown in Figure 2-11, which may cause the cementation of bentonite and make the bentonite more brittle. However, cementation of bentonite by silicate minerals is not considered in the mechanical-chemical coupling in the model and the model is therefore unable to quantify the

change of mechanical properties by cementation. In the near future, the effect of cementation on mechanical properties will be conceptualized and implemented in TOUGHREACT-FLAC3D.

Results from the base case (Figures 2-7 through 2-11) confirm that the clay host rock undergoes a small degree of illitization similar to observations in geological systems (e.g. Wersin et al., 2007; Pusch and Madsen, 1995). This is illustrated by the smectite dissolution at points C and D in Figure 2-7 and illite precipitation at points C and D in Figure 2-8. Results at point D represent the chemical alteration in the clay formation induced only by the long term heating. The volume fraction of smectite in the clay formation, which initially is 0.035, is depleted after 3,500 years for the “high T” case and decreases by 0.0135 (about 40% of initial amount) for the “low T” case. As a comparison, the “no heat” simulation shows that clay formation undergoes a decrease in smectite volume fraction of 0.005 (14% of the initial amount) for undisturbed temperature conditions. At point C near the EBS-NS interface, because the clay formation undergoes interaction with bentonite and experiences higher temperature, illitization is faster in comparison with that at point D. For the “high T” case, in only 650 years, the volume fraction of smectite decreases by 0.034 (about 97% of initial amount) and then in about 1,500 years, all smectite is transformed to illite; for the “low T” case, the volume fraction of smectite decreases about 0.017 (50% of the initial amount) in 100,000 years. As mentioned above, the quick depletion of smectite or the cessation of illitization in the clay formation near the EBS-NS interface has significant impact on the illitization in bentonite.

One of the key findings from Liu et al. (2013) is the critical role that K-feldspar plays on illitization in terms of supplying K, especially in the area far from the NS-EBS interface. Given the uncertainty associated with the reaction rate of K-feldspar, a sensitivity run with a K-feldspar dissolution rate two orders of magnitude higher than that in the base case was conducted in Liu et al. (2013) and model results showed that much more smectite dissolves in 1,000 years if the K-feldspar dissolution rate is higher. However, a question remains whether K-feldspar dissolution rate is still critical if the ultimate concern is the illitization after 100,000 years or even longer.

This year, a simulation with higher K-feldspar dissolution rate was conducted for 100,000 years and model results are given in Figures 2-12 through 2-14. Initially there is 2.9 vol% K-feldspar in the bentonite and increasing the dissolution rate of K-feldspar leads to a quick depletion of K-feldspar, as shown by the plateau of the volume fraction change after about 100 years in Figure 2-12. At point A, the volume fraction changes for K-feldspar (Figure 2-12), smectite (Figure 2-13) and illite (Figure 2-14) follow the same trend, which reveal the importance of K-feldspar dissolution on the illitization. The amount of K-feldspar dissolution determines the amount of smectite dissolution. Furthermore, the dissolution rate of K-feldspar determines the dissolution rate of smectite and the precipitation rate of illite. This is because the geochemical conditions in bentonite at point A are less affected by the host rock, so that the reactions can simply be described as the following reaction in a closed system:



Equation (2-10) clearly shows the interference of K-feldspar on illitization (dissolution of smectite and precipitation of illite). As shown in Table 2-4, the dissolution rate of smectite and precipitation rate of illite is on the order of 10^{-11} mol/m₂/s, but the dissolution rate of K-feldspar is around 10^{-13} mol/m₂/s. Because illitization involves in the current scenarios three minerals: illite, smectite and K-feldspar, the overall reaction rate of illitization depends on the slowest reacting mineral, as a result, the dissolution rate of K-feldspar becomes of the bottle neck of illitization. This is why at point A, the volume fraction change of smectite follows that of K-feldspar. However, at point B after K-feldspar runs out at around 100 years, smectite continues dissolving and illite continues forming because of the interaction between bentonite and the clay formation.

In the clay formation (see results at points C and D in Figures 2-12 through 2-14), the dissolution of K-feldspar and smectite and the precipitation of illite proceed concurrently because of the controlling of feldspar dissolution on the overall reactions of illitization (see Equation (2-10)). The clay formation at point C undergoes more interaction with bentonite, whereas at point D, the clay formation is much less affected by the interaction with bentonite. However, results at points C and D exhibit a similar trend, although the reactions occur at an earlier time at C than at D because temperature increases earlier at C than at D. This indicates that interaction between EBS bentonite and clay formation has much stronger effect on bentonite than the clay formation.

At the end of 100,000 years, both the base case and the sensitivity case with higher K-feldspar dissolution rate lead to similar quantities of smectite dissolution and illite precipitation, despite the difference at intermediate times. Therefore, if the ultimate concern is the quantity of illitization at 100,000 years (or even longer), it seems that the quantity of K-feldspar is more important than its dissolution rate.

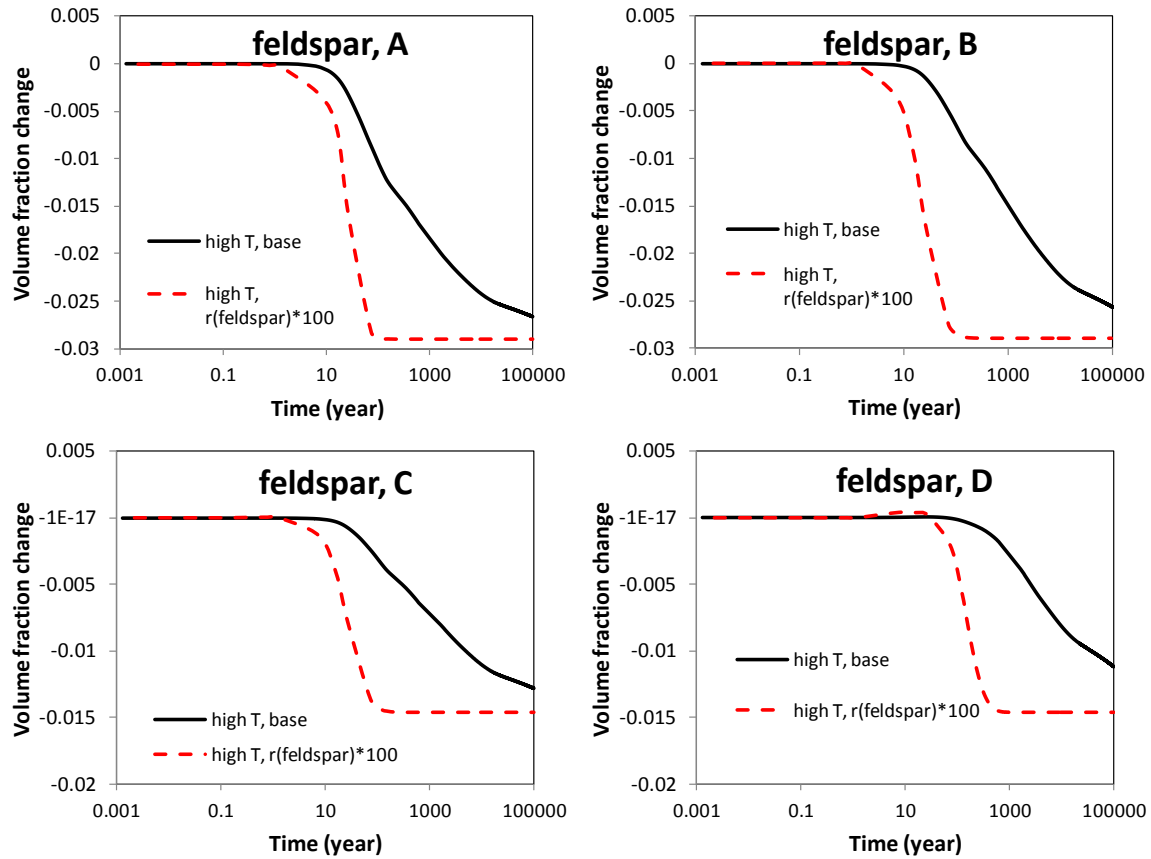


Figure 2-12. The temporal evolution of K-feldspar volume fraction at points A, B, C, and D for the “high T” base run and a sensitivity run with K-feldspar dissolution rate two orders of magnitude higher.

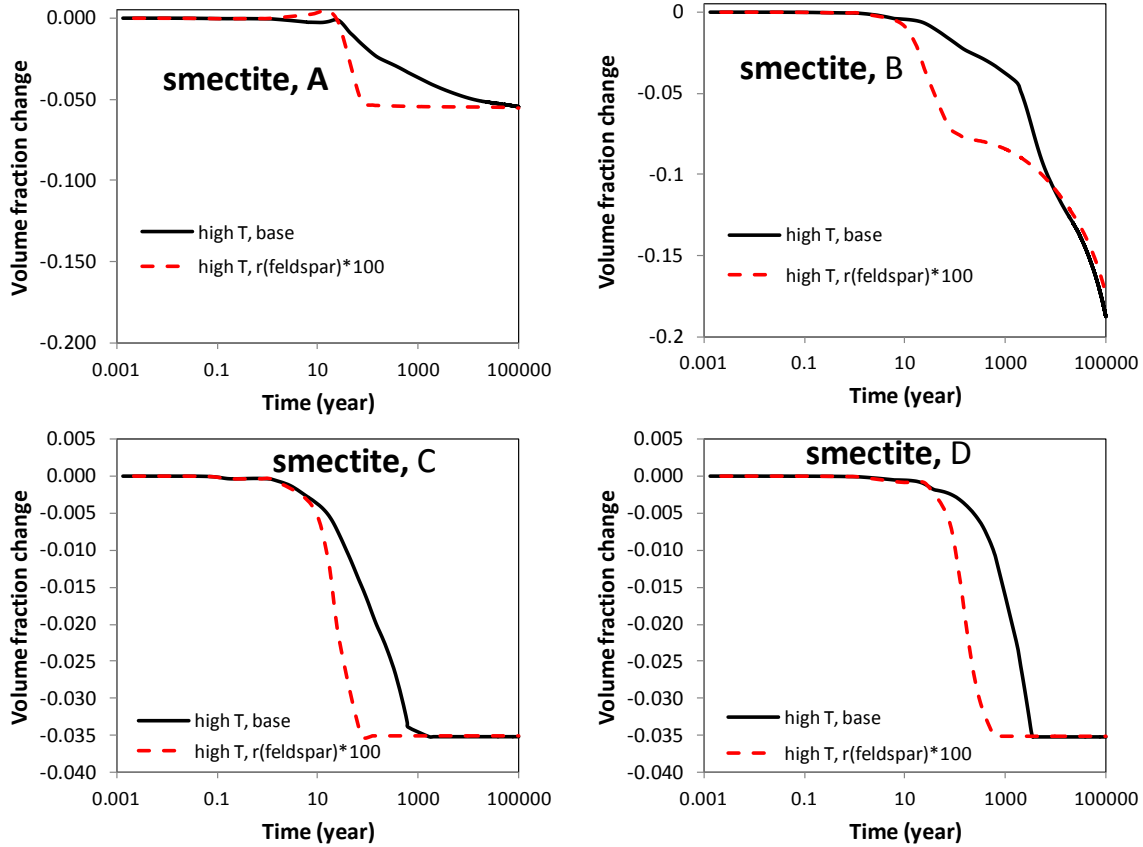


Figure 2-13. The temporal evolution of smectite volume fraction at points A, B, C, and D for the “high T” base run and a sensitivity run with K-feldspar dissolution rate two orders of magnitude higher.

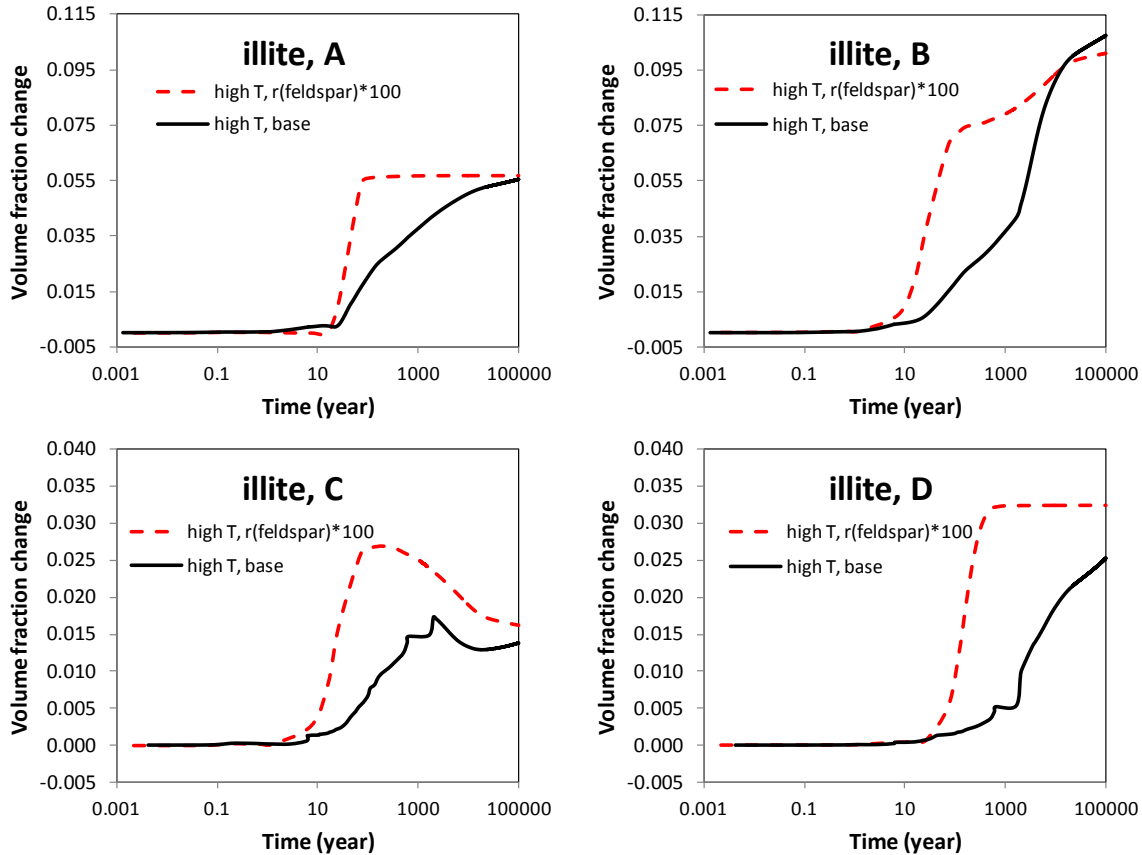
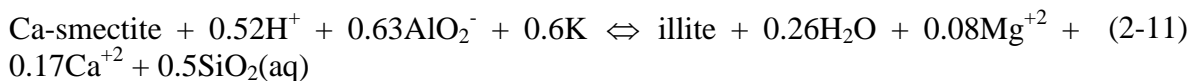


Figure 2-14. The temporal evolution of smectite volume fraction at points A, B, C, and D for the “high T” base run and a sensitivity run with K-feldspar dissolution rate two orders of magnitude higher.

Na-smectite and Ca-smectite are two representative smectites, with Na being the dominant interlayer cations for Na-smectite and Ca being the dominant interlayer cation for Ca-smectite. In the base cases for Kunigel-VI bentonite, illitization is modeled as the dissolution of Na-smectite and precipitation of illite, as shown in Equation (2-9). In the base case, we also observed that calcite dissolves and Ca^{+2} concentration increases. In the base case, because Na-smectite is considered in the model, the dissolution of calcite has no direct interaction with illitization. However, if Ca-smectite rather than Na-smectite were present in the mineral assemblage, calcite dissolution might affect the illitization. To evaluate this scenario, we create a hypothetical case in which Ca-smectite rather than Na-smectite is included in the model and overall reaction of illitization can be written as:



The log K for the above reactions is just slightly different from that for Equation (2-9) (the transformation from Na-smectite to illite).

Model results for calcite, smectite and illite are shown in Figures 2-15 through 2-17. Examination of these model results leads to the following observations:

- In general, switching Na-smectite to Ca-smectite does not have significant impact in terms of illitization.
- If Ca-smectite is present in the bentonite, the dissolution of calcite delays the start of smectite dissolution because higher Ca^{+2} concentration caused by the dissolution of calcite inhibit illitization.
- Eventually Ca-smectite leads to only slightly less illitization (less dissolution of smectite and less precipitation of illite) for both “high T” and “low T” cases. The reason is that the quantity of calcite that dissolves is quite small.

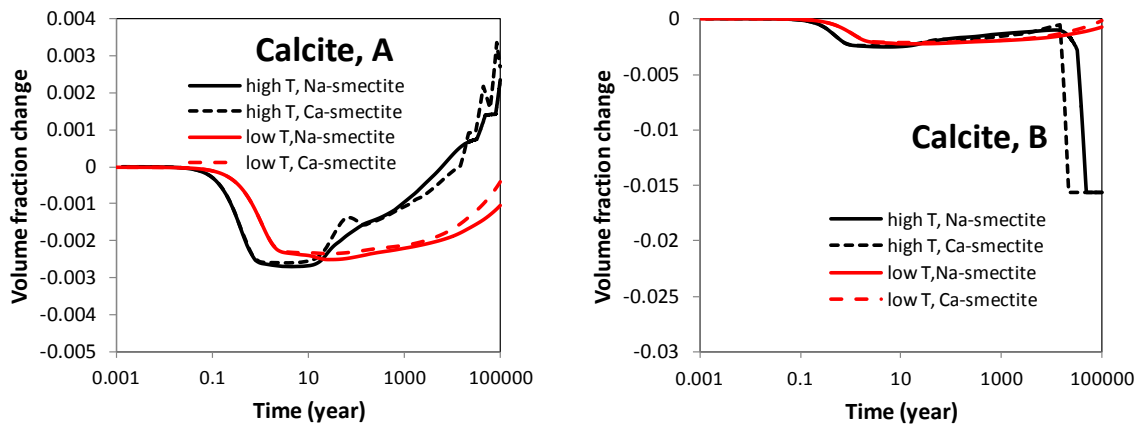


Figure 2-15. The temporal evolution of calcite volume fraction at points A, B for the case with Ca-smectite and Na-smectite in Kunigel-VI bentonite.

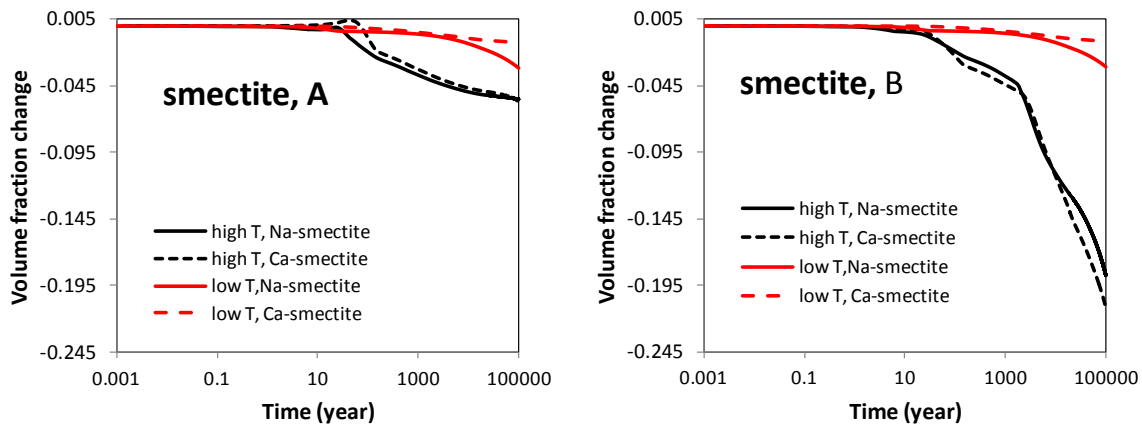


Figure 2-16. The temporal evolution of smectite volume fraction at points A, B for the case with Ca-smectite and Na-smectite in Kunigel-VI bentonite.

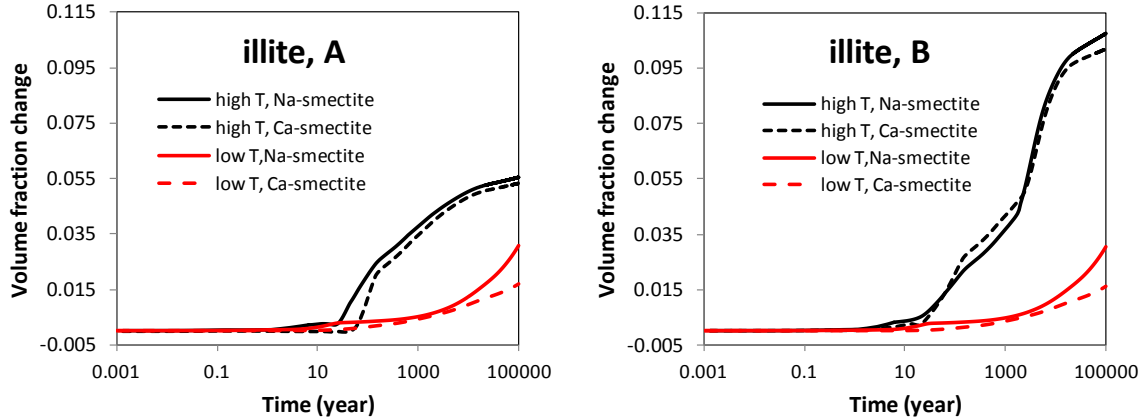


Figure 2-17. The temporal evolution of illite volume fraction at points A, B for the case with Ca-smectite and Na-smectite in Kunigel-VI bentonite.

2.3.1.2 Stress Evolution

The mechanical-chemical coupling implemented in the current model allows us to evaluate how the chemical changes described in Section 2.3.1.1 may affect the mechanical behavior of the EBS bentonite in terms of swelling and total stress. We limit our analysis to the effects of ion concentration and illitization on swelling and do not include other potential effects of chemical changes on mechanics, such as changes in mechanical properties due to cementation.

Figures 2-18 and 2-19 show the stress changes at point A and B for both “low T” and “high T” cases. Several processes combine to drive the peak stress in bentonite up to about 5 MPa for the “low T” case and 13 MPa for the “high T” case, both at around 100 years. Reasons for the stress increase include the increase in pore pressure due to hydration and thermal pressurization (a processes caused by the difference in thermal expansion of the fluid and solid host rock), bentonite swelling, and thermal expansion. Clearly the stronger thermal pressurization in the “high T” case leads to much higher stress in the bentonite than the “low T” case. For both the “high T” and “low T” cases, the major contribution to total stress within the buffer is pore pressure, with smaller contributions from swelling and thermal stresses. After 100 years, the stress gradually goes down and stabilizes somewhat after 30,000 years. By the end of 100,000 years, the difference between the “high T” and “low T” cases is minimal.

The constitutive relationship described by Equation (2-5) provides an opportunity to evaluate the effect of chemical changes on swelling stress. The mechanical results presented in this section are based on the chemical results in the previous section. In order to isolate the contributions of ion concentration changes versus smectite changes on swelling stress changes, we present three sets of calculated swelling stress. In the first set, denoted in Figures 2-19 and 2-20 as “ $\sigma=f(SI,C,Ms)$ ”, the swelling stress is calculated according to Equation (2-5) as a function of liquid saturation changes (SI), ion concentration (C) changes, and smectite (Ms) changes. In the second set, denoted as “ $\sigma=f(SI,C)$ ”, the contribution from smectite changes in Equation (2-5) is disregarded, and the swelling stress is only a function of liquid saturation and ion concentration. In the third set, denoted as “ $\sigma=f(SI)$ ”, all chemical effects are neglected, and the swelling stress is only a function of liquid saturation changes.

At early time (< 20 years), the fact that results for “ $\sigma=f(SI,C,Ms)$ ” and “ $\sigma=f(SI,C)$ ” cases are indistinguishable (Figures 2-20 and 2-21) indicates that smectite changes have not yet contributed to the stress change because the volume fraction of smectite changes significantly only after about 20 years (see Figure 2-7). Ion concentration changes start to affect stress at early times (< 20 years) and maintain such effects afterwards. Initially bentonite near the canister undergoes desaturation and therefore negative swelling stress (see Figure 2-5 for changes at point A). At point A, for the “low T” case, the ion concentration increase leads to a drop in swelling stress of about 0.11 MPa and the dissolution of smectite reduces the swelling stress a little further by about 0.06 MPa after 100,000 years. For the “high T” case, ion concentration changes cause about a 0.08 MPa decrease in swelling stress and the loss of smectite due to dissolution results in about a 0.09 MPa reduction of swelling stress after 100,000 years, (see Figure 2-20). In general, the chemical changes in bentonite have a fairly moderate effect on swelling stress, with about 17% swelling stress reduction being due to chemical change for the “low T” and “high T” cases at point A (Figure 2-20). In terms of the effect of ion concentration change on swelling stress, bentonite near the EBS-NS interface (point B) behaves similarly to bentonite near the canister. After 100,000 years, the ion concentration increase leads to a drop in swelling stress of about 0.1 MPa in both “low T” and “high T” case. In terms of the effect of smectite dissolution on the reduction in swelling stress, bentonite near the EBS-NS (point B) interface behaves similarly to those near the canister (point A) for the “low T” case, but not for the “high T” case. The chemical changes in bentonite lead to about 54% swelling stress reduction “high T” case (see Figure 2-21), which is much higher than the 17% swelling stress reduction at point B for the “low T” case. This is caused by more dissolution of smectite in bentonite near EBS-NS interface (see Figure 2-7 at point B) for the “high T” case. In terms of the total stress, the decrease of swelling stress accounts for about a 3-10% reduction of the total stress after 100,000 years.

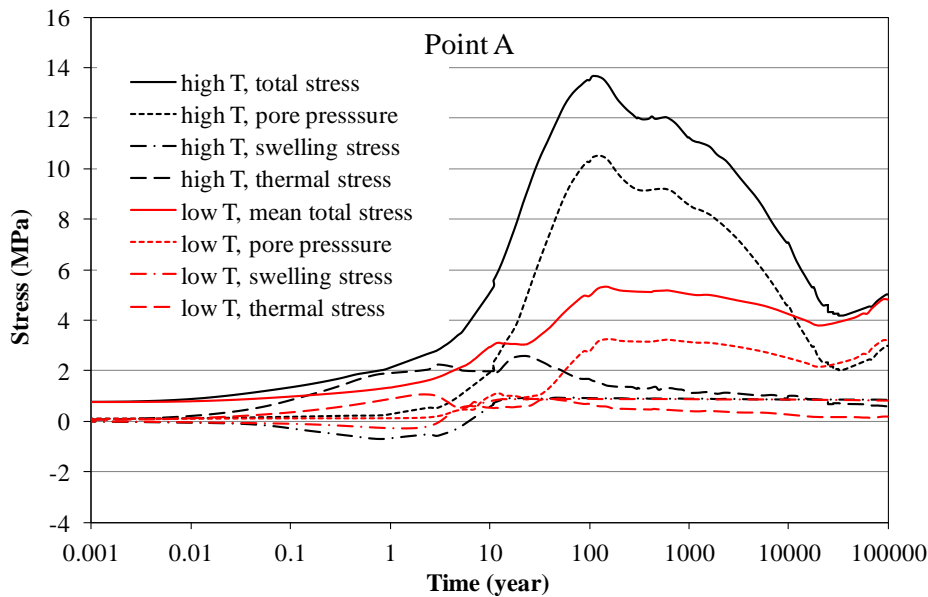


Figure 2-18. Simulation results of mean total stress, pore pressure, and thermal stress at point A for the “low T” and “high T” scenario, respectively.

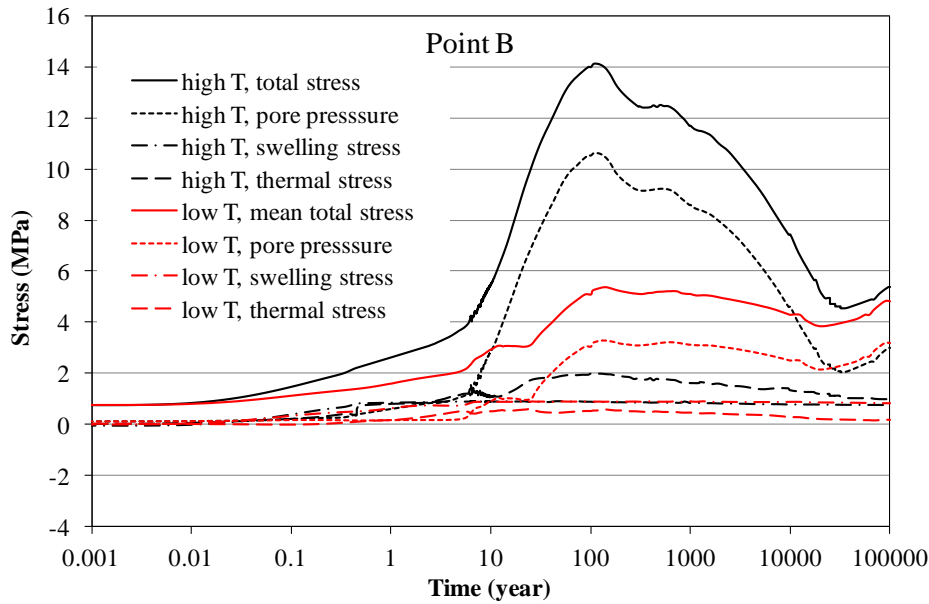


Figure 2-19. Simulation results of mean total stress, pore pressure, and thermal stress at point B for the “low T” and “high T” scenario, respectively.

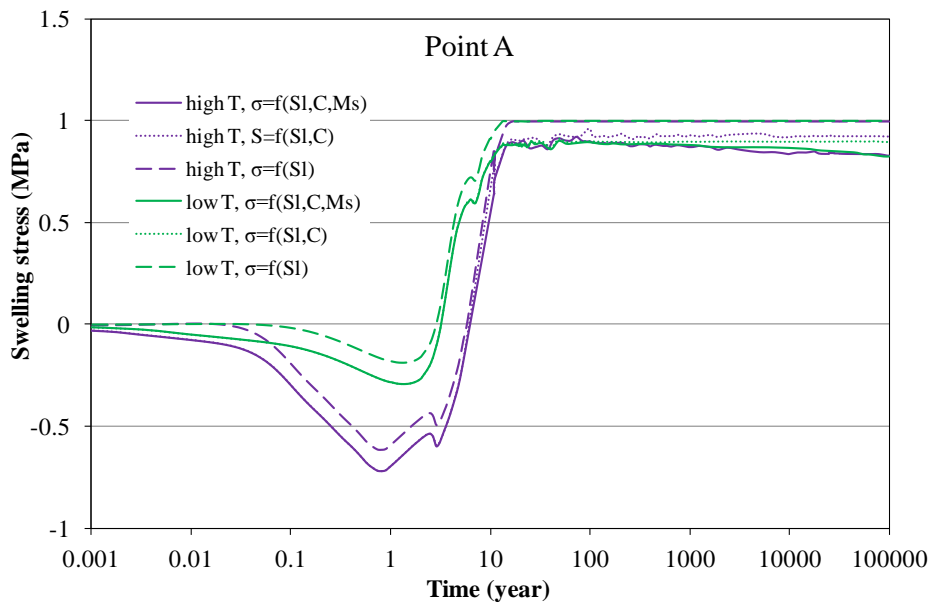


Figure 2-20. Simulation results of swelling stress at point A for the “low T” and “high T” scenarios, respectively.

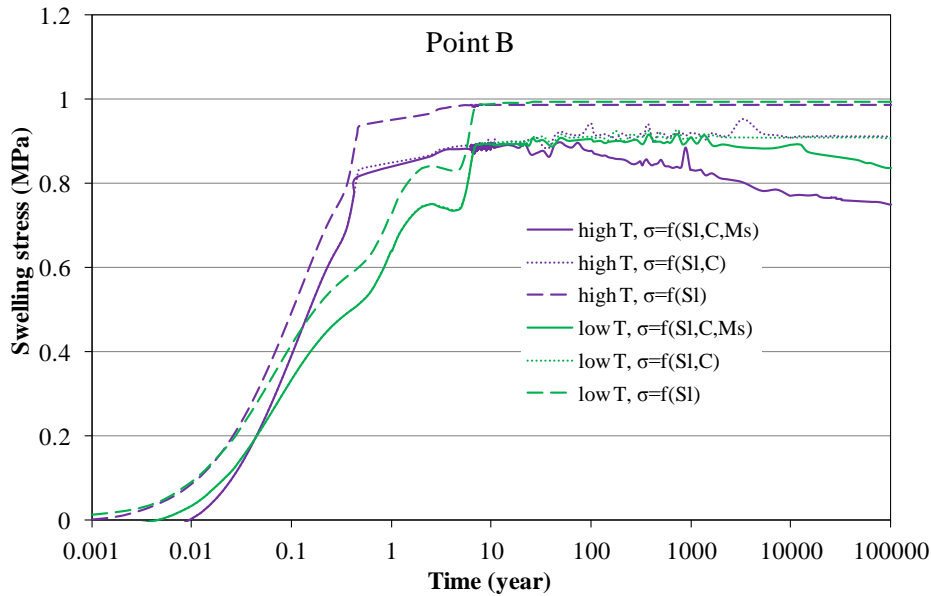


Figure 2-21. Simulation results of swelling stress at point B for the “low T” and “high T” scenarios, respectively.

Figures 2-22 and 2-23 show the evolution of total stress and pore pressure at points C and D in the clay formation. After a sharp increase in stress at about 100 years, stress decreases. After 20,000 to 30,000 years the stress field becomes stable and the difference between the “high T” and “low T” case is fairly small.

In FY15, the mechanical model for clay formation is also linked to the chemical changes with a similar coupling scheme to that used for bentonite, which provides an opportunity to check the effect of chemical change in the clay formation on stress. In the “high T” base case the effect of ion concentration and smectite change on stress are considered. We developed two sensitivity runs in which the contribution of ion concentration and smectite volume fraction change to stress are alternatively neglected to check on the contribution of chemical changes on the stress. The “high T, no Sc” case in which the contribution of smectite change to stress is neglected and the “high T, no C, no Sc” case in which both the contribution of smectite change and ion concentration to stress is neglected, are shown in Figures 2-24 and 2-25. Model results for these three cases show that the effects on stress are very small, especially at point D. By the end of 100,000 years at point C, the dissolution of smectite leads to a decrease in stress of about 0.14 MPa and ion concentration change cause another decrease in stress of about 0.14 MPa. Therefore, in total, the chemical changes in the clay formation result in about a 0.28 MPa decrease in stress, or 2.6%. At point D, chemical changes account for only about a 0.1 MPa difference in stress.

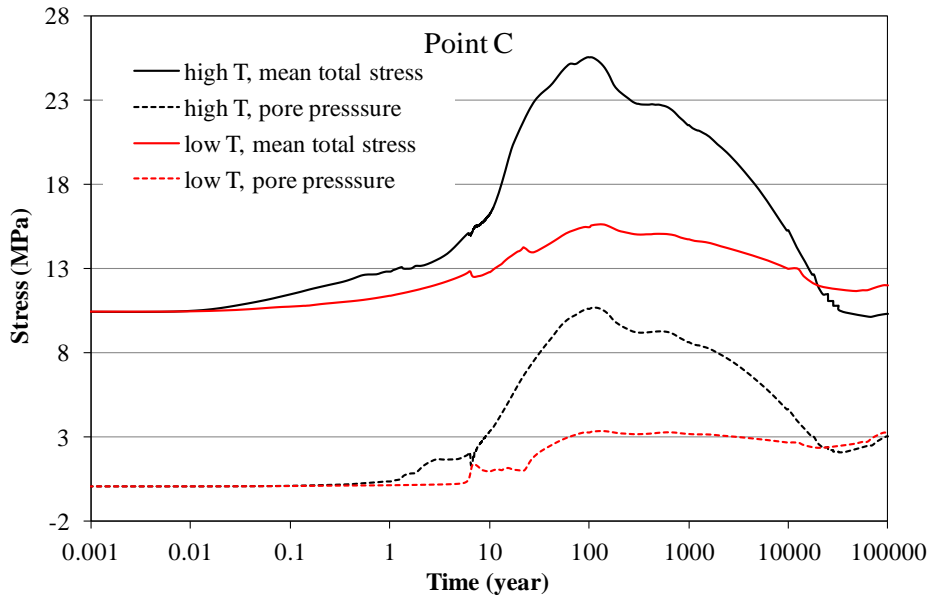


Figure 2-22. Simulation results of mean total stress, pore pressure, and thermal stress at point C for the “low T” and “high T” scenario, respectively.

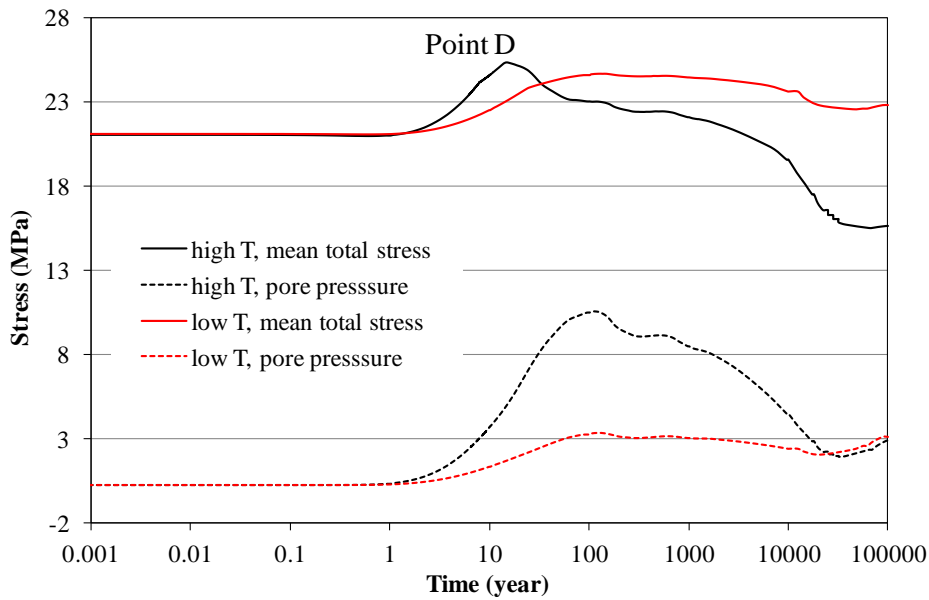


Figure 2-23. Simulation results of mean total stress, pore pressure, and thermal stress at point D for the “low T” and “high T” scenario, respectively.

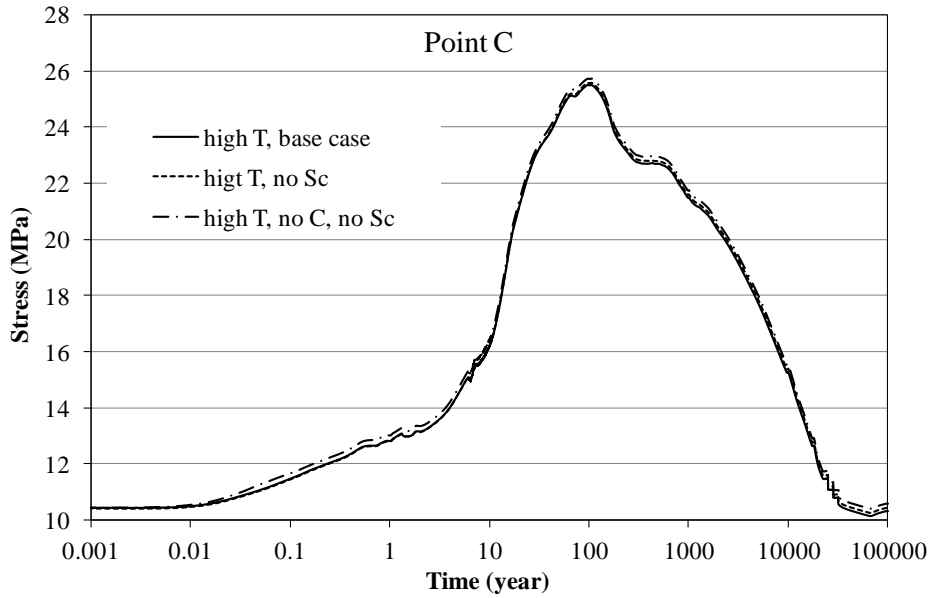


Figure 2-24. Simulation results of mean total stress at point C for the “high T” scenarios in three cases: the “high T, base case” in which the effect ion concentration and smectite change on stress are considered; the “high T, no Sc” case in which the contribution of smectite change to stress is neglected and the “high T, no C, no Sc” case in which both the contribution of smectite change and ion concentration to stress are neglected.

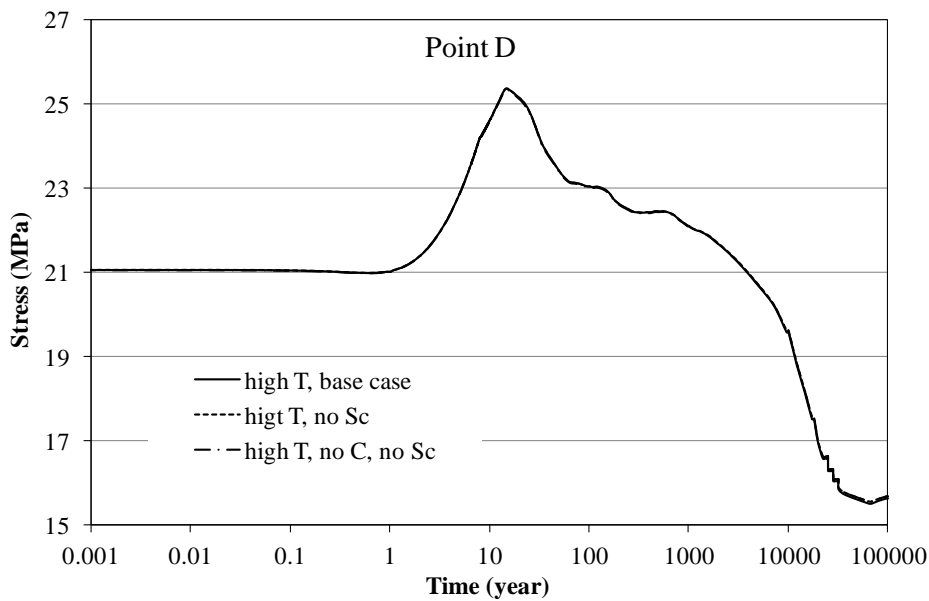


Figure 2-25. Simulation results of mean total stress at point D for the “high T” scenarios in three cases: the “high T, base case” in which the effect ion concentration and smectite change on stress are considered; the “high T, no Sc” case in which the contribution of smectite change to stress is

neglected and the “high T, no C, no Sc” case in which both the contribution of smectite change and ion concentration to stress are neglected.

2.3.2 Cases for FEBEX Bentonite

In order to understand the change in THMC properties under high temperature for different conditions, models were also developed for FEBEX bentonite as an alternative to Kunigel-VI bentonite discussed in Section 2.3.1. Kunigel-VI bentonite (Ochs et al., 2004) is one of those that have low smectite content and relative low swelling capacity, whereas FEBEX bentonite (ENRESA, 2000) represents a type of bentonite that has high fraction of smectite and high swelling capacity. Kunigel-VI bentonite differs from the FEBEX bentonite in the following aspects (Zheng et al., 2014):

1. In terms of mineralogical composition, the most pronounced and relevant difference between FEBEX and Kunigel-VI bentonite is content of smectite, with FEBEX bentonite containing about 60 vol% smectite and Kunigel-VI bentonite having only about 31 vol% smectite (see Table 2-1). FEBEX bentonite also has less K-feldspar, which could affect illitization. The published mineralogical compositions vary slightly (Zheng et al., 2014), and the average was used in the model. Note that Table 2-1 lists the volume fraction whereas most published values are mass fraction.
2. In terms of aqueous chemistry, FEBEX bentonite has a higher ion concentration in pore water than Kunigel-VI bentonite, as shown in Table 2-2. The concentration of major cations, i.e. Ca, Mg, Na, K for FEBEX bentonite is about 2 orders of magnitude higher than that for Kunigel-VI bentonite, which could affect illitization over the course of heating and hydration.
3. The swelling pressure for FEBEX bentonite, ranging from 4.5 MPa (Castellanos et al., 2008) to 7 MPa (ENRESA, 2000), is higher than the swelling pressure for Kunigel-VI bentonite, with a swelling pressure of around 1 MPa (Börgesson et al. 2001; Komine and Ogata, 1996) measured using distilled water. Therefore the β_{sw} in Equation (2-4) for FEBEX bentonite is 0.238 (Rutqvist et al., 2011), which is higher than that used for Kunigel-VI bentonite (0.048).
4. Another difference between FEBEX and Kunigel-VI bentonite is the parameter A_{sc} that relates swelling stress with the abundance of smectite. For FEBEX bentonite, A_{sc} is $6.5E+6 \text{ Pa}^{-1}$ (Zheng et al., 2014), which is higher than $2.5E+6 \text{ Pa}^{-1}$ used for Kunigel-VI bentonite.

2.3.2.1 Chemical Evolution

In order to delineate the effect of differences in chemical and mechanical properties on the long term chemical changes and the subsequent mechanical changes, the same thermal conductivity and permeability are used for FEBEX bentonite as used for Kunigel-VI bentonite. The temperature, water saturation and pore pressure for FEBEX bentonite are therefore the same as shown in Figures 2-4 through 2-6. Changes in smectite and illite volume fractions are shown in Figures 2-26 and 2-27. An examination of the model results for Kunigel-VI and FEBEX bentonite reveals that some changes are common to both bentonites and some are distinct. Some common observations for both bentonites are as follows:

- Illitization (dissolution of smectite and precipitation of illite) occurs in bentonite and is enhanced at higher temperature.
- Bentonite near the NS-EBS interface undergoes more illitization than that near the waste package.
- Starting from about 1,600 years for the “high T” case, coincident with the time that smectite is depleted and illitization ceases in the clay formation near the NS-EBS interface, the dissolution of smectite is accelerated.
- In the far field of the clay formation (e.g. point D), it takes about 3,400 years to transform all smectite to illite for the “high T” case, but there is still 60% left after 100,000 years for the “low T” case.

However, in comparison with the model results for Kunigel-VI bentonite, several distinct features have been observed for FEBEX bentonite.

- There is less smectite dissolution for FEBEX bentonite for both “high T” and “low T” scenarios after 100,000 years. For the “high T” case, smectite volume fraction decreases about 0.03 at point A and 0.14 at point B, about 5% and 23% of the initial smectite volume fraction, respectively. These changes are significantly lower than a decrease of 0.05 (17% of initial amount) at point A and 0.19 (60% of the initial amount) for Kunigel-VI bentonite.
- The enhancement of illitization (expressed as smectite dissolution and illite dissolution) by temperature is less pronounced for FEBEX, i.e. the difference between the amount of smectite dissolving for the “low T” and “high T” scenarios is less significant for FEBEX bentonite than for Kunigel-VI bentonite.
- Although the different types of EBS bentonite have almost no impact on the chemical changes in the clay formation away from the EBS-NS interface (illustrated by results at point D Figures 2-26 and 2-27), the type of bentonite does have a moderate impact on the clay formation near the EBS interface. As shown by the results at point C in Figures 2-26 and 2-27, with FEBEX bentonite, smectite dissolution occurs earlier in the clay formation. The reason is that FEBEX bentonite has a higher K concentration (see Table 2-2) so that the diffusion of K from the clay formation into the bentonite is at lower rate, and subsequently more K is available in the clay formation for illitization.

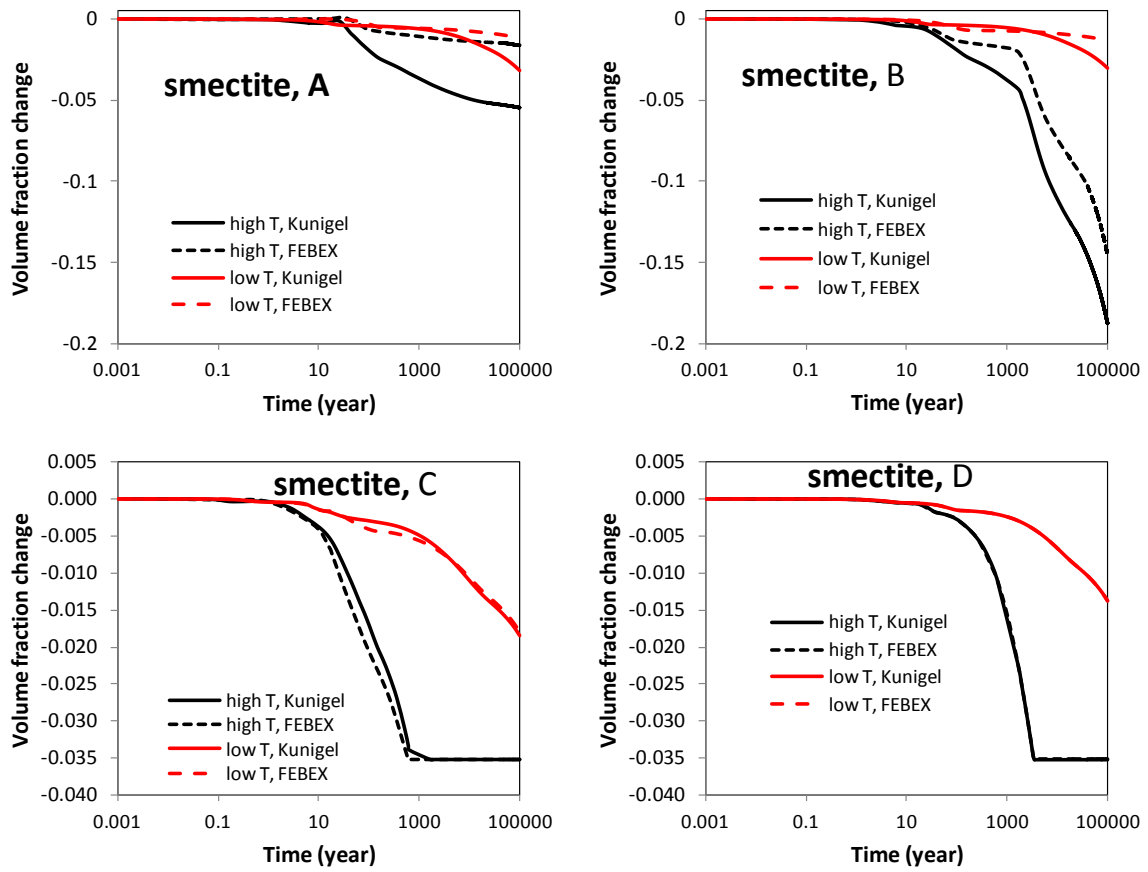


Figure 2-26. The temporal evolution of smectite volume fraction at points A, B, C, and D for Kunigel and FEBEX bentonite.

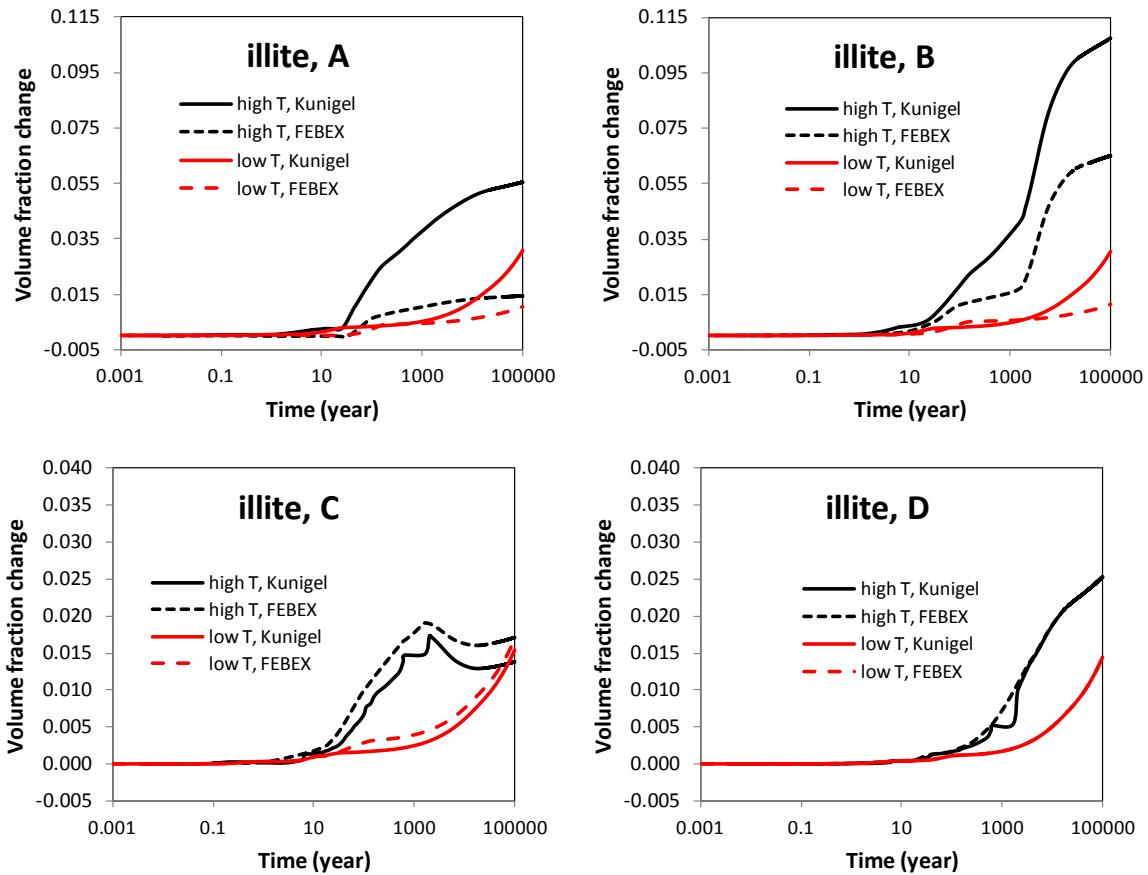


Figure 2-27. The temporal evolution of illite volume fraction at points A, B, C, and D for Kunigel and FEBEX bentonite.

A sensitivity analysis of illitization in the EBS to key chemical parameters was documented in Liu et al. (2013), which confirms the importance of available K to illitization. This sensitivity has also been widely observed in geological formations (e.g. Cuadros, 2006), which further demonstrates that the source of K is actually the dissolution of K-feldspar. When FEBEX bentonite is used as the EBS material, much less K-feldspar dissolution occurs compared with the case using Kunigel-VI bentonite, as illustrated in Figure 2-28. This is the reason why in Figure 2-26 there is less smectite dissolution for FEBEX bentonite than that for Kunigel-VI bentonite. Less dissolution of K-feldspar for FEBEX bentonite can be attributed to two factors: a lower content of K-feldspar and a higher K concentration in pore water for FEBEX bentonite.

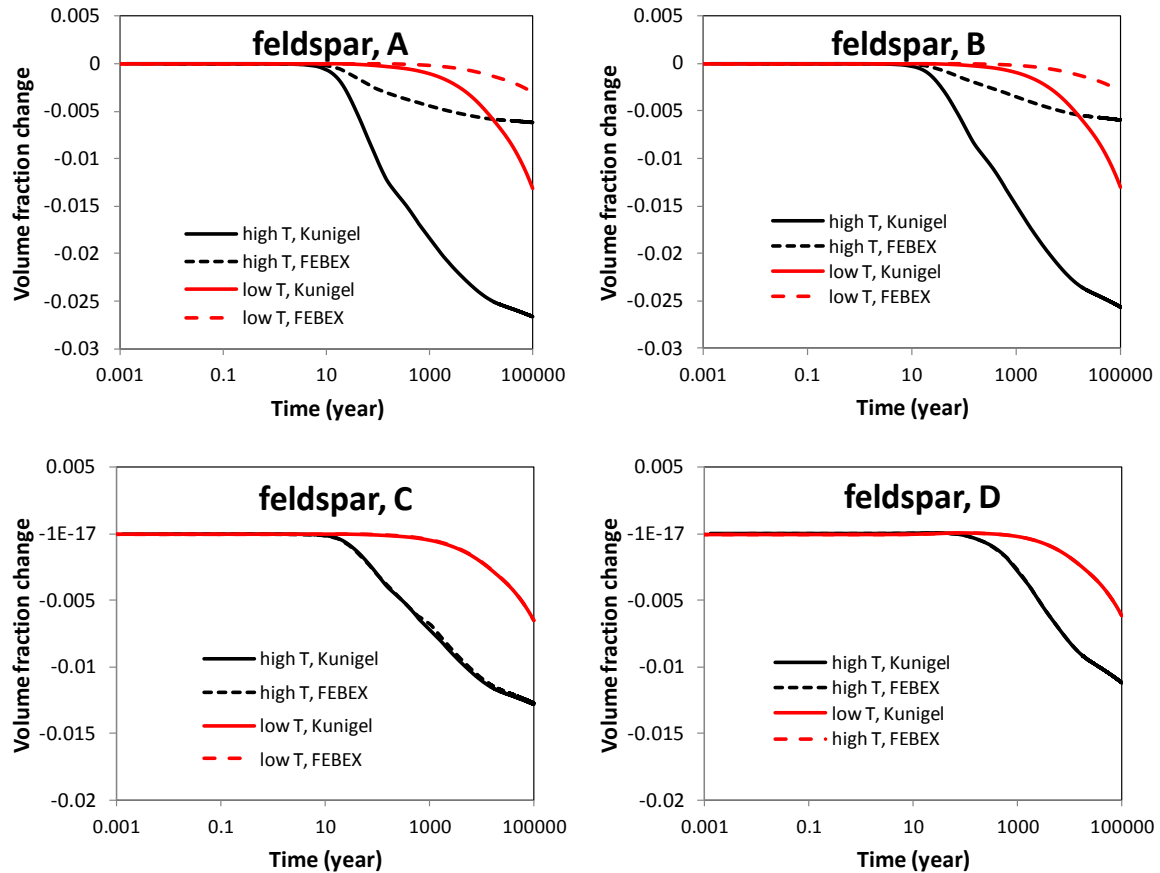
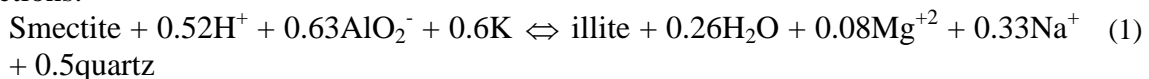


Figure 2-28. The temporal evolution of K-feldspar volume fraction at points A, B, C, and D in the base case with Kunigel bentonite and a sensitivity case with FEBEX bentonite.

One of the byproducts of illitization is the precipitation of quartz as shown in the following reactions:



The cementation by quartz (or amorphous SiO₂ minerals) might lower the swelling of bentonite and increase the brittleness of the bentonite. In comparison with Kunigel-VI bentonite, there is less quartz precipitation for the case with FEBEX bentonite (see Figure 2-19). For the “high T” scenario, the amount of quartz formed in FEBEX bentonite is only about 30% of that for Kunigel-VI bentonite.

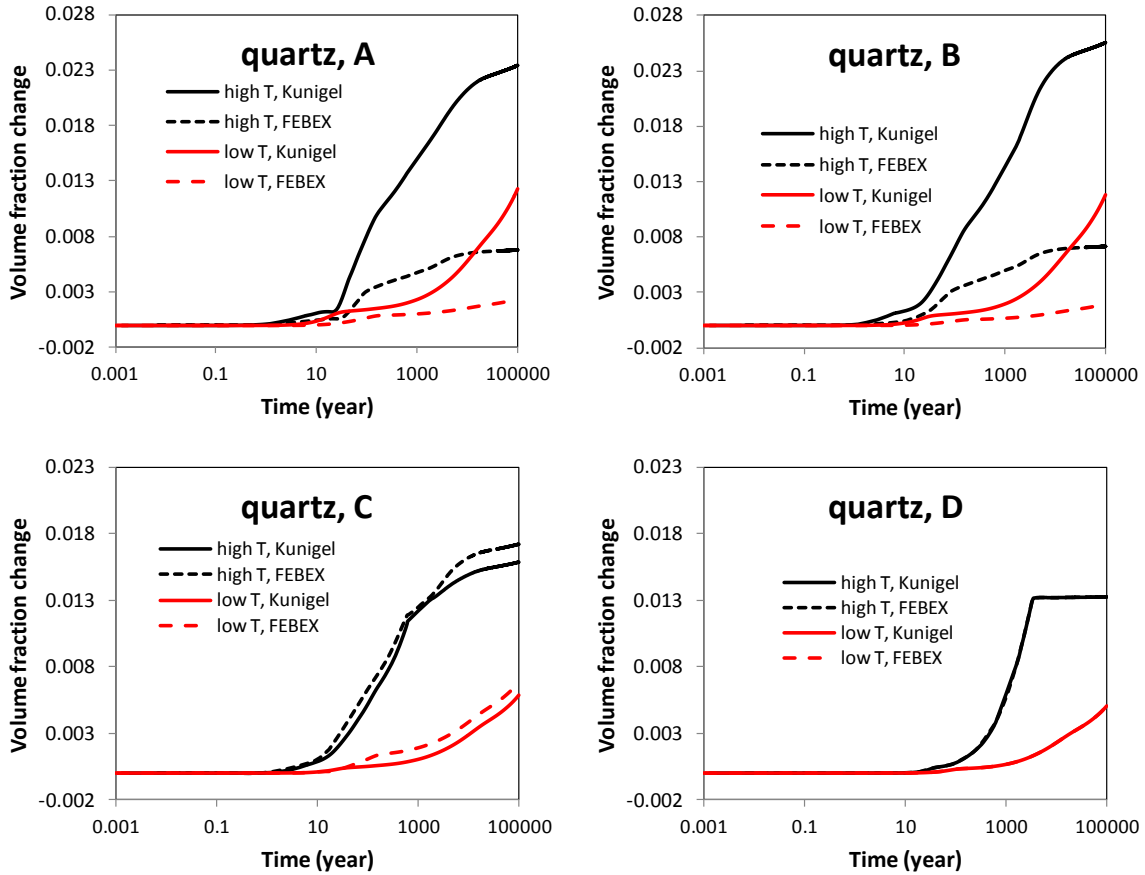


Figure 2-29. The temporal evolution of quartz volume fraction at points A, B, C, and D in the base case with Kunigel bentonite and a sensitivity case with FEBEX bentonite.

We also tested the behavior of FEBEX bentonite containing Na-smectite versus Ca-smectite to investigate the effects of calcite dissolution on long term illitization, as done for Kunigel-VI bentonite in Section 2.3.1. The reaction of Ca-smectite is given in Equation (2-10) above.

Calcite dissolution is a fairly fast process. For the “low-T” case, it takes about 7 years to dissolve all the calcite initially present, as manifested by the plateau of the volume fraction change in Figure 2-30. For the “high-T” case, higher temperature leads to a faster reaction rate, so it takes only about 3 years to deplete calcite if Ca-smectite is considered in the model compared with 5 years if Na-smectite is modeled. Because there is only a small amount of calcite initially in the bentonite and the dissolution of calcite is fast, the effect of calcite on the illitization is short-lived. In Figure 2-31, the volume fraction of illite in the first 200 years is plotted to highlight this effect. If Ca-smectite is used, because of the dissolution of calcite, the formation of illite is delayed in comparison with the case that Na-smectite is used because calcite interferes with illitization. But after 200 years (see Figures 2-32 and 2-33), the difference in illitization between the Ca-smectite and Na-smectite is very small.

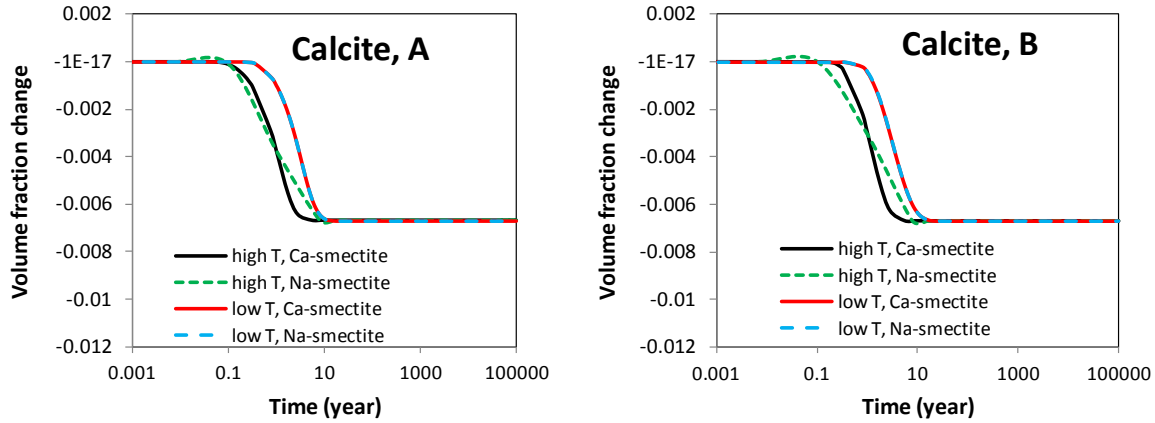


Figure 2-30. The temporal evolution of calcite volume fraction at points A and B for the case with Ca-smectite and Na-smectite in FEBEX bentonite.

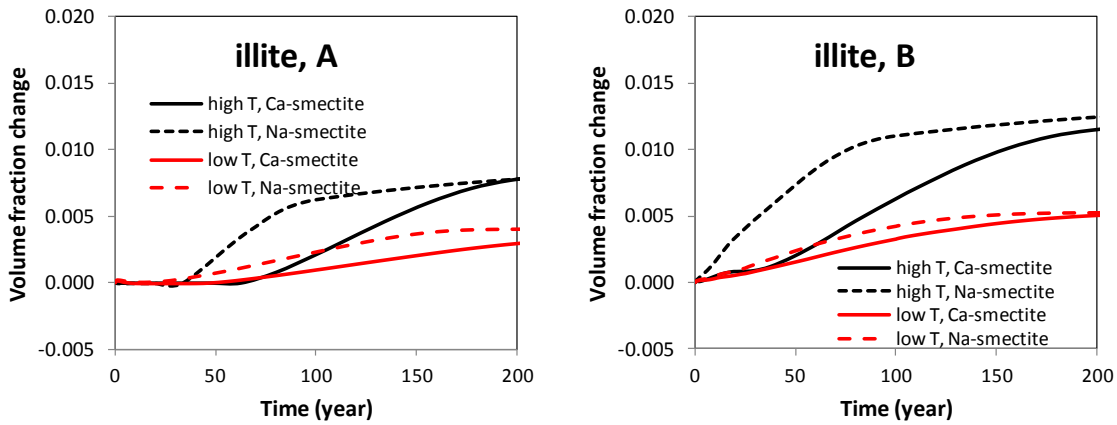


Figure 2-31. The temporal evolution of Ca-smectite/Na-smectite volume fraction for 200 years at points A and B for the case with Ca-smectite and Na-smectite in FEBEX bentonite.

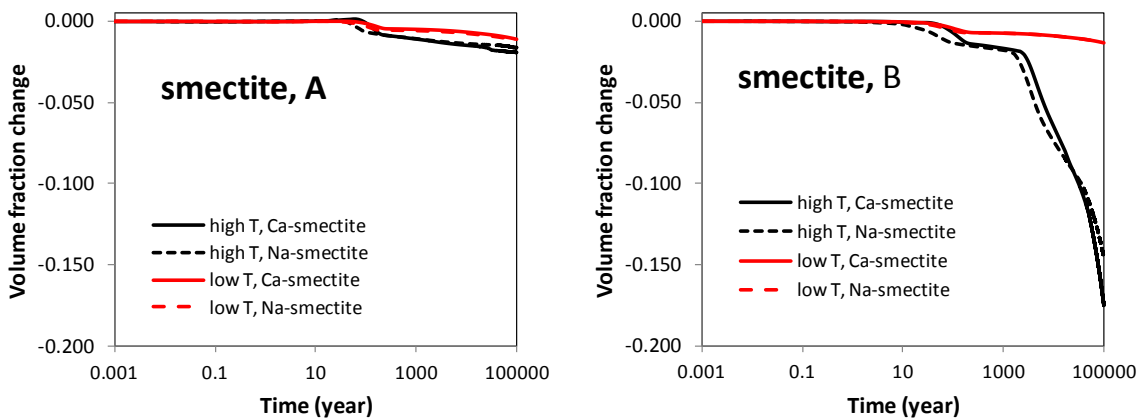


Figure 2-32. The temporal evolution of illite volume fraction at points A and B for the case with Ca-smectite and Na-smectite in FEBEX bentonite.

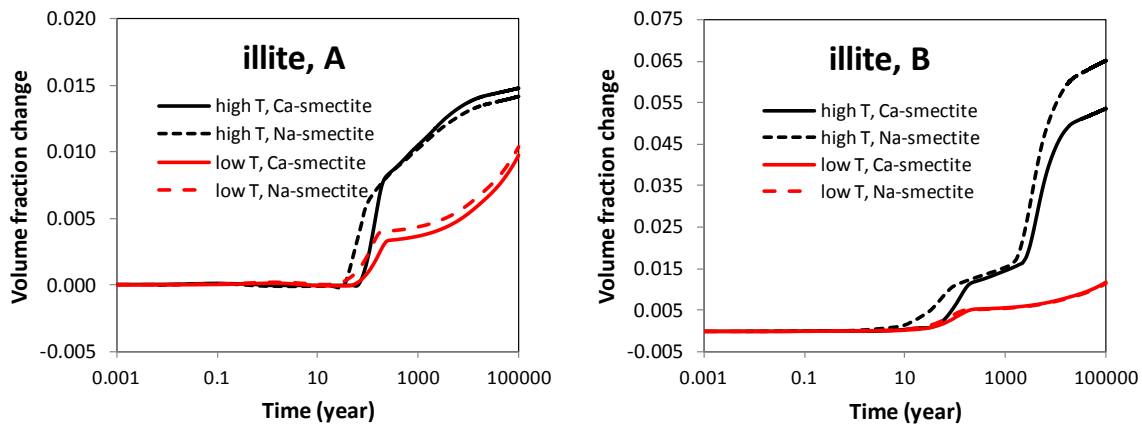


Figure 2-33. The temporal evolution of illite volume fraction at points A, B for the case with Ca-smectite and Na-smectite in FEBEX bentonite.

2.3.2.2 Stress Evolution

Figures 2-34 and 2-35 show the stress changes in the sensitivity run using FEBEX bentonite at points A and B for both “low T” and “high T” cases. As discussed in Section 2.3.1.2, the increase in pore pressure due to hydration and thermal pressurization (a processes caused by the difference in thermal expansion of the fluid and solid host rock), bentonite swelling, and thermal expansion are the main driving force for the increase in total stress in bentonite. In comparison with the “low T” case, the stronger thermal pressurization in the “high T” case clearly leads to much higher stress in the bentonite. For both the “high T” and “low T” cases, the major contribution to the total stress within the buffer is from pore pressure, with smaller contributions from swelling and thermal stress. As observed for Kunigel-VI bentonite, the stress peak occurs at around 100 years and then decreases thereafter. After 20,000 to 30,000 years, the stress seems to reach a stable state.

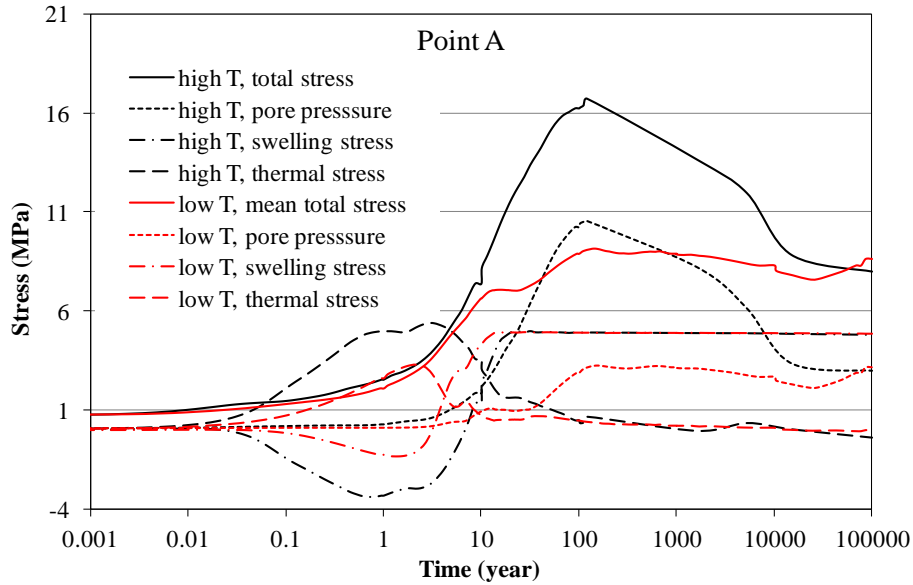


Figure 3-34. Simulation results of mean total stress, pore pressure, swelling stress, and thermal stress at point A in the sensitivity case with FEBEX bentonite for the “low T” and “high T” scenarios, respectively.

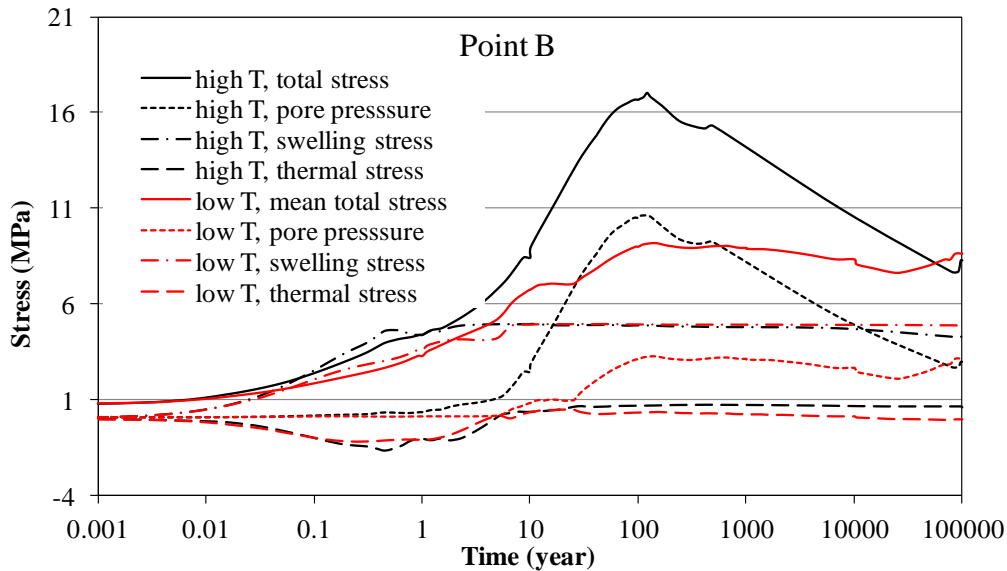


Figure 2-35. Simulation results of mean total stress, pore pressure, swelling stress, and thermal stress at point B in the sensitivity case with FEBEX bentonite for the “low T” and “high T” scenarios, respectively.

Figures 2-36 and 2-37 compare the total stress calculated for the Kunigel-VI and FEBEX bentonite. Because FEBEX bentonite has higher swelling pressure, the total stress for FEBEX bentonite at points A and B are 3-4 MPa higher than that for Kunigel bentonite at the peak (100 years) and this difference persists until the end of the simulation at 100,000 years.

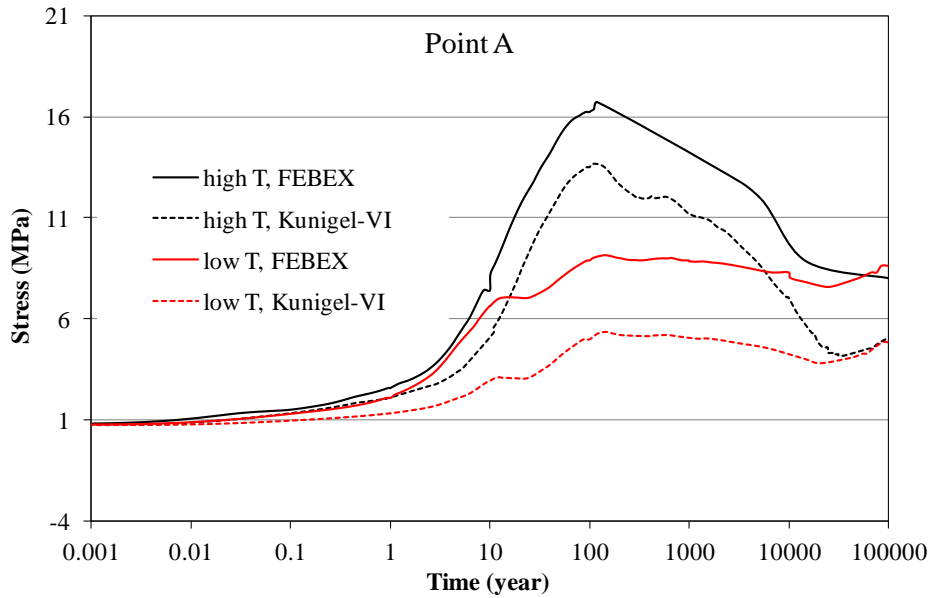


Figure 2-36. Simulation results of mean total stress at point A for Kunigel-VI and FEBEX bentonite for the “low T” and “high T” scenarios, respectively.

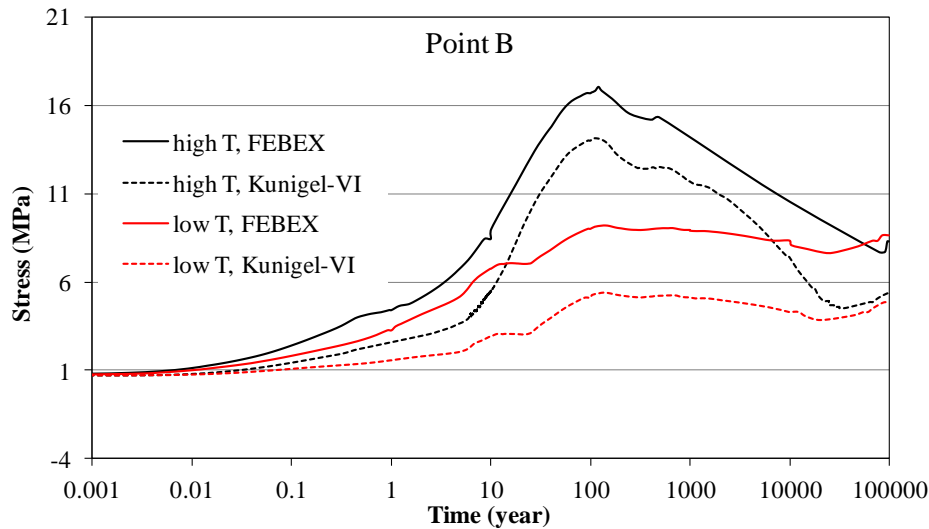


Figure 2-37. Simulation results of mean total stress at point B for Kunigel-VI and FEBEX bentonite for the “low T” and “high T” scenarios, respectively.

The constitutive relationship described by Equation (2-5) shows that the swelling stress changes have contributions from moisture, ion concentration and smectite changes. Similar to what has been done for the Kunigel-VI bentonite, we also present three sets of calculated swelling stresses for FEBEX bentonite to delineate the contribution from each process. In the first set, denoted in Figures 2-38 to 2-41 as “ $\sigma=f(SI,C,Ms)$ ”, the swelling stress is calculated according to Equation (2-5) as a function of liquid saturation changes (SI), ion concentration (C) changes, and smectite

(Ms) changes. In the second set, denoted as “ $\sigma=f(SI,C)$ ”, the contribution from smectite changes in Equation (2-5) is disregarded, and the swelling stress is only a function of liquid saturation and ion concentration. In the third set, denoted as “ $\sigma=f(SI)$ ”, all chemical effects are neglected, and the swelling stress is only a function of liquid saturation changes. At point A near the canister, pore water in the bentonite evaporates causing the liquid saturation to decrease. This results in a decrease of swelling stress (shrinkage) until about 4 years for “low T” scenario and 8 years for “high T” scenario (Figure 2-38). After that, increases in liquid saturation induce swelling and swelling stress keeps increasing until reaching the swelling capacity of 5 MPa. Figure 2-39 zooms in to show the stress from 4.5 to 5 MPa and illustrate the contribution from ion concentration and smectite changes. In comparison with the swelling stress for Kunigel-VI bentonite at point A, presented in Section 2.3.1.2, the swelling stress for FEBEX bentonite has two distinct features. First, ion concentration has a minimal effect on the swelling stress because the ion concentration of the pore water in FEBEX bentonite is fairly close to that in the clay formation. Second, a greater stress reduction due to smectite dissolution has been observed for FEBEX bentonite. Despite that, less smectite dissolution has been observed for FEBEX bentonite (Figure 2-26) and a higher A_{sc} (a parameter that relates swelling stress with the abundance of smectite) for FEBEX bentonite leads to slightly higher reduction in swelling stress. Table 2-5 lists the stress reduction by ion concentration and smectite dissolution at point A for Kunigel-VI and FEBEX bentonites. In total, chemical changes leads to about 0.17 MPa stress change for Kunigel-VI bentonite and 0.18 MPa for FEBEX bentonite. In comparison with the swelling stress obtained with “ $\sigma=f(SI)$ ”, chemical change causes about 16% reduction in swelling stress for Kunigel-VI bentonite, but only 3.4% for FEBEX bentonite.

Model results at point B (Figures 2-40 and 2-41) lead to the same observation in terms of the difference between Kunigel-VI and FEBEX bentonite, although the specific values differ significantly from those at point A. As we discussed in the previous section, because of the interaction between bentonite and the clay formation, bentonite near the interface goes through further dissolution of smectite after about 20,000–30,000 years when the dissolution of smectite in bentonite near the waste package become stable, which lead to further decrease in swelling stress. By the end of 100,000 years, as illustrated in Figure 2-41 and articulated in the Table 2-5, Kunigel-VI bentonite has lost more than half of its swelling capacity whereas FEBEX bentonite has lost about 13% of its swelling capacity. Generally speaking, in absolute numbers, Kunigel-VI and FEBEX bentonites undergo similar magnitudes of reduction in swelling stress, but relative to their swelling capacity (the maximum swelling stress which is typically measured by hydrating bentonite with deionized water), chemical changes cause a stronger reduction in swelling capacity for Kunigel-VI than for FEBEX bentonite. Therefore, using bentonite with a high swelling capacity such as FEBEX bentonite is always beneficial with respect to stress reduction caused by illitization.

Table 2-5. The geochemically induced swelling stress for Kunigel and FEBEX bentonite at points A and B for “high T” scenario. Stress reduction by ion concentration is the difference between the swelling stress obtained with “ $\sigma=f(SI)$ ” and “ $\sigma=f(SI,C)$ ”, and the stress reduction by smectite dissolution is the difference between the swelling stress obtained with “ $\sigma=f(SI,C)$ ” and “ $\sigma=f(SI,C,Ms)$ ” (see Figure 2-26), where the relative amount (%) use the results from “ $\sigma=f(SI)$ ” as the basis.

	Kunigel-VI bentonite				FEBEX bentonite			
	Stress reduction by ion concentration		Stress reduction by smectite dissolution		Stress reduction by ion concentration,		Stress reduction by smectite dissolution	
	MPa	%	MPa	%	MPa	%	MPa	%
Point A	0.07	7%	0.09	9%	0.006	0.1%	0.17	3.4%
Point B	0.08	8%	0.45	45%	0.06	1.1%	0.6	12%

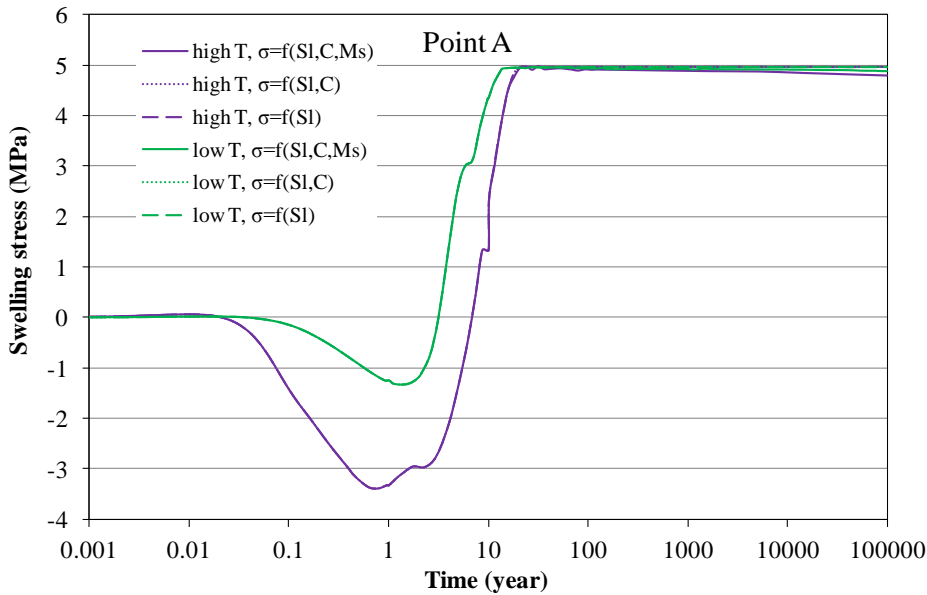


Figure 2-38. Simulation results of swelling stress at point A for the FEBEX bentonite for the “low T” and “high T” scenarios, respectively, focusing on the stress range from 4.5 to 5 MPa.

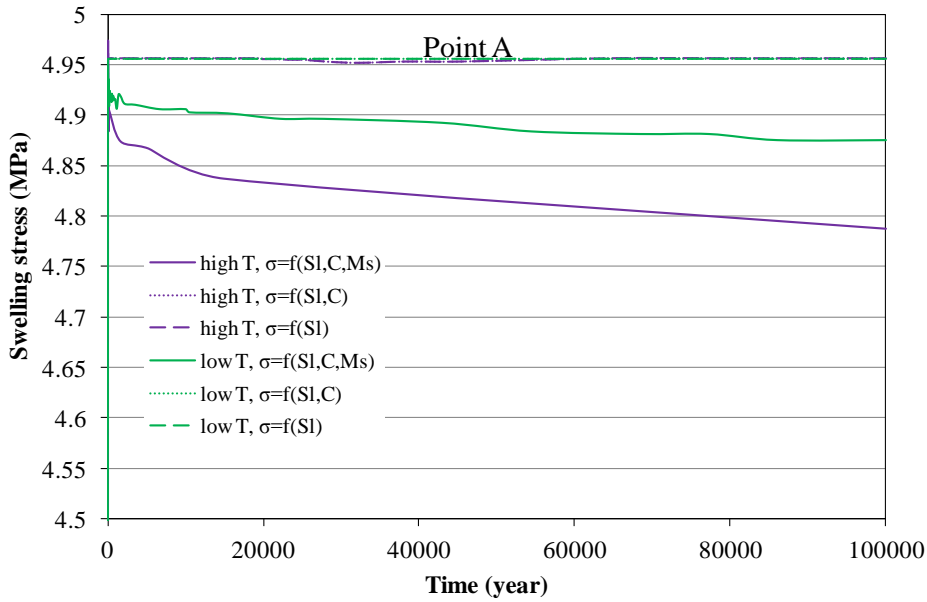


Figure 2-39. Simulation results of swelling stress at point A for the FEBEX bentonite for the “low T” and “high T” scenarios, respectively, focusing on the stress range from 4.5 to 5 MPa.

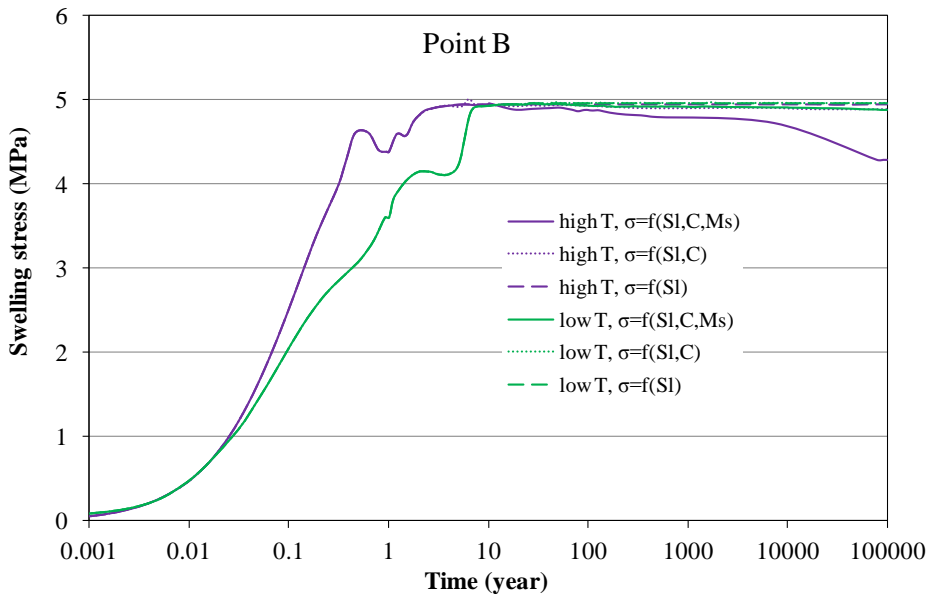


Figure 2-40. Simulation results of swelling stress at point B for the FEBEX bentonite for the “low T” and “high T” scenarios, respectively, focusing on the stress range from 4.5 to 5 MPa.

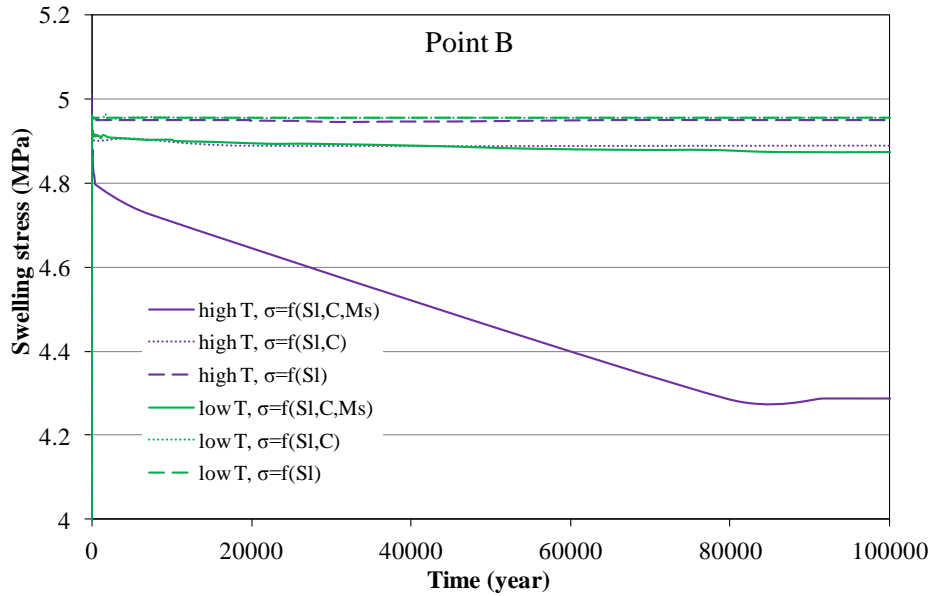


Figure 2-41. Simulation results of swelling stress at point B for the FEBEX bentonite for the “low T” and “high T” scenarios, respectively, focusing on the stress range from 4.5 to 5 MPa.

2.4 Conclusions

2.4.1 Summary of current modeling work

This part of the report documents our progress in FY15 to investigate the impact of strongly elevated temperature on the bentonite backfill and near-field clay host rock in a geologic repository for radioactive waste. Since FY13, we have been using coupled THMC modeling to evaluate the chemical alteration and associated mechanical changes in a generic repository to consider the interaction between EBS bentonite and the NS clay formation. Two main scenarios were developed for comparison: a “high T” case in which the temperature near the waste package can reach about 200 °C and a “low T” scenario in which the temperature peaks at about 100 °C. Conducting coupled THMC modeling is very challenging — it requires significant expansion of our modeling capability in terms of considering more processes and improving the numerical stability and efficiency of the current simulator TOUGHREACT-FLAC3D. One of the major achievements in FY15 is the implementation of a time-step management scheme in the TOUGHREACT-FLAC3D simulator to reduce the simulation time, which enables us to extend the simulations from 1,000 years to 100,000 years. The simulator was also revised to include chemical-mechanical coupling for clay formations. We also performed an evaluation of Ca-smectite illitization, which sheds light on the potential for calcite to interfere with smectite illitization.

Our model results for 100,000 years confirm some findings from the 1,000-year simulations (Liu et al., 2013; Zheng et al., 2014). There is some degree of illitization in the EBS bentonite and NS clay formation and illitization is enhanced under higher temperature. In addition to illitization, major chemical alterations include the dissolution of K-feldspar and calcite, the precipitation of quartz, chlorite, and kaolinite. The quantity of illitization, expressed as the smectite volume

fraction change, is affected by many chemical factors and as a result varies over a wide range. The most important chemical factors for illitization are the concentration of K and dissolution rate of K-feldspar. However, 100,000-year simulations also lead to some distinct observations regarding illitization, especially for the high temperature condition:

- Model results reveals that for the “high T” scenario, illitization is stabilized after about 2,000 years in bentonite near the waste package, but continues in bentonite near the EBS-NS interface. For the “low T” scenario, illitization is nearly stabilized after 2,000 years for the entire volume of EBS bentonite.
- The geochemical interaction between EBS bentonite and the clay formation has a strong effect on long term illitization in bentonite. Previous simulations, namely the 1,000-years simulations in Liu et al., (2013) and Zheng et al., (2014), showed that illitization reactions in bentonite are tied to the dissolution rate of K-feldspar that occurs locally, and as a result, illitization is fairly homogeneous in the entire bentonite barrier. However, the 100,000-year simulations show that bentonite near the EBS-NS interface undergo more illitization than that near the waste package by the end of 100,000 years for the “high T” scenarios. The reason is that after 2,000–3,000 years, the illitization process ceases in the clay formation and the K ion is not consumed by the local illitization and is, therefore, transported into the EBS bentonite to facilitate further illitization.
- The dissolution rate of K-feldspar, which was thought to be critical for illitization as revealed by the 1,000-years simulations, is not as important as the amount of K-feldspar available for longer time periods. The reason is that fast dissolution of K-feldspar leads to a quicker depletion of K-feldspar (in about 1,000 years) that permits greater illitization to occur within 1,000 years. However, for the 100,000 year time period, the amount of K-feldspar available controls how much illitization can occur rather than the dissolution rate of K-feldspar.

The simulations conducted in FY15 also reveal that the dissolution of calcite delays illitization by around 30 to 50 years for the case of Kunigel-VI and FEBEX bentonite if Ca-smectite is the major smectite phase in the bentonite. Although this effect is short-lived and not important as far as long-term illitization is concerned, calcite dissolution might explain why illitization was not observed in some laboratory and field experiments.

In terms of the effect of chemical changes on swelling stress for bentonite, the current modeling results show a more significant reduction in swelling stress as a result of smectite dissolution after 100,000 years than previously revealed by the 1,000-years simulations. This is particularly true for bentonite near the EBS-NS interface as illitization continues in these areas. For the “high T” case, Kunigel-VI bentonite near the EBS-NS loses as much as 53% swelling capacity and FEBEX bentonite near the EBS-NS has about 13% reduction in swelling stress, whereas bentonite near the waste package undergoes a small reduction in swelling stress — 16% reduction for Kunigel-VI and 3.4% for FEBEX bentonite, respectively. For the “low T” case, the stress reduction by chemical change is relatively homogeneous, 16% reduction for Kunigel-VI bentonite and around 3% reduction for FEBEX bentonite after 100,000 years.

In FY15, chemical effects were incorporated in the mechanical model for the clay formation and the effect of chemical change in clay formation on the total stress was evaluated. Chemical change leads to about a 2.6% decrease in stress near the EBS-NS interface and about 0.7% in the

far field. In general, chemical change does not have significant impact on the stress in the clay formation.

2.4.2 FUTURE WORK

The current coupled THMC model greatly improves our understanding of the coupled processes contributing to chemical and mechanical alteration in EBS bentonites and NS argillite formations and answers questions regarding the thermal limit of EBS bentonite in clay repository. However, more questions remain to be answered regarding the THMC alteration of bentonites and clay formations under high temperature. Further refinement of current models and improvements for the TOUREACT-FLAC3D simulator are needed in the future. In the remaining months of FY15 and FY16 the following activities are proposed:

- A more rigorous approach to link chemistry to mechanics is needed for more accurate calculations than the current extended linear elastic swelling model. More comprehensive links between chemistry and mechanics, taking advantage of the framework provided by a dual-structure model, was implemented in TOUGHREACT-FLAC (Rutqvist et al., 2014), and could be used to simulate the chemical-mechanical coupling for EBS bentonite in the future.
- In the current model, the canister serves only as a heat source; chemical changes on the surface of the canister are neglected for simplification. Further model analysis is needed to consider chemical changes in the canister, specifically the release of Fe^{+2} , which might enhance the dissolution of smectite by forming chlorite.
- Current models show significant precipitation of silicate minerals during illitization, which could result in the cementation of bentonite and subsequently lead to change in the mechanical properties of bentonite. While the current model can quantify the formation of silicate minerals, the change of mechanical properties as result of cementation needs to be quantified. This requires a mechanical-chemical coupling scheme for cementation to be incorporated and tested in the next version of the simulator.

References

- Alonso, E. E., J. Vaunat and A. Gens 1999. Modeling the mechanical behaviour of expansive clays. *Engineering Geology* 54: 173-183.
- Bossart P. (2011) Characteristics of the Opalinus Clay at Mont Terri, http://www.mont-terri.ch/internet/mont-terri/en/home/geology/key_characteristics.html
- Börgesson, L., Chijimatsu, M., Nguyen, T.S., Rutqvist, J., Jing L. (2001) Thermo-hydro-mechanical characterization of a bentonite-based buffer material by laboratory tests and numerical back analyses. *Int. J. Rock Mech. & Min. Sci.* 38, 105-127.
- Bucher, F., and Müller-Vonmoos, M. (1989) Bentonite as a containment barrier for the disposal of highly radioactive waste. *Applied Clay Science*, 4(2): 157–177.
- Castellanos, E., M. V. Villar, E. Romero, A. Lloret and A. Gens 2008. Chemical impact on the hydro-mechanical behaviour of high-density FEBEX bentonite. *Physics and Chemistry of the Earth, Parts A/B/C* 33, Supplement 1(0): S516-S526.
- Chen, Y., C. Zhou and L. Jing 2009. Modeling coupled THM processes of geological porous media with multiphase flow: Theory and validation against laboratory and field scale experiments. *Computers and Geotechnics* 36(8): 1308-1329.
- Cuadros, J. 2006. Modeling of smectite illitization in burial diagenesis environments. *Geochimica et Cosmochimica Acta* 70(16): 4181-4195.
- ENRESA 2000. Full-scale engineered barriers experiment for a deep geological repository in crystalline host rock FEBEX Project, European Commission: 403.
- Fernández, A. M., B. Baeyens, M. Bradbury and P. Rivas (2004). Analysis of the porewater chemical composition of a Spanish compacted bentonite used in an engineered barrier. *Physics and Chemistry of the Earth, Parts A/B/C* 29(1): 105-118.
- Fernández, A., Cuevas, J., Rivas, P., 2001. Pore water chemistry of the FEBEX bentonite. *Mat. Res. Soc. Symp. Proc.* 663, 573–588.
- Fernández, A. M., Turrero, M. J., Sánchez, D. M., Yllera, A., Melón, A. M., Sánchez, M., Peña, J., Garralón, A., Rivas, P., Bossart, P. and Hernán, P. (2007) On site measurements of the redox and carbonate system parameters in the low-permeability Opalinus Clay formation at the Mont Terri Rock Laboratory. *Physics and Chemistry of the Earth, Parts A/B/C* 32(1-7): 181-195.
- Horseman S.T. and McEwen, T. J. (1996) Thermal constrains on disposal of heat-emitting waste in argillaceous rocks, *Engineering Geology* 41, 5-16.
- Hicks, T.W., White, M.J. and Hooker, P.J. (2009) Role of Bentonite in Determination of Thermal Limits on Geological Disposal Facility Design, Report 0883-1, Version 2, Falson Sciences Ltd., Rutland, UK, Sept. 2009.
- Itasca, 2009. FLAC3D, Fast Lagrangian Analysis of Continua in 3 Dimensions, Version 4.0, Minneapolis, Minnesota, Itasca Consulting Group.
- JNC, Japan Nuclear Cycle Development Institute. (1999) H12: project to establish the scientific and technical basis for HLW disposal in Japan: supporting report 2 (respiratory design and engineering Technology). Japan Nuclear Cycle Development Institute, Tokyo.
- Komine, H., and Ogata, N. (1996) Prediction for swelling characteristics of compacted bentonite. *Canadian Geotechnical Journal*, 33: 11–22.
- Karland, O., Olsson, S. and Nilsson, U. (2006) Mineralogy and sealing properties of various bentonites and smectite-rich clay materials, SKB Technical Report TR-06-30.

- Laredj, N., Missoum, H. and Bendani, K. (2010) Modeling the effect of osmotic potential changes on deformation behavior of swelling clays. *Journal of Porous Media* 13(8): 743-748.
- Lasaga, A. C., J. M. Soler, J. Ganor, T. E. Burch and K. L. Nagy 1994. Chemical weathering rate laws and global geochemical cycles. *Geochimica et Cosmochimica Acta* 58: 2361-2368.
- Lauber, M., B. Baeyens and Bradbury, M. H. (2000) Physico-Chemical Characterisation and Sorption Measurements of Cs, Sr, Ni, Eu, Th, Sn and Se on Opalinus Clay from Mont Terri. PSI Bericht Nr. 00-10 December 2000 ISSN 1019-0643.
- Liu, H.H., J. Houseworth, J. Rutqvist, L. Zheng, D. Asahina, L. Li, V. Vilarrasa, F. Chen, S. Nakagawa, S. Finsterle, C. Doughty, T. Kneafsey and J. Birkholzer. (2013) Report on THMC modeling of the near field evolution of a generic clay repository: Model validation and demonstration, Lawrence Berkeley National Laboratory, August, 2013, FCRD-UFD-2013-0000244.
- Nguyen, T. S., A. P. S. Selvadurai and G. Armand 2005. Modelling the FEBEX THM experiment using a state surface approach. *International Journal of Rock Mechanics and Mining Science* 42(5-6): 639-651.
- Ochs, M., Lothenbach, B., Shibata, M. and Yui, M. (2004) Thermodynamic modeling and sensitivity analysis of porewater chemistry in compacted bentonite. *Physics and Chemistry of the Earth, Parts A/B/C* 29(1): 129-136.
- Pusch R. and Karnland, O. (1996) Physico/chemical stability of smectite clays, *Engineering Geology* 41: 73-85.
- Pusch, R., Kasbohm, J. and Thao, H. T. M. (2010) Chemical stability of montmorillonite buffer clay under repository-like conditions—A synthesis of relevant experimental data. *Applied Clay Science* 47(1–2): 113-119.
- Pusch, R. and Madsen, F. T. (1995) Aspects on the illitization of the kinnekulle bentonites. *Clays and Clay Minerals* 43(3): 261-270.
- Ramírez, S., J. Cuevas, R. Vigil and S. Leguey 2002. Hydrothermal alteration of “La Serrata” bentonite (Almeria, Spain) by alkaline solutions. *Applied Clay Science* 21(5–6): 257-269.
- Rutqvist, J., Y. Ijiri and H. Yamamoto 2011. Implementation of the Barcelona Basic Model into TOUGH–FLAC for simulations of the geomechanical behavior of unsaturated soils. *Computers & Geosciences* 37(6): 751-762.
- Rutqvist, J., Zheng, L., Chen, F., Liu, H.-H. and Birkholzer, J. (2013). Modeling of Coupled Thermo-Hydro-Mechanical Processes with Links to Geochemistry Associated with Bentonite-Backfilled Repository Tunnels in Clay Formations. *Rock Mechanics and Rock Engineering*: 1-20.
- Rutqvist, J., Zheng, L., Chen, F., Liu, H.-H. and Birkholzer, J. (2014) Modeling of Coupled Thermo-Hydro-Mechanical Processes with Links to Geochemistry Associated with Bentonite-Backfilled Repository Tunnels in Clay Formations. *Rock Mechanics and Rock Engineering*: 47(1): 167-186.
- Sánchez, M., A. Gens, L. J. D. N. Guimarães and S. Olivella 2005. A double structure generalized plasticity model for expansive materials. *International Journal for numerical and analytical methods in geomechanics* 29: 751-787.
- Soler, J. M. 2001. The effect of coupled transport phenomena in the Opalinus Clay and implications for radionuclide transport. *Journal of Contaminant Hydrology* 53: 63-84.
- Sonnenthal, E. Chapter 5 in: Birkholzer, J. Rutqvist, E. Sonnenthal, and D. Barr, Long-Term Permeability/Porosity Changes in the EDZ and Near Field due to THM and THC

- Processes in Volcanic and Crystalline-Bentonite Systems, DECOVALEX-THMC Project Task D Final Report, 2008.
- Wersin P., Johnson, L.H. and McKinley, I.G. (2007) Performance of the bentonite barrier at temperature beyond 100oC: A critical review, *Physics and Chemistry of the Earth* 32: 780-788.
- Wolery, T. J. 1993. EQ3/6, A software package for geochemical modelling of aqueous systems (Version 7.2). , Lawrence Livermore National Laboratory.
- Xu, T., E. Sonnenthal, N. Spycher and K. Pruess 2006. TOUGHREACT: A Simulation Program for Non-isothermal Multiphase Reactive Geochemical Transport in Variably Saturated Geologic Media. *Computers and Geosciences* 32: 145-165.
- Xu, T., Spycher, N., Sonnenthal, E., Zhang, G., Zheng, L. and Pruess, K. (2011) TOUGHREACT Version 2.0: A simulator for subsurface reactive transport under non-isothermal multiphase flow conditions. *Computers & Geosciences* 37(6): 763-774.
- Zheng, L., Li, L., Rutqvist, J., Liu, H. and Birkholzer, J.T., (2012). Modeling Radionuclide Transport in Clays. Lawrence Berkeley National Laboratory. FCRD-URD-2012-000128
- Zheng, L., J. Samper and L. Montenegro 2011. A coupled THC model of the FEBEX in situ test with bentonite swelling and chemical and thermal osmosis. *Journal of Contaminant Hydrology* 126(1-2): 45-60.
- Zheng, L., Jonny Rutqvist, Carl Steefel, Kunhwi Kim, Fei Chen, Victor Vilarrasa, Seiji Nakagawa, Jiangtao Zheng, James Houseworth, Jens Birkholzer. (2014) Investigation of Coupled Processes and Impact of High Temperature Limits in Argillite Rock. FCRD-UFD-2014-000493, LBNL-6719E.

3. Developing THMC Models for FEBEX-DP

3.1 Introduction

The multi-barrier system in a nuclear waste repository typically consists of the natural barrier system (NBS), which includes the repository host rock and its surrounding subsurface environment, and the engineered barrier system (EBS). The EBS represents the man-made, engineered materials placed within a repository, including the waste form, waste canisters, buffer materials, backfill, and seals (OECD 2003).

The most common buffer material for EBS is compacted bentonite, which features low permeability and high retardation of radionuclide transport. The safety functions of EBS bentonite include limiting transport in the near field; damping the shear movement of the host rock; preventing the sinking of canisters (if emplaced in the center of the tunnel), limiting pressure on the canister and rock, and reducing microbial activity. To assess whether EBS bentonite can maintain these favorable features when undergoing heating from the waste package and hydration from the host rock, we need a thorough understanding of the thermal, hydrological, mechanical, and chemical evolution of bentonite under disposal conditions. While numerous laboratory experiments, field tests, and numerical models have been conducted to improve the understanding of each individual process or coupled THC/THM processes, there is a lack of studies on coupled THMC processes due to the challenges of conducting experiments and developing models that can cover all the THMC processes. Recently in the UFD program, coupled THMC models have been developed for a generic disposal system in clayey host rock with EBS bentonite (Liu et al., 2013; Zheng et al., 2014). However, model validation was difficult for lack of THMC data from long-term, large-scale experiments. The FEBEX (Full-scale Engineered Barrier EXperiment) *in situ* test, which has been operated for 18 years, provides a unique opportunity of validating coupled THMC models.

In the FEBEX *in situ* test, two heaters surrounded by bentonite blocks about 0.7 m thick were emplaced in a tunnel excavated in granite. The heaters were switched on in 1997. In 2002, heater 1 was dismantled; in 2015, the second heater is being dismantled in the FEBEX-DP project, which is comprised of extensive THMC and biological characterization of bentonite, and development of numerical models. LBNL/DOE joined FEBEX-DP project in FY15. The ultimate goal is to use THMC data from FEBEX-DP to validate THMC models and therefore enhance our understanding of coupled THMC process. In this section, we describe our progress in FY15, which includes the development of a TH model with Non-Darcian flow, a coupled THC model, and evaluation of these models with TH data obtained from the bentonite surrounding heater 2 and chemical data obtained from the dismantling of heater 1.

3.2 A Brief Description of FEBEX Experiments

The objective of the FEBEX experiment was to study the behavior of components in the near-field for a high-level radioactive waste (HLW) repository in crystalline rock. Specifically, the project aimed to demonstrate the feasibility of fabricating and assembling the EBS and developing methodologies and models for evaluation of the thermo-hydro-mechanical (THM) and thermo-hydro-chemical (THC) behavior of the near-field (ENRESA, 2000). These objectives were to be attained through the combination of *in situ* and mock-up tests, and numerous small

scale laboratory tests, and THM/THM modeling. The project was initially scheduled for a period of 7 years, from 1994 to 2001, but was extended several times as the experiments continued. Figure 3-1 shows the history of FEBEX projects, with different project names representing different operational stages. In 2002, the *in situ* test was partially dismantled — the heater 1 was turned off and the bentonite blocks surrounding heater 1 were sampled for THM/THC characterization. The final dismantling started in April 2015 and is expected to finish in August 2015.



Figure 3-1. The operational stages of FEBEX *in situ* test (Vomvoris, personal communication).

The bentonite used in the FEBEX project was from the Cortijo de Archidona deposit in the south of Spain. It has about 92% mass fraction of smectite, with a dry density of 1.6–1.7 g/cm³ and a swelling pressure of around 5 MPa. The average permeability of FEBEX bentonite is on the order of 10⁻²¹ m². Extensive THMC characterization of FEBEX bentonite was conducted at the early stage of the FEBEX project.

Small scale THM/THC experiments were also conducted to improve the understanding of the THM/THC changes in bentonite under simultaneous heating and hydration, which facilitated the design of large scale experiments and helped the calibration of key parameters for THM/THC models. Figure 3-2 shows an example of a THC experiment. A 4.29 kg FEBEX bentonite block 13 cm in height and 15 cm in diameter was placed in a stainless steel cylindrical hermetic cell (Figure 3-2). A heater maintained a constant temperature of 87.5 °C in the upper part of the cell. At the same time, the lower part of the bentonite block was hydrated with distilled water injected at a pressure of 1 MPa through a 2.4 cm thick porous stone. After 183 days of heating and hydration, the heater was switched off, hydration was stopped and the bentonite sample was allowed to reach the ambient temperature. Then, the bentonite block was sliced into five sections to measure the aqueous concentration of pore water.

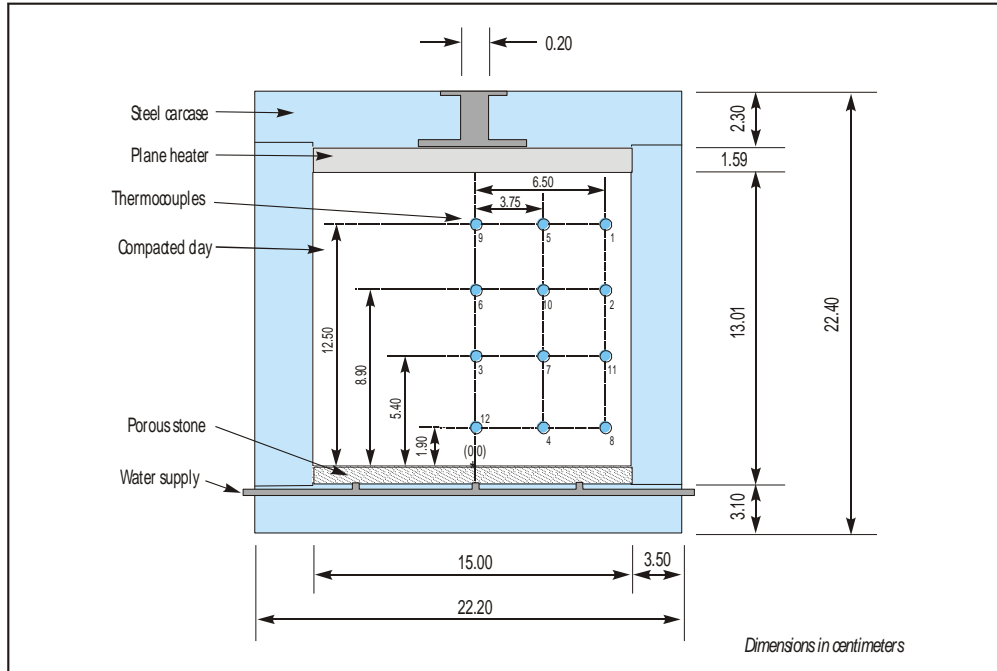


Figure 3-2. Schematic design of the heating and hydration laboratory experiment in the cell CT23 (ENRESA, 2006a).

In parallel with the *in situ* test, a mock-up test was conducted at CIEMAT facilities in Madrid, Spain (Martín and Barcala, 2005; Martín et al., 2006). Components of the mock-up test (Figure 3-3) are similar to those of *in situ* test: two electric heaters, a 0.64 m-thick bentonite barrier, instrumentation, automatic control of heaters, and a data-acquisition system. In the mock-up test the buffer is confined in a steel structure which ensures a uniform temperature and water pressure around the external surface of the buffer (Figure 3-3). The clay barrier is made of compacted bentonite blocks of dry density of 1.7 Mg/m^3 . Heating and hydration of the clay buffer started in February 1997 and has continued uninterruptedly until now.

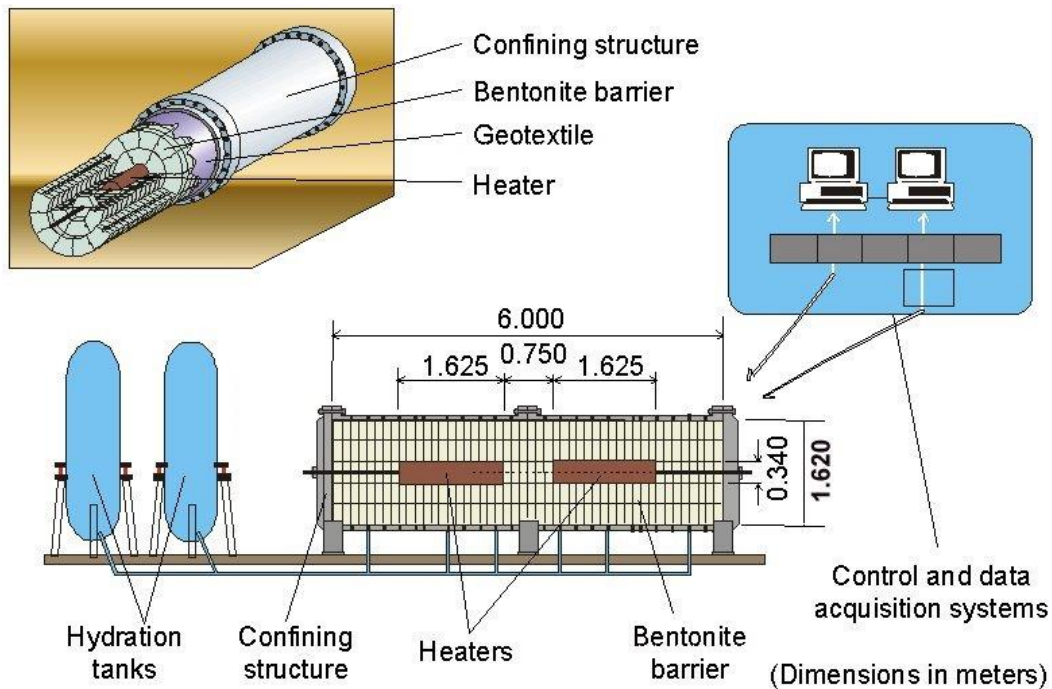


Figure 3-3. Schematic design of mock-up test (Martín et al., 2006).

The centerpiece of FEBEX experiments is, of course, the *in situ* test conducted at the Grimsel underground laboratory, Switzerland. The test consists of five basic units: the drift, the heating system, the bentonite barrier, the instrumentation, and the monitoring and control system (Figure 3-4). The drift is 70.4 m long and 2.28 m in diameter. The test area which was sealed with a concrete plug is located at the last 17.4 m of the drift where heaters, bentonite and instrumentation were installed. The main elements of the heating system are two heaters (1 and 2), 1 m apart, which simulate full-sized canisters. Heaters were placed inside a cylindrical steel liner. Each heater is made of carbon steel, measures 4.54 m in length and 0.9 m in diameter, and has a wall thickness of 0.1 m. Heaters were operated at a constant power output of 1200 W/heater during the first 20 days and 2000 W/heater for the following 33 days. Afterwards, the heaters were switched to a constant-temperature control mode to maintain a maximum temperature of 100 °C at the steel liner/bentonite interface.

The bentonite barrier is made of blocks of highly compacted bentonite, situated in vertical sections normal to the axis of the tunnel. The average values of the initial dry density and the water content of bentonite blocks are 1.7 g/cm³ and 14.4%, respectively.

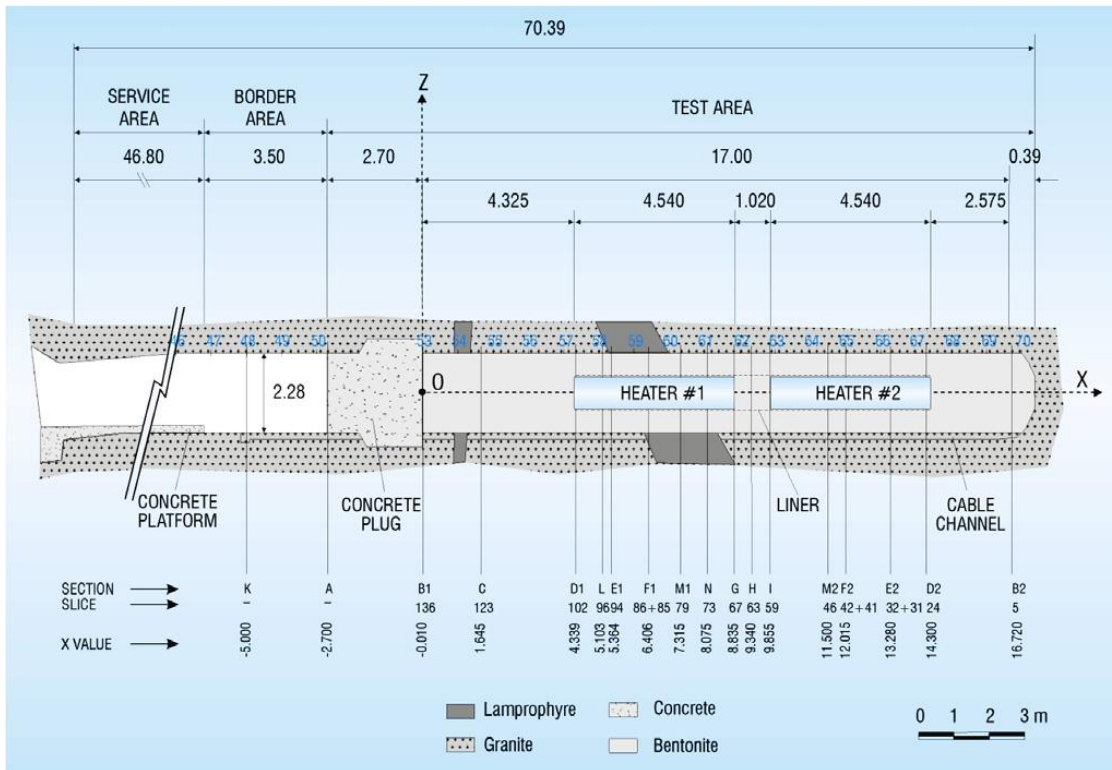


Figure 3-4. The initial configuration of FEBEX in situ test at the Grimsel underground laboratory (Switzerland) (ENRESA, 2000).

The *in situ* test began on February 27, 1997. Heater 1 was switched off in February 2002 and dismantled from May to September 2002. A comprehensive post-mortem bentonite sampling and analysis program was performed on the solid and liquid phases to check the physical and chemical changes induced by the combined effect of heating and hydration and to test THM and THC model predictions (ENRESA 2006a, b). Figure 3-5 shows the moisture content at section 15 after the dismantling of heater 1. The location of section 15 is shown in Figure 3-6. Note that the sections during dismantling of heater 1 are different from that was originally designated in the initial configuration as shown in Figure 3-4.

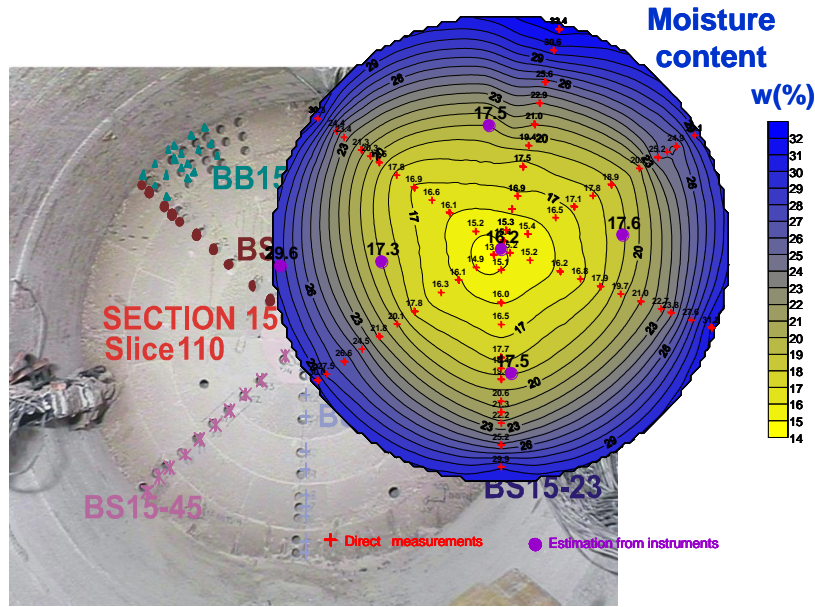


Figure 3-5. The moisture content (gravimetric water content) at section 15(Vomvoris, personal communication).

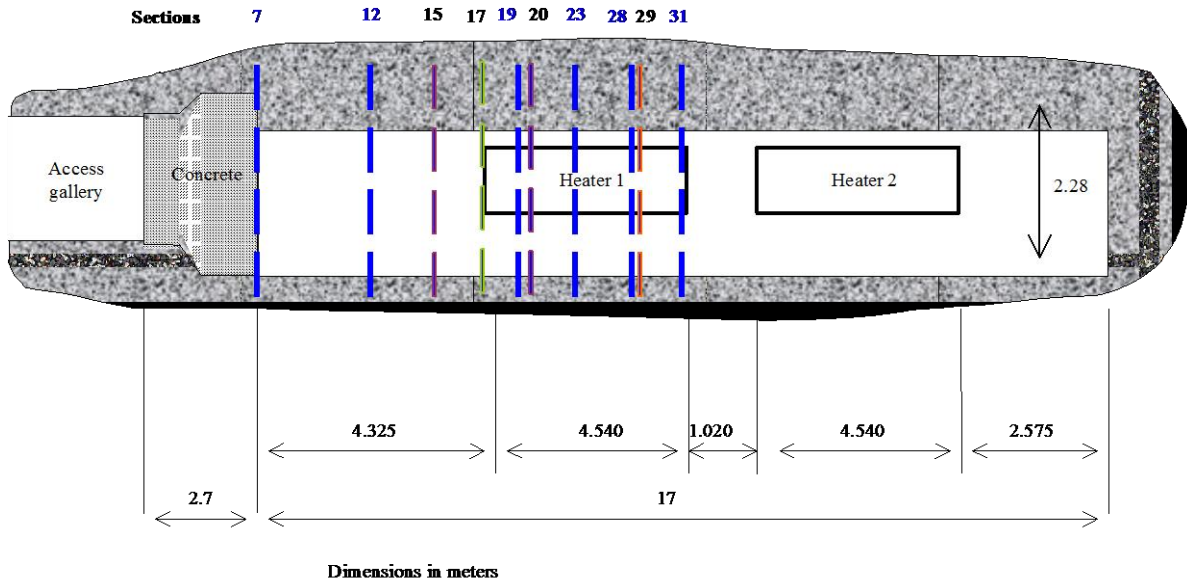


Figure 3-6. Layout of the sampling sections during the dismantling of heater 1 in 2002. In blue color are the common sections for THG and THM analyses (Fernandez and Rivas, 2003)

After the dismantling of heater 1, the tunnel was plugged with shotcrete (Figure 3-7) and heater 2 was kept working under normal conditions to maintain a constant 100 °C at the steel liner/bentonite interface. In 2014, considering that changes in the state of bentonite buffer is very slow and it is unlikely for bentonite to reach fully saturation in the project lifetime, decision was

made to dismantle the heater 2. On April 24, 2015, heater 2 was switched off. After a short cool off time period, samples were taken for THMC and microbiological characterization.

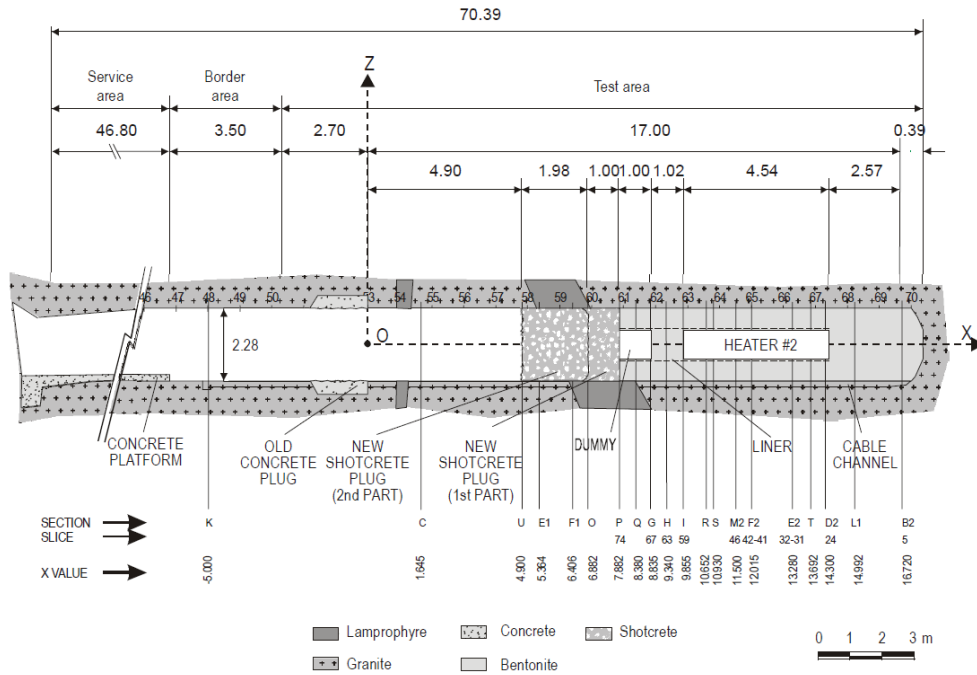


Figure 3-7. *In situ* test configuration following dismantling of heater 1 (Huertas et al., 2005)

The long-term FEBEX *in situ* test with comprehensive THMC data provides a unique opportunity to validate coupled THMC models and strengthen our understanding of the coupled processes in bentonite. In addition, experiments at different scales with the same type of bentonite are also very useful to evaluate the key parameters obtained at different scales and study the scaling effect of modeling THMC processes. Up to now, several THM/THC models have been developed to interpret the FEBEX experiments, including the THM model for the mock-up test (Sánchez et al., 2005; 2012a) and *in situ* test (Sánchez et al., 2012b), and THC models for the small scale heating and hydration experiment (Zheng et al., 2010), mock-up test (Zheng and Samper, 2008), and *in situ* tests (Samper et al., 2008a; Zheng et al., 2011).

3.3 Model Development

In this section, we describe the model development effort so far in FY15, starting from a TH model and then building THC models; eventually a coupled THMC models will be completed in the future.

3.3.1 Simulator

The numerical simulations are conducted with TOUGHREACT-FLAC3D, which sequentially couples the multiphase fluid flow and reactive transport simulator, TOUGHREACT (Xu et al., 2011), with the finite-difference geomechanical code FLAC3D (Itasca, 2009). The coupling of TOUGHREACT and FLAC was initially developed in Zheng et al. (2012) to provide the necessary numerical framework for modeling fully coupled THMC processes. It was equipped with a linear elastic swelling model (Zheng et al., 2012; Rutqvist et al., 2013) to account for

swelling as a result of changes in saturation and pore-water composition and the abundance of swelling clay (Liu et al., 2013; Zheng et al., 2014). A recent addition to the code is the capability of simulating Non-Darcian flow.

Non-Darcian flow refers to a phenomenon where the flux is not linearly proportional to the hydraulic gradient. It has been fairly well known for clay media, as manifested in the “pressure seal” studies in the petroleum literature (Deming, 1994). Researchers have proposed different relationship to describe non-Darcian flow, such as the flux being proportional to a power function (Hansbo, 1960; 2001), or exponential function (Swartzendruber, 1963), of hydraulic gradient. Zou (1996) developed a nonlinear flux-gradient relationship depending on the activation energy of pore liquid. Liu and Birkholzer (2012) proposed more generalized equations that encompass the relationship proposed by other researchers, which are given below and implemented in the simulator.

$$q = K \left[i - \frac{I}{\gamma\left(\frac{1}{\alpha}\right)} \gamma\left(\frac{1}{\alpha}, \left(\frac{i}{I^*}\right)^\alpha\right) \right] \quad (3-1)$$

where q (m/s) is the water flux, K (m/s) is the hydraulic conductivity, and I is the threshold gradient. I^* is calculated as:

$$I^* = \frac{I \cdot \alpha}{\gamma\left(\frac{1}{\alpha}\right)} \quad (3-2)$$

γ refers to Gamma functions

$$\gamma(a, x) = \int_0^x t^{a-1} e^{-t} dt \quad (3-3)$$

$$\gamma(a) = \int_0^\infty t^{a-1} e^{-t} dt \quad (3-4)$$

where α and I are fitting parameters. Liu and Birkholzer (2012) found out that $\alpha = 5$ leads to a good match between Equation (3-1) and data. How to calculate the threshold gradient will be discussed later.

3.3.2 Modeling Setup

As shown in Figure 3-5, the hydration of bentonite is fairly symmetrical, and radial symmetry has also been observed for heating (as shown later in Figures 3-9 to 3-12). We therefore use an axi-symmetrical mesh (Figure 3-8) to save computation time so that we can focus on the key coupling processes. However, such a model can only be used to interpret and predict the THMC behavior in the “hot” sections, i.e. sections of bentonite block surrounding the heater such as section F1 and F2 in Figure 3-4. 3-D models that have both “hot” and “cold” sections could be developed in the future.

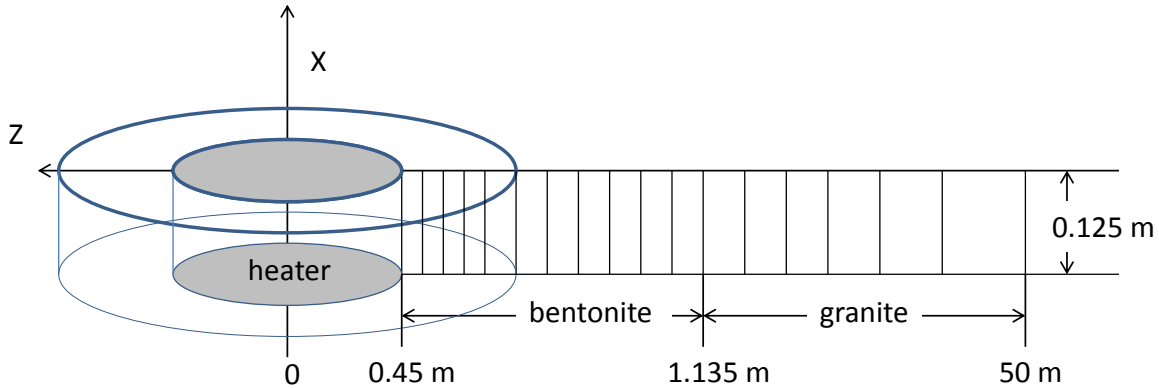


Figure 3-8. Mesh used for the model, not to the scale.

The model considers two material zones for the bentonite and granite. The first two nodes (1 and 2) are located on the external wall of the heater ($r = 0.45\text{--}0.46\text{ m}$). Bentonite is located within $0.45\text{ m} < r < 1.135\text{ m}$. The remaining domain up to 50 m is used to simulate the granite. The simulation time starts on February 27, 1997 and ends on July 1, 2015, a total of 6,698 days. The initial temperature is uniform and equal to 12 °C. A constant temperature of 100 °C is prescribed at the heater/bentonite interface ($r = 0.45\text{ m}$) while temperature is assumed to remain constant at its initial value of 12 °C at the external boundary ($r = 50\text{ m}$) because the thermal perturbation induced by the heaters does not extend to this boundary.

The bentonite has initially a gravimetric water content of 14% which corresponds to a saturation degree of 59% and a suction of $1.11 \times 10^5\text{ kPa}$. The boundary conditions for flow include: 1) no flow at $r = 0.45\text{ m}$ and 2) a prescribed liquid pressure of 7 bars at $r = 50\text{ m}$.

3.3.3 The TH model

In previous modeling work (e.g. Sánchez et al., 2012b; Zheng and Samper, 2008), significant effort has been invested to find out why the hydration of FEBEX bentonite is slower than predicted by the typical Darcy flow model. Several processes have been proposed to explain the discrepancy between measured data and predictions by the Darcy flow model. These include the permeability decrease due to the dual-structural behavior of bentonite (Sánchez et al., 2005, 2012b), thermal osmosis, in which a moisture flux induced by the thermal gradient in the bentonite is in the opposite direction of water infiltration from the granite (Zheng et al., 2011),

and permeability decrease due to swelling (Zheng and Samper, 2008). Another possibility could be the Non-Darcian flow (Liu and Birkholzer, 2012) which has been observed for clay rock and shale. However, before we use a more complex THMC model to identify exactly which processes are at play, we should keep in mind that uncertainty in the parameters could also affect the hydration of bentonite. Therefore, for this work we started first with a TH model. Parameters for the base case are listed in Table 3-1. Sensitivity analyses to key parameters are given in the following sections. The parameters in Table 3-1 are largely based on the information from ENRESA (2000), Sánchez et al. (2012) and Zheng et al. (2011), with more detailed discussion about their uncertainties in Section 3.4.1.2 when we present the sensitivity analyses.

Table 3-1. Thermal and hydrodynamic parameters.

Parameter	Granite	Bentonite
Grain density [kg/m ³]	2700	2700
Porosity ϕ	0.01	0.41
Saturated permeability [m ²]	2.0×10^{-18}	3.75×10^{-21}
Relative permeability, k_{rl}	$k_{rl} = S$	$k_{rl} = S^3$
Van Genuchten α [1/Pa]	1.1×10^{-8}	4.76×10^{-4}
Van Genuchten m	0.45	0.7
Compressibility, β [1/Pa]	3.2×10^{-9}	5.0×10^{-8}
Thermal expansion coeff., [1/°C]	1.0×10^{-5}	1.5×10^{-4}
Dry specific heat, [J/kg-°C]	793	1091
Thermal conductivity [W/m-°C] dry/wet	3.2/3.3	0.47/1.15
effective vapor diffusion coefficient (m ² /s)	1.03×10^{-4}	1.03×10^{-4}

3.3.4 Chemical Model

The establishment of the chemical model requires first the knowledge of initial chemical conditions in bentonite and granite, i.e. the initial mineralogical and pore water composition. Extensive mineralogical characterization had been conducted by ENRESA (2000) and Fernández et al. (2004). Ramírez et al. (2002) also reported the mineralogical composition of FEBEX bentonite, which is slightly different from that in ENRESA (2000). In the part of the report, we take the average of mass fraction reported in ENRESA (2000), Fernández et al. (2004) and Ramírez et al. (2002) (all listed in Table 3-2) and transformed mass fraction to volume fraction (ratio of the volume for a mineral to the total volume of medium) using a porosity of 0.41 (see Table 3-3). Note the minerals that have zero volume fractions are the secondary minerals that could be formed. Detailed mineralogical composition of granite has not been found in current literature search, probably because the chemical conditions in granite are not supposed to be actively changed by repository conditions. Previous THC models for the *in situ* test (Samper et al., 2008a; Zheng et al., 2011) only include quartz in the minerals assemblage in granite. Siitari-Kauppi et al., (2007) reported that Grimsel granite is composed of quartz, K-feldspar, plagioclase and a small amount of “dark material”. In the current model, we consider quartz, K-feldspar, plagioclase in granite with their volume fractions listed in Table 3-3.

Table 3-2. Mass fraction of minerals for FEBEX bentonite from different publications (%)

Mineral	ENRESA (2000), Fernández et al. (2004)	Ramírez et al. (2002)
Calcite	trace	1 ± 0.7
Dolomite	0.0	0
Illite	0.0	0
Kaolinite	0.0	0
Smectite	92 ± 3	93 ± 3
Chlorite	0.8	-
Quartz	2 ± 1	2 ± 0.5
K-Feldspar	trace	2 ± 1
Siderite	0.0	0
Ankerite	0.0	0

Table 3-3. Mineral volume fraction (dimensionless, ratio of the volume for a mineral to the total volume of medium) FEBEX bentonite (ENRESA, 2000; Fernández et al., 2004; Ramírez et al., 2002) and granite (Zheng et al., 2011).

Mineral	FEBEX Bentonite	Granite
Calcite	0.00472	0
Smectite	0.546	0.
Chlorite	0.0024	0
Quartz	0.012	0.37
K-Feldspar	0.0059	0.35
Plagioclase	0	0.27
Dolomite	0.0	0
Illite	0.0	0
Kaolinite	0.0	0
Siderite	0.0	0
Ankerite	0.0	0

FEBEX bentonite blocks have an initial gravimetric water content of 13.5–14% (ENRESA 2000). As described in Bradbury and Baeyens (2003), obtaining the pore-water chemistry of compacted bentonite with such a low water content is difficult. Because the concentration of ions for the initial state of compacted bentonite cannot be measured directly, indirect measurement methods must be used. Squeezing and aqueous extract are the most commonly used methods. Squeezing is a straight forward method — pore-water is squeezed out and concentrations are measured. However, pore water cannot be extracted by squeezing from clay samples with gravimetric water contents less than 20% (Fernández et al. 2001, 2004), which means that squeezing cannot be done for FEBEX bentonite blocks. In an aqueous extract test, a crushed sample is placed in contact with water at a low solid/liquid ratio (ranging from 1:16 to 1:1). After establishing equilibrium, the solid phase is separated and the liquid phase is analyzed (Fernández

et al., 2001). Geochemical modeling was needed to retrieve the aqueous ion concentrations at low water content (Zheng et al. 2008). Therefore, any uncertainties associated with the geochemical models affect the evaluation of initial aqueous concentration levels at low water content (the water content at the initial state). The model presented in this part of the report uses the pore water composition (see Table 3-4) inferred by Fernández et al. (2001) from aqueous extract data. The pore water composition for granite (Table 3-4) is taken from Zheng et al., (2011).

Table 3-4. Pore-water composition (mol/kg water except for pH) of FEBEX bentonite (Fernández et al., 2001) and granite (Zheng et al., 2011).

	EBS Bentonite: FEBEX	Granite
pH	7.72	8.35
Cl	1.60E-01	1.31E-05
SO ₄ ⁻²	3.20E-02	7.86E-05
HCO ₃ ⁻	4.1E-04	3.97E-04
Ca ⁺²	2.2E-02	1.81E-04
Mg ⁺²	2.3E-02	1.32E-06
Na ⁺	1.3E-01	3.76E-04
K ⁺	1.7E-03	7.80E-06
Fe ⁺²	2.06E-08	2.06E-08
SiO ₂ (aq)	1.1E-04	6.07E-04
AlO ₂ ⁻	1.91E-09	3.89E-08

In the chemical model, we consider aqueous complexation, cation exchange, surface complexation and mineral dissolution/precipitation. Aqueous complexes and their disassociation constants for reactions that are written in terms of the primary species in Table 3-4 are listed in Table 3-5. These thermodynamic data were taken from Data0.dat.YMPv4.0, an EQ3/6 (Wolery, 1993) database qualified by the U.S. Department of Energy for the Yucca Mountain project. Surface protonation reactions are given in Table 3-6 and cation exchange reactions are given in Table 3-7.

The equilibrium constants for precipitation/dissolution of primary minerals (minerals that are present initially) and secondary minerals are listed in Table 3-8. Note that plagioclase is a solid solution with albite and anorthite as its end members. In the current model, we assume plagioclase contains 10% anorthite and 90% albite so that there is a quasi-equilibrium between pore water and plagioclase.

Mineral dissolution/precipitation is kinetically controlled. The kinetic law for mineral dissolution/precipitation is given in Xu et al. (2011). The kinetic rates and surface areas for the minerals considered in the model were taken mostly from Xu et al. (2006) (Table 3-9). However, the illitization rate (the rate of illite precipitation and smectite dissolution) was calibrated (Liu et al., 2013) based on the measured illite percentage in an illite/smectite (I/S) mixed layer from Kinnekulle bentonite, Sweden (Pusch and Madsen, 1995).

Table 3-5. Aqueous complexes and their dissociation constants

Species	Log K (25°C)	Species	Log K (25°C)
OH ⁻	13.99	MgHCO ₃ ⁺	-1.03
Al ⁺³	-22.88	CO ₂ (aq)	-6.34
HAlO ₂ (aq)	-6.45	CO ₃ ⁻²	10.33
NaAlO ₂ (aq)	0.75	CaCO ₃ (aq)	7.01
AlOH ⁺²	-17.87	KCl(aq)	1.50
Al(OH) ₂ ⁺	-12.78	MgCl ⁺	0.14
Al(OH) ₃ (aq)	-6.72	MgSO ₄ (aq)	-2.38
CaCl ⁺	0.70	NaSO ₄ ⁻	-0.81
CaCl ₂ (aq)	0.65	KSO ₄ ⁻	-0.88
CaSO ₄ (aq)	-2.10	NaHSiO ₃ (aq)	8.30
NaCl(aq)	0.78	CaOH ⁺	12.85
FeCl ⁺	0.17	NaOH(aq)	14.15
FeHCO ₃ ⁺	-2.04	NaCO ₃ ⁻	9.82
FeCO ₃ (aq)	4.88	NaHCO ₃ (aq)	-0.17
FeCl ₄ ⁻²	1.94	CaHCO ₃ ⁺	-1.04

Table 3-6. Surface protonation reactions on montmorillonite (Bradbury and Baeyens, 2005)

Surface complexation	Log K
mon_sOH ₂ ⁺ = mon_sOH + H ⁺	-4.5
mon_sO ⁻ + H ⁺ = mon_sOH	7.9
mon_w1OH ₂ ⁺ = mon_w1OH + H ⁺	-4.5
mon_w1O ⁻ + H ⁺ = mon_w1OH	7.9
mon_w2OH ₂ ⁺ = mon_w2OH + H ⁺	-6
mon_w2O ⁻ + H ⁺ = mon_w2OH	10.5

Table 3-7. Cation exchange reactions on montmorillonite and illite (Bradbury and Baeyens, 2005)

Cation exchange reaction	K _{Na/M}
Na ⁺ + mon-H = mon -Na + H ⁺	1
Na ⁺ + mon -K = mon -Na + K ⁺	0.0775
Na ⁺ + 0.5 mon -Ca = mon -Na + 0.5Ca ⁺²	0.302
Na ⁺ + 0.5 mon -Mg = mon -Na + 0.5Mg ⁺²	0.302

Table 3-8. Equilibrium constants for mineral precipitation/dissolution

Primary Mineral	log(K)	Secondary Mineral	log(K)
Calcite	1.85	Siderite	1.543
Smectite-Na	-34.62	Dolomite	2.524
Quartz	-3.75	Ankerite	-1.035
K-feldspar	-22.91	Illite	-47.33
Albite	-20.133	Chlorite	4.298
Anorthite	-19.19	Kaolinite	-39.9

Table 3-9. Kinetic properties for minerals considered in the model (Xu et al., 2006).

Mineral	A (cm ² /g)	Parameters for Kinetic Rate Law							
		Neutral Mechanism		Acid Mechanism			Base Mechanism		
		k ₂₅ (mol/m ² -s)	E _a (kJ/mol)	k ₂₅ (mol/m ² -s)	E _a (kJ/mol)	n(H ⁺)	k ₂₅ (mol/m ² -s)	E _a (kJ/mol)	n(H ⁺)
Quartz	9.8	1.023×10 ⁻¹⁴	87.7						
K-feldspar	9.8	3.89×10 ⁻¹³	38	8.71×10 ⁻¹¹	51.7	0.5	6.31×10 ⁻¹²	94.1	-0.823
Kaolinite	151.6	6.91×10 ⁻¹⁴	22.2	4.89×10 ⁻¹²	65.9	0.777	8.91×10 ⁻¹⁸	17.9	-0.472
Illite	1.18×10 ⁴⁽¹⁾	1.66×10 ⁻¹³	105 ⁽²⁾						
Chlorite	9.8	3.02×10 ⁻¹³	88	7.76×10 ⁻¹²	88	0.5			
Calcite	3.5	1.63×10 ⁻⁷	23.5						
Dolomite	12.9	2.52×10 ⁻¹²	62.76	2.34×10 ⁻⁷	43.54	1			
Ankerite	9.8	1.26×10 ⁻⁹	62.76	6.46×10 ⁻⁴	36.1	0.5			
Smectite -Na	1.18×10 ⁴⁽¹⁾	1.66×10 ⁻¹³	105 ⁽²⁾						

(1) calibrated based on the field illitization data (Liu et al., 2013)

(2) from Pusch and Madsen (1995)

3.4 Model Results

The ultimate goal of modeling the FEBEX *in situ* test is to develop a coupled THMC model that can simultaneously match the measured temperature, relative humidity, water content, stress, aqueous concentrations, and minerals phase change. While the development of a mechanical model is still under way, we report here the results from THC models. First, result from TH models and sensitivity analyses to key hydrological parameters are presented and then preliminary model results for the chemical changes in bentonite are discussed.

3.4.1 The TH model

3.4.1.1 The TH base model

Figures 3-9 through 3-12 compare the measured temperatures to simulation results. Because the current model simulates only the “hot” sections that normally are located at the middle of the 4.5 m long heater, we used temperature measured at section F2 and E2 (see Figure 3-4) surrounding heater 2 to constrain the thermal calculation. Starting February 27, 1997, a constant power of 1200 W was applied to each heater for 20 days and then a constant power of 2000 W for another 33 days. After that, the system was switched to the constant temperature mode, allowing the power to fluctuate freely, but the maximum temperature at the surface of steel liner of the heater was maintained at 100 °C. After the shutdown of heater 1 on February 2, 2002 (1827 days), the temperature field changed, as manifested by the temperature evolution after 1827 days in Figures 3-9 to 3-12. Unfortunately the thermal sensors at radial distances of 0.48 m and 1.09 m failed shortly after 1827 days, but the temperature data from some sensors at radial distance of 0.8 m (Figure 3-10) and 1.05 m (Figure 3-11) show the decrease in temperature after the shutdown of heater 1. Models results match well the temperature data at all the radial distances. Near the steel liner, e.g., radial distance of 0.48 m in Figure 3-9, the temperature is almost the same as at the surface of the steel liner, but it decreases noticeably at radial distance of 1.09 m (very close to the bentonite/granite interface) after the shutdown of heater 1 (Figure 3-12). The current model is a 1-D axi-symmetrical model that is designed to simulate the conditions of “hot” sections around heater 2. In order to account for the heat dissipation from “hot” sections to “cold” sections (located outside of the heater in X direction, such as sections B1 and B2 in Figure 3-4), we used

a semi-analytical solution implemented in TOUGH2 (Pruess et al., 1999) with an adjusted heat exchange surface area to match the temperature data. After 1827 days, the heat exchange surface area was adjusted again to match the data to mimic further heat loss from heater 2 when heater 1 was removed. In general, a fairly good match between the model and data was archived.

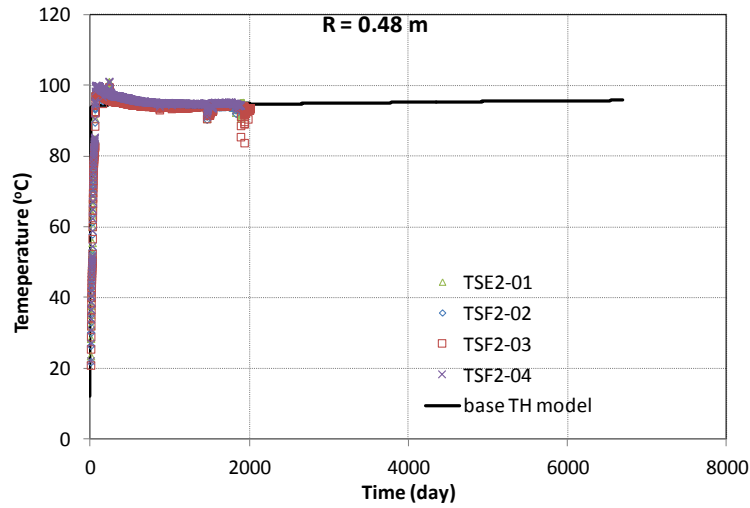


Figure 3-9. Measured temperature by sensors located at radial distance of 0.48 m in sections E2 and F2 and model results from the base TH model.

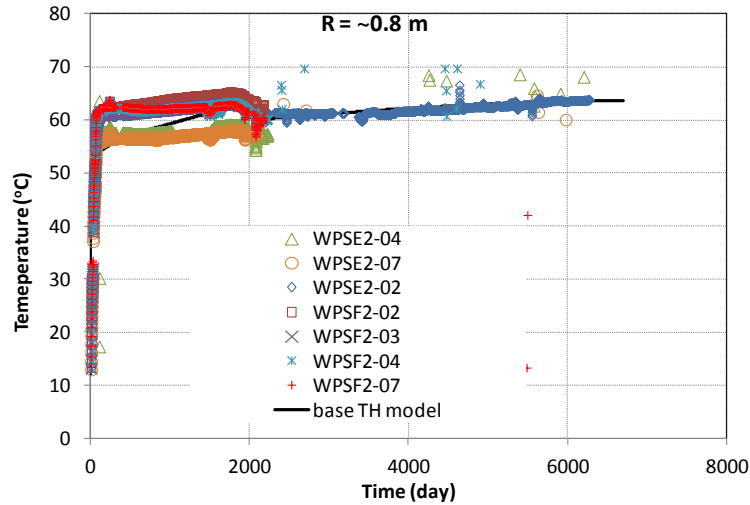


Figure 3-10. Measured temperature by sensors located at radial distance of 0.8 m in sections E2 and F2 and model results from the base TH model.

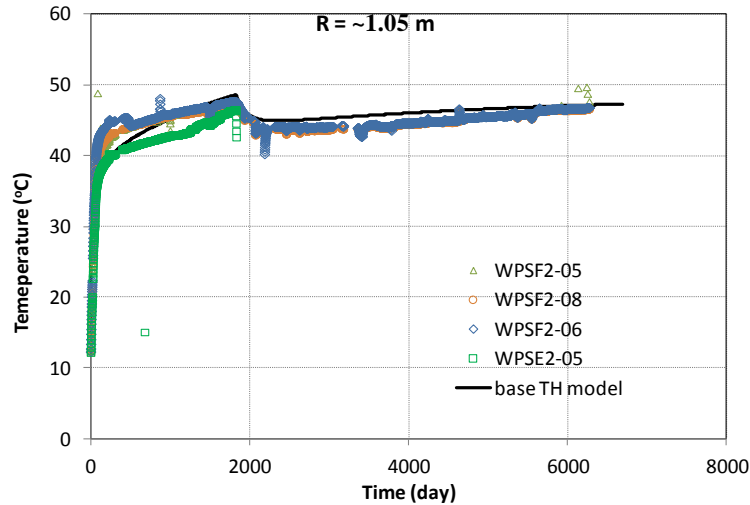


Figure 3-11. Measured temperature by sensors located at radial distance of 1.05 m in sections E2 and F2 and model results from the base TH model.

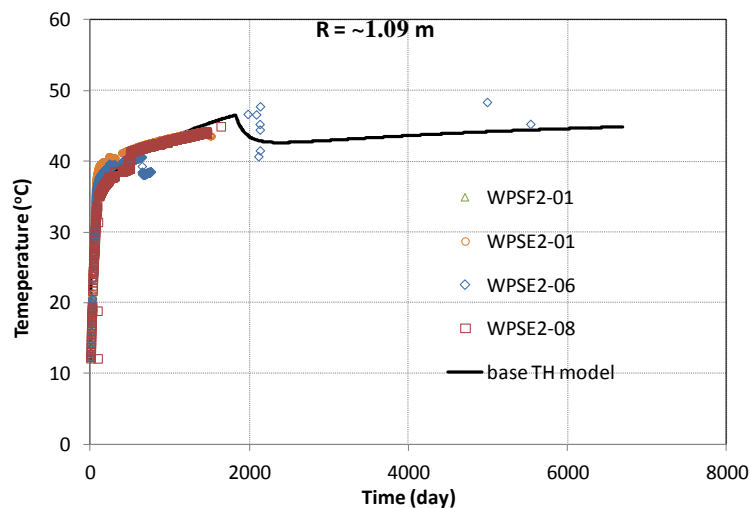


Figure 3-12. Measured temperature by sensors located at radial distance of 1.09 m in sections E2 and F2 and model results from the base TH model.

Relative humidity data measured by sensors at various positions in the bentonite were compared with models results. These data were grouped by the radial distance of the sensors. Previous modeling exercises (e.g. Zheng et al., 2011) showed that relative humidity near the heater has been overestimated and was the key data to test the models. Unfortunately, most sensors for relative humidities failed for sections around heater 2, especially near the heater. For example, as shown in Figure 3-13, sensors at section E2 (WCSE2-03, WCSE2-04) only provide data until 147 days. We therefore have to rely on the relative humidity data measured at section E1 (located around heater 1) to constrain our model. A fairly good match between model results and relative humidity was achieved. A better fit between the model and data was obtained at the outer rings of the bentonite barrier (large radial distance, see Figure 3-15 and 16) and in the

middle of the bentonite barrier (radial distance of 0.8 m, Figure 3-14). However, the match between the model and data near the heater (radial distance of 0.52 m, Figure 3-13) was slightly worse.

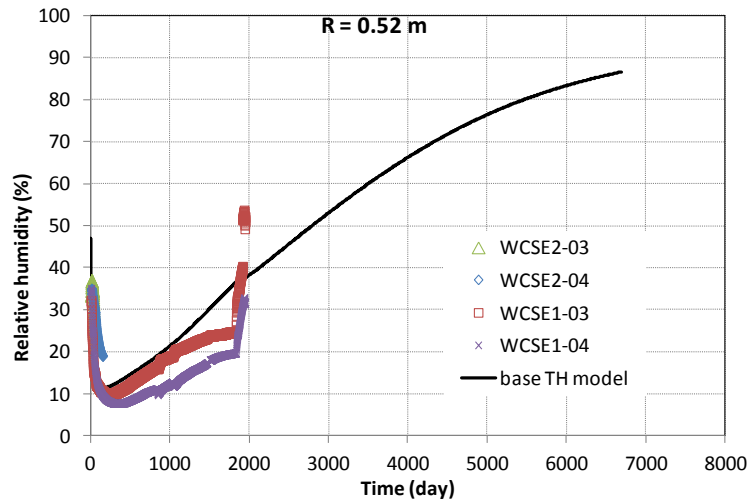


Figure 3-13. Measured relative humidity by sensors located at radial distance of 0.52 m in sections E2 and E1 and model results from the base TH model.

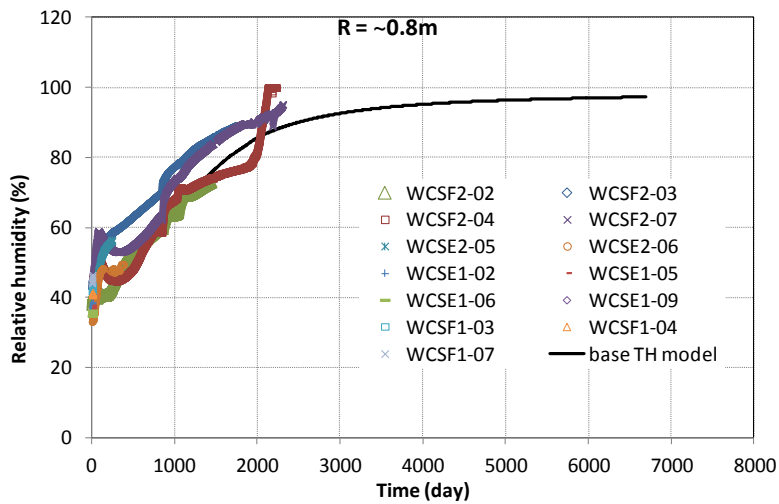


Figure 3-14. Measured relative humidity by sensors located at radial distance of ~0.8 m in sections E1, E2, F1 and F2 and model results from the base TH model.

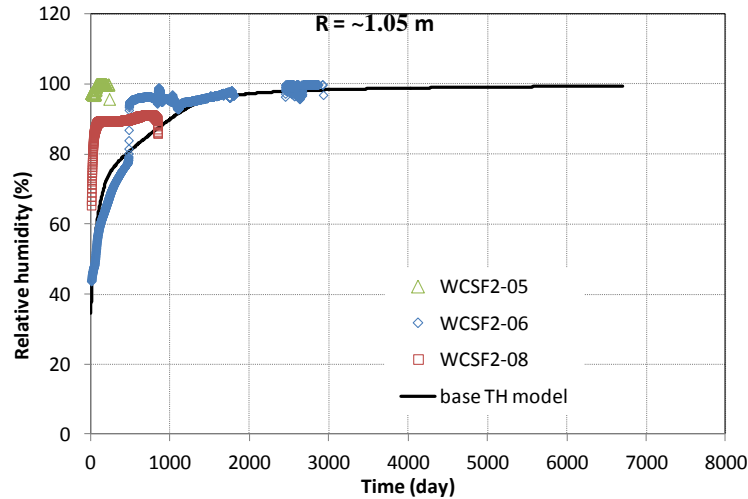


Figure 3-15. Measured relative humidity by sensors located at radial distance of ~ 1.05 m in section F2 and model results from the base TH model.

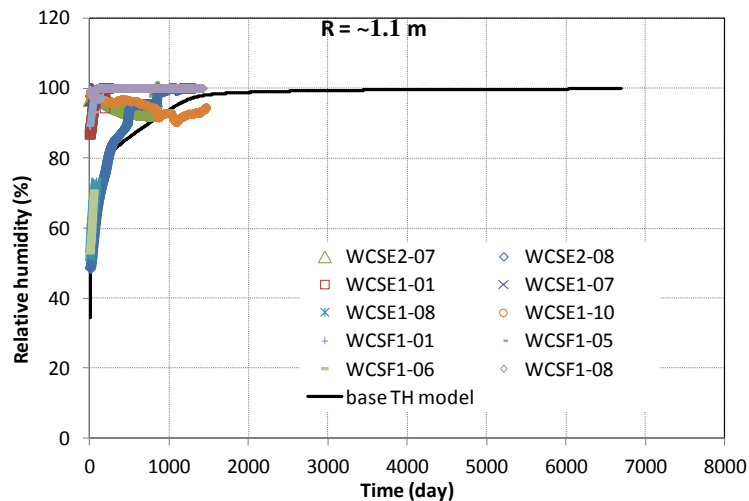


Figure 3-16. Measured relative humidity by sensors located at radial distance of ~ 1.1 m in sections E1, E2 and F1 and model results from the base TH model.

3.4.1.2 Sensitivity analyses to key hydrological parameters

The key parameters affecting the hydration of bentonite are the permeability of granite, the relative permeability and retention curves of bentonite, and the vapor diffusion coefficient. In this section, we discuss the most plausible values for these parameters and illustrate how they affect the simulated relative humidity.

Granite is a fractured medium and should ideally be represented by fractures and matrix. Just as previous models for *in situ* tests (Samper et al., 2008a; Sánchez et al., 2012b), current model also assumes granite is a homogeneous porous medium, which requires us to use an equivalent permeability. Based on the total water flow at the entire test zone (17.4 m, see Figure 3-4)

(ENRESA, 2000), the permeability of granite is around 5×10^{-18} to $8 \times 10^{-18} \text{ m}^2$. ENRESA (2000) also reports that the most frequent permeability is 1×10^{-18} but deems it is more representative of rock matrix. Zheng et al., (2011) used $8 \times 10^{-18} \text{ m}^2$, Kuhlman and Gaus (2014) estimated a permeability of $6.8 \times 10^{-19} \text{ m}^2$, and Sanchez et al., (2012b) used a surprisingly small value, $8.18 \times 10^{-21} \text{ m}^2$. Based on the published values, it seems that a permeability between 7×10^{-19} to $8 \times 10^{-18} \text{ m}^2$ is plausible. In the base model, a permeability of $2 \times 10^{-18} \text{ m}^2$ is used and Figure 3-17 shows the relative humidity results obtained with permeability of $6.8 \times 10^{-19} \text{ m}^2$ and $8 \times 10^{-18} \text{ m}^2$ for granite. Lower granite permeability significantly limits the water infiltration into bentonite, and subsequently lowers the computed relative humidity. A permeability of 6.8×10^{-19} for granite actually leads to a better match of measured relative humidity data at radial distance of 0.52 m (near the heater, Figure 3-17); however, it results in a marked underestimation of the relative humidity in the middle of bentonite barrier (radial distance of 0.8 m, Figure 3-18) and near the bentonite/granite interface (radial distance of 1.05, 1.21 m). A permeability of $8 \times 10^{-18} \text{ m}^2$ for granite leads to reasonable fit of the relative humidity in the middle of bentonite barrier and near the bentonite/granite interface, but causes overestimation of the relative humidity near the heater. Permeability of granite is certainly a very important parameter for determining the hydration rate of bentonite, but adjusting it will not result in a good match of the relative humidity data over the entire bentonite barrier.

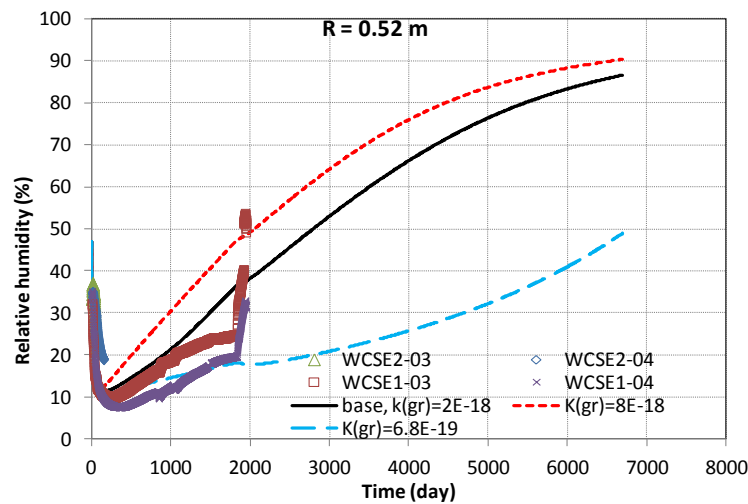


Figure 3-17. Measured relative humidity by sensors located at radial distance of 0.52 m and model results from the base model and two sensitivity runs with different permeability for granite.

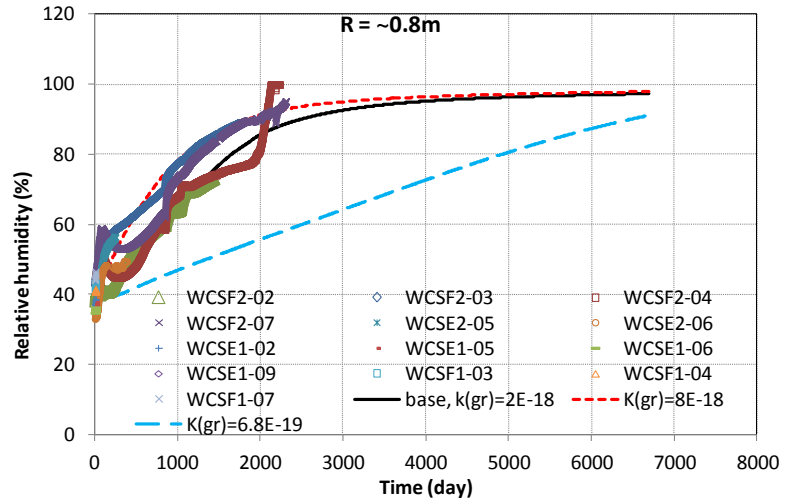


Figure 3-18. Measured relative humidity by sensors located at radial distance of 0.8 m and model results from the base model and two sensitivity runs with different permeability for granite.

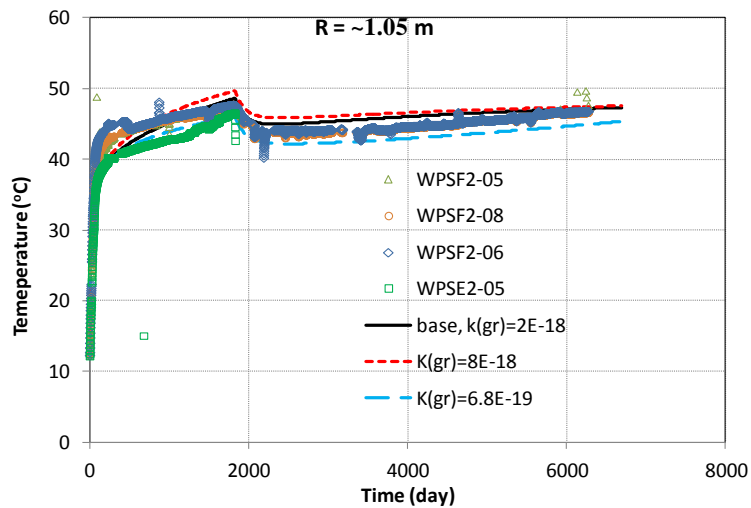


Figure 3-19. Measured temperature by sensors located at radial distance of ~1.05 m and model results from the base model and two sensitivity runs with different permeability for granite.

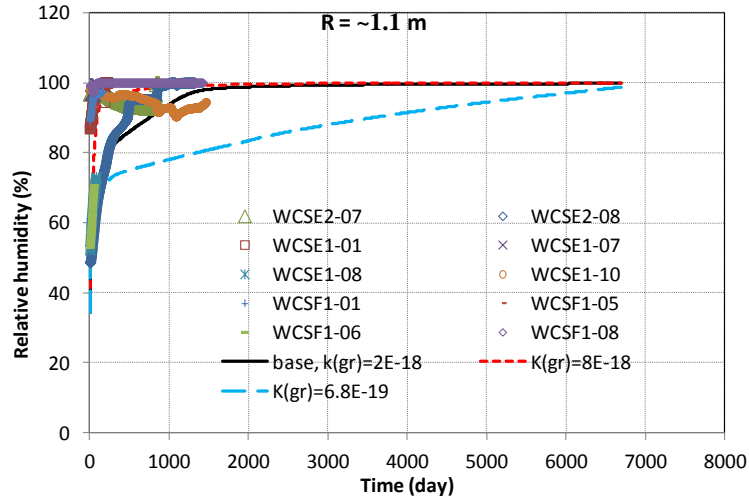


Figure 3-20. Measured relative humidity by sensors located at radial distance of 1.1 m and model results from the base model and two sensitivity runs with different permeability for granite.

The effective permeability of bentonite has been under scrutiny by modelers (e.g. Zheng et al., 2011) due to its critical role in determining the hydration of bentonite. It is the product of saturated permeability (k) and relative permeability (k_r). Because $k_r = S_l^3$ (where S_l is water saturation degree) has been consistently used by different models (Zheng et al., 2011; Sánchez et al., 2012b; Kuhlman and Gaus, 2014), we focus here on the impact of saturated permeability on relative humidity. Dry density is the primary factor that affects the permeability of bentonite, as shown in Figure 3-21. The bentonite blocks used in the *in situ* test initially have a dry density of 1.7 g/cm^3 , which gives a saturated permeability of around $2.5 \times 10^{-21} \text{ m}^2$ ($2.5 \times 10^{-14} \text{ m/s}$ in term of saturated hydraulic conductivity). In addition to dry density, the water (distilled, granitic or saline water) used to measure the permeability also give different values (see Figure 3-21). Considering the possible small variation in the initial dry density and impact of water type on the permeability, the plausible saturated permeability for FEBEX bentonite could be in a range from 1×10^{-21} to $9 \times 10^{-21} \text{ m}^2$. In a THM model for the *in situ* test Chen et al., (2009) use $2 \times 10^{-21} \text{ m}^2$ which is within that range, but a permeability of 9.4×10^{-22} estimated based on inverse modeling by Kuhlman and Gaus (2014) seems a bit low. Results from two sensitivity runs using permeabilities of 1×10^{-21} and $9 \times 10^{-21} \text{ m}^2$ for bentonite are shown in Figures 3-22 to 3-24. The impact of permeability of bentonite on the computed relative humidity is not obvious: higher permeability leads to higher relative humidity near the heater but actually lower relative humidity near the bentonite/granite interface. The reason is that higher permeability, on the one hand, accelerates the water infiltration overall, which leads to higher relative humidity near the heater; on the other hand, it also induces stronger suction that causes desaturation in granite and maintains the unsaturated state in bentonite near the bentonite/granite for longer time.

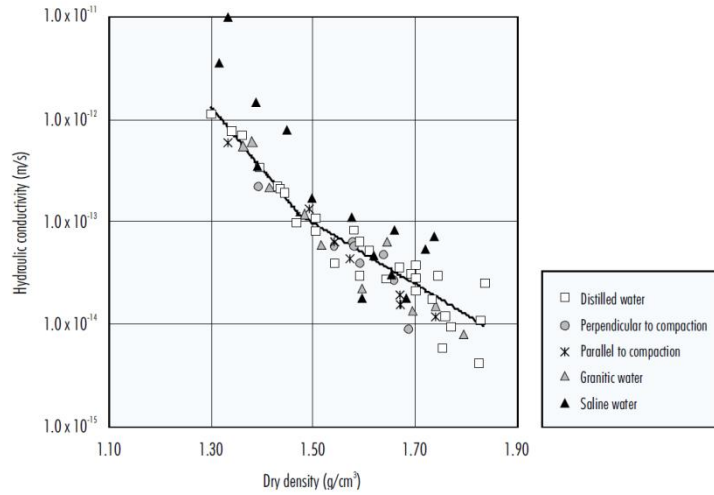


Figure 3-21. Saturated hydraulic conductivity as a function of dry density (ENRESA, 2000)

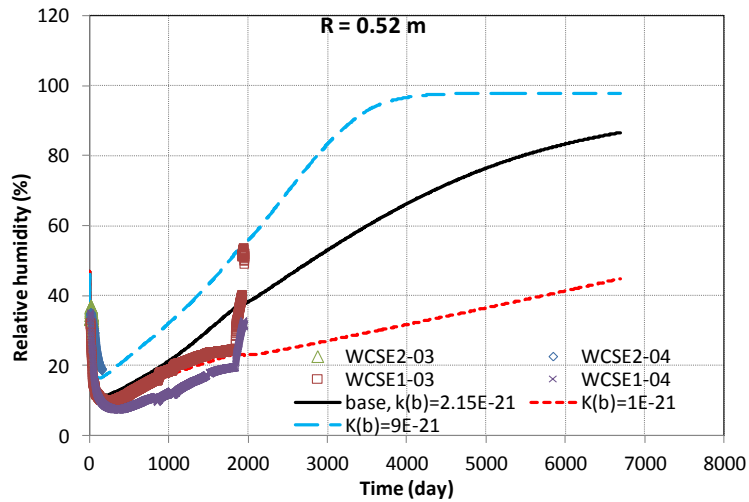


Figure 3-22. Measured relative humidities by sensors located at radial distance of 0.52 m and model results from the base model and two sensitivity runs with different permeability for bentonite.

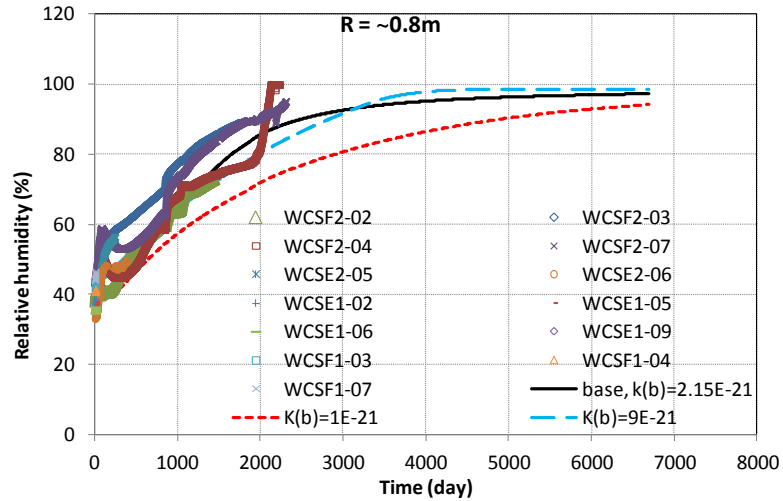


Figure 3-23. Measured relative humidities by sensors located at radial distance of 0.8 m and model results from the base model and two sensitivity runs with different permeability for bentonite.

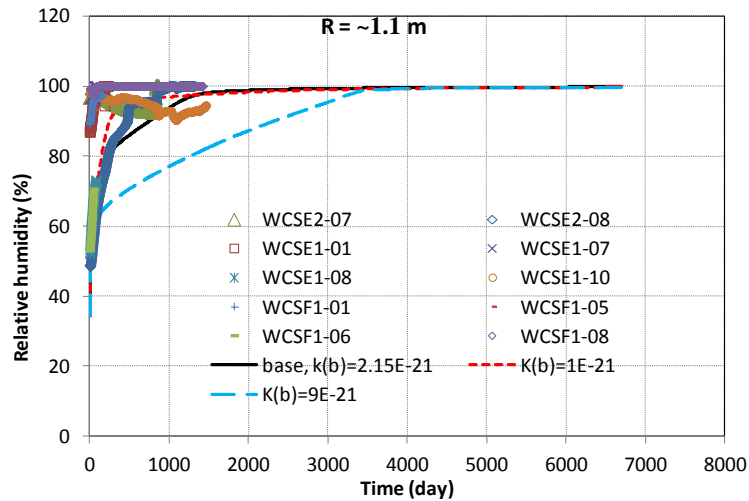


Figure 3-24. Measured relative humidities by sensors located at radial distance of 1.1 m and model results from the base model and two sensitivity runs with different permeability for bentonite.

While it is obvious that permeability has a strong effect on the hydration of bentonite, it is also clear that a constant saturated permeability cannot lead to a satisfactory match of relative humidity data at all the locations. Then the question is how saturated permeability changes over the course of hydrating bentonite. Zheng et al. (2011) related saturated permeability to porosity using the Kozeny-Carman (KC) equation (Bear, 1972):

$$k = k_0 \frac{\phi^3}{(1-\phi)^2} \frac{(1-\phi_0)^2}{\phi_0^3} \quad (3-5)$$

where k_0 (m^2) and ϕ_0 are the reference values of bentonite permeability and porosity, respectively, with $k_0 = 3.75 \cdot 10^{-21} \text{ m}^2$ and $\phi_0 = 0.41$. The porosity changes were calculated by a mechanical model using a state surface approach (Nguyen *et al.*, 2005). Although the Kozeny-Carman (KC) equation was derived for granular material, other studies have shown (Odong, 2007) that it can be used for a wide range of soils. Eventually Zheng *et al.* (2011) managed to achieve a good match between models and data using Equation (3-1) and thermal osmosis which leads to outward (from heater to granite) moisture flux. Sanchez *et al.* (2012b) used also the KC equation to relate porosity change with permeability, with $k_0 = 1.9 \cdot 10^{-21} \text{ m}^2$ and $\phi_0 = 0.40$, and the porosity changes as a result of swelling which is calculated based on the BBM. In the near future, when mechanical models are developed, we can explore which one leads to a better fit of the measured data.

3.4.2 The relevance of Non-Darcian flow to the hydration of bentonite

THM/THC models for mock-up tests (Zheng and Samper, 2008; Sánchez *et al.*, 2012b) clearly showed that the typical Darcy flow model overestimated the hydration of FEBEX bentonite. While summarizing the main findings from 15 years of operation of the mock-up and *in situ* tests, Lanyon *et al.* (2013) identified three second-order processes that may be relevant: thermal osmosis, threshold gradient for flow (i.e. the Non-Darcian flow) within bentonite, and the evolution of pore structure during hydration. One of the objectives of conducting THMC simulations is to sort out which one (or ones) of these processes plays an important role in slowing down the hydration of bentonite. In this section, we tested a TH model with Non-Darcian flow.

3.4.2.1 Calibrating threshold gradient with a permeability test

The key of having Non-Darcian flow model is to be able to calculate the threshold gradient reliably. Based on data from various sources, the threshold gradient I and permeability k (m^2) have the following relationship (Liu and Birkholzer, 2012):

$$I = Ak^B \quad (3-6)$$

with $A = 4.0\text{E-}12$ and $B = -0.78$. However, as the data set have some scatter, A and B have to be calibrated for a particular case, even though Equation (3-6) with $A = 4.0\text{E-}12$ and $B = -0.78$ can give a good first-cut estimate. The uncertainties regarding threshold gradient likely dictate the relevance of Non-Darcian flow to the hydration of bentonite. Fortunately, a permeability test using FEBEX bentonite (Samper *et al.*, 2008b) provides a great opportunity for calculating the threshold gradient (parameters A and B) that can be applied to the FEBEX *in situ* test. In this part of the report, we first developed a Non-Darcian flow model for the permeability test and then applied the calibrated parameters to the TH model for *in situ* test.

The experimental column used for the permeability test consists of a stainless steel cell in which a sample of FEBEX compacted bentonite is subjected to water flow (Figure 3-25). The cell has an internal diameter of 5 cm and a length of 2.5 cm. It contains 99.7 g of dry bentonite and 19.09 mL of water. A HPLC pump injects a solution at a pressure of 4 MPa through a porous stainless

steel filter providing a nearly-constant flow rate of approximately 2 mL/month. Outflowing water comes out through another stainless steel filter and is sampled inside a syringe. The test lasted for 1393 days, during which a total volume of 106 mL (which amounts to 5 pore volumes) was collected. The saturated hydraulic conductivity of the clay is 2.9×10^{-14} m/s.

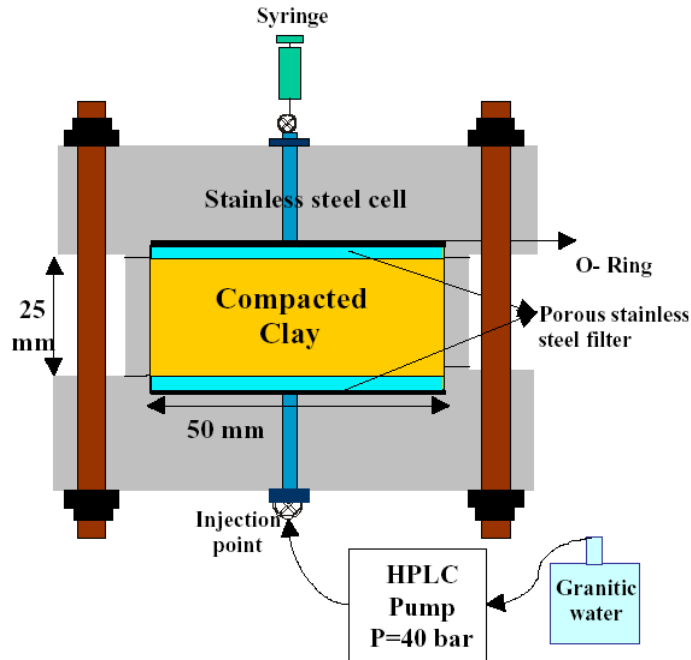


Figure 3-25. Schematic design of the permeation test (Samper et al., 2008b).

Darcy flow models with this measured hydraulic conductivity and the Non-Darcian flow model with different parameters were developed to match the cumulative water flux measured in the test. As shown in Figure 3-26, a Darcy flow model overestimates the water flux data and Non-Darcian flow with A of $4E-12$ completely shuts down the water flow through the bentonite sample. Eventually we calibrated that A of 2×10^{-13} gives the best fit of measured data. Model results are very sensitive the choice of B as well, as illustrated in Figure 3-27, and the best value for B is -0.78.

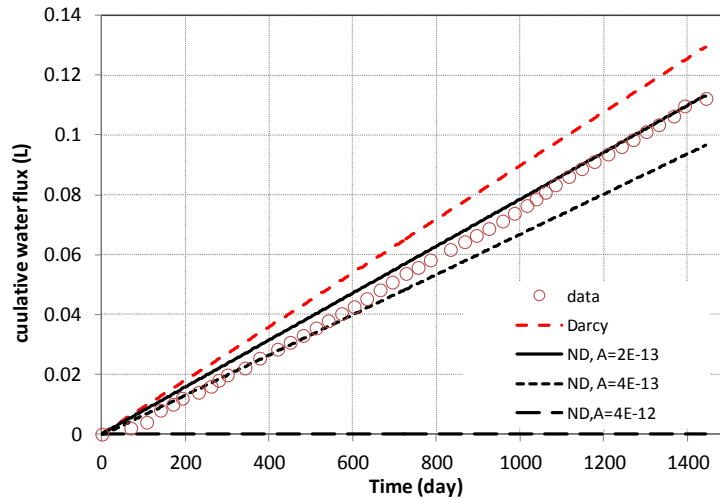


Figure 3-26. Measured cumulative water flux data and Darcy flow model, marked “Darcy” in the figure and Non-Darcian flow model, marked as “ND” in the figure with different A values while keeping B equal to -0.78.

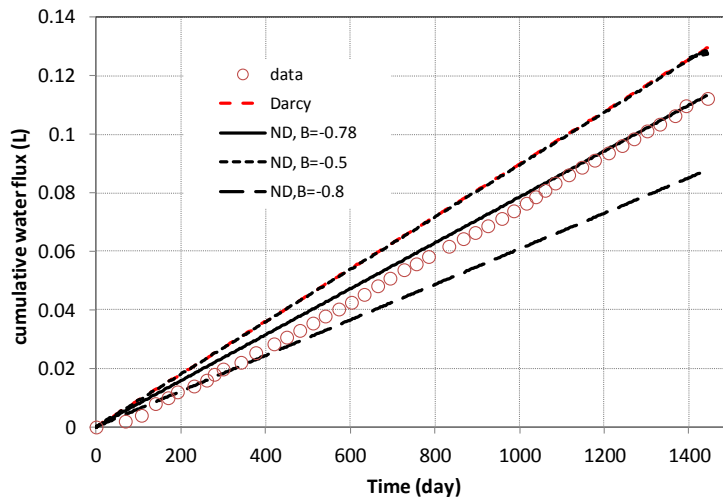


Figure 3-27. Measured cumulative water flux data and Darcy flow model, marked “Darcy” in the figure and Non-Darcian flow model, marked as “ND” in the figure with different B values while keeping A equal to 2×10^{-13} .

3.4.2.2 TH model with Non-Darcian flow

After we obtained the optimal A and B to reliably calculate the threshold gradient for FEBEX bentonite, a Non-Darcian flow model was developed for the FEBEX *in situ* test. Except for Non-Darcian flow, all the rest of the parameters remain the same as in the base model presented in 3.4.1.1. Comparison between relative humidity data and model results from the Darcy and Non-Darcian flow models at several radial distances are presented in Figures 3-28-3-30. The Non-Darcian flow models significantly underestimate the relative humidity data, even in bentonite near the bentonite/granite interface (at the radial distance of 1.1 m in Figure 3-30).

The relevance of Non-Darcian behaviour is clear for saturated flow in clay rock (Liu and Birkholzer, 2012 and references cited therein) and intuitively one would think that Non-Darcian behaviour should also be relevant to unsaturated flow in clay rock. However, when the numerical model is used to demonstrate such relevance, there are a couple of issues that might prevent us from clearly delineating the contribution of Non-Darcian flow to unsaturated clay or bentonite. First and foremost, the calibration of the relative permeability and retention curves overshadows the effect of Non-Darcian flow. The non-linear relationship between water flux and hydraulic gradient which motivates the relevance of Non-Darcian behaviour to water flow, is already accounted for, at least partially, by the relative permeability (which in turn is a function of the retention curve) in the flux-gradient relationship for unsaturated flow. In other words, the non-linear relationship between water flux and hydraulic gradient for unsaturated flow might be affected by two features: Non-Darcian flow and relative permeability. However, in most modelling exercises, relative permeability is calibrated based on a Darcy-type flow. As a result, the calibration of the parameters associated with relative permeability overshadows the contribution of Non-Darcian flow—the parameters for relative permeability might be “over-calibrated” so that the effect of Non-Darcian flow looks irrelevant. For FEBEX bentonite, the relative permeability and retention curve were calibrated based on Darcy type of flow model (ENRESA, 2000), which essentially obviates the Non-Darcian flow for unsaturated bentonite. Thus, if Darcian flow is added on top of relative permeability that is calibrated based on Darcy flow, as in the model presented in this section, we double count the non-linearity between flux and gradient, and consequently the model significantly underestimates the water inflow from granite to bentonite, as shown in Figures 3-28 to 3-30. This is essentially an issue of process uncertainty versus parameter uncertainty, which is faced by many complex models. Second, Cui et al., (2008) reported that threshold gradients are different for different capillary pressure. In this part of the report, we used the equation proposed in Liu and Birkholzer (2012) in which threshold gradient is solely a function of saturated permeability. Further research is needed to take into account the effect of capillary pressure when a threshold gradient is calculated. However, even though we can improve our threshold gradient calculation by taking into account capillary pressure, it is unlikely to eliminate the aforementioned issue of process uncertainties versus parameter uncertainties.

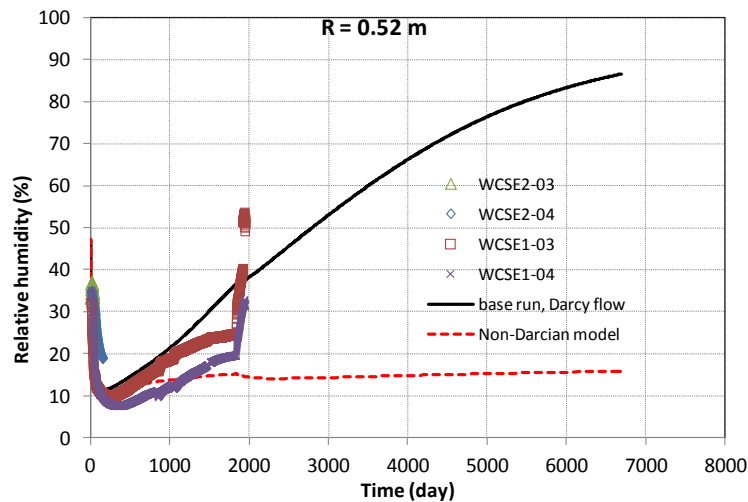


Figure 3-28. Measured relative humidities by sensors located at radial distance of 0.52 m and model results from the base model and the Non-Darcian flow model.

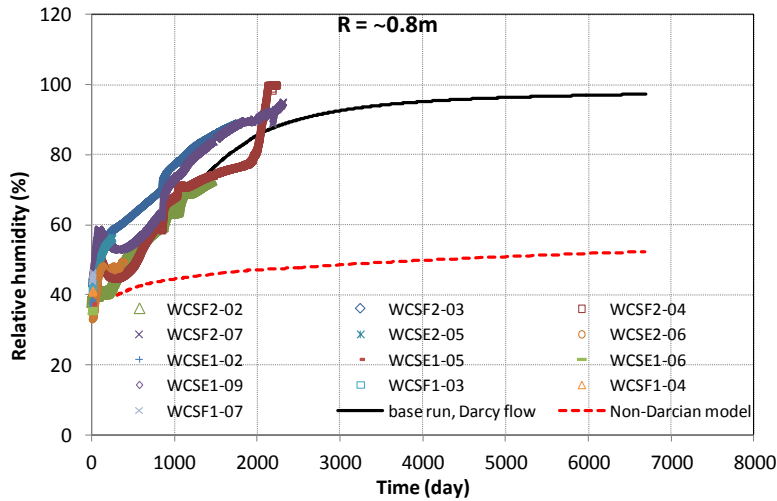


Figure 3-29. Measured relative humidities by sensors located at radial distance of 0.8 m and model results from the base model and the Non-Darcian flow model.

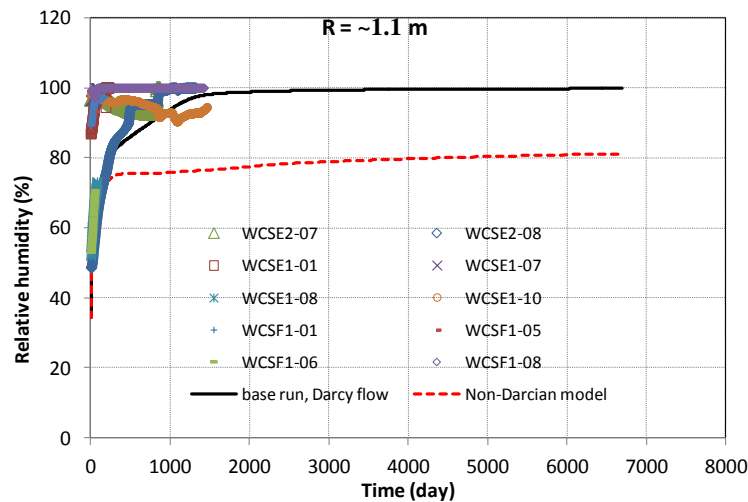


Figure 3-30. Measured relative humidities by sensors located at radial distance of 1.1 m and model results from the base model and the Non-Darcian flow model.

Figures 3-31 and 3-32 show the temperature computed by the TH model with Non-Darcian flow. The model results illustrate perfectly the coupling between thermal and hydrological processes — underestimation of relative humidity by Non-Darcian flow model is accompanied by underestimation of temperature because thermal conductivity of bentonite is a function of water saturation.

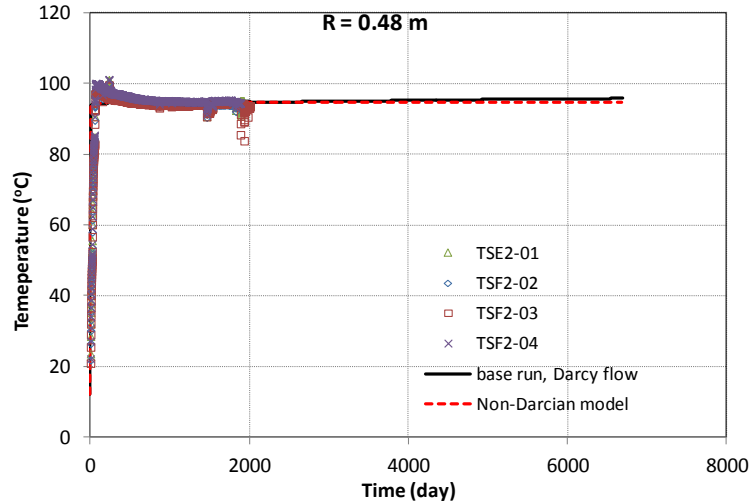


Figure 3-31. Measured temperature by sensors located at radial distance of 0.48 m and model results from the base model and the Non-Darcian flow model.

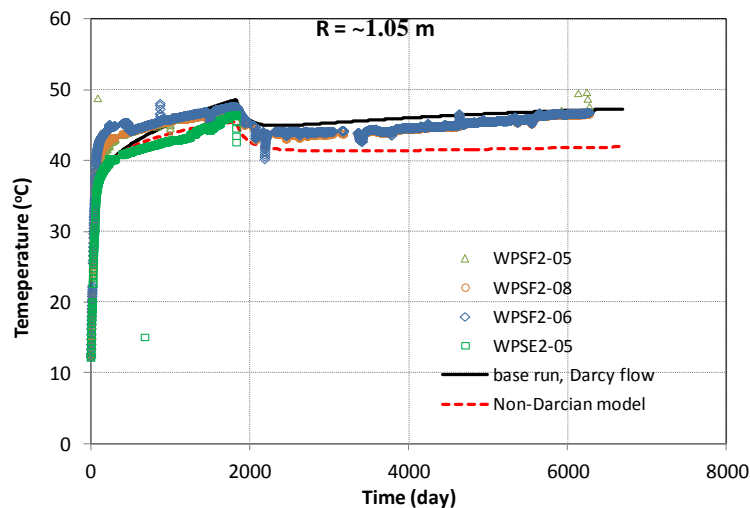


Figure 3-32. Measured temperature by sensors located at radial distance of 1.1 m and model results from the base model and the Non-Darcian flow model.

3.4.3 The THC model

Previous THC modeling work focused on the interpretation of the aqueous concentration of major cations and anions measured after the dismantling of heater 1. In this section, these data are compared with the results from the preliminary THC model as well. Because the TH model cannot match perfectly the hydrological data, namely relative humidity, which means the water inflow to bentonite still needs improvement (with the permeability change due to swelling being the last piece of the puzzle), it is expected that the THC model cannot match the chemical data perfectly. The comparison between chemical data and results from the THC model will illustrate

how much discrepancy can be introduced by neglecting the mechanical changes and the subsequent permeability decrease in bentonite. However, because hydrological and mechanical processes shape the concentration profile very differently from chemical processes, as will be discussed below, the THC model is still very useful to test the chemical model and guide its future refinement.

3.4.3.1 Geochemical data after dismantling of heater 1

Bentonite samples were taken from vertical sections normal to the axis of the tunnel. Samples were taken along several radii in each section (Zheng et al., 2011). Bentonite samples were taken for THC analyses from three sections surrounding the heater 1: s19, s28, and s29; see Figure 3-6 for the positions of these sections. Each sampling section consists of an outer, central and inner layer of bentonite blocks. The locations of bentonite blocks in section 29 collected after dismantling of heater 1 are shown in Figure 3-33. A total of 9 bentonite blocks were sampled at several radial distances. Bentonite blocks were preserved immediately after their extraction in plastic films, with two layers of aluminized PET sheets and vacuum-sealed plastic bags. Protection against mechanical damage was used to ensure the integrity of the material (ENRESA, 2006a).

Aqueous extract tests (AET) were used to obtain pore water chemistry for compacted FEBEX bentonite. AET is a method to quantify the total content of soluble salts of a clay sample. A $1:R$ AET consists on adding to a mass M_s of powdered clay sample a mass of distilled water equal to R times M_s . The clay sample and water are stirred during a period of time, usually 2 days, during which water and clay are allowed to equilibrate. Chemical analyses are performed on the supernatant solution after phase separation by centrifugation (Sacchi et al., 2001). In addition to dilution, chemical reactions take place during pore water extraction which changes the concentrations of dissolved species in a complex nonlinear manner. This makes it difficult to derive the chemical composition of the original pore water from the aqueous extract data (Bradbury and Baeyens, 1998; Sacchi et al., 2001). The inference of dissolved concentrations for reactive species requires geochemical modeling based on mineralogical data (Fernández and Rivas, 2005; Zheng et al., 2008). Aqueous extract tests and concentration of exchangeable cations are available for sections 19, 28 and 29 (Fernández and Rivas, 2003). Aqueous extract data from sections 29 and 19 (see Figure 3-6) were interpreted by inverse geochemical modeling (Zheng et al., 2008) and used to test the model predictions (Zheng et al., 2011). In this part of the report, we use the same data set to evaluate our THC models.

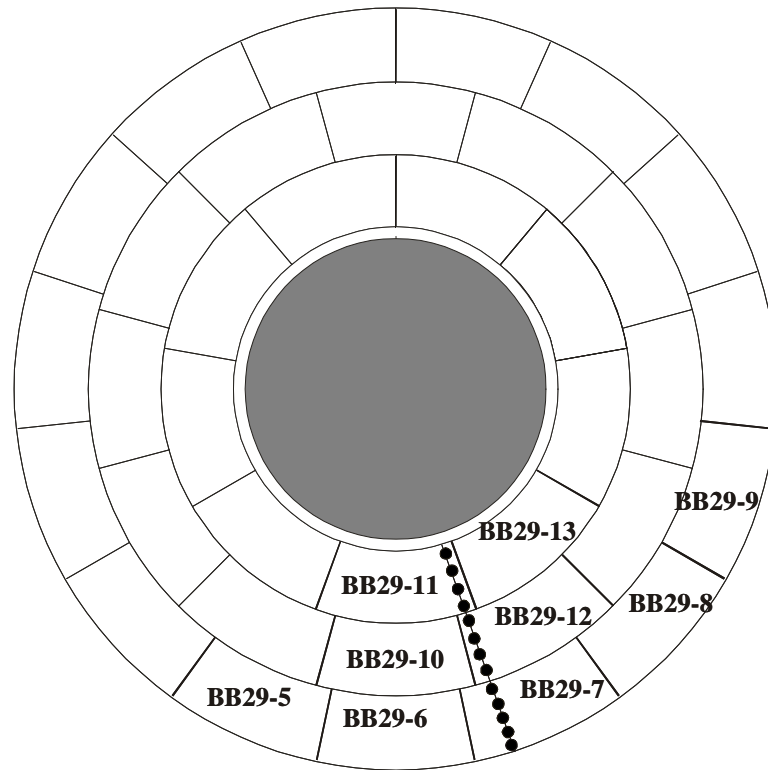


Figure 3-33. The positions where samples were taken for geochemical analyses at section 29 after the dismantling of heater 1 in 2002 (Zheng et al., 2011).

3.4.3.2 Testing the THC model with data and predictions

In Figure 3-34, we compare the chloride data and model results at 1930 days. Note that heater 1 was turned off after 1827 days, but the sample for THC analyses were actually taken at 1930 days after a three-month cooling period. The model captures the general trend of the measured profiles, but overestimates the concentration near the heater and the bentonite/granite interface. A similar discrepancy has been observed for the THC models in Zheng et al. (2011). When water infiltrates into bentonite, the swelling of bentonite allows more water to reside near the bentonite/granite interface and this dilutes the chloride. The current THC model cannot capture such behavior, but it is expected that including swelling in the model would alleviate the discrepancy.

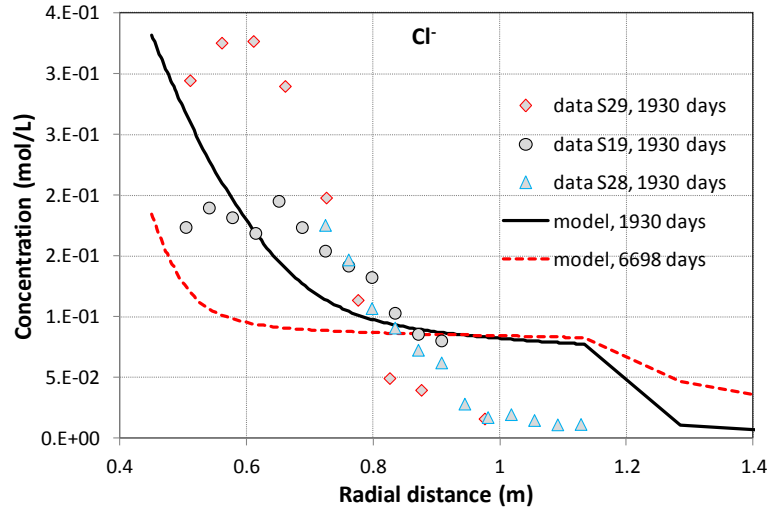


Figure 3-34. The concentration profile of chloride at 1930 days (Zheng et al., 2011) and model results from the base model.

The concentration profiles of major cations are shown in Figures 3-35 through 3-38. In addition to the base model results at 1930 days when samples were taken after the dismantling of heater 1, also shown in the figures are the results from a sensitivity run that does not consider chemical reactions. The comparison between the base model and sensitivity run allows one to distinguish the contribution of chemical reactions in shaping the concentration profile along the bentonite barrier. Concentration profiles of major cations largely follow the profile of conservative species such as chloride, indicating that flow and transport play major roles in shaping the profile. Similarly, just as the model overestimates the concentration of chloride near the bentonite/granite interface and near the heater, it also overestimates the concentration of sodium, calcium, magnesium, and potassium as well. In addition to the transport processes, sodium concentration could also be affected by cation exchange and dissolution of smectite (Figure 3-39). However, because sodium concentration is much higher than other cations and the concentration perturbation of other cations is fairly small, sodium concentration is not impacted noticeably by cation exchange, and the amount of smectite dissolved is too small to meaningfully alter the sodium concentration; the results from the base model and sensitivity run are almost indistinguishable as shown in Figure 3-35.

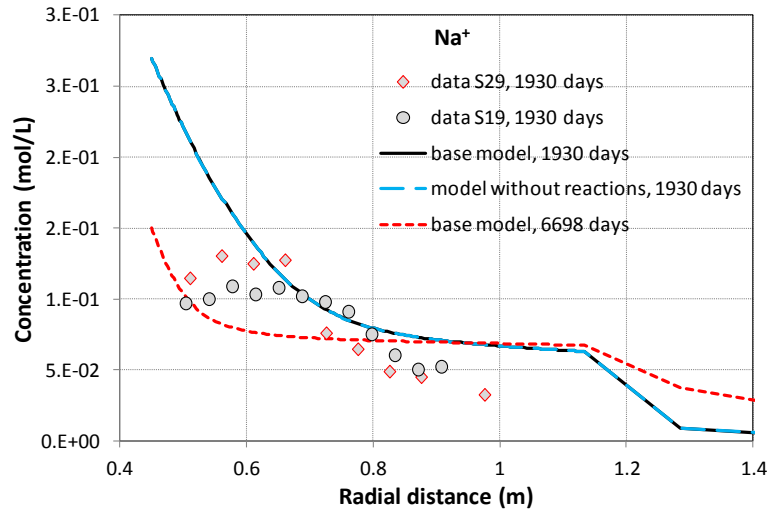


Figure 3-35. The concentration profile of sodium at 1930 days (Zheng et al., 2011) and model results from the base model and sensitivity run that does not consider any chemical reaction.

The base model leads to slightly lower calcium concentration than the sensitivity run (Figure 3-36). This is because of precipitation of dolomite (which decreases calcium concentration) (Figure 3-40), which outperforms the dissolution of calcite (which increases calcium concentration) (Figure 3-41). Eventually the model needs to delicately balance the pH, bicarbonate, calcium concentration, calcite dissolution, and dolomite precipitation to capture the concentrations of all of them.

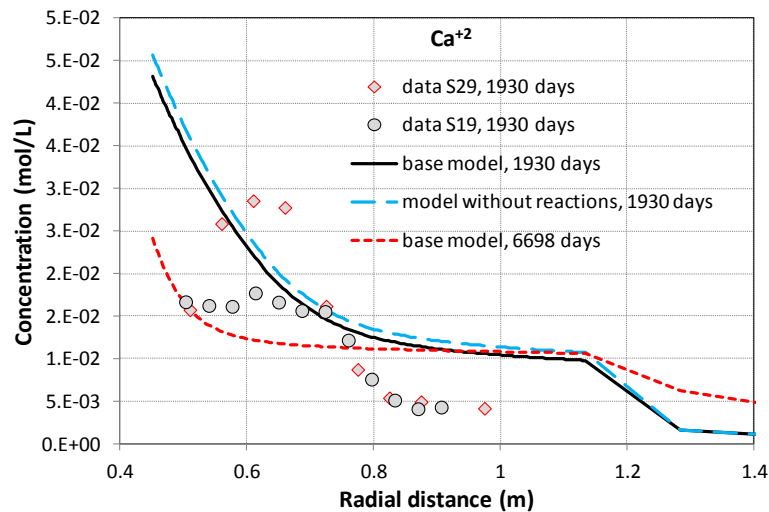


Figure 3-36. The concentration profile of calcium at 1930 days (Zheng et al., 2011) and model results from the base model and sensitivity run that does not consider any chemical reaction.

Magnesium is involved in the dissolution/precipitation of smectite, the precipitation of dolomite, and cation exchange (Figure 3-37). Eventually these reactions seem to cancel each other out, and

magnesium concentration in the base model is just slight lower than that from the sensitivity run without any reactions.

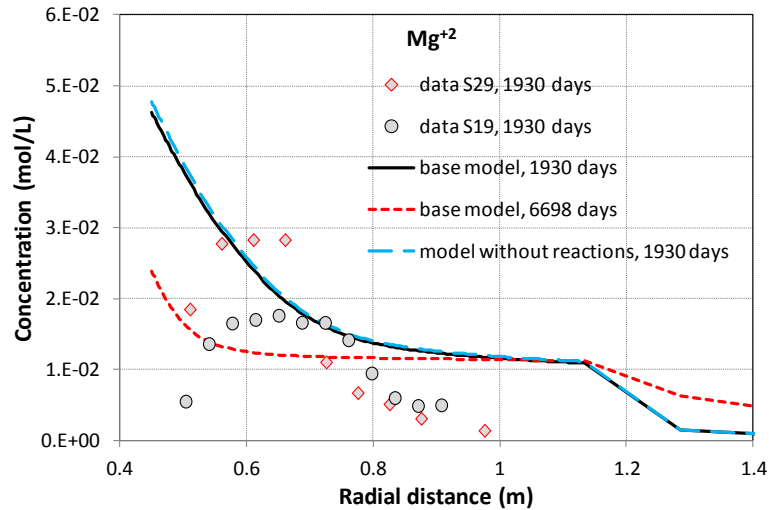


Figure 3-37. The concentration profile of magnesium at 1930 days (Zheng et al., 2011) and model results from the base model and sensitivity run that does not consider any chemical reaction.

The computed concentration of potassium from the base model is actually lower than that from the sensitivity run (Figure 3-38), suggesting that some reactions consume potassium in the pore water, which aligns well with the precipitation of illite (Figure 3-42). However, the fact that measured concentration is just slightly lower than computed from the sensitivity run (which has no reactions) seems to suggest there is only minimal precipitation of illite. In Figure 3-44, the maximum volume fraction increase is about $2E-6$ after 1930 days, which could be too small to be detected.

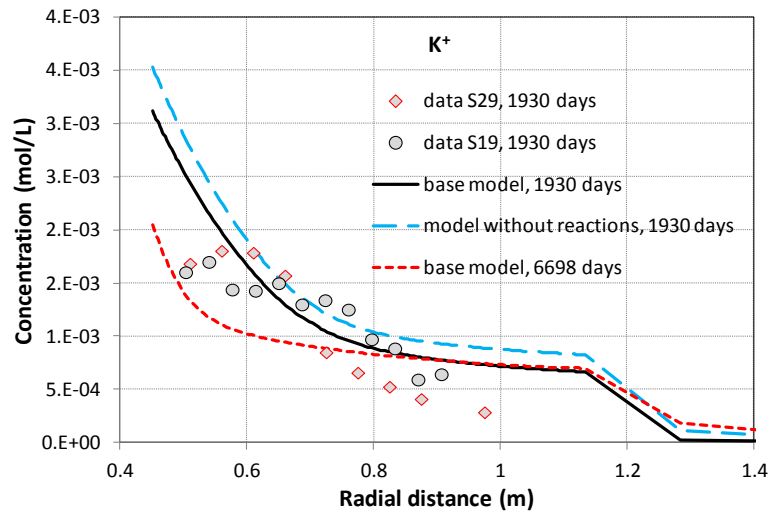


Figure 3-38. The concentration profile of potassium at 1930 days (Zheng et al., 2011) and model results from the base model and sensitivity run that does not consider any chemical reaction.

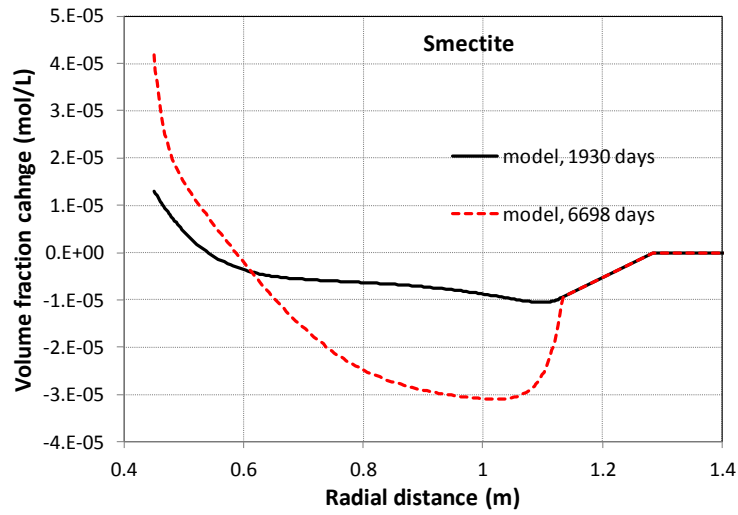


Figure 3-39. Computed profile of volume fraction change of smectite at the 1930 days (after the dismantling of heater 1) and at 6698 days (July 1, 2015).

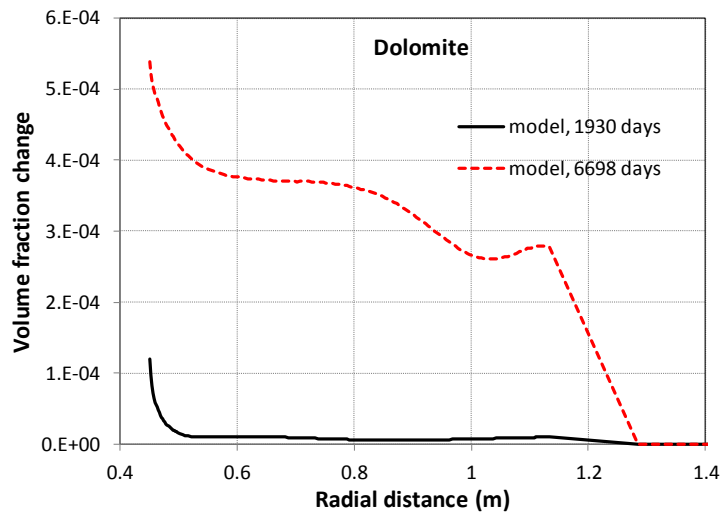


Figure 3-40. Computed profile of volume fraction change of dolomite at the 1930 days (after the dismantling of heater 1) and at 6698 days (July 1, 2015).

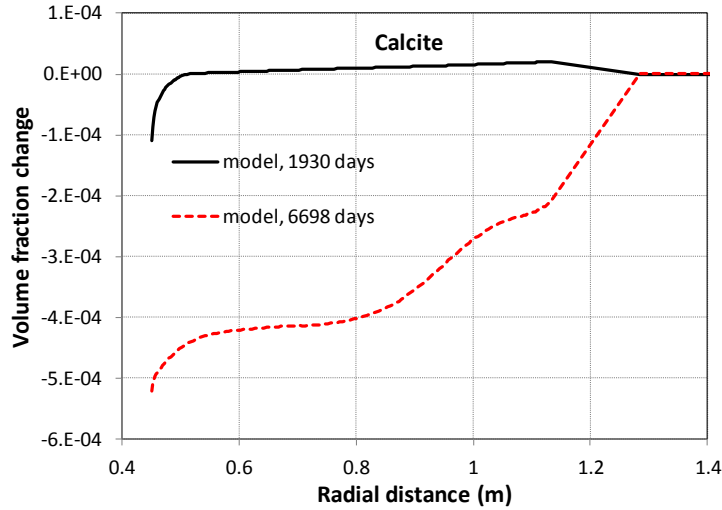


Figure 3-41. Computed profile of volume fraction change of calcite at the 1930 days (after the dismantling of heater 1) and at 6698 days (July 1, 2015).

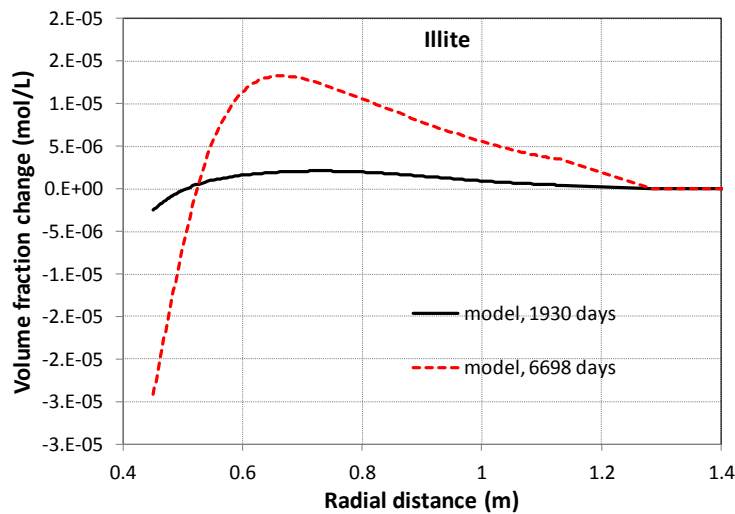


Figure 3-42. Computed profile of volume fraction change of illite at the 1930 days (after the dismantling of heater 1) and at 6698 days (July 1, 2015).

pH is usually very difficult to predict because it involves many reactions. As shown in Figure 3-43, in the sensitivity run that has no reactions, the computed pH is too low. For FEBEX bentonite, pH is mainly regulated by carbonate reactions involving calcite and dolomite and surface protonation reactions. Zheng et al. (2011) showed that surface protonation has strong pH buffering capacity and the model in this part of the report confirms that observation. However, the base model still underestimates the measured pH slightly by 0.1 unit, which may be attributed to the uncertainties in the initial amount of calcite. Figure 3-44 shows the concentration profile of bicarbonate. The base model produces lower bicarbonate concentration than the sensitivity run and results from the base model are lower than measured data. Previous

modeling work (e.g. Samper et al., 2008) showed that bicarbonate concentration is very sensitive to the alteration of calcite and dolomite and is entangled with pH changes. The current model does not consider the dissolution/exsolution of CO₂ gas, which may be a key reaction to explain the underestimation of pH and bicarbonate by the model. Also as mentioned above, inference processes using geochemical modeling were needed to obtain the chemical composition of pore water in bentonite under *in situ* conditions based on the measured concentrations by aqueous extract (Zheng et al., 2008a). However, during the aqueous extract, there was CO₂ exsolution that changed the inventory of total carbonate, which was difficult to capture accurately in the geochemical model that was used to infer the concentration under the *in situ* conditions (Zheng et al., 2008). This is another source of uncertainty regarding the pH and concentration of bicarbonate.

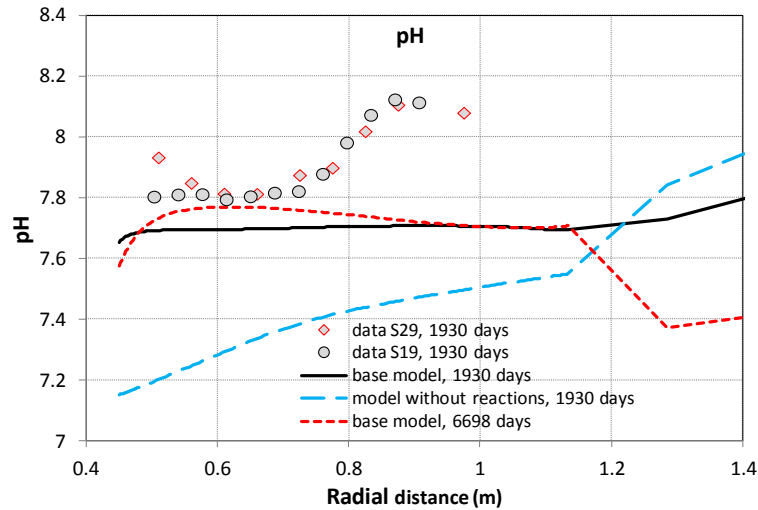


Figure 3-43. The profile of pH at 1930 days (Zheng et al., 2011) and model results from the base model.

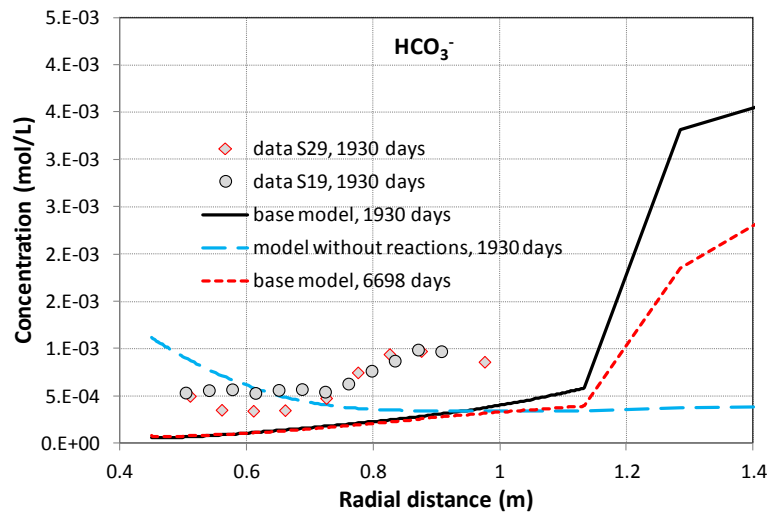


Figure 3-44. The concentration profile of bicarbonate at 1930 days (Zheng et al., 2011) and model results from the base model.

FEBEX bentonite contains a small amount of gypsum (ENRESA, 2000). But the amount is very small and gypsum is very soluble, so a small change in the water saturation may make gypsum disappear, which makes it debatable whether there is gypsum initially in the bentonite. The presence of gypsum had been one of the major uncertainties when the pore water compositions under in situ conditions were inferred from aqueous extract data (Zheng and Samper, 2008). Figure 3-45 shows the inferred data and model results. Unlike cations, the data for sulfate does not follow the trend of chloride, which indicated strong interference by chemical reactions. In the current model, no gypsum is present in the bentonite. Model results underestimate the data. Refinement of the current chemical model is warranted when the swelling of bentonite is properly accounted for.

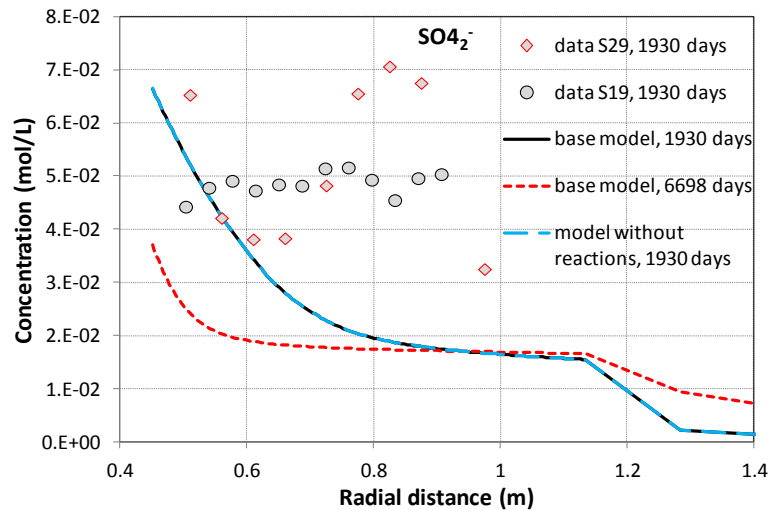


Figure 3-45. The concentration profile of sulfate at 1930 days (Zheng et al., 2011) and model results from the base model.

The concentration profile along the EBS bentonite is the result of complex reaction networks under the influence of coupled THMC processes. For FEBEX bentonite, the inability to obtain concentrations directly (Zheng et al., 2008) adds another layer of uncertainty. In this part of the report, we conducted a few sensitivity analyses to illustrate how these parameters affect the concentration profile in bentonite after the dismantling of heater 1; more analyses will be conducted in the future.

In section 3.4.1.2, we explore the sensitivity of relative humidity to several hydrological parameters. One of these is the permeability of granite, which significantly affects the hydration of bentonite; consequently it will affect profiles of concentration. As we can see from Figure 3-46, lower permeability for granite leads to higher concentration of chloride because less infiltration of granite water leads to less dilution of bentonite pore water, and vice versa, higher permeability of granite leads to lower concentration of chloride in bentonite.

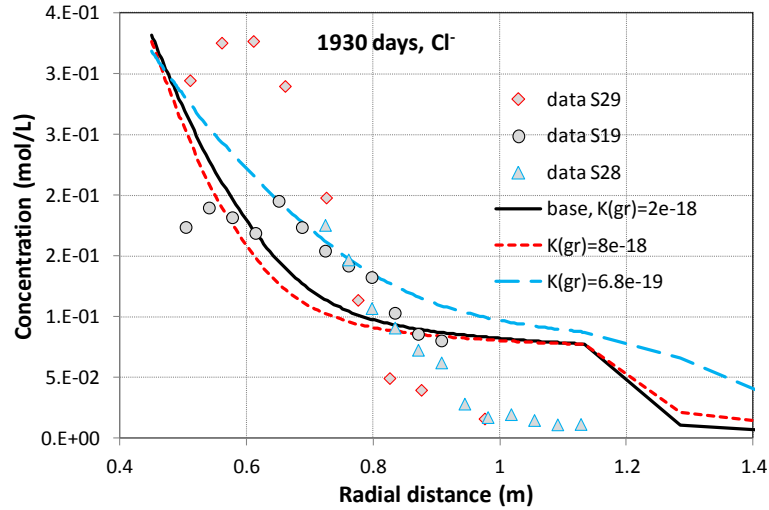


Figure 3-46. The concentration profile of chloride at 1930 days (Zheng et al., 2011) and model results from the base model and two sensitivity runs with different permeability for granite.

Another uncertainty is the initial concentration of major cations and anions in pore water, which stems mostly from the complex pore structure of bentonite. While defining the right pore structure and modeling approach has been, and will be, a challenge for modeling the chemical change in bentonite, here we simply vary the initial concentration of chloride to illustrate how important the initial concentration is in term of controlling the concentration profile for the FEBEX in situ test. Figure 3-47 shows the concentration profile of chloride with three different initial concentrations. Differences in initial concentrations change the overall level of concentration but not the general trend of concentration profile across the bentonite barrier.

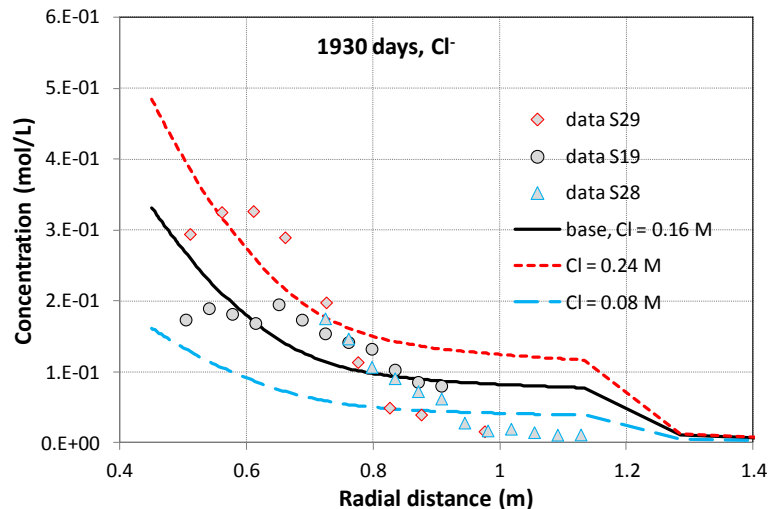


Figure 3-47. The concentration profile of chloride at 1930 days (Zheng et al., 2011) and model results from the base model and two sensitivity runs with different chloride initial concentrations.

Figures 3-34 to 3-45 also show the concentration profiles of major cations and anion and minerals phase changes at 6698 days, corresponding to July 1, 2015. The dismantling of heater 2 started on April 2015 and is expected to finish in August, 2015. July 1, 2015 is just an approximation of the time that samples for geochemical analyses were to be taken. When we know the time that samples are taken, the appropriate simulation data will be used for comparison. Regarding the evolution of concentration of major cations in pore water, after 6698 days (18.3 years) the model predicts lower concentrations near the heater than after 1930 days, but concentration near granite similar to the level of 1930 days (Figures 3-35 through 3-38). Sulfate concentration will be further diluted as more water coming to saturate bentonite (Figure 3-45), but pH and bicarbonate at 6698 days stay roughly the same level as at 1930 days (Figures 3-43, 3-44). Regarding the mineral change at 6698 days, calcite continues dissolving and dolomite keeps precipitating; smectite dissolves more in the bentonite blocks near the bentonite/granite interface and start to precipitate in bentonite blocks near the heater. Illite acts the opposite — wherever smectite dissolve it precipitates and vice versa. However, the amount that smectite dissolves and illite precipitates is still very small, which might be difficult to detect.

3.5 Summary and Future Work

The FEBEX *in situ* test that lasted more than 18 years is extremely valuable for validating coupled the THMC model. In the FEBEX-DP project, heater 2 will be dismantled and extensive THMC characterization will be conducted to evaluate the THMC alteration of the bentonite block. LBNL/DOE joins the FEBEX-DP in FY15 and aims to develop a THMC model and test it with data from FEBEX-DP. Specifically we would like to answer the following questions:

- What causes the hydration of bentonite to be slower than typically predicted by a Darcy flow model: Non-Darcian flow behavior, thermal osmosis that counteracts flow towards the heater, decrease of intrinsic permeability of the buffer due to changes in microstructure, or a combination of all these processes?
- What is the spatial density variation of the bentonite as a result of long term hydration and swelling?
- What is the chemical evolution in the bentonite, especially the changes of more soluble minerals (gypsum, calcite and pyrite) and aqueous concentration, evolution of pH and Eh and alteration of smectite?

We planned to start the development of the TH model, then expand the TH model to a THC or THM model and eventually establish the coupled THMC model. This part of the report documents our modeling effort so far in FY15, which encompasses the development the TH model with Non-Darcian flow and the THC model, and comparison between model results with TH data from the bentonite surrounding heater 2 and chemical data obtained from the dismantling of heater 1. The key findings from current modeling work are as follows:

- Adjusting key hydrological parameters such as permeability of bentonite and granite may lead to a good fit of measured relative humidity at given location, but cannot explain relative humidity across the entire bentonite barrier. Mechanical change (especially swelling) has to be considered.
- Including Non-Darcian flow into the TH model leads to a significant underestimation of the relative humidity data in the entire bentonite barrier (even in bentonite near the

bentonite/granite interface). The reason could be that the calibration of relative permeability (and retention curve) already encompasses the nonlinear relationship between gradient and flux for bentonite, which would obviate the consideration of Non-Darcian flow in the model. Non-Darcian flow under unsaturated conditions still needs more study.

- In comparison with the chemical data obtained after the dismantling of heater 1 in 2002, the THC model captures the general trend of the concentration profiles of major cations and anions. However, the model overestimates the concentration level in bentonite near the bentonite/granite interface; this effect will be reduced when mechanical change is included in the model, i.e. with THMC models.
- The preliminary prediction of the chemical change after the dismantling of heater 2 shows that concentration levels of aqueous species will continue going down in bentonite near the heater; calcite dissolves and dolomite forms, and illite precipitates in bentonite near the bentonite/granite interface, accompanied by the dissolution of smectite at the same place.

In the remaining months of FY15 and FY16, the following work is planned:

- The mechanical processes will be added to the current THC model. Once the coupled THMC model is developed, mechanical-hydrological coupling will be calibrated against measured stress, dry density, water content and relative humidity data.
- The chemical model will be further refined. Once the concentration profile of chloride can be matched by the THMC model, predictions will be made for other chemical species and mineral phases.
- Once the corrosion of the steel liner is analyzed, chemical changes of steel will be included in the chemical model to evaluate the interaction of steel and bentonite.

Ultimately, after the THMC models for FEBEX *in situ* test are fully validated with data, they will be used to explore THMC changes in the long run under higher temperature.

References

- Bear, J., (1972). Dynamics of fluids in porous media. American Elsevier Publishing Company Inc., New York. ISBN 0-486-65675-6.
- Bradbury, M.H., Baeyens, B., (1998). A physicochemical characterization and geochemical modelling approach for determining porewater chemistries in argillaceous rocks. *Geochimica et Cosmochimica Acta* 62, 783–795.
- Bradbury, B., Baeyens, B., (2003). Porewater chemistry in compacted resaturated MX-80 bentonite. *Journal Contaminant Hydrology* 61, 329–338.
- Bradbury, M. H. and B. Baeyens (2005). Modelling the sorption of Mn(II), Co(II), Ni(II), Zn(II), Cd(II), Eu(III), Am(III), Sn(IV), Th(IV), Np(V) and U(VI) on montmorillonite: Linear free energy relationships and estimates of surface binding constants for some selected heavy metals and actinides. *Geochimica et Cosmochimica Acta* 69(4): 875-892.
- Chen, Y., Zhou, C., Jing, L., (2009). Modeling coupled THM processes of geological porous media with multiphase flow: theory and validation against laboratory and field scale experiments. *Computers and Geotechnics* 36 (8), 1308–1329.
- Cui YJ, Tang AM, Loiseau C, Delage P (2008). Determining the unsaturated hydraulic conductivity of a compacted sand-bentonite mixture under constant-volume and free-swell conditions. *Physics and Chemistry of the Earth* 33, S462-S471
- Deming D (1994). Factors necessary to define a pressure seal. *AAPG Bulletin* 78(6): 1005-1009
- ENRESA (2000). Full-scale engineered barriers experiment for a deep geological repository in crystalline host rock FEBEX Project, European Commission: 403.
- ENRESA, (2006a). FEBEX: Updated final report. ENRESA Tech. Publ. PT 05-0/2006, 589 pp.
- ENRESA, (2006b). FEBEX: Final THG modelling report. ENRESA Tech. Publ. PT 05-3/2006, 155 pp.
- Fernández, A., Rivas, P., (2003). Task 141: post-mortem bentonite analysis. geochemical behaviour. CIEMAT/DIAE/54520/05/03, Internal Note 70-IMA-L-0-107 v0.
- Fernández, A.M., Rivas, P., (2005). Pore water chemistry of saturated FEBEX bentonite compacted at different densities. In: Alonso, E.E., Ledesma, A. (Eds.), *Advances in Understanding Engineered Clay Barriers*. A.A Balkema Publishers, Leiden, The Netherlands, pp. 505–514.
- Fernández, A. M., B. Baeyens, M. Bradbury and P. Rivas (2004). Analysis of the porewater chemical composition of a Spanish compacted bentonite used in an engineered barrier. *Physics and Chemistry of the Earth, Parts A/B/C* 29(1): 105-118.
- Fernández, A.M., Cuevas, J., Rivas, P. (2001). Pore water chemistry of the FEBEX bentonite. *Mat. Res. Soc. Symp. Proc.* 603, 573-588.
- Hansbo S (1960). Consolidation of clay, with special reference to influence of vertical sand drains. *Swed Geotech Inst Proc* 18, Stockholm
- Hansbo S (2001). Consolidation equation valid for both Darcian and non-Darcian flow. *Geotechnique* 51(1): 51-54
- Huertas, F. B. de la Cruz, J. L. Fuentes-Cantillana, et al. (2005). Full-Scale Engineered Barriers Experiment for a Deep Geological Repository for High-Level Waste in Crystalline Host Rock – Phase II. EUR 21922
- Itasca, (2009). FLAC3D, Fast Lagrangian Analysis of Continua in 3 Dimensions, Version 4.0, Minneapolis, Minnesota, Itasca Consulting Group.
- Kuhlman U., Gaus I. (2014). THM Model validation modelling of selected WP2 experiments:

- Inverse Modelling of the FEBEX in situ test using iTOUGH2. DELIVERABLE-Nº: D3.3-1, NAGRA.
- Lanyon, G. W., I. Gaus, M. Villar, P.L.Martín, A. Gens, J. García-Siñeriz, I. Bárcena, (2013). Main outcomes and review of the FEBEX In Situ Test (GTS) and Mock-Up after 15 years of operation, Arbeitsbericht NAB 13-96
- Liu, H.H., J. Houseworth, J. Rutqvist, L. Zheng, D. Asahina, L. Li, V. Vilarrasa, F. Chen, S. Nakagawa, S. Finsterle, C. Doughty, T. Kneafsey and J. Birkholzer. (2013). Report on THMC modeling of the near field evolution of a generic clay repository: Model validation and demonstration, Lawrence Berkeley National Laboratory, August, 2013, FCRD-UFD-2013-0000244.
- Liu, H.-H. and J. Birkholzer (2012). On the relationship between water flux and hydraulic gradient for unsaturated and saturated clay. *Journal of Hydrology* 475: 242-247.
- Martín, P.L. and J.M. Barcala, (2005). Large scale buffer material test: Mock-up experiment at CIEMAT, *Engineering Geology* 81, 298– 316.
- Martín, P.L., J.M. Barcala, and F. Huertas, (2006). Large-scale and long-term coupled thermo-hydro-mechanic experiments with bentonite: the FEBEX mock-up test, *Journal of Iberian Geology* 32 (2) 259-282.
- Nguyen, T. S., A. P. S. Selvadurai and G. Armand (2005). Modelling the FEBEX THM experiment using a state surface approach. *International Journal of Rock Mechanics and Mining Science* 42(5-6): 639-651.
- Odong, J. (2007). Evaluation of empirical formulae for determination of hydraulic conductivity based on grain-size analysis. *The Journal of American Science* 3 (3), 54–60.
- Pusch, R. and Madsen, F. t. (1995). Aspects on the illitization of the kinnekulle bentonites. *Clays and Clay Minerals* 43(3): 261-270.
- Pruess, K., C. Oldenburg and G. Moridis (1999). TOUGH2 User's Guide, Version 2.0, Lawrence Berkeley National Laboratory, Berkeley, CA.
- Ramírez, S., J. Cuevas, R. Vigil and S. Leguey (2002). Hydrothermal alteration of “La Serrata” bentonite (Almeria, Spain) by alkaline solutions. *Applied Clay Science* 21(5–6): 257-269.
- Rutqvist, J., Zheng, L., Chen, F., Liu, H.-H. and Birkholzer, J. (2013). Modeling of Coupled Thermo-Hydro-Mechanical Processes with Links to Geochemistry Associated with Bentonite-Backfilled Repository Tunnels in Clay Formations. *Rock Mechanics and Rock Engineering*: 1-20.
- Sacchi, E., Michelot, J.L., Pitsch, H., Lalieux, P., Aranyossy, J.F., (2001). Extraction of water and solution from argillaceous rock for geochemical characterisation: methods, processes, and current understanding. *Hydrogeology Journal* 9, 17–33.
- Sánchez, M., A. Gens, L. J. D. N. Guimarães and S. Olivella (2005). A double structure generalized plasticity model for expansive materials. *International Journal for numerical and analytical methods in geomechanics* 29: 751-787.
- Sánchez, M., A. Gens and L. Guimarães (2012a). Thermal–hydraulic–mechanical (THM) behaviour of a large-scale in situ heating experiment during cooling and dismantling. *Canadian Geotechnical Journal* 49(10): 1169-1195.
- Sánchez, M., A. Gens and S. Olivella (2012b). THM analysis of a large-scale heating test incorporating material fabric changes. *International Journal for Numerical and Analytical Methods in Geomechanics* 36(4): 391-421.

- Samper, J., L. Zheng, L. Montenegro, A. M. Fernández and P. Rivas (2008a). Coupled thermo-hydro-chemical models of compacted bentonite after FEBEX in situ test. *Applied Geochemistry* 23(5): 1186-1201.
- Samper, J., L. Zheng, A. M. Fernández and L. Montenegro (2008b). Inverse modeling of multicomponent reactive transport through single and dual porosity media. *Journal of Contaminant Hydrology* 98(3-4): 115-127.
- Siitari-Kauppi, M.; Leskinen, A., Kelokaski, M.; Togneri, L. Alonso, U.; Missana, T.; García - Gutiérrez, (2007). Physical Matrix Characterisation: Studies of Crystalline Rocks and Consolidated Clays by PMMA Method and Electron Microscopy as Support of Diffusion Analyses. CIEMAT Technical Report, 1127, December 2007.
- Swartzendruber D (1961). Modification of Darcy's law for the flow of water in soils. *Soil Science* 93: 22-29
- Wolery, T. J., (1993). EQ3/6, A software package for geochemical modelling of aqueous systems, Version 7.2. Lawrence Livermore National Laboratory, USA.
- Xu, T., Spycher, N., Sonnenthal, E., Zhang, G., Zheng, L. and Pruess, K. (2011). TOUGHREACT Version 2.0: A simulator for subsurface reactive transport under non-isothermal multiphase flow conditions. *Computers & Geosciences* 37(6): 763-774.
- Xu, T., E. Sonnenthal, N. Spycher and K. Pruess (2006). TOUGHREACT: A Simulation Program for Non-isothermal Multiphase Reactive Geochemical Transport in Variably Saturated Geologic Media. *Computers and Geosciences* 32: 145-165.
- Zheng, L. and J. Samper (2008). A coupled THMC model of FEBEX mock-up test. *Physics and Chemistry of the Earth, Parts A/B/C* 33, Supplement 1: S486-S498.
- Zheng, L., J. Samper and L. Montenegro (2008). Inverse hydrochemical models of aqueous extracts tests. *Physics and Chemistry of the Earth, Parts A/B/C* 33(14-16): 1009-1018.
- Zheng, L., J. Samper, L. Montenegro and A. M. Fernández (2010). A coupled THMC model of a heating and hydration laboratory experiment in unsaturated compacted FEBEX bentonite. *Journal of Hydrology* 386(1-4): 80-94.
- Zheng, L., J. Samper and L. Montenegro (2011). A coupled THC model of the FEBEX in situ test with bentonite swelling and chemical and thermal osmosis. *Journal of Contaminant Hydrology* 126(1-2): 45-60.
- Zheng, L., Li, L., Rutqvist, J., Liu, H. and Birkholzer, J.T., (2012). Modeling Radionuclide Transport in Clays. Lawrence Berkeley National Laboratory. FCRD-URD-2012-000128
- Zheng, L., Jonny Rutqvist, Carl Steefel, Kunhwi Kim, Fei Chen, Victor Vilarrasa, Seiji Nakagawa, Jiangtao Zheng, James Houseworth, Jens Birkholzer. (2014). Investigation of Coupled Processes and Impact of High Temperature Limits in Argillite Rock. FCRD-UFD-2014-000493, LBNL-6719E
- Zou Y (1996). A non-linear permeability relation depending on the activation energy of pore liquid. *Geotechnique* 46(4): 769-774

4. THM Modeling: FE Heater Test and DECOVALEX

In this section, we present LBNL's activities related to THM modeling of underground heater experiments in clay formations, including studies related to the Development of Coupled Models and their Validation against Experiments (DECOVALEX)-2015 project and the Mont Terri FE (Full-scale Emplacement) Experiment. DECOVALEX-2015 is an acronym for the sixth and current phase of the "Development of Coupled Models and their Validation against Experiments" project, ongoing from 2012 through 2015. In DECOVALEX-2015, LBNL participates in Task B, which includes:

Subtask B1—Mont Terri HE-E Experiment: A heating experiment to evaluate sealing and clay-barrier performance, in a micro-tunnel at the Mont Terri URL in Switzerland; and

Subtask B2—Horonobe Engineered Barrier System (EBS) Experiment: A heating experiment to study the thermo-hydro-mechanical-chemical (THMC) behavior of the EBS and its interaction with the mudstone host rock, in a vertical emplacement hole at the Horonobe URL in Japan

In addition to the modeling work in these two DECOVALEX tasks; LBNL participates in the Mont Terri FE Experiment as one of the participating modeling teams. The FE Experiment is undertaken as an ultimate test for the performance of geologic disposal in Opalinus Clay, focusing on both the EBS components and the host-rock behavior; it will be one of the largest and longest running heater tests worldwide.

UFD objectives for participating in these international activities are to develop expertise and test advanced models of coupled processes in clay-based backfill in interaction with clay host rock. Through participation in modeling these field experiment, the models will be developed and experience will be gained for a range of different backfill materials (e.g., bentonite pellets and sand/bentonite mixture), as well as different host rocks (e.g., Opalinus clay and mudstone).

The main software developed and used for these simulations is the TOUGH-FLAC (Rutqvist et al. 2002; 2011; 2014). For nuclear waste isolation, TOUGH-FLAC provides UFD with a model framework for modeling coupled THM processes in the EBS and host rock and their interactions using state-of-the-art macroscopic constitutive models for bentonite, crushed rock salt backfill, clay, salt and crystalline host rocks. For rigorous modeling of the THM behavior of bentonite-based (swelling) buffer and back-fill materials, the BBM (Barcelona Basic Model) and BExM (Barcelona Expansive Model) have been implemented into TOUGH-FLAC. Modeling of the in situ heater experiments provides a unique opportunity to validate and test the models at realistic, large-scale, in-situ conditions, including the interactions between the host rock and EBS. Finally, through the numerical modeling of these experiments and being at the forefront of modeling coupled THMC processes our goal is also to advance the state-of-the-sciences in the field of coupled processes modeling of clay barriers.

In the following Subsection 4.1, the modeling approach and the status of model development will be summarized. Then the modeling work conducted associated with field experiments is presented in Subsections 4.2 through 4.4. Finally, in Subsection 4.5, the current status and future plans for THM m modeling are summarized.

4.1 Modeling Approach

LBNL uses two independent numerical simulators (TOUGH-FLAC and ROCMAS) for modeling of coupled THM processes associated with nuclear waste disposal and for modeling of the aforementioned heater experiments. The TOUGH-FLAC simulator developed at LBNL is the primary analysis tool, because this simulator has the required capabilities to model a large variety of problems associated with nuclear waste disposal for various engineering and natural systems. The ROCMAS code, also developed at LBNL, is in this project used for confidence building through code-to-code verification. That is, models of a particular problem might be built in both TOUGH-FLAC and ROCMAS, and if the simulation results agree, that provides confidence in the models.

Both the TOUGH-FLAC and ROCMAS codes solve THM coupled problems, but are two different codes with different characteristics. TOUGH-FLAC can simulate coupled THM processes under multiphase flow conditions through a sequential coupling of the TOUGH2 multiphase flow simulator with the FLAC3D geomechanical code (Rutqvist et al., 2002; Rutqvist 2011). TOUGH-FLAC has recently been modified for applications related with to bentonite-backfilled repositories in clay host formations (Rutqvist et al., 2014). ROCMAS simulates coupled THM processes in unsaturated media, including single-phase liquid flow and vapor diffusion in a static gas phase (Rutqvist et al., 2001a). The code has been extensively applied in earlier phases of the DECOVALEX project for THM analysis in bentonite-rock systems (Rutqvist et al., 2001b, 2005, 2009). In the following, the TOUGH-FLAC simulator (primary analysis tool) is described in more detail.

The TOUGH-FLAC simulator (Rutqvist 2011), is based on linking the TOUGH2 multiphase flow and heat transport simulator (Pruess et al., 2011) with the FLAC3D geomechanical simulator (Itasca 2011). In this approach, TOUGH2 (Pruess et al., 2011) is used for solving multiphase flow and heat transport equations, whereas FLAC3D (Itasca, 2011) is used for solving geomechanical stress-strain equations. The two codes are sequentially coupled so that a TOUGH-FLAC simulation runs seamlessly.

For analysis of coupled THM problems, TOUGH2 and FLAC3D are executed on compatible numerical grids and linked through a coupled THM model (Figure 4-1) with coupling functions to pass relevant information between the field equations that are solved in the respective codes. In the coupling scheme between TOUGH2 and FLAC3D, the TOUGH2 multiphase pressures, saturation, and temperature are provided to update temperature, and pore pressure to FLAC3D (Figure 4-1). After data transfer, FLAC3D internally calculates thermal expansion, swelling, and effective stress. Conversely, element stress or deformation from FLAC3D is supplied to TOUGH2 to correct element porosity, permeability, and capillary pressure for the fluid-flow simulation in TOUGH2. The corrections of hydraulic properties are based on material-specific functions.

In a TOUGH-FLAC simulation, the calculation is stepped forward in time with the transient multiphase fluid flow analysis in TOUGH2, and at each time step or at the TOUGH2 Newton iteration level, a quasi-static mechanical analysis is conducted with FLAC3D to calculate stress-induced changes in porosity and intrinsic permeability. In this scheme, the fluid-flow sequence is solved first under fixed stress, and the resulting pressure and temperature are prescribed in the mechanical sequence. This corresponds to so-called stress-fixed iterations in the sequential scheme, in which the solution becomes unconditionally stable. The resulting THM analysis may

be explicit sequential, meaning that the porosity and permeability is evaluated only at the beginning of each time step, or the analysis may be implicit sequential, with permeability and porosity updated on the Newton iteration level towards the end of the time step using an iterative process.

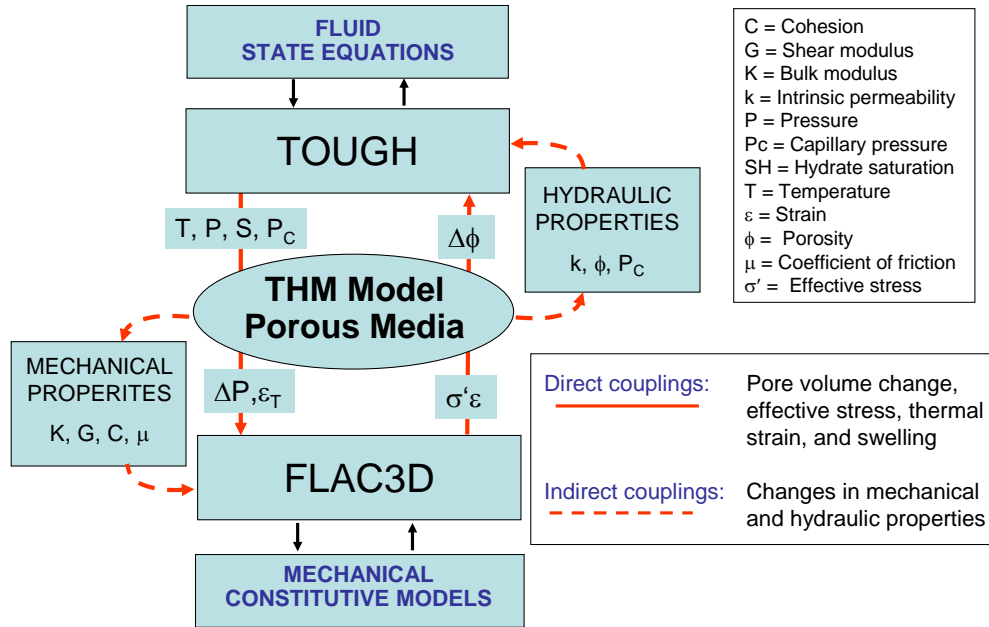


Figure 4-1. Schematic of linking of TOUGH2 and FLAC3D in a coupled TOUGH-FLAC simulation.

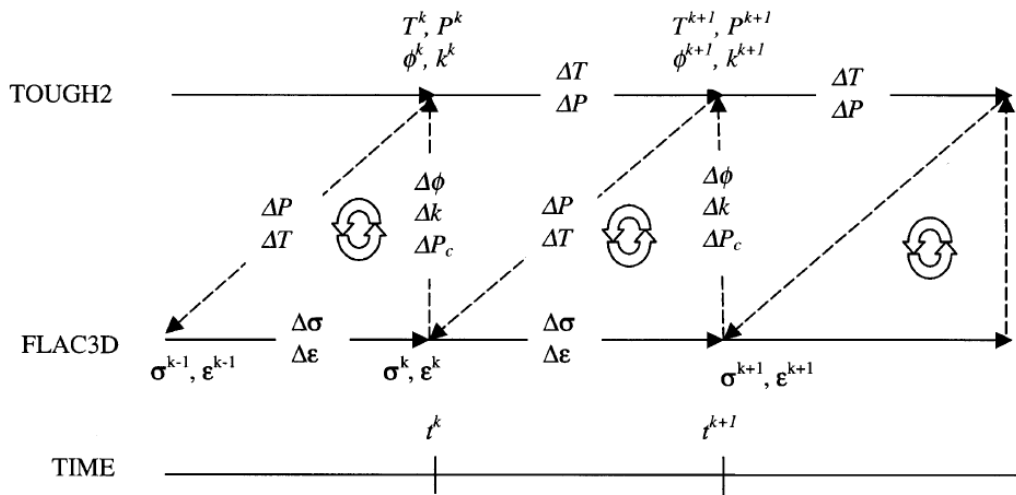


Figure 4-2. Numerical procedure of a linked TOUGH2 and FLAC3D simulation.

A great advantage with this adopted approach is that both codes are continuously developed and widely used in both academia and industry. In TOUGH2, a large number of fluid equation-of-state modules are available, while in FLAC3D, a large number of geomechanical constitutive models are available. This means that the simulator can be relatively easily extended to new application areas.

As part of the UFD effort, the TOUGH-FLAC simulator has been extended and applied to issues related to nuclear waste disposal with bentonite backfilled tunnels (Rutqvist et al., 2011; 2014). This includes implementation of the Barcelona Basic Model (BBM) (Alonso et al., 1990), for the mechanical behavior of unsaturated soils, which has been applied for modeling of bentonite backfill behavior (Rutqvist et al., 2011). The BBM was first developed and presented in the early 1990s as an extension of the Modified Cam Clay (MCC) model to unsaturated soil conditions (Alonso et al., 1990). The model can describe many typical features of unsaturated-soil mechanical behavior, including wetting-induced swelling or collapse strains, depending on the magnitude of applied stress, as well as the increase in shear strength and apparent preconsolidation stress with suction (Gens et al., 2006). Figure 4-3 presents the yield surface of the BBM model in q - p - s space. The shaded surface corresponds to the elastic region at fully water-saturated conditions, which is equivalent to the modified MCC model. The figure also shows how the yield surface expands at unsaturated and dryer conditions when suction increases. There is an increase in both the apparent pre-consolidation pressure along the load collapse (LC) yield surface and by the increasing tensile strength, which in turn leads to an increased cohesion and shear strength.

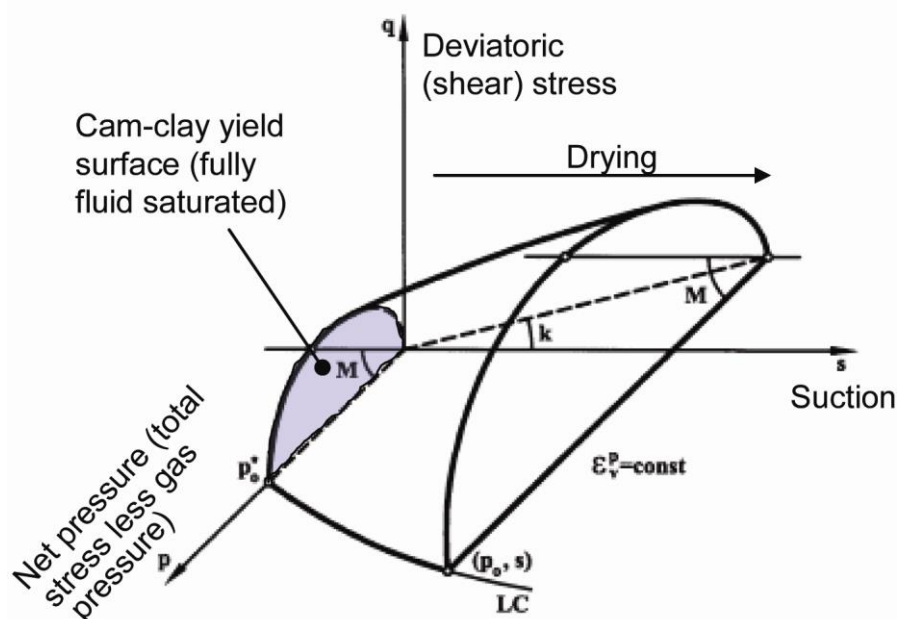


Figure 4-3. BBM constitutive model showing the yield surface in q - p - s space.

The BBM has been used for modeling bentonite-buffer behavior in various national nuclear waste programs in Europe and Japan. For example, the BBM was successfully applied to model the coupled THM behavior of unsaturated bentonite clay associated with the FEBEX *in situ* heater test at the Grimsel Test Site, Switzerland (Gens et al., 2009). The BBM has also been applied to other types of bentonite-sand mixtures based on MX-80, considered as an option for an isolating buffer in the Swedish KBS-3 repository concept (Kristensson and Åkesson 2008). As part of the UFD program, the BBM was also used by Rutqvist et al. (2014), for the modeling of coupled THM processes around a generic repository in a clay host formation.

Recently, as part of the UFD EBS program, the BBM has been extended to a dual structure model, corresponding to the Barcelona Expansive Model (BExM). In a dual-structure model, the material consists of two structural levels: a microstructure in which the interactions occur at the particle level, and a macrostructure that accounts for the overall fabric arrangement of the material comprising aggregates and macropores (Figure 4-4) (Gens et al., 2006, Sánchez et al., 2005, Gens and Alonso 1992). A dual-structure model has important features for modeling the mechanical behavior of a bentonite buffer, such as irreversible strain during suction cycles. However, most importantly, a dual-structure model provides the necessary link between chemistry and mechanics, enabling us to develop a coupled THMC model for the analysis of long-term EBS behavior. This approach enables mechanistic modeling of processes important for long-term buffer stability, including effects of pore-water salinity on swelling (loss of swelling), conversion of smectite to nonexpansive mineral forms (loss of swelling), and swelling pressure versus exchangeable cations. Details of the development, testing and applications of the dual structure model, were presented in the FY2014 milestone report titled “Investigation of Coupled THMC Processes and Reactive Transport: FY14 Progress” (Rutqvist et al. 2014).

Based on model simulation in the DECOVALEX-2015 project with TOUGH-FLAC, considering full multiphase flow (gas and liquid) we found that a gas intrinsic permeability several orders of magnitude higher than the intrinsic permeability related to liquid flow would be required. In the following simulations of the three heater experiments we simulated high intrinsic gas permeability in the bentonite through the Klinkenberg parameter according to:

$$K_g = K_l(1+b/P) \quad (4-1)$$

where K_g is intrinsic permeability for gas flow, K_l is intrinsic permeability of water flow, b is the Klinkenberg parameter, and P is pressure. In this case, we assigned a high value of the Klinkenberg parameter of $2.5 \times 10^{11} \text{ Pa}^{-1}$, which means that the intrinsic permeability for gas flow would be about 6 orders of magnitude higher than the intrinsic permeability for water flow. This was necessary as otherwise it is not possible to simulate the drying that usually occurs near the heaters.

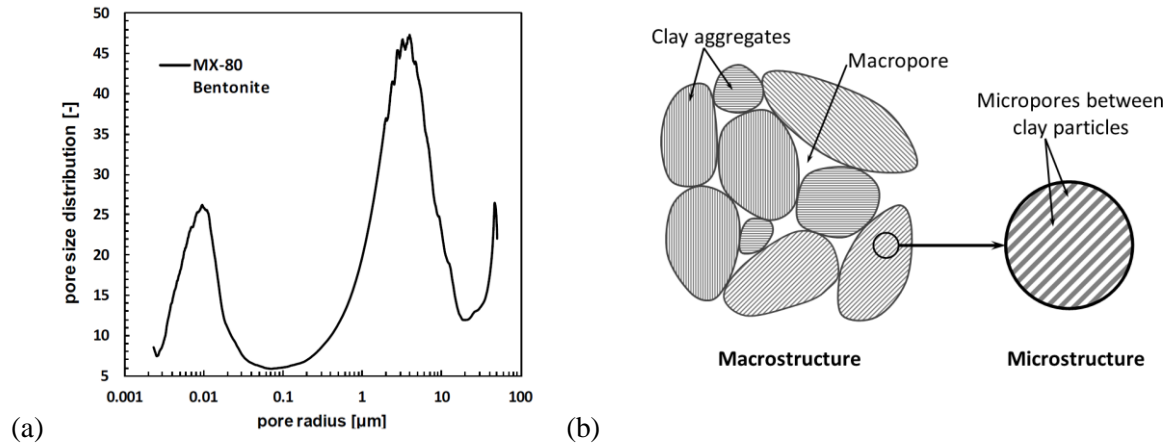


Figure 4-4. (a) Pore size distribution and (b) schematic representation of the two structural levels considered in the dual structure model. Clay particles are represented by the gray lines.

As will be discussed in Section 4.5, future model developments related to THM process modeling with TOUGH-FLAC will be focused on improving the BExM implementation (especially in terms of efficiency) and to implement and use the model for the evolution of the excavation disturbed zone, starting with implementation and use of the Two-Parts Hooke's Model (TPHM) that has been developed and applied previously in LBNL's work package for UFD.

4.2 Mont Terri HE-E Experiment (DECOVALEX)

The Mont Terri HE-E Experiment focuses on the THM behavior of bentonite barriers in the early nonisothermal resaturation stage and their THM interaction with Opalinus Clay (Figure 4-5). The objective is to better understand the evolution of a disposal system for high level waste in the early post-closure period, with emphasis on the thermal evolution, buffer resaturation (*in situ* determination of the thermal conductivity of bentonite and its dependency on saturation), pore-water pressure in the near field, and the evolution of swelling pressures in the buffer (Gaus et al., 2014). Because the test is conducted in a micro-tunnel (at half scale), it is considered a validation, not a demonstration experiment. The heating test involves two types of bentonite buffer materials (Figure 4-5, left). The heater-buffer interface is heated to a maximum temperature of 135°C and a temperature of 60–70°C is expected at the buffer-rock interface. A dense instrumentation network was in place in the host rock surrounding the micro-tunnel from a previous experiment testing the impact of ventilation on the clay host rock, and has been improved for the purpose of the HE-E Heater Test (up to 40 piezometers in total); various sensors have also been placed in the buffer material. The heating phase started in the late summer of 2011 and is still ongoing.

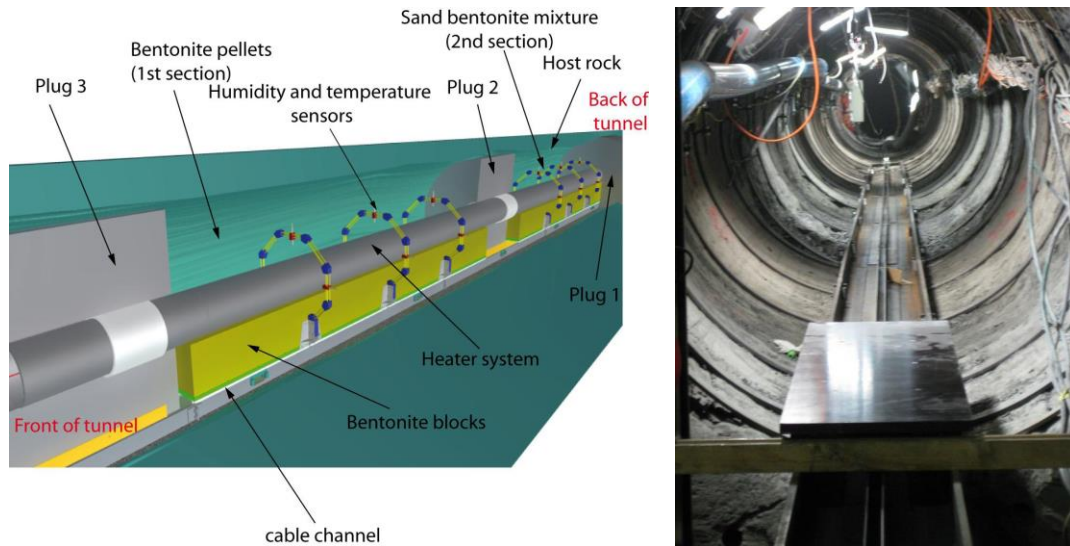


Figure 4-5. Schematic setup of HE-E experiment at Mont Terri and photo of micro-tunnel (Garritte, 2012).

In DECOVALEX-2015 (Task B1), eight international research teams are participating in the modeling of the HE-E experiment. Task B1, which is running over 3 years, is divided into the following steps:

- Step 1a: Opalinus Clay study including HE-D experiment, literature study, processes understanding and parameter determination.
- Step 1b: Buffer material study including CIEMAT column cells, literature study, processes understanding and parameter determination.
- Step 2: HE-E predictive modeling using as-built characteristics and true power load. Modeling is 2-D (axisymmetric, plane strain or combination) and 3-D.
- Step 3: HE-E interpretative modeling when data are made available.

Step 1a started in 2012 with the modeling of the previous HE-D experiment for *in situ* characterization of THM material parameters for the Opalinus Clay and was completed in November 2013. The HE-D experiment involved 1 year of heating of the Opalinus Clay without any bentonite buffer. The modeling of the HE-D experiment and comparison of the TOUGH-FLAC modeling results to the results of other modeling teams were reported in the FY2013 milestone report titled “Report on THMC modeling of the near field evolution of a generic clay repository: Model validation and demonstration” (Liu et al., 2013). Step 1b, which is a study of buffer material properties through modeling of laboratory experiments on buffer material samples, has been completed by all the modeling teams in DECOVALEX-2015. LBNL’s final analysis of the CIEMAT column experiments associated with Step 1b was presented in the FY14 milestone report entitled “Investigation of Coupled Processes and Impact of High Temperature Limits in Argillite Rock” (Zheng et al., 2014). In this part of the report we present the results of the predictive analysis of the HE-E experiment, conducted before the field data were available to the DECOVALEX-2015 participants. We also present a comparison of the model predictions

with experimental results. A final interpretive modeling of the field experimental data is also ongoing and will be completed during the rest of FY2015.

4.2.1 TOUGH-FLAC model prediction of the Mont Terri HE-E experiment

Figure 4-6 shows a 3-D model grid for the HE-E experiment and its location within the Mont Terri URL, whereas Figure 4-7 shows more details of the materials in a vertical cross-section that is also the geometry of a 2-D plane strain model. It is a half symmetric model with a vertical symmetry plane along the tunnel axis. In the model, the relevant materials are represented, including the different types of bentonite materials. The most important thermal and hydraulic properties, listed in Table 4-1, were derived from literature data and from material properties derived by modeling of various THM laboratory experiments on bentonite. The intrinsic permeability of gas flow in the bentonite is orders of magnitude higher than the intrinsic permeability for liquid flow and this is simulated in TOUGH2 using a high value of the Klinkenberg parameter (see Section 4.1 and Equation (4-1)). The material properties of the Opalinus Clay are based on the results of the modeling of the HE-D experiment as described Liu et al. (2013).

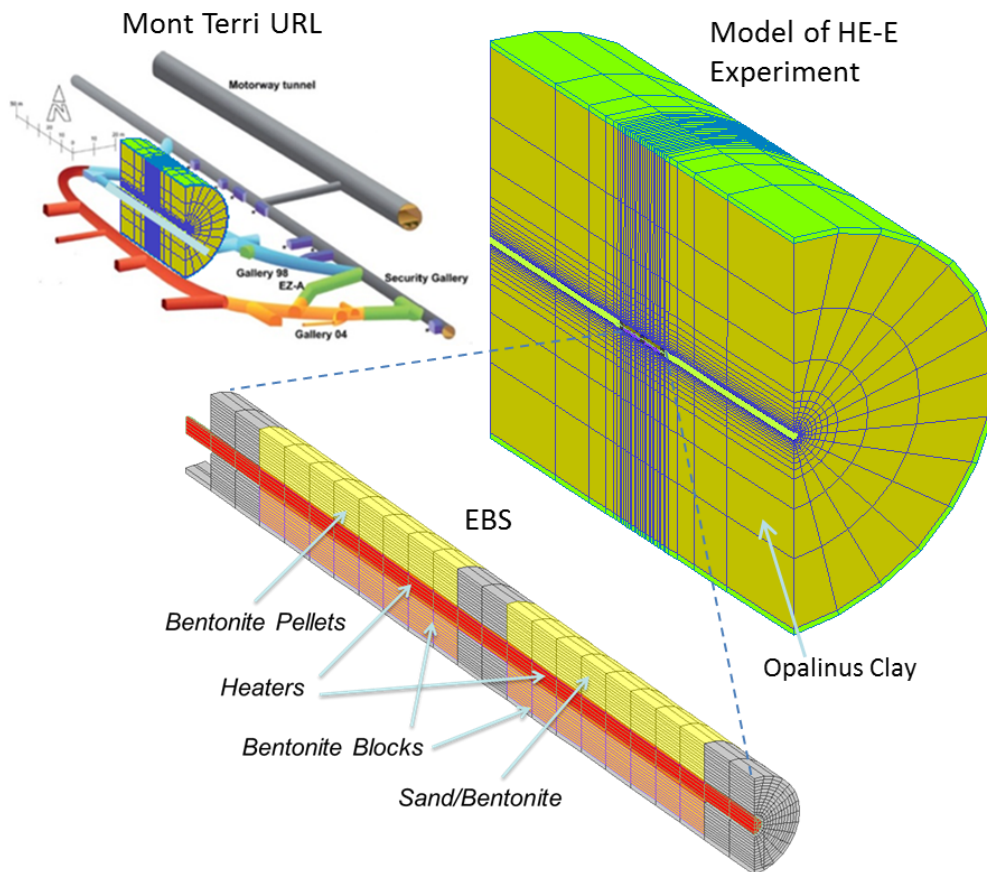


Figure 4-6. TOUGH-FLAC 3-D model of the Mont Terri HE-E experiment.

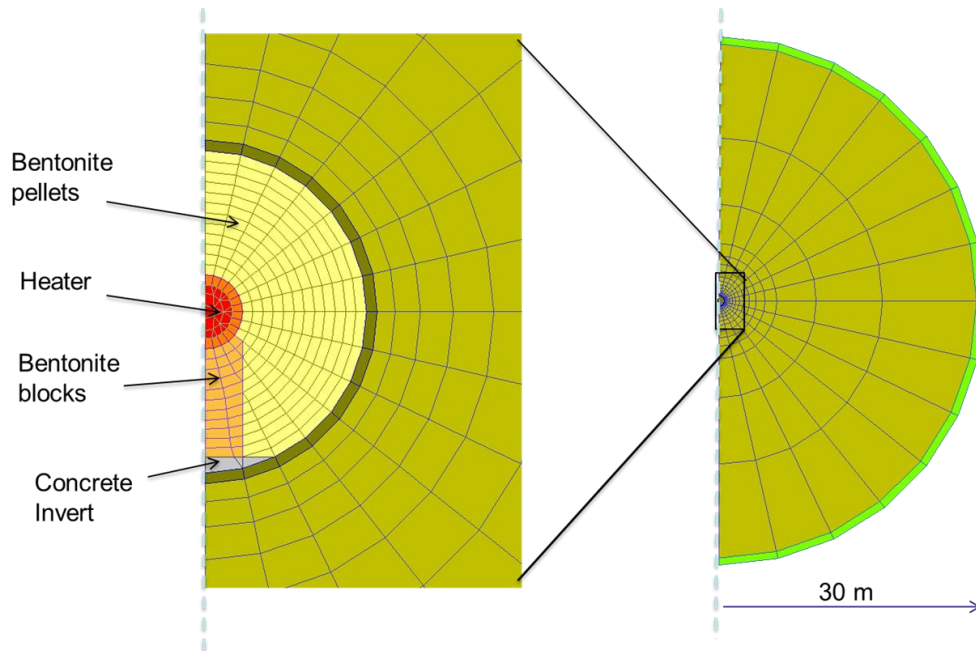


Figure 4-7. Vertical cross-section through the model grid.

Table 4-1. Parameters used in the modeling of the Mont Terri HE-E experiment.

Parameters	Symbol	Opalinus Clay	Granular Bentonite	Bentonite blocks	Concrete (shotcrete and plugs)	Unit
Grain density	ρ_g	2.7×10^3	2.7×10^3	2.7×10^3	2.7×10^3	kg/m ³
Porosity	\emptyset	0.15	0.46	0.389	0.15	-
Intrinsic permeability	k	5.0×10^{-20}	5.0×10^{-21}	2.0×10^{-21}	3.5×10^{-21}	m ²
Liquid relative permeability $k_{rw}(S_w) = \left(\frac{S_w - S_r}{S_m - S_r}\right)^A$	A	-	5	3	-	-
Liquid relative permeability $k_{rw}(S_w) = \left(\frac{S_w - S_r}{S_m - S_r}\right)^{1/2} \left[1 - \left\{1 - \left(\frac{S_w - S_r}{S_m - S_r}\right)^{1/m}\right\}^m\right]^2$	m	0.52	-	-	0.52	-
Capillary curve $\psi(S_w) = P_0 \left\{ \left(\frac{S_w - S_r}{S_m - S_r}\right)^{-1/m} - 1 \right\}^{1-m}$	P_0	1.09×10^7	1.0×10^7	3.0×10^7	1.09×10^7	Pa
	m	0.29	0.4	0.32	0.29	-
	S_{ls}	1.0	1.0	1.0	1.0	-
	S_{lr}	0.01	0.0	0.0	0.01	-
Thermal conductivity (wet)	λ_{sat}	1.7	1.3	1.0	1.7	W/m-K
Thermal conductivity (dry)	λ_{dry}	1.06	0.3	0.5	1.06	W/m-K
Grain specific heat	C	800	950	950	800	J/kg-K

The modeling of the HE-E experiment was conducted in several steps (Figure 4-8), including

- 1) The tunnel being open for 13 years at a constant relative humidity of 98%
- 2) Bentonite buffer and heaters emplaced for 75 days before start of heating
- 3) Heating for 1000 days

The simulation of the tunnel open for 13 years at a constant relative humidity of 98% is simulated applying a constant suction value of 2.6 MPa at the tunnel wall. In reality, the tunnel was exposed to a complex history including ventilation experiments, and the average 98% relative humidity was inferred from information in Gaus et al. (2014). This creates a pressure sink around the tunnel with a slight desaturation of the near field rock. The bentonite buffer and heaters were then installed into the model by changing material properties for elements within the tunnel. Also the initial saturation of about 20% in the granular bentonite buffer was assumed based on in-situ observations. Finally, after another 75 days, the heaters were turned on following the heater power used in the actual experiment. In the simplified 2-D model simulations used for the initial model predictions, the actual heat power was scaled down to represent the heat input per meter tunnel.

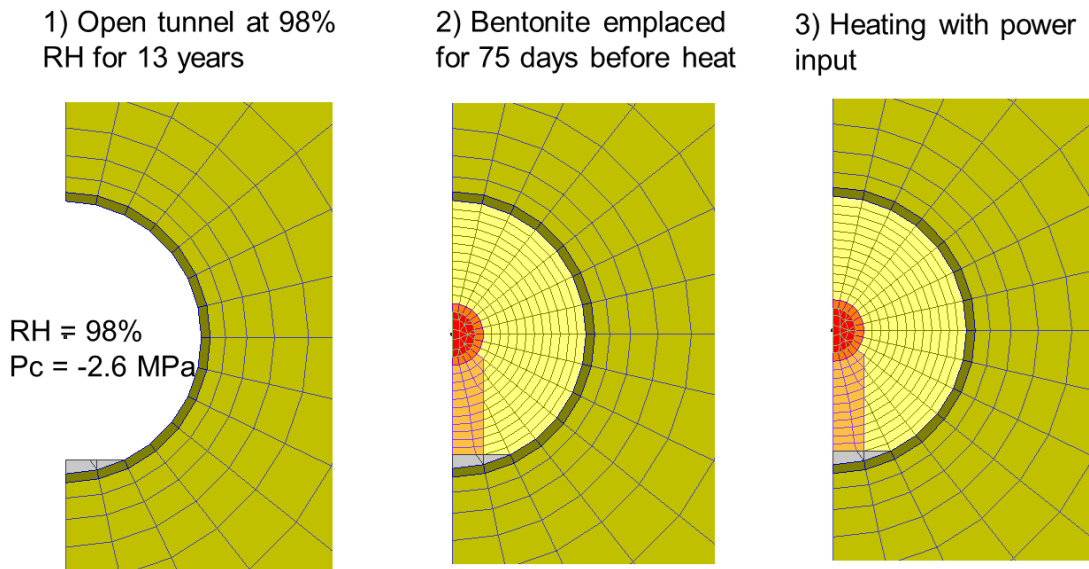


Figure 4-8. Steps for modeling the Mont Terri HE-E experiment.

Figure 4-9 shows the simulation results related to the evolution of liquid saturation and temperature from -100 to 1000 days, i.e. from 100 days before the start of the heating. Figure 4-9a shows that as soon as the bentonite buffer is installed (at -75 day), water is sucked into the bentonite from the adjacent rock. This is seen as a drop in liquid saturation in the rock (orange curve), while the saturation in the bentonite adjacent to the rock wall increases (blue curve). When the heating is turned on, a typical drying occurs at the inner part of the buffer (e.g. red line). Using the given heat power input, the maximum temperature of about 140°C is reached in less than 400 days, while the temperature at the rock wall gradually increases to about 60°C.

In Figure 4-10 compares the simulated responses at two points located in the granular bentonite section with two points located within bentonite blocks, but located at about same distance from the heater. In this case the results are presented in terms of relative humidity and temperature. At the initial saturation of 20% in the granular bentonite, the relative humidity is about 40%, whereas in the bentonite block initial saturation was about 65% with a relative humidity of about 60%. The relative humidity for a given degree of saturation depends on the capillary pressure

and hence the water retention curve. A higher saturation in the bentonite blocks, results in a higher thermal conductivity which explains the difference in the temperature between the monitoring points in the granular bentonite and the bentonite blocks.

A comparison of the predicted and observed evolutions of relative humidity and temperature is shown in Figure 4-11. The figure shows that the general humidity behavior of the bentonite at the rock wall and drying of the inner parts of the bentonite buffer are captured in the modeling. Model results for relative humidity, which is related to saturation, shows very good agreement with measurements for the blue and red curves (i.e. close the rock wall and close to the heater). However, the model overestimates relative humidity in the mid part of the bentonite buffer (green curve). A parameter study was performed as to identify possible reasons for this discrepancy in the wetting of the bentonite buffer. The included variation of buffer absolute permeability (no significant effect), diffusion coefficient (did not help) and buffer relative permeability (tried to reduce relative permeability, but this did not help). A possible reason that will be investigated next is the high suction part of the water retention curve with the van-Genuchten water retention model may cause important deviations from the experimental data at low saturation. Nevertheless, the overall evolution of relative humidity was reasonably predicted by the modeling.

Figure 4-12 shows the evolution of fluid pressure within Opalinus Clay at a monitoring point located 3.54 m from the tunnel wall. This increase in fluid pressure is a result of so-called thermal pressurization, caused by thermal expansion of the pore fluid that cannot escape in the relatively low-permeability host rock. The magnitude and duration of this excess pressure pulse depends on parameters such as rock permeability, and compressibility of water and rock (Rutqvist et al., 2014). Using the Opalinus Clay properties determined from the modeling of the HE-D experiments, it appears that the model could predict this pressure increase fairly well.

The next step will be to complete the interpretive analysis by detailed comparison to measured data for final model comparison within the DECOVALEX-2015 project.

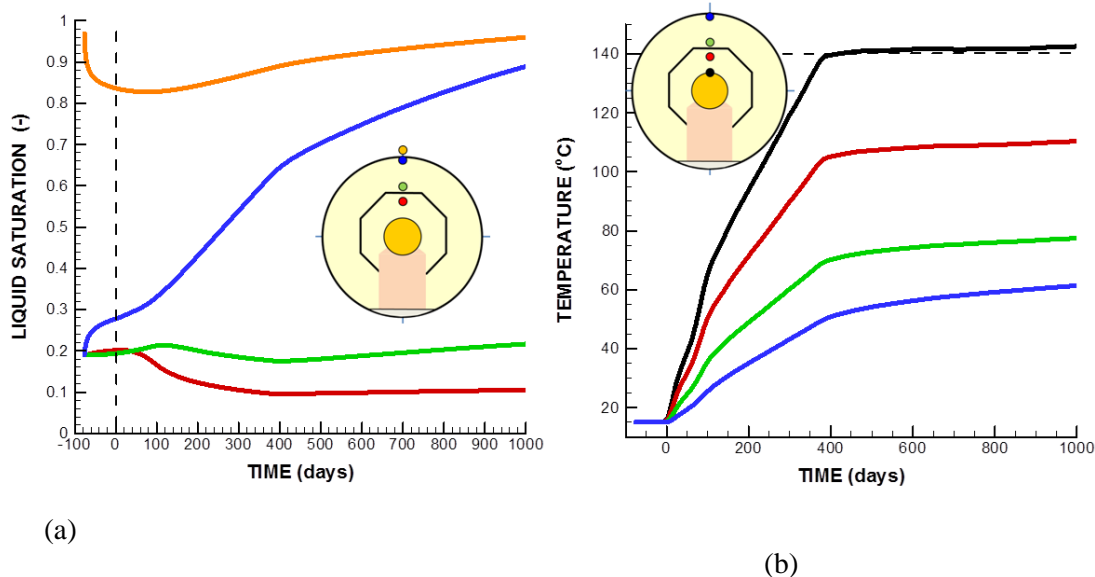


Figure 4-9. Calculated evolution of (a) liquid saturation and (b) temperature.

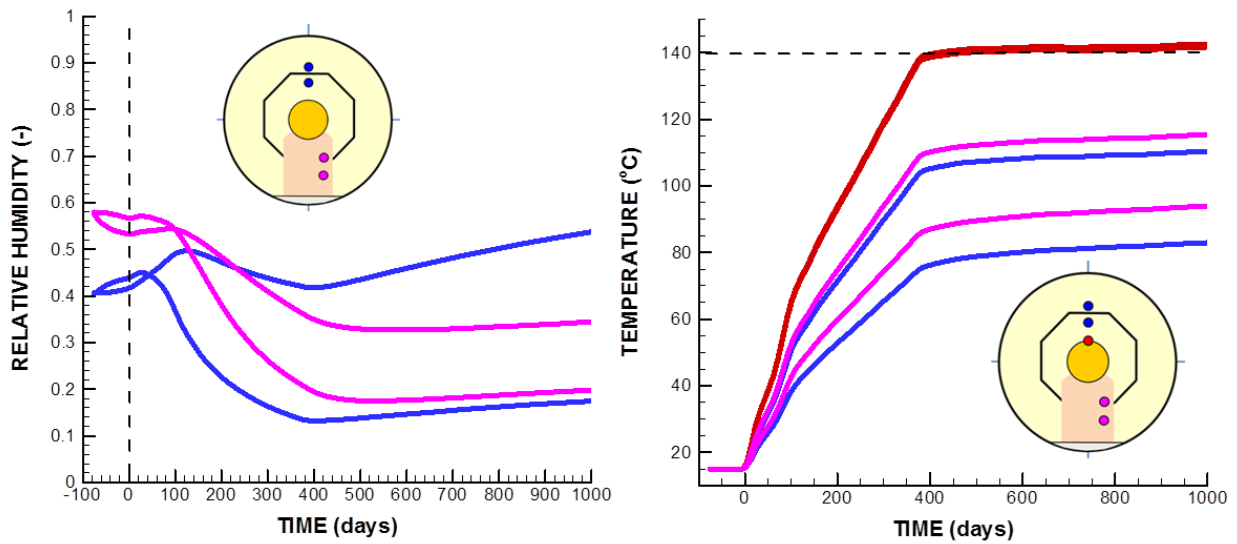


Figure 4-10. Calculated evolution of (a) liquid saturation relative humidity and (b) temperature at monitoring points in the granular bentonite (above heater) and bentonite blocks (below heater).

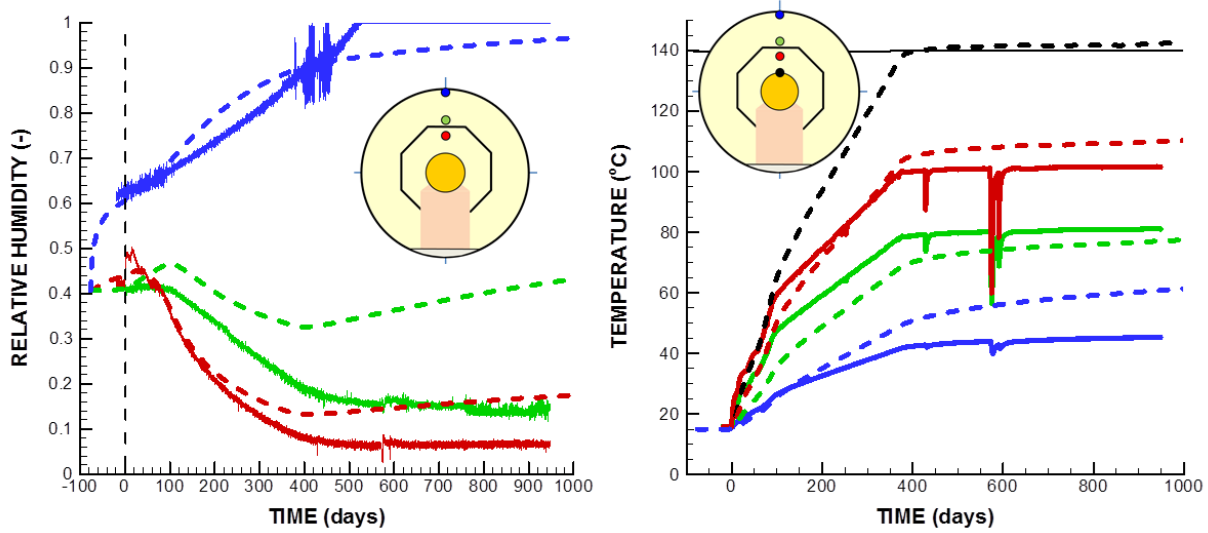


Figure 4-11. Comparison of predicted (dashed lines) and measured (solid lines) evolutions of (a) liquid saturation relative humidity and (b) temperature.

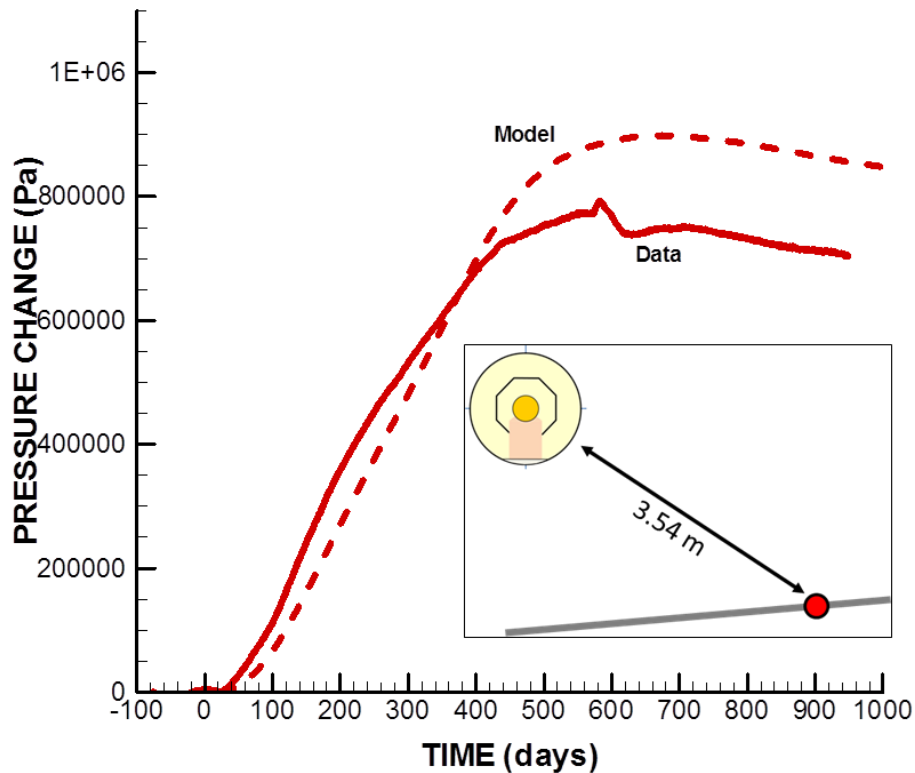


Figure 4-12. Comparison of predicted (dashed lines) and measured (solid lines) evolutions of pore pressure in Opalinus Clay at a point located 3.54 m from the tunnel wall.

4.3 Horonobe EBS Experiment (DECOVALEX)

This task focuses on coupled THMC modeling of a planned full-scale EBS experiment conducted by the Japan Atomic Energy Agency (JAEA) at the Horonobe URL, Hokkaido, Japan (Figure 4-13). The EBS experiment is carried out at a depth of 350 m in a very porous and soft, siliceous mudstone with the following basic properties:

- Porosity 35-60%
- Permeability $10^{-20} - 10^{-18} \text{ m}^2$
- UCS (Strength) 5-25 MPa
- Young's Modulus 1-4 GPa
- Thermal Conductivity 1.34-1.53 W/mK

Figure 4-14 shows the experimental layout with a vertical heater emplacement installed in a test pit at the bottom of an experimental drift. The detailed sequence of the experiment is given in Table 4-2. The experimental drift was backfilled after the installation of the heater and bentonite buffer into the test pit. Bentonite buffer and backfill materials are based on the Japanese Kunigel V1 bentonite. For the buffer, Kunigel V1 bentonite is mixed with sand and emplaced at a dry density of 1.6 g/cm^3 , whereas for the backfill, rock debris is mixed in, for an emplacement dry

density of 1.4 g/cm^2 . The experimental area was then isolated by a concrete plug and the heater was finally turned on January 15, 2015. Sensors have been installed in buffer, backfill, and rock to monitor temperature, stress, strain, pore pressure, humidity, displacement, pH, resistivity, electric potential, and seismic velocity.

Figure 4-15 shows some early time measurements of heater surface temperature as well as pore pressure at the bottom of the test pit (within the sand layer). During the construction and installation of the buffer, backfill and plug, water was pumped out of the test pit. The pump was turned off on December 22, 2014 i.e. 24 days before the heater was turned on. Figure 4-15a shows that the water pressure increases due to inflow from the rock and reaches a steady value about 60 kPa after 15 to 20 days.

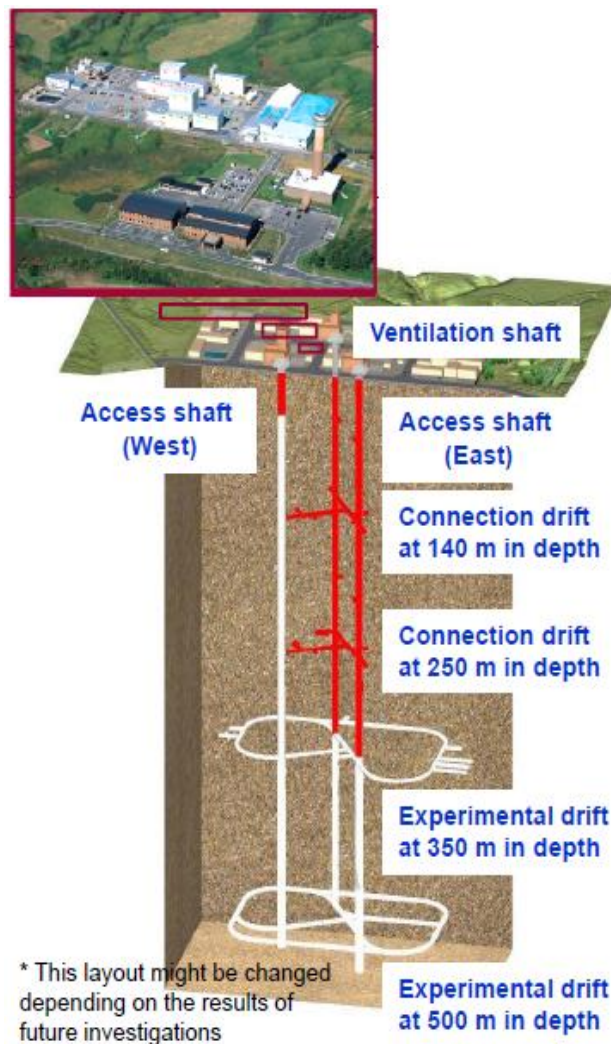


Figure 4-13. Layout of the Horonobe URL in Hokkaido, Japan.

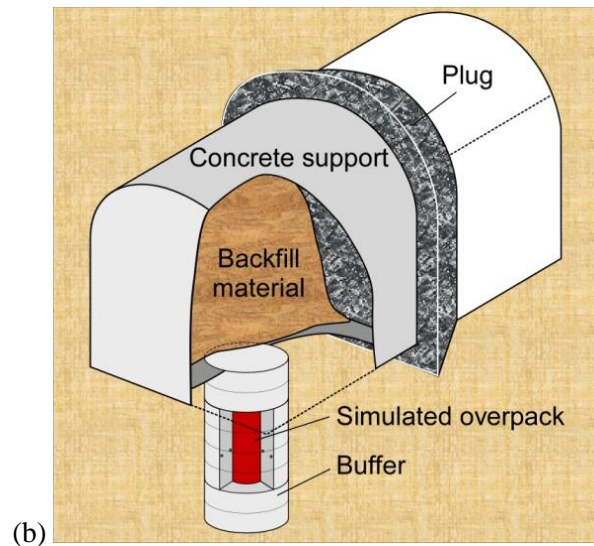
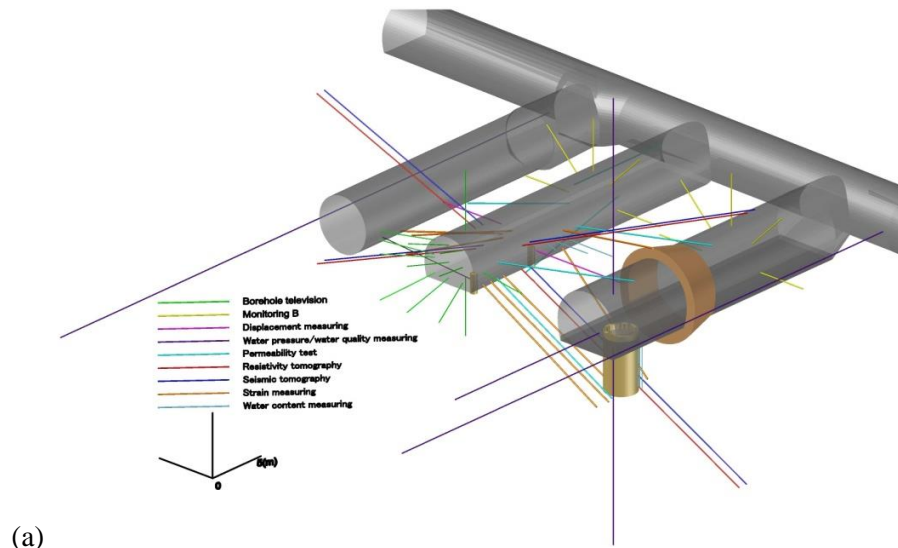
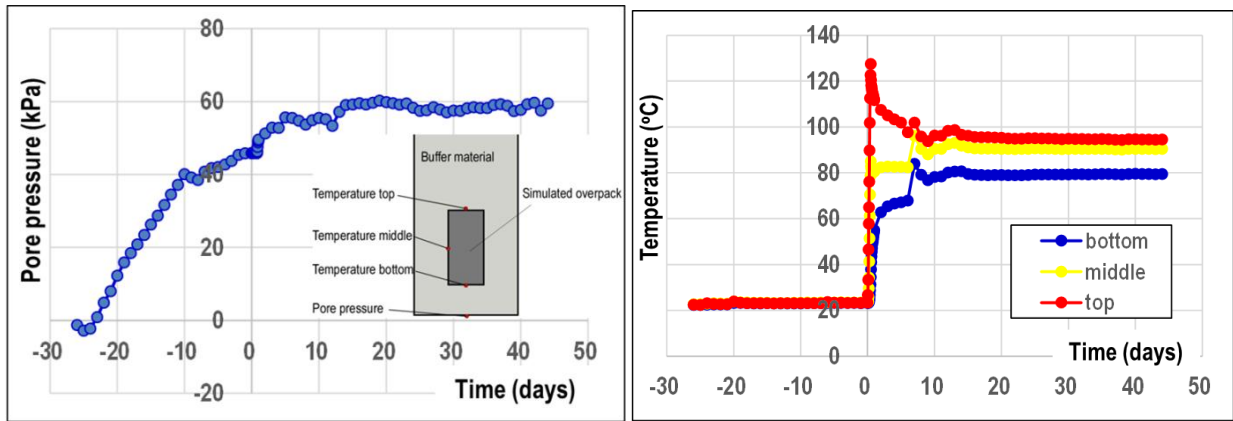


Figure 4-14. General description of the EBS experiment at the Horonobe URL Project in Japan.

Table 4-2. Details on the sequence of construction and installation of the Horonobe EBS experiment

Sequence of the Horonobe EBS Experiment	
Excavation of the experimental gallery	Oct 29 – Dec 6, 2013
Opening of the test pit	Feb 3 – 8, 2014
Emplacement of the buffer	Aug 18 – Sept 6, 2014
Emplacement of the backfill	Sep 8 – Oct 3, 2014
Plugging	Oct 9 – 27, 2014
Stop pumping up water from pit	Dec 22, 2014 at 14:00
Start of heating	Jan 15, 2015 at 14:20



(a)

(b)

Figure 4-15. Early time monitored fluid pressure in the test pit and temperature evolution at the heater surface that will help to define boundary conditions in the interpretive modeling of the Horonobe EBS experiment.

4.3.1 DECOVALEX modeling tasks and status related to Horonobe EBS experiment

The DECOVALEX Task B2 related to the Horonobe EBS experiment is divided into the following steps;

- Step 1 (1D benchmark test with comparison of numerical models)
- Step 2 (Prediction analysis)
- Step 3 (Calibration analysis)

The 1D benchmark test (Step 1) was defined with exact properties and boundary conditions given by the JAEA. The benchmark test was conducted for the teams to familiarize themselves with the problem and for precise comparison of computer codes before going into the more complex full-scale case. Thereafter, in Step 2, a model of the real experimental design should be constructed and a first predictive analysis was to be performed for several years from the start of the heating. The heating started on January 15, 2015, and JAEA will eventually provide the monitored data for the first six months of heating to the research teams. The research teams should then calibrate their models against this first 6 months of field data and then carry out coupled numerical analysis for long-term predictions (100–1,000 years) using the test conditions of the EBS experiment.

JAEA provides reports from the investigations at the Horonobe URL for input parameters related to the mudstone host rock and buffer material properties for the Kunigel V1 bentonite from the previous H12 project, whereas properties for the backfill are being investigated along with this project.

DECOVALEX-2015 Task B2 started in May 2013 with Step 1, which has been completed. In the FY14 milestone report entitled “Investigation of Coupled Processes and Impact of High Temperature Limits in Argillite Rock” (Zheng et al., 2014), we presented the final results of the

Step 1 benchmarking with comparison to the results of other DECOVALEX-2015 teams. In this part of the report we present Step 2 model predictions of the full scale EBS experiment with comparison of the results to other DECOVALEX-2015 modeling teams. In DECOVALEX-2015, five research teams are participating in the modeling of the Horonobe EBS experiment with the models listed in Table 4-3. Some of the models listed in Table 4-3 have been extensively applied in previous DECOVALEX project phases, whereas some are new and being developed.

Table 4-3. DECOVALEX research teams and numerical simulators in modeling Horonobe EBS experiment

Research Team	Numerical Simulator	Brief Description of Numerical Simulator
DOE U.S. Department of Energy's Research Team: Lawrence Berkeley National Laboratory (LBNL)	TOUGH-FLAC	TOUGH-FLAC is a simulator for analysis of coupled THM processes under multiphase fluid flow conditions being developed at the LBNL (Rutqvist et al., 2002). The simulator is based on linking of the existing computer codes TOUGH2 and FLAC3D, and has been extended for modeling of coupled THM and THMC processes associated with nuclear waste disposal with backfilled emplacement tunnels in clay formations (Rutqvist et al., 2014).
	ROCMAS	ROCMAS is a finite element program for analysis of coupled THM processes in porous and fractured rock developed at LBNL (Rutqvist et al., 2001a). It can model unsaturated media with single-phase liquid flow and vapor diffusion in a static gas phase. The code has been extensively applied in earlier phases of the DECOVALEX project for THM analysis in bentonite-rock systems (Rutqvist et al., 2001b; 2005).
BGR Bundesanstalt für Geowissenschaften und Rohstoffe's Research Team: University of Tübingen	GeoSys/ Rockflow	GeoSys/Rockflow is based on object-oriented programming (Kolditz et al., 2003). It was first applied in previous DECOVALEX phases for analysis of thermal-hydrological and thermal-mechanical processes and has been extended to THM (Wang et al., 2006). For the present study, an unsaturated single-phase liquid flow and vapor diffusion is considered.
CAS Chinese Academy of Sciences' Research Team	EPCA3D	The EPCA code (Elasto-Plastic Cellular Automata) uses the concept of cellular automata inspired by the self-organizing theory in biology. This code has been successfully used to simulate the failure process of heterogeneous rocks with and without consideration of hydro-mechanical coupling (Feng et al., 2006; Pan et al., 2008).
JAEA Japan Atomic Energy Agency's Research Team, including Hazama Cooperation	THAMES	THAMES is a finite element program for analyzing coupled THM processes in porous and fractured rock developed at the Kyoto University (Ohnishi and Kobayashi, 1996). The code has been extended to unsaturated media with single-phase liquid flow and vapor diffusion in a static gas phase (Chijimatsu et al., 2005).
KAERI Korean Atomic Energy Research Institute	FLAC/ FLAC3D/ Tough2	Simulation tools being developed along with the DECOVALEX-2015 project based on FLAC and FLAC3D linked with TOUGH2.

4.3.2 TOUGH-FLAC Model prediction of the full scale Horonobe EBS experiment

We made a 3-D model and a prediction of the THM responses at the Horonobe EBS experiment. The model is half symmetric, including half of the tunnel and half of the deposition hole (Figure 4-16). It contains all relevant materials, including mudstone rock, buffer, backfill, a sand layer at

the rock/buffer interface, concrete lining and plug. In this model prediction, we use the properties of the buffer and rock developed associated with the 1D benchmark calculation (Table 4-4). Additional properties for the backfill, sand layers, concrete lining and plug were provided by the JAEA to DECOVALEX -2015 modeling teams. The intrinsic permeability of gas flow in the bentonite is orders of magnitude higher than the intrinsic permeability for liquid flow and this is simulated in TOUGH2 using a high value of the Klinkenberg parameter (see Section 4.1 and Equation (4-1)).

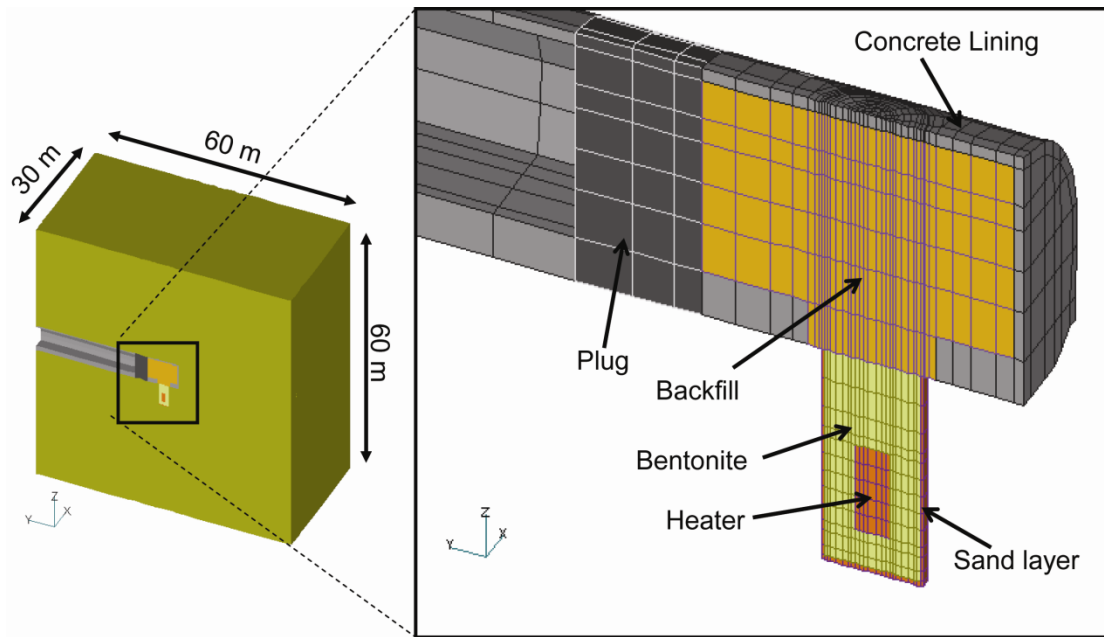


Figure 4-16. TOUGH-FLAC 3-D numerical grid of the Horonobe EBS experiment.

Table 4-4. Material parameters for modeling Horonobe EBS experiment.

Parameter	Symbol	Overpack	Buffer	Backfill	Rock
Grain density (kg/m ³)	ρ_g	10,000.	2680.	2680.	2454.
Porosity	ϕ	0.403	0.403	0.460	0.4482
Permeability (m ²)	K	5×10^{-51}	4×10^{-20}	1.5×10^{-19}	1.33×10^{-15}
Thermal conductivity (saturated) (W/m°C)	λ_{wet}	20	1.986	1.250	1.231
Specific heat (solids) (J/kg°C)	C	10,000	341	341	626
Thermal conductivity (desaturated) (W/m°C)	λ_{dry}	20	0.444	0.444	0.579
Water relative permeability parameters using power function $k_{rw}(S_w) = \left(\frac{S_w - S_r}{S_m - S_r}\right)^A$	A	1.3	1.3	1.3	NA
	S_r	0	0	0	NA
	S_m	1	1	1	NA
Water relative permeability parameters using van-Genuchten equations $k_{rw}(S_w) = \left(\frac{S_w - S_r}{S_m - S_r}\right)^{1/2} \left[1 - \left\{ 1 - \left(\frac{S_w - S_r}{S_m - S_r}\right)^{1/m} \right\}^m \right]^2$	M	NA	NA	NA	0.503
	S_r	NA	NA	NA	0
	S_m	NA	NA	NA	1
Capillary pressure parameters using van-Genuchten equation $\psi(S_w) = 1/\alpha \left\{ \left(\frac{S_w - S_r}{S_m - S_r}\right)^{-1/m} - 1 \right\}^{1-m}$	$\alpha (m^{-1})$	8×10^{-3}	8×10^{-3}	8×10^{-3}	9.928×10^{-3}
	m	0.375	0.375	0.375	0.503
	S_r	0	0	0	0
	S_m	1	1	1	1
Vapor diffusion coefficients (m ² /s)	D_v	3.5×10^{-6}	3.5×10^{-6}	3.5×10^{-6}	3.5×10^{-6}
Young's modulus E, (MPa)	E	200,000	37	3	1820.0
Poisson's ratio (-)	ν	0.3	0.3	0.4	0.21
Linear thermal expansion coefficient (C ⁻¹)	C^{-1}	1×10^{-6}	1×10^{-6}	1×10^{-6}	1.33×10^{-5}
Moisture swelling coefficient, β_{sw}	β_{sw}	0	0.0108	0.0108	0

We simulated the experiment in 3 steps:

- 1) Excavations are open for 3 months.
- 2) Excavations are filled with backfill and the heater, buffer and plug are all installed for 6 months.
- 3) Then heating starts.

In this model prediction, we simulated heating for about 2 years. The results of temperature and saturation evolution for points located in the buffer and near-field rock are shown in Figures 4-17 and 4-18. When keeping the heater temperature constant at 100°C, the simulation shows that the temperature at the buffer-rock interface (P3, P4 in Figure 4-17) increases to about 60°C after 2 years. The liquid saturation in the buffer increases slowly by water infiltration from the surrounding rock (Figure 4-18). Also, a slight desaturation was predicted in the sand layer during the first 200 days. The liquid saturation at the inner part of the buffer decreases due to evaporation and vapor flow transport (P1 in Figure 4-18). Figure 4-19 presents results of displacements relative to an anchor at the rock wall. The calculated results in Figures 4-17 through 4-19 are sensible and show that we are able to use this full 3-D TOUGH-FLAC model of the Horonobe EBS experiment for making a model prediction of the THM responses during the heating.

The results of the model predictions provided by all the DECOVALEX-2015 modeling teams, have been compared. Figure 4-20 and 4-21 shows example of comparison related to the evolution of temperature and liquid saturation in the bentonite buffer. The results are quite consistent and in good agreement between the modeling teams, though some outliers can be observed. The next step is to complete Step 3, which is the calibration analysis using measured data to be provided by the JAEA.

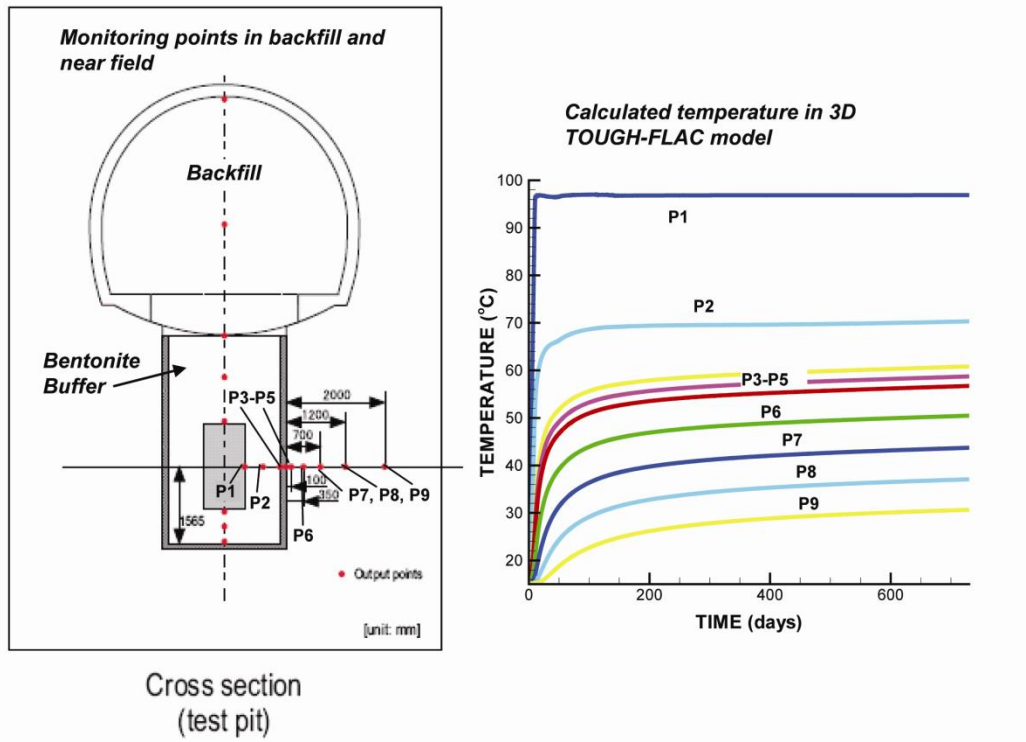


Figure 4-17. TOUGH-FLAC simulation results of temperature in the buffer and rock.

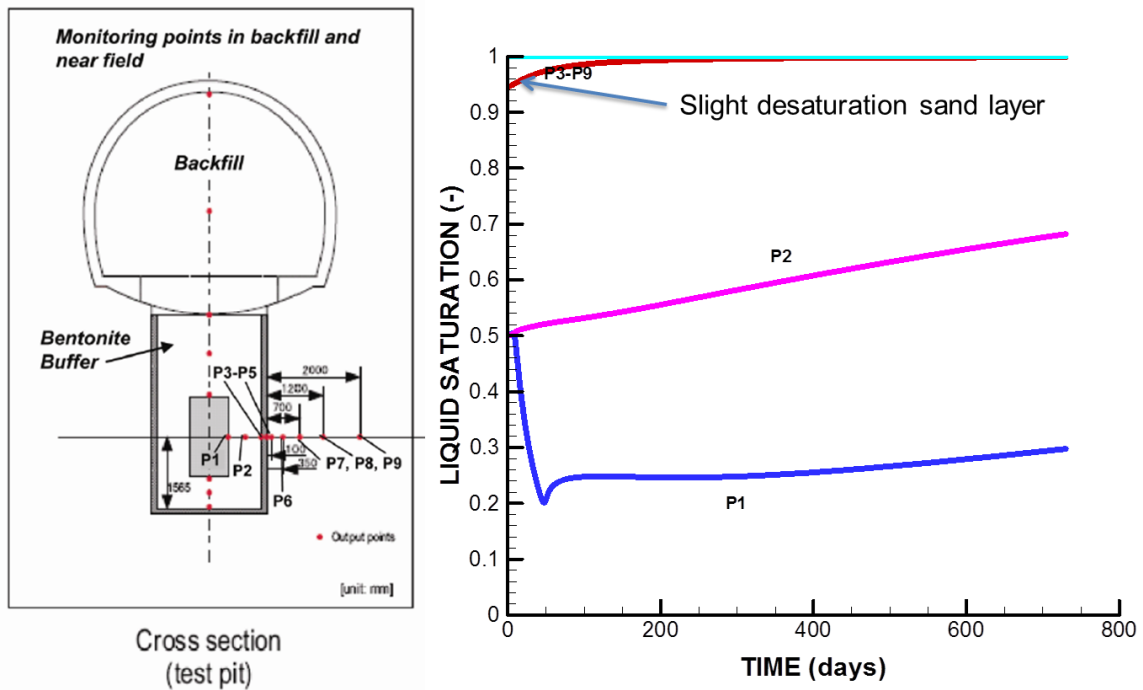


Figure 4-18. TOUGH-FLAC simulation results of liquid saturation in the buffer, sand layer and rock.

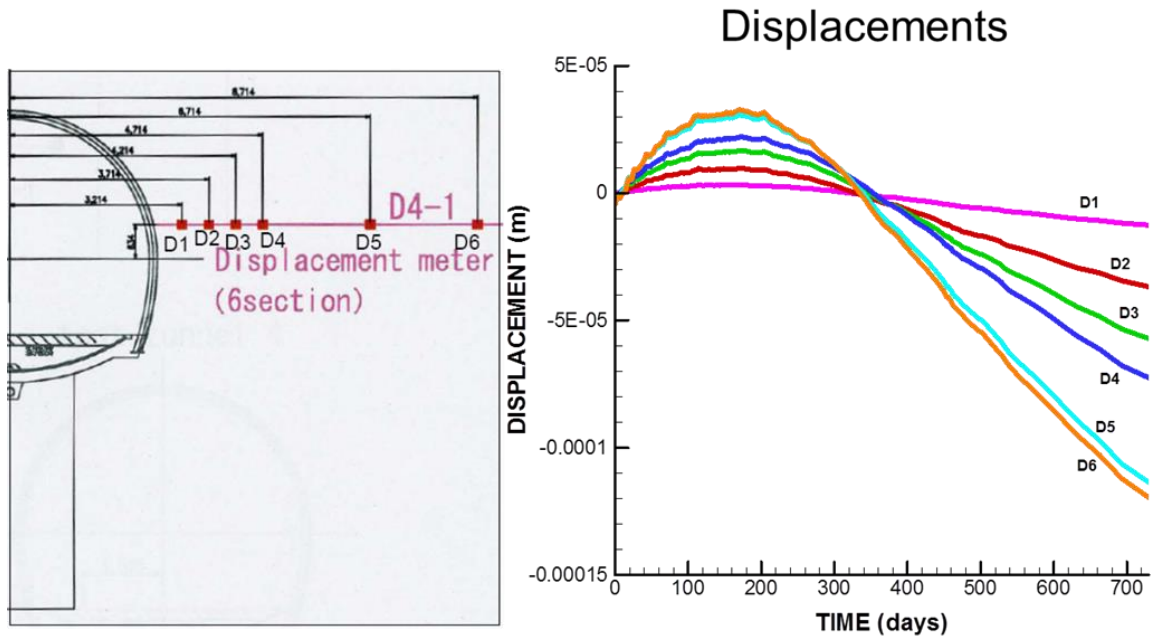


Figure 4-19. TOUGH-FLAC simulation results of extensometer displacements in the rock.

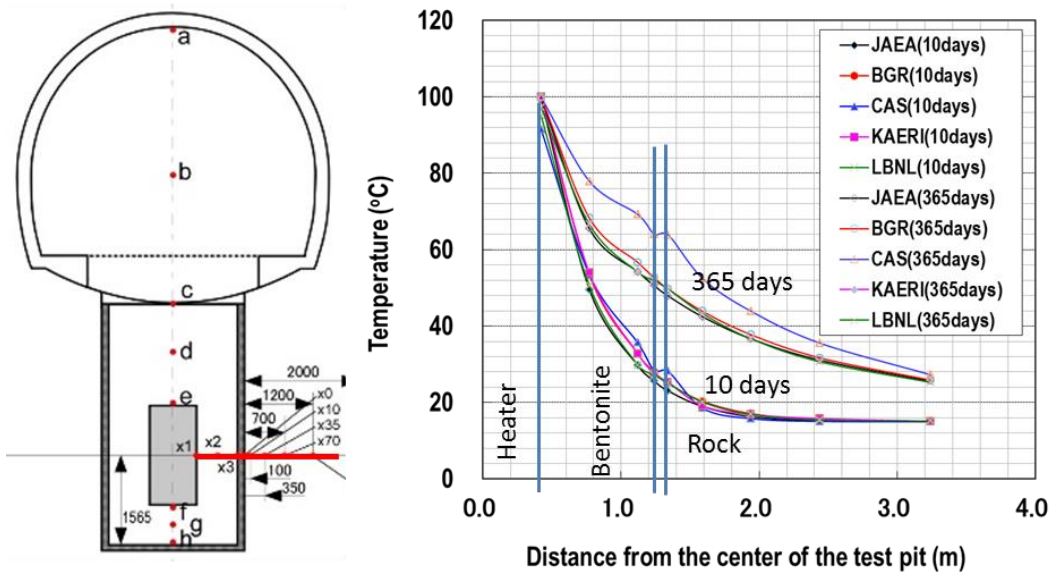


Figure 4-20. Comparison of simulated temperature profiles at 10 and 365 days among the DECOVALEX modeling teams.

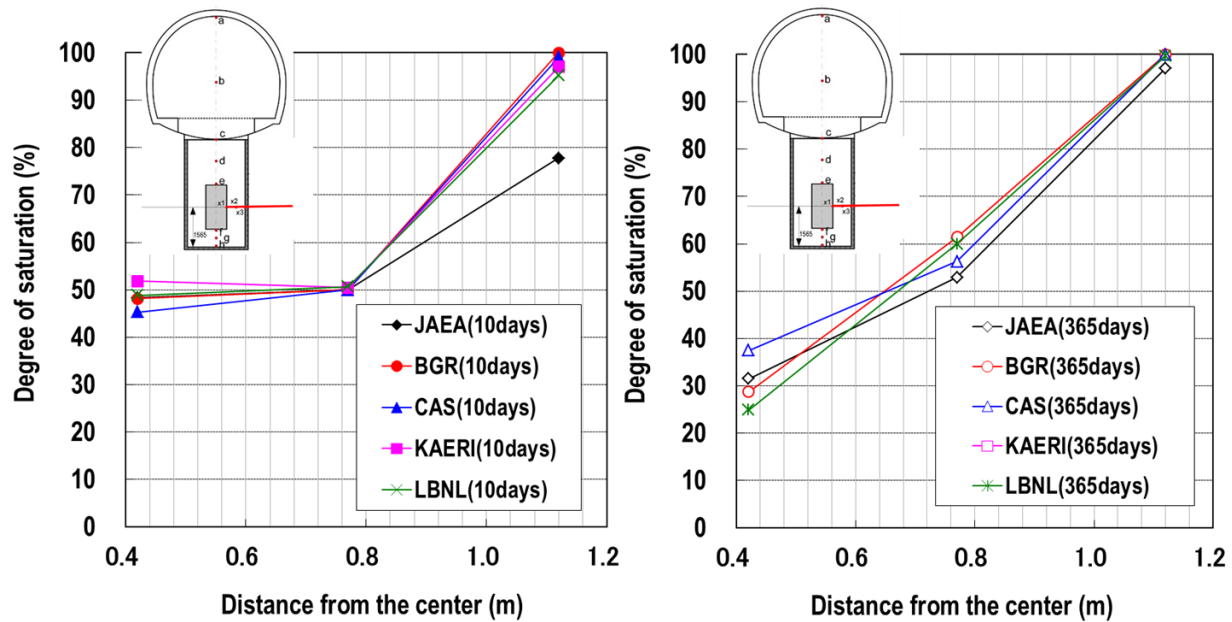


Figure 4-21. Comparison of simulated saturation profiles at 10 and 365 days among the DECOVALEX modeling teams.

4.4 FE Experiment at the Mont Terri Site (Mont Terri Project)

In this section, we present the current status of the FE Experiment and modeling. The current status of the Mont Terri FE experiment is that all the heaters, bentonite buffer and instrumentation have been installed, the tunnel has been plugged, and the final heater was turned on February 15, 2015 (Figure 4-22). The modeling activities during this year have been focused on the prediction of the temperature evolution as part of the experimental field test design. In the final design, a staged heating approach was employed in which the three heaters were turned on in stages, to monitor and validate the models for predicting the temperature in the buffer. Moreover, we are actively working on defining the material properties for the granular bentonite and bentonite blocks that were placed in the experimental tunnel.

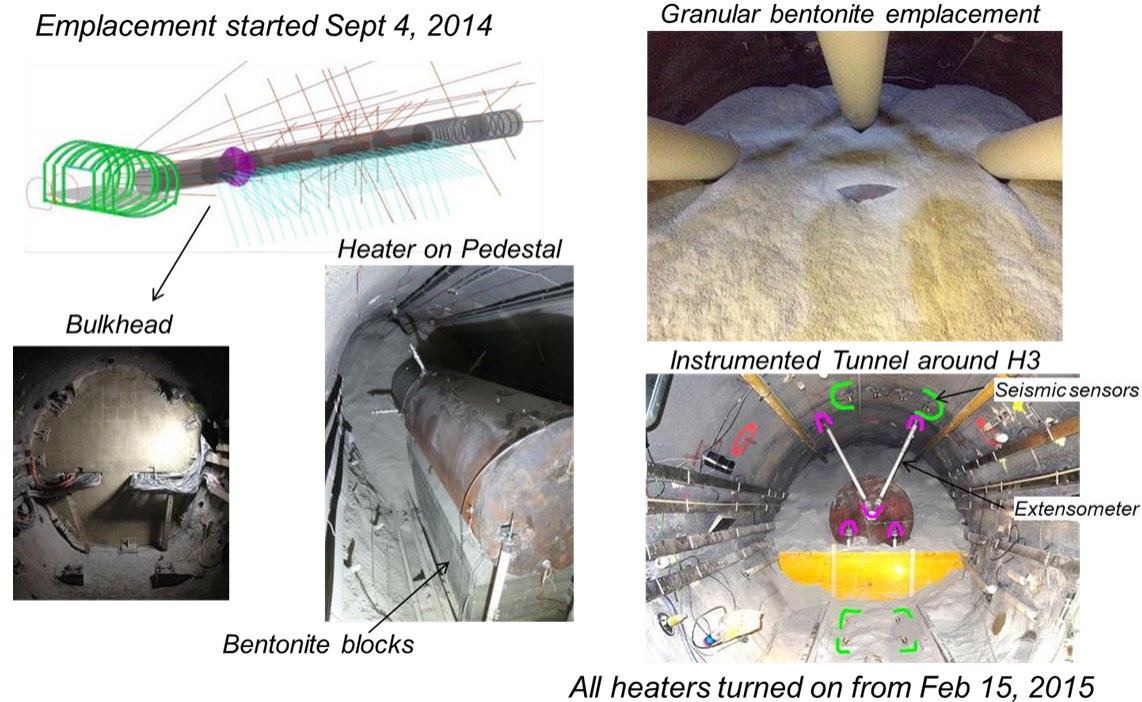


Figure 4-22. Images from the construction and installation of heaters, bentonite buffer and plugs from NAGRA daily reports by Herwig Müller, NAGRA.

As mentioned, the Mont Terri FE Experiment will be one of the largest and longest-duration heater tests worldwide, with focus on both the EBS components and the host-rock behavior. The FE experiment is conducted in a side tunnel at Mont Terri, excavated along the claystone bedding planes for this purpose, extending 50 m in length and about 2.8 m in diameter (Figure 4-23). Heating from emplaced waste will be simulated by three heat-producing canisters of 1500 W maximum power. The temperature is expected to exceed 100°C, with a target temperature 125 to 135°C at the inner parts of the buffer. A sophisticated monitoring program is planned, including dense pre-instrumentation of the site for *in situ* characterization, dense instrumentation of the bentonite buffer and host rock, and extensive geophysical monitoring (seismic and electric tomography).

The experiment will provide data useful for the validation of THM coupling effects regarding the processes in the host rock, while correctly accounting for (and examining) the conditions in the emplacement tunnel (temperature, saturation, and swelling pressure). Due to the 1:1 scale of the experiment, it will be possible to achieve realistic temperature, saturation, and stress gradients. It will also be possible to test backfilling technology with granular bentonite, as well as lining technology with shotcrete, anchors, and steel ribs. Processes examined in the test cover many aspects of repository evolution, such as creation and desaturation of the EDZ during tunnel excavation and operation (including ventilation for about one year), as well as reconsolidation of

the EDZ, resaturation, thermal stresses, and thermal pore-pressure increase after backfilling and heating (heating and monitoring period > 10 years).

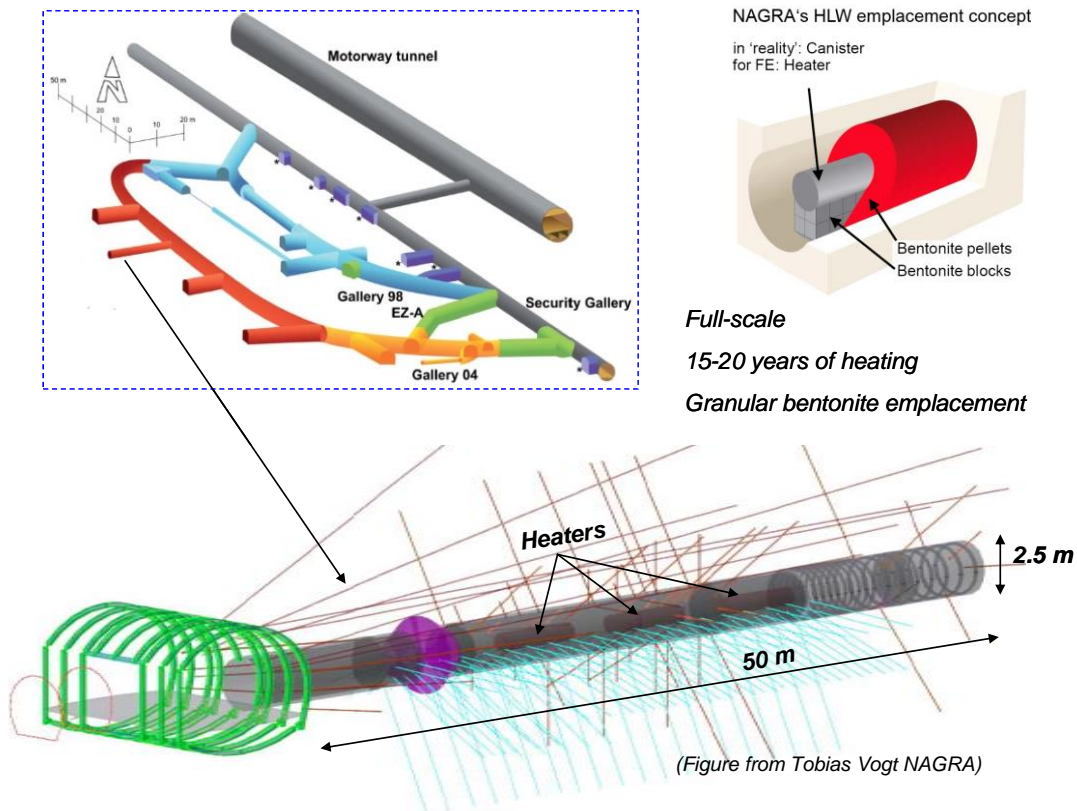


Figure 4-23. Plan view of experiment setup and borehole layout.

In 2011, a niche in front of the FE tunnel was constructed, followed by a first phase of instrumentation of the rock mass surrounding the tunnel, using boreholes from the niche. The FE tunnel was then excavated by road-header in 2012; this was followed by another phase of instrumentation. The tunnel was open for a 1-year ventilation period. This was followed by the emplacement of the heaters, bentonite buffer, and a concrete plug, after which the heating was gradually turned on during the fall of 2014. The heating is then expected to go on for at least 15 years, with continuous monitoring of THM processes in both the bentonite buffer and surrounding rock.

4.4.1 FE-E experiment modeling tasks

DOE is one of the experimental partners for the FE heater experiment, and LBNL is one of the modeling teams. In addition to LBNL, six other modeling teams are currently involved in the Mont Terri FE experiment from Germany (2 teams), U.K., Spain, Switzerland, and Canada.

The THM modeling program includes three types of computations:

- 1) Scoping calculations
- 2) Bench Marking

3) Predictive computations

The scoping calculations include brainstorming on potential ongoing processes, evaluating their significance and parameter range, comparing simulation results and input parameters derived by each team, and lessons learned (parameter range, importance, expected response). The benchmarking uses well-defined geometry problems with exact parameter values given to the teams, focusing on process modeling with precise comparison of codes. In the predictive calculations, likely parameters values and the as-built information of the experiment will be frozen.

Each modeling team develops its conceptual models and material properties using available literature (papers and reports) on lab experiments and previous Mont Terri *in situ* tests, etc. Moreover, this is complemented with a restricted benchmark test for code comparison, in which properties and model geometry are set by NAGRA. In the FY13 UFD milestone report titled “Report on International Collaboration Involving the FE Heater and HG-A Tests at Mont Terri (Houseworth et al., 2013), we presented results on the scoping calculations and the benchmarking which was completed in April 2014. We also made a first full THM 3-D simulation of the FE heater test, including the BBM model for calculating the mechanical responses. These were scoping and preliminary predictions with the material properties available at the time, though in some cases including a different kind of bentonite.

In the following, we present the current LBNL model of the Mont Terri FE experiment, including numerical grid and thermal and hydraulic material properties. Finally, we present some simulation results related to the thermal evolution for different heat power schemes. This includes a staged heating during the first few months of the experiment, perhaps using only one of the three heaters. The staged heating schedule will be conducted to enable an early model calibration of the *in situ* thermal properties that can then be used to make a more reliable prediction of the peak temperature, once the full thermal power is applied. This will be done to ensure that the temperature will not be so high as to damage the monitoring system.

4.4.2 TOUGH-FLAC model prediction of the Mont Terri FE Experiment

For the modeling of the FE experiment, we have developed a conceptual model and modeling approach that was presented previous milestone report (Houseworth et al., 2013; Zheng et al., 2014). The host rock is modeled using TOUGH-FLAC with anisotropic properties considering bedding planes of the Opalinus Clay. The bedding planes across the FE tunnel are inclined, as can be seen in Figure 4-24. To accurately model anisotropic thermal and hydrological behavior, we created an inclined TOUGH2 mesh. Anisotropic mechanical material behavior is simulated using the FLAC3D ubiquitous joint model, with initial properties of those derived from the excavation design analysis of the experimental tunnels. In the ubiquitous joint model weak planes are assumed along the bedding planes of the Opalinus Clay in which the shear strength properties are different along bedding versus across bedding. The mechanical model used for the Opalinus Clay was presented in Houseworth et al. (2013), but is not used in this study of peak temperature. For the bentonite, we started with the BBM model as applied by the CINEMAT and UPC (Garitte and Gens, 2012), and derived specific input material parameters for the MX-80 bentonite pellets that will be used as the emplaced bentonite buffer around the heaters. With this modeling approach, we are able to simulate THM processes in both, the bentonite and host rock, as well as their interactions.



Figure 4-24. View of FE tunnel face from the FE niche showing beddings dipping 45° (Vietor, 2012).

Figure 4-25 presents the 3-D TOUGH-FLAC numerical grid of the FE experiment. This model grid includes all vital material components for the modeling of the FE experiment, including layered Opalinus Clay host rock; excavation disturbed zone, tunnel, three heaters, bentonite buffer, concrete liner, and concrete plug. The initial conditions for the model simulation are 2 MPa pore-fluid pressure and 15°C temperature for the host rock. The 2 MPa pore pressure is not under hydrostatic conditions, and the process is affected by the existing tunnel system at the site. In our simulations, we first run a simulation with an open tunnel at atmospheric pressure for 1 year, creating a pressure drop and hydraulic gradient around the tunnel. Thereafter, we assume instantaneous emplacement of the heater and buffer, and start our heating simulation.

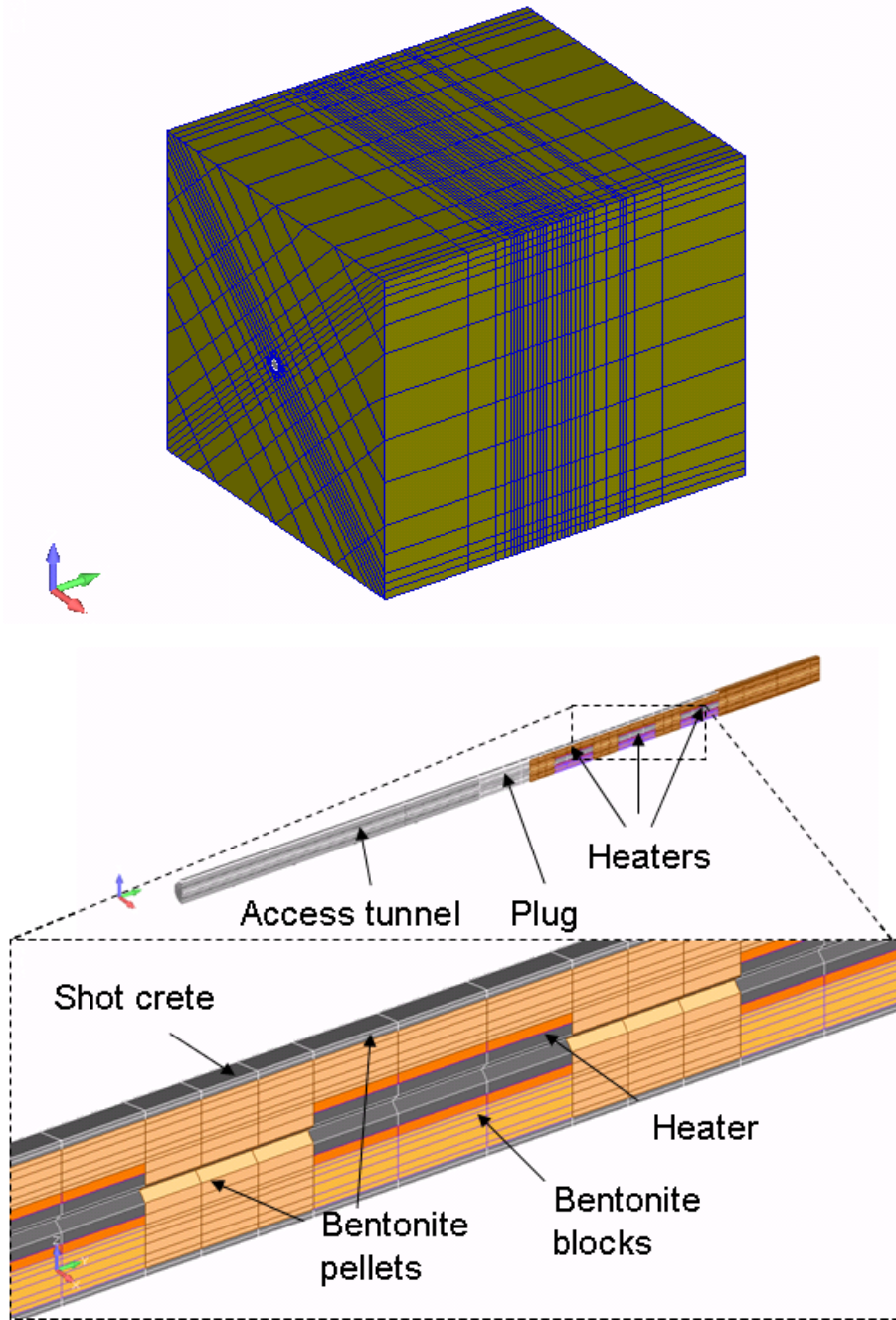


Figure 4-25. TOUGH-FLAC 3-D numerical grid of the FE experiment.

The thermal and hydraulic material properties for modeling the FE experiment are given in Table 4-5. These include properties defined by NAGRA and used for the 1-D benchmarking exercise and reported in FY2013 milestone report “Report on International Collaboration Involving the FE Heater and HG-A Tests at Mont Terri” (Houseworth et al., 2013), and is considered the current best estimate of the properties. The intrinsic permeability of gas flow in the bentonite is orders of magnitude higher than the intrinsic permeability for liquid flow and this is simulated in TOUGH2 using a high value of the Klinkenberg parameter (see Section 4.1 and Equation (4-1)). In this simulation of temperature and moisture evolution we did not invoke the mechanical part, though a preliminary simulation using the BBM model was presented in Houseworth et al. (2013).

Table 4-5. Parameters for the Opalinus and Bentonite clay used in the modeling of the FE experiment.

Parameters	Symbol	Opalinus Clay	Bentonite	Concrete (shotcrete and plug)	Unit
Grain density	ρ_g	2.7×10^3	2.7×10^3	2.7×10^3	kg/m ³
Porosity	\emptyset	0.15	0.46	0.15	-
Intrinsic permeability	k	5.0×10^{-20}	2.0×10^{-21}	3.5×10^{-21}	m ²
Liquid relative permeability using power law $k_{rw}(S_w) = \left(\frac{S_w - S_r}{S_m - S_r}\right)^A$	A	-	5	-	-
Liquid relative permeability using van-Genuchten model $k_{rw}(S_w) = \left(\frac{S_w - S_r}{S_m - S_r}\right)^{1/2} \left[1 - \left\{1 - \left(\frac{S_w - S_r}{S_m - S_r}\right)^{1/m}\right\}^m\right]^2$	m	0.52	-	0.52	-
Capillary curve using van-Genuchten model $\psi(S_w) = P_0 \left\{ \left(\frac{S_w - S_r}{S_m - S_r}\right)^{-1/m} - 1 \right\}^{1-m}$	P_0	1.09×10^7	1.00×10^7	1.09×10^7	Pa
	m	0.29	0.4	0.29	-
	S_{ls}	1.0	1.0	1.0	-
	S_{lr}	0.01	0.0	0.01	-
Thermal conductivity (wet)	λ_{sat}	1.7	1.0	1.7	W/m-K
Thermal conductivity (dry)	λ_{dry}	1.06	0.3	1.06	W/m-K
Grain specific heat	C	800	950	800	J/kg-K

The simulation of the heating is conducted with the initial saturation in the bentonite equal to 20%. Although the bentonite pellets when emplaced will be very dry, with a saturation of a few percent, experience and monitoring in the Mont Terri HE-E experiment shows that moisture is quickly taken up by the pellets from the surrounding humid air. This means that an initial saturation of 20% is realistic. In our modeling, we assign an initial capillary pressure, corresponding to the initial saturation of 20% (Figure 4-26).

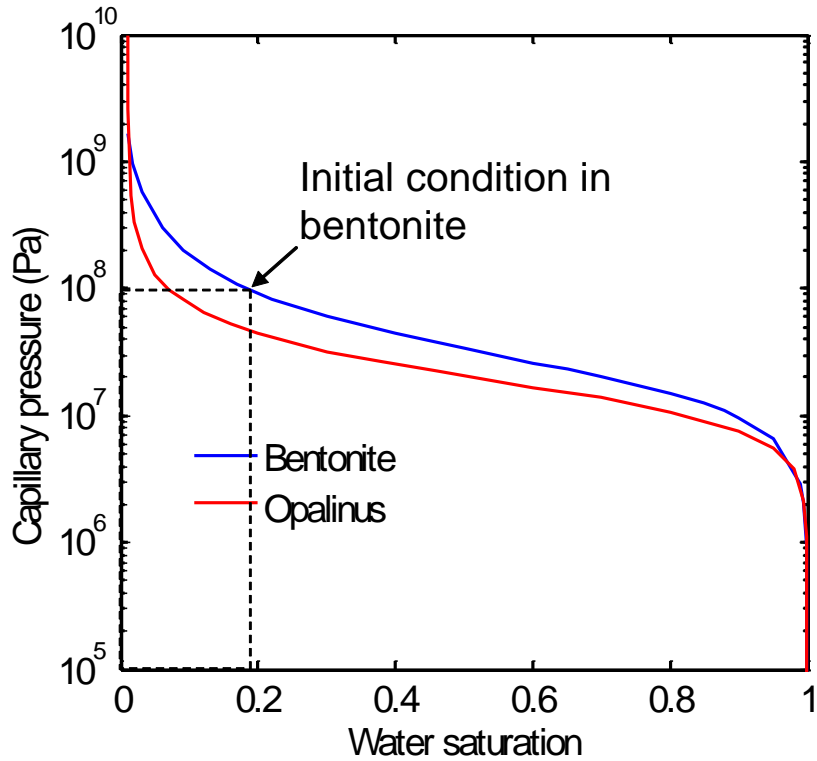


Figure 4-26. Capillary curves for Bentonite and Opalinus clays.

Figure 4-27 shows our prediction of temperature and saturation evolution considering a staged heating only in the heater that is emplaced first, i.e., the one placed farthest into the tunnel. Figure 4-27 includes the temperature and saturation evolution at all three heaters, although heating is turned on only at one heater. We can conclude that during the first 100 days, the temperature and saturation evolution is identical at heaters that are turned on (solid lines). That is, the temperature and saturation evolution at one heater is not affected by the heating, temperature, saturation at the other two heaters. Figure 4-27 also shows the difference in temperature and saturation evolution between heaters that are turned on or off. At heaters that are turned off, there is no drying near the heater (red dashed line) and there is some slow infiltration from the rock, causing a slow increase in saturation (blue dashed line). The results indicate that for the heating design it is possible to first turn on only one heater with the staged heating test to calibrate the THM models. It might be possible to turn on the heater emplaced first and make this initial heating test before the entire test tunnel is completely backfilled. In the experiment, the temperature should not exceed 150°C, because this could be damaging for some of the monitoring sensors.

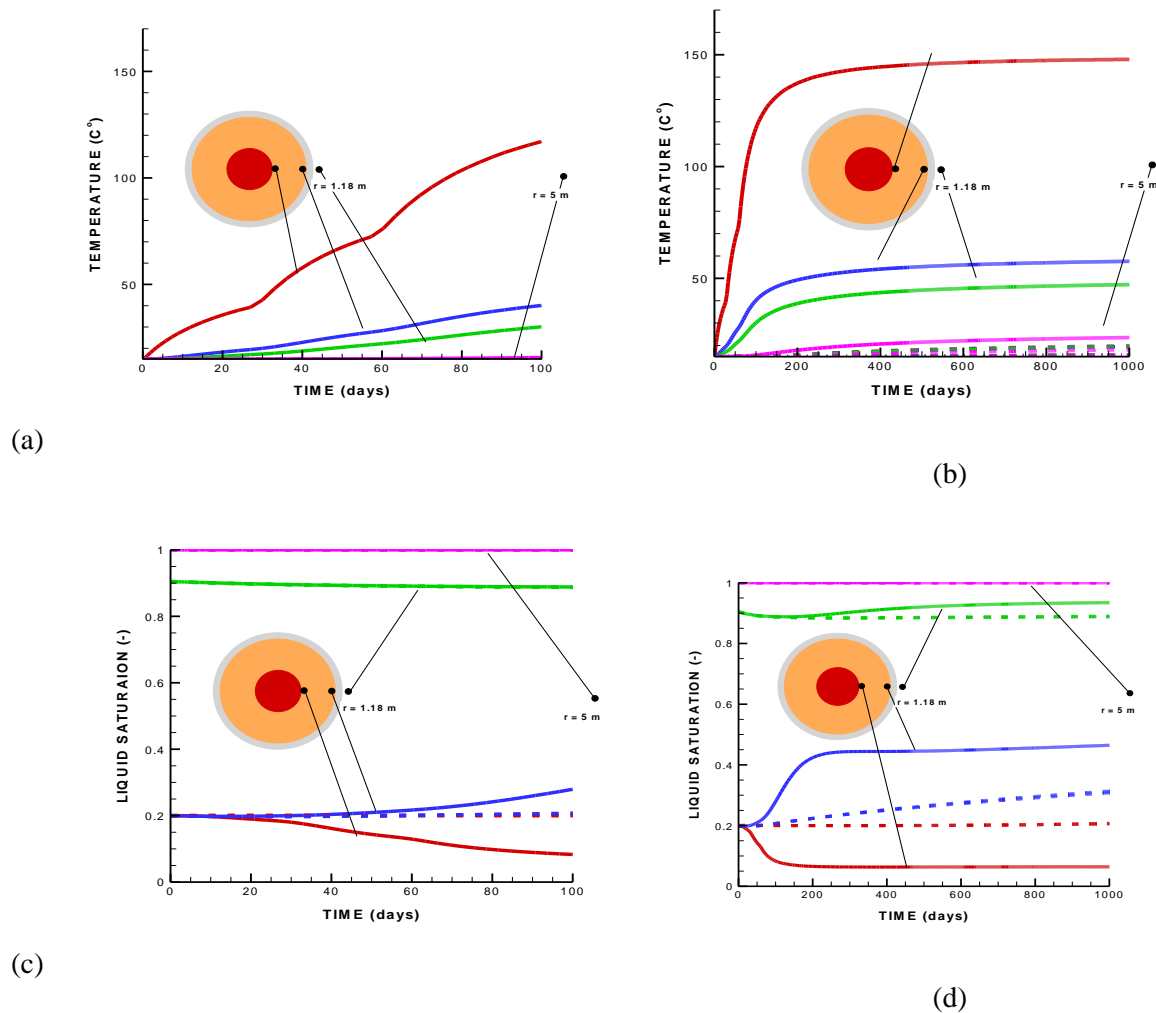


Figure 4-27. Model prediction of (a, b) temperature and (c, d) liquid saturation for staged power in first emplaced heater. The results in (a) and (b) and (c) and (d) are the same but using different range on the time axis to highlight the early time behavior (a) and (c) of the first 100 days and longer term response (b) and (d) up to 1000 days. Solid lines refer to evolution at the heater that is turned on, whereas dashed lines refers to evolution at heater that are turned off.

4.5 Status of THM Modeling of Heater Experiments and Plans

UFD and LBNL greatly benefit from participating in these international activities for developing expertise and testing advanced models for coupled THM processes. LBNL is leveraging previous experience and existing models (e.g. TOUGH-FLAC) that are extended to meet technical requirements for being able to predict the long-term THM and THMC evolution of a multibarrier nuclear waste repository system, involving backfilled emplacement tunnels in argillite host formations. While the work in previous years has been focused on model development and testing, in FY2015 work has been focused on modeling of the large scale in situ heater experiments involving both bentonite and rock, the Mont Terri HE-E, Horonobe EBS, and Mont Terri FE experiments. Modeling these require large 3-D models, involving all relevant

components, such as simulated waste package, bentonite buffer, and host rock, as well as their interactions. Modeling the real system at full scale is the ultimate test of the numerical models developed in this project.

The main accomplishment in FY2015 is that we have been able to successfully conduct model predictions of the THM responses at all these three experiments using state-of-the-art constitutive models for bentonite and host rocks. Some comparison to measured data has been conducted in the case of the Mont Terri HE-E experiment. The heating has just started in 2015 for the Horonobe EBS experiment and the Mont Terri FE experiment, and comparison between measured and predicted responses can be started once the data is provided to the modeling teams.

For the remainder of FY2015 we plan to complete interpretive modeling of the Mont Terri HE-E experiment and Horonobe EBS experiment as part of the DECOVALEX-2015 project, which is due to end at the end of year 2015. The last DECOVALEX-2015 workshop will be held in October 2015. Related to the Mont Terri FE experiment, LBNL will participate in a joint journal paper with the Swiss nuclear waste organization NAGRA and other organization in a Mont Terri 20-years anniversary, scientific paper for the Swiss Journal of Geosciences. This will include work done by FE experiment modeling teams, including code benchmarking and design modeling predictions.

Our work for FY2016 will be first to complete and document work related to DECOVALEX-2015 and at the same time initiate work related to DECOVALEX-2019. It is very likely that the Mont Terri FE experiment will be part of DECOVALEX-2019; it will be an upscaling from the half-scale HE-E experiment to the full scale FE experiment. We also propose that our work on coupled THM modeling be focused on 1) improving and gaining experiences in applying the dual-structure model for granular bentonite and 2) implementing and applying damage models for the evolution of the excavation damaged zone in host rocks.

We have previously shown the importance of considering the dual-structure behavior of bentonite clay associated with the permeability and long-term resaturation behavior. This is at the forefront of research on bentonite behavior and currently only a few codes, including TOUGH-FLAC are capable of modeling such behavior using a constitutive model similar to the Barcelona Expansive Model (BExM). However, there is still a lack of experimental data and experience to use such a complex model with confidence. Moreover, the highly non-linear behavior and the way it is implemented into TOUGH-FLAC make it, at the moment, computationally demanding. One of the main Tasks for FY2016 will be the improvement of the BExM in TOUGH-FLAC and to gain experience in applying it efficiently, including gaining confidence in the determination of input parameters. The inclusion of the FE heater experiment into DECOVALEX-2019 will be helpful for international collaboration on this, including collaboration with the University of Catalonia (UPC), which is the only other group in the world that has implemented BExM into a numerical simulator.

The implementation and application of a damage model for the evolution of the excavation disturbed zone will be an important addition to the current model for calculating the evolution of permeability along with damage as well as sealing and healing. Different approach can be tested, including to build upon previous work on the Two-Part Hooke's Model (TPHM), as well as other continuum damage models considering fracture evolution implicitly. Such a model can be benchmarked against discrete fracture modeling of damage-zone fractures using TOUGH-RBSN.

The goal is to build a pragmatic continuum model that can be validated against field experiments such as sealing experiments conducted in underground research laboratories.

Finally, we note that by participating in these international activities we are making significant progress toward achieving UFD goals to fill data needs and confirm advanced modeling approaches (by 2015), and to have a robust modeling and experimental basis for evaluation of multiple disposal system options (by 2020).

References

- Alonso EE, Gens A, Josa A (1990) A constitutive model for partially saturated soils. *Geotechnique*. 40: 405-430.
- Chijimatsu M, Nguyen TS, Jing L, de Jonge J, Kohlmeier M, Millard A, Rejeb A, Rutqvist J, Souley M, Sugita Y (2005) Numerical study of the THM effects on the near-field safety of a hypothetical nuclear waste repository – BMT1 of the DECOVALEX III project. Part 1: Conceptualization and characterization of the problems and summary of results. *Int. J Rock Mech & Min Sci* 42:720–730.
- Garitte B. and Gens A. (2012) TH and THM Scoping computations for the definition of an optimal instrumentation layout in the Full-scale Emplacement (FE) experiment NAGRA NIB 10-34, March 2012.
- Gaus I, Wieczorek K, Schuster K, Garitte B, Senger R, Vasconcelos R and Mayor JC(2014) EBS behaviour immediately after repository closure in a clay host rock: HE-E experiment (Mont Terri URL). Geological Society, London, Special Publications, first published March 7, 2014; doi 10.1144/SP400.11
- Gens, A, Alonso, E. A framework for the behaviour of unsaturated expansive clays. *Can. Geotech. J.* 29, 1013–1032 (1992).
- Gens A, Sánchez, M Sheng, D (2006) On constitutive modelling of unsaturated soils. *Acta Geotechnica*. 1, 137-147
- Gens, A., Sánchez, M., Guimaraes, L.D.N., Alonso, E.E., Lloret, A., Olivella, S., Villar, M.V., Huertas, F. (2009) A full-scale in situ heating test for high-level nuclear waste disposal: observations, analysis and interpretation. *Geotechnique* 59, 377–399.
- Feng Xia-Ting, Pan Peng-zhi, Zhou Hui (2006) Simulation of rock microfracturing process under uniaxial compression using elasto-plastic cellular automata. *Int J Rock Mech & Min Sci* 43: 1091–1108.
- Houseworth J., Rutqvist J., Asahina D., Chen F., Vilarrasa V., Liu H.H., Birkholzer J. Report on International Collaboration Involving the FE Heater and HG-A Tests at Mont Terri. Prepared for U.S. Department of Energy, Used Fuel Disposition Campaign, FCRD-UFD-2014-000002, Lawrence Berkeley National Laboratory (2013).
- Itasca, FLAC3D V5.0, Fast Lagrangian Analysis of Continua in 3 Dimensions, User's Guide. Itasca Consulting Group, Minneapolis, Minnesota (2011).
- Kristensson O, Åkesson M (2008) Mechanical modeling of MX-80 – Quick tools for BBM parameter analysis. *Phys Chem Earth, Parts A/B/C*. 33, Supplement 1: S508-S515.
- Liu H.H., Houseworth J., Rutqvist J., Zheng L., Asahina D., Li L., Vilarrasa V., Chen F., Nakagawa S., Finsterle S., Doughty C., Kneafsey T., Birkholzer J. Report on THMC Modeling of the Near Field Evolution of a Generic Clay Repository: Model Validation and Demonstration. Prepared for U.S. Department of Energy, Used Fuel Disposition Campaign, FCRD-UFD-2013-000244, Lawrence Berkeley National Laboratory (2013).
- Pan Peng-zhi, Feng Xia-Ting, Huang Xiao-Hua, Cui Qiang, Zhou Hui (2008) Study of coupled THMC processes in crystalline rock in the EDZ using an ECPA code. *Environmental Geology*.
- Pruess, K., Oldenburg, C.M., Moridis, G. (2011) TOUGH2 User's Guide, Version 2.1, LBNL-43134(revised), Lawrence Berkeley National Laboratory, Berkeley, California.
- Rutqvist, J., Börgesson, L., Chijimatsu, M., Kobayashi, A., Nguyen, T.S., Jing, L., Noorishad, J., Tsang, C.-F. (2001a) Thermohydromechanics of partially saturated geological media –

- Governing equations and formulation of four finite element models. *Int. J. Rock Mech. & Min. Sci.* 38, 105-127.
- Rutqvist J., Börgesson L., Chijimatsu M., Nguyen T. S., Jing L., Noorishad J., Tsang C.-F. (2001b) Coupled Thermo-hydro-mechanical Analysis of a Heater Test in Fractured Rock and Bentonite at Kamaishi Mine – Comparison of Field Results to Predictions of Four Finite Element Codes. *Int. J. Rock Mech. & Min. Sci.* 38, 129-142.
- Rutqvist, J., Wu, Y.-S., Tsang, C.-F. and Bodvarsson, G. (2002). A modeling approach for analysis of coupled multiphase fluid flow, heat transfer and deformation in fractured porous rock. *International Journal of Rock Mechanics & Mining Sciences*, 39, 429-442.
- Rutqvist J., Chijimatsu M., Jing L., De Jonge J., Kohlmeier M., Millard A., Nguyen T.S., Rejeb A., Souley M., Sugita Y. and Tsang C.F. Numerical study of the THM effects on the near-field safety of a hypothetical nuclear waste repository – BMT1 of the DECOVALEX III project. Part 3: Effects of THM coupling in fractured rock *Int. J. Rock Mech. & Min. Sci.* 42, 745-755 (2005).
- Rutqvist J., Barr D., Birkholzer J.T., Fujisaki K., Kolditz O., Liu Q.-S., Fujita T., Wang W. and Zhang C.-Y. A comparative simulation study of coupled THM processes and their effect on fractured rock permeability around nuclear waste repositories. *Environ Geol*, 57, 1347–1360 (2009)
- Rutqvist J. Status of the TOUGH-FLAC simulator and recent applications related to coupled fluid flow and crustal deformations. *Computers & Geosciences*, 37, 739–750 (2011).
- Rutqvist, J., Ijiri, Y. and Yamamoto, H. (2011). Implementation of the Barcelona Basic Model into TOUGH-FLAC for simulations of the geomechanical behavior of unsaturated soils. *Computers & Geosciences*, 37, 751-762.
- Rutqvist J., Davis J., Zheng L., Vilarrasa V., Houseworth J., Birkholzer J. Investigation of Coupled THMC Processes and Reactive Transport: FY14 Progress. Prepared for U.S. Department of Energy, Used Fuel Disposition, FCRD-UFD-2014-000497, Lawrence Berkeley National Laboratory, LBNL-6720E (2014a).
- Rutqvist J., Zheng L., Chen F, Liu H.-H, and Birkholzer J. Modeling of Coupled Thermo-Hydro-Mechanical Processes with Links to Geochemistry Associated with Bentonite-Backfilled Repository Tunnels in Clay Formations. *Rock Mechanics and Rock Engineering*, 47, 167–186 (2014b).
- Sánchez, M., Gens, A., Guimarães, L. do N., Olivella, S. A double structure generalized plasticity model for expansive materials. *Int. J. Numer. Anal. Meth. Geomech.*, 29, 751–787 (2005).
- Vietor T. (2012). Mont Terri Project - FE Experiment Modelling Kick-off Meeting. February 9, 2012, Mont Terri, Switzerland. NAGRA Technical Discussion TD-217
- Wang W, Xie M, Nowak T, Kunz H, Shao H, Kolditz O (2006) Modeling THM coupled problem of Task D of the DECOVALEX project. *Proc. GEOPROC2006 International symposium: 2nd International Conference on Coupled Thermo-hydro-mechanical-chemical processes in Geosystems and Engineering*, HoHai University, Nanjing, China, May 22-25, 2006, 226–232, HoHai University.
- Zheng L., Rutqvist J., Steefel C., Kim K., Chen F., Vilarrasa V., Nakagawa S., Houseworth J., and Birkholzer J. Investigation of Coupled Processes and Impact of High Temperature Limits in Argillite Rock Prepared for U.S. Department of Energy, Used Fuel Disposition, FCRD-UFD-2014-000493, Lawrence Berkeley National Laboratory, LBNL-6719E (2014).

5. Discrete Fracture Network (DFN) Approach for THM Damage Modeling in Argillaceous Rock

Mechanical and hydrological interactions in porous geologic media are fundamental and universal mechanisms that deform the geologic structure and control the behavior of water and other fluids in its pores (Neuzil, 2003). Geotectonic phenomena produce deformations and strains that tend to alter fluid pressure. Resulting pressure perturbations can be dramatic, and many cases of so-called “anomalous” pressure generation appear to have occurred in this manner. Conversely, the effects of fluid pressure on mechanical behavior are also profound. Pore fluids control deformation of porous media by bearing loads, and consequently geologic structures deform and fail largely in response to effective stress (i.e. skeleton stress or grain-to-grain stress).

In argillaceous rocks, fractures are typical mechanical features of particular importance to determine hydrological properties. While the clay-rich formations usually exhibit low permeability, under certain conditions there may be fractures which increase the permeability. Fracturing has been often observed as a result of fluid overpressure. Due to the low permeability of argillaceous rocks, fluids can only be transmitted very slowly. Consequently, the rock systems are not in pressure equilibrium (Gonçalvès et al., 2004), and the overpressure conditions can trigger hydraulic fracturing if the effective stress resulting from fluid pressure exceeds the rock tensile strength (Cosgrove, 2001). This fluid-driven fracturing process is relevant to many geoenvironmental applications. For example, hydraulic fracturing and stimulation of fracture networks are utilized by the energy industry (e.g., shale gas extraction, enhanced geothermal systems, etc.) to increase permeability of geological formations. From the opposite perspective, related to underground CO₂ sequestration, fracturing of the repository rock could be detrimental for geo-environmental issues due to increasing the risk of contaminant leakage (Bossart et al., 2004; Chiaramonte et al., 2008). Fluid-driven fracturing needs to be considered as a tightly coupled hydro-mechanical process if it is to be accurately modeled. Especially in the presence of multiple fractures (e.g., propagating fractures and pre-existing natural fractures), modeling the fracturing process can be very challenging because of the complex interactions between propagating fractures and natural fractures (e.g., Fu et al., 2013).

This section of the report covers an overview of the TOUGH-RBSN code for coupled THM processes in Sections 5.1 and 5.2. The simulation code combines TOUGH2 with the rigid-body-spring network (RBSN) model, which enables a discrete representation of individual fractures and fracture networks in rock formations. The discrete fracture network (DFN) approach is facilitated in the Voronoi discretization via a fully automated modeling procedure. In Section 5.3, the numerical program is verified through a single fluid-driven fracture simulation, and hydraulic fracturing simulations within complex fracture networks are conducted to demonstrate the modeling capabilities for coupled hydro-mechanical processes. Subsequently, some numerical problems with the current modeling scheme are presented to recognize the necessity for a new dynamic modeling approach. Section 5.4 documents the development phase of the new dynamic simulation code based on the lattice modeling approach (i.e., RBSN) based upon kinematics of particles.

5.1 RBSN for Mechanical Damage Modeling of Geomaterials

5.1.1 Voronoi discretization

Voronoi discretization is an effective approach to partition a computational domain into a set of spatial regions or cells. Each Voronoi cell is associated with an individual nodal point, which can be either prescribed or randomly generated. Discretization process is basically carried out in three steps: nodal point generation, Delaunay tessellation, and Voronoi tessellation (Figure 5-1).

In the first step, a set of nodal points are positioned regularly or irregularly inside the domain (Figure 5-1a). For random point generation, the points are sequentially generated with a minimum allowable distance l_{min} between neighboring points, which defines the desired nodal density to fill in the domain so that the grid size can be controlled. Furthermore, gradient grid geometry is attainable using a user-specified spatial correlation function for l_{min} . The random point generation involves choosing an arbitrary trial point within the domain by a pseudo-random number generator. If the trial point does not violate the l_{min} constraint, it is secured to be a member of the final nodal point set; otherwise, it is discarded and a new trial point is randomly selected. This process continues until either a specified total number of nodal points has been obtained or the domain is saturated with points. Practically, it is assumed that the domain becomes saturated when no more trial points are secured after a certain large number of trials. Nodal points also can be predefined at a specific position from input if necessary for assignment of boundary conditions.

The second step provides the Delaunay tessellation in which a collection of tetrahedra connect the nodal points (Figure 5-1b). The Delaunay tessellation is constructed using the concept of a super-tetrahedron (Sloan, 1987; Taniguchi et al., 2002). The circumsphere of each tetrahedron is the smallest sphere that circumscribes the corresponding four nodal points. The Delaunay tessellation is defined by the disjoint tetrahedra that do not include any other nodal point inside their circumspheres. In general, a randomly distributed point set corresponds to a unique Delaunay tessellation, in which no two coincidental circumspheres exist. The resulting Delaunay tessellation represents the unstructured grid of lattice elements. Each tetrahedral edge connects two adjacent nodes, by which the nodal connectivity of the lattice element is defined.

Following the Delaunay tessellation, the dual Voronoi tessellation is constructed with convex polyhedra called Voronoi cells (Figure 5-1c). The Voronoi diagram is also uniquely determined by the given set of nodal points, where each nodal point corresponds to exactly one Voronoi cell. The Voronoi cell for a nodal point is a territory in which the locations are closer to the corresponding point than any other points. Locations on a cell boundary are equally close to the neighboring nodal point for which the Voronoi cell shares that boundary (i.e., common Voronoi cell boundary). Consequently, the domain is collectively filled with the disjoint Voronoi cells through the recursive discretization process for all the nodal points. Also, the Voronoi diagram has a unique geometric correspondence with the Delaunay tessellation (Okabe et al. 2000). These geometric characteristics are used for the RBSN element formulation, which will be discussed in the next subsection.

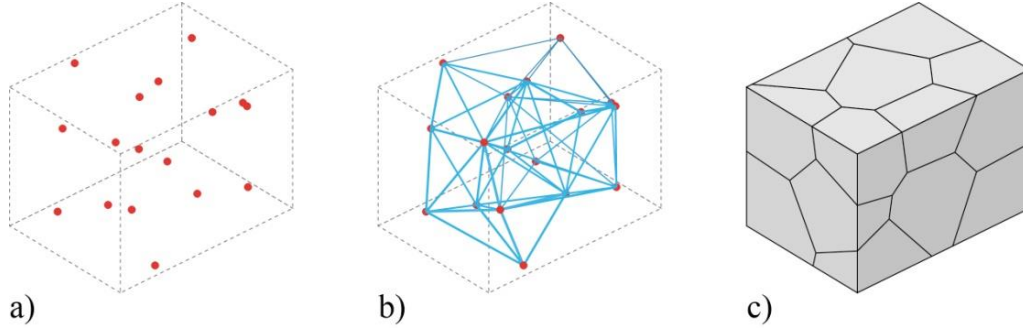


Figure 5-1. Discretization process: a) nodal point generation; b) Delaunay tessellation; and c) Voronoi tessellation.

5.1.2 Model formulation

The geometry of a RBSN is defined by the dual Delaunay tessellation of the nodal points. A basic unit of the lattice element that connects arbitrary nodes i and j consists of: 1) a zero-size spring set that is located at position C (the centroid of the common Voronoi cell boundary); and 2) rigid arm constraints that link the spring sets and the nodal degrees of freedom (Figure 5-2b). Each node has six degrees of freedom for the case of 3-D modeling. The spring set is formed from three axial springs and three rotational springs as shown in Figure 5-2c (the rotational springs have been intentionally omitted for clear illustration).

Note that the Voronoi cell is basically considered to be rigid in the sense that it maintains its original shape during the process of loading and material deformation (assumption of small strain). The flexibility of the motion is lumped into the spring sets; therefore, the separation and interpenetration of the cells are permitted.

The spring coefficients are scaled in proportion to the distance between the element length h_{ij} , and the area of the Voronoi cell boundary A_{ij} :

$$k_s = k_t = \alpha_1 k_n = \alpha_1 \alpha_2 E \frac{A_{ij}}{h_{ij}}, k_{\phi n} = E \frac{J_p}{h_{ij}}, k_{\phi s} = E \frac{I_{ss}}{h_{ij}}, k_{\phi t} = E \frac{I_{tt}}{h_{ij}} \quad (5-1)$$

in which E is the elastic modulus, J_p , I_{ss} , and I_{tt} are the polar and two principal moments of inertia of the Voronoi cell boundary with respect to the centroid, respectively. By adjusting α_1 and α_2 in accordance with experimental results, macroscopic modeling of both elastic constants (E and Poisson ratio, ν) is possible. For the special case of $\alpha_1 = \alpha_2 = 1$, the Voronoi scaling of the spring coefficients enables the model to be elastically homogeneous under uniform modes of straining, albeit with zero effective Poisson ratio (Bolander and Saito, 1998; Asahina et al., 2011).

The relationship between the generalized spring displacement, \mathbf{d} (6×1 column vector), and the generalized nodal displacements in local coordinates, \mathbf{u}_e (12×1 column vector), can be expressed by

$$\mathbf{d} = \mathbf{B} \mathbf{u}_e \quad (5-2)$$

where \mathbf{B} is a 6×12 geometric transformation matrix:

$$\mathbf{B} = \begin{bmatrix} -\mathbf{I} & \mathbf{B}_{12} & \mathbf{I} & \mathbf{B}_{14} \\ \mathbf{0} & -\mathbf{I} & \mathbf{0} & \mathbf{I} \end{bmatrix} \quad (5-3)$$

Submatrices \mathbf{B}_{12} and \mathbf{B}_{14} are defined by

$$\mathbf{B}_{12} = \begin{bmatrix} 0 & -z_C & y_C \\ z_C & 0 & -h/2 \\ -y_C & h/2 & 0 \end{bmatrix} \text{ and } \mathbf{B}_{14} = \begin{bmatrix} 0 & z_C & -y_C \\ -z_C & 0 & -h/2 \\ y_C & -h/2 & 0 \end{bmatrix} \quad (5-4)$$

where y_C and z_C are the distances between the centroid C and the intersection of the y - and z -axes and the Voronoi cell boundary, respectively (Figure 5-2b). The element stiffness matrix, \mathbf{K}_e , can be obtained by

$$\mathbf{K}_e = \mathbf{B}^T \mathbf{D} \mathbf{B} \quad (5-5)$$

The local spring stiffness matrix \mathbf{D} is filled with the spring coefficients from Equation (5-1):

$$\mathbf{D} = \text{diag}[k_s, k_t, k_n, k_{\phi n}, k_{\phi s}, k_{\phi t}] \quad (5-6)$$

The system matrix \mathbf{K} is assembled for all the lattice elements and nodal displacements \mathbf{u} are computed by solving the system equations:

$$\mathbf{K} \mathbf{u} = \boldsymbol{\phi} \quad (5-7)$$

where $\boldsymbol{\phi}$ is the global vector of nodal forces. At the stage of constructing the system stiffness matrix, which is usually sparse, a skyline matrix storage form is used to economize the use of computer memory. Then, the system equations are solved by the Crout elimination scheme.

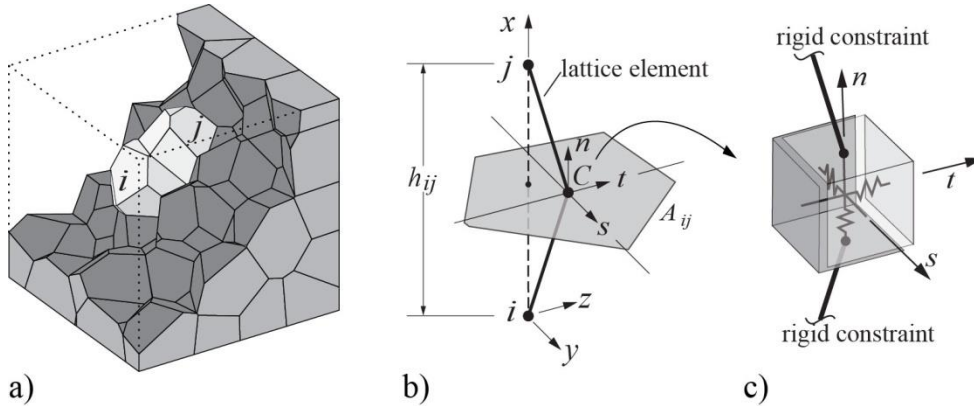


Figure 5-2. Typical RBSN element ij : a) within a Voronoi grid; b) isolated from the network; and c) a zero-size spring set located at centroid C of Voronoi cell boundary area A_{ij} .

5.1.3 Evaluation of criticality of element stress state

The RBSN model provides a discrete representation of fracture by damaging/breaking the local springs. For the damaged spring set, the local stiffness matrix is

$$\mathbf{D}' = (1 - \omega) \mathbf{D} \quad (5-8)$$

where ω is a scalar damage index with a range from 0 (undamaged) to 1 (completely damaged). In the modeling of brittle fracturing, which is applied to the cases presented in this part of the report, ω is either 0 or 1. Fracture may initiate within a lattice element when the stress state exceeds the given material strength. To determine the criticality of the stress state, a stress ratio is calculated for each lattice element:

$$R_f = \sigma_e / \hat{\sigma} \quad (5-9)$$

where σ_e is the element stress state and $\hat{\sigma}$ is the critical stress defined by fracture criteria. During iterative calculations, only one element, with the most critical stress state (i.e., the largest $R_f \geq 1$), is allowed to break per iteration, and the fracture event entails a reduction of spring stiffnesses and a release of the associated elemental forces. To date, three types of fracture modeling in the RBSN have been used to evaluate the criticality of stress state with different fracture criteria, which will be presented and reviewed herein.

Resultant stress measures

The RBSN models have been applied to simulate fracture process predominantly subjected to tensile loading (Berton and Bolander, 2006). In general, the global loading direction is mostly skewed to the local element axes; therefore, all the normal and tangential components of spring forces are activated in the direction of the element axes. Nodal displacements produce forces F_n , F_s , and F_t in the respective axial springs, and the resultant vector of the spring forces with a measure of $F_R = (F_n^2 + F_s^2 + F_t^2)^{0.5}$ is used to obtain a stress state:

$$\sigma_R = F_R / A_{ij}^P \quad (5-10)$$

where A_{ij}^P is the projected area of A_{ij} on a plane perpendicular to the direction of the resultant force. σ_R serves as σ_e in Equation (5-9), whereas $\hat{\sigma}$ varies according to a tensile softening relation. The tension/compression condition is determined by the direction of the normal spring force.

This uniaxial, vectorial stress approach is energy-conserving and mesh-insensitive for predominantly tensile stress fields. For example, Thomure et al. (2001) demonstrated the model objectivity with respect to size and geometry of the lattice network. A random mesh provides uniform, controllable energy consumption which gives practically the same result as a straight line discretization of the crack trajectory. However, complications arise when such uniaxial notions of stress are applied to modeling cases of multiaxial stress.

Maximum principal stress from tensorial stress state

Asahina et al. (2011) have used the stress tensor to determine the failure of RBSN elements. The calculation of stress tensor at a Voronoi cell node is possible by considering the equilibrium conditions of the spring forces. Sets of the spring forces are applied at the boundaries surrounding a Voronoi cell (Figure 5-3a), and nodal force components F_{nn} , F_{ns} , and F_{nt} can be calculated for an arbitrary section passing through the Voronoi cell node with its corresponding local n - s - t coordinates, which satisfy the equilibrium condition with all the forces acting on the remaining cell boundaries (Figure 5-3b). Moment contributions to equilibrium are not considered here. By dividing these force components by the cut-face area, the corresponding stress components σ_n , σ_s , and σ_t can be obtained. By repeating this process for three mutually

perpendicular sections, the full stress tensor is obtained (Figure 5-3c). Details are given elsewhere (Yip et al., 2005).

From the stress tensors at two neighboring nodes, the stress tensor of the inter-element is calculated according to

$$\bar{\sigma} = (\sigma_i + \sigma_j)/2 \quad (5-11)$$

where σ_i and σ_j are the stress tensors at the neighboring nodes i and j , respectively. The maximum principal tensile stress of $\bar{\sigma}$ serves as σ_e in Equation (5-9). In this way, fracture under multiaxial stress conditions can be simulated. However, this approach does not readily account for the possibility of softening behavior since the ambiguity still exists for calculation of the nodal stress tensor from the damaged spring forces.

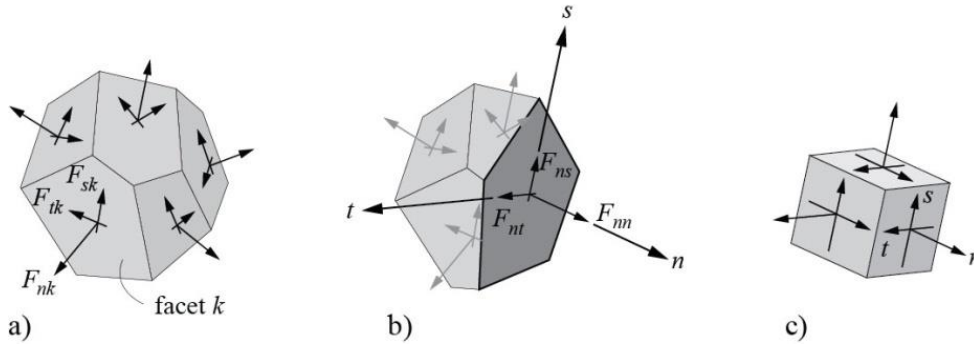


Figure 5-3. Stress tensor at a Voronoi cell node: a) components of spring force local coordinates; b) a set of nodal forces satisfying the equilibrium; and c) complete stress tensor at Voronoi cell node (Adapted from Yip et al., 2005).

Stress components with Mohr-Coulomb surface

Strength properties of each element are determined as critical stress components on a Mohr-Coulomb surface. Figure 5-4 shows the fracture surface with a tension cut-off, where the envelop is defined by three parameters: the angle of internal friction ψ (surface inclination with respect to σ_n -axis); cohesive strength c (surface intersection with the shear axes); and the tensile strength f_n . Measures of stress $P(\sigma_n, \sigma_s, \sigma_t)$ are derived by averaging the axial spring forces F_n , F_s , and F_t over the cell boundary area A_{ij} . The criticality of the stress state is assessed as $R_f = \overline{OP}/\overline{OP}_O$, where P_O is the point at which \overline{OP} intersects the fracture surface. At the present stage of model development, there is no option to gradually damage the springs (e.g., with softening behavior) for fracturing. However, other studies have indicated the possibility of modeling damage process by shrinking the Mohr-Coulomb surface (Shen and Shen, 2002; Kim and Lim, 2011). This fracture modeling approach will be utilized for the simulations in Section 5.3.

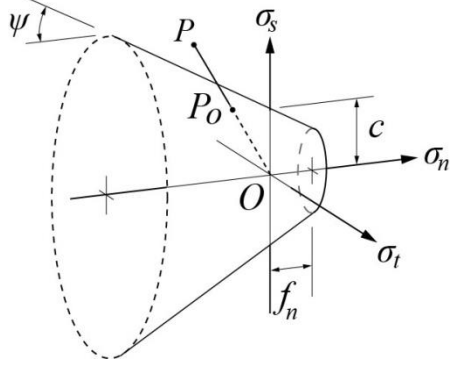


Figure 5-4. Mohr-Coulomb fracture surface with tension cut-off.

5.2 Hydro-Mechanical Modeling Using TOUGH-RBSN

5.2.1 Linkage between TOUGH2 and RBSN

TOUGH2 is a general-purpose simulator for flow and mass transfer in porous and fractured media (Pruess et al., 2011), which has an applicability to diverse modeling problems by adopting various equation-of-state (EOS) modules. Simulations presented in this paper use the EOS1 module for single-phase flow problems with isothermal conditions. The modeling approach is based on the integral finite difference method (IFDM), thus possesses the advantage of being compatible with regular or irregular gridding in any number of spatial dimensions. It also allows for flexibility of fracture representation, in which fractures and fracture networks form in response to the hydro-mechanical forces and conditions (Zhang et al., 2004; Rutqvist et al., 2013).

For modeling of coupled hydro-mechanical processes, the TOUGH2 simulator is linked with the RBSN approach. The general coupling procedure of TOUGH-RBSN is basically similar to that of the TOUGH-FLAC software (Rutqvist et al., 2002), but the coupling modules are substantially modified for the DFN approach. Figure 5-5 shows a schematic flow diagram of the coupling procedure between TOUGH2 and RBSN, which are linked through external modules that handle two-way coupling of the relevant quantities at each time step.

First, the TOUGH2 to RBSN link, shown on the left side of Figure 5-5, supplies pressure and degree of saturation to update the mechanical quantities. From the pore pressure P , the effective (grain-to-grain) stress σ_n' , applied to the lattice element, is calculated using Biot's theory (Biot and Willis, 1957):

$$\sigma_n' = \sigma_n + \alpha_p P \quad (5-12)$$

where σ_n is the total normal stress obtained from overall loading, including external loads; α_p is Biot's effective stress parameter. Note that tensile stress is taken to be positive. By averaging the nodal pressure, Equation (5-12) can be modified to calculate the effective stress applied to a lattice element ij in incremental form:

$$\Delta\sigma' = \Delta\sigma + \alpha_p(\Delta P_i + \Delta P_j)/2 \quad (5-13)$$

where ΔP_i and ΔP_j are the pressures increments measured at nodes i and j .

It is assumed that the saturation change induces the strain increment in the element ij as follows:

$$\Delta\varepsilon_s = \alpha_s(\Delta S_i + \Delta S_j)/2 \quad (5-14)$$

where ε_s is shrinkage/swelling strain; and α_s is the hydraulic shrinkage coefficient. If an expansible matrix material is subjected to constant stress conditions in an elastic region, the effective stress can be affected by the swelling/ shrinking strain as

$$\Delta\sigma' = \Delta\varepsilon_s E \quad (5-15)$$

Thereafter, the RBSN to TOUGH2 link, shown on the right side of Figure 5-5, supplies the effective stress and the strain calculated at the lattice element to update the hydrological properties of the corresponding Voronoi cells i and j in the TOUGH2 model. Porosity, permeability, and capillary pressure are generally related with the effective stress and strain values (Rutqvist and Tsang, 2002).

If fracturing occurs at the element ij (i.e., $\omega \neq 0$), the associated fracture node and additional connections are activated in the TOUGH2 model. The permeability of an individual fracture can be defined by the fracture aperture b (Bear, 1972; Bear et al., 1993), however, herein the fracture is simply assumed to have a constant permeability very high relative to that of the rock matrix.

The TOUGH-RBSN simulator has several advantages that stem from the availability of sharing the same grid geometry based on the Voronoi discretization. This simplifies coupling of nodal quantities and data exchange between the two numerical models. Also, discrete fractures for hydrological behavior can be more easily introduced in the grid and directly related to mechanical damage. The modeling scheme for the DFN approach in the unstructured grid geometry is described in the next subsection.

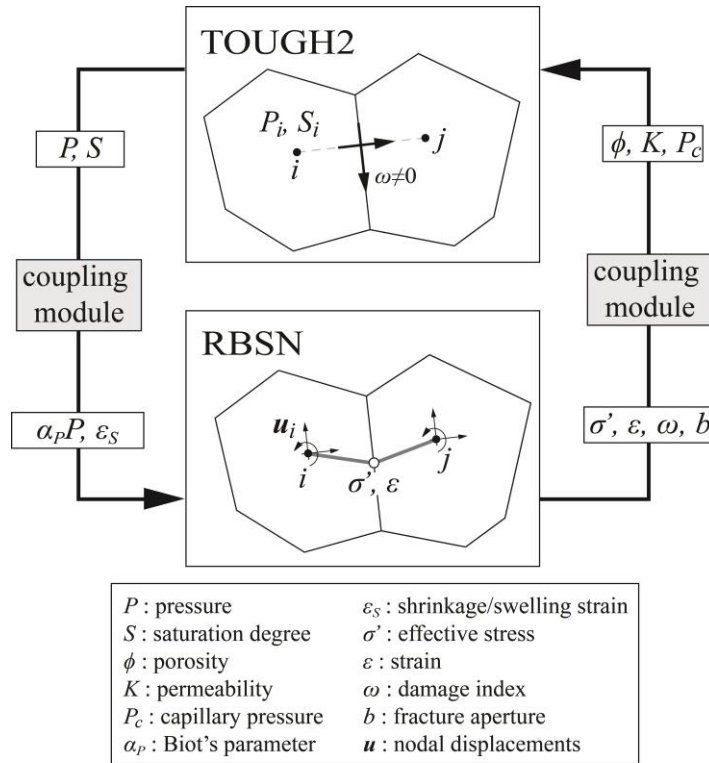


Figure 5-5. Flow diagram of the coupling procedure between TOUGH2 and RBSN (adapted from Asahina et al., 2014).

5.2.2 Representation of discrete fractures in rock formations

Fractures within geological systems may facilitate storage and flow of fluids and contribute to discontinuous mechanical responses. Such fractures and discontinuities are explicitly modeled as discrete features within the Voronoi grid.

The Voronoi grid represents the matrix component of geomaterial structures, and pre-existing or newly generated fractures are placed on the Voronoi cell boundaries. Descriptors of fractures (e.g., orientation, length, curvature) can be obtained by field mapping, computer-generated statistical representations, or the simulation outcomes of mechanical models. An example of the discretization procedure in 2-D modeling involving a straight fracture path is as follows:

- i. Generate a Voronoi unstructured grid for the spatial domain.
- ii. Overlay the reference fracture path onto the grid.
- iii. Test all connections of natural neighboring nodes to check if they cross the fracture path. For example, compare connections ij and jk in Figure 5-6.
- iv. The collection of the Voronoi cell boundaries corresponding to the nodal connections that cross the reference fracture (such as ij) forms discretized fractures.

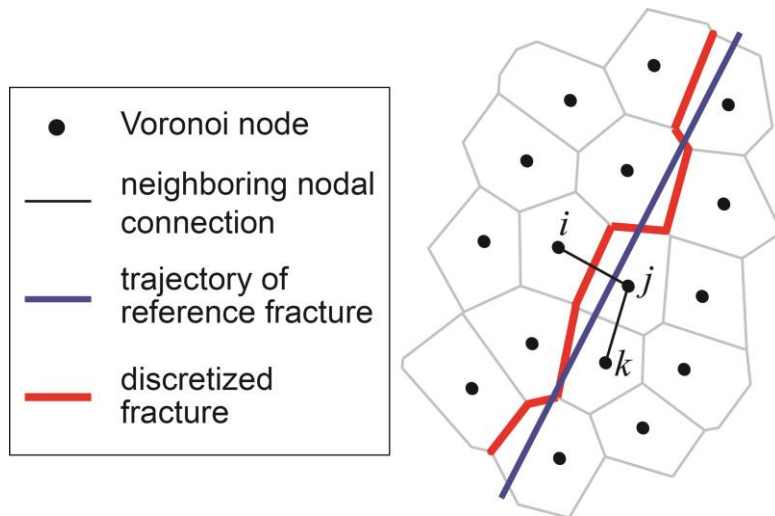


Figure 5-6. Fracture mapping and discretization within an unstructured Voronoi grid.

By repeating the above process for multiple fractures, a network of discrete fractures can be generated. This fracture discretization process is completely automated and can be easily extended to more complicated geometries in 3-D modeling. The grid size should be carefully chosen to obtain a sufficiently accurate representation of the reference fracture. With a finer grid, the discretized fractures correspond more closely to the reference path, but the computational effort may be increased.

In TOUGH2 simulations using a basic Voronoi grid, flow and mass transfer are enacted only through the connections of the neighboring matrix nodes (called matrix-matrix connections in Figure 5-7a). However, if fracturing occurs within the matrix, substantial flow may arise through the fracture apertures. For the DFN approach, dynamic formation of such flow channels is implemented by introducing fracture nodes and the associated connections within the Voronoi grid. As shown in Figure 5-7b, a fracture node is inserted on the Voronoi cell boundary where the matrix-matrix connection crosses. The original matrix-matrix connection is divided into two matrix-fracture (and vice versa) connections by the newly inserted fracture node. In addition, the connections between the fracture nodes are established to activate flow channels in discrete fractures. Hydrological properties of the discrete fractures are related to the grid geometry and the local fracture aperture. Fracture geometries can be either assigned as a pre-existing fracture property or computed by the mechanical-damage analysis of the RBSN model.

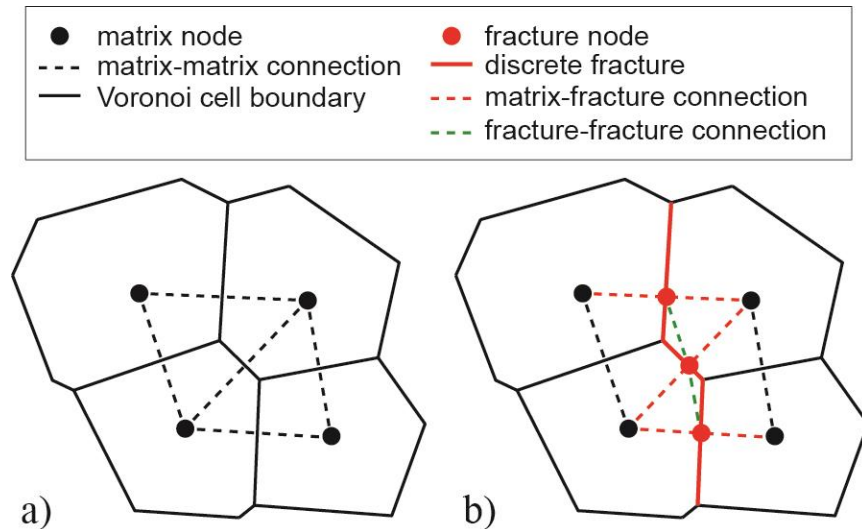


Figure 5-7. Adjustment of nodal connections for flow modeling with discrete fractures: a) original matrix nodes and connections; and b) insertion of fracture nodes and connections.

5.3 Fluid-Driven Fracture Simulations

5.3.1 Model verification

Fracture initiation and propagation incurred by the pressurized fluid are simulated to verify the TOUGH-RBSN simulator. A 2-D rectangular domain with dimensions of 100×120 m is prepared, in which an unstructured Voronoi grid is generated with graded nodal density for computational efficiency (Figure 5-8a). A reference line is prescribed in the middle of the domain such that a single, straight fracturing path results. Symmetric boundary conditions are applied through a slipping (roller) configuration on the left side boundary. The point of fluid injection is located on this boundary at the end of the reference line.

The fracture geometry from the simulation result is compared to the analytical solutions for fracture opening versus length relationship. Classic 2-D fracture models, such as the Khristianovic-Geertsma-de Klerk (KGD) model (Khristianovic and Zheltov, 1955; and Geertsma and de Klerk, 1969) and the Perkins-Kern-Nordgren Model (PKN) model (Perkins and Kern, 1961; and Nordgren, 1972), have considered that the cross section of the fracture would be an elliptical shape based on the linear elastic fracture mechanics theory and the assumption of uniform fluid pressure along the fracture length.

The aperture width of the resulting fracture is measured by the generalized displacement of the fractured lattice element, and the fracture profiles are plotted at times 10, 15, and 20 sec. in duration of fluid injection (Figure 5-8b). As the hydraulically driven fracture gets wider and longer with time, the fracture profiles retain elliptic shapes, which are analytically drawn with the fracture length and the wellbore aperture chosen as the principal radii of ellipses.

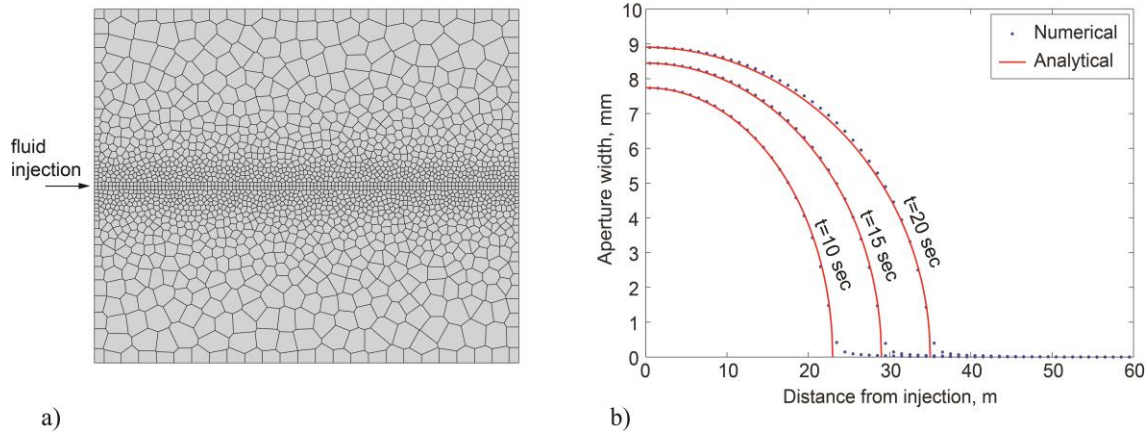


Figure 5-8. Hydraulic fracturing simulation of a single fracture: a) 2-D model set up; and b) comparison between the numerical model and the analytical approximation in terms of fracture aperture profiles.

5.3.2 Hydraulic fracturing within discrete fracture networks

The purpose of this study is to demonstrate the current TOUGH-RBSN modeling capabilities extended to hydraulic fracturing simulations through the prediction of actual laboratory experimental behavior. In the experiments, pre-existing fracture networks are designed and fabricated within soda-lime glass blocks by generating thermally induced micro-cracks with the 3-D laser-engraving technique. The fracture network pattern is made up of clouds of these micro-cracks and its geometric topology is obtained for numerical modeling (Figure 5-9a). In the numerical model, the discrete fractures are replicated using the scheme presented in Section 5.2.2. In Figures 5-9b and c, two cases of fracture modeling with different mesh density show a similarity of the fracture pattern.

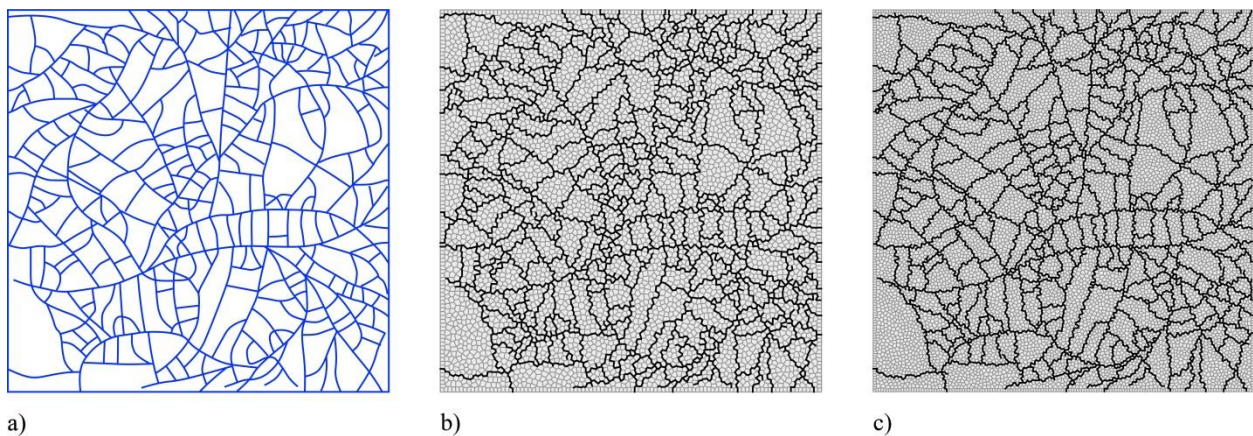


Figure 5-9. Modeling of discrete fracture networks: a) geometric topology of fracture networks; and mapping of the fracture pattern onto unstructured Voronoi grids with different mesh density: approximately b) 5000 and c) 10000 Voronoi cells, respectively.

For simplicity, the matrix (soda-lime glass) is assumed to be impermeable and non-porous. An 88.9 mm square domain is discretized for modeling. Mechanical properties of the matrix are as follows: Young's modulus $E = 73.8$ GPa, tensile strength $f_t = 30$ MPa. Parameters for the Mohr-Coulomb fracture criterion are cohesive strength $c = 22.5$ MPa and internal friction angle $\psi = 45^\circ$. In the experiment, overall strength of the pre-existing fractures can be varied by modifying the micro-crack density. Since the strength of these fractures have not been determined at this point, for the numerical modeling, it is assumed that pre-fractured elements have Young's modulus and tensile strength reduced from those of the intact glass by 50%.

Hydrological properties of the pre-existing fractures are set as those of the intact glass unless the fractures are activated by subsequent hydro-mechanical responses. Once a new fracture occurs or a pre-existing fracture is activated, the mechanical resistance is removed and the permeability and the porosity are increased (e.g., a permeability of 1 darcy and a porosity of 0.8) for the fractured element while compressibility remains at zero. The borehole is assigned a permeability of 1 darcy, porosity of 1, and zero compressibility.

Because the glass is prone to brittle fracturing, the injection needs to be performed very carefully to capture the fracture propagation. As a suggestion, this simulation is conducted with injecting water into a borehole at the center of the domain. The injection rate is chosen to be 2×10^{-7} kg/s per unit millimeter. Anisotropic confining stresses of 7.24 MPa and 4.83 MPa (in the vertical and horizontal directions, respectively) are applied at the boundary edges.

Figure 5-10a presents the deformed shape at a final stage of hydraulic fracturing ($t = 1.25$ sec), in which the nodal displacements are exaggerated (50 times) for better visibility. The fluid pressure triggers fracturing process and induces fracture opening throughout the activated fractures. Figure 5-10b illustrates the fracture propagation (in red) overlaid on the pre-existing fracture network (in blue). Two dominant fractures are shown stretching from the borehole in the direction sub-parallel to the maximum confining stress, and the details of the fracturing paths show a preference for forming along pre-existing fractures.

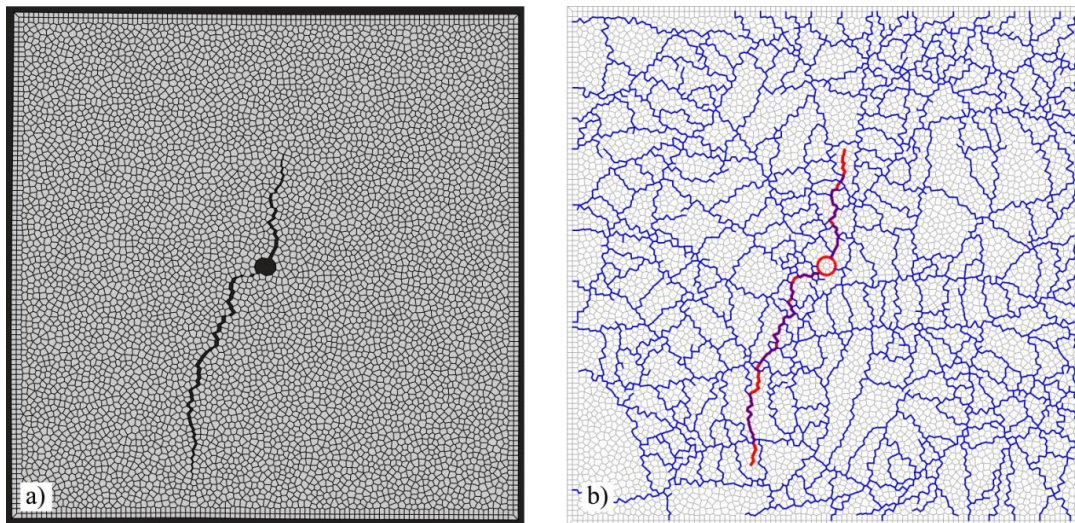


Figure 5-10. Simulation results at a final stage of hydraulic fracturing: a) deformed shape; and b) fracture propagation paths overlaid on the pre-existing fracture network.

Figure 5-11 arranges snapshots of pressure distributions, captured at the point of fracture initiation, at the intermediate stages of fracture propagation, based on the length of the fracture, and at the final stage of the simulation. Up until fracture initiation, the pressure at the borehole increases due to the fluid injection (Figure 5-11a). During hydraulic fracture propagation the fluid is directly transferred from the borehole into newly created volume along the fracture paths, so the fluid pressure at the borehole decreases with the advance of fractures (Figures 5-11b through d). Figure 5-11d shows the pressure distribution at the final stage, in which the region with higher pressure clearly indicates the hydraulic fracture paths illustrated in Figure 5-10b.

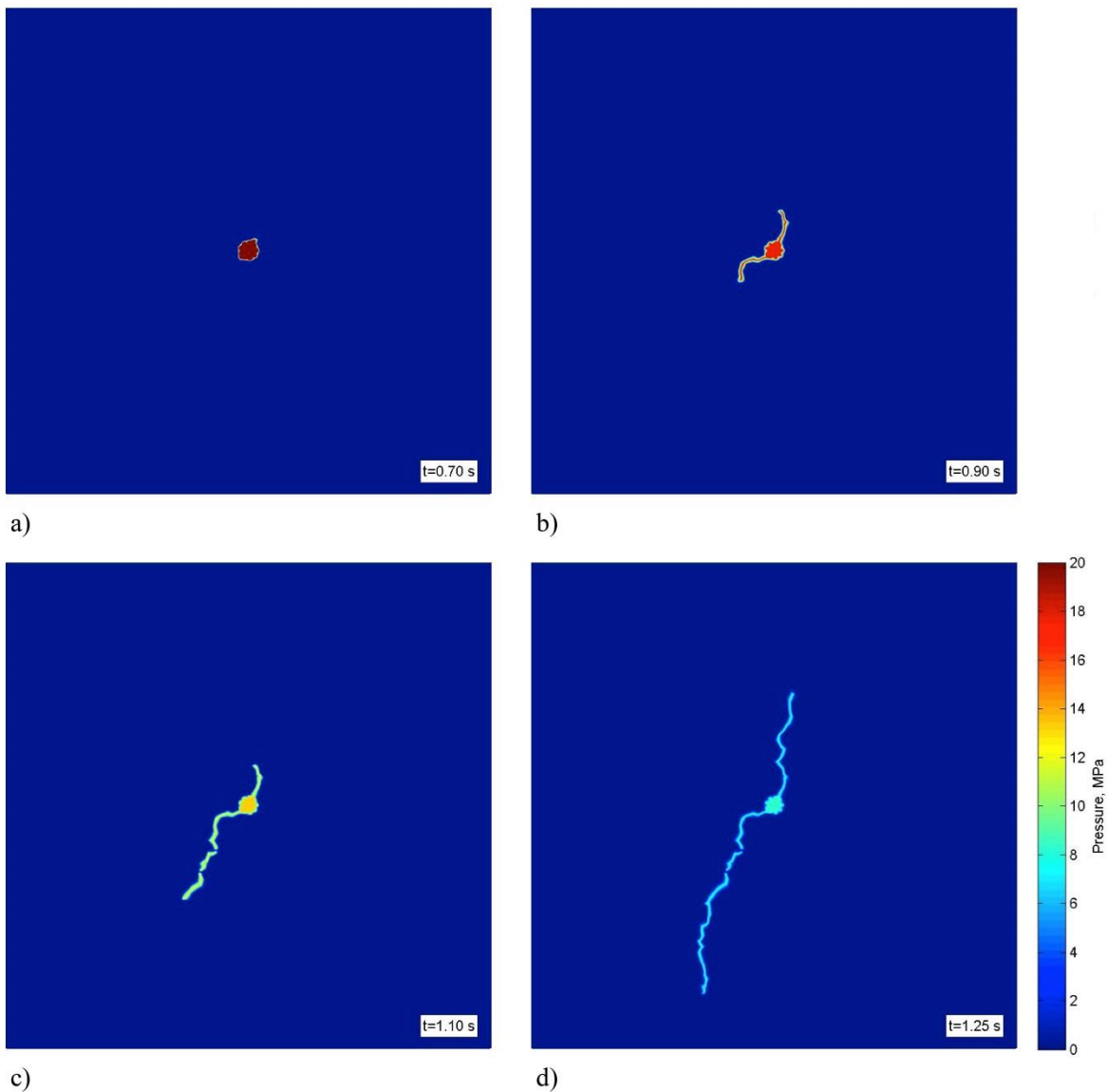


Figure 5-11. Pressure distributions captured at: a) at the point of fracture initiation; b) at the early stage; c) at the latter stage; and d) at the final stage of fracture propagation.

Next, a sensitivity analysis for fracture formation was conducted by varying the storage coefficient as an independent variable. For accurate modeling of the system response, it is crucial to represent the specific storage of the injection device correctly (including the storage resulting from the compliance of the borehole) as well as the storage created by the opening of hydraulic fractures. The storage coefficient is apparently related to the compressibility of the model domain. Two cases of the compressibility parameters for the borehole blocks are considered: zero and $4.6 \times 10^{-9} \text{ Pa}^{-1}$. Note that all the other conditions and parameters, including the injection rate, are identical in the simulations.

Figure 5-12 compares the pressure evolutions at the borehole for the two cases. As depicted by the blue curve, zero compressibility allows gradual fracture propagation from the borehole with intermittent pressure release at the borehole. In contrast, the red curve for the higher compressibility case leads to a longer period for pressure development up to the triggering pressure. The delayed fracture initiation results in greater strain energy stored in the system, thus rapid fracture develops with a subsequent instantaneous pressure drop after fracture initiation. This analysis suggests that a stiff injection system with a low storage coefficient is desirable for producing stable propagation of hydraulic fractures.

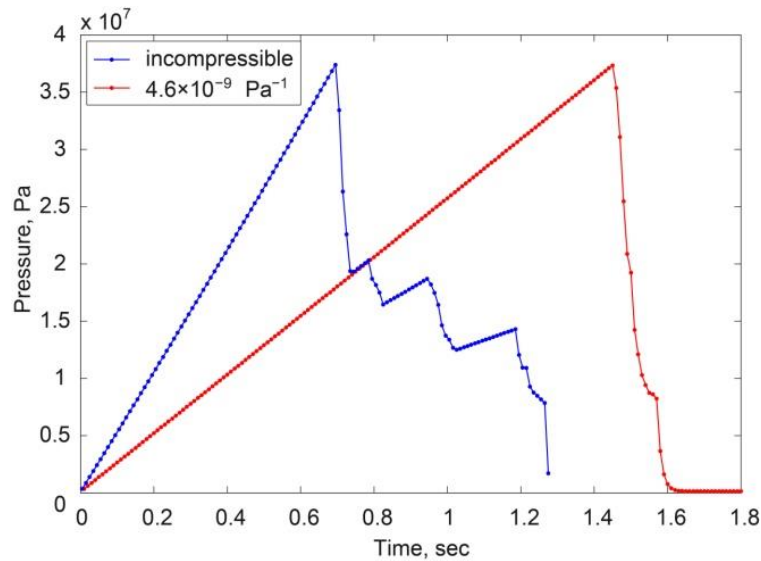


Figure 5-12. Evolutions of injected fluid pressure for different compressibility coefficients of the borehole region.

5.3.3 Observations of problems with the current modeling scheme

This study demonstrates the modeling capacities of the TOUGH-RBSN simulator for coupled hydro-mechanical processes. The mechanical effect of the excessive pressure produced by fluid injection (i.e., hydraulic fracturing) and the preferential flow features through the newly generated fracture path are realistically represented. However, the simulator inherently has shortcomings due to the equilibrium-based calculations generated by the RBSN model. While the main coupling procedure is driven by TOUGH which computes hydrological behavior with

the passage of time, the RBSN model does not have the terms of time in its governing equations (i.e., static simulations).

For nonlinear calculations with fracturing processes, damaging/breaking the elements are iterated to retain the convergence to the equilibrium-state of the system, in which the LHS and RHS of Equation (5-7) are balanced. However, especially when fracture propagation reaches the domain boundary, the system keeps trying to make fracturing at irrelevant elements in absurd places since no more elements at the boundary can be fractured. In that respect, the simulation results sometimes lead to unreal fracture behavior or the system becomes unstable and the numerical solution fails to converge.

This type of behavior has been found in the above simulation example. Figure 5-13 shows fractured elements at two consecutive time steps ($t = 1.25$ sec and 1.26 sec). The fracture paths in Figure 5-10b are redrawn in Figure 5-13a for comparison. As can be seen in Figure 5-13b, after the main fracture paths reach the boundaries, trivial fractures are generated over the boundaries to break up the domain. These numerical artifacts may be reduced by choosing smaller time increment, but that cannot be guaranteed.

To resolve this problem, a new dynamic simulation framework has been being developed based on the RBSN. Equations of motion are solved at each time step for mechanical behavior, so the time variables are retained in the two-way coupling procedure. Details of the methodology are presented in the next section.

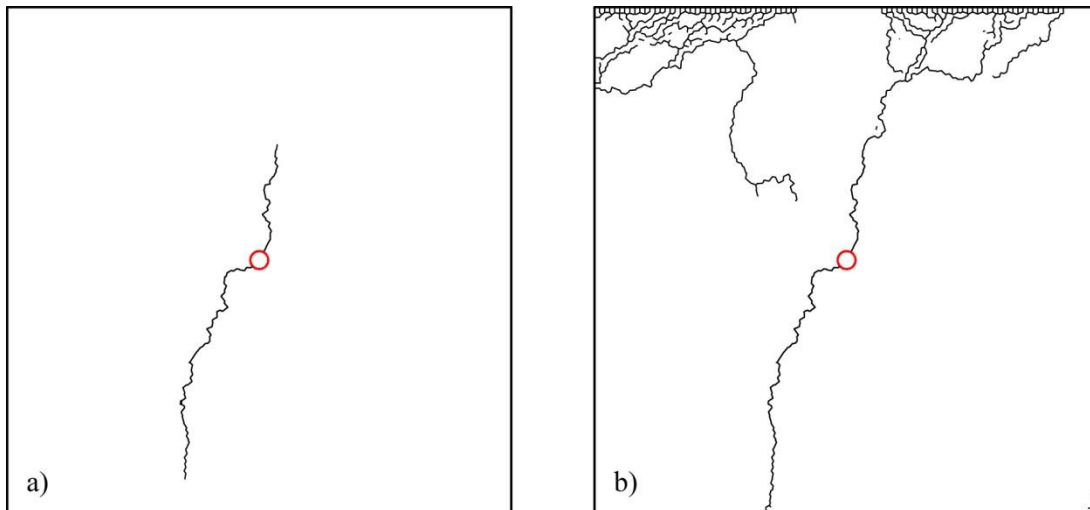


Figure 5-13. Abnormal break-up of the domain due to numerical instability: a) final time step as a meaningful result; and b) abrupt fracture generation at the next time step.

5.4 Development of Dynamic Simulation Code

5.4.1 Equation of motion and time stepping method

In dynamic modeling of mechanical behavior, the motion of the system is governed by a differential equation of the displacements of the Voronoi nodes. The nodal displacements,

velocities, and accelerations are calculated by a time-stepping method for integrating the equation of motion. The governing equation is constructed based on Newton's second law of motion.

Figure 5-14 shows a free-body diagram of a Voronoi cell subjected to external load applied at the node and local internal forces generated at the spring sets. Let us consider the external load vector $\mathbf{p}(p_x, p_y, p_z, \tau_x, \tau_y, \tau_z)$ in the global X - Y - Z coordinates and a local internal force vector $\mathbf{f}_k(f_{nk}, f_{sk}, f_{tk}, m_{nk}, m_{sk}, m_{tk})$ for a Voronoi facet k . Both the external and internal force sets have six components (three translations and three rotations), in the figure the rotational components (i.e., m_{nk}, m_{sk}, m_{tk}) of the spring forces are omitted for visibility. With coordinate transformations, the local internal force vectors for n facets are assembled into a global internal force vector:

$$\mathbf{f} = \sum_{k=1}^n \mathbf{\Gamma}_k^T \mathbf{f}_k \quad (5-16)$$

where $\mathbf{\Gamma}_k$ is a 6×6 matrix for coordinate transformation from global X - Y - Z to local n - s - t for individual Voronoi facet k .

The governing equation for nodal displacements and rotations varying with time can be constructed as

$$\mathbf{M}\ddot{\mathbf{u}} + \mathbf{f} = \mathbf{p}(t) \quad (5-17)$$

where $\ddot{\mathbf{u}}$ is a second derivative of displacement vector (i.e., acceleration) \mathbf{M} is the inertia matrix containing mass and moment of inertia tensor of the Voronoi cell. For numerical modeling, Equation (5-17) is discretized in the time domain.

$$\mathbf{M}\ddot{\mathbf{u}}_n + \mathbf{f}_n = \mathbf{p}_n \quad (5-18)$$

The time scale is divided into a series of time steps by uniform duration Δt and a discrete time instant $t_n = n\Delta t$, denoted as time n .

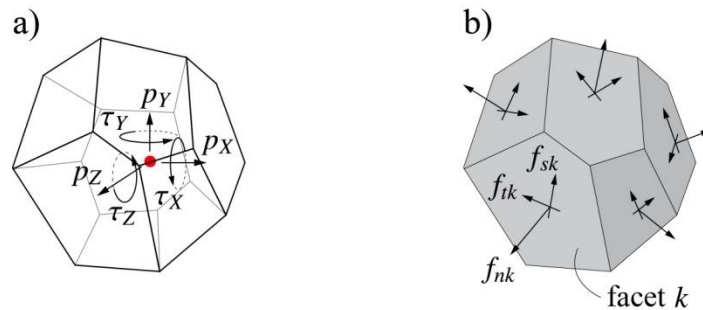


Figure 5-14. Free-body diagram of a Voronoi cell: a) with external nodal forces; and b) with internal spring forces.

Time stepping-methods enable the evaluation of the response that satisfies Equation (5-17) at time $n + 1$:

$$\mathbf{M}\ddot{\mathbf{u}}_{n+1} + \mathbf{f}_{n+1} = \mathbf{p}_{n+1} \quad (5-19)$$

When applied successfully with $n = 0, 1, 2, 3, \dots$ the numerical time-stepping procedure gives the desired response at all time $n + 1$. In this study, an explicit time integration scheme, the velocity Verlet algorithm, is used to conduct time-stepping procedure.

From the known kinematic information up to time n , the unknown displacement at time $n + 1$ can be calculated as

$$\mathbf{u}_{n+1} = \mathbf{u}_n + \dot{\mathbf{u}}_n \Delta t + \frac{\ddot{\mathbf{u}}_n}{2} \Delta t^2 \quad (5-20)$$

Then, the internal force \mathbf{f}_{n+1} is explicitly evaluated as a function of nodal displacement \mathbf{u}_{n+1} . By manipulating Equation (5-19), the acceleration $\ddot{\mathbf{u}}_{n+1}$ is derived from the unbalanced internal and external forces:

$$\ddot{\mathbf{u}}_{n+1} = \mathbf{M}^{-1}[\mathbf{p}_{n+1} - \mathbf{f}_{n+1}] \quad (5-21)$$

Finally, the unknown velocity $\dot{\mathbf{u}}_{n+1}$ is calculated as

$$\dot{\mathbf{u}}_{n+1} = \dot{\mathbf{u}}_n + \frac{\ddot{\mathbf{u}}_{n+1} + \ddot{\mathbf{u}}_n}{2} \Delta t \quad (5-22)$$

This second-order time integration scheme is known to be more accurate than single-step integration schemes such as the Euler method, and therefore commonly used in the molecular dynamics and particle dynamics simulations (Amini et al., 1987; Martys and Mountain, 1999; Kim et al., 2008). Also, unlike the static analysis program of the RBSN approach, the solution procedure using an explicit time integration scheme is simple and does not require building the whole system matrix equation. In that regard, the program code is expected to be easily parallelized for large-scale computations.

5.4.2 Suppression of boundary artifacts

The dynamic RBSN method offers more flexibility with boundary conditions than the current equilibrium model for geomechanical and fracture damage modeling. Boundary effects are important to control because earth models almost always must use artificial boundaries in numerical models for systems that are effectively unbounded. One method to control these effects is to implement damping (or frictional) effects of movement near the boundary. This tends to reduce reflections of disturbances from the boundaries, which is needed if the boundaries are artificial. The following analysis provides an example of how damped boundary masses in a mass-spring system can suppress reflections from boundaries.

Mass-spring system

As shown in Figure 5-15, a one-dimensional mass-spring system with rigid boundaries consists of N masses and $N + 1$ springs. This is the simplest mechanical analogue available to investigate the effects of boundary conditions on mechanical disturbances. Each mass is characterized by m

and each spring has an associated spring constant, k . Each spring has a neutral (no force) length of ℓ . The spring force on mass n connected on each side to a springs n and $n + 1$.

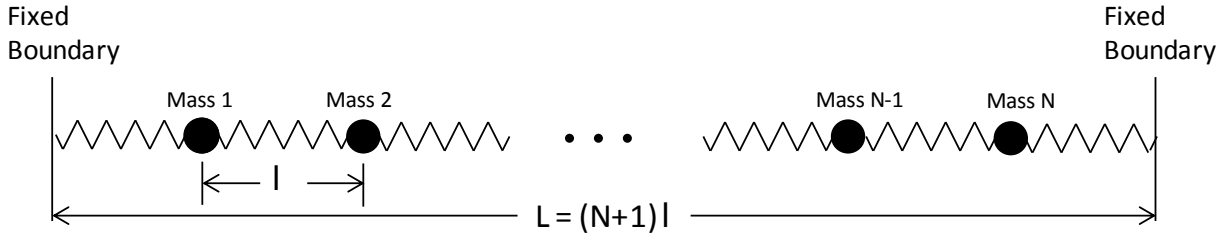


Figure 5-15. Conceptual drawing of mass-spring system.

The time-dependent positions of each mass is given by $x_n(t)$.

$$F_n = -k(x_n - x_{n-1} - \ell) + k(x_{n+1} - x_n - \ell) \quad (5-23)$$

An additional resistive damping (or frictional) force acts on each mass and is proportional to the negative of the velocity of the mass with a coefficient r_n . Therefore,

$$m \frac{d^2 x_n(t)}{dt^2} = -r_n \frac{dx_n(t)}{dt} - k(x_n(t) - x_{n-1}(t) - \ell) + k(x_{n+1}(t) - x_n(t) - \ell) \quad (5-24)$$

This may be written as the following pair of first-order differential equations by letting

$$\frac{dx_n(t)}{dt} = y_n(t) \quad (5-25)$$

$$\frac{dy_n(t)}{dt} = -\frac{r_n}{m} y_n(t) - \frac{k}{m} (x_n(t) - x_{n-1}(t) - \ell) + \frac{k}{m} (x_{n+1}(t) - x_n(t) - \ell) \quad (5-26)$$

with $x_0 = 0$ and $x_{N+1} = L$ being the fixed endpoints of the first and last spring. For $n = 2$ to $n = N - 1$ these may be written as

$$\frac{dx_n(t)}{dt} = y_n(t) \quad (5-27)$$

$$\frac{dy_n(t)}{dt} = -\frac{r_n}{m} y_n(t) - \frac{2k}{m} x_n(t) + \frac{k}{m} x_{n-1}(t) + \frac{k}{m} x_{n+1}(t) \quad (5-28)$$

For $n = 1$,

$$\frac{dx_1(t)}{dt} = y_1(t) \quad (5-29)$$

$$\frac{dy_1(t)}{dt} = -\frac{r}{m} y_1(t) - \frac{2k}{m} x_1(t) + \frac{k}{m} x_2(t) \quad (5-30)$$

and for $n = N$,

$$\frac{dx_N(t)}{dt} = y_N(t) \quad (5-31)$$

$$\frac{dy_N(t)}{dt} = -\frac{r}{m}y_N(t) - \frac{2k}{m}x_N(t) + \frac{k}{m}x_{N-1}(t) + \frac{kL}{m} \quad (5-32)$$

In non-dimensional form for $n = 2$ to $N - 1$,

$$\frac{dx_{dn}(\tau)}{d\tau} = y_{dn}(\tau) \quad (5-33)$$

$$\frac{dy_{dn}(\tau)}{d\tau} = -2x_{dn}(\tau) + x_{dn-1}(\tau) + x_{dn+1}(\tau) \quad (5-34)$$

For $n = 1$,

$$\frac{dx_{d1}(\tau)}{d\tau} = y_{d1}(\tau) \quad (5-35)$$

$$\frac{dy_{d1}(\tau)}{d\tau} = -r_d y_{d1}(\tau) - 2x_{d1}(\tau) + x_{d2}(\tau) \quad (5-36)$$

and for $n = N$,

$$\frac{dx_{dN}(\tau)}{d\tau} = y_{dN}(\tau) \quad (5-37)$$

$$\frac{dy_{dN}(\tau)}{d\tau} = -r_d y_{dN}(\tau) - 2x_{dN}(\tau) + x_{dN-1}(\tau) + 1 \quad (5-38)$$

The dimensionless variables are defined as:

$$\tau = \sqrt{\frac{k}{m}} t \quad (5-39)$$

$$r_d = \frac{r}{\sqrt{km}} \quad (5-40)$$

$$x_{dn}(\tau) = \frac{x_n(t)}{L} \quad (5-41)$$

$$y_{dn}(\tau) = \sqrt{\frac{m}{k}} \frac{y_n(t)}{L} \quad (5-42)$$

Computed Example

Equations (5-33) through (5-38) are solved using explicit time integration with a constant dimensionless time step of 0.001. A disturbance is introduced through the initial condition in which mass 1 is displaced 0.04 dimensionless distance units towards mass 2 relative to its neutral position. All other masses are initialized at their neutral positions. After mass 1 returns to a

position close to its neutral position (at a dimensionless time of 1.121), its damping coefficient is changed from 0 to 0.01 (strong damping) such that the initial disturbance is a simple pulse. For the damped case, the dimensionless damping coefficients are incremented by 0.0001 starting from a value of 0.0001 for mass 11 up to a value of 0.001 for mass 20. Using a set of ever-increasing damping coefficients over the 10 masses closest to the far boundary was found to do a better job at reducing reflected disturbances from the far boundary than the use of a single highly damped mass next to the far boundary.

Solving for a system of 20 masses and 21 springs gives the results in Figure 5-16. Figure 5-16a shows the reflected disturbance that propagates away from the far boundary ($x_d = 1$). The reflected disturbance is a boundary artifact if the model boundary is not a physical boundary but an artificial numerical model boundary. Figure 5-16b shows the elimination of the reflected disturbance for the case in which damping is used for masses 11 through 20. Damping has little effect on the initial disturbance propagating through the undamped masses (masses 2 through 10). This is shown by superimposing the two cases in Figure 5-17. The responses for masses 2 through 10 diverge only at later times when the reflected wave moves through the undamped system (red lines in Figure 5-17). The comparison also shows the effects of damping for masses 11 through 20 on the propagation of the initial disturbance.

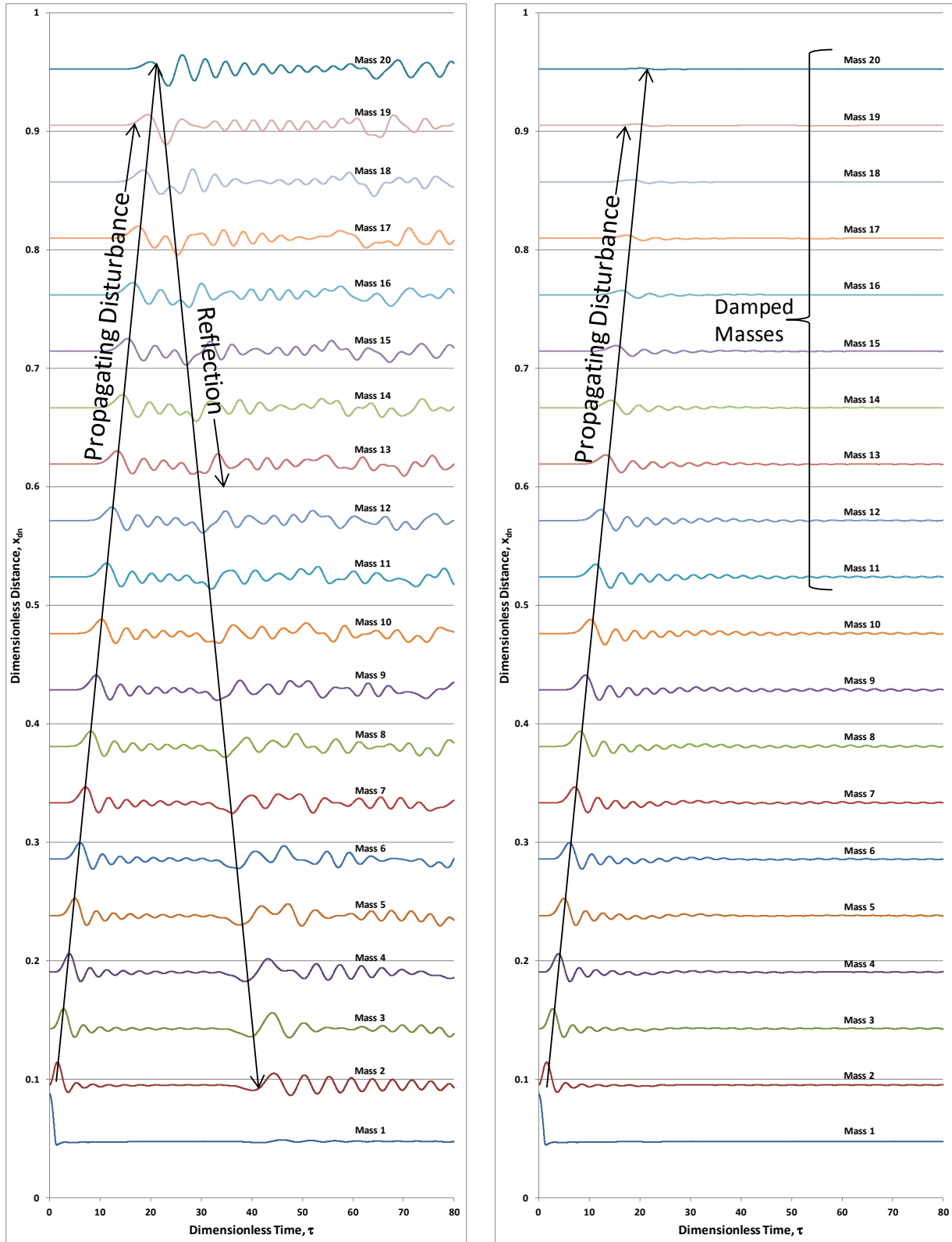


Figure 5-16. Propagation of a disturbance in the mass-spring system: a) no damping except for mass 1; and b) damping for masses 11 through 20 and mass 1.

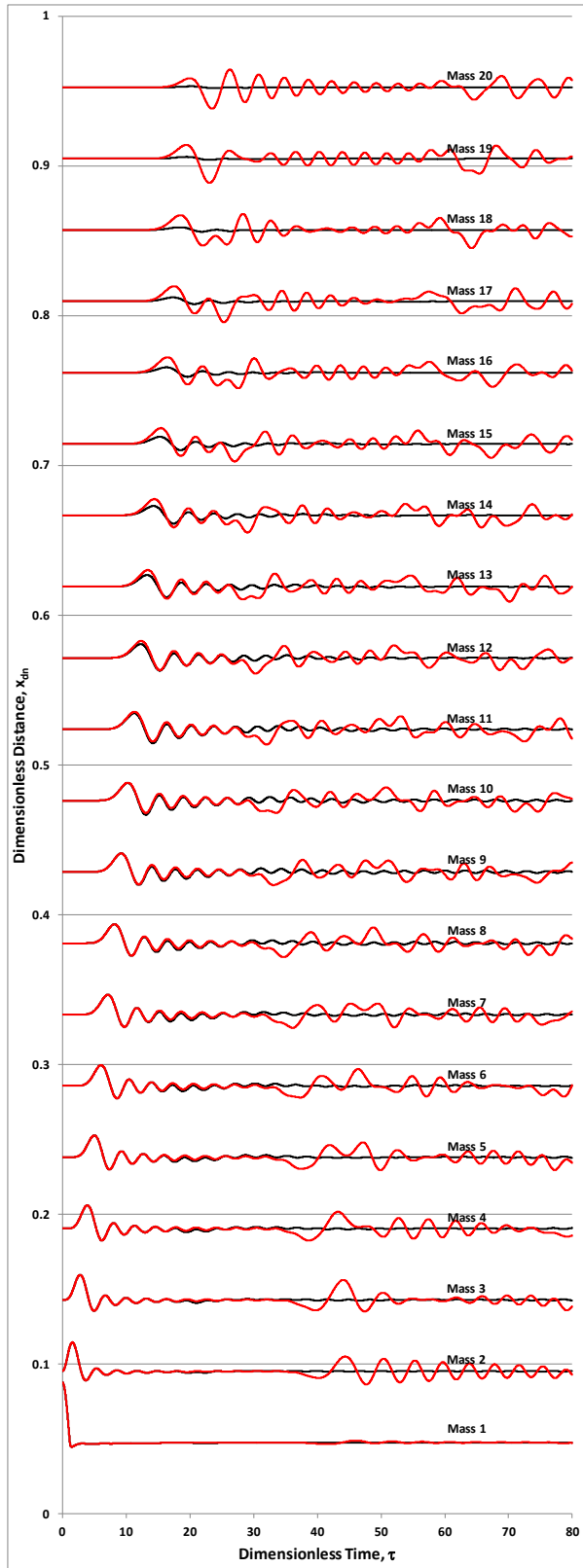


Figure 5-17. Comparison of damping with no damping of masses 11 through 20. Black lines for damped case, red lines for undamped case (except mass 1 which is damped in both cases).

5.5 Conclusions

In this study, an effective coupling between the TOUGH2 and the RBSN approach has been implemented and applied to hydraulic fracturing simulations. The simulator provides a discrete representation of hydrological (flow and mass transfer through fracture networks) and mechanical (fracture initiation and propagation) responses within geomaterials using the DFN approach within unstructured Voronoi grids.

The numerical program is verified through a simulation of a single fluid-driven fracture, in which the elliptical fracture aperture profiles are in close agreement with the analytical solution based upon the linear elastic fracture mechanics theory. Subsequently, predictive simulations including a sensitivity study of the effect of injection system compliance are conducted for hydraulic fracturing within complex pre-existing fracture networks. The simulation results demonstrate relevant modeling capabilities of TOUGH-RBSN, and the sensitivity analysis provides insights for controlling hydraulic fracture propagation. In addition, an inherent shortcoming of the current RBSN approach due to the equilibrium-based calculations is observed, where abrupt and unstable fractures break up the computational domain at near-final stage of the simulation.

As a part of efforts to resolve the problems with the current RBSN approach, we have initiated development of a new dynamic simulation framework. In the new methodology, the terms of time exist in the governing equation and the force unbalance is naturally allowed, so that the numerical instability found in the static modeling approach can be prevented. Nodal kinematic information (displacements, velocities, and accelerations) is calculated through the explicit time integration scheme, by which the code implementation with parallelization can be easily realized. Finally, a specific boundary configuration with damping is discussed for reduction of the effects of artificial boundary conditions. An example calculation with a mass-spring model proves that the propagation of a disturbed displacement is absorbed by damped masses at the boundary.

5.6 Future Work

A modeling program using the DFN approach for coupled THM processes has been developed and verified through fluid-driven fracture simulations. While the simulation results demonstrate the relevant modeling capabilities of TOUGH-RBSN for tightly coupled hydro-mechanical behavior, unphysical features exist due to the equilibrium-based calculations of the RBSN models within the current THM coupling procedure. To resolve the numerical artifacts, we have set to develop a new dynamic simulation framework for RBSN. A summary of the accomplishments so far is as follows:

- The basic methodology to compute the elemental forces (i.e., force-displacement relationship) is based on the existing RBSN approach.
- The equations of motion of Voronoi cells are solved to get the nodal accelerations, which are integrated through a time-stepping procedure (e.g., velocity Verlet algorithm) to derive the nodal velocities and displacements.
- Boundary effects due to the wave reflection can be suppressed using layered damped masses over the boundary.

Recommended work for FY16 includes:

- Regarding the RBSN to TOUGH2 coupling module, hydrological properties (e.g., permeability) of an individual fracture will be defined on the basis of the fracture aperture in order to conduct rather quantitative simulations.
- Also, in the Mohr-Coulomb fracture criterion, gradual damage by shrinking the fracture surface will be implemented for more realistic energy-based fracture processes.
- The dynamic simulation framework uses explicit time integration schemes without building the whole system matrix and its inverse, so the program code is expected to be easily parallelized for large-scale computations.
- Verifications of the dynamic simulation framework will be provided through simple geomechanics examples.

5.7 References

- Amini, M., Eastwood, J.W., and Hockney, R.W. (1987) Time integration in particle models, *Computer Physics Communications*, 44, 83–93.
- Asahina, D., Houseworth, J.E., Birkholzer, J.T., Rutqvist, J., and Bolander, J.E. (2014) Hydro-mechanical model for wetting/drying and fracture development in geomaterials, *Computers & Geosciences*, 65, 13–23.
- Asahina, D., Landis, E.N., and Bolander, J.E. (2011). Modeling of phase interfaces during pre-critical crack growth in concrete. *Cement & Concrete Composites*, 33, 966–977.
- Bear, J. (1972) *Dynamics of Fluids in Porous Media*, Elsevier, New York, New York.
- Bear, J., Tsang, C.-F., and de Marsily, G. (1993) *Flow and Contaminant Transport in Fractured Rock*, Academic Press, San Diego, Calif.
- Berton S. and Bolander, J.E. (2006) Crack band model of fracture in irregular lattices, *Computer Methods in Applied Mechanics and Engineering*, 195, 7172–7181.
- Biot, M.A. and Willis, D.G. (1957) The elastic coefficients of the theory of consolidation, *Journal of Applied Mechanics*, 24, 594–601.
- Bolander, J.E. and Saito, S. (1998) Fracture analyses using spring networks with random geometry, *Eng. Fract. Mech.*, 61, 569–91.
- Bossart, P., Meier, P.M., Moeri, A., Trick, T., and Mayor, J.-C. (2004) Structural and hydrogeological characterisation of the excavation-disturbed zone in the Opalinus Clay (Mont Terri Project, Switzerland), *Applied Clay Science*, 26, 429–448.
- Chiaromonte, L., Zoback, M.D., Friedmann, J., and Stamp, V. (2008) Seal integrity and feasibility of CO₂ sequestration in the Teapot Dome EOR pilot: geomechanical site characterization, *Environ. Geol.*, 54, 1667–1675.
- Cosgrove, J.W. (2001) Hydraulic Fracturing during the Formation and Deformation of a Basin: A Factor in the Dewatering of Low-Permeability Sediments, *AAPG Bulletin*, 85(4), 737–748.
- Fu, P., Johnson, S.M., and Carrigan, C.R. (2013) An explicitly coupled hydro-geomechanical model for simulating hydraulic fracturing in arbitrary discrete fracture networks, *Int. J. Numer. Anal. Meth. Geomech.*, 37, 2278–2300.
- Geertsma J. and de Klerk, F. (1969) A rapid method of predicting width and extent of hydraulically induced fractures, *Journal of Petroleum Technology*, 21, 1571–1581.
- Gonçalvès, J., Violette, S., and Wendling, J. (2004) Analytical and Numerical Solutions for Alternative Overpressuring Processes: Application to the Callovo-Oxfordian Sedimentary Sequence in the Paris Basin, France, *Journal of Geophysical Research*, 109, 14.
- Khristianovic, S.A. and Zheltov, Y.P. (1955) Formation of vertical fractures by means of highly viscous liquid, *Proceedings of the Fourth World Petroleum Congress, Rome*, 579–586.
- Kim, K., Lim J., Kim J., and Lim, Y.M. (2008) Simulation of material failure behavior under different loading rates using molecular dynamics, *Structural Engineering and Mechanics*, 30(2), 177–190.

- Kim, K. and Lim, Y.M. (2011) Simulation of rate dependent fracture in concrete using an irregular lattice model, *Cement & Concrete Composites*, 33, 949–955.
- Martys, N.S., and Mountain, R.D. (1999) Velocity Verlet algorithm for dissipative particle-dynamics-based models of suspensions, *Physical Review E*, 59(3), 3733–3736.
- Neuzil, C.E. (2003) Hydromechanical coupling in geologic processes, *Hydrogeology Journal*, 11, 41–83.
- Nordgren, R.P. (1972) Propagation of a vertical hydraulic fracture, *Society of Petroleum Engineers Journal*, 12, 306–314.
- Okabe, A., Boots, B., Sugihara, K., and Chiu, S.N. (2000) *Spatial Tessellations: Concepts and Applications of Voronoi Diagrams*, 2nd ed., Wiley, NYC, 696 pages.
- Perkins, T.K. and Kern, L.R. (1961) Widths of hydraulic fractures, *Journal of Petroleum Technology*, 13, 937–949.
- Pruess, K., Oldenburg, C., and Moridis, G. (2011) *TOUGH2 User's Guide, Version 2*, Report LBNL-43134 (Revised), Lawrence Berkeley National Laboratory, Berkeley, Calif.
- Rutqvist, J., Leung, C., Hoch, A., Wang, Y., and Wang, Z. (2013) Linked multicontinuum and crack tensor approach for modeling of coupled geomechanics, fluid flow and transport in fractured rock, *J. Rock Mech. Geotech. Eng.*, 5, 18–31.
- Rutqvist, J. and Tsang, C.-F. (2002) A study of caprock hydromechanical changes associated with CO₂-injection into a brine formation, *Environmental Geology*, 42, 296–305.
- Rutqvist, J., Wu, Y.-S., Tsang, C.-F., and Bodvarsson, G. (2002) A modeling approach for analysis of coupled multiphase fluid flow, heat transfer and deformation in fractured porous rock, *International Journal of Rock Mechanics & Mining Sciences*, 39, 429–442.
- Shen, X. and Shen, G. (2002) A fracture-energy-based elasto-softening-plastic constitutive model for joints of geomaterials, *Applied Mathematics and Mechanics*, 23(9), 1097–1104.
- Sloan, S.W. (1987) A fast algorithm for constructing Delaunay triangulations in the plan, *Advances in Engineering Software*, 9(1), 34–55.
- Taniguchi, T., Yamashita, Y., and Moriwaki, K. (2002) Generation of arbitrary 3-dimensional domain from nodes on its surface, *8th Conference on Numerical Grid Generation*, Hawaii, USA.
- Thomure, J.L., Bolander, J.E., and Kunieda, M. (2001) Reducing mesh bias on fracture within rigid-body-spring networks, *Journal of Structural Mechanics and Earthquake Engineering*, 18(2), 95–103.
- Yip, M., Mohle, J., and Bolander, J. (2005) Automated modeling of three-dimensional structural components using irregular lattices, *Computer-Aided Civil and Infrastructure Engineering*, 20, 393–407.
- Zhang, K., Wu, Y.S., Bodvarsson, G.S., and Liu, H.H. (2004) Flow focusing in unsaturated fracture networks: a numerical investigation, *Vadose Zone Journal*, 3, 624–633.

6. Summary

(1) Investigation of the Impacts of High Temperature Limits with THMC modeling

This section documents progress on simulations to analyze the impact of strongly elevated temperature on the bentonite backfill and near-field clay host rock in a geologic repository for radioactive waste. One of the major achievements in FY15 is the implementation of a time-step management scheme in the TOUGHREACT-FLAC3D simulator to reduce the simulation time, which enables us to extend the simulations from 1,000 years to 100,000 years. The simulator was also revised to include chemical-mechanical coupling for clay formations. Specific findings are as follows:

- Results for 100,000-year simulations have found some degree of illitization in the EBS bentonite and NS clay formation and that illitization is enhanced under higher temperature. Other major chemical alterations include the dissolution of K-feldspar and calcite, the precipitation of quartz, chlorite, and kaolinite. The most important chemical factors for illitization are the concentration of K and dissolution rate of K-feldspar.
- Model results reveal that for the “high T” scenario, illitization is stabilized after about 2,000 years in bentonite near the waste package, but continues in bentonite near the EBS-NS interface. For the “low T” scenario, illitization is nearly stabilized after 2,000 years for the entire volume of EBS bentonite.
- In contrast to the previous 1,000-year simulations in Liu et al., (2013) and Zheng et al., (2014), the simulation results at 100,000 years show that bentonite near the EBS-NS interface undergo more illitization than that near the waste package for the “high T” scenarios.
- The dissolution rate of K-feldspar, which was thought to be critical for illitization as revealed by the 1,000-years simulations, is not as important as the amount of K-feldspar available for longer time periods.
- The simulations conducted in FY15 also reveal that the dissolution of calcite delays illitization by around 30-50 years for the case of Kunigel-VI and FEBEX bentonite if Ca-smectite is the major smectite phase in the bentonite. Although this effect is short-lived and not important as far as long term illitization is concerned, calcite dissolution might explain why illitization was not observed in some laboratory and field experiments.
- The effect of chemical changes on swelling stress as a result of smectite dissolution in bentonite was analyzed for a time period of 100,000 years. The results show more significant reductions in swelling stresses, ranging from 3% to 53%, than previously revealed by the 1,000-year simulations. Greater reductions in swelling stress were found at higher temperatures for Kunigel-VI bentonite compared with FEBEX bentonite.
- Chemical effects were incorporated in the mechanical model for the clay formation and the effect of chemical change in clay formation on the total stress was evaluated. Chemical change leads to about a 2.6% decrease in stress near the EBS-NS interface and about 0.7% in the far field. In general, chemical change does not have significant impact on the stress in the clay formation.

In the remaining months of FY15 and FY16 the following activities are proposed:

- A more rigorous approach to link chemistry to mechanics is needed for more accurate calculations than the current extended linear elastic swelling model. More comprehensive links between chemistry and mechanics, taking advantage of the framework provided by

a dual-structure model, was implemented in TOUGHREACT-FLAC (Rutqvist et al., 2014), and could be used to simulate the chemical-mechanical coupling for EBS bentonite in the future.

- In the current model, the canister serves only as a heat source; chemical changes on the surface of the canister are neglected for simplification. Further model analysis is needed to consider chemical changes in the canister, specifically the release of Fe^{+2} , which might enhance the dissolution of smectite by forming chlorite.
- Current models show significant precipitation of silicate minerals during illitization, which could result in the cementation of bentonite and subsequently lead to change in the mechanical properties of bentonite. While the current model can quantify the formation of silicate minerals, the change of mechanical properties as result of cementation needs to be quantified. This requires a mechanical-chemical (MC) coupling scheme for cementation to be incorporated and tested in the next version of the simulator.

(2) Developing THMC models for FEBEX-DP

The key findings from current modeling work are as follows:

- Adjusting key hydrological parameters such as permeability of bentonite and granite may lead to the good fit of measured relative humidity at given location, but cannot explain relative humidity across the entire bentonite barrier. Mechanical change (especially swelling) has to be considered.
- Including non-Darcian flow into the TH model leads to a significant underestimation of the relative humidity data in the entire bentonite barrier (even in bentonite near the bentonite/granite interface). The reason could be that the calibration of relative permeability (and retention curve) already encompasses the nonlinear relationship between gradient and flux for bentonite, which would obviate the consideration of Non-Darcian flow in the model. Non-Darcian flow under unsaturated conditions still needs more study.
- In comparison with the chemical data obtained after the dismantling of heater 1 in 2002, the THC model captures the general trend of the concentration profiles of major cations and anions. However, the model overestimate the concentration level in bentonite near the bentonite/granite interface; this effect will be reduced when mechanical change is included in the model, i.e. with THMC models.
- The preliminary prediction of the chemical change after the dismantling of heater 2 shows that concentration levels of aqueous species will continue going down in bentonite near the heater; calcite dissolves and dolomite forms, and illite precipitates in bentonite near the bentonite/granite interface, accompanied by the dissolution of smectite at the same place.

In the remaining months of FY15 and FY16, the following activities are recommended:

- The mechanical processes will be added to the current THC model. Once coupled THMC model is developed, mechanical-hydrological coupling will be calibrated against measured stress, dry density, water content and relative humidity data.

- The chemical model will be further refined. Once the concentration profile of chloride can be nicely matched by the THMC model, predictions will be made for other chemical species and mineral phases.
- Once the corrosion of the steel liner is analyzed, chemical changes of steel will be included in the chemical model to evaluate the interaction of steel and bentonite.

Ultimately, after the THMC models for FEBEX *in situ* test are fully validated with data, they will be used to explore THMC change in the long run under higher temperature.

(3) THM modeling: FE heater test and DECOVALEX

While the work in previous years has been focused on model development and testing, in FY2015 work has been focused on modeling of the large scale *in situ* heater experiments involving both bentonite and rock, the Mont Terri HE-E, Horonobe EBS, and Mont Terri FE experiments. The main accomplishment in FY2015 is that we have been able to successfully conduct model predictions of the THM responses at all three of these experiments using state-of-the-art constitutive models for bentonite and host rocks. Some comparison to measured data has been conducted in the case of the Mont Terri HE-E experiment.

The heating has just started in 2015 for the Horonobe EBS experiment and the Mont Terri FE experiment, and comparison between measured and predicted responses can be started once the data is provided to the modeling teams. In the remaining months of FY15 and FY16 the following activities are recommended:

- For the remainder of FY2015 we plan to complete interpretive modeling of the Mont Terri HE-E experiment and Horonobe EBS experiment as part of the DECOVALEX-2015 project, which is due to end at the end of year 2015. Related to the Mont Terri FE experiment, LBNL will participate in a joint journal paper with the Swiss nuclear waste organization NAGRA and other organizations in a Mont Terri 20-year anniversary, scientific paper for the Swiss Journal of Geosciences. This will include work done by FE experiment modeling teams, including code benchmarking and design modeling predictions.
- Our work for FY2016 will be first to complete and document work related to DECOVALEX-2015 and at the same time initiate work related to DECOVALEX-2019. It is very likely that the Mont Terri FE experiment will be part of DECOVALEX-2019; it will be an upscaling from the half-scale HE-E experiment to the full scale FE experiment. We also propose that our work on coupled THM modeling be focused on 1) improving and gaining experience in applying the dual-structure model for granular bentonite and 2) implementing and applying damage models for the evolution of the excavation damaged zone in host rocks.
- One of the main Tasks for FY2016 will be the improvement of the BExM in TOUGH-FLAC and to gain experience in applying it efficiently, including gaining confidence in the determination of input parameters. The inclusion of the FE heater experiment into DECOVALEX-2019 will be helpful for international collaboration on this, including collaboration with the University of Catalonia, which is the only other group in the world that has implemented BExM into a numerical simulator.
- The implementation and application of a damage model for the evolution of the excavation disturbed zone will be an important addition to the current model for

calculating the evolution of permeability along with damage as well as sealing and healing. Different approaches can be tested, building upon previous work on the Two-Part Hooke's Model (TPHM), as well as other continuum damage models considering fracture evolution implicitly. Such a model can be benchmarked against discrete fracture modeling of damage-zone fractures using TOUGH-RBSN. The goal is to build a pragmatic continuum model that can be validated against field experiments such as sealing experiments conducted in underground research laboratories.

- These activities will allow significant progress to be made toward achieving UFD goals to fill data needs and confirm advanced modeling approaches (by 2015), and to have a robust modeling and experimental basis for evaluation of multiple disposal system options (by 2020).

(4) Discrete Fracture Network (DFN) Approach for THM Damage Modeling in Argillaceous Rock

In this study, an effective coupling between the TOUGH2 and the RBSN approach has been implemented and applied to hydraulic fracturing simulations. The simulator provides a discrete representation of hydrological (flow and mass transfer through fracture networks) and mechanical (fracture initiation and propagation) responses within geomaterials using the DFN approach within unstructured Voronoi grids. The numerical program is verified through a simulation of a single fluid-driven fracture which is found to be in close agreement with an analytical solution. The model has also been used for predictive simulations of hydraulic fracturing within complex pre-existing fracture networks. The simulation results demonstrate relevant modeling capabilities of TOUGH-RBSN, and the sensitivity analysis provides insights for controlling hydraulic fracture propagation.

While the simulation results demonstrate the relevant modeling capabilities of TOUGH-RBSN for tightly coupled hydro-mechanical behavior, unphysical features exist due to the equilibrium-based calculations of the RBSN models within the current THM coupling procedure. To resolve the numerical artifacts, we have initiated development of a new dynamic simulation framework for RBSN. A summary of the accomplishments so far is as follows:

- The basic methodology to compute the elemental forces (i.e., force-displacement relationship) is based on the existing RBSN approach.
- The equations of motion of Voronoi cells are solved to get the nodal accelerations, which are integrated through a time-stepping procedure (e.g., velocity Verlet algorithm) to derive the nodal velocities and displacements.
- Boundary effects due to the wave reflection can be suppressed using layered damped masses over the boundary.

In the remaining months of FY15 and FY16 the following activities are recommended:

- Regarding the RBSN to TOUGH2 coupling module, hydrological properties (e.g., permeability) of an individual fracture will be defined on the basis of the fracture aperture in order to conduct quantitative simulations.
- Also, in the Mohr-Coulomb fracture criterion, gradual damage by shrinking the fracture surface will be implemented for more realistic energy-based fracture processes.
- The dynamic simulation framework uses explicit time integration schemes without building the whole system matrix and its inverse, so the program code is expected to be easily parallelized for large-scale computations.

- Verifications of the dynamic simulation framework will be provided through simple geomechanics examples.

Acknowledgement

Funding for this work was provided by the Used Fuel Disposition Campaign, Office of Nuclear Energy, of the U.S. Department of Energy under Contract Number DE-AC02-05CH11231 with Lawrence Berkeley National Laboratory.

**Summary of Baseline Experiments for Generic Repository Engineered Barriers
(PART III)**

1 Introduction

The U.S. Department of Energy has designed the Used Fuel Disposition Campaign to investigate the design and safety function of generic nuclear geologic repositories in a variety of geologic settings. The evaluation of engineered barrier system (EBS) concepts and interaction with the wall rock (i.e., natural barriers), waste canisters, or other EBS interfaces are important to the long term performance and safety of geologic repositories (Nutt et al., 2011, Jove-Colon et al., 2011). The European community (EC), especially the French, have investigated bentonite stability in contact with steel under a variety of experimental conditions in an attempt to replicate repository conditions (Pusch 1979; Madsen 1998; Meunier et al. 1998; Guillaume et al. 2003; Wersin et al. 2007; Mosser-Ruck et al. 2010; Ferrage et al. 2011). The majority of their research was focused on lower temperature environments and atmospheric pressures. With the US considering the possibility of either dense packing or the use of dual purpose canisters, the differences in heat load associated with dual purpose canisters were summarized by Caporuscio et al. (2014) and described as follows. “At present, dual purpose canister designs vary greatly, but, in most cases, canisters will be constructed from steel or stainless steel with a steel reinforced concrete overpack (IAEA 2000). In some designs, copper cladding can be added on to the steel canister (Pusch 2008). These canisters can have up to 32 spent fuel assemblies (32 pressurized water reactors or 32-PWR), while many of the European concepts are limited to four spent fuel assemblies (4-PWR) (Pusch 2008; Greenburg and Wen 2013). This increased number of spent fuel assemblies will generate a greater amount of heat radiating into the host rock. High-level modeling suggests a 32-PWR waste package (at 60 gigawatt-days per metric ton burnup) disposed in a clay/shale host rock, has the potential to reach 299°C after 85 years within 1 meter from the waste package (25 years ventilation; 15 m package spacing; Greenberg and Wen 2013). These results are just one of many models or designs for a U.S. nuclear repository, but, this particular model provides one possible high temperature scenario (Figure 1)”. Our experimental program aims to characterize how EBS components react and change at reasonable high temperature in-situ repository conditions.

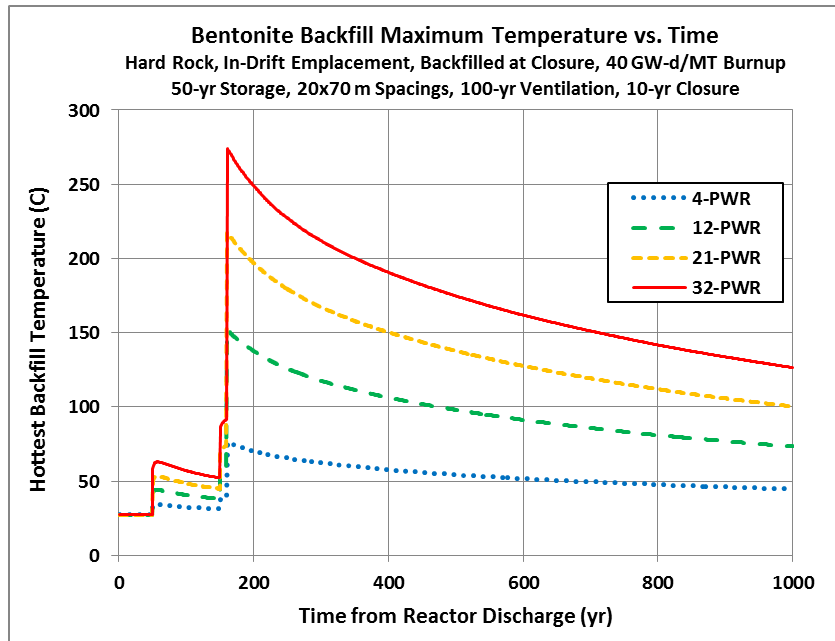


Figure 1. Bounding backfill temperature histories at the waste package surface, for in-drift emplacement in crystalline rock (2.5 W/m-K) with a compacted bentonite backfill (0.6 W/m-K). Backfill rehydration is neglected as a bounding approximation. Waste packages with various capacities are plotted, for fuel with 40 GW-d/MT burnup. For this comparative calculation all packages would be stored at the surface 50 years, then ventilated in the repository 100 years, and finally backfilled over a period of 10 years before permanent closure (personal communication from Ernest Hardin). (From Caporuscio et al., 2014)

2 Background

One of the more accepted ideas for high-level nuclear waste disposal is to emplace the steel waste canister in a geological repository with a bentonite barrier between the canister and host rock (Pusch 1979; Meunier et al. 1998). Bentonite is used to provide 1) a physical barrier to prevent fluid seeping in from natural surroundings and interacting with the waste package, 2) a chemical barrier by attenuating actinide migration if a release occurs. Furthermore, the bentonite's swelling capacity has the capability of self-sealing if cracks develop within the bentonite due to shrink-swell phenomena. However, there remain large uncertainties regarding the long-term stability of bentonite at potential repository conditions, particularly, under prolonged periods of high thermal loads. There have been numerous investigations on the stability of bentonites under various repository conditions and in contact with various metals replicating possible canister compositions (Pusch 1979; Madsen 1998; Meunier et al. 1998; Guillaume et al. 2003; Wersin et al. 2007; Mosser-Ruck et al. 2010; Ferrage et al. 2011).

This part of the report summarizes the various authigenic minerals occurring within hydrothermal experiments replicating a high temperature repository environment. Various reactions include unprocessed Wyoming bentonite, the clay/metal interface, and the metal/clay/host rock components. Much of the characterization and discussion on the early EBS (1-12) results have been published in Cheshire et al. (2013; 2014). Characterization of both the pre-run materials and post experiment phases of experiments EBS-1 through -17 (experiment conditions are listed in Table 1) have been included to better describe the processes that progress during the hydrothermal reactions. In addition to expanded analyses of the earlier reactions,

experiments on host-rock interaction and post-heat cooling were conducted to further our understanding of this complex system. The synthetic brine chemistry had slight variation between different batches, with all 4 Stripa brines listed in Table 2, and the initial Opalinus clay synthetic groundwater depicted in Table 3.

Table 1 Initial components and reaction conditions for EBS experiments. EBS-8 developed a leak during experiment. This experiment was discarded and repeated as EBS-11.

Experiment	Clay, g	Brine, g	EBS Component	Run temp, °C	Run time
EBS-1	7.4	79	Bentonite only	25/100/200/300/25	4 weeks
EBS-2	7.2	62	304SS	25/100/200/300/25	4 weeks
EBS-3	6.79	59.4	316SS	25/100/200/300/25	5 weeks
EBS-4	16.21	145	Cu	25/100/200/300/25	5 weeks
EBS-5	15.77	135.9	304SS	300	6 weeks
EBS-6	12.11	104.2	Low-C Steel	25/100/200/300/25	5 weeks
EBS-7	14.63	157.9	Graphite	25/100/200/300/25	5 weeks
EBS-8	15.28	131.9	Cu (FAILED)	300	6 weeks
EBS-9	15.52	167.6	Quartz sand	25/100/200/300/25	5 weeks
EBS-10	21.11	182.3	316SS	300	6 weeks
EBS-11	15.04	129.8	Cu	300	6 weeks
EBS-12	208.5	41.7	Run for LBNL	300	7 weeks

Table 1 (cont.)

6 MONTH EXPERIMENTS

EBS-13	29.62	245.3	316 SS	300 to 120	6 months
EBS-16	29.62	248.3	Cu	300 to 120	6 months

OPALINUS CLAY EXPERIMENTS

EBS-14	14.86	128.1	Opalinus Clay	300	6 weeks
EBS-15	14.72	158.5	Opal - 316SS	300	6 weeks
EBS-17	14.44	155.2	Opal - Cu	300	6 weeks

Table 2 Synthetic groundwater chemistries used in the hydrothermal experiments. All values were measured at 25°C.

	Stripa V2.1	Stripa V2.2	Stripa V2.3	Stripa V2.4
Species	mg/L	mg/L	mg/L	mg/L
Ca ²⁺	93	95	43	61
Cl ⁻	931	455	686	882
K ⁺	583	9	299	559
Na ⁺	171	166	162	201
Si	1	2	2	1
SO ₄ ²⁻	46	48	31	53
Sr ²⁺	0.05	<0.05	<0.05	0.06
TDS	1863	773	1226	1759
pH	7.35	9.48	6.93	11.2
Experiment Used	EBS 1-5	EBS 6-9	EBS 10-12	EBS 13, 16

Table 3 Synthetic groundwater chemistry used in the Opalinus Clay experiments. All values were measured at 25°C. n.m. = not measured

	Type Solution	Actual Solution
Species	mg/L	mg/L
Ca ²⁺	421	426
Cl ⁻	5672	6470
CO ₃ ²⁻	162	n.m.
K ⁺	221	225
Na ⁺	3885	3846
Si	5	1
SO ₄ ²⁻	2305	998
Sr ²⁺	27	0.16
TDS	11502	12153
pH	7.24	7.50
Experiment Used		EBS 14, 15, 17

3 Methods

All three of the following descriptions (Experimental Setup, Mineral characterization, and Aqueous geochemical analyses) are included here for completeness in this summary document. The three sections are taken verbatim from Caporuscio, et al. (2014).

3.1 Experimental Setup

The bentonite used in this experimental work is mined from a reducing horizon in Colony, Wyoming. The bentonite was pulverized and sieved to < 3 mm and used with a free moisture of ~15.5 wt. %. The synthetic groundwater solution was chosen to replicate a deep groundwater composition (Table 1, Stripa sample V2 (69-4), Frape et al. 2003). The groundwater solution was prepared using reagent grade materials dissolved in double deionised water. NaOH and HCl were added to adjust the initial solution pH. This solution was then filtered through a 0.45 μm filter and sparged with He before each experiment. The salt solution was added at 9:1 water: bentonite ratio. Initial components for all experiments have been summarized in Table 3.

A second series of experiments were performed to examine the bentonite system with host rock inclusion. Host-rock experiments focused on Opalinus Clay from the Swiss Underground Research Laboratory located at Mont Terri. The core was collected from BFE-A10 drillcore (interval from 11 to 12 m and interval from 33 to 34 m from the borehole head). A portion of the Opalinus Clay was crushed and sieved with 10 mesh (~2 mm). Opalinus Clay to be used in experiments was reconstituted at 80 wt.% -10 mesh and 20 wt.% +10 mesh. Synthetic groundwater was chosen to replicate the groundwater composition that represents Opalinus Clay porewater (Table 2, Pearson et al., 2003). The salt solution was added at 9:1 water: rock ratio.

The redox conditions for each system were buffered using a 1:1 mixture (by mass) of Fe_3O_4 and Fe° added at 0.07 wt. % of the bentonite mass. Approximately 7 wt. % (of total solids mass) 304 stainless steel (NIST SRM 101g), 316 stainless steel (NIST SRM 160b), Cu-foil, and low-carbon steel (provided by Sandia National Laboratory) were added to the experiments to mimic the presence of a waste canister.

Reactants were loaded into either a flexible gold or titanium bag and fixed into a 500 mL Gasket Confined Closure reactor (Seyfried et al. 1987). Experiments were pressurized to 150 - 160 bar and were heated following three different temperature profiles: 1) 120°C for 2 weeks, 210°C for 2 weeks, and then 300°C for 1 week, 2) isothermal at 300 °C for 6 weeks and 3) 300°C for 4 months, 210°C for 1 month, and 120°C for 1 month. Reaction liquids were extracted during the experiments and analyzed to investigate the aqueous geochemical evolution in relationship to mineralogical alterations. The sampled reaction liquids were split three-ways producing aliquots for unfiltered anion, unfiltered cation, and filtered (0.45 μm syringe filter) cation determination. All aliquots were stored in a refrigerator at 1°C until analysis.

3.2 Mineral Characterization

X-ray diffraction (XRD) analyses of experimental materials determined mineral compositions. Each sample was ground with 20 wt. % corundum (Al_2O_3) for quantitative XRD analysis of the bulk rock (Chung 1974). XRD measurements were conducted with a Siemens D500 diffractometer using Cu-K α radiation. Data were collected from 2 to 70 $^\circ 2\theta$ with a 0.02 $^\circ 2\theta$ step-size and count times of 8 to 12 seconds per step. To better analyze the non-clay and clay

fractions, the < 2 μm particles were separated via sedimentation in DI H₂O. An aliquot of the < 2 μm suspension was dropped on a zero-background quartz plate and dried. This oriented mount was X-rayed from 2 to 40 °2θ at 8 to 12 s per step. The oriented mount was then saturated with ethylene glycol in a 60 °C oven for 24 hours and XRD analysis was repeated. A portion of the > 2 μm particles was ground with a mortar/pestle, deposited on a zero-background quartz plate, and X-rayed under the same parameters as the bulk powder material. The remaining > 2 μm portion was used for electron microscopy. Mineral identification and unit-cell parameters analysis was performed using Jade[®] 9.5 X-ray data evaluation program with ICDD PDF-4 database. Quantitative phase analysis (QXRD) was performed using FULLPAT (Chipera and Bish 2002). Illite-smectite composition of higher-ordered (R1-3) illite-smectites were modeled via ClayStrat+ (developed by Hongji Yuan and David Bish). Expandable component abundances for the disordered illite-smectites were calculated via the Δ°2Θ method (Środoń 1980; Eberl et al. 1993; Moore and Reynolds 1997). A regression from calculated data were used to calculate the % expandable (%Exp) component in each untreated and reacted bentonite. The equations are:

$$\% \text{Exp} = 973.76 - 323.45\Delta + 38.43\Delta^2 - 1.62\Delta^3 \text{ (Eberl et al. 1993, Eq. 3, } R^2=0.99),$$

with Δ corresponding to Δ°2Θ between the 002 and 003 peak positions for the oriented, ethylene glycol saturated samples.

Analytical electron microscopy was performed using a FEI[™] Inspect F scanning electron microscope (SEM). All samples were Au/Pd-coated prior to SEM analysis. Imaging with the SEM was performed using a 5.0 kV accelerating voltage and 1.5 spot size. Energy dispersive X-ray spectroscopy (EDX) was performed at 30 kV and a 3.0 spot size.

Electron microprobe (EMP) analyses were performed at the University of Oklahoma using a Cameca SX50 electron microprobe equipped with five wavelength-dispersive spectrometers and PGT PRISM 2000 energy-dispersive X-ray detector. Petrographic characterization was performed by backscattered electron imaging coupled with energy-dispersive X-ray analysis, using beam conditions of 20 kV acceleration and 20 nA sample current. Quantitative analysis was performed by wavelength-dispersive spectrometry using 20 kV accelerating voltage, 20 nA beam current, and 2 μm spot size. Matrix corrections employed the PAP algorithm (Pouchou and Pichoir 1985), with oxygen content calculated by stoichiometry. Counting times were 30 seconds on peak for all elements, yielding minimum levels of detection (calculated at 3-σ above mean background) in the range of 0.01 to 0.03 wt. % of the oxides for all components except F (0.16 wt. %). All standards for elements in the silicates were analyzed using 30 second count times on peak, using K-alpha emissions. Extensive appendices on the analytical data collected in this work are included as a separate volume (Vol. II)

. The standards and oxide detection limits are presented in Appendix A, with analytical data presented in Appendix B. Aqueous geochemical results are presented in Appendix C.

3.3 Aqueous Geochemical Analyses

Major cations and trace metals were analyzed via inductively coupled plasma-optical emission spectrometry (Perkin Elmer Optima 2100 DV) and inductively coupled plasma-mass spectrometry (Elan 6100) utilizing EPA methods 200.7 and 200.8. Ultra-high purity nitric acid was used in sample and calibration preparation prior to sample analysis. Internal standards (Sc, Ge, Bi, and In) were added to samples and standards to correct for matrix effects. Standard Reference Material (SRM) 1643e Trace Elements in Water was used to check the accuracy of the multi-element calibrations. Inorganic anion samples were analyzed by ion chromatography (IC) following EPA method 300 on a Dionex DX-600 system. Again, aqueous geochemical results are presented in Appendix C.

4 Results/Discussion

4.1 Summary of Previous Work

Caporuscio, et al. (2014) and Cheshire et.al. (2014) have written extensively on the results of most of the experiments produced for the Argillite EBS research program. To that effect, I will first summarize our findings from FY-14 and then provide updates on experimental characterization results from 2015.

4.1.1 Layer Charge

A series of 45 capsule experiments were designed to interrogate if any layer charge increase took place during the EBS experiments (Caporuscio, et al., 2014). Smectite swelling is the competing effects between the interlayer cation hydration energy (hydration-repulsion) and the Coulombic attractive forces between negatively-charged 2:1 layers and positively-charged interlayer cations (Laird, 1996; 2006). When Coulombic attractive forces dominate over hydration-repulsion collapse of the interlayer spaces occurs. Collapse can be cause by several possible scenarios, increased layer charge (i.e., illitization), increased interlayer cation charges (i.e., interlayer exchange reactions), or decreased interlayer cation hydration energy (i.e., interlayer exchange reactions). Alternatively, swelling occurs when the hydration-repulsion dominates over the Coulombic attractive forces. . It is evident (Caporuscio etal, 2014) that there is variation in the layer charge within the starting montmorillonite, but the current EBS reaction conditions do not significantly alter the layer charges or charge distribution. This is also confirmed by the CEC measurement showing no change in CEC values between all reaction products and the starting montmorillonite.

4.1.2 Illitization

There was no evidence of illite-smectite mixed-layering during the six-month cooling experiment where montmorillonite was heated to 300°C for four months, consistent with the other EBS experiments in our Na-dominated hydrothermal systems. The following description from Caporuscio et al. (2014) summarizes the smectite-illite transformation complexity and explains why our experiments do not generate illite:

“Smectite-to-illite transformation is not well understood and probably follows several different reaction pathways, i.e. solid-state transformation and dissolution-precipitation (Güven 2001; Dong 2005; Zhang et al. 2007). These different reaction mechanisms may be due to

different geological or experimental conditions, including variables such as water/rock ratio, fluid composition, redox state, occurrence of microbial organisms, and presence or absence of organic matter (Small et al. 1992; Small 1993; Güven 2001; Dong 2005; Zhang et al. 2007). Solid-state transformation may be operative in closed systems with a low water/rock ratio, whereas, dissolution-precipitation may be the dominant mechanism in open systems with high water/rock ratios (Zhang et al. 2007). In our experiments, it appears that two major parameters are preventing smectite-to-illite alteration: alkali and silica solution compositions.

Current experimental results are consistent with other experimental data showing that a limited supply of K^+ along with a relatively high Na^+ activity significantly decreases dioctahedral smectite illitization rates (Eberl and Hower 1977; Eberl 1978, Eberl et al. 1978; Roberson and Lahann 1981; Mosser-Ruck et al. 1999). Their studies also show that, in general, dioctahedral smectites with low hydration-energy interlayer-cations (e.g., K^+ , Rb^+ , Cs^+) are more susceptible to smectite-to-illite alteration reaction compared to dioctahedral smectites with higher hydration-energy interlayer-cations (e.g., Na^+ , Ca^{2+} , Mg^{2+}). These results are consistent with capsule experiments from the current work. However, the presence of a Na-rich system does not preclude smectite illitization. There have been numerous occurrences of illite and illite/smectite occurring in natural or experimental systems that are Na-dominated (Bannister 1943; Frey 1969; Eberl and Hower 1977; Eberl et al. 1978; Whitney and Velde 1993; Mosser-Ruck et al. 1999; Środoń 1999). But, in all these cases, either the temperatures exceeded 300°C or there was a significant potassium source from groundwater or coexisting minerals. Temperatures beyond 300°C exceed the upper temperature limits expected for a repository environment and the experimental temperature from this investigation (Greenburg and Wen 2013). Additionally, Na-bentonites are currently the bentonite of choice for a repository backfill, thereby, providing a K-depleted and Na-enrich system. Even though the aqueous solutions in the experiments were K-rich, the overall system (bentonite + water) was Na^+ dominant (~ 2,400 mg Na/L) and K^+ poor (~ 1,000 mg K/L). Include Ca^{2+} (~750 mg/L, bentonite + water) in the discussion, the overall ($Na^+ + Ca^{2+}$)/ K^+ ratio is greater than 3.0. It is evident that the dominance of Na^+ and Ca^{2+} along with the low abundance of K^+ does not facilitate illite-smectite formation after 45 days at 300°C.

Silica activities in these experiments appear to be controlled partially by silicate mineral dissolution and precipitation, in addition to clinoptilolite to analcime alteration. Solutions saturated with respect to cristobalite probably contributed to illitization retardation in these current experiments. Systems with silica concentrations higher than quartz saturation have been shown to significantly retard illitization rates (Eberl et al. 1978; Lahann and Roberson 1980; Abercrombie et al. 1994). Abercrombie et al. (1994) has shown that a K-smectite to be the stable phase, potentially up to 200°C, provided silica activity is higher than $\sim 10^{-2}$. It was noted by Abercrombie et al. (1994) that as silica levels decreased, due to quartz precipitation, illitization progressed within the system. Therefore, an environment with silica concentrations saturated with respect to cristobalite at temperatures less than 300°C, such as the current experiments, smectite-to-illite alteration should further be inhibited. However, it is important to consider differences between closed, experimental systems versus geological or repository environments that open to the surrounding environment. Many processes that are observed in a closed, experimental system might be mitigated in an open system where solutes can freely move in and out of the environment.

We have shown that at higher silica activities (i.e., cristobalite saturation) clinoptilolite is altered to a high-silicon analcime under the current experimental conditions. Again, these reactions were observed in the other EBS experiments with extended periods at 300°C. Previous studies (Smyth 1982; Wilkin and Barnes 1998; 2000; Cheshire et al., 2014) have linked changes in Na, Al, and Si activities with the alteration of clinoptilolite by analcime. However, experimental work ($T < 300^{\circ}\text{C}$) from Wilkin and Barnes (1998) indicate silica activity influences clinoptilolite alteration by affecting the reaction affinity rather than controlling the reaction equilibrium. Wilkin and Barnes (1998) also show that analcime can form in an environment saturated with respect to cristobalite provided there is a sufficient change in the Na and/or Al activities.

The effect on the repository due the changes in the system's silica phases and concentrations appears to be a significant issue regarding the repository stability and physical properties. Cementation via silica precipitation is believed to pose the greatest risks to the repository stability and isolation capability compared other mineral reaction (Pusch et al. 1998). Silica precipitation has the potential to weld the smectite lamellae together and reduce the smectite expandability (Pusch et al. 1998; Pusch 2002). The primary mechanism for silica liberation includes smectite illitization, silica/silicate dissolution/saturation, and zeolite alteration.”

4.1.3 $\text{H}_2\text{S}_{(\text{aq,g})}$ Generation

All experiments generated $\text{H}_2\text{S}_{(\text{aq,g})}$, with the 300°C isothermal reactions producing the gas faster and in greater quantities. The $\text{H}_2\text{S}_{(\text{aq,g})}$ is most likely related to pyrite solubility in a chloride-bearing solution (Crerar et al. 1978; Ohmoto et al. 1994). The reducing nature of the experimental system easily preserved the $\text{H}_2\text{S}_{(\text{aq,g})}$ species. Pyrite contents obtained by QXRD analyses for the Colony Wyoming bentonite (0.4 wt%) and Opalinus Clay (1.1 wt%) are listed in Table 4. Sulfide-induced corrosion of the waste canisters is the primary concern for the Swedish repository systems (Börjesson et al. 2010), therefore the Swedish Nuclear Fuel and Waste Management Company (SKB) have emplaced fairly strict sulfur specifications (sulfide content < 0.5 wt. %; total sulfur < 1 wt. %) for the bentonite buffer used in their repositories (Börjesson et al. 2010).

Table 4 Quantitative X-Ray Diffraction (QXRD) analyses of the buffer clay (Wyoming Bentonite) the wall rock (Opalinus Clay) and end product results of all seventeen experiments. Values are in weight percent.

b.d.l. = below detection limit, n.s. = not sampled

	Wyoming Bentonite	Opalinus Clay Switzerland	EBS-1 --	EBS-2 304 SS	EBS-3 316 SS	EBS-4 Cu	EBS-6 LC Steel	EBS-7 Graphite	EBS -9 Quartz	EBS-5 304 SS	EBS-10 316 SS	EBS-11 Cu	EBS-12 20% H ₂ O
			Stepped Heating from 25/100/200/300/25							Isothermal 300°C			
Smectite	72	24.1	81	75	79	79	81	75	73	79	79	80	71
Chlorite	b.d.l.	9.1	n.s.-	n.s.	n.s	n.s	n.s	n.s	n.s	n.s	n.s	n.s	n.s
Kaolinite	b.d.l.	16.9	n.s	n.s	n.s	n.s	n.s	n.s	n.s	n.s	n.s	n.s	n.s
Clinoptilolite	13	0.0	8	9	6	6	7	5	6	2	6	8	4
Analcime / Wairakite	b.d.l.	0.0	b.d.l.	b.d.l	b.d.l	b.d.l	b.d.l	b.d.l	b.d.l	3	1	1	1
Quartz	1	13.8	2	1	2	1	2	3	16	2	3	2	3
Cristobalite/ Opal-C	2	0.0	2	3	2	1	4	5	6	2	6	8	4
Biotite	3	7.4	2	4	1	2	1	+	+	2	1	+	+
Pyrite	0.4	1.1	b.d.l	b.d.l	b.d.l	b.d.l	b.d.l	b.d.l	b.d.l	b.d.l	b.d.l	b.d.l	+
Plagioclase	9	3	4	6	7	6	3	2	2	5	6	5	7
K-Feldspar	b.d.l.	5.9	2	3	3	3	1	1	1	2	2	2	3
Calcite	6	16.4	n.s	n.s	n.s	n.s	n.s	n.s	n.s	n.s	n.s	n.s	n.s
Dolomite	+	0.7	n.s	n.s	n.s	n.s	n.s	n.s	n.s	n.s	n.s	n.s	n.s
Siderite	2	0.1	n.s	n.s	n.s	n.s	n.s	n.s	n.s	n.s	n.s	n.s	n.s
Magnetite		0.0	b.d.l.	b.d.l	2	1	+	+	1	1	b.d.l	b.d.l	b.d.l
Graphite		0.0	b.d.l.	b.d.l	b.d.l	b.d.l	b.d.l	12	b.d.l	b.d.l	b.d.l	b.d.l	b.d.l
Gypsum		0.0	n.s	n.s	n.s	n.s	n.s	n.s	n.s	n.s	n.s	n.s	n.s
Total:	100.4	100	101	101	100	99	99	99	101	100	100	100	99

Table 4 cont. b.d.l. = below detection limit, n.s. = not sampled

	Wyoming Bentonite	Opalinus Clay Switzerland	EBS-13 316 SS	EBS-16 Cu	EBS-14 Opalinus Clay	EBS-15 Opal -316 SS	EBS-17 Opal -Cu
			6 month 300°C to 120°C		6 weeks Isothermal 300°C		
Smectite	72	24.1	69.8	65.2	39.8	51.6	63.8
Chlorite	b.d.l.	9.1	0.0	0.0	11.1	1.3	1.1
Kaolinite	b.d.l.	16.9	0.0	0.0	1.8	0.2	0.0
Clinoptilolite	13	0.0	0.0	1.8	0.0	15.0	11.7
Analcime / Wairakite	b.d.l.	0.0	3.4	4.4	5.5	1.3	3.0
Quartz	1	13.8	2.6	3.2	8.4	5.5	3.3
Cristobalite/ Opal-C	2	0.0	5.1	6.9	0.0	0.0	0.0
Biotite	3	7.4	1.5	2.6	11.9	9.7	2.0
Pyrite	0.4	1.1	0.0	0.0	0.7	0.0	0.2
Plagioclase	9	3	10.3	10.6	3.5	11.8	11.3
K-Feldspar	b.d.l.	5.9	4.7	3.7	4.3	2.3	3.1
Calcite	6	16.4	0.0	0.2	9.4	0.0	0.0
Dolomite	+	0.7	0.0	0.0	0.0	0.0	0.0
Siderite	2	0.1	0.0	0.0	0.0	0.0	0.0
Magnetite		0.0	2.8	1.4	3.1	1.1	0.5
Graphite		0.0	n.s	n.s	n.s	n.s	n.s
Gypsum		0.0	0.0	0.0	0.5	0.3	0.1
Total:	100.4	100	100	100	100	100	100

4.1.4 Dry Clay Experiment for LBNL

At the request of Lawrence Berkley National Laboratory an experiment was run using a bentonite water (15 wt %) mix and held at 300°C for seven weeks. It turns out that dry system kinetics and mineral solubility are highly restricted. Many of the chemical reactions observed in the wet system (9:1 water: rock systems) either do not take place or are restricted in the dry (~ 15 wt. %) system. Pyrite does not undergo decomposition and clinoptilolite undergoes limited dissolution with limited analcime formation. It is evident that reaction kinetics are accelerated under water saturation due to increased ion mobility and minerals' saturation limits.

4.1.5 Mineral Reactions

Caporuscio et al. (2014) provided a succinct and explicit discussion of mineral phase changes during various heating profiles, corrosion effects in bentonite backfill, and reactions with Opalinus Clay (zeolite formation, clay mineralogy, and pH effects). To make this summary document fully usable, that discussion is repeated here:

Heating profile. The mineral evolution and geochemical processes are consistent between all three reactions with differing heating profiles. These profiles were designed to mimic the maximum heating profile during a repository's lifetime, with exception to the duration of each stage: (1) heating from 120°C (2 weeks); 220°C (2 weeks); 300°C (1 week); (2) isothermal, 300°C (6 weeks); (3) cooling from 300°C (16 weeks), 220°C (4 weeks); 120°C (4 weeks). There were no retrograde reactions observed during the cooling phase. Essentially EBS-10 and EBS-13 show no significant differences between the two reaction products.

It would be expected during the early emplacement of the waste canister that silica saturation, exchange reaction will take place under limited conditions. The relatively dry environment of the early bentonite would significantly restrict the mineral reactions due to the limited ion mobility and early saturation. It is possible that sulfide gas could be generated, but as shown in the 15 wt. % free moisture experiment (EBS-12) pyrite decomposition was not readily observed due to the restricted solubility. As temperatures increase to peak temperature (currently unknown and will be determine during repository design), various possible zeolite reactions (mordenite, laumontite, analcime, wairakite formation) will occur due to the precursor clinoptilolite and volcanic glasses. These zeolite reactions, along with silica saturation reactions, will control the porewater solution chemistry and determine any further mineral alteration. Illite formation can still progress, if a K-source is available, but, K-source stability with respect to the repository conditions will determine the illitization rates. As shown in the capsule experiments, adding K-bearing minerals does not necessarily force illitization; dissolution of those mineral phases has to take place. Illitization thermodynamics and kinetics are strongly tied to the alkali, alkaline earth, silica, and hydrogen (pH) activities; therefore, it is difficult to predict whether illitization will occur in a repository. After the high temperature pulse passes and temperatures begin to decrease, retrograde reaction have the potential to further change the high temperature mineralogy. As observed in current work, no significant retrograde reactions took place, but as with any experimental work slow kinetics of such reactions make them difficult to show experimentally. It would be expected silica saturation is maintained at continuing lower temperatures by releasing silica from solution. This in turn should partially cement and fill pores in the bentonite. Retrograde zeolite reactions are expected, but currently the extent of such reaction and types are unknown.

Corrosion in bentonite. Results from these experiments have shown the more dynamic environment associated with this system is at the bentonite-metal interface. Trioctahedral, Fe-rich saponite crystallized on steel surfaces forming a reactive substrate with a high surface area compared to the original steel surfaces. Partial dissolution of the steel plates contributes ferrous iron into the fluid phase while silica and aluminum facilitates Fe-saponite (smectite) crystallization (Figure 2). Liberated Ni, from the steel, partitions into the sulfide phases forming pentlandite ((Fe,Ni)₉S₈) and millerite (NiS). Oxidative leaching of Fe and Ni forms a chromite (Cr_{1.04},Fe_{0.96})(Fe_{0.69},Ni_{0.31})O₄ passivation layer on the outer surface of the 316SS plates, restricting corrosion rates (0.1 μm·d⁻¹ stainless steel) compared to non-alloyed metals (0.6 μm·d⁻¹ low-carbon steel and 0.8 μm·d⁻¹ copper). Formation mechanism for Fe-saponite is not completely understood for this system. There are two possible scenarios for Fe-saponite formation: 1) direct crystallization in a Fe- and Si-rich solution as a result from bulk mineralogy influences or 2) Fe + montmorillonite interactions breaking down montmorillonite and producing Fe-saponite. The latter mechanism would be a deleterious reaction to the overall repository as montmorillonite is primary mineral in the barrier.

Fe-phyllsilicates tend to have strong sorption properties towards actinides and other radioactive materials; therefore, they have the potential to provide added barrier properties for actinide containment. The dynamics and reactivity of actinide adsorption need to be incorporated into the long term repository performance evaluation models. However, this work has never been addressed in repository studies. Inclusion of a reactive, high surface-area canister into used-fuel repositories performance assessments should help provide a viable repository evaluation.

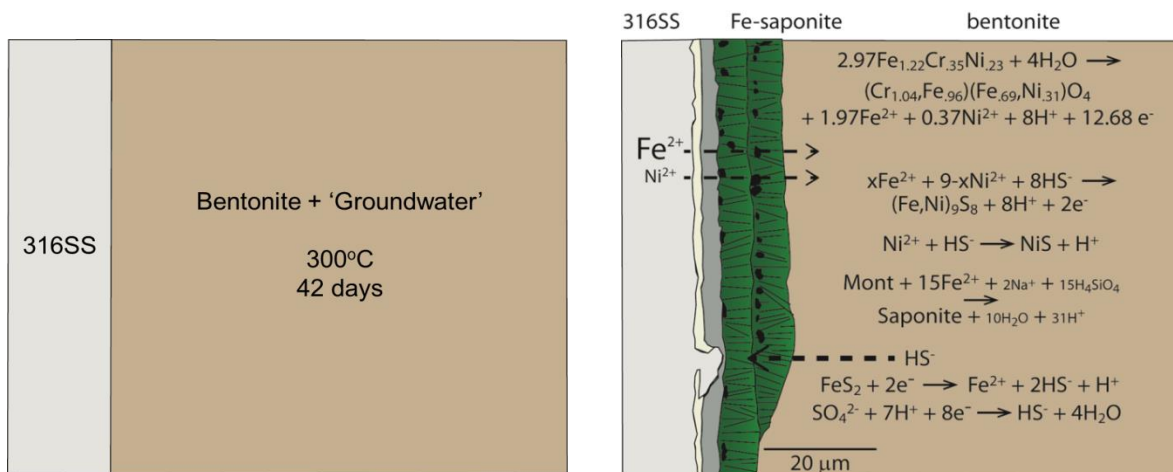


Figure 2. Cartoon of corrosion processes related to EBS experiments containing 316SS.

Opalinus Clay

There are very limited cation exchange reactions associated with the Opalinus Clay and solution chemistry due to no significant amount of smectite. Opalinus Clay is dominated with clay phases (i.e., illite, I-S, kaolinite, and chlorite) that typically do not freely exchange cations.

Zeolite formation. The primary authigenic zeolite in experiments with Opalinus Clay alone differs from the Opalinus Clay experiments with bentonite. These differences appear to be strongly related to the solution chemistry. Bentonite-bearing experiments most likely exchanged Ca into the montmorillonite interlayer producing a Ca depleted solution compared to the

Opalinus Clay experiments. Solution chemistry associated with the Opalinus clay will remain fairly unchanged unless mineral alteration occurs. The changing of solution chemistry as function of the types of clays in the system appears to indirectly control zeolite stability.

The analcime-wairakite series typically forms through dissolution-precipitation mechanisms through an intermediate mineral or glass phase. In the other EBS experiments, it appears that analcime formed from a direct dissolution-precipitation at the expense of precursor clinoptilolite and volcanic glass. This paragenetic sequence has been previously observed by many other researchers (Smyth, 1982; Masuda et al., 1996; Wilkin and Barnes, 1998). Natural paragenetic sequences suggest that clinoptilolite to analcime may progress at temperatures as low as 75 - 90° C (Smyth 1982; Masuda et al. 1996). Alternatively, work from Wilkin and Barnes (1998; 2000) shows analcime formation kinetics are significantly increased at alkaline pH's (9 - 10), whereas, experiments with circum-neutral pH's showed limited to no analcime formation even at with temperatures > 100° C lasting up to 26 days. It is evident that onset temperatures associated with mineral alterations that pH, along with many other solution chemistry parameters, are important to understand.

Wairakite primarily forms when excess silica is present and typically crystallizes through either an intermediate Ca-mordenite ($\text{CaAl}_2\text{Si}_{10}\text{O}_{24}\cdot 7\text{H}_2\text{O}$) or laumontite ($\text{CaAl}_2\text{Si}_4\text{O}_{12}\cdot 4\text{H}_2\text{O}$) phase (Ames and Sands, 1958; Jové and Hacker, 1997). In their experimental works, wairakite was observed to be stable between 315°C and 450°C. However, the inclusion of small amount of Na-substitution lowers the formational conditions for wairakite. Additionally, there are limited isomorphous substitutions between analcime and wairakite making Na- or Ca-enriched end members, as opposed of a true intermediate analcime-wairakite (Steiner, 1955; Coombs, 1955; Ames and Sands, 1958). Na-mordenite has an experimental stability range between 190 to 300°C, whereas, Ca-mordenite ranges from 340 to 380°C (Ames and Sand, 1958).

The possible presence of mordenite and laumontite combined with information from Ames and Sand (1958) and Jové and Hacker (1997) strongly suggests that wairakite in this system is probably from the decomposition of mordenite and/or laumontite. Mordenite and laumontite, therefore, appears to have crystallized from the decomposition of kaolinite in the silica and Na/Ca-rich fluids. This reaction would have progressed either until the reaction was quenched or when one of the reactants was depleted and in this case, kaolinite appears to be the limiting resource as it has been completely removed. The presence of Na in our system appears to have lowered the formation temperatures to below 300°C for Na-enriched wairakite.

However, when bentonite is included into Opalinus Clay experiments, the solution chemistry changes significantly forcing the formation of a high-silicon, Ca-enriched analcime. The analcime composition from this experiment is similar to analcime from EBS experiments with bentonite as the only clay. However, it is evident that the reaction mechanisms are very different. In bentonite only reactions, high-silicon analcime crystallized from clinoptilolite and unaltered glass with in the high Na and $\text{SiO}_{2(aq)}$ fluids. EBS experiments with 20 wt. % Opalinus Clay much of the original clinoptilolite is preserved, but kaolinite is completely removed. When kaolinite and clinoptilolite are present in a Na/Ca-rich fluid, kaolinite is preferentially recrystallized into either Na/Ca-mordenite and laumontite or analcime.

Clay mineralogy. *Following the clay mineral evolution within Opalinus materials is complicated due to the variety of clay minerals present in the Opalinus experimental systems. Two systems were tested: (1) Opalinus Clay and (2) bentonite with 20 wt. % Opalinus Clay. The*

latter experiment was setup to represent mixing between a repository host rock with a bentonite backfill to determine what effects (if any) the host rock has on the backfill material. After thermal processing in brine, the Opalinus Clay appears to have an increase in the I-S distribution. The original Opalinus material appeared to have an R3 illite (0.8-0.9)-smectite, but after 300°C for 6 week in an Opalinus brine an R3 illite (0.9)/smectite and a R1 illite (0.7)/smectite was produced. However, illitization in the host rock may not be a major concern as Opalinus Clay is primarily a low-permeable barrier with very limited swelling capacity due to the low amounts of swelling smectite within the Opalinus Clay. The major concern is the reactivity of Opalinus Clay with the bentonite causing alteration to the bentonite constituents. There was negligible illitization within the bentonite fraction in the mixed reaction (EBS-15). This is consistent with the capsule experiments containing a bentonite with a secondary rock phase. It is important to note that these experiments do not preclude the possibility of host rock – bentonite interaction at these temperatures because kinetics may not allow the observation of mineral alterations under the current experimental duration. With any of these experiments representing repository system, kinetics is always an issue that has to be taken into account when interpreting data.

***pH effects.** Many of the reactions described above are strongly influence by the pH of the system. Most mineral reaction rates that are of concern to a repository are increased under high pH systems. Chermak (1992) showed that under pH conditions of 11-13, Na-rectorite was formed at 150 – 200°C within 17 days. Fully formed Na-mica (paragonite) developed after 32 days. Work from Eberl and Hower (1977) and Eberl (1978) do not show illitization until 260 – 400°C at quenched pH's ranging from 4 – 5. These observations are consistent with the current research. The Opalinus Clay experiment starts with a 7.5 – 7.8 solution pH, but during the reaction the pH drops to 4 – 5. The reactions experience significant zeolite reactions, but it appears illitization does not occur under the Na-dominated environment. These high pH dependent reactions will play a major factor within the bentonite backfill near the concrete liners, especially if the concrete used contains significant K⁺ concentrations. However, these same reactions should have a minor impact on the bentonite backfill near the waste package because steel and copper corrosion tend to lower the pH.*

5 New Information and Interpretation from Characterization of Experiments in FY15

5.1 Illite formation in experimental runs

As discussed in Caporuscio et al. (2014), the bulk composition of the experimental material dominates the formation of illite in a closed system. The experiments with Colony bentonite, Stripa synthetic brine, and metal never generated any measurable illite. It was determined that a combination of silica and Na saturation, along with low K concentrations precluded illitization of the smectites at 300°C. Clay mineral evolution with Opalinus Clay material is more diverse. The starting Opalinus Clay is dominated with illite-smectite (I-S) mixed-layers and discrete illite with minor amounts of smectite. The resultant clay reaction products of EBS-14, EBS-15 and EBS-17 have a bimodal clay composition. The montmorillonite from the bentonite component has not significantly reacted to illite, while the post reaction Opalinus Clay fraction has a clay characteristic similar to the starting Opalinus Clay. Caporuscio et al. (2014) describes the post reaction Opalinus Clay material as a well-crystalline illite and a poorly-crystalline illite displaying a low, broad reflection superimposed on a sharp 10 Å illite reflection. The I-S appears to be a R0 illite (0.1)/smectite and expands to 16.8 Å with a $\Delta 2\theta$ (002/003) values of 5.44°,

corresponding to 91% expandability. R1-3 ordered I-S were not detected. In summary, the starting material, maximum pressure / temperature attained, and the overall bulk chemistry of a specific EBS system will dictate whether secondary illite will form.

5.2 Zeolite phase transformations at elevated temperatures

Cheshire et al. (2014) noted that clinoptilolite (Figure 3a) was the precursor zeolite that transformed to analcime (Figure 3b) at high temperature. The reaction was listed as:

Generalized:



Detailed:

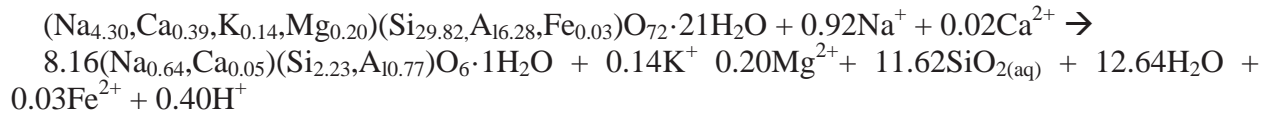
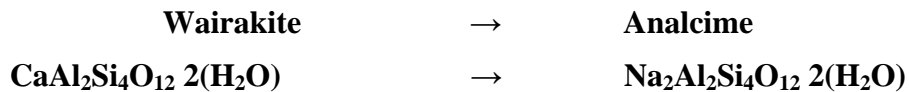
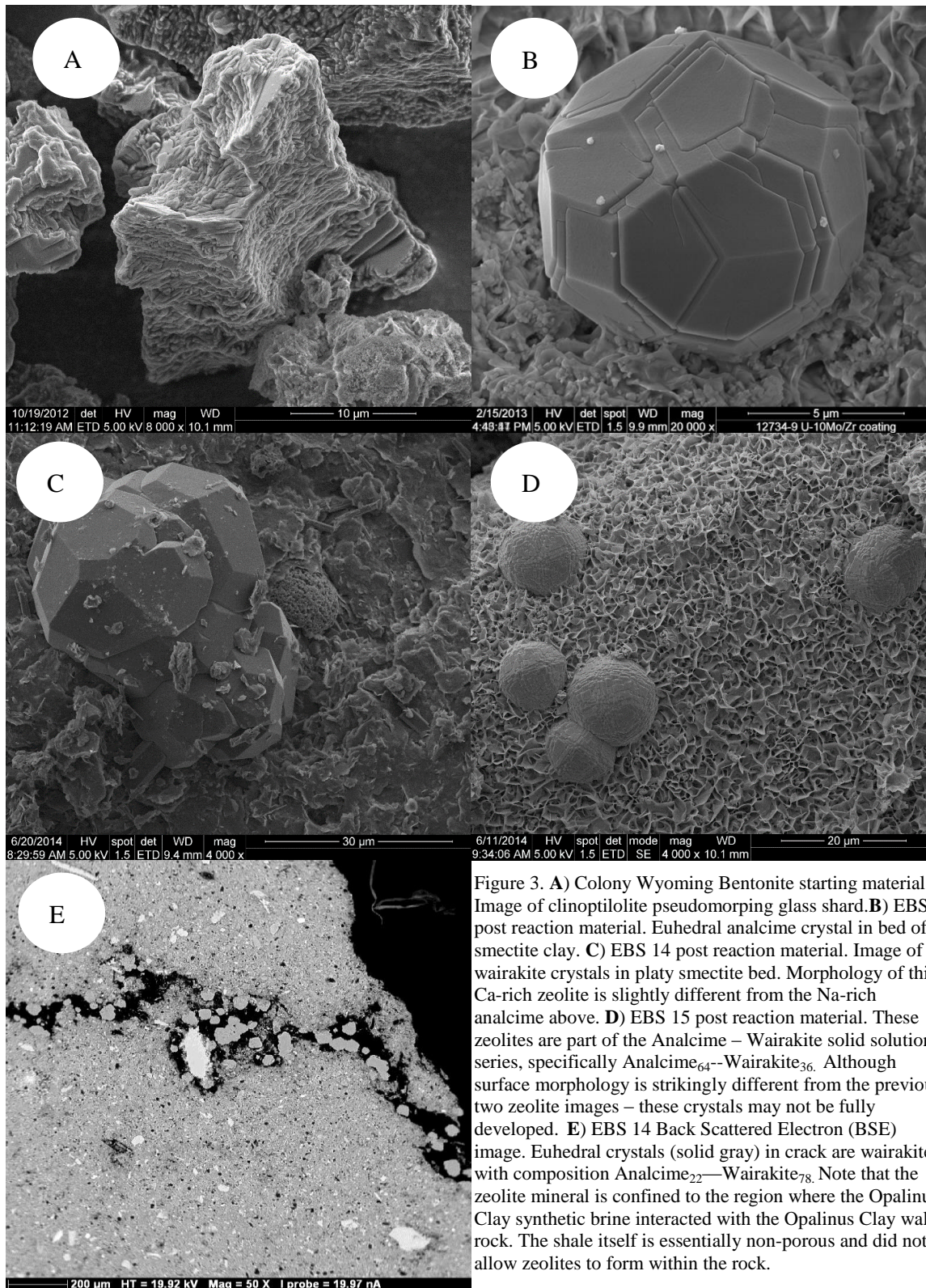


Table 5 presents data on the high temperature zeolite phase in all EBS experiments to date. Note that the experiments with bentonite only produce analcime (Na-rich, monoclinic) phases (Figure 3b). The experiment with Opalinus Clay only (EBS-14) indicates the zeolite wairakite (Ca-rich, triclinic, Figure 3c) has grown at high temperature. Of great interest are experiments EBS-15 and EBS-17, which contain a mixture on Wyoming bentonite as backfill and Opalinus Clay as the wall rock. The resultant zeolite produced (Figure 3d) is intermediate between analcime and wairakite in composition (Table 5). This is in agreement with Seki (1971) and expands the solid solution fields that described therein. Figure 4 depicts the range of wairakite and analcime compositions in terms of the solid solution Na-Ca join. The generalized reaction between the two zeolite phases with complete exchange of Na and Ca is shown below:



Further analysis of this analcime-wairakite solid solution along with that of aluminous and siliceous analcime needs to be performed to accurately describe the zeolite paragenesis of bentonite and clay rock degradation. These analyses emphasizes the importance of solid solutions in the stability of secondary mineral assemblages, particularly within the thermal range between diagenetic and metamorphic systems. There are thermodynamic approaches to model mineral solid solutions, however, their use and application to diagenetic/metamorphic systems is rather restricted given the limited amount of data.



Analcime

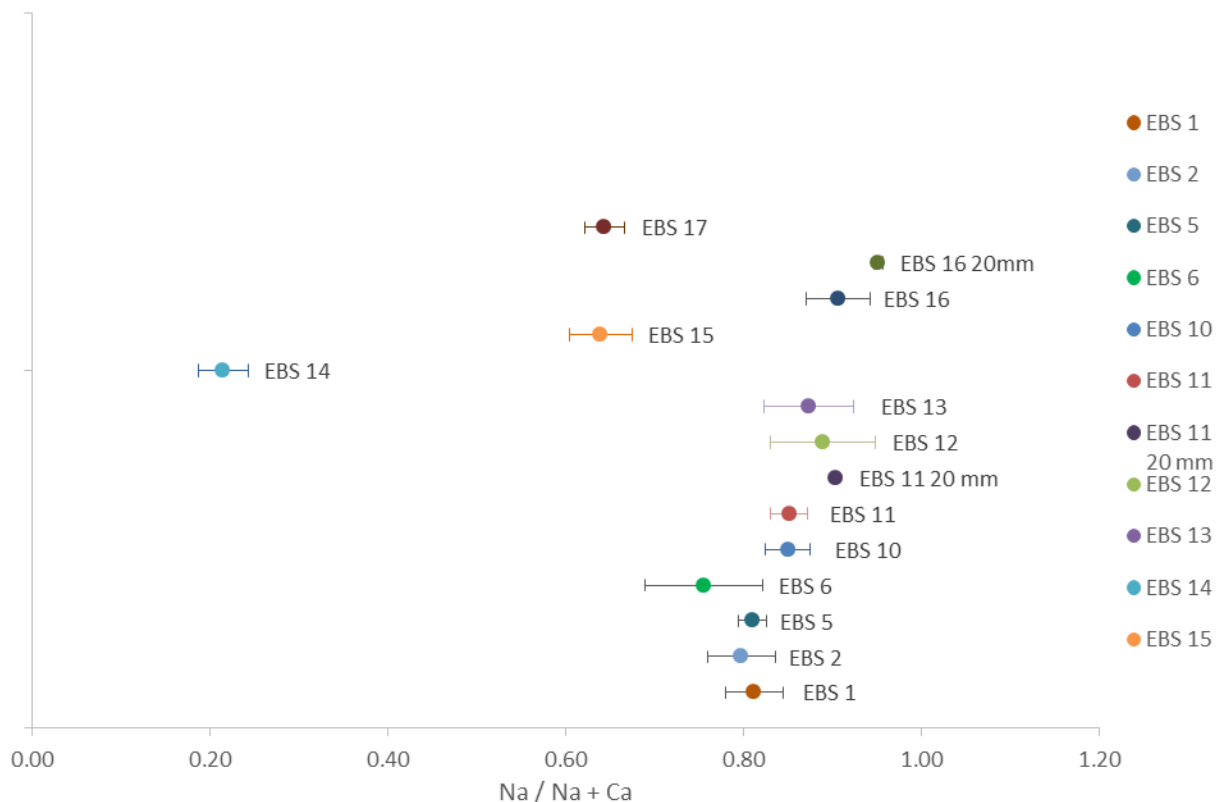


Figure 4. Plot of the analcime—wairakite solid solution compositions for the Na-Ca join. Vertical axis represents the experiments pertaining to the analcime sample analyses. The average compositions (and standard deviations) were obtained from the electron microprobe values given in Appendix B. High Na-dominated zeolites (Analcime) were typically generated in Colony Wyoming bentonite. The highest Ca zeolite (Wairakite₇₈—Analcime₂₂) was observed in in the Opalinus Clay only reaction product. Two experiments (EBS-15 and EBS-17) with both Colony Wyoming bentonite and Opalinus Clay result in intermediate composition analcime—wairakite solid solution minerals.

Table 5 Average (post reaction) zeolite compositions from mineral sample analyses.

Sample	Analcime-Wairakite Solid solution
EBS 1	An ₈₁ -Wrk ₁₉
EBS 2	An ₈₀ -Wrk ₂₀
EBS 5	An ₈₁ -Wrk ₁₉
EBS 6	An ₇₅ -Wrk ₂₅
EBS 10	An ₈₅ -Wrk ₁₅
EBS 11	An ₈₅ -Wrk ₁₅
EBS 11 spot	An ₉₁ -Wrk ₉
EBS 12	An ₈₈ -Wrk ₁₂
EBS 13	An ₈₇ -Wrk ₁₃
EBS 14	An ₂₂ -Wrk ₇₈
EBS 15	An ₆₄ -Wrk ₃₆
EBS 16	An ₉₁ -Wrk ₉
EBS 16 spot	An ₉₅ -Wrk ₅
EBS 17	An ₆₄ -Wrk ₃₆

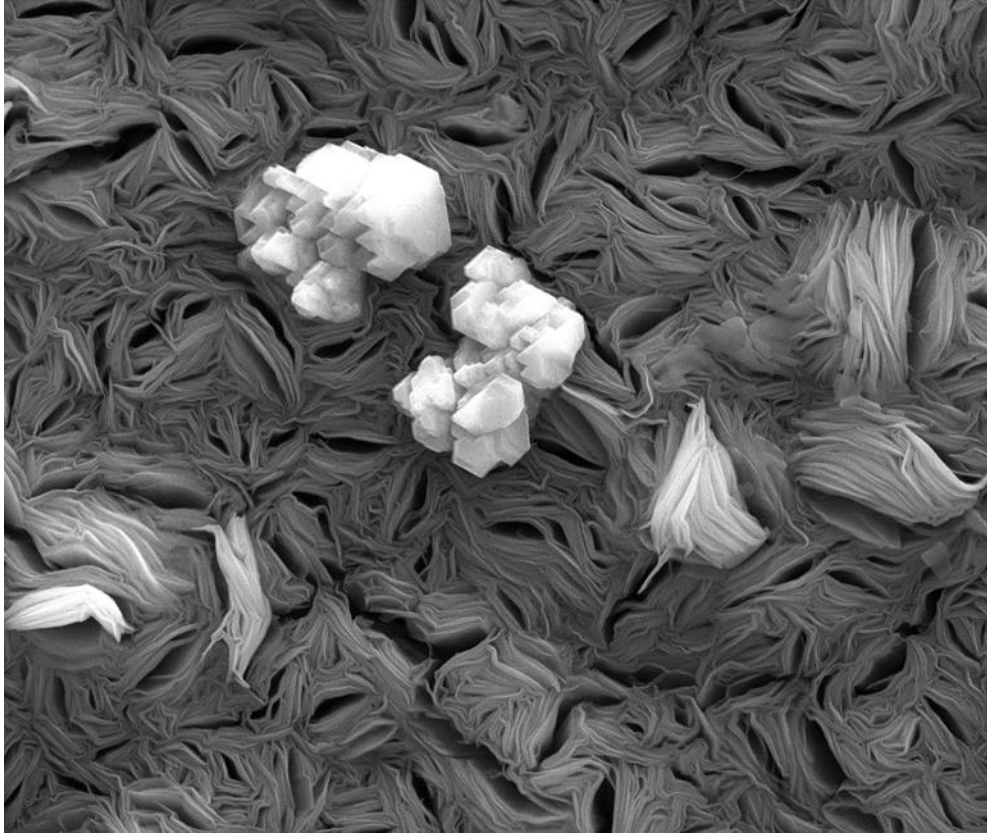


Figure 5. Pentlandite (white) sitting on a bed of Fe-saponite, all of which form as a mantling material on 316 stainless steel.

Figure 3e, which is a reflected light image of the reacted Opalinus Clay, depicts wairakite crystals that formed within a crack in the wall rock material. This is indicative of the complete sample, in that the zeolite forms only on the edges or within cracks of the Opalinus Clay. All petrographic evidence indicates that the Opalinus Clay shale has such limited porosity and permeability that the resultant wairakite crystals can not grow in the matrix. They are relegated to leaching aluminum and silica from the wall rock and nucleating at the rock surface.

5.3 Steel corrosion during elevated pressure/temperature EBS experiments

The following mineral phases have been previously identified (Caporuscio et al., 2014) as growing at the interface between bentonite backfill and various steels: Fe-saponite $[(Ca/2,Na)_{0.3}(Fe^{++})_3(Si,Al)_4O_{10}(OH)_2]$, pentlandite $((Fe,Ni)_9S_8)$ (Figure 5), chromite $(Fe^{++}Cr_2O_4)$, pyrrhotite (FeS) (Figure 7), millerite (NiS) . Figure 6 depicts the growth of the interface assemblage perpendicular to the steel. We have just recently identified another interface material: stilpnomelane (Appendix B.1 and Figure 8.). This Fe-bearing phase seems to only occur when mantling iron metal is present (one of our solid buffer materials). Although stilpnomelane is a common metamorphic mineral and occurs over a wide P, T spectra (Winkler, 1976) there is a dearth of occurrences reported in experimental literature.

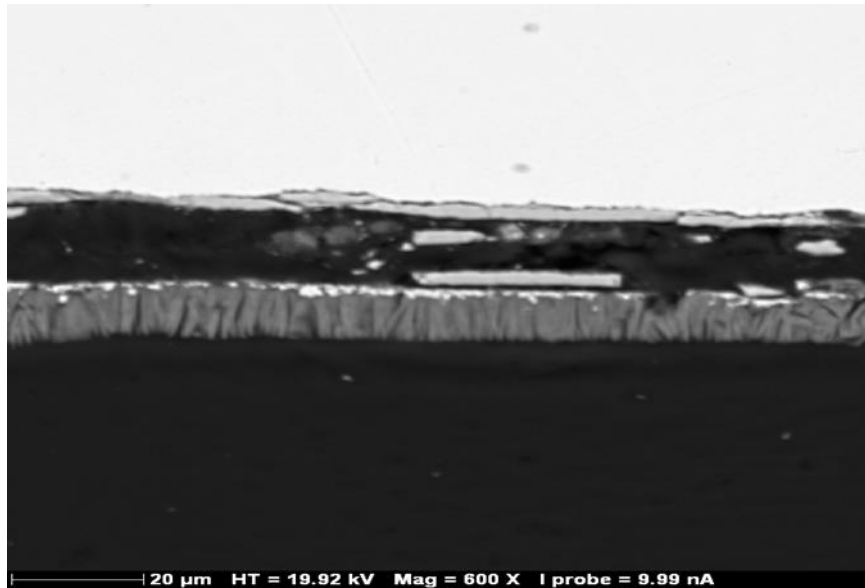


Figure 6. BSE image of steel and Fe-saponite interface from experiment EBS-13. Note the perpendicular growth pattern of the Fe-saponite with respect to the steel (white material at top). This interface material has been forcibly removed from the steel during preparation of the sample by vacuum injected epoxy.

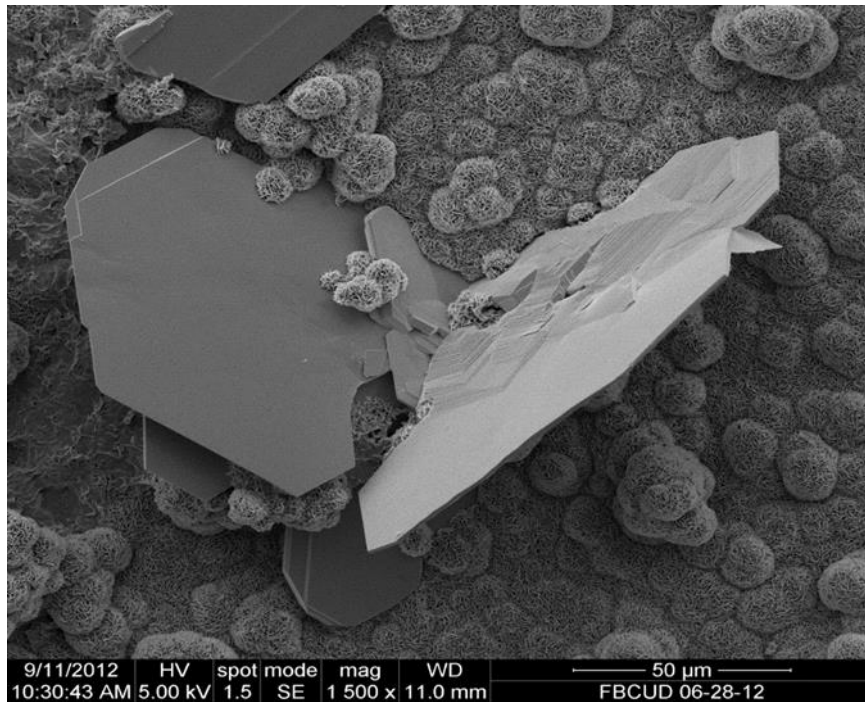


Figure 7. SEM image of pyrrhotite nested in bed of Fe-saponite rosettes. Sample EBS-6: the growth substrate is low carbon steel.

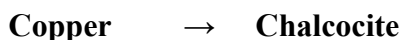
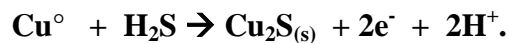


Figure 8. BSE image of iron metal with concentric alteration zones. Bright white core is remnant iron metal, dark grey is iron oxide, light grey is an iron sulfide (probably pyrrhotite) remaining mottled intermediate grey is stilpnomelane. Sample is EBS-15.

Similar experimental work by Ferrage (2011), Mosser-Ruck et al. (2010), Guillaume, et al. (2003) and Munier (1998) do not report this mineral phase in their reaction products. The chemical formula of stilpnomelane $[K(Fe^{++}, Mg, Fe^{+++})_8(Si, Al)_{12}(O, OH)_{27}]$ indicates that iron occurs in both oxidation states. Given that the iron metal in our experiments (Figure 8) is mantled first by an iron oxide (magnetite?), followed by an Fe sulfide (pyrrhotite) and finally by stilpnomelane, there is a potential that micro-domains of differing oxygen fugacity may be at play. This phenomena and mineral genesis deserves further investigation concerning iron corrosion.

5.4 Copper corrosion

Caporuscio et al (2014) discussed copper corrosion in the high P,T EBS experiments in some detail. We have since performed two further experiments (EBS-16 – 6 month, EBS-17- 6 week, Opalinus clay). The primary reaction associated with sulfide-induced copper corrosion is reaction to chalcocite:



This is well illustrated in an image from EBS-4 (Figure 9). The type of corrosion encountered in all four experiments is pit corrosion (Figure 10). Chalcocite formed a hexagonal morphology ranging from discrete plates to completely coalesced patches on the copper surface (Figures 11 and 12). Chalcocite crystallized on the copper surfaces due to available H_2S from the decomposition of pyrite in the hydrothermal environment. It is evident that the formation of these surface bound minerals was from the direct crystallization from solution in the localized environments surrounding the metal plates.

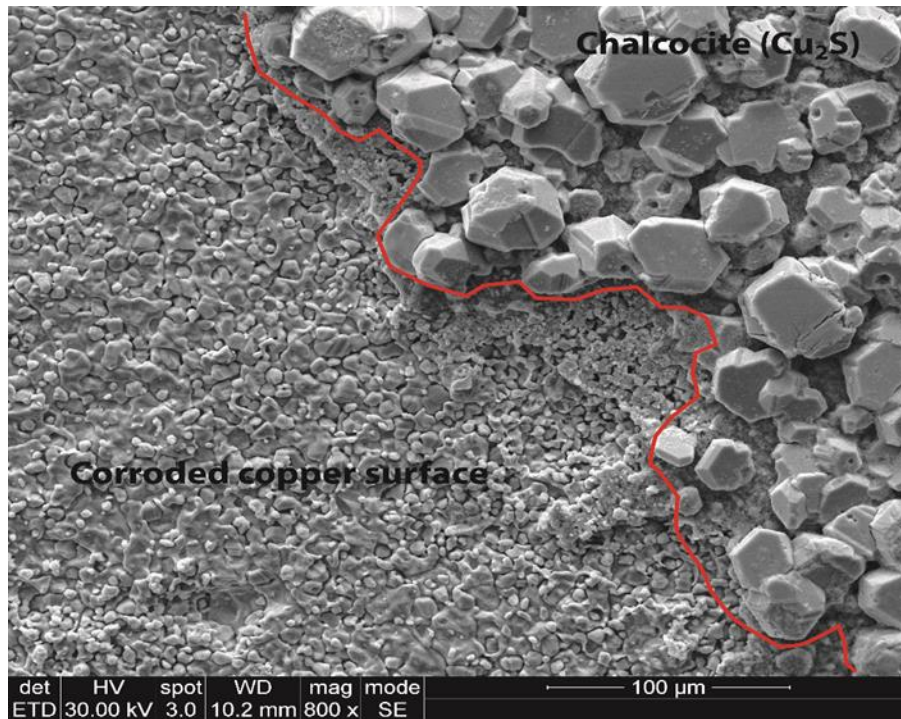


Figure 9. Corroded copper surface (lower left) and the covering chalcocite secondary growth (upper right). Sample EBS-4.

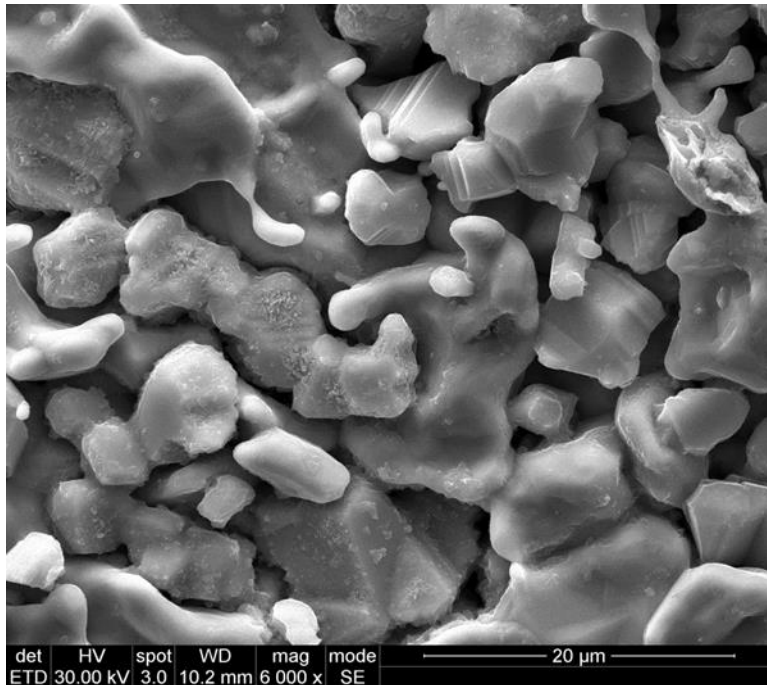


Figure 10. Plan view of pit corrosion in Sample EBS-4

The corrosion and growth of chalcocite typically begins as individual crystals and / or aligned stringers of crystals (Figure 12). This growth of chalcocite in a linear fashion may be due to nucleation along striations and defects in the copper foil. Eventually the copper corrodes further and the surface is totally mantled by chalcocite (Figure 12). Other mineral phases have recently been identified, namely covellite (CuS) and atacamite ($\text{Cu}_2\text{Cl}(\text{OH})_3$). Covellite was recognized in reflected light microscopy during corrosion thickness measurements, while atacamite was identified by morphologic characteristics (Figure 13). The very late stage atacamite growth is most likely due to late stage scavenging of Cl from solution.

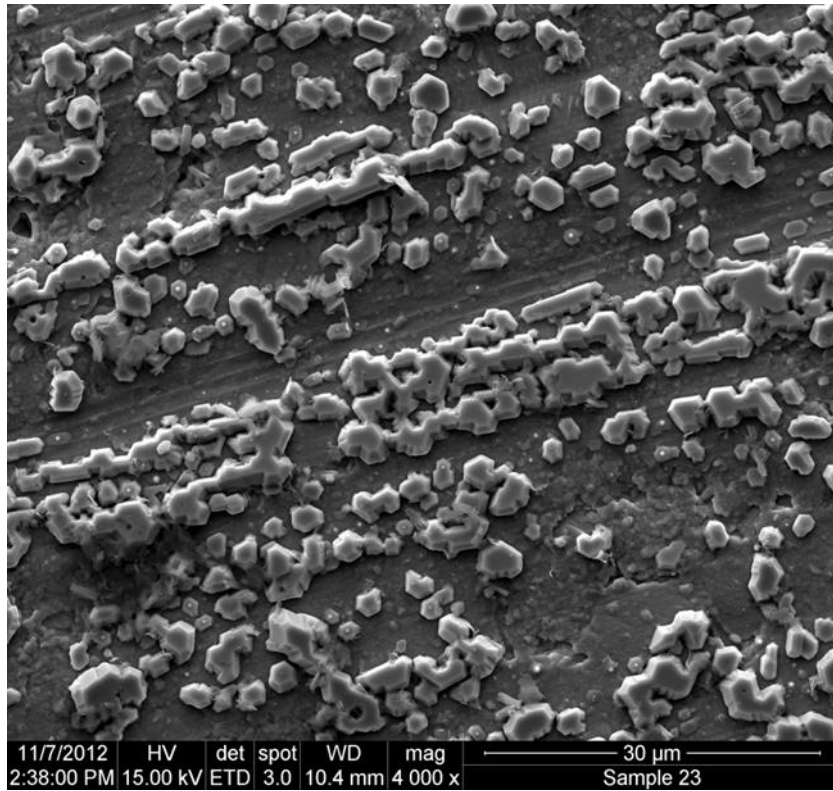


Figure 11. Sample EBS-8. Initial growth of chalcocite on copper

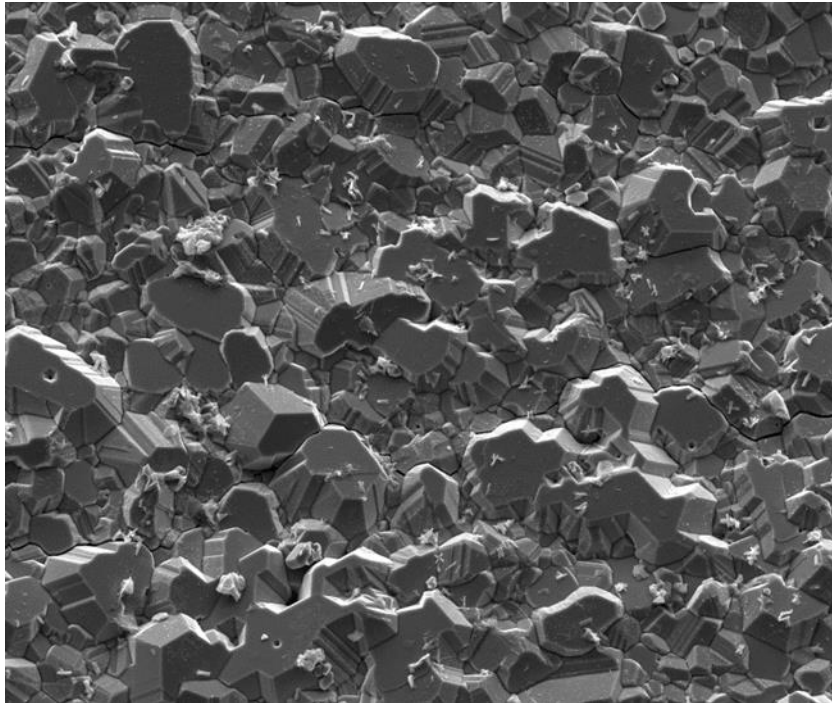


Figure 12. Total coverage of copper by chalcocite. Sample EBS-8.

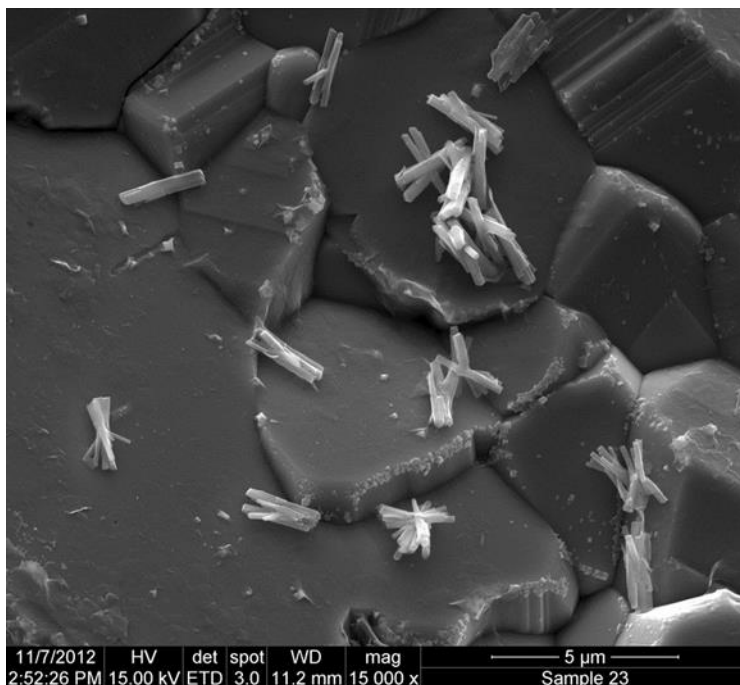


Figure 13. Atacamite (orthorhombic laths) resting on top of chalcocite crystals. Their growth is due to late stage scavenging of Cl from the brine. Sample EBS-8

5.5 Copper corrosion rate determination

The thickness of the chalcocite layer and the depth of the corrosion pitting varied with both temperature profile and experiment duration. In most of the experiments the chalcocite forms a thick layer over a corroded/pitted layer. A notable exception to this is the Opalinus Clay run, EBS-17, where the chalcocite layer was found to be either absent or extremely thick. For the ramped temperature experiment, EBS-4, the average chalcocite thickness was 3.0(13) μm . In the isothermal experiments in both bentonite (EBS-11) and opalinus (EBS-17) clay, the layer was notably thicker, 8.2(42) μm and 5.6(40) μm respectively. The chalcocite layer was dramatically thinner in the six month long-term cooling run (EBS-16) with a depth of only 2.6(13) μm .

The thickness of the chalcocite layer generally correlated with the amount of pitting corrosion the Cu foil had undergone. The initial overall thicknesses of the copper foils are ~ 63 μm . The short term isothermal experiments in both bentonite and opalinus clay yielded similar average pit corrosion, 13.5(63) μm and 13.1(58) μm respectively. The ramped experiment (EBS-4) incurred less corrosion, having an average pit depth of only 5.7(22) μm . The most significant result comes from the six month experiment. The average pit depth of EBS-16 was 4.3(14) μm , which is similar to that of EBS-4, but sustained over a much longer period of time. These average corrosion depths were determined from corrosion pitting occurring on the exterior surfaces of the rolled copper foil. The surfaces within the rolled copper foil were protected from the brine and thus did not suffer significantly from either chloride or sulfide attack.

Table 6 Copper corrosion rate data. Note that the EBS-16 (6 month experiment) corrosion rate is an order of magnitude lower than the other 3 experiments (5-6 week run time). The longer run time experiment likely formed complete coverage of chalcocite over the copper and passivated the reaction. Numbers in parentheses for average thickness, depth, and corrosion rate are standard deviations.

Experiment	Components	Temperature (K)	Duration (days)	Average Chalcocite Thickness (Microns)	Average Corrosion Pit Depth (Microns)	Average Corrosion rate (Microns/day)
EBS4 RLM	Cu + Bentonite	25/100/200/300/25	5 weeks/35 days	2.5(10)	4.2(16)	0.12(4)
EBS4 SEM	Cu + Bentonite	25/100/200/300/25	5 weeks/35 days	3.5(15)	6.7(20)	0.19(6)
EBS4 All	Cu + Bentonite	25/100/200/300/25	5 weeks/35 days	3.0(13)	5.7(22)	0.16(6)
EBS11 RLM	Cu + Bentonite	300	6 weeks/42 days	6.1(37)	10.0(38)	0.24(9)
EBS11 SEM	Cu + Bentonite	300	6 weeks/42 days	9.8(38)	16.3(65)	0.39(15)
EBS11 All	Cu + Bentonite	300	6 weeks/42 days	8.2(42)	13.5(63)	0.32(15)
EBS16 RLM	Cu + Bentonite	300 to 120	6 months/180 days	2.0(7)	4.3(13)	0.024(7)
EBS16 SEM	Cu + Bentonite	301 to 120	6 months/180 days	2.9(14)	4.2(15)	0.023(9)
EBS 16 All	Cu + Bentonite	302 to 120	6 months/180 days	2.6(13)	4.3(14)	0.024(8)
EBS17 RLM	Cu + Opalinus	300	6 weeks/42 days	4.0(26)	12.0(54)	0.29(13)
EBS17 SEM	Cu + Opalinus	300	6 weeks/42 days	7.3(45)	13.8(59)	0.32(14)
EBS17 All	Cu + Opalinus	300	6 weeks/42 days	5.6(40)	13.1(58)	0.31(14)

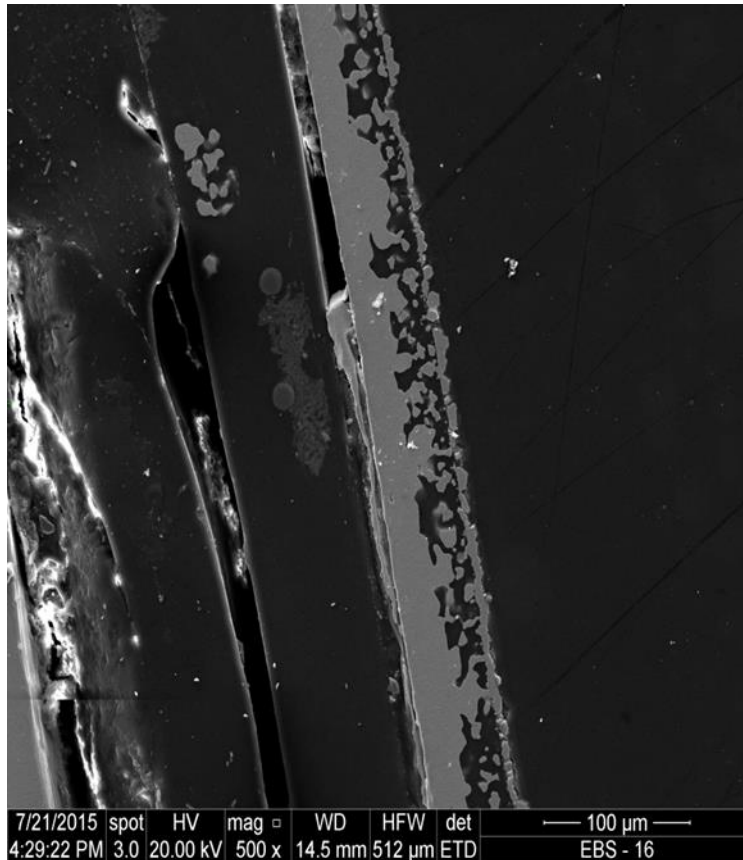


Figure 14 Experiment EBS-17. Note that pit corrosion of this copper foil has progressed to nearly 50% of the total thickness of the sample.

The corrosion rates listed in Table 6 were determined by dividing the average corrosion pit depth by the number of days in the run. Table 6 was compiled from over 850 data points. The corrosion rates from the two isothermal experiments on bentonite and Opalinus Clay were within experimental error of each other and the highest measured. The corrosion of the Cu mixed with Opalinus Clay exhibited several regions of extreme corrosion (Figure 14). These parts of the copper foil were corroded fifty percent or more and show deep channeling in the Cu foil. The corrosion rate for the five week ramped experiment (EBS-4) was half that of the isothermal experiments, $0.16(6) \mu\text{m}/\text{day}$ for the ramped versus $\sim 0.31 \mu\text{m}/\text{day}$ for the isothermal experiments. The six month long-term cooling experiment had a much smaller average corrosion rate of $0.024(8) \mu\text{m}/\text{day}$. This is consistent with the reduced corrosion found in the long term experiment.

The nature of corrosion pitting in the copper foils was similar for all experiments. The average aspect ratio of the width to the depth of the corrosion pits found in the experiment with the least corrosion, the six month extended cooling run, was $1.4(9)$. The run with the most corrosion, the six week Opalinus Clay run, had a nearly identical aspect ratio of $1.3(8)$. The similarity of these aspect ratios indicates that although more rapid corrosion is occurring during the six week experiment, the pit shapes are unaffected by rate and retain the same nature regardless of the

amount of corrosion the copper foil has undergone. A wide variety of corrosion pit structures exist, but extremely deep corrosion pits are just as common as shallow wide ones.

6 Conclusions

This document summarizes the last four years of experiments and attempts to compile pertinent 1) SEM images, 2) electron microprobe data for major mineral phases, and 3) aqueous geochemistry data from both starting materials and the 17 major experiments conducted so far into one source. There is also a discussion of more recent characterization results and interpretation of copper corrosion rates.

6.1 Major concepts developed so far include:

- 1) Illitization of smectites may be restricted due to the bulk chemistry of the overall system.
- 2) P yrite within bentonite that may be used as backfill reacts readily in groundwater and the resulting $H_2S(aq,g)$ reacts in a minor fashion with steel and aggressively with copper.
- 3) Bentonite heated to $300^\circ C$ in a dry environment has very restricted reactivity.
- 4) Experiments held at $300^\circ C$ for 4 months and then stepped down in temperature over two more months exhibit no discernable retrograde reactions. This may well be due to kinetic effects of metastable phases.
- 5) The interface between bentonite and steel develops a well characterized new mineral phase, Fe-saponite (especially at $300^\circ C$), that grows perpendicular to the steel surface.
- 6) Another Fe layered phyllosilicate, stilpnomelane, grows in the presence on native iron (one of our solid buffer materials), which alludes to the idea that oxygen fugacity may be quite variable, depending on scale.
- 7) Zeolites transform as temperature increases. Mine run bentonite contains clinoptilolite, and transforms to analcime at higher temperature, releasing both SiO_2 and water. Opalinus Clay upon heating develops wairakite along cracks and edges. The location of these new growth zeolites is due to the impermeable nature of the shale. Mixtures of Opalinus Clay and Colony bentonite produce an intermediate composition Analcime-Wairakite solid solution phase, indicating ease of cation exchange for this zeolite.
- 8) Pit corrosion is the driving force in copper degradation. The copper reacts with $H_2S(aq,g)$ to produce chalcocite and covellite. At latter times in the reaction pathway Cl may combine with copper to produce atacamite.
- 9) Systematic measurements ($N > 850$) of copper corrosion cross sections have determined corrosion reaction rates at experimental temperatures and pressures. At 6 week duration, corrosion rates ranged from 0.12 to 0.39 micron/day, depending on heating profiles and bulk composition. However, in the 6 month experiment, the corrosion rate dropped by an order of magnitude, to 0.024 micron/day. We believe that complete coverage by the reaction product chalcocite pacifies the corrosion reaction.

This database, along with summary conclusions will be of use to other experimental teams on the DOE complex, system modeler, and the international repository science community.

6.2 FY16 Research Outlook

Further research is needed in the following areas:

- Corrosion of steels and copper must be the focus of research activities in the upcoming year.
- Provide further information on complete repository thermal pulse event, using long term (6 month) experiments with and without host rocks.
- Performed detailed geochemical modeling of F13-FY15 experimental reactions. Investigate the role of solid solution in the parageneses of secondary zeolite minerals.
- International FEBEX-DP – hydrothermal treatment of FEBEX samples expanding the thermal range in addition to routine mineral/geochemical interrogations.
- Perform transmission electron microscope (TEM) investigation looking at very local chemical changes at a single metal surface.
- Purify mineral phases for thermodynamic investigations using solution calorimetry.

Acknowledgements

We would like to thank Emily Kluk and Diana Brown for XRF analyses. Scanning electron microscopy facilities were provided by Materials Science and Technology group at Los Alamos National Laboratory. Dr. George Morgan at the University of Oklahoma was instrumental in the obtaining of EMP analyses. I thank James Maner for both many discussions and a critical review.

7. References

- Abercrombie, H.J., Hutcheon, I.E., Bloch, J.D., and de Caritat, P. (1994) Silica activity and the smectite-illite reaction. *Geology*, 22, 539-542.
- Ames, L.L. and Sand, L.B. (1958) Hydrothermal synthesis of wairakite and calcium-mordenite. *The American Mineralogist*, 43, 476-480.
- Bannister, R.A. (1943) Brammalite (sodium-illite) a new mineral from Llandebie, South Wales. *Mineralogical Magazine*, 26, 304-307.
- Börjesson, L., Gunnarsson, D., Johannesson, L-E., and Jonsson, E. (2010) Design, production and initial state of the buffer. *Svensk Kärnbränslehantering Technical Report, TR-10-15*, pp. 89.
- Caporuscio, F.A., Cheshire, M.C., Rearick, M.S., and Jove-Colon, C. (2014). - LANL Argillite EBS Experimental Program 2014. FCRD-USED-2014-000491.
- Chermak, J.A. (1992) Low temperature experimental investigation of the effect of high pH NaOH solutions on the Opalinus Shale, Switzerland. *Clays and Clay Minerals*, 40, 650-658.
- Cheshire, M.C., Caporuscio, F.A., Jové-Colón, C., and McCarney, M.K. (2013) Alteration of clinoptilolite into high-silica analcime within a bentonite barrier system under used nuclear fuel repository conditions. *Proceeding from the 14th International High-Level Radioactive Waste Management Conference*, 410-415.
- Cheshire, M.C., Caporuscio, F.A., Jove-Colon, C., and McCarney, M.K. (2014) Bentonite Clay Evolution at Elevated Pressures and Temperatures: An experimental study for generic nuclear repositories. *American Mineralogist*, V99, pp1662-1675
- Chipera, S.J. and Bish, D.L. (2002) FULLPAT: a full-pattern quantitative analysis program for X-ray powder diffraction using measured and calculated patterns. *Journal of Applied Crystallography*, 35, 744-749.
- Chung, F.H. (1974) Quantitative interpretations of X-ray diffraction patterns of mixtures. I. Matrix flushing method for quantitative multicomponent analysis. *Journal of Applied Crystallography*, 7, 519-525.
- Coombs, D.S. (1955) X-ray observations on wairakite and non-cubic analcime. *Mineralogical Magazine*, 30, 699-708.
- Crerar, D.A., Susak, N.J., Borcsik, M., and Schwartz, S. (1978) Solubility of the buffer assemblage pyrite + pyrrhotite + magnetite in NaCl solution from 200 to 350°C. *Geochimica et Cosmochimica Acta*, 42, 1427-1437.
- Dong, H. (2005) Interstratified illite-smectite: A review of contributions of TEM data to crystal chemical relation and reaction mechanisms. *Clay Science*, 12, Supplement 1, 6-12.
- Eberl, D. and Hower, J. (1977) The hydrothermal transformation of sodium and potassium smectite into mixed-layer clay. *Clays and Clay Minerals*, 25, 215-227.
- Eberl, D. (1978) Reaction series for dioctahedral smectites. *Clays and Clay Minerals*, 26, 327-340.
- Eberl, D., Whitney, G., and Khourym, H. (1978) Hydrothermal reactivity of smectite. *American Mineralogist*, 63, 401-409.

- Eberl, D.D., Velde, B., and McCormick, T. (1993) Synthesis of illite-smectite from smectite at Earth surface temperatures and high pH. *Clay Minerals*, 28, 49-60.
- Ferrage, E., Vidal, O., Mosser-Ruck, R., Cathelineau, M., and Cuadros, J. (2011) A reinvestigation of smectite illitization in experimental hydrothermal conditions: Results from X-ray diffraction and transmission electron microscopy. *American Mineralogist*, 96, 207-223.
- Frey, M. (1969) A mixed-layer paragonite/phengite of low-grade metamorphic origin. *Contribution to Mineralogy and Petrology*, 24, 63-65.
- Greenburg, H.R. and Wen, J. (2013) Repository layout and host rock thermal gradient trade study for large waste packages in clay/shale: Using the DSEF thermal analytical model. LLNL-TR-639869-DRAFT, pp. 38.
- Guillaume, D., Neaman, A., Cathelineau, M., Mosser-Ruck, R., Peiffert, C., Abdelmoula, M., Dubessy, J., Villieras, F., Baronnet, A., and Michau, N., (2003) Experimental synthesis of chlorite from smectite at 300 °C in the presence of metallic Fe. *Clay Minerals*, 38, 281-302.
- Güven, N. (2001) Mica structure and fibrous growth of illite. *Clays and Clay Minerals*, 49, 189-196.
- International Atomic Energy Agency (IAEA) (2000) Multi-purpose container technologies for spent fuel management. IAEA Technical Document, IAEA-TECDOC-1192, pp. 56.
- Jové, C. and Hacker, B.R. (1997) Experimental investigation of laumontite \square wairakite + H₂O: A model diagenetic reaction. *American Mineralogist*, 82, 781-789.
- Jové-Colón, C. F., Caporuscio, F. A., Levy, S. S., Sutton, M., Blink, J., Greenberg, H. R., Fratoni, M., Halsey, W. G., Wolery, T. J., Rutqvist, J., et al. (2011) Disposal Systems Evaluations and Tool Development - Engineered Barrier System (EBS) Evaluation (Fuel Cycle Research and Development). Sandia National Laboratory, FCRD-USED-2011-000132, 1-192.
- Lahann, R.W. and Roberson, H.E. (1980) Dissolution of silica from montmorillonite: effect of solution chemistry. *Geochimica et Cosmochimica Acta*, 44, 1937-1943.
- Laird, D.A. (1996) Model for crystalline swelling of 2:1 phyllosilicates. *Clays and Clay Minerals*, 44, 553-559.
- Laird, D.A. (2006) Influence of layer charge on swelling of smectites. *Applied Clay Science*, 34, 74-87.
- Madsen, F.T. (1998) Clay mineralogical investigations related to nuclear waste disposal. *Clay Minerals*, 33, 109-129.
- Masuda, H., O'Neil, J.R., Jiang, W-T, and Peacor, D.R. (1996) Relation between interlayer composition of authigenic smectite, mineral assemblages, I/S reaction rate and fluid composition in silicic ash of the Nankai Trough. *Clays and Clay Minerals*, 44, 443-459.
- Meunier, A., Velde, B., and Griffault, L. (1998) The Reactivity of Bentonites: a Review. An Application to Clay Barrier Stability for Nuclear Waste Storage. *Clay Minerals*, 33, 187-196.
- Moore, D. M. and Reynolds, R.C. (1997) X-ray Diffraction and the Identification and Analysis of Clay Minerals. Oxford University Press, New York, New York, pp. 377.

- Mosser-Ruck, R., Cathelineau, M., Baronnet, A., and Trouiller, A. (1999) Hydrothermal reactivity of K-smectite at 300 °C and 100 bar: dissolution-crystallization process and non-expandable dehydrated smectite formation. *Clay Minerals*, 34, 275-290.
- Mosser-Ruck, R., Cathelineau, M., Guillaume, D., Charpentier, D., Rousset, D., Barres, O., and Michau, N. (2010) Effects of Temperature, pH, and Iron/Clay and Liquid/Clay Ratios on Experimental Conversion of Dioctahedral Smectite to Berthierine, Chlorite, Vermiculite, or Saponite. *Clays and Clay Minerals*, 58, 280-291
- Nutt, M. Voegelé, M., Jové-Colón, C.F., Wang, Y., Howard, R., Blink, J., Liu, H.H., Hardin, E., and Jenni, K. (2011) Used fuel disposition campaign disposal research and development road map (Fuel cycle research and development). Sandia National Laboratory, FCRD-USED-2011-000065, 1-121.
- Ohmoto, H., Hayashi, K-I, and Kajisa, Y. (1994) Experimental study of the solubilities of pyrite in NaCl-bearing aqueous solutions at 250-350°C. *Geochimica et Cosmochimica Acta*, 58, 2169-2185.
- Pearson, F.J., Arcos, D., Bath, A., Boisson, J.-Y., Fernandez, A.M., Gabler, H.-E., Gaucher, E., Gautschi, A., Griffault, L., Hernan, P., and Waber, H.N. (2003) Mont Terri Project- Geochemistry of water in the Opalinus Clay Formation at the Mont Terri Rock Laboratory. – Reports of the Federal Office for Water and Geology (FOWG), Geology Series No. 5.
- Pouchou, J.L. and Pichoir, F. (1985) “PAP” $\square(\square z)$ correction procedure for improved quantitative microanalysis. *Microbeam Analysis*. Ed. Armstrong, J.T. San Francisco Press, pp. 104-106.
- Pusch, R. (1979) Highly compacted sodium bentonite for isolating rock-deposited radioactive waste products. *Nuclear Technology*, 45, 153-157.
- Pusch, R. Takase, H., and Benbow, S. (1998) Chemical Processes causing cementation in heat-affected smectite- the Kinnekulle bentonite. *Svensk Kärnbränslehantering Technical Report*, TR-98-25, pp. 62.
- Pusch, R. and Kasbohm, J. (2002) Alteration of MX-80 by hydrothermal treatment under high salt content conditions. *Svensk Kärnbränslehantering Technical Report*, TR-02-06, pp. 44.
- Pusch, R. (2008) *Geological Storage of Radioactive Waste*. Springer-Verlag, Berlin, Germany, pp. 379.
- Roberson, H.E. and Lahann, R.W. (1981) Smectite to illite conversion rates: Effects of solution chemistry. *Clays and Clay Minerals*, 29, 129-135.
- Seki, Y. (1971) Some Physical Properties of Analcime-Wairakite Solid Solutions. *Journal of the Geologic Society of Japan*. 77, 1-8
- Seyfried, J.R., Janecky, D.R., and Berndt, M.E. (1987) Rocking autoclaves for hydrothermal experiments II. The flexible reaction-cell system. *Hydrothermal Experimental Techniques*. Eds. Ulmer, G.C. and Barnes, H.L. John Wiley & Sons, pp. 216 – 239.
- Small, J.S., Hamilton, D.L., and Habesch, S. (1992) Experimental simulation of clay precipitation within reservoir sandstones 2: Mechanism of illite formation and controls on morphology. *Journal of Sedimentary Petrology*, 62, 520-529.

- Small, J.S. (1993) Experimental determination of the rates of precipitation of authigenic illite and kaolinite in the presence of aqueous oxalate and comparison to the K/Ar ages of authigenic illite in reservoir sandstones. *Clays and Clay Minerals*, 41, 191-208.
- Smyth, J.R. (1982) Zeolite stability constraints on radioactive waste isolation in zeolite-bearing volcanic rocks. *Journal of Geology*, 90, 195-201.
- Środoń, J. (1980) Precise identification of illite/smectite interstratifications by X-ray powder diffraction. *Clays and Clay Minerals*, 28, 401-411.
- Środoń, J. (1999) Nature of mixed-layer clays and mechanisms of their formation and alteration. *Annual Review of Earth and Planetary Sciences*, 27, 19-53.
- Steiner, A. (1955) Wairakite, the calcium analogue of analcime, a new zeolite mineral. *Mineralogical Magazine*, 30, 691-698.
- Wersin, P., Johnson, L.H., and McKinley, I.G. (2007) Performance of the bentonite barrier at temperatures beyond 100°C: A critical review. *Physics and Chemistry of the Earth*, 32, 780-788.
- Whitney, G. and Velde, B. (1993) Changes in particle morphology during illitization: An experimental study. *Clays and Clay Minerals*, 41, 209-218.
- Wilkin, R.T. and Barnes, H.L. (1998) Solubility and stability of zeolites in aqueous solution: I. Analcime, Na-, and K-clinoptilolite. *American Mineralogist*, 83, 746-761.
- Wilkin, R.T. and Barnes, H.L. (2000) Nucleation and growth kinetics of analcime from precursor Na-clinoptilolite. *American Mineralogist*, 85, 1329-1341.
- Winkler, H.G.F. (1976) *Petrogenesis of Metamorphic Rocks*. Springer-Verlag, New York, 329 pp.
- Zhang G., Kim, J., Dong, H., and Sommer, A. (2007) Microbial effects in promoting the smectite to illite reaction: Role of organic matter intercalated in the interlayer. *American Mineralogist*, 92, 1401-1410.

**Evaluation of Thermodynamic and Sorption Data; Applications of First-Principles Modeling in the Assessment of Thermal-Mechanical Properties of Kaolinite Clay
(Part IV)**

1 Introduction

Ongoing efforts on the assessment of thermodynamic and sorption data has been described in Jove Colon et al. (2013, 2014). These are focused on the evaluation of recent thermodynamic data of EBS components such as clays and associated sheet silicates. This data is then used as key inputs to geochemical and transport models to simulate fluid-mineral interactions under given pressure and temperature conditions. For example, accurate predictions of mineral solubilities, phase stability relations, and coupled geochemical processes like reactive transport at elevated temperatures are necessary in the evaluation of process models for disposal of heat-generating waste. Therefore, a comprehensive assessment of key thermodynamic data issues and inconsistencies are necessary for applications to the UFDC R&D.

This part of the report describes the following:

- Progress on the assessment of thermodynamic and sorption data.
- Interplay between structural and thermal-mechanical properties of argillite disposal systems: First-principles study of kaolinite clay. This work is described in Weck et al. (2015).

2 Thermodynamic and Sorption Data Evaluation

Thermodynamic modeling of Engineered Barrier System (EBS) materials and properties also requires the development of thermodynamic databases to evaluate the stability of EBS materials. The core of this model-data evaluation lies in the complex fluid-interactions at various physico-chemical conditions represented by (geo)chemical reactions relevant to subsurface repository environments. The development and implementation of equilibrium thermodynamic models are intended to describe chemical and physical processes such as solubility, sorption, and diffusion which are key to radionuclide transport and therefore repository isolation performance. The scope of the effort included the following:

1. Develop thermodynamic databases and models to evaluate the stability of barrier materials and their interactions with fluids at various physico-chemical conditions relevant to subsurface repository environments (in collaboration with Sandia National Laboratory (SNL)).
2. Evaluate sorption processes such as surface complexation (SC) and cation exchange (CE). Develop a methodology to test various SC models using global approaches to digitized data available in the literature. The ultimate goals are 1) the integration of all available sorption data with updated thermodynamic speciation databases 2) development and testing of surface complexation modeling formulations, and 3) the development of a flexible and comprehensive methodology for determining K_{ds} and associated uncertainties for use in Performance Assessment (PA) models.
3. Enhance international collaborations with other groups on the development of thermodynamic data and benchmarks to evaluate and perform quality assessments and model testing that is key to the geochemical evaluation of repository performance. SC methodologies will be coordinated with international effort headed by Helmholtz Zentrum Dresden Rossendorf (HZDR).
4. Integrate efforts with the the argillite and crystalline crystalline work packages for the evaluation of experiments on uranium and neptunium sorption/diffusion onto clay and related modeling efforts.

The thermodynamic database development effort is a continuation of FY14 work. It includes reviewing and revising the previously developed thermodynamic databases and expanding them to cover the needs of the repository types currently under consideration by the Used Fuel Disposition (UFD) program (i.e. clay, granite, deep borehole). The effort is a collaboration between LLNL and SNL. A draft manuscript summarizing this effort was prepared for submission later this fiscal year; we include only a short summary of that effort here.

A second effort involves development of surface complexation and cation exchange models and databases for use in PA models. This effort is also a continuation of FY14 work, in collaboration with Dr. V. Brendler (HZDR).

A third effort involves participation of Cynthia Atkins-Duffin (LLNL) in the Nuclear Energy Agency (NEA) Thermochemical Database (TDB) project. Dr. Atkins-Duffin is the UFD representative for thermodynamic database development efforts at the NEA in support of international nuclear waste repository research.

A fourth effort is integrated with the crystalline control account and focused on the study of radionuclide sorption and diffusion through clay. This has relevance to both clay/bentonite barrier systems in crystalline repository scenarios and clay rock in argillite repository scenarios. This fourth effort was recently summarized in the UFD R&D deliverable for disposal in a crystalline repository effort.

3 Thermodynamic Database Development

The following abstract was prepared as part of the manuscript in preparation and authored by Thomas J. Wolery (LLNL) and Carlos F. Jové-Colón (SNL). The manuscript, entitled “Chemical Thermodynamic Data. I. The Concept of Links to the Chemical Elements and the Historical Development of Key Thermodynamic Data” will be submitted for publication later this fiscal year.

“Chemical thermodynamic data remain a keystone for geochemical modeling and reactive transport simulation as applied to an increasing number of applications including geologic disposal of nuclear waste, carbon sequestration, climate change, and environmental analysis and remediation, as well as applications outside the earth sciences such as metallurgy, material science, and industrial process design. The last century has seen the development of large quantities of thermodynamic data and numerous compilations of such. In addition, the past several decades have seen the development of thermodynamic databases in digital form designed to support computer calculations. Nevertheless, problems with thermodynamic data appear to be persistent. Here we examine some of these problems and argue that many of them arise from a “data value” focused perspective that fails to account for the full origin of resulting values. As a partial solution to this problem as it pertains to Gibbs energies and enthalpies of formation at 298.15K and 1 bar pressure (reference temperature and pressure), we propose a formal concept of “links” to the chemical elements in their reference forms. This concept involves a documented understanding of all reactions and calculations leading to values for a formation property (Gibbs energy or enthalpy). A valid link consists of two parts: (a) the path of reactions and corrections and (b) the associated data. Such a link differs from a bare “key” or “reference” datum in that it requires additional information, although some or perhaps all of its associated data may also be considered key data. In evaluating a reported thermodynamic datum, one should identify the links to the

elements, a process which can be time-consuming and which may lead to a dead end (and hence an unsupported hence invalid link). The use of two or more inconsistent links to the same elemental reference form in a thermodynamic database will necessarily result in an inconsistency in the database. Thus, in constructing a database, it is important to first establish a set of reliable links and then correct all data adopted subsequently for consistency with that set. Key reference data of concern include atomic weights, entropies of the elements in their reference forms at reference temperature and pressure, and formation properties at reference temperature and pressure of various key species including simple oxides and principal aqueous ions. Recommended values have not been constant through history, and data derived from such values have apparently been passed on in a number of compilations and databases without consistent correction to a single set of preferred reference data values. In this paper, we review some of this history and note a number of problem areas. Finally, we illustrate the concepts developed in this paper by applying them to some key species of geochemical interest. These species include liquid water, quartz and aqueous silica, and gibbsite, corundum, and the aqueous aluminum ion.”

This paper describes a methodology for evaluating consistency in thermodynamic data and building thermodynamically consistent databases. It reviews nearly a century of thermodynamic data. It then applies the methodology to key data for (1) water, (2) quartz and aqueous silica, and (3) gibbsite, corundum, and the aluminum ion. Follow-on efforts will focus on further illustrating these concepts and applying them to mineralogic components of greatest interest to the UFD program.

We illustrate the process with an example from the paper. We want to use CODATA (Cox et al., 1989) key reference data as much as possible, especially in that this will maintain consistency with the NEA-TDB works. Aluminum is a key component of both natural geochemical systems and EBS materials such as aluminosilicates including clays and zeolites. In the case of the aqueous ion Al^{3+} we found newer and more reliable data in the work of Tagirov and Schott (2001), who made a comprehensive study of the solubility of gibbsite ($\text{Al}(\text{OH})_{3(c)}$) over a wide range of temperature. In contrast, the CODATA development for the aluminum ion focuses on low temperature data, is rather complex, and averages various reported results where culling might have been more appropriate. The CODATA report does not give recommended data for gibbsite, although data for it are used in part in its development of recommended data for Al^{3+} . For gibbsite, we chose the enthalpy (calorimetrically determined) and entropy from Robie et al. (1978). However, we recalculated the corresponding Gibbs energy from these data using the CODATA recommendations for the entropies of the requisite standard elemental reference forms, resulting in a slight correction to the value given by Robie et al. (1978) (Table 1). Although in this case the Gibbs energy correction is only -0.004 kJ/mol, this illustrates the practice that must be employed to maintain consistency with chosen key reference data.

Table 1 G-H-S data for Al(OH)₃ (Gibbsite) at 298.15K, 1 bar. Data from Robie et al. (1978) are shown, along with corrections (affecting only the Gibbs energies of formation) for consistency with other data from CODATA.

		Al(OH) ₃ (Gibbsite)		
Source	Year of	ΔG°_f	ΔH°_f	S°
	Publication	kJ/mol	kJ/mol	J/mol-K
Robie et al. (1978)	1978	-1154.889	-1293.128	68.440
Robie et al. (1978), corrected	this work	-1154.903	-1293.128	68.440

Tagirov and Schott (2001) obtained the corresponding data for the aluminum ion by fitting the “HKF equation of state” model to solubility data over a wide range of temperature, consistent with the reaction $Al(OH)_3(c) + 3 H^+ = Al^{3+} + 3 H_2O$. They first determined the Gibbs energy and entropy of reaction. Using data for the other species in the reaction, they obtained the Gibbs energy and entropy of the aluminum ion. With some elemental reference form data, the enthalpy for the aluminum ion was obtained from the Gibbs energy and the entropy. We recalculated their results to be consistent with our corrected data for gibbsite (Table 1), the CODATA recommendations for liquid water, and the CODATA recommendations for the requisite elemental entropies. No correction is associated with the aqueous hydrogen ion, as the requisite values for it are zero by convention. The results, which preserve the Tagirov and Schott values for the Gibbs energy and entropy of the reaction, are shown in Table 2.

Table 2 G-H-S data for Al³⁺ at 298.15K, 1 bar. Data from Tagirov and Schott (2001) are shown along with corrections for consistency with other data from CODATA.

		Al ³⁺		
Source	Year of	ΔG°_f	ΔH°_f	S°
	Publication	kJ/mol	kJ/mol	J/mol-K
Tagirov and Schott (2001)	2001	-487.478	-538.769	-339.753
Tagirov and Schott (2001), corrected	this work	-487.621	-538.937	-339.834

The corrections in this case are larger. A notable cause is that Tagirov and Schott (2001) developed their model for use with the SUPCRT92 code (Johnson et al., 1992), which contains a hard-coded model for the thermodynamic properties of water that is affected by a small but significant error (1 atm data were used as 1 bar data). Implementing the CODATA recommended values for water in SUPCRT92 will be explained in the Part II paper.

4 Surface Complexation and Ion Exchange Model and Database Development

The need to develop self-consistent surface complexation/ion exchange models, in concert with thermodynamic models, for nuclear waste repository performance assessment was identified many years ago (Bradbury and Baeyens, 1993). This issue was expressly identified in the recent NEA Sorption project reports (Davis et al., 2005; Ochs et al., 2012). However, significant progress on this issue has been made only recently in various international nuclear waste repository programs (e.g. (Bradbury and Baeyens, 2009), (Dresden-Rosendorf, 2013), (Geckeis et al., 2013)). Hybrid approaches have also been attempted (Bradbury et al., 2010). The best path forward for developing such databases remains an open question (Geckeis et al.,

2013), particularly in cases where generic repositories are being investigated resulting in a need to model radionuclide behavior over a very broad range of solution and mineralogic conditions.

The RES³T project is a recent effort by HZDR to develop a digital open source thermodynamic sorption database. It includes mineral-specific surface complexation constants that can be used in additive models of more complex solid phases such as rocks or soils. It includes an integrated user interface to access selected mineral and sorption data and export data into formats suitable for other modeling software. Data records comprise mineral properties, specific surface areas, characteristics of surface binding sites and their protolysis constants, sorption ligand information, and surface complexation reactions (SC models include the Non-Electrostatic, Diffuse Double Layer, Constant Capacitance, Triple Layer, Basic Stern, and the 1-pK Model as extended to CD-MUSIC). The database also includes a comprehensive list of publications that are the primary sources of the surface complexation data. In total, the database includes over 100 minerals, 4000 surface complexation reaction constants, and 2000 references. The database provides a comprehensive list of reaction constants reported in the literature for a very large number of radionuclide-mineral reaction pairs. However, this database project does not provide recommended values. It also does not capture the primary sorption data or provide information on the aqueous speciation constants used in determining those surface complexation constants. As a result, the RES³T project provides a foundation for developing a comprehensive surface complexation database but does not go so far as to provide one.

Three key issues prevent the application of the RES³T database in performance assessment and other radionuclide transport/risk assessment models. They are:

- An inability to integrate disparate data sets and surface complexation model constructs into single unified model and associated set of reaction constants
- An inability to produce self-consistent reaction constants based on a common set of aqueous speciation constants and surface properties.
- The absence of error propagation in the sorption data and/or database constants needed to assess model uncertainties.

To address these limitations, the inclusion of primary sorption data in the RES³T database is needed. This would allow for integration of all available literature data, error propagation, and database updating and ensure self-consistency between aqueous speciation, mineral solubility, and surface complexation databases.

In our FY14 progress report, we developed a test-case for U(VI) sorption to quartz and demonstrated how a self-consistent set of surface complexation constants could be produced from ~400 batch sorption data digitized from the published literature (10 publications in total). The minimization routine was performed using the software developed at LLNL (Zavarin et al., 2004) and based on the FITEQL software (Herbelin and Westall, 1994). However, this approach did not provide the flexibility needed to easily evaluate and test various surface complexation models. Thus, an alternative approaches have been investigated. One promising approach that has become available is a recently released PHREEQC module, PreeqcRM (Charlton and Parkhurst, 2011; Parkhurst and Wissmeier, 2015). The module was developed to facilitate operator splitting approaches to reactive transport modeling. The module may also be ideal for performing equilibrium calculations on individual batch sorption data. When linked to a parameter estimation software (e.g. PEST (Doherty, 2003)), the PhreeqcRM module may provide a framework for testing various surface complexation models on large sets of sorption data in a comprehensive manner. This new approach will be tested in the following months.

5 NEA Thermodynamic database development

Dr. Atkins-Duffin is the UFD representative for thermodynamic database development efforts at the NEA in support of international nuclear waste repository research. In the following table (Table 3), we provide a summary of the ongoing efforts by the NEA TDB project and the upcoming releases of new data compilations. A history of NEA TDB activities was recently published and summarizes the accomplishment of the project since its inception in 1984 (Ragoussi and Brassinnes, 2015).

The Ancillary Data Review (Table 3) may be useful for comparison with the thermodynamic database efforts of Wolery and Jove-Colon described in Section 2. All draft content for aqueous species, with the exception of the phosphate data, was sent to the NEA in March 2015. These sections are being reviewed by the Chairman of the activity. A completed draft for solids should have been sent to the NEA by the end of June 2015 and all synopses for Appendix A should be received at the NEA by July 2015. A complete peer-review draft is planned to be readied by the end of the summer 2015. The document will be provided to UFD as soon as it becomes available.

Table 3. Summary of NEA TDB Activities.

Activity	Status	Final milestone
Fe – Part II Review	Most single contributions concluded All first drafts expected to be ready by end of summer 2015	Book to peer-review in beginning 2016.
Mo Review	Big part of single contributions concluded All first drafts expected to be ready by end of 2015	Book to peer-review in 2016.
Ancillary Data Review	Aqueous drafts completed. Solids drafts expected by June 2015 Synopses expected by July 2015	Book to peer review end 2015
State-of-the Arts Report Cements	Ongoing	Completion of 1st draft in mid-2017
State-of-the Arts Report Pitzer	Just initiated	Completion of 1st draft end of 2016
Update Actinides	Just initiated	Completion of 1st draft end of 2016

6 Planned FY16 Efforts

In FY16, we plan to continue our efforts in the development of thermodynamic databases in support of the UFD program. These include

- Illustrating the concepts developed by Wolery and Jove-Colon and applying them to mineralogic components of greatest interest to UFD research
- Testing the PhreeqcRM-PEST framework for testing various surface complexation models on large sets of sorption data in a comprehensive manner.
- Continued engagement with the NEA TDB project through the support of Dr. Atkins-Duffin as the UFD representative for international thermodynamic database development effort.

A second paper, “Chemical Thermodynamic Data. II. Analysis and Revision of the Mineral Thermodynamic Dataset of Helgeson et al. (1978)” is in preparation and will be completed FY16. The objective of this paper is to examine the key thermodynamic data used in the original work and to revise the original dataset for consistency with a more appropriate set of key thermodynamic data, much of it taken from CODATA (Cox et al., 1989). The revised results, along with some corresponding revisions to aqueous species data, will be incorporated into a new database for the SUPCRT92 program. A methodology for revising the built-in model of

water properties for consistency with CODATA will be described and applied. Although the original development of Helgeson and co-workers is known to have a number of flaws, it is less well known that the original development incorporates a number of ties to key reference data for aqueous species. This likely gives it an advantage (specifically when the known flaws are corrected) in modeling mineral-aqueous solution interactions at relative low temperatures (less than 300°C). Other more recent models that have obtained thermodynamic data from mineral phase equilibria at high temperature and pressure, such as that of Holland and Powell (2011), have done so without making ties to key reference data for aqueous species, other than water itself. However, these models do have features that allow them to extend accurately to significantly higher temperature and pressure, and such models will be considered in the future. The main issue is whether or not these models can be accurately applied to mineral-aqueous solution interactions at relatively low temperature and pressure. To meaningfully compare such models, it is necessary to put them on the same footing with regard to key reference data. The benefit can be maximized by linking, as much as possible, to the key reference data associated with the NEA-TDB project.

In FY16 we will complete and publish the Part II paper, create a modified SUPCRT92 data file, and produce a modified version of SUPCRT92 that contains a modified water model consistent with the CODATA (Cox et al., 1989) recommendations. This will provide a core for additional database development. As much as possible, we will leverage the efforts of the NEA TDB effort and other investigators.

7 References

- Bradbury, M. H. and Baeyens, B., 1993. A general application of surface complexation modeling radionuclide sorption in natural systems. *J. Colloid Interface Sci.* 158, 364-371.
- Bradbury, M. H. and Baeyens, B., 2009. Sorption modelling on illite. Part II: Actinide sorption and linear free energy relationships. *Geochim. Cosmochim. Acta* 73, 1004-1013.
- Bradbury, M. H., Baeyens, B., and Thoenen, T., 2010. Sorption Data Bases for Generic Swiss Argillaceous Rock Systems. Nagra, Wettingen, Switzerland.
- Charlton, S. R. and Parkhurst, D. L., 2011. Modules based on the geochemical model PHREEQC for use in scripting and programming languages. *Computers & Geosciences* 37, 1653-1663.
- Cox J. D., Wagman D. D., and Medvedev V. A., eds. (1989) CODATA Key Values for Thermodynamics. CODATA Series on Thermodynamic Values. Hemisphere Publishing Corp., New York. 271 pp. ISBN 0-89116-758-7.
- Davis, J., Ochs, M., Olin, M., Payne, T., and Tweed, C., 2005. Interpretation and prediction of radionuclide sorption onto substrates relevant for radioactive waste disposal using thermodynamic sorption models. OECD/Nuclear Energy Agency, Paris.
- Doherty, J., 2003. PEST: Model-Independent Parameter Estimation. Watermark Numerical Computing.
- Dresden-Rossendorf, H.-Z., 2013. RES³T - Rossendorf Expert System for Surface and Sorption Thermodynamics. RES³T - Rossendorf Expert System for Surface and Sorption Thermodynamics, Dresden, Germany.
- Geckeis, H., Lützenkirchen, J., Polly, R., Rabung, T., and Schmidt, M., 2013. Mineral–Water Interface Reactions of Actinides. *Chemical Reviews* 113, 1016-1062.
- Johnson J. W., Oelkers E. H., and Helgeson H. C. (1992) SUPCRT92: A software package for calculating the standard molal thermodynamic properties of minerals, gases, aqueous species, and reactions from 1 to 5000 bar and 0 to 1000°C. *Comp. Geosci.* 18, 899-947.
- Helgeson H. C., Delany J. M., Nesbitt H. W., and Bird D. K. (1978) Summary and critique of the thermodynamic properties of rock forming minerals. *Am. J. Sci.* 278-A, 1-229.
- Herbelin, A. L. and Westall, J. C., 1994. FITEQL, A computer program for determination of chemical equilibrium constants from experimental data. Department of Chemistry, Oregon State University.
- Holland T. J. B. and Powell R. (2011) An improved and extended consistent thermodynamic dataset for phases of petrological interest, involving a new equation of state for solids. *J. Meta. Geol.* 29, 333-383.
- Ochs, M., Payne, T. E., and Brendler, V., 2012. Thermodynamic sorption modeling in support of radioactive waste disposal safety cases. A guideline document. OECD/NEA, Paris.
- Parkhurst, D. L. and Wissmeier, L., 2015. PhreeqcRM: A reaction module for transport simulators based on the geochemical model PHREEQC. *Advances in Water Resources* 83, 176-189.

- Robie R. A., Hemingway B. S., and Fischer J. R. (1978) *Thermodynamic Properties of Minerals and Related Substances at 298.15K and 1 Bar (105 Pascals) Pressure and at Higher Temperatures*. U.S. Geol. Surv. Bull. 1452, United States Government Printing Office, Washington, DC. 456 pp. [Reprinted with corrections, 1979]
- Ragoussi, M. E. and Brassinnes, S., 2015. The NEA Thermochemical Database Project: 30 years of accomplishments. *Radiochimica Acta*, 2392.
- Tagirov B. and Schott J. (2001) Aluminum speciation in crustal fluids revisited. *Geochim. Cosmochim. Acta* 64, 3965-3992.
- Zavarin, M., Turner, G. D., and Westall, J. C., 2004. FIT4FD. Modification of the Program FITEQL to Facilitate Rapid Evaluation of Complex Datasets, Livermore (CA).

8. Interplay Between Structural and Thermal-Mechanical Properties of Argillite Disposal Systems: First-Principles Study of Kaolinite Clay¹

8.1 Background

Thermodynamic parameters for the corrosion phases of spent nuclear fuel (SNF), engineered barrier systems (EBS) materials and natural system (NS) minerals are critical to assess their stability and behavior in geologic disposal environments for safety assessments. Among the thermodynamic data gaps and research needs, the thermal properties of NS minerals surrounding the waste package (e.g. clays, complex salts, granite...) are of particular importance to determine phase stability of materials and interfacial processes leading to the degradation of the waste package.

The main objectives of the present study using first-principles methods are to:

- Calculate missing thermodynamic data needed for EBS materials, in a fast, systematic, way to avoid using expensive materials and time-consuming approaches but also to complement experiments.
- Provide an independent assessment of existing experimental thermodynamic data and resolve contradictions in existing calorimetric data.
- Validate our computational approach using high-quality calorimetric data.

In order to assess our first-principles computational approach, structural optimization of kaolinite clay was carried out using density functional theory (DFT), followed by density functional perturbation theory (DF-PT) calculations to determine its phonon, elastic and thermal properties.

Kaolin-group minerals, which exhibit a high degree of structural order and chemical purity, are important members of the clay minerals family. Kaolinite, dickite, nacrite and halloysite are the four polytypes in the kaolin group, with a chemical composition of $\text{Al}_2\text{Si}_2\text{O}_5(\text{OH})_4$. These minerals, formed as a result of weathering or hydrothermal alteration of micas and feldspars, are significant resources of the Earth's permeable near-surface layer and have therefore played a prominent role in Earth and human history (Schroeder and Erickson, 2014; Balan, Calas, and Bish, 2014; Cygan and Tazaki, 2014). Owing to their large surface area and their ability to adsorb both cationic and anionic pollutant species, kaolin-group minerals can serve as efficient migration barriers at nuclear waste repositories, or as soil amendments for heavy-metals remediation.

As outlined by Pauling in 1930, minerals in the kaolin group consist of repeating $\text{Al}_2\text{Si}_2\text{O}_5(\text{OH})_4$ layers, each made of covalently bonded 1:1 sheets of silica tetrahedra (siloxane sheet) and alumina octahedra (gibbsite-like sheet) (Pauling, 1930). Since the layers are electronically neutral, the bonding between layers occurs through hydrogen bonds and van der Waals dispersion forces. Kaolinite, dickite and nacrite essentially differ in stacking sequences of the layers (Balan, Calas, and Bish, 2014). Kaolin-group minerals feature plate-like morphologies, with the exception of halloysite, which can also naturally occur as nanotubes upon hydration (Hughes and King, 2010).

¹ See Weck et al. (2015).

Because kaolinite is among the most abundant clay minerals in modern soils and sediments, it has been a subject of active research over the last few decades. However, experimental studies of the kaolinite structure, using X-ray and neutron diffraction (Giese and Datta, 1973; Suitch and Young, 1983; Young and Hewat, 1988; Bish, 1993; Akiba, et al., 1997; Neder, et al., 1999), infrared and Raman spectroscopy (Wada, 1967; Frost, 1995; Frost and Klopogge, 1999; Frost, et al., 2002; Johansson, et al., 1998; Johnston, Agnew, and Bish, 1990), nuclear magnetic resonance spectroscopy, and inelastic neutron scattering spectroscopy (White, et al., 2013), have reported conflicting results regarding its space group and the bond lengths and orientations of hydroxyl groups. In addition, large discrepancies exist between measured values of the elastic constants, bulk and shear moduli, transverse and longitudinal wave velocities, and Poisson's ratio (Katahara, 1996; Lonardelli, Wenk, Ren, 2007; Wenk, et al., 2008; Woeber, Katz, and Ahrens, 1963; Wang, Wang, and Cates, 2001; Vanorio and Prasad, 2003; Welch and Crichton, 2010). Calorimetric data, such as the isobaric heat capacity and entropy, reported so far also show some differences (Schieltz and Soliman, 1966; Robie and Hemingway, 1995; Robie and Hemingway, 1991).

Numerous computational studies using first-principles methods have also investigated the structure and properties of kaolinite (White, et al., 2013; Hess and Saunders, 1992; Hobbs, et al., 1997; Balan, et al., 2001; Benco, et al., 2001; Sato, et al., 2005; Hu and Michaelides, 2008; Ugliengo, et al., 2009; White, et al., 2009; Mercier, Le Page, and Desgreniers, 2010; Mercier and Le Page, 2011; Militzer, et al., 2011; Tunega, Bucko, and Zaoui, 2012). However, very few of those studies utilized dispersion-corrected methods, which were found to significantly improve the agreement between calculated and measured structural parameters (Ugliengo, et al., 2009; Tunega, Bucko, and Zaoui, 2012). Indeed, a well-known limitation of standard density functional theory (DFT) functionals utilized in previous investigations of kaolinite is their inability to account for non-local electron correlation. A pragmatic method to work around this problem has been given by density functional theory corrected for dispersion (Wu, et al., 2001), which consists in adding a semi-empirical dispersion potential (R^{-6} terms) to the conventional Kohn-Sham total-energy functional. While this computational approach was successfully tested to determine the relaxed structure of kaolinite, little is known about its ability to accurately predict the mechanical and thermal properties of kaolin-group minerals.

In this work, the structural, mechanical and thermodynamic properties of kaolinite clay, with ideal $\text{Al}_2\text{Si}_2\text{O}_5(\text{OH})_4$ stoichiometry, have been investigated using first-principles methods. In particular, computational approaches going beyond the standard density functional theory framework are utilized here and include corrections for possible van der Waals dispersion interactions. Details of our computational approach are provided in the next section, followed by a discussion of our results and conclusions.

8.2 Computational Methods

First-principles total energy calculations were performed using density functional theory, as implemented in the Vienna Ab initio Simulation Package (VASP) (Kresse and Furthmüller, 1996). The exchange-correlation energy was calculated within the generalized gradient approximation (GGA) (Perdew, et al., 1992), with the parameterization of Perdew, Burke, and Ernzerhof (PBE) (Perdew, Burke and Ernzerhof, 1996). Standard functionals such as the PBE or PW91 functionals were found in previous studies to correctly describe the structural parameters

and properties of various minerals characterized experimentally (Weck, et al., 2012, 2013, 2014; Weck and Kim, 2014a, 2014b).

The interaction between valence electrons and ionic cores was described by the projector augmented wave (PAW) method (Kresse and Joubert, 1999; Blöchl, 1994). The O(2s,2p), Al(3s,3p) and Si(3s,3p) electrons were treated explicitly as valence electrons in the Kohn-Sham (KS) equations and the remaining core electrons together with the nuclei were represented by PAW pseudopotentials. The KS equation was solved using the blocked Davidson (Davidson, 1983) iterative matrix diagonalization scheme. The plane-wave cutoff energy for the electronic wavefunctions was set to 500 eV, ensuring the total energy of the system to be converged to within 1 meV/atom.

Since the structure of kaolinite consists of tightly bonded siloxane and gibbsite-like layers, with weak attractive interactions between silicate/gibbsite paired layers, it can be inferred that hydrogen bonds and van der Waals dispersion forces may play a role in the structure and properties of this compound. However, popular density functionals are unable to describe correctly van der Waals interactions resulting from dynamical correlations between fluctuating charge distributions. A pragmatic method to work around this problem has been given by density functional theory corrected for dispersion (DFT-D), which consists in adding a semi-empirical dispersion potential to the conventional Kohn-Sham GGA total-energy functional, E_{DFT} , i.e.,

$$E_{\text{DFT-D}} = E_{\text{DFT}} + E_{\text{disp}}.$$

In the DFT-D method of Grimme (2006) (aka, DFT-D2) utilized in this study, the van der Waals interactions are described via a simple pair-wise force field, which is optimized for DFT functionals. The dispersion energy for periodic systems is defined as:

$$E_{\text{disp}} = -\frac{s_6}{2} \sum_{i=1}^N \sum_{j=1}^N \sum_L' \frac{C_6^{ij}}{|\vec{r}^{i,0} - \vec{r}^{j,L}|^6} f(|\vec{r}^{i,0} - \vec{r}^{j,L}|),$$

where the summation are over all atoms N and all translations of the unit cell $L = (l_1, l_2, l_3)$, with the prime sign indicating that cell $i \neq j$ for $L = 0$, s_6 is a global scaling factor, C_6^{ij} is the dispersion coefficient for the atom pair ij , and $\vec{r}^{j,L}$ is a position vector of atom j after performing L translations of the unit cell along lattice vectors. In practice, terms corresponding to interactions over distances longer than a certain suitably chosen cutoff radius contribute only negligibly to the dispersion energy and can be ignored. The term $f(r^{i,j})$ is a damping function:

$$f(r^{i,j}) = \frac{1}{1 + e^{-d(r^{i,j}/R_0^{ij}-1)}},$$

whose role is to scale the force field such as to minimize contributions from interactions within typical bonding distances. Combination rules for dispersion coefficients C_6^{ij} and van der Waals radii R_0^{ij} are:

$$C_6^{ij} = \sqrt{C_6^i C_6^j},$$

and

$$R_0^{ij} = R_0^i + R_0^j.$$

The global scaling parameter s_6 has been optimized for several different DFT functionals and corresponds to a value of $s_6 = 0.75$ for the PBE functional used in this study (Grimme, 2006). The parameters used in the empirical force-field of Grimme (2006) are summarized in Table 4.

Table 4 Parameters used in the empirical force-field of Grimme for the elements in kaolinite.^a

Parameters	Al	Si	O	H
R_0 (Å)	1.716	1.716	1.342	1.001
C_6 (Jnm ⁶ mol ⁻¹)	10.79	9.23	0.70	0.14

^a [Grimme, 2006].

The crystal structure was optimized with periodic boundary conditions applied. Ionic relaxation was carried out using the quasi-Newton method and the Hellmann-Feynman forces acting on atoms were calculated with a convergence tolerance set to 0.01 eV/Å. Structural optimization and properties calculations were carried out using the Monkhorst-Pack special k -point scheme (Monkhorst and Pack, 1976) with a $6 \times 6 \times 6$ mesh for integrations in the Brillouin zone (BZ) of kaolinite. The tetrahedron method with Blöchl corrections (Blöchl and Jepsen, 1994) was used for BZ integrations. A periodic unit cell containing 34 atoms ($Z = 2$) was used in the calculations. Ionic and cell relaxations of the kaolinite bulk structure were performed simultaneously, without symmetry constraints, using the crystallographic structure resolved by Bish (1993) as an initial guess.

Table 5 Structural unit-cell parameters of kaolinite.^a

Parameter	DFT ^a	DFT-D2 ^c	DFT ^b	GULP ^c	Expt. ^d	Expt. ^e
<i>a</i> (Å)	5.212	5.177	5.225	5.168	5.1535(3)	5.154(9)
<i>b</i> (Å)	9.051	8.985	9.071	8.974	8.9419(5)	8.942(4)
<i>c</i> (Å)	7.461	7.329	7.464	7.059	7.3906(4)	7.401(10)
α (°)	91.83	91.95	91.44	91.400	91.926(2)	91.69(9)
β (°)	104.97	105.22	104.67	104.85	105.046(2)	104.61(5)
γ (°)	89.77	89.82	89.77	89.71	89.797(2)	89.82(4)
<i>V</i> (Å ³)	339.84	328.73	342.12	316.34	328.70(5)	329.91(5)

^a This study.^b VASP/GGA by Militzer *et al.*, 2011.^c GULP classical results from Benazzouz *et al.*, 2012.^d Neutron powder diffraction data from Bish, 1993.^e Single-crystal XRD data from Neder *et al.*, 1999.

For the sake of comparison, the structural unit-cell parameters calculated by Benazzouz *et al.* (2012) using the classical GULP software were also reported in Table 5. While both DFT-D2 and GULP slightly overestimate dispersion forces between sheets, classical calculations significantly underestimate both the *c* parameter along the stacking direction and the cell volume by ~4%.

In this 1:1-type clay, one silicate tetrahedral sheet is covalently connected to one oxide/hydroxide gibbsite octahedral sheet *via* apical oxygen atoms and the resulting paired layers, stacked perpendicularly to the *c* axis (cf. Figure 1), are held together predominantly by O–H···O hydrogen bonds and by van der Waals forces to some extent. In kaolinite, both inner hydroxyl groups [O(h1)H(1)] and outer surface hydroxyl groups [O(h2)H(2), O(h3)H(3), and O(h4)H(4)] terminating the octahedral sheet are present, but only the latter are responsible for layers stacking. Only two-thirds of the octahedral sites in the sheet are occupied by trivalent Al(III) cations in dioctahedral kaolinite.

Table 6 Selected interatomic distances (Å) in the structure of kaolinite.

Parameters ^a	DFT ^b	DFT-D2 ^b	Expt. ^c	Expt. ^d
Si(1)–O(1)	1.620	1.616	1.618	1.614
Si(1)–O(3)	1.644	1.640	1.611	1.620
Si(1)–O(4)	1.640	1.638	1.620	1.618
Si(1)–O(5)	1.648	1.644	1.619	1.628
Si(2)–O(2)	1.618	1.613	1.612	1.605
Si(2)–O(3)	1.643	1.640	1.617	1.622
Si(2)–O(4)	1.640	1.636	1.616	1.616
Si(2)–O(5)	1.648	1.644	1.608	1.615
Al(1)–O(1)	1.970	1.976	1.927	1.948
Al(1)–O(2)	2.046	2.034	1.930	2.001
Al(1)–O(h1)H(1)	1.940	1.944	1.913	1.921
Al(1)–O(h2)H(2)	1.870	1.864	1.890	1.853
Al(1)–O(h3)H(3)	1.863	1.856	1.865	1.849
Al(1)–O(h4)H(4)	1.864	1.853	1.915	1.862
Al(2)–O(1)	2.036	2.025	1.931	1.990
Al(2)–O(2)	1.958	1.961	1.919	1.946
Al(2)–O(h1)H(1)	1.938	1.941	1.912	1.921
Al(2)–O(h2)H(2)	1.870	1.866	1.896	1.867
Al(2)–Oh(3)H(3)	1.869	1.863	1.886	1.858
Al(2)–O(h4)H(4)	1.868	1.859	1.910	1.853
O(h1)–H(1)	0.975	0.976	0.975	0.75
O(h2)–H(2)	0.971	0.972	0.982	0.76
O(h3)–H(3)	0.972	0.974	0.976	0.77
O(h4)–H(4)	0.971	0.972	0.975	0.88
O(h2)H(2)···O(4)	3.088	2.933	3.087	3.088
O(h3)H(3)···O(3)	2.992	2.862	2.980	2.989
O(h4)H(4)···O(5)	2.941	2.822	2.945	2.953

^a Atomic labels are from Figure 1, ^b This study, ^c Neutron powder diffraction data from Bish, 1993.

^d Single-crystal XRD data from Neder *et al.*, 1999.

Selected calculated and measured interatomic distances in the structure of kaolinite are given in Table 6. Good agreement is obtained overall between computed equilibrium bond distances and the values measured at finite temperature by Bish (1993) and Neder *et al.* (1999). As observed in XRD experiments, the computed Si tetrahedra exhibit Si–O_{apical} distances [i.e. Si(1)–O(1) and Si(2)–O(2)] shorter than Si–O_{basal} bonds. The calculated Al–(O,OH) distances are similar to experimental data, with Al–O_{apical} bonds being longer than Al–OH distances and the Al–OH(1) bond to the intralayer hydroxyl group being longer than Al–OH bonds to interlayer hydroxyl groups. Let us note that the O–H bond distances calculated with DFT and DFT-D2 (i.e. ~0.97 Å) are nearly identical with the neutron powder-diffraction data reported by Bish, while the hydroxyl bond distances proposed by Neder and co-workers based on single-crystal XRD data are significantly shorter (i.e. 0.75–0.88 Å). In agreement with the neutron diffraction data of Bish (Bish, 1993), the computed intralayer hydroxyl groups are nearly parallel to the (001) plane (~1–2°, compared to 0.38° in experiments), while the angle between the interlayer hydroxyl groups and the (001) plane is in the range 63–80° (60.28–73.16° in experiments).

Although the cell volume and lattice parameters calculated with DFT-D2 are in good agreement with experiment, the computed O–H···O hydrogen bonds are systematically shorter than distances determined using XRD and neutron diffraction, i.e. another indication that attractive dispersion forces between layers are slightly overestimated by DFT-D2. This contrasts with standard DFT, which closely reproduces hydrogen bonds measured in kaolinite. Consistent with crystallographic data (Bish, 1993; Neder *et al.*, 1999) and infrared spectroscopy (Wada, 1967), DFT-D2 and DFT predict that O(h4)H(4)···O(5) is the shortest (i.e. strongest) H-bond and O(h2)H(2)···O(4) is the longest (i.e. weakest).

9.2 Mechanical properties:

Using the equilibrium structures of kaolinite relaxed with DFT and DFT-D2, the elastic constants were calculated at $T = 0$ K with VASP as the second derivatives of the energy with respect to the strain, i.e.

$$C_{ij} = \frac{1}{V} \left(\frac{\partial^2 U}{\partial \varepsilon_i \partial \varepsilon_j} \right)$$

where V is the volume, U is the total energy of the systems, and ε is the infinitesimal displacement. The Voigt notation, which relates the elastic stiffness coefficients C_{ijkl} ($i, j, k, l = x, y, z$) in the different directions in the crystal to the C_{ij} ($i, j = 1, \dots, 6$) elastic constants, was adopted in this study, i.e. $xx \rightarrow 1$, $yy \rightarrow 2$, $zz \rightarrow 3$, $yz \rightarrow 4$, $zx \rightarrow 5$, and $xy \rightarrow 6$. The 6×6 elasticity tensor was determined by performing six finite distortions of the equilibrium lattice and deriving the elastic constants from the strain-stress relationship (Le Page and Saxe, 2002). The elastic behavior of the triclinic kaolinite crystal is determined by 21 non-degenerate elastic constants in the symmetric elasticity tensor C (Nye, 1985):

$$C = \frac{1}{V} (D_{\varepsilon\varepsilon} - D_{\varepsilon i} D_{ij}^{-1} D_{j\varepsilon}),$$

with

$$D_{\varepsilon\varepsilon} = \left(\frac{\partial^2 U}{\partial \varepsilon \partial \varepsilon} \right)_{\text{internal}},$$

$$D_{\varepsilon i} = \left(\frac{\partial^2 U}{\partial \varepsilon \partial \alpha_i} \right)_{\varepsilon},$$

and

$$D_{ij} = \left(\frac{\partial^2 U}{\partial \alpha_i \partial \beta_j} \right)_{\varepsilon}.$$

The total elastic moduli calculated with DFT and DFT-D2, including both the contributions for distortions with rigid ions and the contributions from the ionic relaxations, are summarized in Table 7, along with experimental results and previous quantum and classical predictions. The in-plane C_{11} and C_{22} elastic constants calculated with DFT are larger than with DFT-D2, while the C_{33} constant along the normal to the sheets is larger with DFT-D2 as a result of attractive dispersion forces. Although a meaningful comparison with experiments is difficult, owing to the large spread in measured values, the primary-direction elastic constants calculated here for an ideal single crystal appear larger than most experimental values obtained using samples with various levels of crystallinity, defects, and impurity and water content. The C_{44} , C_{55} , and C_{66} shear constants and off-diagonal elastic constants computed in this study appear overall in line with available measurements and previous theoretical results, although discrepancies remain.

Table 7 Calculated and measured elastic constants of kaolinite (in GPa).

C_{ij}	DFT ^a	DFT-D2 ^a	DFT ^b	GULP ^c	Expt. and Extrapolation
C ₁₁	187.20	175.16	178.5	249.12	171.51 ^d 48.1 ^e 79.3 ^e 121.1 ^e 126.4 ^f
C ₂₂	180.56	168.65	200.9	259.22	
C ₃₃	88.02	133.99	32.1	52.09	52.62 ^d 45.2 ^e 72.5 ^e 112.5 ^e 57.8 ^f
C ₄₄	9.63	10.07	11.2	12.48	14.76 ^d 16.7 ^e 25.6 ^e 41.1 ^e 31.6 ^f
C ₅₅	12.36	12.78	22.2	16.03	
C ₆₆	62.10	62.30	60.1	66.65	66.31 ^d 16.9 ^e 26.3 ^e 41.3 ^e 53.6 ^f
C ₁₂	66.42	54.10	71.5	124.82	
C ₁₃	15.63	28.58	2.0	14.52	27.11 ^d 12.9 ^e 24.1 ^e 34.8 ^e 8.5 ^f
C ₁₄	-0.74	-1.90	-0.4	6.40	
C ₁₅	1.18	-0.79	-41.7	0.08	
C ₁₆	-6.14	-5.79	-2.3	-0.85	
C ₂₃	16.00	28.46	-2.9	18.72	
C ₂₄	-0.30	-2.70	-2.8	5.69	
C ₂₅	-0.04	-1.42	-19.8	1.44	
C ₂₆	0.58	0.96	1.9	6.42	
C ₃₄	-0.96	-3.57	-0.2	1.57	
C ₃₅	-0.56	-2.44	1.7	-4.15	
C ₃₆	0.37	0.71	3.4	-0.64	
C ₄₅	-0.45	-0.84	-1.2	-0.17	
C ₄₆	-1.20	-1.78	-12.9	-1.03	
C ₅₆	-0.02	-0.13	0.8	-1.05	

^a This study.

^b CASTEP results from Sato *et al.*, 2005.

^c GULP classical results from Benazzouz *et al.*, 2012.

^d Extrapolation by Katahara, 1996.

^e Lonardelli *et al.*, 2007.

^f Wenk *et al.*, 2008.

For the sake of comparison with the DFT results from Sato *et al.* (2005) and the classical results of Benazzouz *et al.* at $T = 0$ K (Benazzouz *et al.*, 2012), the Reuss (1929) approximation was used to compute the isotropic elastic properties of kaolinite polycrystalline aggregates. The method proposed by Reuss for calculating the elastic moduli of an aggregate of crystals is based on the averaging, over all possible lattice orientations, of the relations expressing the strain in a single crystal in terms of a given stress.

The bulk modulus by the Reuss approximation, K_R , was obtained using the expression:

$$K_R = [S_{11} + S_{22} + S_{33} + 2(S_{12} + S_{13} + S_{23})]^{-1}$$

where the elastic compliances, S_{ij} , can be readily obtained by inverting the elastic constant tensor, i.e. $S = C^{-1}$. The K_R values calculated with DFT and DFT-D2 are 59.21 and 74.25 GPa, respectively, i.e. significantly larger than the value of 23 GPa obtained by Sato *et al.* (Sato *et al.*, 2005) with DFT and the value of 44.85 GPa predicted by Benazzouz *et al.* (Benazzouz *et al.*, 2012) using the classical GULP software. As shown in Table 8, the value predicted in this study with DFT at $T = 0$ K is in close agreement with the experimental estimate of 59.7 ± 0.7 GPa recently reported by Welch and Crichton (Welch and Crichton, 2010) at 298 K and slightly overestimates the value of 56 GPa extrapolated by Katahara (1996).

The shear modulus by the Reuss approximation, G_R , was also calculated from elastic compliances using the formula:

$$G_R = \frac{15}{4(S_{11} + S_{22} + S_{33} - S_{12} - S_{13} - S_{23}) + 3(S_{44} + S_{55} + S_{66})}$$

The G_R values predicted with DFT and DFT-D2 are 20.91 and 21.70 GPa, respectively. These estimates are consistent with the values of 17 and 24.11 GPa previously obtained with DFT and GULP, as well as with the experimental values of 19.7 and 22.1 GPa determined by Wang *et al.* (2001) for samples with poor and good crystallinity, respectively.

The Young's modulus, defined as the ratio of the stress to strain, i.e. $Y = \sigma/\varepsilon$, was derived from the elastic compliances, with its components along the a , b , and c directions expressed as $Y_x = S_{11}^{-1}$, $Y_y = S_{22}^{-1}$, and $Y_z = S_{33}^{-1}$. The values computed with DFT are $Y_x = 160.85$ GPa, $Y_y = 155.61$ GPa, and $Y_z = 85.89$ GPa, while the values predicted with DFT-D2 are $Y_x = 154.20$ GPa, $Y_y = 148.54$ GPa, and $Y_z = 125.42$ GPa. Young's modulus along the z stacking direction is much stiffer with DFT-D2 than with DFT as a result of attractive dispersion forces, while softening occurs along the x and y in-plane directions with DFT-D2.

Table 8 Calculated bulk modulus (K), shear modulus (G), transverse wave velocity (V_s), longitudinal wave velocity (V_p), Poisson's ratio (ν), and Young's modulus components along the a , b , c directions (Y_x , Y_y , Y_z) of kaolinite. Suffixes R, V and H denote values calculated using the Reuss, Voigt, and Hill approximations. Experimental values are also reported for comparison. Moduli are expressed in GPa and velocities in km.s^{-1} .

	DFT ^a	DFT-D2 ^a	DFT ^b	GULP ^c	Expt. and Extrapolation
K_R	59.21	74.25	23	44.85	44 ^d 47.9 ^d 56 ^e 6-11 ^f 1.43 ^g 59.7 ^h
K_V	72.43	77.79			
K_H	65.82	76.02			
G_R	20.91	21.70	17	24.11	22.1 ^d 19.7 ^d 31.8 ^e 6 ^f 1.38 ^g
G_V	40.66	41.48			
G_H	30.79	31.59			
V_{pR}	5.75	6.26	7.34	16.85	5.488 ^d 5.509 ^d 6.23 ^e 2.695 ^f 1.4 ^g
V_{pV}	6.93	7.11			
V_{pH}	6.37	6.70			
V_{sR}	2.82	2.87	3.50	9.43	3.010 ^d 2.839 ^d 3.55 ^e 1.436 ^f 0.93 ^g
V_{sV}	3.93	3.97			
V_{sH}	3.42	3.46			
V_{pR}/V_{sR}	2.04	2.18	2.10	1.787	1.823 ^d 1.755 ^e
V_{pV}/V_{sV}	1.76	1.79			
V_{pH}/V_{sH}	1.86	1.93			
ν_R	0.342	0.367	0.352	0.272	0.285 ^d 0.319 ^d 0.26 ^e 0.301 ^e 1.14 ^f
ν_V	0.264	0.274			
ν_H	0.298	0.317			
Y_x	160.85	154.20	92	187.22	
Y_y	155.61	148.54	170	192.57	
Y_z	85.89	125.42	31	49.35	

^a This study; ^b CASTEP results from Sato *et al.*, 2005; ^c GULP classical results from Benazzouz *et al.*, 2012; ^d Wang *et al.*, 2001; ^e Extrapolation by Katahara, 1996; ^f Vanorio *et al.*, 2003; ^gWoeber *et al.*, 1963; ^h Welch and Crichton, 2010.

The acoustic transverse wave velocity, V_{sR} , and longitudinal wave velocity, V_{pR} , of kaolinite were further derived from the Reuss bulk modulus and shear modulus using the formulas:

$$V_{sR} = \sqrt{\frac{G_R}{\rho}}$$

and

$$V_{pR} = \sqrt{\frac{4G_R + 3K_R}{3\rho}}$$

where ρ is the density of kaolinite. The V_{pR}/V_{sR} ratio computed with DFT and DFT-D2 are 2.04 and 2.18, respectively, i.e. slightly larger than the values of 1.823 and 1.755 reported by Wang *et al.* (2001) and Katahara (1996), respectively.

Poisson's ratio, ν_R , was derived from the ratio of the acoustic wave velocities, using the expression:

$$\nu_R = \frac{(V_{pR}/V_{sR})^2 - 2}{2[(V_{pR}/V_{sR})^2 - 1]}$$

The values predicted with DFT and DFT-D2 are 0.342 and 0.367 km.s⁻¹, overestimating the experimental values of 0.285 and 0.319 km.s⁻¹ determined by Wang *et al.* (2001) and the values of 0.260 and 0.301 km.s⁻¹ extrapolated by Katahara (1996).

All the results calculated using the Reuss approximation are summarized in Table 8, along with the corresponding experimental values.

While the stress is assumed to be uniform throughout the aggregate of crystals in the method of Reuss, the approximation proposed by Voigt (1928), on the other hand, considers that the strain is uniform and the averaging of the relations expressing the stress is carried out.

The bulk modulus by the Voigt approximation, K_V , was calculated using the formula:

$$K_V = \frac{C_{11} + C_{22} + C_{33} + 2(C_{12} + C_{13} + C_{23})}{9}$$

where C_{ij} are the elastic constants.

The shear modulus by the Voigt approximation, G_V , was also obtained using the expression:

$$G_V = \frac{C_{11} + C_{22} + C_{33} - C_{12} - C_{13} - C_{23} + 3(C_{44} + C_{55} + C_{66})}{15}$$

Based on energy considerations, it was shown by Hill (1952) that Reuss and Voigt approximations result in lower and upper limits, respectively, of polycrystalline constants and practical estimates of the polycrystalline bulk and shear moduli in the Hill approximation were computed using the formulas:

$$K_H = \frac{K_R + K_V}{2}$$

and

$$G_H = \frac{G_R + G_V}{2}$$

In a similar way as described above for the Reuss approximation, the acoustic wave velocities and Poisson's ratio were calculated with DFT and DFT-D2 in the Voigt and Hill approximations; results are also reported in Table 8.

Starting from the equilibrium structure of kaolinite relaxed with DFT-D2, two types of unit-cell deformation were investigated, namely hydrostatic deformation and uniaxial deformation along the z -axis (c direction) normal of the layers. Both deformation modes and the corresponding calculated total energies are shown in Figure 2. Significant differences exist between hydrostatic and uniaxial deformations of kaolinite, i.e. uniaxial deformation resulting in a stiffer material than when deformed hydrostatically; this shows the importance of anisotropy in layered materials such as kaolinite.

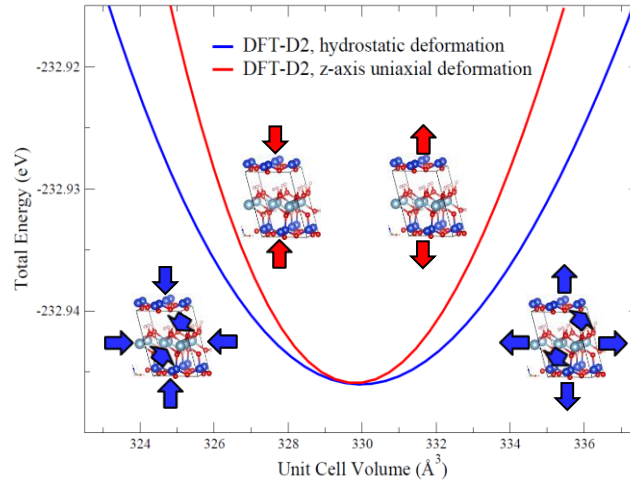


Figure 2. Energetics of the hydrostatic and uniaxial (z -axis) deformations of the kaolinite unit cell calculated with DFT-D2 at the GGA/PBE level of theory.

For the sake of comparison with experiments and previous calculations, the bulk modulus K_0 was calculated with DFT-D2 for uniform hydrostatic pressure using the third-order Birch-Murnaghan isothermal equation of state (EoS) (Birch, 1947; Murnaghan, 1944):

$$P(V) = \frac{3K_0}{2} \left[\left(\frac{V_0}{V} \right)^{\frac{7}{3}} - \left(\frac{V_0}{V} \right)^{\frac{5}{3}} \right] \left\{ 1 + \frac{3}{4} (K'_0 - 4) \left[\left(\frac{V_0}{V} \right)^{\frac{2}{3}} - 1 \right] \right\},$$

where P is the pressure, V_0 is the reference volume, V is the deformed volume, and

$$K_0(T) = -V \left(\frac{\partial P}{\partial V} \right)_{P=0} \quad \text{and} \quad K'_0(T) = \left(\frac{\partial K}{\partial P} \right)_{P=0}.$$

In addition, the bulk modulus was computed using the universal Vinet (Vinet, et al., 1989) EoS,

$$P(V) = 3K_0 \frac{(1-x)}{x^2} \exp \left[\frac{3}{2} (K'_0 - 1)(1-x) \right],$$

where

$$x = \left(\frac{V}{V_0} \right)^{\frac{1}{3}}.$$

The bulk moduli computed at 0 K with the third-order Birch-Murnaghan and Vinet EoS are $K_0 = 69.42$ and 69.40 GPa, respectively. These values are slightly below the calculated $K_R = 74.25$ GPa and $K_V = 77.79$ GPa derived from elastic compliances and elastic constants, respectively, and above the values measured at ambient temperature, i.e., $K_0 = 1.43\text{--}59.7$ GPa (see Table 8). However, as will be shown in the next section, a significant softening of the bulk modulus occurs as the temperature increases from 0 to 298 K.

9.3 Thermodynamic properties:

The forces exerted on atoms of the equilibrium structure of kaolinite were computed using density functional perturbation theory (DFPT) with VASP at the DFT-D2/GGA/PBE level of theory and phonon frequencies were calculated.

Phonon analysis was performed at constant equilibrium volume in order to derive the phonon contribution to the Helmholtz free energy, which was calculated using the following formula:

$$F_{phonon}(T) = \frac{1}{2} \sum_{\mathbf{q},v} \hbar \omega_{\mathbf{q},v} + k_B T \sum_{\mathbf{q},v} \ln[1 - e^{-\beta \hbar \omega_{\mathbf{q},v}}],$$

where \mathbf{q} and v are the wave vector and band index, \hbar is the reduced Planck constant, $\hbar \omega_{\mathbf{q},v}$ is the energy of a single phonon with angular frequency $\omega_{\mathbf{q},v}$, k_B is the Boltzmann constant, T is the temperature of the system, and $\beta = (k_B T)^{-1}$.

The isochoric heat capacity, C_V , and entropy, S , were also computed at constant equilibrium volume using the expressions:

$$C_V(T) = k_B \sum_{\mathbf{q},v} (\beta \hbar \omega_{\mathbf{q},v})^2 \frac{e^{\beta \hbar \omega_{\mathbf{q},v}}}{[e^{\beta \hbar \omega_{\mathbf{q},v}} - 1]^2}$$

and

$$S(T) = -k_B \sum_{\mathbf{q},v} \ln[1 - e^{-\beta \hbar \omega_{\mathbf{q},v}}] - \frac{1}{T} \sum_{\mathbf{q},v} \frac{\hbar \omega_{\mathbf{q},v}}{e^{\beta \hbar \omega_{\mathbf{q},v}} - 1}$$

As shown in Figure 3, the calculated entropy using uniaxial deformation along the z -axis of the unit cell is in good overall agreement with experimental values derived by Robie and Hemingway (Robie and Hemingway, 1995) using well-crystallized Georgia kaolinite (“KGa-1b” sample (Robie and Hemingway, 1991)). At 298 K, the computed value of $191 \text{ J}\cdot\text{mol}^{-1}\cdot\text{K}^{-1}$ underestimates by 4.7% the value obtained by Robie and Hemingway (i.e. $200.4 \text{ J}\cdot\text{mol}^{-1}\cdot\text{K}^{-1}$), while it overestimates by 11.3% the value reported by Schieltz and Soliman (i.e. $169.45 \text{ J}\cdot\text{mol}^{-1}\cdot\text{K}^{-1}$) (Schieltz and Soliman, 1966). At 800 K, the computed and experimentally-derived entropy values differ by less than 3%. The entropy increases steadily with temperature as a result of the larger number of microstates in the system, W , which in turn increases logarithmically the entropy according to Boltzmann’s entropy formula, $S = k_B \cdot \log(W)$. However, the entropy calculated using hydrostatic deformation consistently underestimates data derived from calorimetry. This shows that uniaxial deformation of the cell maximizes the entropy compared to hydrostatic deformation. Maximizing the entropy appears to be the thermodynamic driving force for the formation of layered structures. The upper temperature limit is set to *ca.* 800 K in this study, since it is well-known that kaolinite undergoes significant structural changes as the result of the loss of its lattice OH groups in the 800–900 K temperature range.

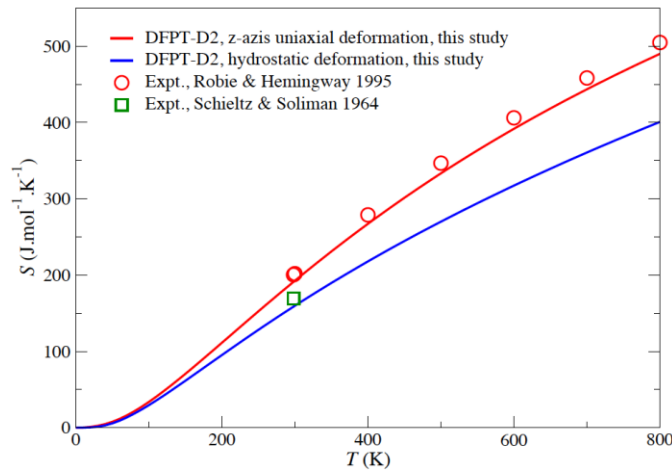


Figure 3. Thermal evolution of the entropy of kaolinite computed with DFT-D2 at the GGA/PBE level along with the experimental values of Robie and Hemingway (1995) and Schieltz and Soliman (1966).

Further analysis from a set of phonon calculations in the vicinity of the computed equilibrium crystal structure was carried out to obtain thermal properties at constant pressure (e.g., the Gibbs free energy and the isobaric heat capacity) within a quasi-harmonic approximation (QHA). The

QHA mentioned here introduces a volume dependence of phonon frequencies as a part of anharmonic effect (Togo, Oba and Tanaka, 2008).

The Gibbs free energy is defined at a constant pressure by the transformation:

$$G(T, P) = \min_V [U(V) + F_{\text{phonon}}(T; V) + PV],$$

where \min_V [function of V] corresponds to a unique minimum of the expression between brackets with respect to the volume V , U is the total energy of the system, and P is the pressure. $U(V)$ and $F_{\text{phonon}}(T; V)$ were calculated and the thermodynamic functions of the right-hand sides of the equation above were fitted to the integral forms of the Vinet EoS and the third-order Birch-Murnaghan EoS. The thermal evolution of the bulk modulus of kaolinite computed with both EoS is depicted in Figure 4. The bulk modulus values calculated with Vinet and Birch-Murnaghan EoS are essentially identical up to *ca.* 350 K, while differences of up to 50% appear at higher temperatures. The estimates of 56.17 and 56.01 GPa predicted at 298.15 K with the Vinet and Birch-Murnaghan EoS, respectively, are slightly below the most recent experimental value of 59.7 ± 0.7 GPa reported by Welch and Crichton (2010) at 298 K (with well-crystallized kaolinite sample from Keokuk, Iowa) using a second-order Birch-Murnaghan EoS, and above the values of 47.9 ± 8 GPa for well-crystallized Georgia kaolinite (“KGa-1b” sample with grain density of 2.444%) and 44.0 ± 8 GPa for poorly crystallized Georgia kaolinite (“KGa-2” sample with grain density of 2.439%) reported by Wang *et al.* at 294 K (2001). The estimates calculated in the present study at 298.15 K are in excellent agreement with the estimate of 56 GPa extrapolated by Katahara (1996). These values are also in line with bulk moduli determined experimentally for typical clays (see, e.g. comparative histogram in Benazzouz, et al., 2012), while the values of 6–11 GPa measured at ambient temperature by Vanorio *et al.* (2003) (“KGa-1b” sample) and 1.43 GPa by Woeber *et al.* (1963) most likely underestimate the bulk modulus of well-crystallized kaolinite. Previous studies also pointed out the unusually low bulk moduli obtained by Vanorio *et al.* using extrapolation of acoustic measurements on cold-pressed samples with different porosities, compared to values obtained from compressibility measurements and Brillouin scattering (Chen and Evans, 2006; Sone and Zoback, 2013).

Assuming that the thermal evolutions of the bulk modulus calculated with DFT-D2 and DFT are similar and that the difference $\Delta K_H = K_H^{\text{DFT-D2}} - K_H^{\text{DFT}} \approx 10$ GPa calculated at $T = 0$ K (cf. Table 8) is nearly constant, it can be inferred that a value of ~ 46 GPa value would be obtained at $T = 298$ K with standard DFT. While smaller than the value of 59.7 ± 0.7 GPa reported by Welch and Crichton (2010) at 298 K, this estimate would still be in close agreement with the value of 47.9 ± 8 GPa reported by Wang *et al.* (2001) for well-crystallized kaolinite at 294 K.

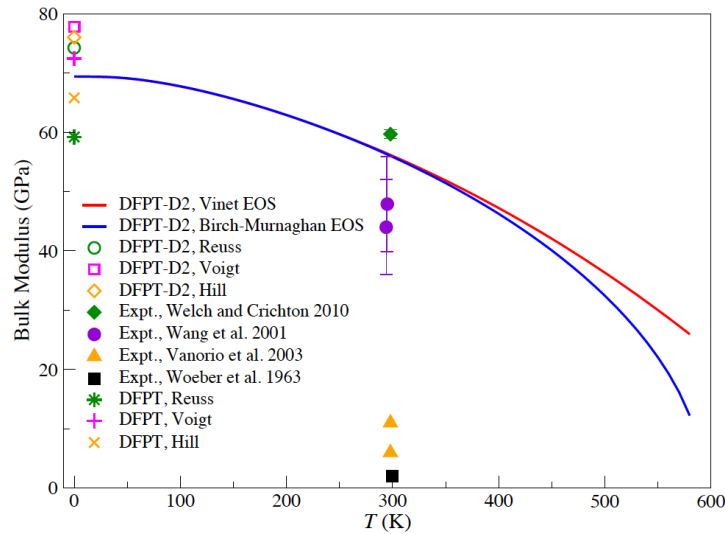


Figure 4. Thermal evolution of the bulk modulus of kaolinite computed with the Vinet and third-order Birch-Murnaghan EoS with DFPT-D2 at the GGA/PBE level of theory. Experimental data and Reuss-Voigt-Hill values computed with DFPT and DFPT-D2 from Table 8 are also displayed for comparison.

The isobaric heat capacity versus temperature was also derived from the Gibbs free energy according to:

$$C_p(T, P) = -T \frac{\partial^2 G(T, P)}{\partial T^2} = T \frac{\partial V(T, P)}{\partial T} \frac{\partial S(T; V)}{\partial V} \Big|_{V=V(T, P)} + C_V[T, V(T, P)],$$

where $V(T, P)$ is the equilibrium volume at T and P , and the pressure is set to $P = 1$ bar, i.e. the reference pressure for the standard state adopted in calorimetric data tabulated by Robie and Hemingway (1995).

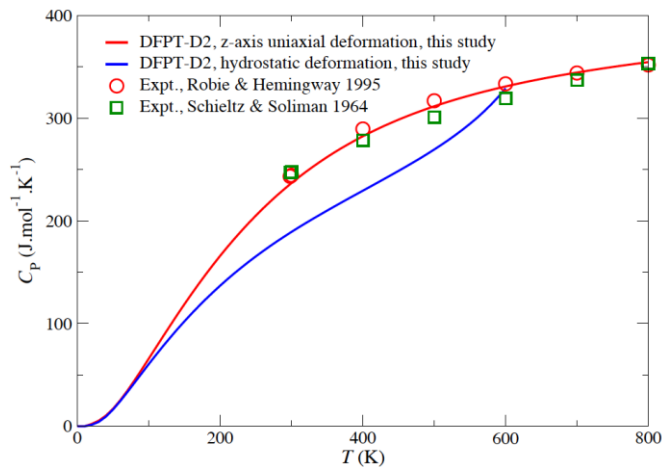


Figure 5. Thermal evolution of the isobaric heat capacity of kaolinite calculated at constant atmospheric pressure with DFPT-D2 at the PBE/GGA level of theory for uniaxial and hydrostatic deformations. The experimental values of Robie and Hemingway (1995) and Schielitz and Soliman (1966) are also depicted for the sake of comparison.

DFPT-D2 calculations of the isobaric heat capacity of kaolinite for uniaxial and hydrostatic deformations are shown in Figure 5. Very good agreement is observed between the computed isobaric heat capacity using uniaxial deformation of the cell and the calorimetric data of Robie and Hemingway (1995), while the values calculated with hydrostatic deformation significantly underestimate calorimetric data for temperatures below 600 K.

At 298 K, the computed C_p value of $236 \text{ J.mol}^{-1}.\text{K}^{-1}$ corresponding to uniaxial deformation along the z -axis underestimates by 4.6 and 3.0 % the fitted values of Schieltz and Soliman (1966) (i.e. $247.4 \text{ J.mol}^{-1}.\text{K}^{-1}$) and Robie and Hemingway (1995) (i.e. $243.4 \text{ J.mol}^{-1}.\text{K}^{-1}$), respectively. Above 400 K, the computed heat capacity lies within the range of calorimetric data from both sets, with overall closer agreement with the data of Robie and Hemingway (Robie and Hemingway, 1995), except nearby the estimated limit of thermal stability at 800 K, where it overestimates experimental data by less than 0.7%. The computed heat capacity of $354 \text{ J.mol}^{-1}.\text{K}^{-1}$ at 800 K remains well below the Dulong-Petit asymptotic value, $C_p = 3nR = 424 \text{ J.mol}^{-1}.\text{K}^{-1}$, where n is the number of atoms per f.u. and R is the universal gas constant.

In order to derive the enthalpy function, $(H_T - H_{298.15}).T^{-1}$, and the Gibbs energy function, $-(G_T - H_{298.15}).T^{-1}$, the thermal evolution of the isobaric heat capacity of kaolinite calculated from DFPT-D2, with uniaxial deformation along the z -axis, was fitted using nonlinear least-squares regression to a Haas-Fisher-type polynomial, i.e.,

$$C_p(T) = a + bT + cT^{-2} + dT^{-0.5} + eT^2,$$

with the resulting optimized coefficients given in Table 9.

Table 9 Coefficients of the Haas-Fisher heat capacity polynomial $C_p(T)$ for kaolinite calculated from DFPT-D2. The range of validity of the fit is 290–800 K.

$a \times 10^2$	$b \times 10^{-1}$	$c \times 10^6$	$d \times 10^4$	$e \times 10^{-4}$	SSD ^a
(T^0)	(T)	(T^2)	($T^{0.5}$)	(T^2)	
9.7638	-3.642	3.8812	-1.1866	1.300	0.007

^a Sum of squared differences between calculated and fitted data.

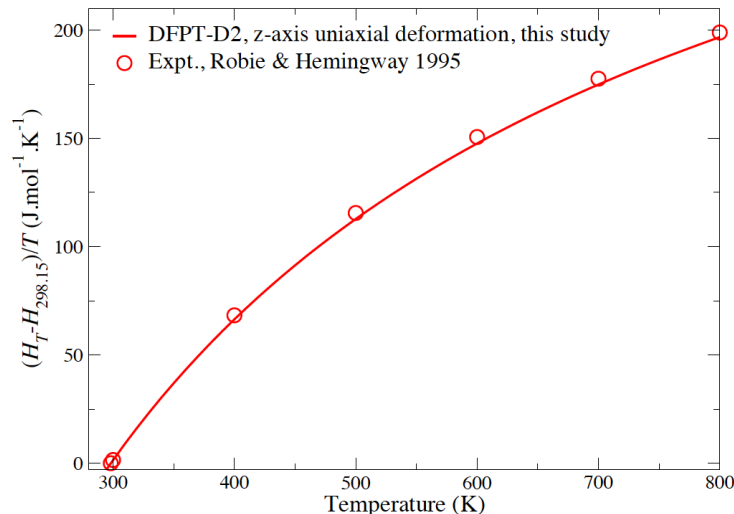


Figure 6. Thermal evolution of the enthalpy function of kaolinite calculated at the DFPT-D2/GGA/PBE level of theory. Experimental estimates derived from calorimetric data by Robie and Hemingway (1995) are also displayed for comparison purpose.

The enthalpy function was then computed by analytical integration of the fit to the isobaric heat capacity using the formula:

$$(H_T - H_{298.15}) \cdot T^{-1} = \int_{298.15}^T (a + bT + cT^{-2} + dT^{-0.5} + eT^2) dT.$$

Results from calculations are shown in Figure 6 along with the experimental estimates derived from calorimetric data by Robie and Hemingway (1995). Calculations essentially reproduce the experimental thermal evolution of the enthalpy function: the computed values systematically underestimate experiment by 2.7–2.0% in the 300–600 K range, and agreement steadily improves with temperature, reaching a difference of only 1.1% (i.e. 2.1 J.mol⁻¹.K⁻¹) at 800 K.

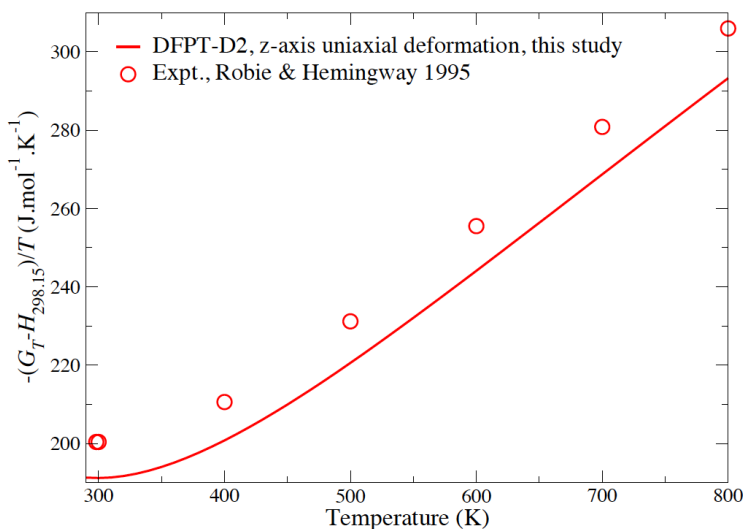


Figure 7. Thermal evolution of the Gibbs energy function of kaolinite calculated at the DFPT-D2/GGA/PBE level of theory. Experimental estimates derived from calorimetric data by Robie and Hemingway (1995) are also displayed for comparison purpose.

The Gibbs energy function was then computed using the following expression:

$$-(G_T - H_{298.15}) \cdot T^{-1} = S_T - (H_T - H_{298.15}) \cdot T^{-1},$$

where S_T is the entropy calculated from DFPT-D2 with uniaxial deformation along the z -axis. As depicted in Figure 7, the values of the Gibbs energy function computed at the DFPT-D2 level of theory are consistently smaller than the experimental estimates of Robie and Hemingway (1995) by 4.6–4.1% in the 298–800 K range. These differences are in line with the 4.7–3.0% underestimation of the experimentally-derived entropy by the computed entropy in this temperature range.

10. Conclusions

Using density functional theory corrected for dispersion interactions (DFT-D2), the structure and mechanical and thermodynamic properties of ideal 1:1 layered dioctahedral kaolinite clay, $\text{Al}_2\text{Si}_2\text{O}_5(\text{OH})_4$, were investigated. While the volume calculated with standard DFT overestimates experiment by $\sim 3\%$, DFT-D2 essentially reproduces the volume determined in recent neutron powder diffraction and single-crystal XRD experiments.

Dispersion forces included in DFT-D2 are also found to impact the elastic properties of kaolinite: the in-plane C_{11} and C_{22} elastic constants calculated with DFT-D2 are smaller than with standard DFT, while the C_{33} constant along the sheet stacking direction is significantly larger with DFT-D2 as a result of attractive long-range forces. The bulk modulus, shear modulus, transverse wave velocity, longitudinal wave velocity, Poisson's ratio, and Young's modulus components were also calculated at $T = 0$ K using the Reuss, Voigt, and Hill approximations; values obtained with DFT-D2 tend to be slightly larger than with standard DFT, and towards the higher end of the broad range of measured values. A significant softening of kaolinite occurs as the temperature increases and the bulk moduli of 56.2 and 56.0 GPa predicted with DFT-D2 at 298.15 K using the Vinet and Birch-Murnaghan equations of state, respectively, are in good agreement with the recent experimental value of 59.7 GPa reported for well-crystallized kaolinite samples.

The isobaric heat capacity computed at the DFPT-D2 level of theory for uniaxial deformation of kaolinite along the stacking direction reproduces the latest calorimetric data available within 0.7–3.0 % from room temperature up to its estimated limit of thermal stability at 800 K. The predicted Gibbs energy function consistently underestimates the most recent experimental estimates by 4.6–4.1% in the 298–800 K range. Some of these discrepancies stem from the 4.7–3.0% underestimation of the experimentally-derived entropy by the computed entropy in this temperature range.

This methodology will be applied in a systematic way to other clays (e.g. montmorillonite clays,...) to expand the applicability of this data set to realistic systems. Such an expanded data set will facilitate investigation of NS, EBS, and SNF thermal-mechanical evolution in geological repositories.

10.1 Proposed Work Scope for FY16

Proposed DFT work scope for FY16:

- Extend DFT/DFPT calculations done for kaolinite to swelling clays (Ca- or Na-montmorillonite)
- Investigate the dehydroxylation of swelling clays (e.g., Ca- montmorillonite).

11. References

- Akiba, E., H. Hayakawa, S. Hayashi, R. Miyawaki, S. Tomura, Y. Shibasaki, F. Izumi, H. Asano, and T. Kamiyama, Structure refinement of synthetic deuterated kaolinite by rietveld analysis using time-of-flight neutron powder diffraction data. *Clays and Clay Minerals*, 1997. **45**(6): p. 781-788.
- Balan, E., G. Calas, and D.L. Bish, Kaolin-Group Minerals: From Hydrogen-Bonded Layers to Environmental Recorders. *Elements*, 2014. **10**(3): p. 183-188.
- Balan, E., A.M. Saitta, F. Mauri, and G. Calas, First-principles modeling of the infrared spectrum of kaolinite. *American Mineralogist*, 2001. **86**(11-12): p. 1321-1330.
- Benazzouz, B.K. and A. Zaoui, A nanoscale simulation study of the elastic behaviour in kaolinite clay under pressure. *Materials Chemistry and Physics*, 2012. **132**(2-3): p. 880-888.
- Benco, L., D. Tunega, J. Hafner, and H. Lischka, Orientation of OH groups in kaolinite and dickite: Ab initio molecular dynamics study. *American Mineralogist*, 2001. **86**(9): p. 1057-1065.
- Birch, F., Finite Elastic Strain of Cubic Crystals. *Physical Review*, 1947. **71**(11): p. 809-824.
- Bish, D.L., Rietveld refinement of the kaolinite structure at 1.5 K. *Clays and Clay Minerals*, 1993. **41**(6): p. 738-744.
- Blöchl, P.E., Projector augmented-wave method. *Physical Review B*, 1994. **50**(24): p. 17953-17979.
- Blöchl, P.E., O. Jepsen, and O.K. Andersen, Improved tetrahedron method for Brillouin-zone integrations. *Physical Review B*, 1994. **49**(23): p. 16223-16233.
- Chen, B. and J.R.G. Evans, Elastic moduli of clay platelets. *Scripta Materialia*, 2006. **54**(9): p. 1581-1585.
- Cygan, R.T. and K. Tazaki, Interactions of Kaolin Minerals in the Environment. *Elements*, 2014. **10**(3): p. 195-200.
- Davidson, E.R., Methods in Computational Molecular Physics, in NATO Advanced Study Institute, G.H.F. Diercksen and S. Wilson, Editors. 1983, Plenum: New York. p. 95.
- Frost, R.L., Fourier transform Raman spectroscopy of Kaolinite, dickite and halloysite. *Clays and Clay Minerals*, 1995. **43**(2): p. 191-195.
- Frost, R.L. and J.T. Kloprogge, Raman Spectroscopy of the Low-Frequency Region of Kaolinite at 298 and 77 K. *Applied Spectroscopy*, 1999. **53**(12): p. 1610-1616.
- Giese, R.F. and F. Datta, Hydroxyl Orientation in Kaolinite, Dickite, and Nacrite. *American Mineralogist*, 1973. **58**: p. 471-479.
- Grimme, S., Semiempirical GGA-type density functional constructed with a long-range dispersion correction. *Journal of computational chemistry*, 2006. **27**(15): p. 1787-99.
- Hess, A.C. and V.R. Saunders, Periodic ab initio Hartree-Fock calculations of the low-symmetry mineral kaolinite. *The Journal of Physical Chemistry*, 1992. **96**(11): p. 4367-4374.

- Hill, R., The elastic behavior of a crystalline aggregate. Proc. Phys. Soc., London, 1952. **65A**: p. 349-354.
- Hobbs, J.D., R.T. Cygan, K.L. Nagy, P.A. Schultz, and M.P. Sears, All-atom ab initio energy minimization of the kaolinite crystal structure. American Mineralogist, 1997. **82**(7-8): p. 657-662.
- Hu, X.L. and A. Michaelides, Water on the hydroxylated (0 0 1) surface of kaolinite: From monomer adsorption to a flat 2D wetting layer. Surface Science, 2008. **602**(4): p. 960-974.
- Hughes, A.D. and M.R. King, Use of naturally occurring halloysite nanotubes for enhanced capture of flowing cells. Langmuir : the ACS journal of surfaces and colloids, 2010. **26**(14): p. 12155-64.
- Johansson, U., R.L. Frost, W. Forsling, and J.T. Kloprogge, Raman Spectroscopy of the Kaolinite Hydroxyls at 77 K. Applied Spectroscopy, 1998. **52**(10): p. 1277-1282.
- Johnston, C., S. Agnew, and D. Bish, Polarised Single-Crystal Fourier-Transform Infrared Microscopy of Ouray Dickite and Keokuk Kaolinite. Clays and Clay Minerals, 1990. **38**(6): p. 573-583.
- Katahara, K.W. Clay mineral elastic properties. in 66th Annual International Meeting. 1996. SEG Expanded Abstracts.
- Kresse, G. and J. Furthmüller, Efficient iterative schemes for ab initio total-energy calculations using a plane-wave basis set. Physical Review B, 1996. **54**(16): p. 11169.
- Kresse, G. and D. Joubert, From ultrasoft pseudopotentials to the projector augmented-wave method. Physical Review B, 1999. **59**(3): p. 1758-1775.
- Lambert, J.F., W.S. Millman, and J.J. Fripiat, Revisiting kaolinite dehydroxylation: a silicon-29 and aluminum-27 MAS NMR study. Journal of the American Chemical Society, 1989. **111**(10): p. 3517-3522.
- Le Page, Y. and P. Saxe, Symmetry-general least-squares extraction of elastic data for strained materials from ab initio calculations of stress. Physical Review B, 2002. **65**(10): p. 104104.
- Lonardelli, I., H.-R. Wenk, and Y. Ren, Preferred orientation and elastic anisotropy in shales. Geophysics, 2007. **72**(2): p. D33-D40.
- Massiot, D., P. Dion, J.F. Alcover, and F. Bergaya, ²⁷Al and ²⁹Si MAS NMR Study of Kaolinite Thermal Decomposition by Controlled Rate Thermal Analysis. Journal of the American Ceramic Society, 1995. **78**(11): p. 2940-2944.
- Mercier, P.H.J. and Y. Le Page, Rational ab initio modeling for low energy hydrogen-bonded phyllosilicate polytypes. European Journal of Mineralogy, 2011. **23**(3): p. 401-407.
- Mercier, P.H.J., Y. Le Page, and S. Desgreniers, Kaolin polytypes revisited ab initio at 10 GPa. American Mineralogist, 2010. **95**(7): p. 1117-1120.
- Militzer, B., H.-R. Wenk, S. Stackhouse, and L. Stixrude, First-principles calculation of the elastic moduli of sheet silicates and their application to shale anisotropy. American Mineralogist, 2010. **96**(1): p. 125-137.

- Monkhorst, H.J. and J.D. Pack, Special points for Brillouin-zone integrations. *Physical Review B*, 1976. **13**(12): p. 5188-5192.
- Murnaghan, F.D., The Compressibility of Media under Extreme Pressures. *Proceedings of the National Academy of Sciences*, 1944. **30**(9): p. 244-247.
- Neder, R.B., M. Burghammer, T. Grasl, H. Schulz, A. Bram, and S. Fiedler, Refinement of the kaolinite structure from single-crystal synchrotron data. *Clays and Clay Minerals*, 1999. **47**(4): p. 487-494.
- Nye, J.F., *The Physical Properties of Crystals: Their Representation by Tensors and Matrices* 1985, New York: Oxford University Press.
- Pauling, L., The Structure of the Chlorites. *Proceedings of the National Academy of Sciences of the United States of America*, 1930. **16**(9): p. 578-82.
- Perdew, J.P., K. Burke, and M. Ernzerhof, Generalized Gradient Approximation Made Simple. *Physical Review Letters*, 1996. **77**(18): p. 3865-3868.
- Perdew, J.P., K.A. Jackson, M.R. Pederson, D.J. Singh, and C. Fiolhais, Atoms, molecules, solids, and surfaces: Applications of the generalized gradient approximation for exchange and correlation. *Physical Review B*, 1992. **46**(11): p. 6671-6687.
- Reuss, A., Berechnung der Fließgrenze von Mischkristallen auf Grund der Plastizitätsbedingung für Einkristalle. *ZAMM-Journal of Applied Mathematics and Mechanics/Zeitschrift für Angewandte Mathematik und Mechanik*, 1929. **9**(1): p. 49-58.
- Robie, R.A. and B.S. Hemingway, Heat capacities of kaolinite from 7 to 380 K and of DMSO-intercalated kaolinite from 20 to 310 K. *Clays and Clay Minerals*, 1991. **39**(4): p. 362-368.
- Robie, R.A. and B.S. Hemingway, Thermodynamic properties of minerals and related substances at 298.15 K and 1 bar (10^5 pascals) pressure and at higher temperatures. *U S Geological Survey bulletin* 1995, Denver, CO: U.S. G.P.O. 461.
- Rocha, J., Single- and Triple-Quantum ^{27}Al MAS NMR Study of the Thermal Transformation of Kaolinite. *The Journal of Physical Chemistry B*, 1999. **103**(44): p. 9801-9804.
- Sato, H., K. Ono, C.T. Johnston, and A. Yamagishi, First-principles studies on the elastic constants of a 1:1 layered kaolinite mineral. *American Mineralogist*, 2005. **90**(11-12): p. 1824-1826.
- Schieltz, N.C. and M.R. Soliman. in *Proceedings of the 13th National Conference on Clays and Clay Minerals*. 1966. Pergamon Press, New York.
- Schroeder, P.A. and G. Erickson, Kaolin: From Ancient Porcelains to Nanocomposites. *Elements*, 2014. **10**(3): p. 177-182.
- Sone, H. and M.D. Zoback, Mechanical properties of shale-gas reservoir rocks - Part 1: Static and dynamic elastic properties and anisotropy. *Geophysics*, 2013. **78**(5): p. D381-D392.
- Suitch, P.R. and R.A. Young, Atom positions in highly ordered kaolinite. *Clays Clay Miner.*, 1983. **31**(5): p. 357.

- Togo, A., F. Oba, and I. Tanaka, First-principles calculations of the ferroelastic transition between rutile-type and CaCl₂-type SiO₂ at high pressures. *Physical Review B*, 2008. **78**(13): p. 134106.
- Ugliengo, P., C.M. Zicovich-Wilson, S. Tosoni, and B. Civalleri, Role of dispersive interactions in layered materials: a periodic B3LYP and B3LYP-D* study of Mg(OH)₂, Ca(OH)₂ and kaolinite. *Journal of Materials Chemistry*, 2009. **19**(17): p. 2564.
- Vinet, P., J.H. Rose, J. Ferrante, and J.R. Smith, Universal features of the equation of state of solids. *Journal of Physics: Condensed Matter*, 1989. **1**(11): p. 1941.
- Voigt, F.F., *Lehrbuch der Kristallphysik* 1928, Leipzig Teubner.
- Wada, K., A study of hydroxyl groups in kaolin minerals utilizing selective-deuteration and infrared spectroscopy. *Clay Minerals*, 1967. **7**(1): p. 51-61.
- Wang, Z., H. Wang, and M.E. Cates, Effective elastic properties of solid clays. *Geophysics*, 2001. **66**(2): p. 428-440.
- Weck, P.F., E. Kim, C.F. Jové Colón, and D.C. Sassani, Structures of uranyl peroxide hydrates: a first-principles study of studtite and metastudtite. *Dalton transactions (Cambridge, England : 2003)*, 2012. **41**(32): p. 9748-52.
- Weck, P.F., E. Kim, C.F. Jové Colón, and D.C. Sassani, On the role of strong electron correlations in the surface properties and chemistry of uranium dioxide. *Dalton transactions*, 2013. **42**(13): p. 4570-8.
- Weck, P.F., E. Kim, C.F. Jové Colón, and D.C. Sassani, First-principles study of anhydrite, polyhalite and carnallite. *Chemical Physics Letters*, 2014. **594**: p. 1-5.
- Weck, P.F., E. Kim, and C.F. Jové-Colón, Relationship between crystal structure and thermo-mechanical properties of kaolinite clay: beyond standard density functional theory. *Dalton Transactions*, 2015.
- Welch, M.D. and W.A. Crichton, Pressure-induced transformations in kaolinite. *American Mineralogist*, 2010. **95**(4): p. 651-654.
- Wenk, H.-R., M. Voltolini, M. Mazurek, L.R. Van Loon, and A. Vinsot, Preferred orientations and anisotropy in shales: Callovo-Oxfordian shale (France) and Opalinus Clay (Switzerland). *Clays and clay minerals*, 2008. **56**(3): p. 285-306.
- White, C.E., G.J. Kearley, J.L. Provis, and D.P. Riley, Structure of kaolinite and influence of stacking faults: reconciling theory and experiment using inelastic neutron scattering analysis. *The Journal of chemical physics*, 2013. **138**(19): p. 194501.
- White, C.E., J.L. Provis, D.P. Riley, G.J. Kearley, and J.S.J. van Deventer, What is the structure of kaolinite? Reconciling theory and experiment. *The journal of physical chemistry. B*, 2009. **113**(19): p. 6756-65.
- Woeber, A.F., S. Katz, and T.J. Ahrens, *Elasticity of Selected Rocks and Minerals*. *Geophysics*, 1963. **28**(4): p. 658-663.
- Wu, X., M.C. Vargas, S. Nayak, V. Lotrich, and G. Scoles, Towards extending the applicability of density functional theory to weakly bound systems. *The Journal of Chemical Physics*, 2001. **115**(19): p. 8748.

Young, R.A. and A.W. Hewat, Verification of the Triclinic Crystal Structure of Kaolinite. *Clays Clay Miner.*, 1988. **36**(3): p. 225.

**Fuel Matrix Degradation Model: Integration with Performance Assessment and
Canister Corrosion Model Development
(Part V)**

1 Introduction and Objective

The importance of used nuclear fuel (UNF) degradation in a repository safety case is that the fuel itself is the initial and primary barrier in a multiple-barrier waste isolation system that must be represented in a quantitative safety analysis. The fuel degradation rate is used directly to calculate radionuclide source term values in the safety analysis reactive-transport model. High confidence in the performance of the sequential barriers used in the safety case requires an accurate representation of the source term due to fuel degradation and coupling with repository engineered barriers and near-field components of repository-scale transport models. The impact of waste form degradation on the safety analysis could depend on the geologic environment owing to the expected interactions during the relevant performance period and importance of the ground water composition on the fuel dissolution rate (dissolved oxygen and hydrogen, ligands affecting dissolved concentration limits, secondary phase, etc.).

The objective of this project is to develop and implement a fundamentals-based process model for the degradation rate of used fuel that can be readily incorporated into the Generic Disposal System Analyses (GDSA) Performance Assessment (PA) code. This model, referred to as the Fuel Matrix Degradation Model (FMDM), was initially based on the Canadian Mixed Potential Model (King and Kolar, 2003), but has since been expanded and customized for the ongoing UFD Argillite and Crystalline rock disposal projects.

The continued development and implementation of the FMDM addresses two high level Features, Events, and Processes (FEPs) that are recognized as high R&D priorities for the UFD (Wang et al., 2014). The FEPs addressed by this model are 2.1.02 (waste form) and 2.1.03 (waste container), which correspond to the high priority research topics P19 (Development of waste form degradation model) and P20 (Development of new waste package concepts and models for evaluation of waste package performance for long-term disposal) identified by Wang et al., 2014.

The FMDM calculates the dissolution rate of used fuel based the interfacial corrosion potential (E_{corr}) determined by the kinetic balance between anodic and cathodic half reactions at the fuel/solution boundary. The dissolution rate is relatively fast under oxidizing conditions (high E_{corr}) but decreases dramatically at E_{corr} values lower than the U(IV)/U(VI) threshold (where solubility based, chemical dissolution is dominant). The FMDM accounts for:

- the generation of radiolytic oxidants based on fuel burn-up,
- the catalyzed oxidation of H_2 , which protects the fuel from oxidative dissolution,
- the precipitation of secondary phases,
- the complexation of uranyl by carbonate,
- the oxidation of ferrous iron,
- temperature variations (by Arrhenius equations),
- the one-dimensional diffusion of all chemical species.

Of these processes, the catalysis of H_2 oxidation on Nobel Metal Particles (NMP) on the fuel surface and the generation rate of radiolytic oxidants (determined by dose rate, which is related to fuel burn-up) are the most important for determining the degradation rate of the fuel (Jerden et al., 2015).

The dissolution rate calculated by the FMDM accounts for oxidation of the fuel by radiolytic H_2O_2 (and decomposition product O_2) the concentration of which is calculated using an analytical form of the radiolysis model developed at PNNL (Buck et al., 2014) and the burn-up/dose rate function described in Section 2 of this part of the report. Fuel oxidation is counteracted by the catalytic oxidation of H_2 on NMP sites that are present on the fuel surface as a distinct phase. The dominant source of H_2 in the repository will be from the anoxic corrosion of steel (Shoosmith, 2008).

As discussed in Section 3 below, the FMDM is being extended to include steel corrosion thus providing a realistic kinetic source of H_2 for key interfacial reactions. It was shown in Jerden et al., 2015 that the FMDM accurately reproduces the experimental observation that relatively low concentrations of dissolved H_2 ($\sim 0.1\text{mM}$) can completely inhibit the oxidative dissolution of the fuel. In the absence of oxidative dissolution, the fuel degrades by solubility based, chemical dissolution, which is over 4 orders of magnitude slower than oxidative dissolution (Röllin et al., 2001). The FMDM accounts for the surface area of the NMPs and is being extended to account for the effects of species that may poison the catalytic effects of the NMP (see Section 4 below).

The key processes currently accounted for in the FMDM as well as the processes that are to be added in FY 2016 are summarized in Figure 1.

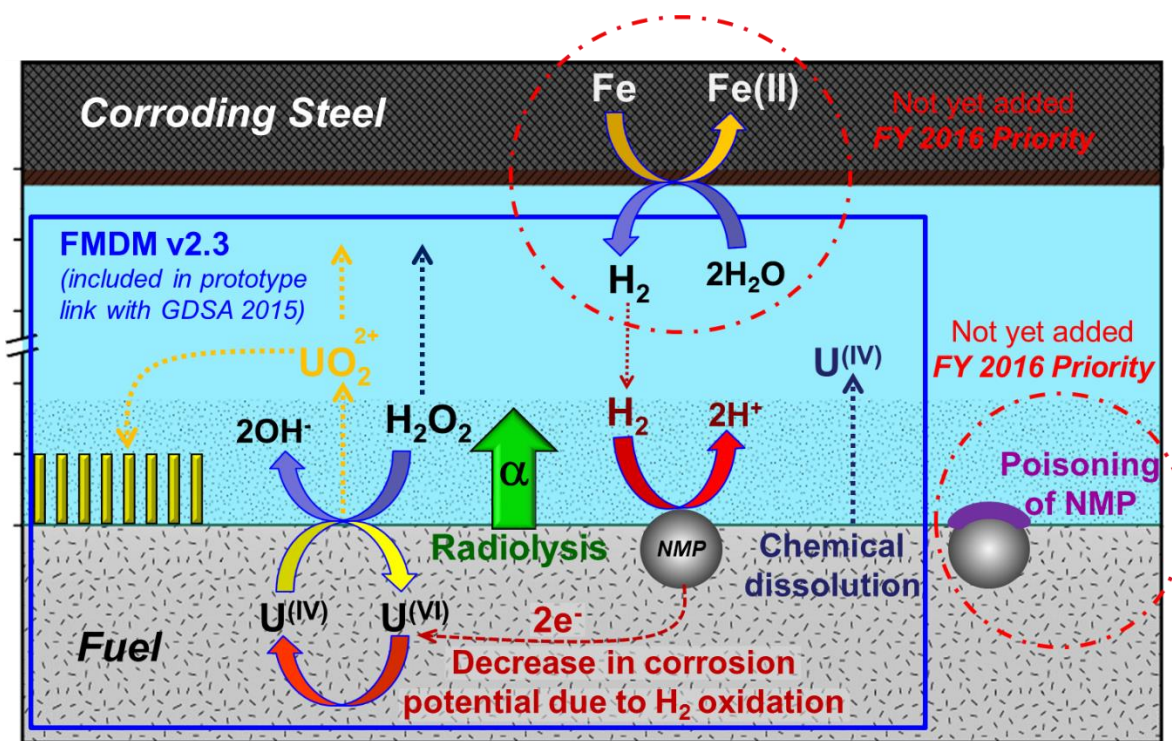


Figure 1. Conceptual diagram identifying the key dissolution rate-determining processes in the FMDM and highlighting the FY 2016 priorities.

2 Fuel Matrix Degradation Model Development and Integration with PFLOTRAN

This section documents model development work that focused on integrating the FMDM with the GDSA PA reactive transport code PFLOTRAN. This involved the conversion of the FMDM from MATLAB to Fortran and the addition of an analytical function that calculates the dose rate at the fuel surface based on a user specified fuel burnup and fuel age (out of reactor). The Fortran version of the FMDM was integrated with PFLOTRAN to produce a prototype PFLOTRAN-FMDM working model. This integrated code was demonstrated for a scaled-down and simplified repository example, which is described in Section 2.3 below.

2.1 Conversion of FMDM from MATLAB to Fortran

The first Fortran version of the FMDM [previously referred to as the Mixed Potential Model (MPM)], was completed and distributed to the GDSA team in October 2014 as version number 2.0 and is documented in Jerden et al., 2014. Versions 2.1 and 2.2 were produced and used internally at Argonne but were not distributed. The Fortran FMDM version 2.3 was distributed to the GDSA team in March 2015. The new features of version 2.3 are described in this part of the report.

One of the major changes is that the Fortran FMDM version 2.3 returns the fuel dissolution rate (`fuelDisRate`) in $\text{g m}^{-2} \text{y}^{-1}$ rather than a matrix of fluxes (as the previous version did). This fuel dissolution rate is equal to the sum of the three interfacial fluxes of uranium leaving the fuel surface: uranyl ion, uranyl tricarbonate and aqueous U(IV) (labeled `UO2_2p`, `UCO3_2n`, `UO2` in the code).

The other major addition to the FMDM v2.3 is that the dose rate at the fuel surface, which determines the generation rate of radiolytic oxidants, is calculated internally rather than provided as an input to the model. This is accomplished through an analytical dose rate – burnup function that was derived by fitting the burnup – dose rate – age of fuel data of Radulescu 2011 (discussed in Section 2.2 below).

The original Fortran FMDM was converted from MATLAB to Fortran 90 for integration with the PFLOTRAN code. The only external library used was LAPACK for its linear algebra solver “`dgesv`” (LAPACK 3.5.0 Windows 32-bit static library). This conversion was a line by line translation of the original MATLAB code. A single call to the FMDM version 2.3 Fortran code requires a call to the subroutine “`AMP_step`” whose interface is shown below.

```
interface
  subroutine AMP_step ( sTme, conc, initialRun, fuelDisRate, status )
    real ( kind = 8), intent( in ) :: sTme
    real ( kind = 8), intent( inout ), dimension (:,:) :: conc
    logical ( kind = 4), intent( in ) :: initialRun
    real ( kind = 8), intent(out) :: fuelDisRate
    integer ( kind = 4), intent(out) :: status
  end subroutine
end interface
```

The first time the code is called, `initialRun` must be set to `“true.”` and the contents of the concentration matrix `“conc”` are ignored. In this case, the initial concentrations are defaulted to the values returned by the subroutine `“enVals”` in file `“AMP_class.f90”`. In subsequent calls to `“AMP_step”`, the concentration from the previous `AMP_step` call must be preserved and used as input to the current `AMP_step` call.

There are eleven components followed by the FMDM version 2.3 Fortran code and the order is defined in the file `“AMP_compList. Inc”`. The first dimension of the concentration matrix is in this order.

<code>UO2_2p</code>	[symbol for UO_2^{2+}]
<code>UCO3_2n</code>	[symbol for $\text{UO}_2(\text{CO}_3)_2^{2-}$]
<code>UO2</code>	[symbol for $\text{UO}_2(\text{aq})$]
<code>CO3_2n</code>	[symbol for CO_3^{2-}]
<code>O2</code>	[symbol for $\text{O}_2(\text{aq})$]
<code>H2O2</code>	[symbol for H_2O_2]
<code>Fe_2p</code>	[symbol for Fe^{2+}]
<code>H2</code>	[symbol for $\text{H}_2(\text{aq})$]
<code>UO2_s1d</code>	[symbol for U(IV) oxide precipitate]
<code>UO3_s1d</code>	[symbol for U(VI) oxide hydrate precipitate]
<code>UO4_s1d</code>	[symbol for U(VI) peroxide precipitate]

Figure 2 identifies the basic order of calculations within the FMDM, identifies the inputs and outputs from and to PFLOTRAN and indicates the new features of v2.3. This Fortran version of the FMDM has been coupled with PFLOTRAN to form a prototype working integrated model as discussed in Section 2.3 below.

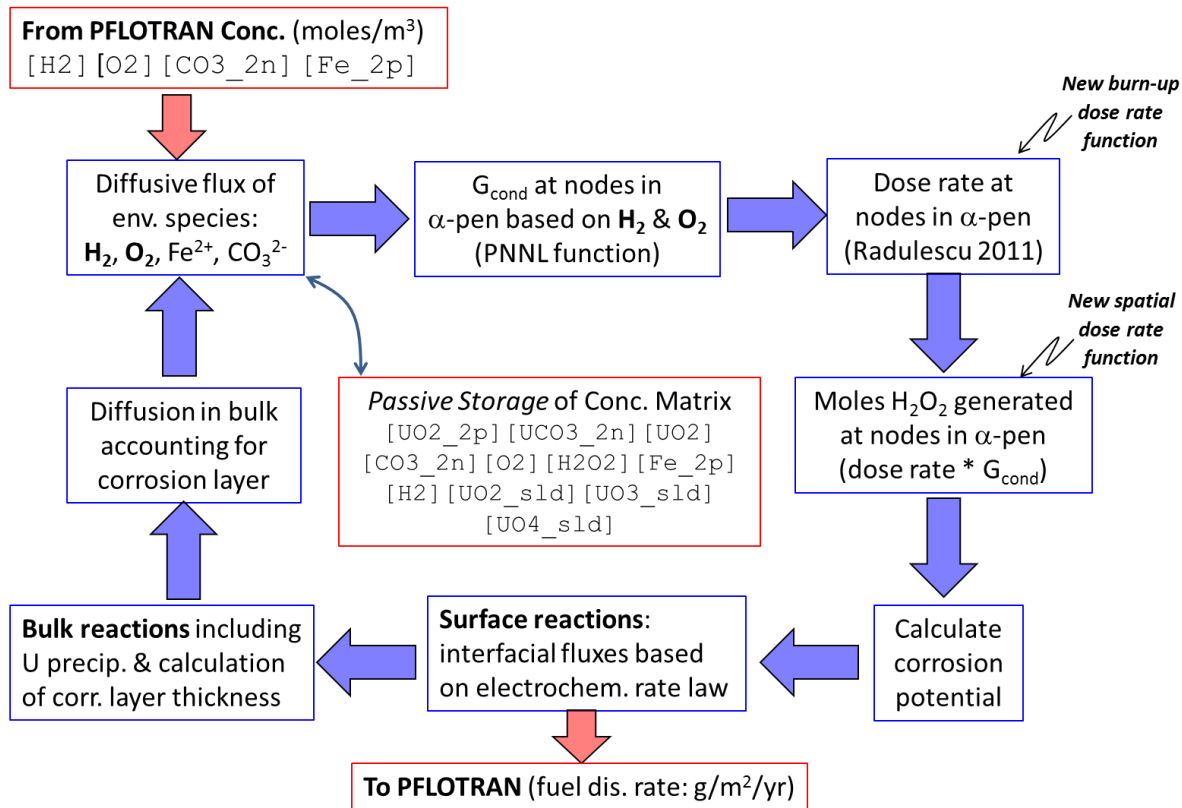


Figure 2. Conceptual flow diagram showing the individual calculations within a single time step of the FMDM. Note that the concentrations of all components must be stored and fed back to the FMDM at the beginning of each new time step. G_{cond} refers to the conditional generation value for H_2O_2 , which determines the peroxide generation rate within the alpha radiation zone (α -pen). In the FMDM v.2.3 the conditional H_2O_2 generation value is calculated by an analytical function. (G_{cond} is a function of $[\text{H}_2]$ and $[\text{O}_2]$) derived from sensitivity runs of the PNNL radiolysis model (Buck et al., 2014).

2.2 Summary of Technical Changes Made to the FMDM Incorporated into Version 2.3

The following changes are incorporated into the Fortran version 2.3 of the FMDM:

- The dose rate function (dose rate as a function of time) was replaced by a function derived from the MCNPX results of Radulescu 2011. The new function calculates the dose rate at the fuel surface as a function of time based on the assumed average burnup of the fuel. The new function is described in Figures 3 and 4.
- The spatial dose rate function, which calculates the dose rate at nodes within the alpha radiation penetration zone (35 micrometers), was replaced with a new function derived from the MCNPX results of Radulescu 2011. The new function is described in Figure 5.

The following is an example section of code showing both the burnup – dose rate function and the spatial dose rate function based on Radulescu 2011. The MATLAB code is shown for clarity – the Fortran implementation is identical except for syntax differences.

```
BU = 60; %Fuel burnup in GWd/MTU
dect = 30; %Decay time of fuel in yr
aof = t/60/60/24/365+dect; %Age of fuel yr

%Relationship between age of fuel, burnup and dose rate (rad0)
%Simple fit from Radulescu 2011 report
f1=log(aof)*log(aof);
f2=log(aof);
f3=1.0/log(aof);
f4=log(aof)/aof;
f5=exp(BU/25.26892627636246);
rad0a = -206.0634818750711-0.7631591788870090*f1...
        +20.97112373957833*f2+678.8463343193430*f3...
        -506.7149017370657*f4+0.1555448893425319*f5;
rad0 = max(exp(rad0a),5.0e-3);

%Constant dose rate option
%rad0 = 1.0; % (J/kg)/s = Gy/s = 100 rad/s

%Dose rate profile with x
rCut = exp(-0.14*(lmat*1.0e6)); %Exponential from Radulescu 2011
%rCut = (max(1 - lmat./penD, 0)); %Linear decrease
%rCut = lmat <= penD; %Step function

rad = rad0.*rCut; %Dose rate used to determine H2O2 generation
```

Simple Fit to Radulescu 2011

$$\text{Function: } \ln z = a + b(\ln x)^2 + c \ln x + d / \ln x + e \ln x / x + f e^{y/w}$$

$r^2=0.9973546$ DF Adj $r^2=0.99680728$ FitStdErr=0.017963849 Fstat=2262.0877

$a=-206.06348$ $b=-0.76315918$ $c=20.971124$

$d=678.84633$ $e=-506.7149$ $f=0.15554489$

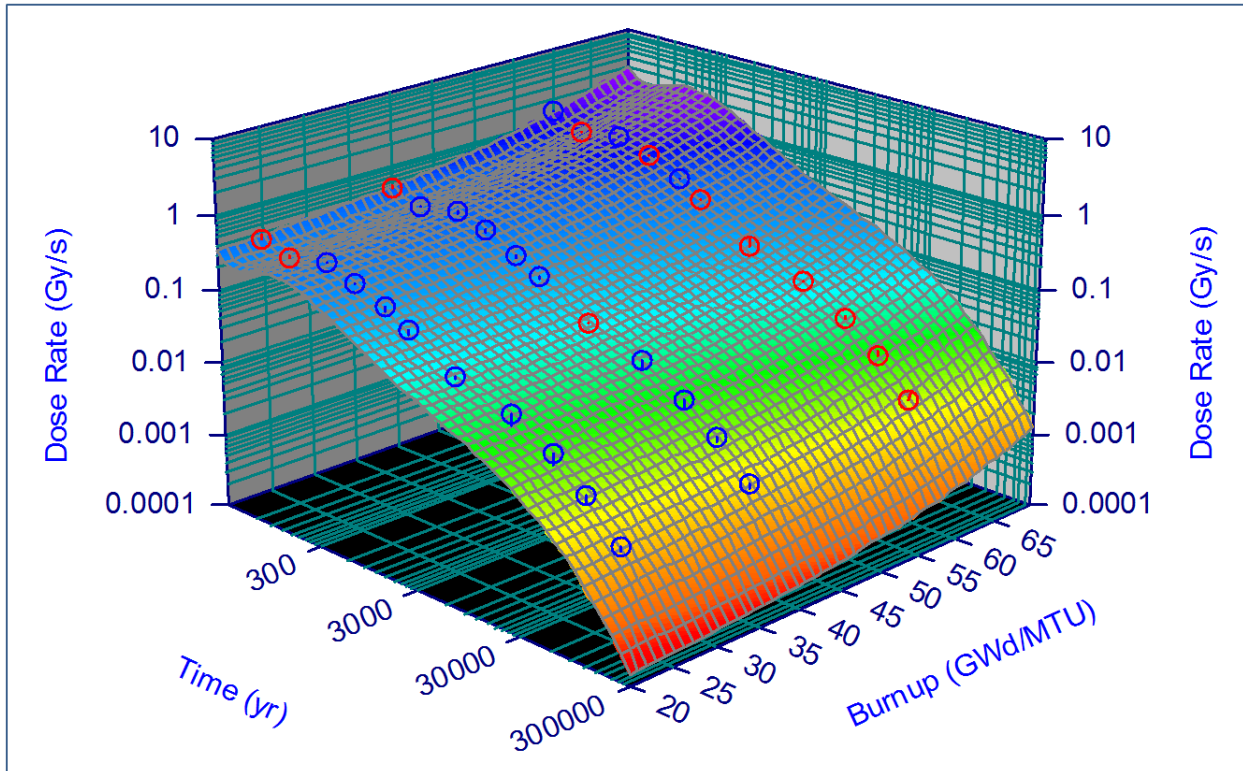


Figure 3. The burnup – dose rate function derived from the MCNPX results of Radulescu 2011 as a polynomial fit. The calculation points from Radulescu 2011 are shown as blue and red circles. Blue indicates that the data point falls below the fit surface and red indicates that the data point is above the fit surface. The derived function is shown as the surface: $x = \text{time}$, $y = \text{burnup}$, $z = \text{dose rate}$, where a , b , c , d , e , f and w are all fitting parameters.

Figure 4 shows a comparison between the new burnup – dose rate function and the MCNPX results of Radulescu, 2011. This figure also shows a comparison between results from the MATLAB version of the FMDM (thin blue line) and the Fortran version (thick red line). This comparison indicates that the Fortran FMDM code accurately reproduces results from the MATLAB FMDM code, which has been validated against experimental data (Jerden et al., 2015).

The results shown in Figure 4 indicate that the burnup – dose rate function accurately reproduces the MCNPX results from Radulescu 2011 and that the Fortran and MATLAB versions of the FMDM produce essentially identical results. It is noted that the increase in dose rate from 100 – 200 years in Figure 4 corresponds with the ingrowth of Am-241.

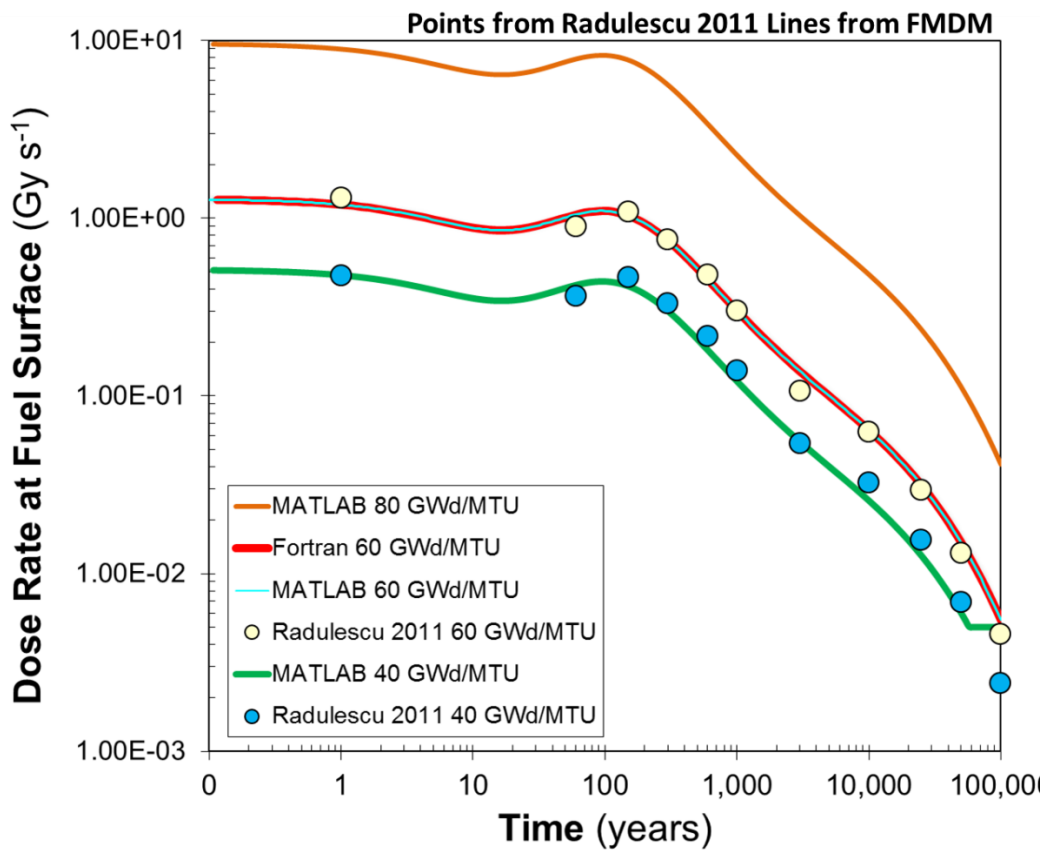


Figure 4. shows three types of results: (1) points from Radulescu 2011, (2) dose rate with time from an example simulation with the Fortran FMDM for 60 GWd/MTU (red), (3) dose rate with time from an example simulation with the MATLAB FMDM for 40, 60 and 80 GWd/MTU.

Figure 5 compares results from the new spatial dose rate function, which calculates the dose rate at each node within the alpha radiation zone, with the MCNPX of Radulescu 2011. The actual function in the code is:

$$\text{Spatial Dose Rate (Gy/hr at } x) = \text{Surface Dose Rate (Gy/hr)} * \exp[-0.14*(x (m)*1.0E+6)]$$

The results shown in Figure 5 indicate that the spatial dose rate function in the FMDM reasonably represents the spatial dose rate calculations of Radulescu 2011.

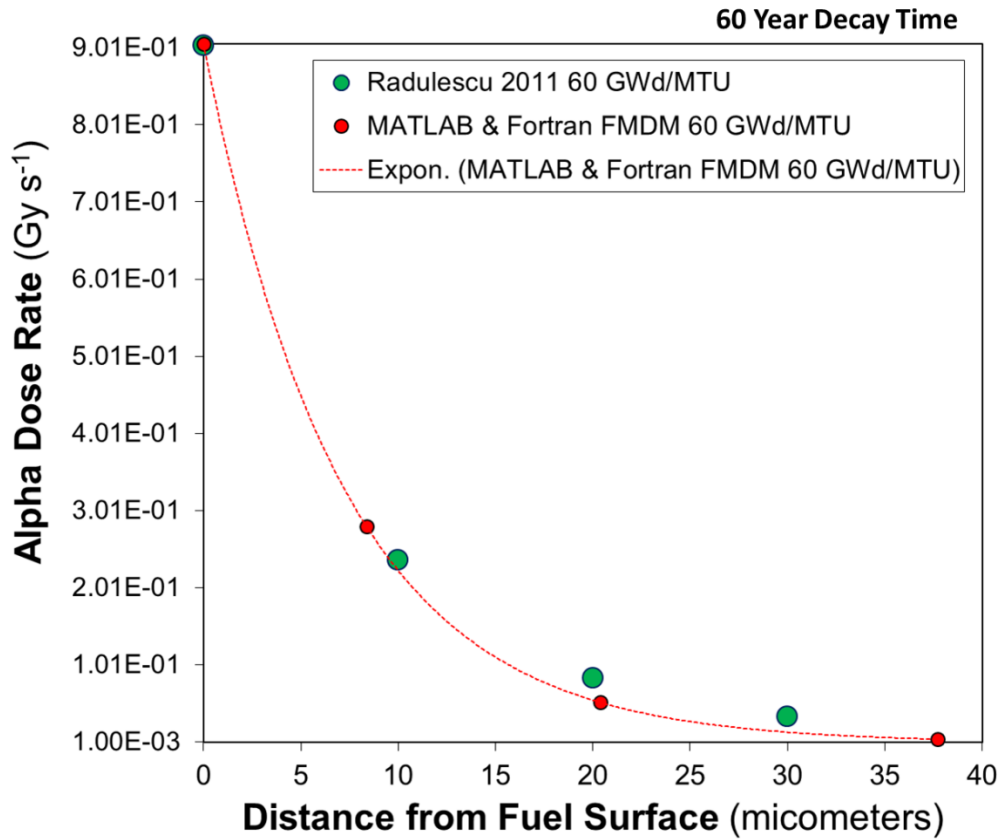


Figure 5. The alpha particle dose rate as a function of distance from the fuel surface. The red line is from example simulations with both the MATLAB and Fortran versions of the FMDM. The green points are from MCNPX calculations presented in Radulescu 2011.

Figure 6 shows direct comparisons of results from the FMDM MATLAB and Fortran versions (v2.3) for cases in which the H₂ concentration is varied. As shown in previous runs with the MATLAB version, the catalyzed oxidation of H₂ on the NMP surfaces at the fuel/solution interface dramatically decrease the fuel dissolution rate at H₂ concentrations around 0.01 mM. This is consistent with experimental investigations as discussed in Jerden et al., 2015.

The runs shown in Figure 6 were performed to confirm that the H₂ catalysis reactions were accurately represented in the Fortran version. The results show that the model outputs are essentially identical and that the breaks in the curves for 0.001mM H₂ and 0.01mM H₂ occur in both MATLAB and Fortran versions of the FMDM. The mathematic cause of these breaks or steps in the results is being studied as part of the continuing model development and optimization work. Note: the increase in dissolution rate at 100 -200 years corresponds with the dose rate increase associated with the ingrowth of Am-241.

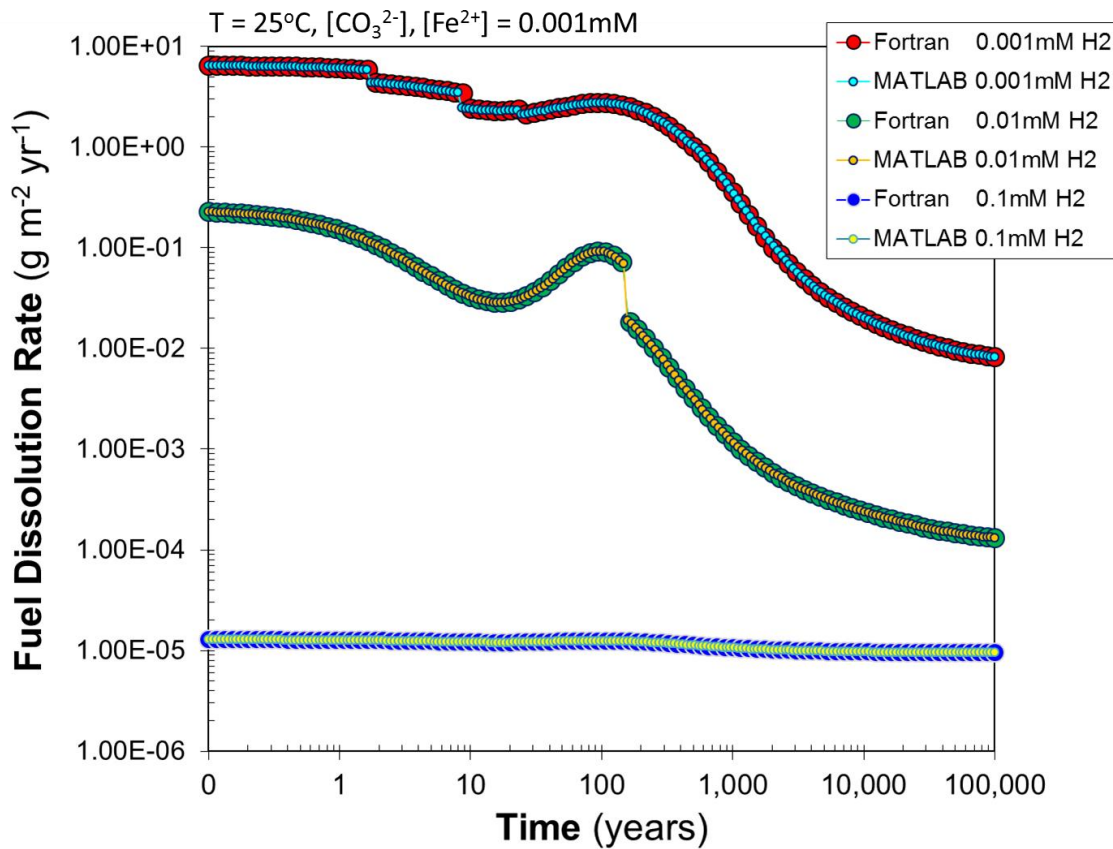


Figure 6. Results from three simulation cases performed with both the MATLAB and Fortran versions of the FMDM. For these cases carbonate and iron were held constant at 1.0×10^{-6} molar while H₂ was varied from 1.0×10^{-6} up to 1.0×10^{-4} . The Fortran simulation used 100 time steps, while the MATLAB run used 200 time steps. The results demonstrate that the Fortran and MATLAB versions of the FMDM give identical results.

2.3 Demonstration of Prototype Integrated PFLOTRAN – FMDM Model for PA

The method of integration of the FMDM Fortran version 2.3 with PFLOTRAN is summarized in Figure 7 (diagrams are from Hammond, 2015). The initial set up that was used to demonstrate the integrated code involved 52 separate 1x1x1 meter fuel bearing cells, each of which degraded at a rate determined by the FMDM (Figure 8). For simplicity, the waste container and fuel cladding were ignored.

Following an initialization step, the PFLOTRAN repository simulation proceeds with energy and mass flow (multiphase flow, heat transfer, reactive transport) calculations, which determine the temperature and solution chemistry inputs for the FMDM (Figure 7 top diagram). The fuel burnup and surface area are currently randomly selected by the code from a relevant range of values. For each time step of the repository simulation, the FMDM returns a fuel dissolution rate for each of the 52 used fuel cells in grams per square meters per year (Figure 7 bottom diagram). This is converted to grams per year using the randomized waste form surface area. This rate is then used to calculate the release of a non-sorbing, non-reacting tracer radionuclide (Figure 8).

The dimensions and conditions used for this initial demonstration of the integrated PFLOTRAN - FMDM code are as follows:

- Spatial discretization: 101x101x21m with 1m resolution (~214K grid cells)
- Temporal discretization: 100 years with 1 year time step (10^{-6} y initial)
- Waste cell spacing: 5m (X), 20m (Y) between 20-80 m
- Prescribed concentrations: $O_2(aq)$, $H_2(aq)$, HCO_3^- , Fe^{2+} all = 1 mM
- Fuel burnup: 55-65 GWd/MTU (random)
- Total fuel reactive surface area: 0.8-1 m^2 (random)
- Pore water velocity: 1 m/yr (X), 0.14 m/yr (Y)
- Computing performance: 66% of total time (~30 minutes) spent in FMDM

It is important to note that the results of the preliminary run with the PFLOTRAN – FMDM model (Figure 8) was for relatively high burnup values and oxidizing conditions. These factors lead to quite high fuel dissolution rates (on the order of $10 - 50 \text{ g m}^{-2} \text{ yr}^{-1}$) and thus rapid radionuclide release. The results from an on-going series of runs for anoxic conditions with both high and low H_2 concentrations will reveal the impact of the FMDM H_2 effect on radionuclide mobilization and will be used to confirm that the integrated model correctly represents the stand-alone FMDM process model.

Due to the relatively rapid fuel dissolution rate and probably high reactive surface area values, the mobilization of the tracer radionuclide is relatively rapid; and while, there is some variation in the tracer concentration among individual waste cells (e.g., t_2 , Figure 8) the overall plume shapes for the four waste cell rows are nearly identical. As mentioned above, results from on-going runs with the integrated model will reveal sensitivities of radionuclide mobilization to key variables such as H_2 , O_2 and CO_3^{2-} concentrations. Based on this initial model coupling experience a number of near-term improvements for the integrated code have been identified:

- Increase flexibility of coupling
- Ability to customize FMDM discretization from PFLOTRAN side

- Incorporate transient surface area
- Update to FMDM v3.0
- Optimized FMDM serial performance
- Integration into simulation of a repository with many waste packages
- Add increasingly mechanistic geochemistry

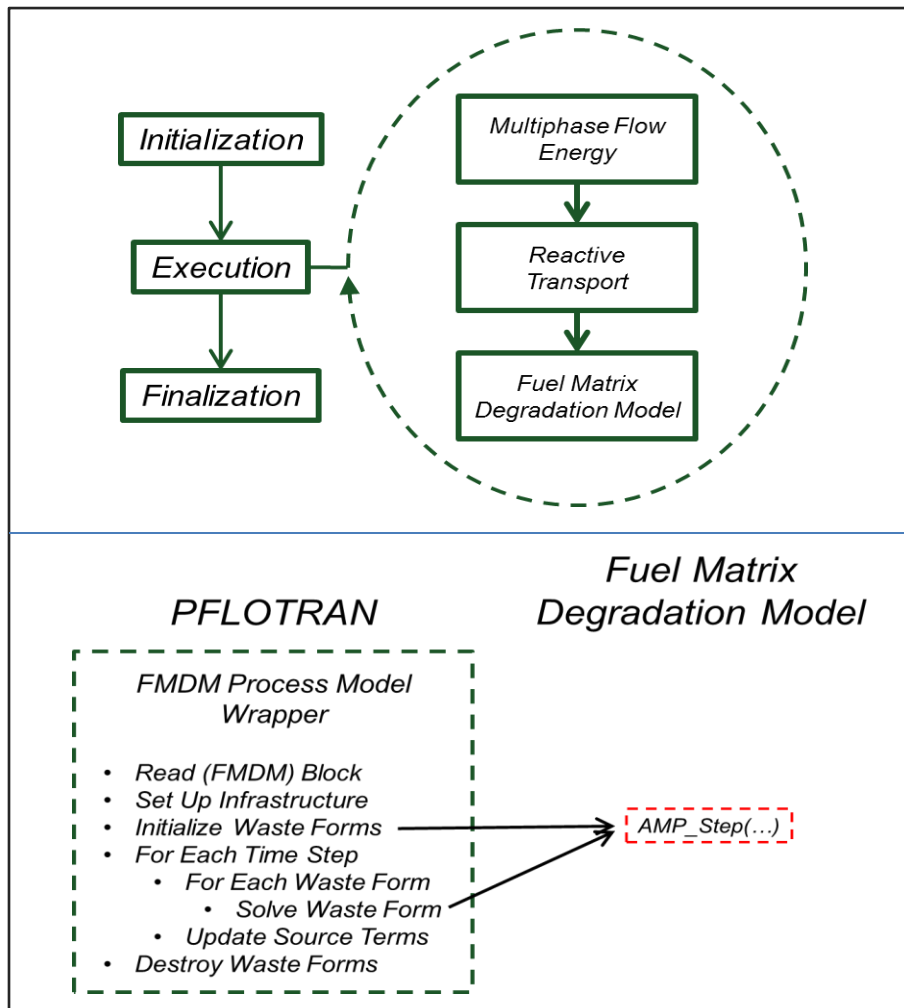


Figure 7. Schematic diagrams summarizing the workflow in the prototype PFLOTRAN – FMDM model (from Hammond, 2015).

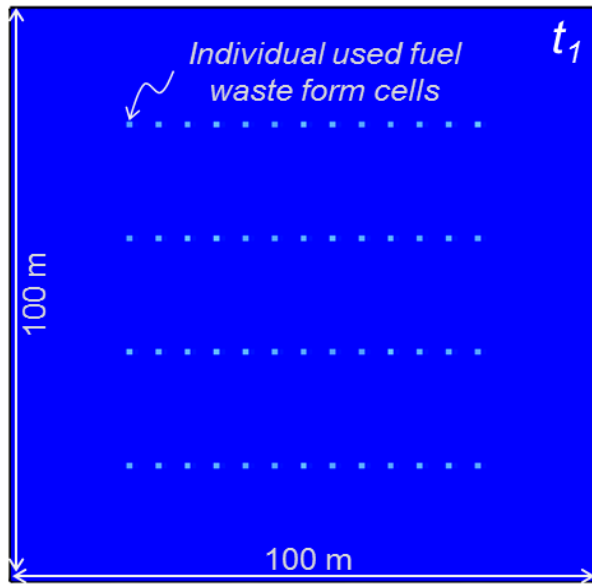
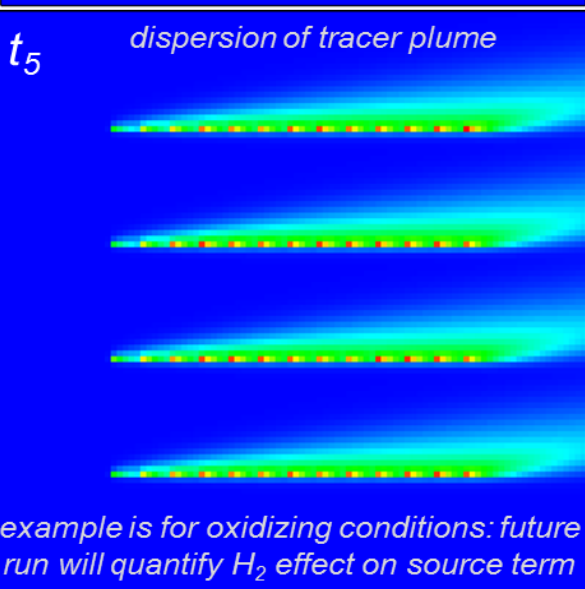
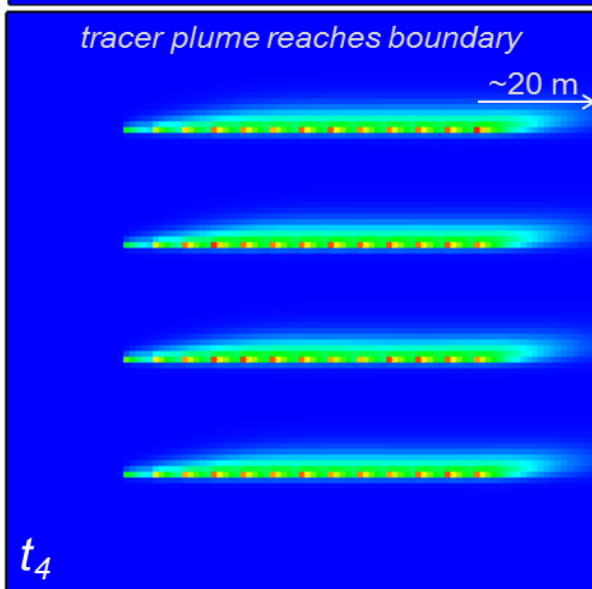
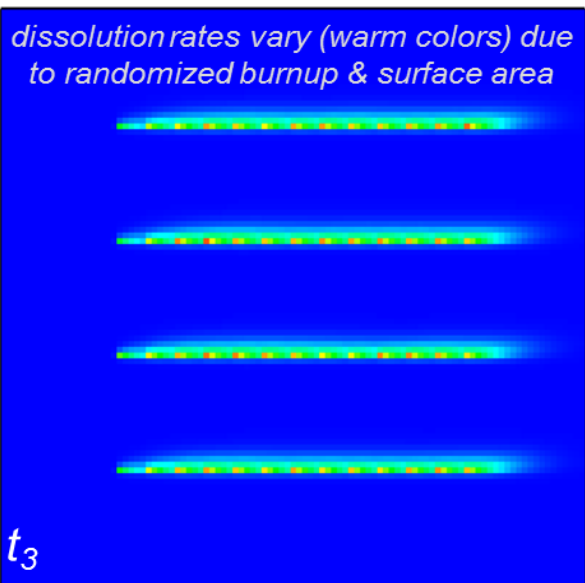
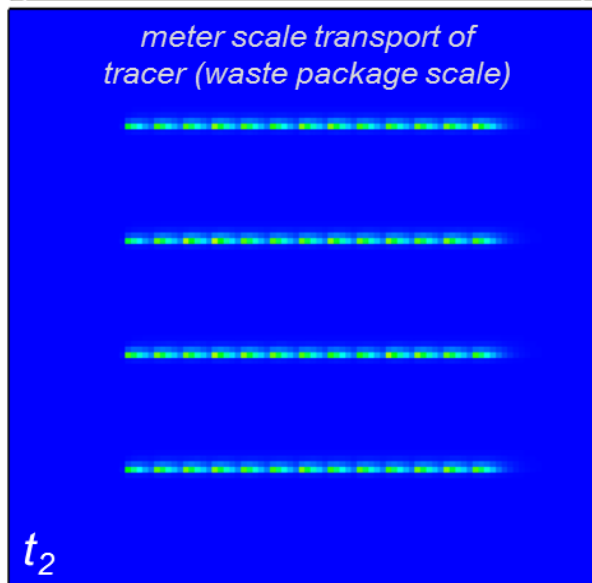
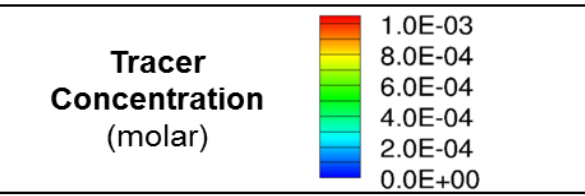


Figure 8. Results from a scaled-down PFLOTRAN repository model in which the FMDM process model has been integrated to determine the dissolution rate of the used fuel and thus the source term of a non-sorbing tracer. The effects of the fuel canister and cladding are ignored. Because this is a prototype model meant only to demonstrate successful model integration, the time scales are left generic (to avoid over-interpretation).



example is for oxidizing conditions: future run will quantify H_2 effect on source term

The on-going model integration work is conceptually summarized in Figure 9, which shows the overall flows of information between the GDSA code (PFLOTRAN) and the FMDM. The FMDM box identifies what processes are currently included in the integrated model (v2.3), and the new processes that need to be added to bring the FMDM up to date with the recent scientific findings on the dissolution behavior of used nuclear fuel.

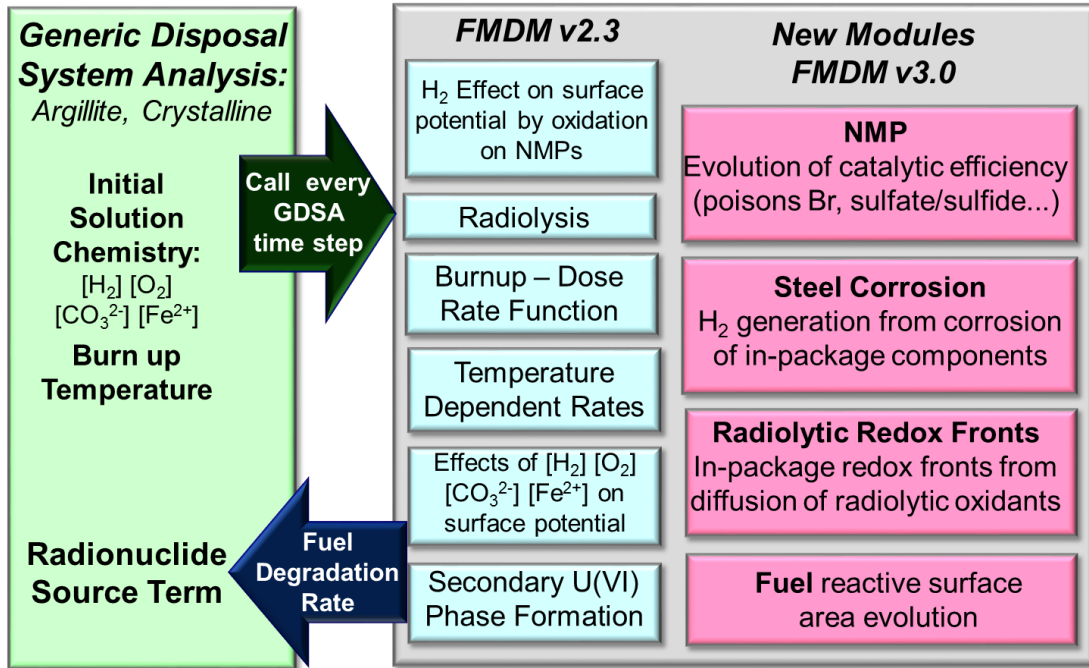


Figure 9. Conceptual summary of the flow of information between the GDSA PA model and the FMDM. Processes currently in the FMDM (v2.3) are shown in blue, while new processes that need to be added to bring the FMDM up to date with current scientific findings are shown in pink.

3 Scoping Work for the Development of a Canister Corrosion Model

The quantification of the long-term corrosion behavior of steels in relevant environmental conditions is central to developing a science-based performance assessment for nuclear waste repositories. The mixed potential theory on which the FMDM is based is ideal for quantifying steel corrosion because it accounts for the fundamental electrochemical mechanisms. Scoping work has thus been initiated to investigate the extension of the FMDM to include the corrosion of a steel surface, which would be located at some distance x from the fuel/NMP surface in the one dimensional FMDM reaction/diffusion domain. That is, the steel corrosion model will have a one-dimensional reaction diffusion layout continuous with the existing FMDM.

As with the FMDM, the steel corrosion model will use mixed potential theory to determine the corrosion rate based on the kinetic balance of all relevant interfacial redox reactions. Homogeneous reactions and diffusion processes that determine the supply of reactants to the steel surface and alteration phase saturation indexes will be taken into account. There are several advantages to this approach of incorporating a steel corrosion model into the FMDM:

- It directly couples fuel degradation and steel corrosion. This is vital, as it has been shown that, even at sub millimolar concentrations, the H_2 produced from the anoxic corrosion of steel can decrease the fuel dissolution rate by over four orders of magnitude (Jerden et al., 2015).
- By directly coupling the fuel and steel degradation, this approach also allows for the quantification of redox fronts that develop within the waste container due to the diffusion of radiolytic oxidants away from the fuel surface and the reactions of these oxidants with the steel surface and the resulting aqueous Fe^{2+} and H_2 . This is also important because these redox fronts represent the Eh of the in package solutions in contact with the waste form and waste container internal components.
- This approach will allow the steel corrosion module to be readily implemented into the GDSA PA PFLOTRAN model, as it will be incorporated into the FMDM, a version of which has already been integrated with PA (see Section 2.3 above).

The original MPM developed as part of the Canadian repository program, on which the FMDM is based, contained a corroding steel surface (see King and Kolar, 2003). In fact, the earliest version of the FMDM included this corroding steel module, but it was removed so that the modeling efforts could focus on quantifying and optimizing the NMP catalyzed H_2 reactions at the fuel surface. By adding the full steel corrosion module, the extended FMDM could be used to quantify a number of processes that are essential for calculating both container life times and the kinetic interdependencies of fuel and steel corrosion. Specifically, the steel module of the envisioned extended FMDM (version 3.0) would quantify the following processes:

- Selection of passive or active corrosion mechanisms depending on the calculated corrosion potential.
- The generation of H_2 during anoxic corrosion, which has been shown to inhibit the dissolution of used fuel and can lead to alloy embrittlement.
- Production of radiolytic oxidants, which can determine whether a type of steel corrodes by aerobic or anaerobic processes.
- Interactions with porewaters to form iron silicate colloids and surface coatings such as Fe-saponite.
- Sorption of radionuclides to colloidal and fixed steel corrosion products. The model layout and context are shown in the figures at the end of this document.

The conceptual layout of the extended FMDM v3.0 is shown in Figure 10. The inputs from the PFLOTRAN PA model would be the same as those discussed in Section 2.0 above. However, the calculated steel dissolution rate (mass per area per time) would be added as an output to PFLOTRAN.

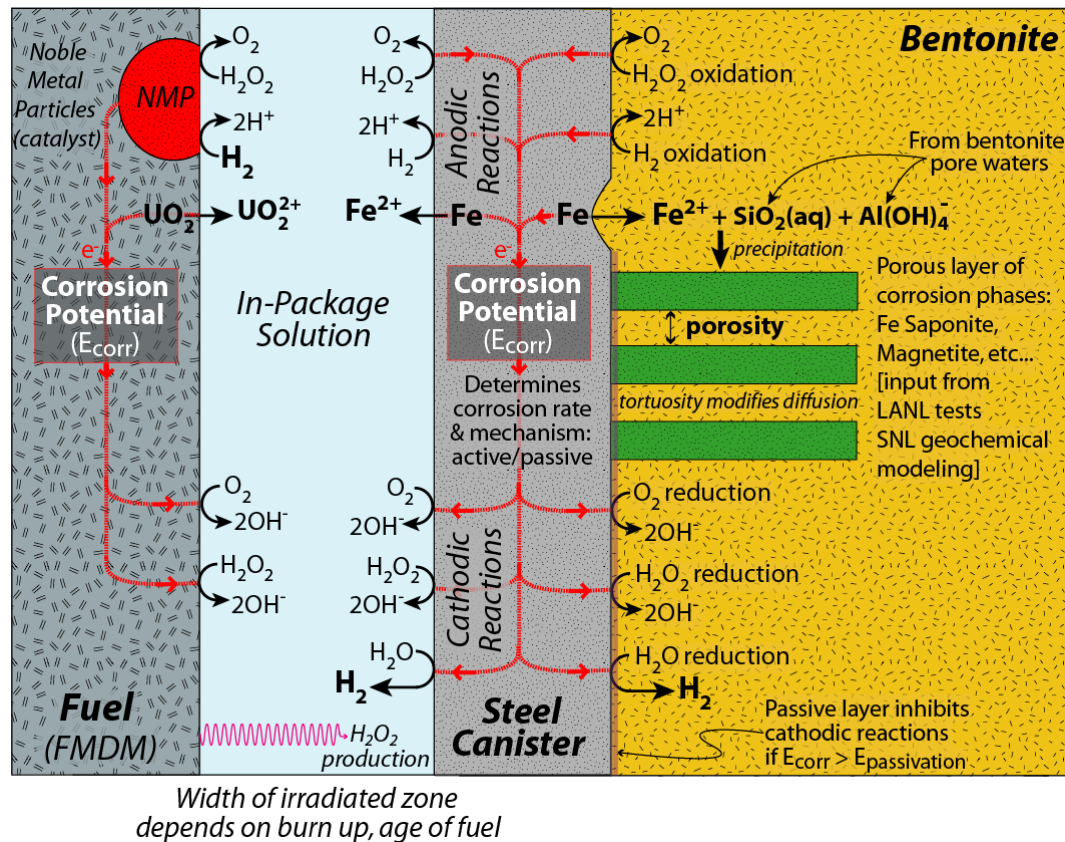


Figure 10. Conceptual layout for the extended FMDM version 3.0 that includes a module quantifying steel corrosion (only key interfacial reactions are shown).

As part of this scoping study the older version of the FMDM that contained the steel corrosion module was run for a number of cases to further investigate how the fuel and steel corrosion reactions would influence each other in the context of the model. Example results from these scoping runs are shown in Figure 11. The examples show how the diffusion of H_2O_2 away from the alpha radiation zone would set up redox fronts within the solution separating the corroding

surfaces (Figure 11, top plot). Figure 11 also shows how the concentration profile for H_2 is predicted to evolve (Figure 11, bottom plot). The time labels for the profiles in Figure 11 are generic because this model is not fully developed and does not include some processes that will affect diffusion rates (e.g., porosity and tortuosity of corrosion layers). That is, the overall shape of the concentration profiles are believed to be accurate, but the absolute time evolution may not be. The overall shape of the concentration profiles, and how they change with time is instructive for understanding the inter-dependencies of the two corrosion processes.

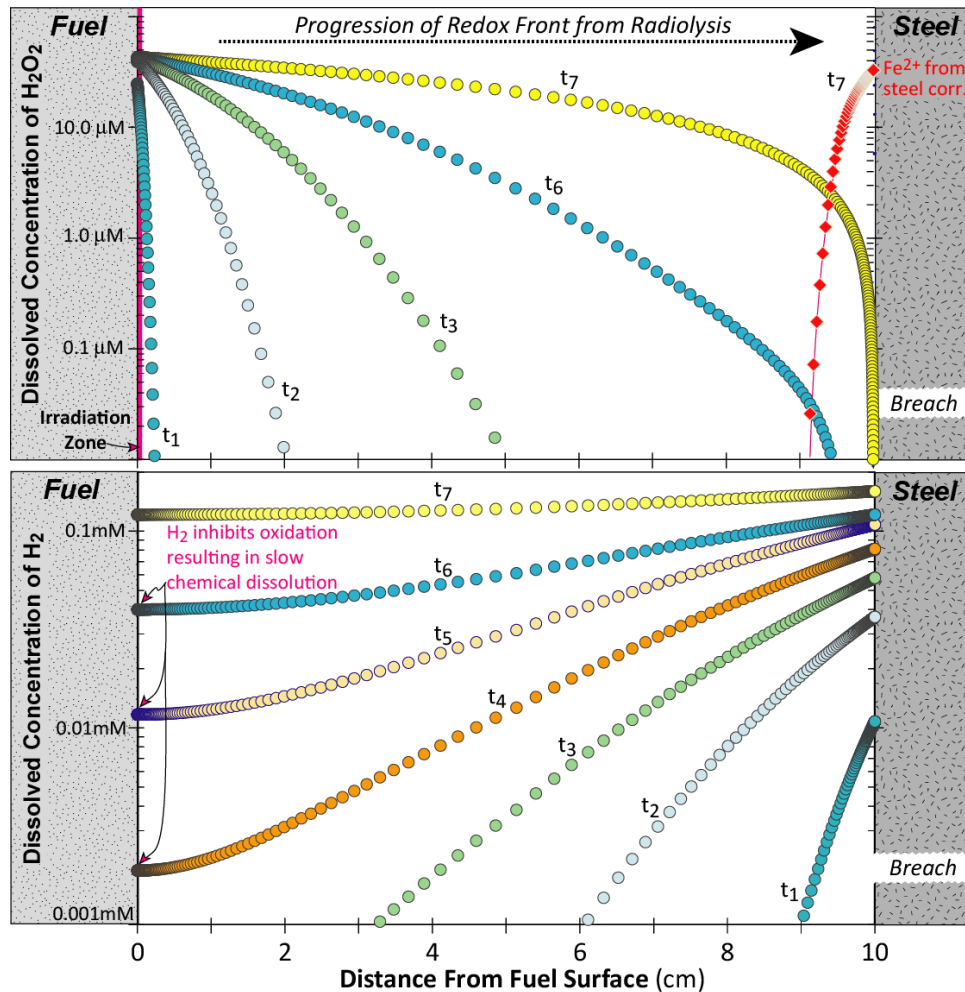


Figure 11. Results from an older version of the FMDM that included a corroding steel surface. The top plot shows how H_2O_2 diffusion away from the irradiation zone can set up redox fronts that evolve through time within the in-package solution. The bottom plot shows H_2 concentration profiles with time. Time labels are generic because this model does not include variables known to influence diffusion rates (porosity and tortuosity of corrosion layers). The overall shape of the concentration profiles are accurate, but the absolute time evolution is uncertain.

4 Results from Scoping Experiments on Poisoning of Noble Metal Particle

In order to ensure that the process models for used fuel degradation and steel corrosion (sections 2.0 and 3.0 above) accurately represent reality within the relevant ranges of repository conditions, the model development efforts need to be coupled with a focused experimental program to quantify key parameters and provide data sets for validation. To this end, the radiological electrochemical testing facilities at Argonne are being used to investigate the interfacial and homogeneous reactions that dominate used fuel degradation.

As shown in Jerden et al., 2015, the catalysis of H₂ oxidation on the NMPs drives the used fuel dissolution rate down by as much as four orders of magnitude when dissolved H₂ concentrations reach approximately 0.1 mM. Because this NMP – H₂ catalysis process plays such a key role in determining the used fuel dissolution rates and its mechanism is not yet fully understood, it is the subject of on-going electrochemical experiments designed to directly inform the process modeling efforts (i.e., the extension of the FMDM to version 3.0).

The experimental set up consists of a 20 mL, three-electrode cell in which the experimental cover gas is continuously bubbled during the experiments (Figure 12). Multiple cells (experiments) are run simultaneously within an oven in a radiological laboratory. Multiple power supplies and potentiostats are available so that tests with two or more working electrodes (e.g., NMP and UO₂) can also be performed. The electrodes are characterized pre- and post-experiment by optical and Scanning Electron Microscopy (SEM). The solutions from selected tests are analyzed for electrode constituents (Ru, Mo, Pd, Rh, Tc, U, and other dopants such as REE) by inductively coupled plasma mass spectrometry (ICP-MS).

Figure 12. Photograph and schematic diagram of the type of cell used for the electrochemical experiments.

The scoping tests performed in FY 2015 focused on the H₂ reactions with a NMP electrode. The electrode was made in house (Argonne) from an alloy produced by Steve Frank at Idaho National Laboratory that closely matches the composition and homogeneity (single alloy phase) of the NMP found in used fuel. The NMP alloy used to make the electrode has a composition of Ru₅₆Mo₂₀Rh₁₁Pd₁₁Tc₂ and, based on SEM characterization, appears to be composed of a single phase with perhaps some minor amounts of TcO₂.

One of the most important experimental observations made regarding the role of H₂ in used fuel dissolution is that the presence of halides, particularly Br⁻, seems to counteract the H₂ effect (Metz et al., 2008). Although poorly understood, our new results (Figure 13) suggest that the NMP surface may be poisoned by halides thus reducing their catalytic efficiency (i.e., counteracting the protective H₂ effect). The poisoning and alteration of the NMP surfaces are not currently accounted for in the FMDM, because these processes are not well understood or quantified. However, due to the importance of the H₂ effect these processes are deemed high priorities for experimental investigations.

To investigate the reaction of H₂ on the NMP electrode scoping tests were performed in which the open circuit potential of the NMP electrode was measured for up to 80 hours in approximately 1 mM NaCl while cover gases of either air, Ar or 2% H₂ in Ar were bubbled through the solution. The possible poisoning effect of Br⁻ was also investigated by performing the 2% H₂ cover gas tests in solutions containing 1 mM NaBr. The pH for all tests remained relatively constant at around 7.0. Typical examples of the results are shown in Figure 13.

The results show a pronounced H₂ effect that causes a decrease in the potential of the NMP electrode from greater than 260 mV (vs. SHE) for the air cover gas tests down to less than 100 mV for tests performed with 2% H₂ in Ar as the cover gas. The observation that this large potential drop is not seen when the test is performed in pure Ar indicates that it is due to the H₂ oxidation on the NMP electrode. This shows that, under near neutral conditions, the NMP surface is hosting anodic reactions that can be generalized as:



As indicated by the green curve in Figure 13, the presence of 1 mM Br⁻ partially counteracts the H₂ effect, shifting the NMP surface potential up by approximately 60 mV. This shows that even over short time frames (minutes) the presence of Br⁻ has an effect on the NMP – H₂ reaction. This is a significant observation as it identifies a key chemical process that is not currently accounted for in the FMDM.

The implication is that, if repository ground waters contain sufficient Br⁻, the H₂ effect, which “protects” the used fuel from dissolution, will be counteracted due to the degradation of NMP catalytic efficiency. This implication was quantified by running the FMDM for a series of case in which the NMP catalytic efficiency was decremented (Figure 14). The results highlight the importance of understanding poisoning or fouling processes that could counteract the NMP catalyzed H₂ effect. More experimental work is needed to quantify these key processes.

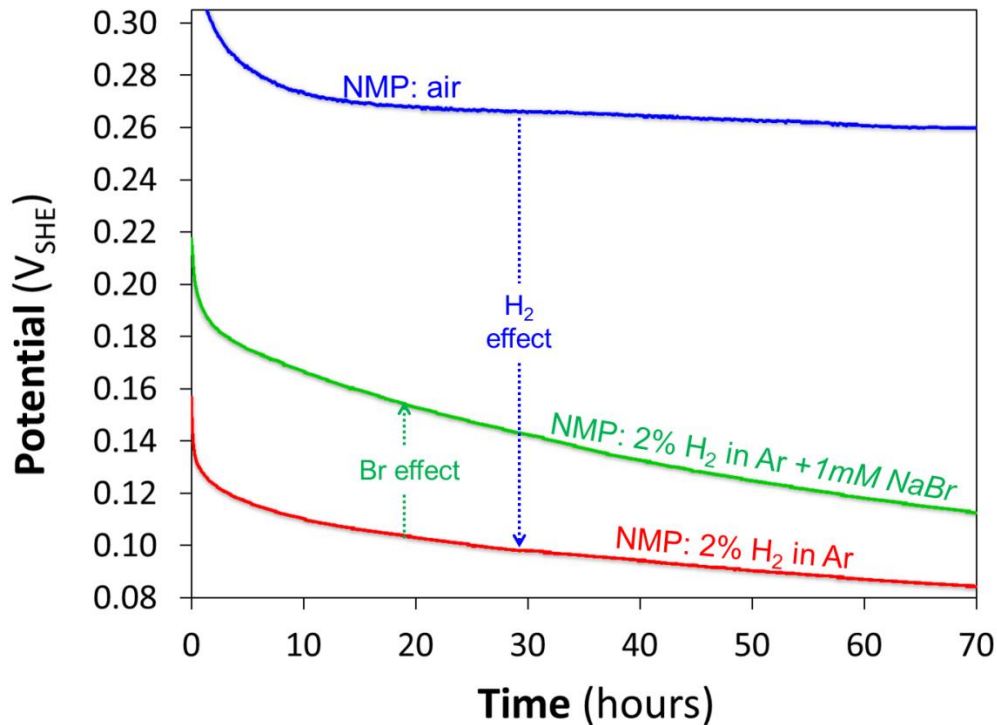


Figure 13. Results from scoping electrochemical tests showing the open circuit potential of the $\text{Ru}_{56}\text{Mo}_{20}\text{Rh}_{11}\text{Pd}_{11}\text{Tc}_2$ (NMP) electrode for three different tests. Note that the presence of Br^- partially counteracts the H_2 effect.

It is important to note that even after 70 hours, the open circuit potentials for the NMP have not reached a constant (steady state) value. This indicates that the surface of the electrode may need to be pre-conditioned in the solutions of interest for extended periods of time to achieve steady state with respect to all redox reactions. Future work will involve the thorough surface characterization of the NMP electrode by SEM before and after the experiments to identify any alteration or pitting that may affect the surface reactions.

Future work will also involve a series of electrochemical tests with simulated used fuel that consists of electrically coupled NMP in a UO_2 matrix. These tests will be used to generate a validation data set for the FMDM.

As mentioned above, to quantify the possible poisoning effect of the catalytic NMPs several sensitivity runs were performed with the FMDM v2.3 in which the poisoning process was simulated by decreasing the active NMP surface coverage while the H_2 concentration, burnup and temperature were held constant from run to run (Figure 14). For these sensitivity runs the fuel burnup was 60 GWd/MTU, the age of the fuel was assumed to be 30 years (out of reactor) and the temperature was held constant at 25°C.

The results show that for a solution containing 1 mM dissolved H_2 , the presence of 1% surface coverage of NMP leads a greater than 5 orders of magnitude decrease in the dissolution rate relative to the no NMP case. This H_2 effect is counteracted by decreasing the active surface area of the NMP. For example, decreasing the NMP surface coverage from 1% to 0.1% causes a

factor of 50 increase in the predicted dissolution rate, while a decrease to 0.01% results in a dissolution rate increase of around 5 orders of magnitude. These FMDM sensitivity runs are quite preliminary as the mechanism and magnitude of the NMP poisoning process is not yet understood. These results do however underscore the need for continued experimental work to quantify processes that may have a significant effect (orders of magnitude) on the fuel degradation rate and thus radionuclide source term in the PA calculations.

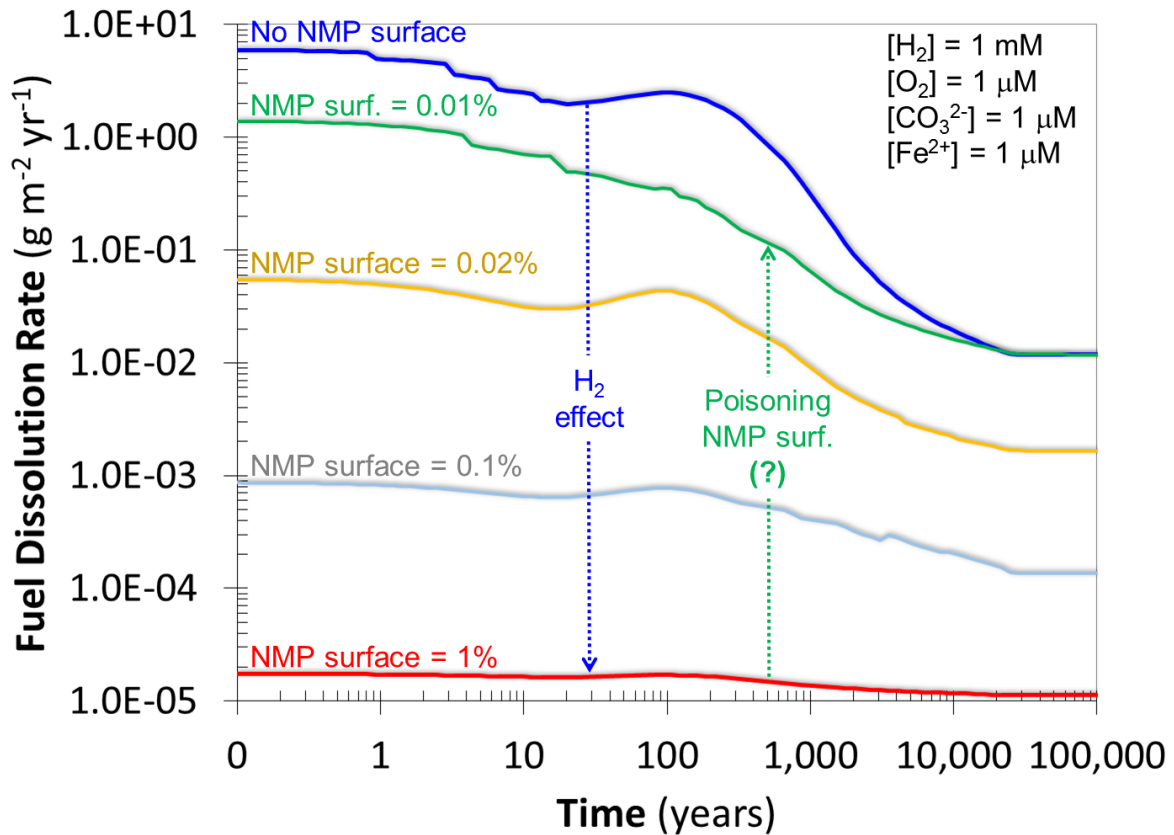


Figure 14. Results from the FMDM v2.3 showing the dramatic decrease in fuel dissolution rate caused by the oxidation of H₂ on the NMP and the possible effect of poisoning of the NMP surface (blocking the H₂ oxidation reaction). For these sensitivity runs the fuel burnup was 60 GWd/MTU, the age of the fuel was assumed to be 30 years (out of reactor) and the temperature was held constant at 25°C. The possible poisoning of the NMP surface was accounted for by decreasing the active surface area of the NMP.

5 Conclusions and Future Work

The main accomplishments for Argonne's FY2015 work on the Fuel Matrix Degradation Model (FMDM) development project are as follows:

- Completed a model validation study in which results from the state of the art FMDM were compared to experimental data from international geologic repository programs. This study was published in the Journal of Nuclear Materials: "A Multiphase Interfacial Model for the Dissolution of Spent Nuclear Fuel" by J. Jerden, K. Frey and W. Ebert, Volume 462, July 2015, Pages 135-146.
- Completed conversion of the state of the art FMDM (version 2.3) to Fortran to facilitate integration with the Generic Disposal System Analysis (GDSA) repository Performance Assessment (PA) code PFLOTRAN.
- Worked with SNL scientists to complete and test a prototype integrated PFLOTRAN-FMDM repository model.
- Completed preliminary model runs focused on expanding the FMDM to account for corrosion of the used fuel steel canister.
- Completed scoping experiments investigating the possible poisoning of the Noble Metal Particles (NMP), which are known to catalyze the oxidation of H₂, thus shutting down the oxidative dissolution of used fuel.

The current version of the FMDM has proven effective for quantifying key processes affecting the rate of used fuel degradation; however, the implementation of FMDM within a performance assessment model requires further model development to account for steel corrosion and the possible poisoning of the NMP phase, which is responsible for the protective H₂ effect. Focused experiments are also needed quantify key parameter values and provide data sets for model validation. In order to take advantage of the work that has been done so far on the FMDM, a number of needs have been identified:

- Take next step in integration of FMDM with PFLOTRAN: demonstrate sensitivity of the Argillite PA model to key variables in the FMDM such as burnup, surface area and the dissolved concentrations of H₂, O₂, carbonate and ferrous iron.
- Extend the FMDM to account for the corrosion of the steel waste canister. This will quantify feedbacks between H₂ production at the corroding steel surface and the dissolution rate of the used fuel.
- Perform focused electrochemical experiments to determine the effect of halides and other possible poisons on the catalytic efficiency of the NMP. These tests will quantify processes that may counteract the protective H₂ effect.

Several specific priorities that have come out of the FMDM – PFLOTRAN integration work are as follows:

- Increase flexibility of coupling
- Ability to customize FMDM discretization from PFLOTRAN side
- Incorporate transient surface area
- Update to FMDM v3.0
- Optimized FMDM serial performance
- Integration into simulation of a repository with many waste packages
- Add increasingly mechanistic geochemistry

6 References

- Buck E., Jerden, J., Ebert, W., Wittman, R., 2013, Coupling the Mixed Potential and Radiolysis Models for Used Fuel Degradation, FCRD-UFD-2013-000290.
- Hammond G., 2015, Generic Disposal System Analysis (GDSA): Coupling of PFLOTRAN to the Fuel Matrix Degradation Model (FMDM), Slide Presentation, Used Fuel Disposition Campaign Annual Working Group Meeting, Las Vegas, NV, June 9-11, 2015
- Jerden J. Copple J., Frey K. Ebert W., 2014, Prototype Fortran Version of the Mixed Potential Process Model for Used Fuel Degradation, Used Fuel Disposition Campaign Milestone: M4FT-15AN0806012, October 15, 2014
- Jerden J. Frey K. Ebert W., 2015, A Multiphase Interfacial Model for the Dissolution of Spent Nuclear Fuel, *Journal of Nuclear Materials*, 462, 135–146
- King F. and Kolar M., 2003, The Mixed-Potential Model for UO_2 Dissolution MPM Versions V1.3 and V1.4., Ontario Hydro, Nuclear Waste Management Division Report No. 06819-REP-01200-10104 R00.
- Metz V., Loida A., Bohnert E., Schild D., Dardenne K., 2008, Effects of Hydrogen and Bromide on the Corrosion of Spent Nuclear Fuel and γ -irradiated $\text{UO}_2(\text{s})$ in NaCl Brine, *Radiochim. Acta* 96, 637–648
- Radulescu, G., 2011, Repository Science/Criticality Analysis, Oak Ridge National Laboratory, Reactor and Nuclear Systems Division, FTOR11UF0334, ORNL/LTR-2011, Oak Ridge National Laboratory, Oak Ridge, TN.
- Röllin S., Spahiu K., Eklunda U., 2001, Determination of Dissolution Rates of Spent Fuel in Carbonate Solutions Under Different Redox Conditions with a Flow-through Experiment, *Journal of Nuclear Materials*, 297, 231–243
- Wang Y. et al., 2014, Used Fuel Disposal in Crystalline Rocks: Status and FY14 Progress, FCRD-UFD-2014-000060, SAND2014, Sandia National Laboratories, Albuquerque, NM.

